

December 2016

# Experimental Methods in Cryogenic Spectroscopy: Stark Effect Measurements in Substituted Myoglobin

Bradley Michael Moran  
*University of Wisconsin-Milwaukee*

Follow this and additional works at: <https://dc.uwm.edu/etd>

 Part of the [Chemistry Commons](#), [Engineering Commons](#), and the [Physics Commons](#)

---

## Recommended Citation

Moran, Bradley Michael, "Experimental Methods in Cryogenic Spectroscopy: Stark Effect Measurements in Substituted Myoglobin" (2016). *Theses and Dissertations*. 1392.  
<https://dc.uwm.edu/etd/1392>

This Dissertation is brought to you for free and open access by UWM Digital Commons. It has been accepted for inclusion in Theses and Dissertations by an authorized administrator of UWM Digital Commons. For more information, please contact [open-access@uwm.edu](mailto:open-access@uwm.edu).

EXPERIMENTAL METHODS IN CRYOGENIC SPECTROSCOPY:  
STARK EFFECT MEASUREMENTS IN SUBSTITUTED MYOGLOBIN

by

Bradley M. Moran

A Dissertation Submitted in  
Partial Fulfillment of the  
Requirements for the Degree of

Doctor of Philosophy

in Chemistry

at

The University of Wisconsin-Milwaukee

December 2016

EXPERIMENTAL METHODS IN CRYOGENIC SPECTROSCOPY:  
STARK EFFECT MEASUREMENTS IN SUBSTITUTED MYOGLOBIN

by

Bradley M. Moran

The University of Wisconsin-Milwaukee, 2016  
Under the Supervision of Professor Peter Geissinger and Professor Jörg C. Woehl

Dawning from well-defined tertiary structure, the active regions of proteins exist as specifically tailored electrostatic microenvironments capable of facilitating chemical interaction. The specific influence these charge distributions have on ligand binding dynamics, and their impact on specificity, reactivity, and biological functionality, have yet to be fully understood. A quantitative determination of these intrinsic fields would offer insight towards the mechanistic aspects of protein functionality. This work seeks to investigate the internal molecular electric fields that are present at the oxygen binding site of myoglobin.

Experiments are performed at 1 K on samples located within a glassy matrix, using the high-resolution technique spectral hole-burning. The internal electric field distributions can be explored by implementing a unique mathematical treatment for analyzing the effect that externally applied electric fields have on the spectral hole profiles. Precise control of the light field, the temperature, and the externally applied electric field at the site of the sample is crucial.

Experimentally, the functionality of custom cryogenic temperature confocal scanning microscope was extended to allow for collection of imaging and spectral data with the ability to modulate the polarization of the light at the sample. Operation of the instrumentation was integrated into a platform allowing for seamless execution of input commands with high temporal inter-instrument resolution for collection of data streams. For the regulated control and cycling of the sample temperature, the thermal characteristics of the research Dewar were theoretically modeled to systematically predict heat flows throughout the system. A high voltage feedthrough for delivering voltages of up to 5000 V to the sample as positioned within the Dewar was developed. The burning of spectral holes with this particular experimental setup is highly repeatable.

The quantum mechanical treatment that is employed during analysis of the experimental data requires the state energies and the transition dipole moments of the porphyrin probe. The configuration interaction, as well as the coupled-cluster approaches, have been investigated for their ability to produce realistic valuations for these calculated quantities as gauged by their ability to accurately reproduce valuations for spectroscopically observable transition energies. A capacitive cell, for the determination of a material's dielectric permittivity, necessary for defining the magnitude of the externally applied electric field at the sample, was developed and shown to successfully yield permittivity valuations for various media in accordance with those reported the literature, while offering the ability to provide measures for permittivities over the temperature range of 1-300 K.

© Copyright by Bradley M. Moran, 2016  
All Rights Reserved

# TABLE OF CONTENTS

**List of Figures**.....xi

**List of Tables**.....xxvii

**List of Symbols**.....xxix

**List of Abbreviations**.....xxxvii

## Book 1 Experimental Foundations

### **1 System and Method of Study**

1.1 Introduction.....1

1.2 Structure Leading Function.....2

1.3 Myoglobin.....3

1.4 Porphyrin.....7

1.5 Chromophores Within Host Matrices.....14

1.6 Spectral Hole-Burning.....20

References.....30

### **2 Mathematical Treatments for the Effect of Electric Fields Applied to Spectral Holes**

2.1 Introduction.....35

2.2 Classical Approach.....36

2.3 Molecular Resolution Approach.....42

2.4 Angular Dependencies of Hole-burning and Stark Profiles.....47

2.5 The Molecular Resolution Modeling Process.....53

References.....60

## Book 2 Experimental Control

### Light

#### **3 Developing Temperature Cycling and Spectral Acquisition Software Platforms**

3.1 Introduction.....	62
3.2 Functional Requirements.....	63
3.3 Software Development.....	63
3.3.1 Spectroscopy.....	65
3.3.2 Hole-Burning.....	68
3.3.3 Temperature Cycling.....	70
3.3.4 Signal Smoothing.....	71

#### **4 Extending Functionality of the Cryogenic Temperature Confocal Scanning Microscope**

4.1 Introduction.....	74
4.2 Microscopy.....	75
4.2.1 Wide-Field Microscopy.....	77
4.2.2 Confocal Microscopy.....	78
4.2.3 Optical Limitations.....	81
4.3 CTCSM.....	85
4.3.1 Illumination.....	87
4.3.2 Construction and Modifications.....	87
4.4 Image Collection.....	95
4.4.1 Calibration Grids.....	95
4.4.2 Fluorescent Microspheres.....	98
4.5 Spectral Collection.....	101
4.6 Image and Spectral collection.....	104

4.7 Outlook.....	106
References.....	108

## **5 Optimizing Signal Collection: Rates, Optics, and Hardware**

5.1 Introduction.....	110
5.2 Scan and Collection Rates.....	112
5.3 Spectral Shape and Filter Studies.....	114
5.4 Final Optical Pathway.....	123
5.5 Hardware Methods.....	126

## Temperature

## **6 Modeling Cryogenic Heat Transfer for Predictive Thermal Regulation**

6.1 Introduction.....	130
6.2 Heat.....	131
6.3 Heat Transfer Mechanisms.....	133
6.3.1 Conduction.....	134
6.3.2 Convection.....	135
6.3.3 Radiation.....	138
6.4 Dimensionless Quantities.....	140
6.4.1 Prandtl Number (Pr).....	141
6.4.2 Reynolds Number (Re).....	142
6.4.3 Rayleigh Number (Ra).....	143
6.4.4 Nusselt Number (Nu <sub>L</sub> ).....	143
6.4.5 Biot Number (Bi).....	144
6.4.6 Fourier Number (Fo).....	145
6.5 Steady State and Transient Heat Transfer.....	145



6.6	Lumped capacitance.....	149
6.7	Extended Dimensions and Geometries.....	151
6.8	Thermal Resistance Networks.....	153
6.9	The Modeled System.....	156
6.9.1	Temperature Cycling.....	157
6.9.2	Resistive Networks.....	160
6.9.3	Thermal Conductivities.....	164
6.9.4	Heat Transfer Coefficients.....	169
6.9.5	Steady State Solutions.....	174
6.9.6	Transient Approximation: Lumped Capacitance.....	177
6.9.7	Heater Ramp.....	180
6.9.8	Sample Lag.....	182
6.9.9	PID Parameters.....	183
6.10	Future.....	184
	References.....	186

## Electric Field

### **7 Engineering a Solution for the Application of High Voltage Electric Fields: Sample Cells, Feedthroughs, Spectral Holes**

7.1	Introduction.....	187
7.2	Sample Cell Design.....	188
7.3	High Voltage.....	191
7.4	Spectral Hole-Burning.....	193
7.5	Problems with High Voltage Field.....	198
7.5.1	Cabling.....	199
7.5.2	Sample Electrode Contact.....	200
7.6	New Sample Cell.....	203
7.7	Glass Cryostat.....	208

7.8 New High Voltage Feedthrough.....	215
7.9 Split Hole Profiles.....	217
References.....	222

## Book 3 Experimental Refinement

### **8 A Capacitive Cell for the Assessment of Dielectric Permittivity**

8.1 Introduction.....	223
8.2 Capacitors.....	224
8.3 Dielectrics in Capacitors.....	226
8.3.1 Dielectrics and Hole-Burning.....	228
8.4 Design of Capacitance Cell.....	231
8.5 Measurement Methods.....	240
8.5.1 DC Approach-RC Time Constant.....	241
8.5.2 AC Approach-Capacitive Reactance.....	253
8.5.3 Comparison of Methods.....	262
8.6 Calibration of Measurement.....	264
8.7 Sample of Interest 3:1 Glycerol:Water.....	275
8.7.1 Temperature Dependence.....	276
8.7.2 Frequency Dependence.....	279
8.7.3 Experimental Permittivity.....	283
8.8 Moving Forward.....	285
References.....	290

### **9 Transition Moments and Energies of Free Base Porphyrin**

#### **Possessing In-Protein Structural Characteristics**

9.1 Introduction.....	293
9.2 The Molecular Geometry of Porphyrin.....	294
9.2.1 The In-Protein Structural Characteristics of Porphyrin.....	296

9.2.2 Selection of an Appropriate Candidate.....	300
9.3 Electronic Structure Theory.....	305
9.4 Configuration Interaction Approaches.....	312
9.4.1 Configuration Interaction Singles.....	314
9.4.2 Configuration Interaction Singles Doubles.....	322
9.4.3 Configuration Interaction Singles Doubles Triples.....	327
9.4.4 Configuration Interaction Singles Doubles Triples Quadruples .....	329
9.5 Coupled-cluster Approaches.....	331
9.5.1 EOM-CCSD(T) and Variants.....	336
9.6 Comparison of Methods.....	344
9.7 Next Steps.....	348
References.....	351
<b>10 Concluding Remarks.....</b>	<b>356</b>

## Appendices

<b>Appendix A: Substitution Process and Temperature Dependence of Qx Transition.....</b>	<b>360</b>
<b>Appendix B: Programmatic Hierarchy for Molecular Resolution Approach...</b>	<b>363</b>
<b>Appendix C: Block Diagrams for Developed Programs.....</b>	<b>365</b>
<b>Appendix D: CTCSM Microscope Head and Component List .....</b>	<b>374</b>
<b>Appendix E: Thermal Modulation Parameters for the Heater Ramp and Temperature Specific PID Settings.....</b>	<b>377</b>
<b>Appendix F: Split Hole Profile.....</b>	<b>381</b>
<b>Appendix G: Computational Studies: Molecular geometries and Method Dependent Qx, Qy, Bx, and By Transition Energies.....</b>	<b>382</b>
<b>Curriculum Vitae.....</b>	<b>400</b>

# LIST OF FIGURES

**Figure 1.1:** Top Left: PPIX (yellow) in myoglobin, with eleven closest residues (green) to oxygen binding center displayed along with van der Waals surfaces. Top Right: PPIX including side groups. Methyl, vinyl and propionic groups outside of red box, are viewed as part of the protein environment for the electronic structure calculations of this particular investigation. Bottom: Distances (Å) of green residue from heme center in table. Image created with SwissPDB. ....5

**Figure 1.2:** Porphine dianion. Protonation of the central nitrogens yields porphine, representative of the parent core that is common to all porphyrin derivatives. Inner 16-membered ring is displayed in red. Peripheral substituents can be added at positions one through twelve. ....8

**Figure 1.3:** Left: Schematic diagram of orbitals and transitions creating the Q and B-bands according to the “four-orbital model” of Gouterman using  $D_{4h}$  symmetry [14]. Using  $D_{2h}$  symmetry, both Gouterman and Hashimoto assign the same irreducible representations. Center: Orbitals and transitions creating the Q and B-bands according to Hashimoto [19], energy levels are spaced for clarity of description. Bottom Left: Transitions responsible for visible transitions (By, Bx, Qy, Qx) of porphyrin [19]. Right: Image of the four orbitals of importance. PPIX hydrogens are oriented along the x-axis, with axis shown. These orbitals were calculated with the GAMESS platform and displayed via MacMolPlt using PPIX with molecular coordinates taken from 1DWT [4, 7, 51]. ....11

**Figure 1.4:** Absorbance spectrum of  $3.99 \times 10^{-5}$  M PPIX in 3:1 glycerol:water acquired using a Perkin Elmer Lambda 650 UV/VIS Spectrometer. Due to its much greater oscillator strength, the Soret band ( $S_0 \rightarrow S_2$ ) is the favored transition and has a significantly larger optical density than the Q-band ( $S_0 \rightarrow S_1$ ) transitions. The Soret band at  $\lambda_{max} \approx 430$  nm is not displayed for enhanced clarity of the Q-band peaks. This experimental investigation involves spectroscopic studies utilizing only the lowest lying energy transition, namely the  $Q_x$  0-0 transition, as highlighted above. ....14

**Figure 1.5:** Upper Right: Representative depiction of a perfect crystalline medium where all embedded chromophores possess the same molecular orientation and reside in identical energetically equivalent local environments resulting in precise spectral overlap across the entire population of chromophores. Bottom Left: Expected line-shape of electronic transition in perfect crystalline medium at liquid helium temperatures. The width of the ZPL defines the homogeneous line-width,  $\Gamma_H$ , is accompanied by the broad phonon sideband. The Debye-Waller factor  $\alpha(T)$ , describes the distribution of integrated intensity between the ZPL and phonon sideband which represents the total oscillator strength of the transition. ....16

**Figure 1.6:** Upper Right: Representative depiction of an amorphous medium where all embedded chromophores possess randomized molecular orientations and reside in energetically inequivalent local environments resulting in a distribution of ZPL center frequencies defining the electronic transition, across the entire population of chromophores. Bottom Left: Expected line-shape of an electronic transition of chromophores in an amorphous medium. The inhomogeneously broadened band follows a Gaussian distribution, has a line-width  $\Gamma_I$ , and is a superposition of the homogeneous line-widths of the individual color centers. Even at liquid helium temperatures,  $\Gamma_I > 10^5 \Gamma_H$ . Forty homogeneous line-shape functions  $F_H(\nu, T)$  with a Debye-Waller factor of  $\alpha=0.8$  are shown, of which represent only a subset of those that constitute the entire inhomogeneously broadened band. ....19

**Figure 1.7:** Depiction of a spectral hole burnt into the inhomogeneously broadened band made up of the homogeneous linewidths of the entire population of absorbing molecules. The appearance of the photoproduct within the inhomogeneously broadened band reflects the outcome for the particular photochemical process for this experiment, namely the tautomerization of the two protons on the inside of the porphyrin ring. For other systems, the photoproduct may appear outside of the inhomogeneous distribution. The pre-burn distribution appears in blue with the post-burn profile appearing in orange. ....23

**Figure 1.8:** Integration of the forty homogeneous line-shape functions displayed in figure 1.6. At higher frequencies, because of their additive nature, the phonon sidebands begin to overwhelm the total contribution to the inhomogeneous band profile in relation to the contribution from the ZPL's. Therefore, spectral holes should be burnt into the low energy side of the band, which is composed of predominantly the ZPL portion of the homogeneous line functions, allowing for the narrowest holes that approach the  $2\Gamma_H$  limit to be obtained. ....27

**Figure 2.1:** Vector representation of the important geometric relationships between the electric field, the source light and the chromophore. Displayed are the applied electric field  $\vec{E}$ , the polarization of the excitation and burning light  $\vec{E}_{hv}$ , and the molecular transition dipole moment  $\vec{\mu}_{mn}$ . The copper electrodes apply the external electric field along the z-axis. The light field interacting with the sample travels along the y-axis with polarization vector represented by  $\vec{E}_{hv}$ . The transition dipole moment  $\vec{\mu}_{mn}$  between the ground and first excited state of porphyrin describing the Qx transition, is the band into which spectral holes are burnt. The matrices depicted above describe the vector components of  $\vec{E}_{hv}$  and  $\vec{\mu}_{mn}$  in terms of the established angles. When used in tandem with the specified equations defining a molecule's contribution to hole shape, the interaction of these vectors quantities for each individual chromophore dictate the weight with which that particular chromophore contributes to the resultant shape of the spectral hole during the orientational averaging process. ....49

**Figure 2.2:** The effect of an externally applied electric field on a spectral hole. These hole profiles are simulated and represent the effect that increasing electric field strength,  $\vec{E}_0 < \vec{E}_1 < \vec{E}_2$ , has on hole profiles when applied both perpendicular and parallel to the polarization of the light used in the burning process. Left: When the applied electric field is perpendicular to the polarization of burning light, and consequently, perpendicular to the transition dipole moments of the population of chromophore molecules responsible for the spectral hole, the spectral hole undergoes broadening. Right: When the applied electric field is parallel to the polarization of burning light, and the transition dipole moments of the population of chromophore molecules responsible for the spectral hole, a splitting of the spectral hole is observed. ....51

**Figure 3.1:** Schematic depicting experimental setup: The three programs developed are indicated as Software P1, P2 and P3. Solid blue, light green and red lines show which instrumentation is addressed in each program. Solid orange line is the laser beam, solid yellow line is an optical fiber, bold curved black lines are optical fibers, and light curved black lines are electrical connections. ....65

**Figure 3.2:** Figure 3.2: Screenshot of the user interface of program P1 "Spectroscopy". User sets timing of data acquisition, values for photon counter discrimination, and adds comments pertaining to the specific run. Recorded data is exported to spreadsheet. ....66

**Figure 3.3:** Example spreadsheet file with time and date stamp, time, frequency, wavelength, wavenumbers, counts per second, and temperature information, and comments. Spreadsheet output files produced by other developed programs appear similar to above. ....67

**Figure 3.4:** Relationship of laser intensity incident upon sample out of objective at base of CTCSM in relation to laser intensity injected into the CTCSM. Intensity losses are due to optics contained within the CTCSM. ....68

**Figure 3.5:** Screenshot of the user interface of program P2 “Hole-Burning”. The user sets the time step for the data acquisition, and the laser power that was measured at the output end of the optical fiber by use of a power meter. The remaining signal, photons counted, frequency drift during burn, laser power and cumulative energy delivered to sample during the burning process are display. Data is exported to spreadsheet. ....69

**Figure 3.6:** Screenshot of the user interface of program P3 “Temperature Cycling”. User sets timing of data acquisition and PID values. Control of heater range and heater output, used when performing temperature cycling studies, are also controlled here. Again, displayed data is exported to spreadsheet. ....70

**Figure 3.7:** Screenshot of the user interface of the signal smoothing program. User enters the raw data set and selects the box size for the Savitzky-Golay smoothing algorithm. Raw data along with smoothed data and signal to noise characteristics are exported to spreadsheet. ....72

**Figure 4.1:** A: Ray diagram within a conventional microscope from the sample through the objective lens  $L_{obj}$  and ocular lens  $L_{occ}$  to the observer’s eye. The intermediate image appears behind the objective at a distance equal to the back focal length  $f'$  of the objective plus the tube length of the microscope. B: Placement of the tube lens  $L_{tube}$  between the infinity corrected objective and ocular allows for inclusion of additional optical elements without affecting the effective tube length of the microscope. ....76

**Figure 4.2:** Wide-Field microscopy, Left: Signal is collected from all depths within the entire sample simultaneously. The collection of out of focus light information leads to enhanced image blurring. Confocal microscopy, Right: Inclusion of pinhole aperture before detector spatially filters the out-of-focus light. Only the signal light that resides in a conjugate focal plane to the sample under investigation is collected, and the optical resolution of the sample is significantly enhanced. ....79

**Figure 4.3:** Depiction of the raster scanning process. Either the source light or the sample is spatially translated in a pattern of successive rows  $Y$ , of parallel scans  $X$ . At each position within the sample, light information is collected and the image is created. Decreasing the step size in either direction increases the number of pixels in the image. This will create clearer and more detailed appearing images with enhanced contrast and perceived resolution. ....80

**Figure 4.4:** Top: Ray diagram of light emanating from a point source through an objective to the image plane. Because the objective collects only a portion of the spherical wave-front, light rays combine in a constructive and destructive fashion yielding the diffraction limited Airy pattern. Bottom left: Light emitting point source, expanded for clarity. Bottom right: Resulting image of the point source, now convolved with the point spread function of the imaging system. ....83

**Figure 4.5:** The head portion of the CTCSM. Excitation arm (left), Emission arm (top right), Reference arm (bottom right), Axial scaffolding structure (center), Polarization modulator (center above cryostat

flange). Light enters the microscope through the excitation arm and is deflected by a dichroic mirror in the central cage cube down towards the optical insert. The bottom cage cube contains a pellicle beam splitter used for deflection of a portion of the signal returning from the objective for rough focus purposes. The rotatable Glan-Taylor prism sits below the bottom cage cube. A mirror or additional polarization cube is housed in the top cage cube to send the signal light down the emission arm for collection by an optical fiber. A second emission arm can be placed vertically atop the microscope for polarization resolved signal collection. ....93

**Figure 4.6:** Left: The complete CTCSM, microscope head and the optical insert. Samples sit below the objective atop the positioners at the base of the optical insert portion of the CTCSM. Center: Insert tube that houses the optical insert when the microscope is used within the cryostat. Right: Close-up of the sample stage and piezo actuators used for coarse positioning and the raster process. Components as numbered 6. sample stage, 5. PI PT 130.14 piezo tube (raster scan), 4. ANSxy100lr (new raster scan positioner), 3. ANPx101 (X direction), 2. ANPx101 (Y direction), 1. ANPz101 (Z direction). ....94

**Figure 4.7:** CTCSM images of Topometrix, model 10-10299 AFM calibration grid in reflection mode. Dimensions of squares  $5.8 \times 5.8 \mu\text{m}$ , ridges have width of  $3.2 \mu\text{m}$ , and pitch of  $9.0 \mu\text{m}$ . Images taken using 100 mW laser intensity ( $\sim 1 \text{ mW}$  at sample), 514.5 nm, and 60x objective. Top left: image size 512x512 pixels, scan size  $25 \times 25 \mu\text{m}$ , temperature 298 K. Top right: 3D of top left. Bottom left: image size 512x512 pixels, scan size  $10 \times 10 \mu\text{m}$ , temperature 82.5 K. Bottom right: 3D of bottom left. ....96

**Figure 4.8:** CTCSM images of  $1.0 \mu\text{m}$  Yellow-green (505/515) Fluospheres<sup>®</sup> in fluorescent mode. Images taken using 100 mW laser intensity ( $\sim 1 \text{ mW}$  at sample), 514.5 nm, and 60x objective. Filters: excitation hq515/10, dichroic z514, emission hq600. Top left: image size 128x128 pixels, scan size  $20 \times 20 \mu\text{m}$ , temperature 298 K. Top right: 3D of top left. Bottom left: image size 256x256 pixels, scan size  $10 \times 10 \mu\text{m}$ , temperature 81.9 K. Bottom right: 3D of bottom left. ....99

**Figure 4.9:** Room and low temperature fluorescent cross-sections of  $1.0 \mu\text{m}$  Yellow-green (505/515) Fluospheres<sup>®</sup> in fluorescent mode with CTCSM. Left: image sections depicted within plotted cross-sections appearing right. FWHM room temperature  $0.91 \mu\text{m}$ , low temperature  $4.03 \mu\text{m}$ . ....100

**Figure 4.10:** Example fluorescence excitation spectra of  $7.67 \times 10^{-5} \text{ M}$  ZnPPIX in 3:1 glycerol:water acquired in CTCSM at room (top) and liquid helium (bottom) temperatures. Optical table neutral density filters: 0.1%; 1%, Time step/Integration time: 1000 ms, Scan increment: 200 (top) and 20 (bottom), Laser intensity: 100 mW ( $\sim 1 \text{ mW}$  at sample). ....102

**Figure 4.11:** Example fluorescence excitation spectra of  $4.0 \times 10^{-5} \text{ M}$  PPIX –Mb in 3:1 glycerol:water acquired in CTCSM with Optical table neutral density filters: 0.1%; 1%, Time step/Integration time: 1000 ms, Scan increment: 100, Laser intensity: 100 mW ( $\sim 1 \text{ mW}$  at sample). Spectral data are of the same sample at various low temperatures, 225 K (top) and 84 K (bottom). Raw data as well as the Savitzky-Golay fit of the data are displayed. ....103

**Figure 4.12:** CTCSM image of single  $1.0 \mu\text{m}$  Red (580/605) Fluospheres<sup>®</sup> in fluorescent mode. Image taken using 100 mW laser intensity ( $\sim 1 \text{ mW}$  at sample), 580 nm, and 60x objective. Filters: dichroic ZT594rdc, emission ET632/60m. Top left: image size 256x256 pixels, scan size  $20 \times 20 \mu\text{m}$ , temperature 297 K. Top right: 3D of top left. Middle: Fluorescence excitation spectrum of the single fluorescent microsphere pictured in the top row. Spectrum was acquired in CTCSM with optical table neutral density filters: 0.1%; 1%, Time step/Integration time: 1000 ms, other optics as stated. Bottom

Left: image section depicted within plotted cross-section appearing bottom right. FWHM 0.87  $\mu\text{m}$ .  
 .....105

**Figure 5.1:** Left: Fluorescence excitation spectrum of  $7.67 \times 10^{-5}$  M ZnPP in 3:1 glycerol:water acquired in CTCSM at room temperature using filters Dichroic: ZT594rdc and Emission: FF01-731/137-25. Time step/Integration time: 1000 ms, Scan increment: 200. Right: Fluorescence excitation spectrum of  $7.67 \times 10^{-5}$  M ZnPP in 3:1 glycerol:water acquired in Horiba Scientific Fluorolog FL3-22 at room temperature using filters Dichroic: ZT594rdc and Emission: FF01-731/137-25. The FL3-22 fluorescence excitation spectrum was created by integrating the individual fluorescence spectra obtained, with excitation every 5 nm from 570 nm to 605 nm. ....111

**Figure 5.2:** Tradeoffs between altering scan speed of the excitation source and the collection rate of the detected signal. The four extreme cases that could be encountered are represented. ....113

**Figure 5.3:** Representative spectra of  $1.42 \times 10^{-4}$  M PPIX in DMSO at various excitation scan and collection rate combinations. Observe the effects of undersampling in the first spectrum and oversampling in the third spectrum of the fluorescent signal and the substantial impact on resultant spectral signatures. ....115

**Figure 5.4:** Pre-Burn and Post-Burn spectrum of  $7.67 \times 10^{-5}$  M ZnPP in 3:1 glycerol:water at 5.5 K. Observe a 20 GHz range of moderate flatness from 507537 to 507557 GHz in the pre-burn trace. Arrow indicates burn frequency, 507547 GHz. Spectral resolution  $\sim 15$  MHz. ....116

**Figure 5.5:** Extended scan of the above post-burn spectrum of  $7.67 \times 10^{-5}$  M ZnPP in 3:1 glycerol:water at 5.5 K. Again, arrow indicates burn frequency. Spectral resolution  $\sim 15$  MHz. Appearance of periodic spectral signal negates positive affirmation of successful spectral hole. ....117

**Figure 5.6:** Effects of various filter sets on observed spectral signal. All spectra obtained at 298 K at resolutions of  $\sim 1$  MHz. Filter sets as indicated above. Set 1: (Ex: ZT594rdc Em: FF01-731/137-25); Set 2: (Ex: Di01-R594 Em: FF01-731/137-25); Set 3: (Ex: T660LPXRXT Em: FF01-731/137-25); Set 4: (Ex: ZT594rdc Em: FF01-675/67-25); Set 5: (Ex: Di01-R594 Em: FF01-675/67-25); Set 6: (Ex: T660LPXRXT Em: FF01-675/67-25). ....119

**Figure 5.7:** Spectral shape obtained in CTCSM using only dichroic filter with no emission filter present. Shape is representative of that obtained for all tested dichroic filters. ....120

**Figure 5.8:** Spectral shape obtained using no filters within the pathway. Observe presence of secondary oscillation with period similar to that seen in the emission filter free case. ....121

**Figure 5.9:** Block diagram of components on optical table. PL: Pump Laser; RDL: Ring Dye Laser; RC: Reference Cavity; M: Silver Coated Mirror; I: Iris; IS: Intensity Stabilizer; MM: Motorized Mirror; BS: Beam Sampler; PSD: Position Sensitive Detector; G-T: Glan-Taylor Prism; FR: Fresnel Rhomb; OBJ: Objective. Orange square: Intensity stabilization optics; Green square: Position stabilization optics; Blue square: Polarization optics. Boxed portions were removed and then sequentially re-incorporated back into optical pathway during signal optimization studies. ....122

**Figure 5.10:** Parallel and perpendicular, excitation light polarization.  $7.67 \times 10^{-5}$  M ZnPP in 3:1 glycerol:water at 298 K. Spectra obtained at 298 K with no windows present within CTCSM, position and intensity stabilization optics included, along with table top Fresnel rhomb, but not the second optics table



Glan-Taylor prism. Slight variation of spectral signal persists, however, lack of large variation within signal allows for possibility of successful spectral hole-burning studies. ....123

**Figure 5.11:** Polarization elements originally used within the optical pathway for control of the polarization of the excitation light. The second Glan-Taylor prism was moved from the optical table into the CTCSM. The first Glan-Taylor prism was eventually completely removed to eliminate the oscillatory behavior observed in collected spectra. ....124

**Figure 5.12:** Left: Previous location on the excitation arm of the CTCSM of the polarization modulator, housing the Glan-Taylor prism. Right: New location of the Glan-Taylor prism, after the dichroic mirror. The prism remains fully rotatable, allowing for any desired angle of linear polarization to be achieved. ....125

**Figure 5.13:** TTL pulse output from APD from detection of fluorescent signal. Blue trace: original pulse with amplitude of 3.68 V. Yellow trace: same pulse after passing through 820 ohm resistor with amplitude of 220.0 mV. ....127

**Figure 5.14:** Representative spectral profiles and statistics taken of PPIX-Mb sample at various discriminator settings on the SR400. Above: no discrimination. Below: 75 mV discrimination. ....128

**Figure 5.15:** Spectral standard deviation of PPIX-Mb sample excited over the range 606-629 nm at various discriminator settings on the SR400. Discrimination thresholds were evaluated at increments of 10 mV over the range of 0 mV to +300 mV. (Specifically: 0, 25, 35, 45, ..., 265, 275, 280, 285, 300 mV) ....129

**Figure 6.1:** Direction and magnitude of heat transfer resulting from a thermal gradient across a boundary. The second law of thermodynamics dictates that heat flows from higher to lower temperatures giving the heat transfer a defined directionality. The heat transfer rate is dependent upon the magnitude of the thermal differential. These two results give heat transfer vector properties. ....132

**Figure 6.2:** The total heat that is transferred between temperature  $T_1$  and temperature  $T_2$  is the sum of heat flows by each of the three aforementioned mechanisms. The equality is mathematically stated in equation 6.1. Conduction is the mechanism of heat transfer in a solid. In fluids, both convective and radiative heat transfer processes occur. In vacuum, radiation is the only form of heat transfer. ....133

**Figure 6.3:** The convective heating or cooling of a body. Laminar flow dominates in regions of low Reynolds numbers where fluid viscous forces outweigh inertial forces. These regions are signified by nearly parallel fluid flow void of lateral mixing. At high Reynolds numbers, inertial forces dominate and flows becomes turbulent resulting in the formation of eddies. Despite depiction, the presence of a body in a flow does not necessarily induce turbulent flow. This is entirely fluid and velocity dependent. Both laminar and turbulent flow patterns facilitate convective heat transfer, yet to differing degrees. ....136

**Figure 6.4:** The development of a boundary layer as a fluid flows tangentially across a solid surface. Interactions between the fluid and surface reduce the propagation velocity of the fluid at the interface. The boundary layer thickness is defined as the distance from the surface to when the flow reaches 99% the flow rate of the bulk fluid. Conduction is mode of transfer between the surface and the boundary layer. Convective processes facilitate heat transport. Depiction is representative of the interaction existing within the boxed region of the previous image. ....136

**Figure 6.5:** Net one-dimensional heat flow through a volume element of planar geometry. The region is defined by a surface of area  $A$ , and a thickness of  $\Delta x$ . By the first law of thermodynamics, a balance of energy exists if and only if, the heat that flows into a region is equivalent to the total sum of the heat energy which flows out of the region and the increase of internal energy that is contained within the region. ....147

**Figure 6.6:** Left: Temperature profile of thermal gradients existing at and across each interface within a multilayer system. This system is composed of four distinct layers. Region one and four represent fluid layers with heat transfer coefficients  $h_1$  and  $h_2$  respectively. Regions two and three represent solid layers of thickness  $L_1$  and  $L_2$ , each layer possessing a different thermal conductivity. Observe the different temperature drop across each of these layers. Due to surface roughness, interstitial spaces exist between the solid layers and thermal contact is imperfect. Thermal transfer in this space is dictated by the heat transfer coefficient  $h_c$ . This results in the development of a thermal gradient at the interface. Right: Thermal resistance network for this system. Each layer, in addition to the contact resistance between the solid layers, contributes thermal resistance to the flow of heat. ....154

**Figure 6.7:** An example temperature profile of the controlled heating of the sample using the heater. The controlled cooling of the sample results in similar profiles. To minimize the time required to heat the sample, the heater is ramped and then turned off. The sample temperature continues to increase until thermal equilibrium is reestablished. Reduced heater output is then used to keep the sample at the heightened temperature. ....158

**Figure 6.8:** The four segments of the temperature cycling curve that require modeling for predictive thermal regulation. The heater is first ramped to an increased temperature following the heater ramp segment. It is then completely turned off and the thermal energy allowed to disperse throughout the system. The loss of heat at the heater is observed as the heater cooling segment. The sample lag segment describes the temporal lag between the start of the heater ramp and the initial change in temperature at the sample. The sample heating segment reflects the increase of sample temperature to the predetermined set point value. ....159

**Figure 6.9:** Left: CAD schematic of research Dewar. External components of the CTCSM are shown at the top of the diagram. Right: Various interfaces within Janis research Dewar providing thermal resistance to heat transfer. Orange and blue squares: positions of sample sensor and heater sensor/heater, respectively. Grey: stainless steel 304 walls. White: space for Air/Vacuum,  $N_2$ , or He gas. The lengths of the concentric cylinders are  $L_1$ ,  $L_2$ , and  $L_3$  with the inner and outer radii of the three cylinders represented by  $r_1$  through  $r_6$ . The outer vacuum jacket of the cryostat is not depicted in the simplified schematic appearing right. The actual quantities for the length and radial components are used for the analysis. Counting outwards, region 1 is annular volume at the sample; region 2 is the solid cylinder around region 1, etc. The liquid cryogen sits in region 7. ....161

**Figure 6.10:** Thermal resistance networks for heat transfer occurring at the sample sensor (top) and the heater sensor (bottom) through the cylindrical interfaces within the research Dewar. Conductive, convective, and radiative resistances are displayed. ....163

**Figure 6.11:** Temperature varying thermal conductivities of the SUS304 cylinders as determined by the NIST method as well as by application of the linear approximation for electrical resistivity used in conjunction with the Wiedemann-Franz law. It was found that the values as calculated by the NIST method yielded fits that more closely reflected experimentally obtained heating and cooling curves in this system. ....166

**Figure 6.12:** The calculated Eucken correction thermal conductivities for the annular layers for the various gaseous species at experimental pressures  $10^{-1}$  -  $10^3$  Pa. The literature values for these species at 1 atm are included for comparison. ....169

**Figure 6.13:** Top: Temperature specific heat transfer coefficient for each gas when liquid nitrogen is the cryogen and the wall temperature is 77K. Bottom: same but liquid helium cryogen at 4.2K or at 1K. ....173

**Figure 6.14:** Top: Temperature profile of thermal gradients existing at and across each interface within the Janis research Dewar. Temperature profiles were calculated using fixed thermal conductivities across all of the thermal interfaces at the seven specified temperatures. The dark blue trace represents the thermal gradients across all thermal interfaces when a variable, temperature dependent thermal conductivity was used for calculation. Bottom: Thermal resistance network for above temperature profile. ....175

**Figure 6.15:** Temperature profile of thermal gradients existing at and across each interface within the Janis research Dewar. Solid line represents exchange gas helium and cryogen liquid nitrogen. Dotted line represents exchange gas helium and cryogen liquid helium. Temperature profiles were calculated using fixed thermal conductivities across all of the thermal interfaces at the seven specified temperatures. The dark blue traces represent the thermal gradients across all thermal interfaces when a variable, temperature dependent thermal conductivity was used for calculation. ....176

**Figure 6.16:** Top: Cooling behavior at the position of the **sample** within the Janis 9VSRD-SVT-22 research Dewar containing the CTCSM. Fits to the cooling curve are modeled using the lumped capacitance transient approximation and using a standard regression approach. Top Right: Plot of residuals of fitting approaches to experimentally obtained results. Below: Fitting models used for the above fitted cooling curve and the goodness of fit parameters. Lumped capacitance uses a system determined (equation 6.23) fixed exponential term and a variable constant term. The regression approach uses a variable exponential term and a fixed constant term. ....178

**Figure 6.17:** Top: Cooling behavior at the position of the **heater** within the Janis 9VSRD-SVT-22 research Dewar containing the CTCSM. Fits to the cooling curve are modeled using the lumped capacitance transient approximation and using a standard regression approach. Top Right: Plot of residuals of fitting approaches to experimentally obtained results. Below: Fitting models used for the above fitted cooling curve and the goodness of fit parameters. Lumped capacitance uses a system determined (equation 6.23) fixed exponential term and a variable constant term. The regression approach uses a variable exponential term and a fixed constant term. ....179

**Figure 6.18:** Five separate ramping cycles of the heater, and the temperature response as recorded at the heater sensor. Included polynomial fits. Ramping appears to follow the curve:  $T(t) = -0.0008t^2 + 0.3256t + 1.3947 + \text{Starting Temp}$ . This polynomial accurately predicts ramp characteristics for the range  $T = 80$  K to  $T = 150$  K. ....181

**Figure 6.19:** Left: Five separate heating response curves of the temperature at the sample in relation to a ramp of the heater. Right: Change in slope of the (left), temperature vs. time trace at the sample in relation to an induced heating by a ramp of the heater. A zero slope followed by continuous positive slope is indicative of initial sample heating and defines the thermal lag times. Lag times: Ramp 1, 24 s; Ramp 2, 33 s; Ramp 3, 72 s; Ramp 4, 15 s; Ramp 5, 36 s. Based on trials, temporal lag for initial heating of sample vs. start of heater ramp is approximately 36 s. ....183

**Figure 7.1:** Above: SolidWorks CAD design of the 1mm dual channel sample cell. Diagram has units of mm. This variation has two channels, allowing for two samples to be held simultaneously. The electrode spacing is 1mm. DuraForm PA is the material used to 3D print these pieces. Left: Depiction of the 1mm single channel design variation. Copper electrodes clip into the 3D printed pieces. Sample sits in recess between electrodes. Coverglass slides into the top of the sample cell to keep the sample in place between the electrodes and isolated from the CTCSM objective. ....190

**Figure 7.2:** Left: Sample cell attached at the base of the optical insert of the CTCSM. The low dielectric properties of the DuraForm PA provide for insulation between the high voltage at the electrodes and the piezo positioners upon which the sample cell sits just below the CTCSM objective. The electrical connections consist of the Kapton insulated voltage carrying lead at the far electrode, and the semi-rigid grounding connection (thick copper wire) which provides for additional positional stability of the affixed sample cell at the front electrode. Right: Close-up of dual channel sample cell with 1 mm electrode spacing. Cover glass is placed atop sample and slides into sample cell. The edge of the cover glass can be seen on the left side of the image. ....192

**Figure 7.3:** Qx band of PPIX in myoglobin at 1.11 K. The raw spectral data appears in red and a Savitzky-Golay smoothed trace of the data appears in grey. Colored arrows indicate the burning positions within the band for the representative hole profiles that follow. Red arrow figure 7.4; blue arrow figure 7.9; green arrow figure 7.12; black arrow figure 7.14. ....196

**Figure 7.4:** Shown above is a representative spectral hole, burnt into the Qx transition of PPIX-Mb. Arrow indicates position of burn. This spectral hole has a FWHM of 0.00148 nm = 1.16 GHz, and a relative depth of 47%. Fitting parameters along with fit statistics reveal good correlation to Lorentzian profile, and successful spectral hole-burning. ....197

**Figure 7.5:** Spectral trace observed during re-scan of a spectral hole burnt into the Qx band of a PPIX-Mb sample upon application of 500 V. Prior to voltage application, the counts were in the range of 4000 cps. ....198

**Figure 7.6:** Left: Original sample holder design. Sample rests in 1mm x 1mm x 1.5 mm channel in direct contact with copper electrodes. Right: Sample holder with electrode spacing of 2mm, sample in 1.5 mm OD KIMAX capillary, isolated from electrode contact. Image shows “tall” capillary for visual clarity. ....201

**Figure 7.7:** Sample trace showing no APD runaway with improvements to connections, shielding of electrical pathway, and isolation of sample from direct contact with electrode surface. ....203

**Figure 7.8:** Newly designed sample holder. Sample rests within 1.4 mm x 1.4 mm x 10 mm square borosilicate glass capillary, isolated from direct contact with Cu electrodes. ....205

**Figure 7.9:** Spectral hole, burnt into the Qx transition of PPIX Mb. Laser polarization parallel to applied electric field (300 V). Low magnitude of externally applied field resulted only in broadening of hole-profile. Spectral splitting is expected at enhanced externally applied field values. Hole (0 V): FWHM 0.00128 nm = 1.0024 GHz; with a relative depth of 18%. Hole (300 V): FWHM 0.00269 nm = 2.11 GHz; with a relative depth of 16%. Lorentzian fit parameters and fitting statistics for the above spectral hole with 0 V applied and 300 V applied. ....207

**Figure 7.10:** Experimental setup for hole-burning with glass cryostat. When Janis Dewar is used, transmission signal, (bottom right) is not present. PL: Pump Laser; RDL: Ring Dye Laser; M: Mirror; I: Iris;

IS: Intensity Stabilizer; MM: Motorized Mirror; BS: Beam Sampler; PSD: Position Sensitive Detector; G-T: Glan-Taylor Prism; F1-6: Neutral Density Filters; OBJ: 10x Objective; OF: Optical Fiber; L: Lens; DIC: Dichroic Mirror; EM: Emission Filter; HV: High Voltage Power Supply; APD: Avalanche Photodiode; SPAD: APD Power Supply; PC: Photon Counter; CPU: Computer; RDL Control: Dye Laser Control Box; TC: Temperature Controller; WM: Wave meter; RC: Reference Cavity. The laser beam is depicted as a solid line, dotted lines are electrical connections. ....211

**Figure 7.11:** Representative spectra of PPIX Mb in pH 7.3 buffered 3:1 Glycerol Water at 2 K, depicting the possible collection modes when sample is placed in the glass cryostat. The reflected and transmitted signal are acquired simultaneously. The top row displays nearly identical spectra of the entire Qx band and the bottom row displays a representative single spectral hole as collected by each mode. The transmitted signal suffers from enhanced noise. Additional efforts placed on alignment of the optics positioned on the transmission side of the cryostat does reduce the noise, yet signal intensity generally remains an order below that of the reflected signal. ....212

**Figure 7.12:** Spectral hole, burnt into the Qx transition of PPIX Mb and resultant broadening of hole profile with application of electric field. Laser polarization parallel to applied electric field. Hole (Post-Burn): FWHM 0.00218 nm = 1.689 GHz; with a relative depth of 44%. Hole (1401 V): FWHM 0.00276 nm = 2.13 GHz; with a relative depth of 31%. Hole (1774 V): FWHM 0.0032 nm = 2.48 GHz; with a relative depth of 26%. Hole (1884 V): FWHM 0.00332 nm = 2.57 GHz; with a relative depth of 24%. At these voltages only broadening of hole profile was observed, profile splitting is expected at enhanced externally applied field values. ....214

**Figure 7.13:** The developed high voltage feedthrough. Right: The entire feedthrough, just over 1 meter in length, is inserted into bath cryostat. Top: close-up of vacuum components at top of feedthrough. Bottom: close-up of the base of the feedthrough. Observe the 1/8 inch stainless conduction rod. Welded endcap ensuring no leakage image right. ....216

**Figure 7.14:** Above, is a representative spectral hole, burnt into the Qx transition of PPIX-Mb. Arrow indicates position of burn. This spectral hole has a FWHM of 0.00249 nm = 1.93 GHz, and a relative depth of 42%. Application of 2750 V and 3750 V resulted in successful splitting of the spectral hole. These applied voltages correspond to applied electric fields of approximately  $1.83 \times 10^6$  V/m and  $2.50 \times 10^6$  V/m, respectively. Each of the split profiles were most basically modeled using a sum of Lorentzian profiles. Lorentzian fit parameters and fitting statistics appear for each split profile. ....218

**Figure 8.1:** Parallel plate capacitor. The capacitor is formed by two parallel plates that share an area of overlap  $A$ , and are separated by a distance  $d$ . After connection to a voltage source, charges accumulate on the inner surface of the plates. Due to the separation of charge that is established, an electric field  $\vec{E}$  develops between the plates. The magnitude of the electric field is directly proportional to the voltage differential of the plates and inversely proportional to their distance from one another. ....225

**Figure 8.2:** Placement of a dielectric material between the plates of a parallel plate capacitor. The polarizable molecules of the dielectric upon orientation towards the external field will collectively establish a counter field that reduces the net field between the plates. To maintain the voltage differential between the plates additional charges flow to the respective plates. ....227

**Figure 8.3:** Capacitors connected in parallel and in series configurations. ....233

**Figure 8.4:** Schematic of charge accumulation on multiple parallel plate capacitors that are connected in parallel. Connection in parallel allows for additive capacitance across the capacitors. The total number of capacitors created in this arrangement is equal to the total number of plates minus one, capacitors = # plates - 1. ....235

**Figure 8.5:** Left: SolidWorks design of an individual capacitor plate, top and tilt view. When plates are successively stacked with a 90-degree rotation the capacitor plate area of overlap is circular. Center: SolidWorks design of entire instrument, used for the CNC fabrication of the capacitor plates and the Teflon bases. Right: An image of the completed capacitance cell. The total height is 76.2 mm, containing 46 plates of diameter 22.86 mm with homogeneous spacing of 0.53 mm. This geometry yields a total capacitive area of 410.4 mm<sup>2</sup> and a theoretical capacitance in air of 310.46 pF at 298 K. The instrument sits in a Vitlab 50mL beaker for solution measurements. ....236

**Figure 8.6:** Theoretically calculated capacitance of air based on the temperature dependent architecture of the capacitance cell. ....239

**Figure 8.7:** RC circuit used for the charging and discharging of a capacitor. Top: Initially at time  $t_0$ , the switch  $S_1$  is open. As soon as switch  $S_1$  is closed, current begins to flow in the direction indicated and the capacitor continues to charge until the voltage across the capacitor is equal to that of the power supply, at time  $t_c$ . Bottom: Initially at time  $t_0$ , the switch  $S_2$  is positioned at point c, and switch  $S_1$  is open, effectively removing the power supply from the circuit. When switch  $S_2$  is positioned at point b, current begins to flow in the indicated direction and the capacitor continues to discharge until the voltage across the capacitor is zero at time  $t_d$ . ....242

**Figure 8.8:** Top: Complete circuit for the measurement of the RC time constant indicating the additional capacitive and resistive contributions of the function generator  $C_{FG}$  and  $R_{FG}$ , and oscilloscope  $C_o$  and  $R_o$ , and the additional capacitive contribution  $C_L$  of the BNC and other electrical leads used for connection of the various components. The resistance values for these instruments were verified by measurement and are indicated in the bottom schematic. The reference resistor is shown as  $R_R$ , the resistance of the leads is  $R_L$ , and the capacitance of the developed measurement cell as  $C_c$ . Bottom: Experimental setup used for the measurement of the RC time constant. During the initial benchtop trials with ambient air as the dielectric medium, an 820 ohm 0.25W  $\pm$ 5% AXIAL Carbon Film CF14JT820R was used for the reference resistor  $R_R$ . Representative example data appears in figure 8.9. For all remaining trials, the 1K ohm 0.6W 0.01% RADIAL Y0062-1.0KA-ND was used as the reference resistor. ....250

**Figure 8.9:** Representative trace of system and cell capacitive charging and discharging in ambient air. Square-wave excitation 10.0 Vpp, 5.0V offset, 100kHz; using an 820-ohm reference resistor before the capacitance measurement cell. The dotted traces indicate the measured voltage and time when  $\tau = RC$ . ....251

**Figure 8.10:** Top: Complete circuit for the measurement of the capacitive reactance indicating the additional capacitive and resistive contributions of the function generator  $C_{FG}$  and  $R_{FG}$ , and oscilloscope  $C_o$  and  $R_o$ , and the additional capacitive contribution  $C_L$  of the BNC and other electrical leads used for connection of the various components. The resistance values for these instruments were verified by measurement and are indicated in the bottom schematic. The reference resistor is shown as  $R_R$ , the resistance of the leads is  $R_L$ , and the capacitance of the developed measurement cell as  $C_c$ . Bottom: Experimental setup used for the measurement of the capacitive reactance. During the benchtop trials with ambient air as the dielectric medium, an 820 ohm 0.25W  $\pm$ 5% AXIAL Carbon Film CF14JT820R was used for the reference resistor  $R_R$ . ....260

**Figure 8.11:** Representative trace of system and cell capacitive charging and discharging in ambient air. Sine-wave excitation of 10.0 Vpp, 1MHz; using an 820-ohm reference resistor before the capacitance cell. ....261

**Figure 8.12:** Location and pressure dependence of the measured capacitance value at ambient temperature. The system capacitance consists of the total sum of the self-capacitance of the function generator, the oscilloscope and the electrical leads used to connect the various components of the RC circuit. The system and cell consists of the system capacitance as well as the additional capacitance of the capacitance cell when it is incorporated into the circuit. The only shift in measured capacitance occurs after the optical insert, containing the electrical leads and optionally the capacitance cell, is placed within the insert tube. Over the pressure range investigated, there was no observed pressure dependence on the measured capacitance value. ....266

**Figure 8.13:** The temperature dependence throughout the liquid nitrogen range of the capacitance of the electrical leads used to connect the various components within the RC circuit, including the leads that extend to the base of the research Dewar. This is representative of the capacitance of the measurement system, which must be accounted for when determining the magnitude of the contribution of the capacitance measurement cell alone, in relation to the total measured capacitance. The jumps in the capacitance trace are equivalent to a differential of 1.905 pF. The magnitude of the differential is dependent upon the frequency of the square wave pulse used during the measurement process, which for these trials was 100 kHz. ....268

**Figure 8.14:** The temperature dependence throughout the liquid nitrogen range of the capacitance measurement cell using nitrogen gas as the dielectric medium within the capacitance cell. The measurements performed during both the cooling and heating of the instrument indicate that no apparent geometric deviation of the instrument occurs throughout the thermal range. The jumps in the capacitance trace are equivalent to a differential of 1.905 pF. The magnitude of the differential is dependent upon the frequency of the square wave pulse used during the measurement process, which for these trials was 100 kHz. ....270

**Figure 8.15:** The measured relative permittivity of 18 MΩ·cm water within the thermal range of 97.7 K to 195.31 K. Displayed are the results of 46 separate measurements that were taken throughout a period of 50 days out of thermal order, during both the heating and the cooling of the sample. The jumps in the above trace are equivalent to a differential in capacitance of 9.5 pF, resulting in a differential of 0.0307 in the value of the relative permittivity. The magnitude of the differential is dependent upon the frequency of the square wave pulse used during the measurement process, which for these trials was 5 kHz. A direct relationship appears between the temperature and the measured relative permittivity. The average value of the relative permittivity throughout this thermal range is equivalent to 2.963. ....272

**Figure 8.16:** The temperature dependence of the relative permittivity of a 3:1 glycerol:water ice sample. This study consists of 42 separate measurements that were all taken at 11 different frequencies, out of thermal order, during both the heating and the cooling of the sample. Top: All 42 measurements, 33 of which occurred between the temperatures of 82.225 K to 200.610 K. Bottom: The nine measurements that were made throughout the range of 1.034 K to 37.168 K. ....278

**Figure 8.17:** The frequency dependence of the relative permittivity of a 3:1 glycerol:water ice sample. This study consists of 45 separate frequency measurements that were taken at 3 different temperature ranges, within the liquid nitrogen thermal range Top: The 45 measurements, for each of the three investigated temperature ranges. Bottom: Magnification of the six lowest frequency

measurements appearing in the above plot. The dotted lines appear only for guidance and represent a least squares regression fourth order polynomial fit to the data. Error bars represent the 95 % confidence interval, and were created using jackknife resampling, a statistical resampling technique. ....281

**Figure 8.18:** The frequency dependence of the relative permittivity of a 3:1 glycerol:water ice sample. This study consists of 45 separate frequency measurements that were taken at 4 different temperature ranges, within the liquid helium thermal range Top: The 45 measurements, for each of the four investigated temperature ranges. Bottom: Magnification of the six lowest frequency measurements appearing in the above plot. The dotted lines appear only for guidance and represent a least squares regression fourth order polynomial fit to the data. Error bars represent the 95 % confidence interval, and were created using jackknife resampling, a statistical resampling technique. ....282

**Figure 8.19:** The relative permittivity of 3:1 glycerol:water ice. These two measurements represent the low temperature and low frequency relative permittivity of the glycerol:water matrix that is used to contain the sample (PPIX-Mb) during the spectral hole-burning and Stark investigations. During the molecular resolution approach to calculating the internal molecular electric field, for the most realistic valuation of the relative permittivity of the surrounding matrix, the value of 3.465 should be used, as this measurement was obtained under environmental conditions that closely reflect those under which the sample exists during the hole-burning and Stark experiments. Error bars represent the 95 % confidence interval, and were created using jackknife resampling, a statistical resampling technique. ....285

**Figure 8.20:** Schematic representation of the Schering bridge circuit that allows for the frequency independent determination of the capacitance of an unknown capacitor. In this circuit, the unknown capacitor under test is  $C_T$  which possesses an in series resistance  $R_T$  representing the loss in the capacitor. ....287

**Figure 9.1:** Representative surface fits to the atomic positions of the porphine core of the porphyrin macrocycle in myoglobin. For each species of origin available in the RCSB-PDB, one surface is displayed. The displayed surfaces include, top left to bottom right (species of origin, PDB identification code and the crystal structure resolution): *Equus caballus* (horse): 3HEO at 2.00 Å [63], *Aplysia limacina* (slug sea hare): 1DM1 at 1.99 Å [13], *Caretta caretta* (loggerhead turtle): 1LHT at 2.00 Å [39], *Sus scrofa* (wild boar): 1M6M at 1.80 Å [31], *Tetrahymena pyriformis* (ciliate protozoa): 3AQ5 at 1.78 Å [25], *Thunnus atlanticus* (blackfin tuna): 2NRL at 0.91 Å [48], *Physeter catodon* (sperm whale): 1MBO at 1.60 Å [41], other porphyrins (not of the above): 1KFR at 1.85 Å [38]. In all of the displayed plots above, the porphine ring is positioned such that the two propionic acid side chains bonded to the porphyrin ring would be oriented towards the front of the image. Across the 380 fits that were performed, additional surface variability that cannot be observed in the above fits did exist. Legends display "Surface Fit", top, and "Atomic Coordinates", bottom. The axes have the units of angstrom. ....298

**Figure 9.2:** Close up of the oxygen binding site of horse heart myoglobin as described by the 1DWT crystal structure [6]. The native heme appears in pink, and the CO is shown in green. The CO is removed from the center of the porphyrin ring by a distance of 4.14 Å. The protein residues also existing within this range to the center of the porphyrin ring are shown in light blue. No electron density associated with the CO appears on the distal side of the porphyrin plane. This image was created using the Swiss-PdbViewer application [19]. ....302

**Figure 9.3:** Photorelaxed horse heart myoglobin CO complex, 1DWT [6]. Above: Surface fit to the atomic coordinates of the porphine core of the porphyrin molecule as it exists in the active site of horse heart myoglobin. The fit reveals that the in-protein structural character of the macrocycle deviates from



planarity by up to 0.516 Å in the z-direction. Left: Top view of the atomic coordinates of the porphine core, displaying the atomic positions, which possess a deviation from idealized molecular symmetry.

.....304

**Figure 9.4:** Predicted Qx transition wavelengths by CISD using the 6-311G(d) basis set. Electron were excited from doubly occupied core orbitals, HOMO down, into unoccupied orbitals from the LUMO upwards. Ten different active electron groups were allowed to populate up to the first 50 orbitals of the virtual space. The inset displays a magnified view of the first portion of the data. ....323

**Figure 9.5:** Predicted Qx transition wavelengths by CISDT using the 6-311G(d) basis set. Electron were excited from doubly occupied core orbitals, HOMO down, into unoccupied orbitals from the LUMO upwards. Ten different active electron groups were allowed to populate up to the first 50 orbitals of the virtual space. The inset displays a magnified view of the first portion of the data. ....328

**Figure 9.6:** Predicted Qx transition wavelengths by CISDTQ using the 6-311G(d) basis set. Electron were excited from doubly occupied core orbitals, HOMO down, into unoccupied orbitals from the LUMO upwards. Ten different active electron groups were allowed to populate up to the first 50 orbitals of the virtual space. The inset displays a magnified view of the first portion of the data. Due to the large scaling of this method,  $N^{10}$ , where N is the number of electrons, calculations could only be performed with all of the different active electron groups populating only a limited portion of the virtual space. ....330

**Figure 9.7:** Predicted Qx transition wavelengths by EOM-CCSD, CR-EOM-CCSD(T) ID/IB, CR-EOM-CCSD(T) IID/IA, and DELTA-CR-EOM-CCSD(T) DEL(IA), using the 6-311G(d) basis set. Electrons were excited from doubly occupied core orbitals, HOMO down, into unoccupied orbitals from the LUMO upwards. Seven different active electron groups were allowed to populate orbitals of the virtual space. Marker positions of the different calculations performed appear in figure 9.8. The experimental Qx transition energy is depicted as the red horizontal line. Several of the selected active spaces, when used with these variants of EOM-CCSD(T), were able to yield transition energies that closely reflect this experimental value. ....338

**Figure 9.8:** Comparison of calculated ground state energies as calculated by the EOM-CCSD and the CR-CCSD(T)\_L methods using the 6-311G(d) basis set. This figure indicated that including greater numbers of occupied and unoccupied orbitals into the active space of the calculation returns lower evaluations of the ground state energy. Improvement to the basis set will undoubtedly lead to further decrease in determined values for the ground state energy. ....340

**Figure 9.9:** Norm of the transition moments of the first four optical transitions of porphine allowing 20 doubly occupied orbitals (40 electrons, HOMO down) to occupy a differing number of unoccupied orbitals in the virtual space (LUMO upwards) for capture of the electron correlation energy by EOM-CCSD, 6-311G(d). ....342

**Figure 9.10:** Performance comparison across the investigated methods. The calculated ground state energy determined by each of the investigated computational approaches using the 6-311G(d) basis set, and the same active space DOC: 10 → VIR: 15. The difference between the ground state energy calculated using the CIS approach and the CISDTQ approach is about 2.5 eV or 240 kJ/mol. ....345

**Figure A.1:** Temperature dependence of the Qx transition of the protoporphyrin-IX substituted myoglobin sample used during the spectral hole-burning investigations. The names of the traces are representative of the temperature in K that the spectra were acquired at. ....361

**Figure A.2:** *Temperature dependence of the peak wavelength of the Qx transition of the protoporphyrin-IX substituted myoglobin sample used during the spectral hole-burning investigations. Peak wavelengths were taken from the fluorescence excitation spectra appearing in figure A1. To guide the eye, the data was fit using a second order polynomial,  $y = 6 \times 10^{-5}x^2 + 0.01x + 620.57$ ;  $R^2 = 0.8725$ , and appears as the dotted trace. ....362*

**Figure C.1:** *Top half of program P1 “Spectroscopy”. The user interface of this block diagram is displayed in figure 3.2. ....366*

**Figure C.2:** *Bottom half of program P1 “Spectroscopy”. The user interface of this block diagram is displayed in figure 3.2. ....367*

**Figure C.3:** *Top left of program P2 “Hole-Burning”. The user interface of this block diagram is displayed in figure 3.5. ....368*

**Figure C.4:** *Top right of program P2 “Hole-Burning”. The user interface of this block diagram is displayed in figure 3.5. ....369*

**Figure C.5:** *Bottom left of program P2 “Hole-Burning”. The user interface of this block diagram is displayed in figure 3.5. ....370*

**Figure C.6:** *Bottom right of program P2 “Hole-Burning”. The user interface of this block diagram is displayed in figure 3.5. ....371*

**Figure C.7:** *Program P3 “Temperature Cycling”. The user interface of this block diagram is displayed in figure 3.6. ....372*

**Figure C.8:** *Program P4 “Signal Smoothing”. The user interface of this block diagram is displayed in figure 3.7. ....373*

**Figure D.1:** *The head of the CTCSM presented in exploded view. The displayed segments correspond to the respective component lists. ....376*

**Figure E.1:** *Thermal ramping dependence of Janis research Dewar based on the specified heater output power and the heater range. The resistive heating element can be modulated within three ranges that correspond to: Low = 500 mW, Med = 5 W, High = 50 W. The heater power is specified as a percentage of total power for a given heater range. ....377*

**Figure F.1:** *Spectral hole, burnt into the Qx transition of PPIX-Mb. Arrow indicates position of burn. This spectral hole has a FWHM of 0.00193 nm = 1.50 GHz, and a relative depth of 46%. The applied voltage corresponds to an applied electric field of approximately  $1.67 \times 10^6$  V/m. This split profile was most basically modeled using a sum of Lorentzian profiles. The Lorentzian fit parameters and the fitting statistics appear the table below. ....381*

**Figure G.1:** *Predicted Qx transition wavelengths by CISD using the 6-311G(d) basis set. Electrons were excited from doubly occupied core orbitals, HOMO down, into unoccupied orbitals from the LUMO upwards. Ten different active electron groups were allowed to populate up to the first 50 orbitals of the virtual space. The inset displays a magnified view of the first portion of the data. ....385*

**Figure G.2:** *Predicted Qy transition wavelengths by CISD using the 6-311G(d) basis set. The inset displays a magnified view of the first portion of the data. ....386*

<b>Figure G.3:</b> Predicted Bx transition wavelengths by CISD using the 6-311G(d) basis set. The inset displays a magnified view of the first portion of the data. ....	387
<b>Figure G.4:</b> Predicted By transition wavelengths by CISD using the 6-311G(d) basis set. The inset displays a magnified view of the first portion of the data. ....	388
<b>Figure G.5:</b> Predicted Qx transition wavelengths by CISDT using the 6-311G(d) basis set. Electrons were excited from doubly occupied core orbitals, HOMO down, into unoccupied orbitals from the LUMO upwards. Ten different active electron groups were allowed to populate up to the first 50 orbitals of the virtual space. The inset displays a magnified view of the first portion of the data. ....	389
<b>Figure G.6:</b> Predicted Qy transition wavelengths by CISDT using the 6-311G(d) basis set. The inset displays a magnified view of the first portion of the data. ....	390
<b>Figure G.7:</b> Predicted Bx transition wavelengths by CISDT using the 6-311G(d) basis set. The inset displays a magnified view of the first portion of the data. ....	391
<b>Figure G.8:</b> Predicted By transition wavelengths by CISDT using the 6-311G(d) basis set. The inset displays a magnified view of the first portion of the data. ....	392
<b>Figure G.9</b> Predicted Qx transition wavelengths by CISDTQ using the 6-311G(d) basis set. Electrons were excited from doubly occupied core orbitals, HOMO down, into unoccupied orbitals from the LUMO upwards. Ten different active electron groups were allowed to populate up to the first 50 orbitals of the virtual space. The inset displays a magnified view of the first portion of the data. ....	393
<b>Figure G.10:</b> Predicted Qy transition wavelengths by CISDTQ using the 6-311G(d) basis set. ....	394
<b>Figure G.11:</b> Predicted Bx transition wavelengths by CISDTQ using the 6-311G(d) basis set. ....	395
<b>Figure G.12:</b> Predicted By transition wavelengths by CISDTQ using the 6-311G(d) basis set. ....	396
<b>Figure G.13:</b> Predicted Qx transition wavelengths by EOM-CCSD, CR-EOM-CCSD(T) ID/IB, CR-EOM-CCSD(T) IID/IA, and DELTA-CR-EOM-CCSD(T) DEL(IA), using the 6-311G(d) basis set. Electrons were excited from doubly occupied core orbitals, HOMO down, into unoccupied orbitals from the LUMO upwards. Seven different active electron groups were allowed to populate orbitals of the virtual space. Marker positions of the different calculations performed appear in figure 9.8. The experimental Qx transition energy is depicted as the red horizontal line. ....	397
<b>Figure G.14:</b> Predicted Qy transition wavelengths by EOM-CCSD, CR-EOM-CCSD(T) ID/IB, CR-EOM-CCSD(T) IID/IA, and DELTA-CR-EOM-CCSD(T) DEL(IA), using the 6-311G(d) basis set. According to experiment, the peak wavelength of this transition occurs at 541 nm. ....	398
<b>Figure G.15:</b> Predicted Bx, By transition wavelengths by EOM-CCSD, CR-EOM-CCSD(T) ID/IB, CR-EOM-CCSD(T) IID/IA, and DELTA-CR-EOM-CCSD(T) DEL(IA), using the 6-311G(d) basis set. The coupled-cluster computations that were performed always return degenerate energies for the Bx and By transitions. According to experiment, these transitions also result in a degenerate peak, with a peak wavelength of 427 nm. Alternate theories predict that the Bx transition occurs at 429 nm, and that the By transition occurs at 425 nm. ....	399

# LIST OF TABLES

**Table 5.1:** *Appropriate filter combinations for use with different intended Porphyrin species to be used for hole-burning investigations. Filters were obtained from Chroma and Semrock.....118*

**Table 6.1:** *Calculated Reynolds numbers for different fluids that could be present within the research Dewar. Fluids that possess turbulent flow characteristics are displayed in blue and those that possess laminar flow appear in orange. ....171*

**Table 7.1:** *Abridged attainable maximum voltages prior to breakdown, or trip condition for various cell configurations and conditions. ....202*

**Table 8.1:** *Coefficients and formula for modeling the temperature dependent length of 304 stainless steel and 6061-T6 aluminum alloy, based on the thermal expansion properties of the material over the temperature range 4-300 K. Formula and coefficients from NIST, reference 24.....238*

**Table 8.2:** *Summary of the measured capacitance values by various methods. The displayed values for the dielectric constant of ambient air at 293 K were calculated using the measured capacitance values and the geometry of the capacitance cell. The percent errors reflect the deviation of the experimentally measured relative permittivity to those reported in reference 9.....263*

**Table 8.3:** *Commonly accepted values appearing in the literature for the relative permittivity of water in the solid, ice phase. Measurement methodologies, as well as investigated thermal ranges vary according to the particular experiment, with no exact overlap between either parameter, and this particular investigation. Work was selected for inclusion for this comparison to reflect similar thermal ranges and measurement techniques in addition to being selected to represent measurement for this quantity across several decades of experiments. This current work represents a determination for the relative permittivity that is within the range of accepted values that appear throughout the literature. ....274*

**Table 9.1** *State energies, transition energies, and transition dipole moment values for the optical transitions ( $Q_x$ ,  $Q_y$ ,  $B_x$ ,  $B_y$ ) of porphine, possessing the molecular geometry of 1DWT. Calculations were performed using the configuration interaction singles (CIS) approach. The first two portions of the table display the effect of calculating properties for a larger number of excited states using the same basis set. The first and third portion of the table display the effect of using basis sets of differing size and quality during the calculation. ....318*

**Table 9.2:** *State energies, transition energies, and transition dipole moment values for the optical transitions ( $Q_x$ ,  $Q_y$ ,  $B_x$ ,  $B_y$ ) of porphine, possessing a molecular geometry that was optimized from the original 1DWT geometry. Calculations were performed using the configuration interaction singles (CIS) approach. The effect of calculating properties for a larger number of excited states using the same basis set can be observed. As compared to the results displayed in table 9.1 that were obtained using the unoptimized molecular geometry, the optimized geometry produces slightly better valuations of the transition energies in relation to what is spectroscopically observable. Again the directionality of the transition moments changes when properties for a greater number of states are calculated. ....320*

**Table 9.3:** State energies, transition energies, and transition dipole moment values for the optical transitions (Qx, Qy, Bx, By) of porphine, possessing the molecular geometry of 1DWT. Calculations were performed using the configuration interaction singles and doubles (CISD) approach with an active space determined by, DOC: 13 → VIR: 4. Displayed are the effect of using basis sets of differing size and quality during the calculation. The ground state energy shows improvement to what was determined using the CIS approach. Similar trends as displayed in tables 9.1 and 9.2 regarding the shift in directionality of the transition moments, continues to occur when the properties are evaluated using CISD. ....326

**Table 9.4:** Representative state energies, transition energies, and transition dipole moment values for the optical transitions (Qx, Qy, Bx, By) of porphine, possessing the molecular geometry of 1DWT. Calculations were performed using the EOM-CCSD approach with an active space determined by, DOC: 20 → VIR: 20. All of the coupled-cluster computation that were performed thus far have yielded degenerate energies for the Bx and By transitions. The directionality of the transition moments typically follows a (X, Y, X, X) polarization. Additional computations that utilize larger basis sets and an increased active space should be performed to determine if this trend continues.....343

**Table 9.5:** Performance comparison across investigated methods. Calculated state energies, highlighted in blue, for the optical transitions (Qx, Qy, Bx, By) of porphine, possessing the molecular geometry as described by 1DWT, determined by each of the investigated computational approaches. The utilized basis set remained consistent across all computations, but the displayed results do represent inclusion of different active spaces during the calculations. For the configuration interaction methods, the active spaces that produced the most experimentally accurate valuations are represented here. For the coupled-cluster methods, a consistent active space across all investigated variants was chosen for display. In relation to the spectroscopically observable transitions [62], highlighted in grey, this comparison reveals that the coupled-cluster approaches generally outperform the truncated configuration interaction methods at least when this basis set is utilized.....347

**Table E.1:** Determined PID value settings for Janis 9VSRD-SVT-22 Research Dewar and Lakeshore 331 Temperature Controller for various temperature regions from 5 K to 300 K. Medium heater range is used in the liquid helium range as it allows for fast equilibration times while not imparting unnecessary additional thermal energy to the cryostat thereby minimizing cryogen losses. High heater range is utilized within the liquid nitrogen range because it yields the fastest equilibration times.....378

**Table G.1:** Atomic coordinates of the porphine core of the porphyrin molecule as it exists in the active site of horse heart myoglobin. Atomic coordinates were obtained from the crystal structure 1DWT. The molecule was repositioned as described in chapter 9.2.1. ....383

**Table G.2:** Atomic coordinates of the porphine core of the porphyrin molecule as it exists in the active site of horse heart myoglobin. Atomic coordinates were obtained from the crystal structure 1DWT. These coordinates represent the optimized geometry that was obtained using a 6-311G basis set at the MP2 level of perturbation theory, and found to be a stationary point by means of a vibrational analysis calculation. ....384

# LIST OF SYMBOLS

$\Gamma_H$	homogeneous line-width (Hz)
$\Gamma_I$	inhomogeneous line-width (Hz)
$\tau$	RC time constant (s)
$\tau_1$	excited electronic state decay time (s)
$\tau^*_2$	phase relaxation time of electronic transition (s)
$F_H(\nu, T)$	homogeneous absorption band
$\nu$	frequency (Hz)
$T$	temperature (K)
$t$	time (s)
$\alpha$	Debye-Waller factor
$\hat{\alpha}$	polarizability tensor (C·m <sup>2</sup> )/N
$\pi$	Pi (3.141592653589793...)
$\vec{\mu}_{mn}$	electronic transition dipole moment (C·m, D)
$\vec{\mu}_{nn}$	electronic dipole moment (C·m, D)
$\vec{\mu}_{per}$	permanent molecular dipole moment (C·m, D)
$\vec{\mu}_{ind}$	induced molecular dipole moment (C·m, D)
$\Omega$	complete set of Euler angles

$\Delta D(\nu)$	change of optical density
$\vec{E}$	electric field (V/m)
$\vec{E}_{tot}$	total electric field (V/m)
$\vec{E}_{int}$	internal electric field (V/m)
$\vec{E}_{loc}$	local electric field (V/m)
$\vec{E}_{hv}$	polarization vector of photon used for burning or reading process
$\delta$	width of spectral hole (Hz)
$h$	Planck's constant $6.626070040 \times 10^{-34}$ J·s
$\hat{f}_{loc}$	local electric field tensor
$H$	Hamiltonian
$\Psi_{HF}$	Hartree-Fock wave function
$\Psi_{CI}$	configuration interaction wave function
$\Psi_{CC}$	coupled-cluster wave function
$\Psi$	true wave function
$\Psi_n$	state specific true wave function
$\mathcal{E}_n$	state specific energy
$\mathcal{O}$	generic operator
$\beta_n$	state specific expectation value of operator $\mathcal{O}$

$\phi_n$	one electron molecular orbital	
$\alpha_{ni}$	characteristic coefficients to scale atomic orbitals	
$\mathbf{a}_i$	configuration interaction coefficients	
$\mathbf{t}_i$	coupled-cluster coefficients	
$\varphi_i$	atomic orbitals or basis functions	
$\Phi$	many electron trial wave function	
$N$	number of electrons in the molecule	
$\mathbf{T}$	excitation operator	
$r$	spatial coordinates (m)	
$\vec{r}$	position vector	
$q$	heat flux (W/m <sup>2</sup> )	Chapter 6
$q$	charge (C)	Chapter 8
$W(n)$	internal molecular electric field free state specific energy	
$L_{\text{obj}}$	objective lens	
$L_{\text{tube}}$	tube lens	
$L_{\text{occ}}$	ocular lens	
$d$	diameter of resolution (m)	Chapter 4
$d$	distance (m)	Chapter 8



$\lambda$	wavelength (nm)
$n$	index of refraction (unitless)
$\theta$	angular resolution (radians)
$NA$	numerical aperture (unitless)
$D$	objective lens diameter (m)
$r$	radial distance (m)
$I$	intensity or amplitude (unitless)
$J_1$	Bessel function of the first kind
$x$	position coordinate in the x axis
$y$	position coordinate in the y axis
$z$	position coordinate in the z axis
$\omega_x$	scale parameter in the direction of the x axis
$\omega_y$	scale parameter in the direction of the y axis
$\omega$	angular frequency (rad/s)
$f$	frequency (Hz)
$M$	molarity (mol/L)
$Q$	heat (J)
$\dot{Q}$	rate of heat flow $W = J/s$

$Q$	total charge (C)	
$k$	thermal conductivity $W/(m \cdot K)$	
$\delta$	boundary layer thickness	
$v$	velocity (m/s)	
$v_{inf}$	velocity of bulk fluid flow (m/s)	
$T_b$	temperature of a body (K)	
$T_{inf}$	temperature of surroundings (K)	
$U$	internal thermal energy (J)	
$C$	specific heat $J/(kg \cdot K)$	Chapter 6
$C_p$	specific heat at constant pressure $J/(kg \cdot K)$	
$C_v$	specific heat at constant volume $J/kg \cdot K$	
$C$	capacitance (F)	
$C$	capacitor	Chapter 8
$m$	mass (g)	
$V$	volume ( $m^3$ )	
$V$	voltage (V)	
$h$	position dependent heat transfer coefficient $W/(m^2 \cdot K)$	
$\bar{h}$	average heat transfer coefficient $W/(m^2 \cdot K)$	

$\alpha_b$	absorptivity coefficient (unitless)
$\epsilon_m$	emissivity coefficient (unitless)
$\epsilon_0$	permittivity of free space, $8.85418 \times 10^{-12}$ (F/m)
$\epsilon_r$	relative permittivity (unitless)
$\epsilon$	absolute permittivity (F/m)
A	surface area (m <sup>2</sup> )
$\sigma_{SB}$	Stefan-Boltzmann constant, $5.670 \times 10^{-8}$ W/(m <sup>2</sup> ·K <sup>4</sup> )
P	radiative power of emission of a blackbody (W)
$F_{1-2}$	radiative view factor
Pr	Prandtl number (unitless)
Re	Reynolds number (unitless)
Ra	Rayleigh number (unitless)
Nu <sub>L</sub>	Nusselt number (unitless)
Bi	Biot number (unitless)
Fo	Fourier number (unitless)
$\alpha$	thermal diffusivity (m <sup>2</sup> /s)
$\nu$	kinematic viscosity (m <sup>2</sup> /s)
$\mu$	dynamic viscosity kg/(m·s)

$\rho$	density (kg/m <sup>3</sup> )
$\rho_r$	electrical resistivity ( $\Omega \cdot m$ )
$L_c$	characteristic length (m)
$L$	length (m)
$L_T$	length (m) at temperature T (K)
$g$	acceleration of gravity in (m/s <sup>2</sup> )
$\beta$	coefficient of thermal expansion of a fluid (1/K)
$\Delta T$	temperature difference between surface and bulk fluid (K)
$G$	rate of heat generation
$V$	voltage (V)
$R$	resistance ( $\Omega$ )
$R$	resistor
$i$	current (Amperes)
$j$	imaginary number $\sqrt{-1}$
$\alpha_r$	temperature coefficient of electrical resistivity
$\sigma$	electrical conductivity ( $\Omega \cdot m$ ) <sup>-1</sup>
$L_z$	Lorentz number, $2.44 \times 10^{-8}$ (W $\cdot\Omega$ /K <sup>2</sup> )
$S$	Sutherland constant (K)

S	switch
l	mean free path (m)
$k_b$	Boltzmann constant $1.38064852 \times 10^{-23} \text{ (m}^2 \cdot \text{kg)/(s}^2 \cdot \text{K)}$
D	diameter of molecule modeled as a hard sphere (m)
P	pressure (Pa, atm)
$\gamma$	specific heat ratio ( $C_p/C_v$ )
$\rho_p$	ideal gas pressure mol/m <sup>3</sup>
$\tilde{v}$	mean molecular gas velocity (m/s)
$\varphi$	angle of impedance in rectangular form
$\angle_Z$	angle of impedance in polar form
$\theta$	phase shift
$X_C$	capacitive reactance ( $\Omega$ )
Z	impedance ( $\Omega$ )
Det.	detector

# LIST OF ABBREVIATIONS

ZPL	zero-phonon line
PSB	phonon sideband
ZnPP	zinc protoporphyrin
PPIX-Mb	protoporphyrin-IX -substituted horse-heart myoglobin
ZnPP-Mb	zinc protoporphyrin-substituted horse-heart myoglobin
PPIXDME-Mb	dimethylester protoporphyrin-IX -substituted horse-heart myoglobin
HOMO	highest occupied molecular orbital
LUMO	lowest unoccupied molecular orbital
MBPT	many-body perturbation theory
MRMP	multireference Møller-Plesset perturbation theory
SAC-CI	symmetry adapted cluster-configuration interaction
EOM-CCSD	equation of-motion coupled-cluster singles and doubles
STEOM-CCSD	similarity transformed equation of-motion coupled-cluster singles and doubles
CASSCF	complete active space self-consistent field
TDDFT	time-dependent density functional theory

DFT	time-independent density functional theory
CI	configuration interaction
CC	coupled-cluster
EOM-CCSD	equation-of-motion coupled-cluster single double
MRCI	multireference configuration interaction
MCSCF	multi-configurational self-consistent field
XMCQDPT2	extended multi-configuration quasi-degenerate perturbation theory
CASPT2	complete active space perturbation theory, 2 <sup>nd</sup> order
MPn	Møller–Plesset perturbation theory, n <sup>th</sup> order
VI	virtual instrument
APD	avalanche photodiodes
CTCSM	cryogenic temperature confocal scanning microscope
S/N ratio	signal to noise ratio
CCD	charge-coupled device
EMCCD	electron multiplying charge-coupled device
PSF	point spread function
CMOS	complementary metal–oxide–semiconductor
AFM	atomic-force microscopy

FWHM	full width at half maximum
HWHM	half width at half maximum
PID	proportional–integral–derivative control
DMSO	dimethyl sulfoxide
SPCM	single photon counting modules
TTL	transistor–transistor logic
PL	pump laser
RDL	ring dye laser
RC	reference cavity
M	silver coated mirror
I	iris
IS	intensity stabilizer
MM	motorized mirror
BS	beam sampler
PSD	position sensitive detector
G-T	Glan-Taylor prism
FR	Fresnel rhomb
OBJ	objective



OF	optical fiber
L	lens
DIC	dichroic mirror
EM	emission filter
SPAD	single-photon avalanche diode
PC	photon counter
CPU	computer central processing unit
RDL Control	ring dye laser control box
TC	temperature controller
WM	wave meter
RC	reference cavity
CAD	computer-aided design
MHV	miniature high voltage connector
BNC	Bayonet Neill–Concelman connector
AWG	American wire gauge
SRS	Stanford Research Systems
HV	high voltage
PMT	photomultiplier tube

Cond	conduction
Conv	convection
Rad	radiation
SUS 304	stainless steel 304
NIST	National Institute of Standards and Technology
AC	alternating current
DC	direct current
RC	resistor- capacitor circuit
Re	real axis
Im	imaginary axis
CNC	computer numeric control
LCAO-MO	linear combination of atomic orbitals to form molecular orbitals
GAMESS	General Atomic and Molecular Electronic Structure System

# I

## Chapter 1

### **System and Method of Study**

#### **1.1 Introduction**

The driving force behind the physical and chemical behavior of molecules are the interaction of the electronic properties of the molecule with the surrounding environment. In environments that possess specifically ordered structures, like those found in the active regions of proteins, it is easy to expect that internally generated electric fields could enhance or even facilitate functionality. Ordered electric fields have been shown to have catalytic effect on bond formation [2] and, in biological systems, have been attributed to processes involving charge separation and transport [8,43]. Thus, the potential for intrinsic fields to play an important role in the electrostatic steering of ligands towards binding sites seems realistic. To allow for a more precise mechanistic understanding of such binding phenomena, gaining a quantitative description of the internal molecular electric fields existing within active sites, as generated by the pocket residues as well as the outer shells of the protein, could be of great benefit.

The following is an introduction to the molecular system of study and to the various spectroscopic techniques that are used for this inquiry. A description of the

underlying physics governing the different spectroscopic techniques used and the properties of the system that are of specific benefit for use in these types of investigations are covered.

## **1.2 Structure Leading Function**

Protein structure is representative of a dynamic environment possessing both ordered and disordered character. The ordered nature arises from the specific sequence of residues that ultimately create and influence the well-defined tertiary structure. For enzymatic proteins, this well-defined tertiary structure allows for the prosthetic groups to be held in active forms. The disordered nature of proteins arises from the mobility, of and in-between domains, allowing for the conformational rearrangement and flexibility necessary to facilitate ligand entrance and exit to active regions. The conformational degrees of freedom available to the protein are then determined by charge distributions as created by various macromolecular assemblies. The specialized microenvironments dawning from tertiary structure, existing around active regions, arise from the specific arrangement of pocket residues capable of exerting directed electric fields that modify prosthetic group charge distributions in order to provide the appropriate complementarity for ligands through noncovalent interactions.

The specific role that these charge distributions play on influencing ligand binding dynamics, facilitating reactivity and specificity, and biological functionality, have yet to be fully understood. Three questions then come to light. What is the relationship between chemical structure and physical properties? What are the

magnitudes and directions of the fields the protein imparts on the prosthetic group? Lastly, can we quantitatively determine the specific internal field required for proper function of the system? At present, many scientists have and are devoting much research effort towards the clarification of the mechanistic aspects of protein functionality [7, 9, 19, 49]. This investigation seeks to determine the internal molecular electric fields that are present at the oxygen binding site of myoglobin. The specific electrostatic nature of the pocket residues and their potential contribution to the functionality of the protein are of interest.

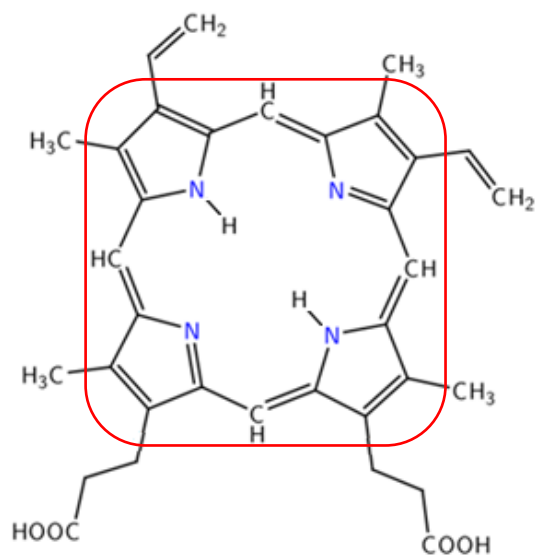
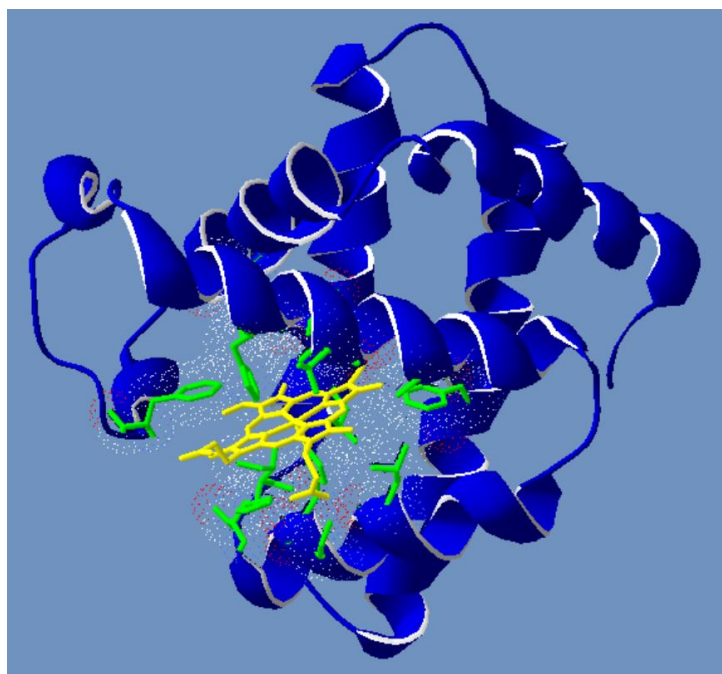
### **1.3 Myoglobin**

The system of interest is the oxygen storage protein myoglobin. Myoglobin is a metalloprotein that is found in the muscle tissues of most mammals. The metal ion cofactor giving native myoglobin its metal character is a single atom of ferrous iron ( $\text{Fe}^{2+}$ ), which is situated at the center of a protoporphyrin crown complex [5]. This prosthetic group, which resides within the protein, is known as heme. A proximal histidine is responsible for binding to the cofactor, and a distal histidine is responsible for keeping the ferrous iron in the reduced state and aids in blocking CO binding. Myoglobin, a 153 amino acid long polypeptide sequence, is a globular protein that is similar in structure to the individual alpha and beta subunits of hemoglobin. Myoglobin possesses a monomeric structure and hemoglobin possesses a tetrameric structure. Despite the fact that myoglobin and the alpha and beta subunits of hemoglobin are identical at only 27 positions within their amino acid sequence, their functionality is

largely the same [40]. The main difference between these two proteins is that the primary function of myoglobin is oxygen storage, and the primary function of hemoglobin is oxygen transport. An additional difference is that myoglobin is capable of binding a single molecule of oxygen, whereas hemoglobin is capable of binding up to four molecules of oxygen. The globular nature of myoglobin arises from the tertiary structure of the molecule, which has hydrophilic charged amino acids organized on its surface, and hydrocarbon-rich hydrophobic amino acids situated towards its core. The iron ion at the center of the heme group has a strong interaction with the oxygen which facilitates the binding of the oxygen molecule. The heme group sits in a deep pocket on one side of the protein. The ligand binding pocket displays a high localization of primarily positive charge, and the asymmetric protein heme pocket creates an electrostatic environment that alters the electronic structure of the prosthetic group heme [40].

Myoglobin was the first protein for which the atomic structure was determined. This work was done in 1958 by John Kendrew and coworkers. This determination was performed on sperm whale myoglobin using the now standard x-ray crystallographic method. This first structure is 1MBN. Since this early work, more than 395 crystal structures for myoglobin from various species have been determined [59]. Myoglobin represents one of the most studied proteins in all of biological science [5, 24, 25].

Figure 1.1 displays a structure of horse-heart myoglobin that was prepared using the platform Swiss-PdbViewer [15]. The structure displayed is that of 1DWT as determined by Chu and coworkers in 2000 by x-ray diffraction at a resolution of 1.40 Å [7]. The ribbon structure is displayed in blue and the heme group is displayed in yellow.



<b>Eleven Closest Amino Acids and Distances to Heme Center (Å)</b>								
HIS 93	<b>(B)</b>	<b>2.14</b>	HIS 97	<b>(B)</b>	<b>5.52</b>	ILE 107	<b>(N)</b>	<b>6.61</b>
HIS 64	<b>(B)</b>	<b>4.34</b>	ILE 99	<b>(N)</b>	<b>5.73</b>	SER 92	<b>(P)</b>	<b>6.7</b>
VAL 68	<b>(N)</b>	<b>4.4</b>	LEU 89	<b>(N)</b>	<b>5.95</b>	LEU 29	<b>(N)</b>	<b>6.99</b>
PHE 43	<b>(N)</b>	<b>5.13</b>	LEU 104	<b>(N)</b>	<b>6.36</b>			
<i><b>B</b> = Basic</i>		<i><b>A</b> = Acidic</i>		<i><b>N</b> = Non-polar</i>		<i><b>P</b> = Polar</i>		

Figure 1.1: Top Left: PPIX (yellow) in myoglobin, with eleven closest residues (green) to oxygen binding center displayed along with van der Waals surfaces. Top Right: PPIX including side groups. Methyl, vinyl and propionic groups outside of the red box, are viewed as part of the protein environment for the electronic structure calculations of this particular investigation. Bottom: Distances (Å) of green residue from heme center in table. Image created with SwissPDB.

The oxygen binding site is at the center of the heme group, on the top side of the porphyrin plane as shown in the image. This occurs on the distal side of the heme, with the oxygen molecule being partially stabilized by the distal histidine [40]. The eleven closest residues to the oxygen binding center are displayed in green along with their van

der Waals surfaces. The adjoining table specifies the distance of these residues to the heme center. Protoporphyrin-IX, the iron-free heme analogue used in spectroscopic studies is also displayed, with the porphine core that is used in electronic state calculations boxed in red.

Advantageous to this particular investigation is the presence of the heme group already present within the binding site [5]. Although a chromophore itself, heme is non-fluorescent. Therefore, fluorescent candidates that have transitions to long lived states, which result in narrow spectral line-widths, are used [33, 49, 53]. Currently, protoporphyrin-IX -substituted horse-heart myoglobin (PPIX-Mb) is used during hole-burning spectroscopic studies. Previous experimenters have found that chromophore replacement does not significantly alter a protein's environment, with the chemical shift of the proton resonances typically changing by only 0.1-0.2 ppm, and therefore, despite this substitution, the electric field that is present in the native protein remains effectively conserved [28]. To more fully understand the various contributing factors defining the electric fields that reside within the protein cavity, eventually, the zinc substituted porphyrin, ZnPPIX-Mb, and dimethylester substituted porphyrin, PPIXDME-Mb, will be placed into myoglobin for hole-burning trials.

For all of the spectra involving protoporphyrin-IX-substituted horse-heart myoglobin that appear throughout this document, the substitution process was graciously performed by Hannah E. Wagie. The substitution process was modeled on the methodology outlined by Teale 1959 and also that of Angiolillo 1998, and uses a methylethylketone extraction procedure for removal of the native heme [1, 57]. An abridged procedure appears in Appendix A. To make a spectroscopic quality glass, the



substituted protein is placed in an amorphous 3:1 (volume:volume) glycerol:water matrix. The 3:1 glycerol:water is used as a host matrix because it possesses a refractive index (1.4353, 20 °C) that is close to that of the objective lens, quartz (1.4601, 20 °C) thereby minimizing any resulting spherical aberrations that are caused by refractive index mismatches, leading to an enhanced quality of the collected signal during optical investigations [21, 31].

## 1.4 Porphyrin

The initial chromophore used for detecting the internal electric field generated within the active site of the myoglobin protein is protoporphyrin-IX (PPIX). The parent structure of all porphyrins and metalloporphyrins is porphine. Porphine has a basic ring structure that is composed of four pyrrole subunits that are linked together by four methine bridges. These linkages create a 24-atom aromatic macrocycle with 26  $\pi$  electrons. The inner 16-membered ring with 18  $\pi$  electrons represents the principal resonance structure and is responsible for the unique absorption properties of porphyrins and porphyrin derivatives. This highly delocalized semi-planar  $\pi$ -framework can be populated with many different peripheral substituents at its eight pyrrole carbon, and four meso-carbon centers, allowing porphyrins to exist in many forms. The ring's ability for metal complex formation is due to the size of the macrocycle. The high flexibility of modifications that can be made to the parent porphine structure has contributed to

porphyrin-related molecules being used as catalysts [35], in creating nonlinear optical materials [55], as dye laser elements [14], as photovoltaic materials [53] and as agents used for photodynamic therapy [49].

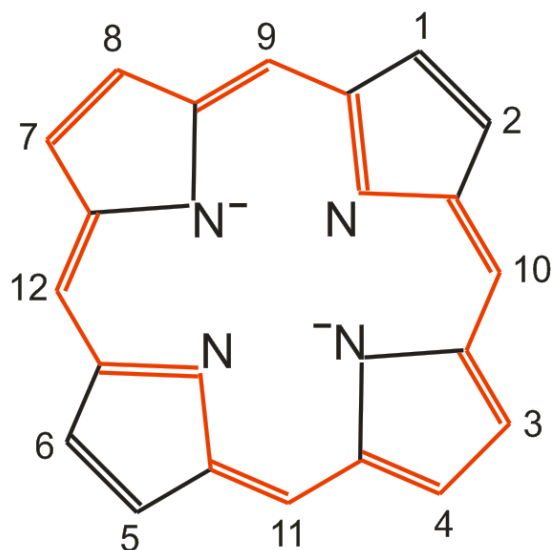


*Figure 1.2: Porphine dianion. Protonation of the central nitrogens yields porphine, representative of the parent core that is common to all porphyrin derivatives. Inner 16-membered ring is displayed in red. Peripheral substituents can be added at positions one through twelve.*

The tunability of the optical properties of these types of molecules comes from the inclusion of hydrogens or metals at the center of the ring, or different substituents at the carbon positions, which are then responsible for the spectral variations observed across different porphyrin species [14]. Variation of peripheral substituents typically tend to have a small influence on recorded spectra, whereas protonation or metalation at the ring center result in large spectral changes. The most notable spectral change occurs in the Q-bands, which collapse from a four-band structure in the free-base case,

PPIX, to a two-band structure upon metalation. This simplification of the spectral profile results from the shift in molecular symmetry from rectangular  $D_{2h}$  to square  $D_{4h}$  when the free-base porphyrin is metalized [14].

The typical features that are characteristic to the optical spectra of porphyrin and porphyrin derivatives are two distinct absorption regions that are designated as the higher energy Soret or B-band appearing between 380-450 nm that has an intense absorption, and the several lower energy Q-bands appearing between 500-800 nm that possess relatively weaker absorptions [11, 39, 52]. These features are commonly and most generally described within the framework of the semi-quantative molecular orbital based “four-orbital model”, as first outlined and applied by Martin Gouterman in the 1960’s [13, 14]. This highly successful yet simplified model, which reproduces the major features of these systems, states that the transitions ( $\pi$ ,  $\pi^*$ ) to low-lying excited states result in the visible absorption spectrum. These are represented as linear combinations of one-electron electronic transitions and correspond to transitions from the two highest occupied molecular orbitals HOMO and HOMO-1, into that of the two lowest unoccupied molecular orbitals, LUMO and LUMO+1. The nearly degenerate HOMO and HOMO-1 are designated as  $a_{2u}(\pi)$  and  $a_{1u}(\pi)$  states and the LUMO and LUMO+1 are degenerate and are both  $e_g(\pi^*)$  states. According to a Hückel theory treatment only, the  $a_{2u} \rightarrow e_g$  results in the lower energy Q-bands with the higher energy B-bands resulting from the  $a_{1u} \rightarrow e_g$  transition. These transitions were shown to have nearly equal transition moments and absorption strengths across the bands and thus only partially explain the observed spectra. The symmetry assignments are only strictly valid for the case where porphyrins possess  $D_{4h}$  symmetry [6, 14, 26, 53]. Upon a relaxation of the symmetry to

$D_{2h}$ , describing that of free-base porphyrin, the assignments for the irreducible representations become HOMO-1  $b_{1u}$ , HOMO  $a_u$ , LUMO  $b_{2g}$ , LUMO+1  $b_{3g}$ . To improve upon the accuracy of the model, implementation of Pariser-Parr-Pople (PPP) Theory, which includes electron correlation amongst the active  $\pi$  electrons, led to a differentiation of energy across the four states involved and a more accurate assignment of the differences in transition strengths that more closely described the observed spectral features.

With the advancements in computational power available to modern researchers, new descriptions have been formulated that seek to enhance the understanding of the optical properties of these porphyrin systems that the four orbital model could not fully explain. Many theoretical studies using different treatments including many-body perturbation theory (MBPT) [41], multireference Møller-Plesset perturbation (MRMP) [19], symmetry adapted cluster-configuration interaction (SAC-CI) [18,38], similarity transformed equation of-motion coupled-cluster singles and doubles (STEOM-CCSD) [16], complete active space self-consistent field (CASSCF) [19, 50], and both time-dependent and time-independent density functional theory (TDDFT, DFT) [18, 41, 50] have been performed. These studies have led to more complete descriptions of the differences in relative absorption intensity across the B-band and Q-band.

In all porphyrins, the absorption intensity of the B-band is much greater than the Q-band. The intensity ratio between these bands is, however, affected by metalation and peripheral substituents [13,50]. It is well studied that the B-band and Q-band arise from linear combinations of one-electron transitions [16, 18, 19, 38, 58]. The Q-band is made of transitions that are dipole allowed but are optically weak due to alternate

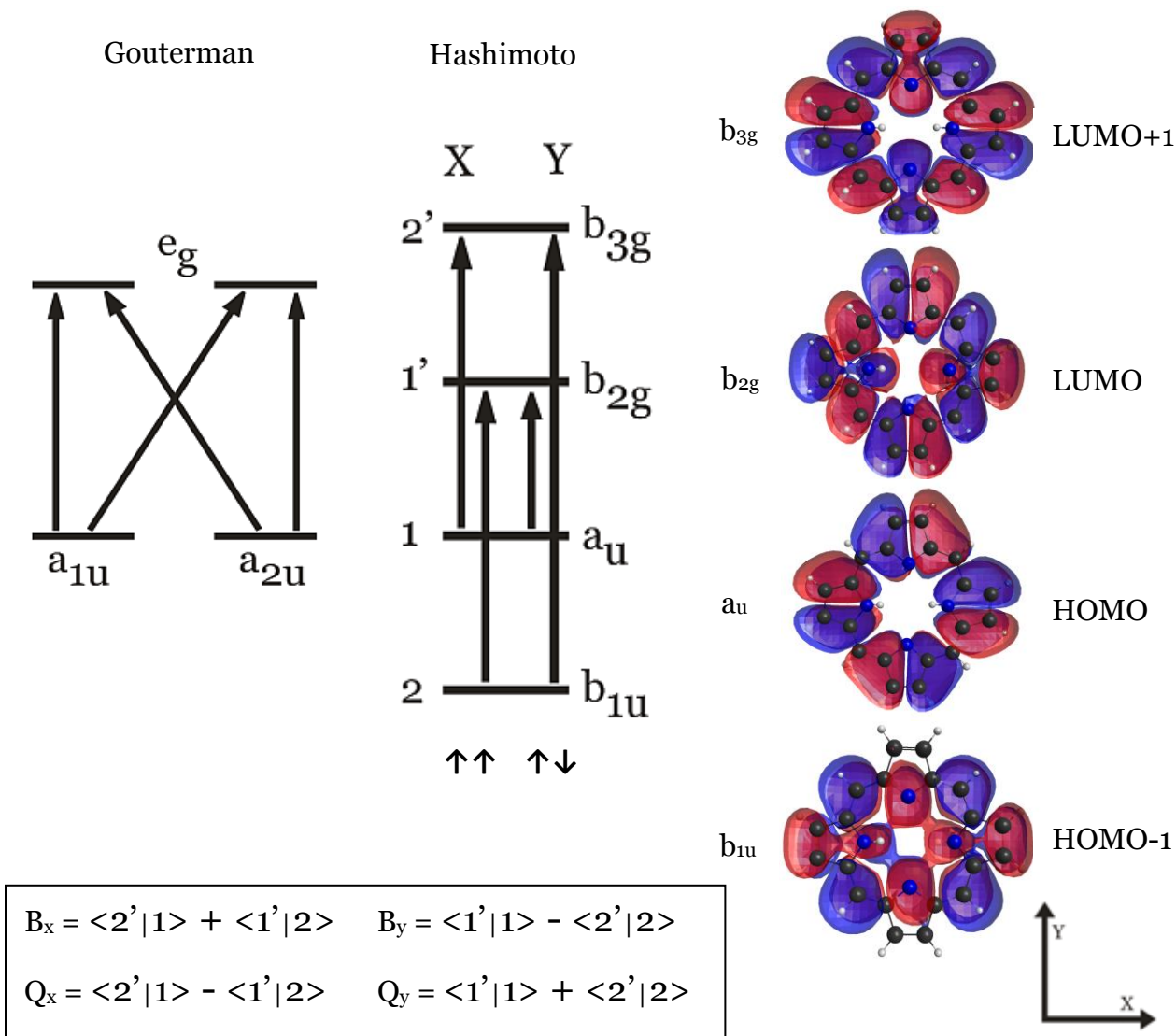


Figure 1.3: Left: Schematic diagram of orbitals and transitions creating the Q and B-bands according to the “four-orbital model” of Gouterman using  $D_{4h}$  symmetry [14]. Using  $D_{2h}$  symmetry, both Gouterman and Hashimoto assign the same irreducible representations. Center: Orbitals and transitions creating the Q and B-bands according to Hashimoto [19], energy levels are spaced for clarity of description. Bottom Left: Transitions responsible for visible transitions ( $B_y, B_x, Q_y, Q_x$ ) of porphyrin [19]. Right: Image of the four orbitals of importance. PPIX hydrogens are oriented along the x-axis, with axis shown. These orbitals were calculated with the GAMESS platform and displayed via MacMolPlt using PPIX with molecular coordinates taken from 1DWT [4, 7, 51].

symmetry, whereas, in the B-band the transitions are reinforced leading to the enhanced absorption intensity. The transitions responsible for the optical spectra of porphyrins and porphyrin derivatives, as presented in the “four-orbital model” of Gouterman, as well as that of Hashimoto *et al.* determined using more modern approaches, appear in figure 1.3. The orbital energies of Hashimoto are pseudo-degenerate across HOMO and HOMO-1, and LUMO and LUMO+1, and have been exaggerated for clarity of discussion. Under a  $D_{2h}$  symmetry, both Gouterman and Hashimoto assign the same irreducible representations to the orbitals involved, which are those that are shown for the Hashimoto model [41,50]. Displayed are the transitions that account for the X and Y components of the B and Q-bands. The one electron transition moment vectors are parallel for transfer between states  $2 \rightarrow 1'$  and  $1 \rightarrow 2'$  and the transition moment vectors are anti-parallel for transfer between states  $1 \rightarrow 1'$  and  $2 \rightarrow 2'$ . In the case of the lowest lying optical excited state transition, the Qx band, the transition energies are nearly degenerate and the two transition moments are parallel and add with opposite parity, and thus nearly cancel resulting in a transition that is formally semi-forbidden, which accounts for its relatively weak absorption properties. In the case of the Bx band, the transition energies are again nearly degenerate and the two transition moments are parallel, but add with the same parity, and thus reinforce resulting in a transition that is allowed and possesses strong absorption properties. The transitions accounting for the Y components of the B and Q-bands have anti-parallel transition moment vectors. For the Qy band, the transition energies are also nearly degenerate, but because the transition moments add with the same parity, they again nearly cancel producing the weak absorption. The By band is again reinforced due to the anti-parallel transition moment vectors being added with opposite parity leading to the strong absorption of

this band. These findings are consistent with those of other researchers that have applied advanced computational treatments [16, 18, 28, 58] to the modeling of porphyrin systems.

A point of note is that both Hashimoto *et al.* [19], and Tokita *et al.* [58] present a consistent description to that outlined above. Hasegawa *et al.* [18] switches the labeling of the transitions accounting for the X and Y components of the bands (with transitions  $1 \rightarrow 1'$  and  $2 \rightarrow 2'$  considered as X, and  $2 \rightarrow 1'$  and  $1 \rightarrow 2'$  considered as Y), and still assigns to the Y components anti-parallel transition moment vectors and parallel transition moment vectors to the transitions X components. The parity assignments describing the linear combinations corresponding to the  $B_y$ ,  $B_x$ ,  $Q_y$ ,  $Q_x$  are, however, conserved. All authors do report that the transition moment vectors of the  $B_x$  and  $Q_x$  bands are orthogonal to the  $B_y$  and  $Q_y$  bands. The accurate understanding of the electronic properties of these types of systems is still a highly active field of research. With the continued growth in computational resources, these systems will undoubtedly continue to receive much attention with our understanding and description continuing to change in the years to come.

Figure 1.4 displays an example of an absorbance spectrum of the Q-band of Protoporphyrin-IX in a 3:1 glycerol:water matrix. The Soret or B-band is not shown in order to enhance the clarity of the Q-bands. Additionally, this investigation relies on spectroscopic studies that involve only the lowest lying energy transition, namely the  $Q_x$  o-o transition. In the case of protoporphyrin-IX, due to the lowering of symmetry from the metalized ( $D_{4h}$ ) to free-base ( $D_{2h}$ ) form, the X and Y components of the Q-band show an additional splitting from two to four separate peaks. The additional bands are the

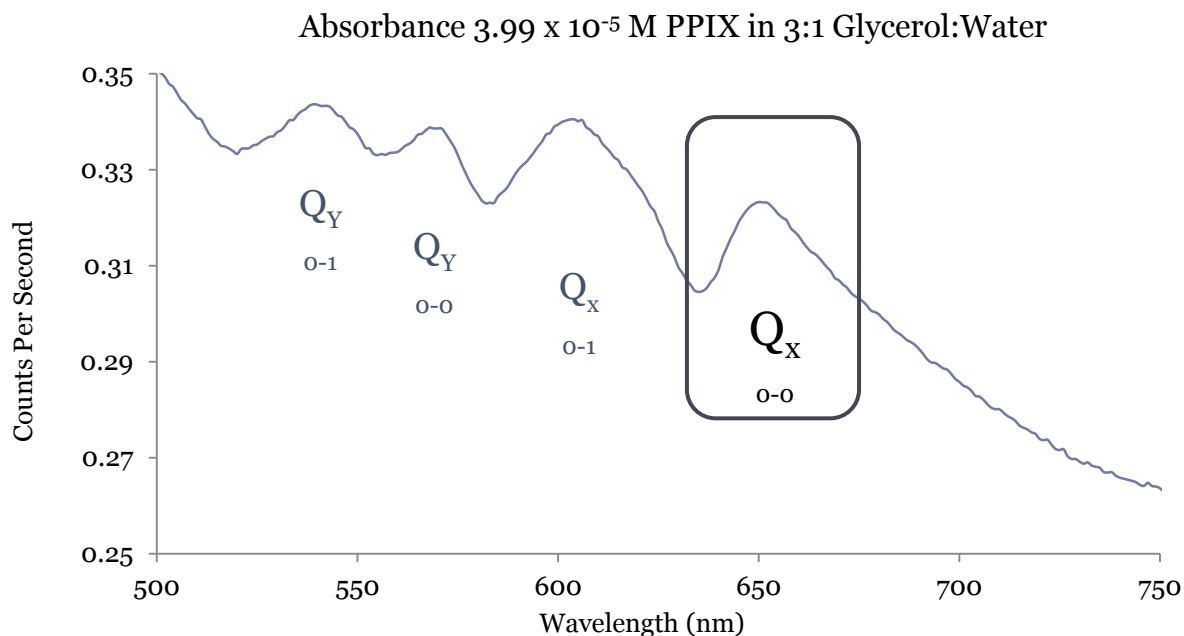


Figure 1.4: Absorbance spectrum of  $3.99 \times 10^{-5}$  M PPIX in 3:1 glycerol:water acquired using a Perkin Elmer Lambda 650 UV/VIS Spectrometer. Due to its much greater oscillator strength, the Soret band ( $S_0 \rightarrow S_2$ ) is the favored transition and has a significantly larger optical density than the Q-band ( $S_0 \rightarrow S_1$ ) transitions. The Soret band at  $\lambda_{max} \approx 430$  nm is not displayed for enhanced clarity of the Q-band peaks. This experimental investigation involves spectroscopic studies utilizing only the lowest lying energy transition, namely the Q<sub>x</sub> 0-0 transition, as highlighted above.

vibrational 0-1 additions to the respective bands. The four components of the Q-band are labelled, with the transition of interest utilized throughout this study during the hole-burning investigations outlined.

## 1.5 Chromophores Within Host Matrices

The absorption profiles of chromophores that either exist as isolated single molecules or exist within the gas phase are populated by narrow peaks corresponding to transitions to excited states that possess line widths limited only by the finite lifetime of the excited



state. When chromophores are placed in either the liquid or solid phase, these peaks consequently broaden due to molecular interaction and the presence of the host matrix [3, 44].

In the specific case of an idealized perfect crystal, in which all of the embedded chromophores are oriented in precisely the same way and thus exist in identical local environments, the absorption lines of the individual chromophores will exactly overlap. Because these absorbers all sit in identical environments, the observed ensemble line-width is simply the intrinsic line-width of the molecular transition, which is called the homogeneous line-width,  $\Gamma_H$ . At liquid helium temperatures typical homogeneous line-widths have been observed to be as narrow as 1 kHz to 100 MHz [36]. The homogeneous line specifying the electronic transition possesses the line-shape of the purely electronic zero-phonon line (ZPL) described by a Lorentzian distribution, and is accompanied by a broad phonon sideband whose shape is that of a Poisson distribution. It is the width of only the ZPL that defines the homogeneous line-width. The thermal characteristics of the system not only dictate the relative width of the ZPL but also the dispersion of intensity across these two coupled regions, the ZPL and the phonon sideband [17, 23]. The total integrated intensity of the ZPL and phonon sideband is representative of the full oscillator strength (intensity) of the electronic transition.

As depicted in figure 1.5, the general line-shape for an electronic transition consists of these two components and the normalized line-shape function that models the homogeneous absorption band  $F_H(\nu, T)$ , is both frequency and temperature dependent and takes the following form.

$$F_H(\nu, T) = \alpha(T)L_{ZPL}(\nu, T) + (1 - \alpha(T))P_{PSB}(\nu, T) \quad (1.1)$$

Here the Lorentzian shaped function describing the zero-phonon line  $L_{ZPL}(\nu, T)$ , and the Poisson shaped function describing the phonon sideband  $P_{PSB}(\nu, T)$ , are related by the Debye-Waller factor  $\alpha(T)$ . The Debye-Waller factor is a ratio of the relative integrated intensity of the ZPL to that of the entire homogeneous absorption band, and indicates

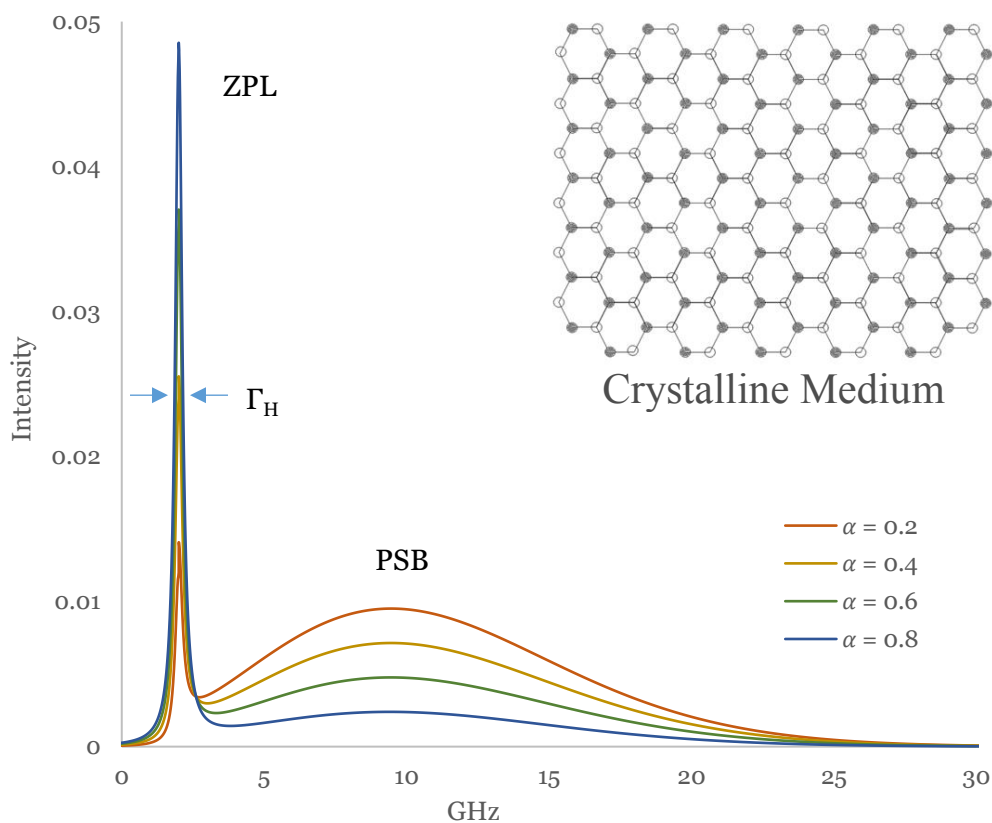


Figure 1.5: Upper Right: Representative depiction of a perfect crystalline medium where all embedded chromophores possess the same molecular orientation and reside in identical energetically equivalent local environments resulting in precise spectral overlap across the entire population of chromophores. Bottom Left: Expected line-shape of electronic transition in perfect crystalline medium at liquid helium temperatures. The width of the ZPL defines the homogeneous line-width,  $\Gamma_H$ , is accompanied by the broad phonon sideband. The Debye-Waller factor  $\alpha(T)$ , describes the distribution of integrated intensity between the ZPL and phonon sideband which represents the total oscillator strength of the transition.

the relative strength of the electron-phonon coupling at a specified temperature.

$$\alpha(T) = \frac{\int L_{ZPL}(\nu, T)}{\int L_{ZPL}(\nu, T) + \int P_{PSB}(\nu, T)} \quad (1.2)$$

Across all temperatures, the total integrated intensity of the ZPL and the phonon sideband remains constant. A result of this specification is that as the temperature of the system is elevated, the Debye-Waller factor decreases and a shift of intensity from the ZPL towards the phonon sideband naturally occurs. At temperatures as high as 10 K, the ZPL component of the homogeneous band becomes greatly diminished, and generally completely disappears at temperatures beyond 20-50 K [17, 46].

Optimally, for high resolution spectroscopic applications the intensity of the electronic transition would reside entirely within the zero-phonon line, with minimal intensity distributed to the phonon sideband. This situation is best realized only at zero kelvin, with elevated temperatures having an ever increasing influence on the shifting of intensity away from the ZPL to the phonon sideband. At zero kelvin only the zero-point motion will exist with the phonon modes, quantized mechanical lattice vibrations, being absent in the matrix within which a chromophore is embedded. In this situation the homogeneous line-width  $\Gamma_H(0)$ , of the ZPL is dependent solely upon the excited electronic state decay time  $\tau_1$ , the energy relaxation time of the particular transition under investigation. For transitions in the optical range, decay times are generally on the order of  $10^{-7}$  to  $10^{-8}$  seconds, and formally under the units of frequency, homogeneous line-widths are determined as follows.

$$\Gamma_H(0) = \frac{1}{2\pi\tau_1(0)} \quad (1.3)$$

The narrow nature of the ZPL results in an exceeding sharp temperature dependence, and these zero-phonon lines display additional broadening, beyond that related to the electronic decay time, at all other temperatures. The presence of thermal phonons increases with temperature as does the electron-phonon coupling interaction at the site of the chromophore. The scattering of phonons at these sites impart no exchange of energy between the electrons and phonons, but shift the coherence of phase of the excited state wave function. This destabilization of the wave function greatly reduces the excited state lifetime. This dephasing mechanism affecting the line-width of the ZPL is accounted for by the inclusion of an additional term  $\tau_2^*$ , the phase relaxation time of the transition, into equation 1.3. At all elevated temperatures, the homogeneous line-width of the ZPL can then be evaluated using the subsequent modified relation [23, 46].

$$\Gamma_H(T) = \frac{1}{\pi} \left( \frac{1}{2\tau_1(T)} + \frac{1}{\tau_2^*(T)} \right) \quad (1.4)$$

In the absence of additional non-radiative pathways, the pure excited state lifetime  $\tau_1$  remains fairly constant regardless of temperature. The high temperature dependence of the phase relaxation time  $\tau_2^*$ , consequently results in phonon dephasing being the primary contributor to the broadening of the homogeneous line.

In realistic crystals even at zero kelvin, the ZPL undergoes additional broadening, which occurs due to point defects in the lattice geometry of the host matrix and equation 1.3 is representative of the lower limit that the line-width of a ZPL could reach. In imperfect systems which possess some form of structural disorder, as is found in real polycrystalline and amorphous materials, the absorption line shape is observed to be

inhomogeneously broadened. This type of broadening is representative of the expected line-shape when chromophores are embedded in glassy matrices, or in proteins. Inhomogeneous broadening arises due to the individual chromophores existing in varied environments and experiencing outside effects anisotropically. This distribution of localized environments results in the chromophores all possessing different absorbing

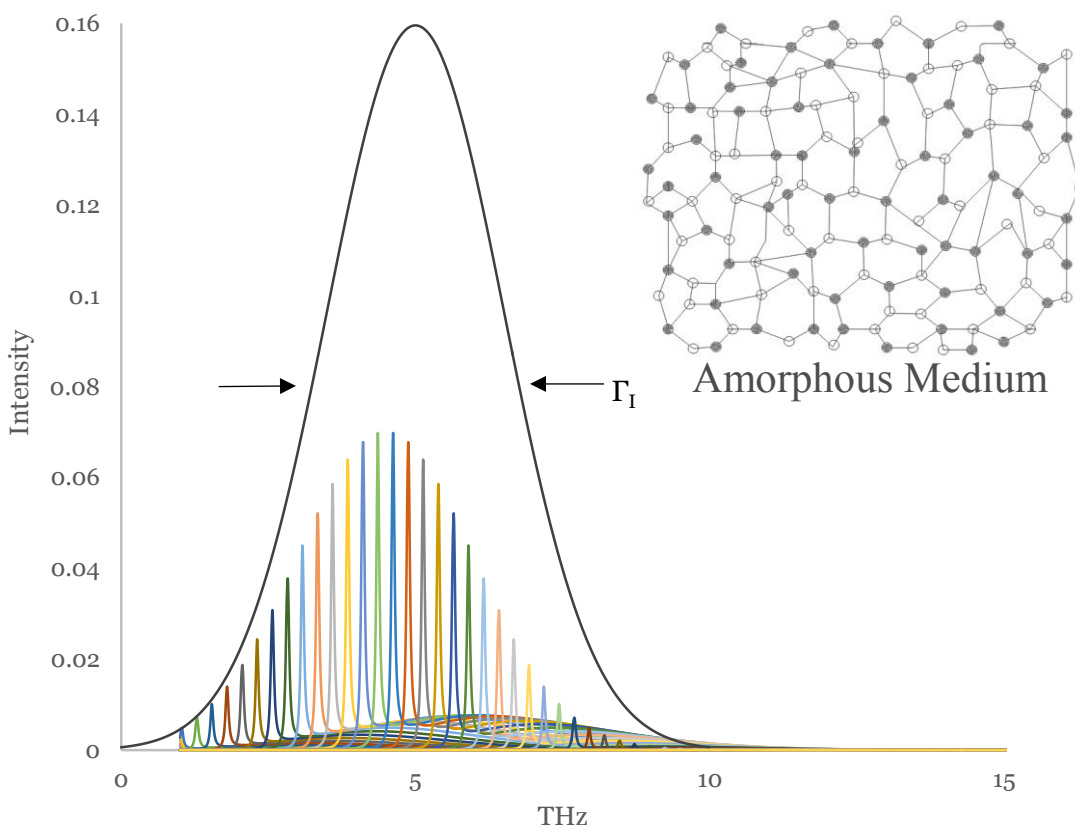


*Figure 1.6: Upper Right: Representative depiction of an amorphous medium where all embedded chromophores possess randomized molecular orientations and reside in energetically inequivalent local environments resulting in a distribution of ZPL center frequencies defining the electronic transition, across the entire population of chromophores. Bottom Left: Expected line-shape of an electronic transition of chromophores in an amorphous medium. The inhomogeneously broadened band follows a Gaussian distribution, has a line-width  $\Gamma_I$ , and is a superposition of the homogeneous line-widths of the individual color centers. Even at liquid helium temperatures,  $\Gamma_I > 10^5 \Gamma_H$ . Forty homogeneous line-shape functions  $F_H(\nu, T)$  with a Debye-Waller factor of  $\alpha=0.8$  are shown, of which represent only a subset of those that constitute the entire inhomogeneously broadened band.*

and emitting energies for a specified electronic transition, across the entire population of molecules. The inhomogeneous band, which takes the form of a Gaussian distribution, is made up of the homogeneous line-widths of the individual chromophores and is representative of this environmentally induced distribution in transition frequencies [30]. The inhomogeneous line-width,  $\Gamma_1$ , can span from several 100 MHz to 10 THz even at liquid helium temperatures, being on the order of up to  $10^5$  times more broad than a typical homogeneous line-width [36, 47].

## 1.6 Spectral Hole-Burning

Spectral hole-burning is a high resolution spectroscopic technique that allows spectral features on the order of the homogeneous line-width to be probed in samples that possess inhomogeneously broadened spectra. Hole-burning can be performed on samples that are placed in an environment at temperatures near zero kelvin, when ZPL's approach their lifetime limited values. This technique [23], along with fluorescent line narrowing spectroscopy [42], single molecule spectroscopy [47], and photon echo experiments [29], are among the few techniques that allow scientists to regain the spectral resolution that is lost due to inhomogeneous broadening.

In order for spectral hole-burning to be performed, a few criteria must first be met by the sample under study. As already specified, the chromophores absorption must be inhomogeneously broadened, and Debye-Waller factors should approach unity, specifying that the oscillator strength defining the optical transition resides predominantly within the ZPL, which is only the case at temperatures around zero

kelvin. The chromophore must be capable of undergoing a photochemical reaction that is induced by either a one or two-photon process. There must exist a stable local conformational ground state configuration for the photoproduct that is energetically different from that of the chromophore. The laser line-width used to induce the photochemical transfer process between the two states, chromophore and photoproduct, must be narrower in frequency space than the energy differential between the two states. Lastly, the relaxation between these two configurations must exceed the time frame of the experiment. At liquid helium temperatures, these requirements have been observed to be met for a variety of rare earth ions, and inorganic and organic dye molecules, when placed in mixed crystals, polymers, glasses, or amorphous matrices [10, 12, 36, 48, 54].

A spectral hole-burning experiment can produce hole profiles that are either transient or persistent in nature. Transient spectral holes arise due to a photo-saturation of the population of the probed absorbers and exist only during the time frame of the experiment, when under maintained illumination of the excitation source. The first spectral holes ever observed were of this variety, and although interesting, the short lived nature of these types of holes greatly limits the ability for perturbative experiments on the spectral hole profiles to be performed [56]. Persistent spectral hole-burning occurs when hole profiles remain after the initial illumination causing the spectral depletion has ceased. Based on the experimental conditions and particular molecules and host matrices involved, these holes can persist for extremely long time frames, and were for a while investigated for potential application in frequency domain optical storage devices [37]. Much of the hole-burning performed to date has been of this type.

The two mechanisms by which spectral holes develop dawn from either a photophysical or a photochemical process. A photophysical process is one by which upon illumination, the environment immediately surrounding the chromophore undergoes a transformation. In this case, the chromophore rearranges within the lattice, or the lattice itself undergoes rearrangement. As a result of these rearrangements, a different set of steric constraints are imparted by the microenvironment on the chromophore. This alters the molecular geometry of the chromophore and induces a shift of the spectral signature of the particular chromophore. In relation to the entire ensemble of absorbers, this then leads to formation of the spectral hole [20]. The other mechanism by which a spectral hole can develop is by a process that is photochemical. In this type of process, the chromophore under investigation undergoes a photochemical transformation. Examples of this type of process are the tautomerization of protons, photoionization or photodecomposition events, hydrogen bond rearrangements or changes of the molecular conformation such as isomerization [23, 36]. In this process, the change to the chemical structure of the molecules leads to different excited state energetics resulting in a photoproduct that absorbs in a different part of the spectrum. This depletion of the total number of absorbers results in a decrease in the observed intensity remaining at the particular burn frequency, thus forming the spectral hole.

These types of experiments require precise control over the sample, the environment of the sample, and the excitation source that is used for the burning and the reading of spectral holes. Samples to be investigated are prepared at low concentration and placed into a host matrix. Typically, concentrations of less than  $10^{-5}$  M are used. Low sample concentrations and low sample volumes that yield small optical



thicknesses are used to assure that chromophores are both non-interacting and undergo uniform exposure. Placing samples at cryogenic temperature contributes to the ability to capture the purely electronic transition during hole-burning. Hole-burning is then performed as a three-step process. The first step is to obtain a spectrum of the sample in its host matrix using a narrow frequency tunable laser. The inhomogeneous distribution

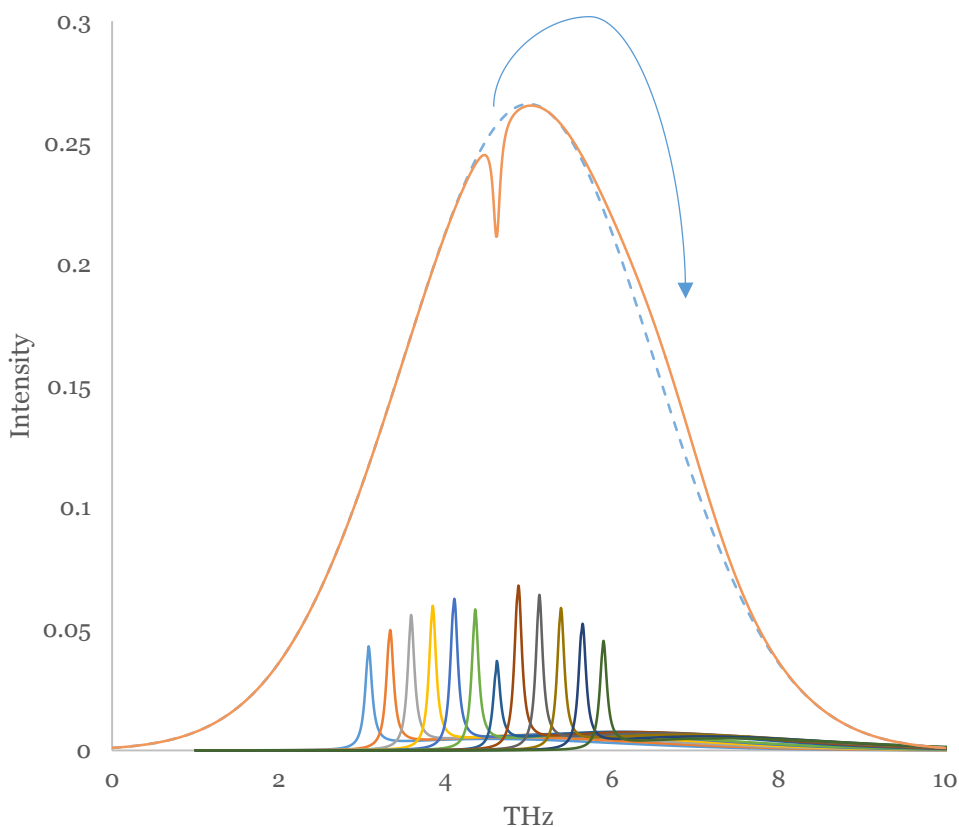


*Figure 1.7: Depiction of a spectral hole burnt into the inhomogeneously broadened band made up of the homogeneous linewidths of the entire population of absorbing molecules. The appearance of the photoproduct within the inhomogeneously broadened band reflects the outcome for the particular photochemical process for this experiment, namely the tautomerization of the two protons on the inside of the porphyrin ring. For other systems, the photoproduct may appear outside of the inhomogeneous distribution. The pre-burn distribution appears in blue with the post-burn profile appearing in orange.*

of the band is typically so broad, that over the frequency range probed (1-10's GHz), the recorded spectrum is essentially constant. Next, a place within the recorded spectrum is chosen, and generally with the same laser, but now at an intensity between 100 to  $10^5$  times greater than during the initial read cycle, a frequency matched sub-ensemble of the sample is photobleached [22, 34, 45]. The final step is to re-scan the sample over the frequency range of the initial read cycle and look for the appearance of the spectral hole within the spectrum.

It becomes instructive to understand which absorbers undergo the induced photochemical change and which absorbers the spectral hole is then in turn defined by. Hole-burning is a high resolution probing technique of the frequency-domain of the corresponding frequency-matched electronic transition. Ideally, the irradiation light is narrower than the homogeneous line-width of the transition. Due to the inhomogeneity of the band, absorbers in different local environments possess an accidental degeneracy. The burning light selects a subensemble of the total population and photobleaches those molecules for which the burning light is in resonance with the specific energy gap between a molecule's ground and excited states, regardless of the absolute energy value of the ground state. Thus, a spectral hole specifies the electronic transition in magnitude only [34]. Therefore, this is an averaging technique and operates only on a subset of all absorbers, allowing information regarding the average electronic transition values to be retrieved. In addition to the resonant energy selection, it is the chromophores that have a small angle between their molecular transition dipole moment and the polarization of the burning light, that will be preferentially selected during burning process and be photochemically affected. Those molecules with their

transition moments exactly aligned with the polarization of the incident light burn first and at a faster rate. The overall hole depth is then dependent on burning times and burning power of the incident radiation. There exists a dispersion in burning rates, whereby shallow holes are representative of those molecules that are more easily burnt and photochemically changed. As holes become deeper, molecules that are more resistant to the photobleaching process are affected and also undergo photochemistry. Any thermal agitation of the system, such as already present phonon modes or a thermal cycling of the sample, can induce spontaneous filling of a spectral hole. In shallow holes, this filling occurs more rapidly as these were the molecules most easily perturbed, with deeper holes displaying hole filling at a reduced rate. A spectral hole thus consists of absorbers that did not undergo phototransformation and remain in the original ground configuration. These remaining absorbers are those which outline the spectral hole and allow experimenters to observe the effects of other externally applied stresses to the sample, such as pressure, thermal or electric field perturbations [27, 32, 36].

As described above, a hole-burning experiment is a multi-step process. These steps being, first an initial scan of the absorption band, next the hole-burning process during which a subset of fluorophores undergo phototransformation, and then finally a re-scan of the absorption band to reveal the spectral hole profile. At minimum, this can be viewed as a two photon process, by which the first photon interacts with the subset of chromophore molecules by altering them photochemically and is responsible for the burning of the spectral hole, and the second photon, which interacts with the remaining fluorophores during the readout of the spectral hole. The resultant hole shape, then is a reflection of both of these processes. The general line-shape function describing a

photochemical hole, which is observed as a loss of optical density  $-\Delta D(\nu)$ , at a given frequency,  $\nu$ , in relation to the initial intensity as recorded during the original scan of the absorption band, is defined as below.

$$-\Delta D(\nu) = K \iint \underbrace{(\vec{\mu}_{mn} \cdot \vec{E}_{h\nu-B})^2}_{\text{Burn Photon}} F_H(\nu_b - \nu_0) \underbrace{(\vec{\mu}_{mn} \cdot \vec{E}_{h\nu-R})^2}_{\text{Read Photon}} F_H(\nu - \nu_0) d\Omega d\nu_0 \quad (1.5)$$

Here,  $\nu_b$  is the burn frequency,  $\nu_0$  is the center frequency for an absorbing molecule,  $K$  is representative of the total absorption cross section and the total number of chromophores present in the illuminated sample volume. Since hole-burning experiments are typically carried out using polarized light, and samples can potentially and frequently do contain randomly oriented chromophore molecules, various geometric considerations become of importance when determining if a molecule will contribute to a spectral hole. Of great importance are the polarization of the incoming photon used for the burning process, which can be denoted by the unit vector  $\vec{E}_{h\nu-B}$ , the unit vector  $\vec{\mu}_{mn}$ , describing the transition moment of the molecular transition, and lastly the unit vector  $\vec{E}_{h\nu-R}$ , denoting the polarization of the reading photon. The overlap of these various vector quantities will then determine if a particular absorber will be photochemically altered and then contribute to the hole shape during readout. To account for the overlap of these particular vector quantities and to account for all possible molecular orientations existing in the amorphous matrix that may contribute to the hole shape, integration over the complete set of Euler angles,  $\Omega$ , relating molecular coordinate frame to the lab coordinate frame is necessary. The remaining terms above

reflect the homogeneous line function from equation 1.1, for the burning and reading cycles. Specifically, the hole shape contribution from the burning photon is related to the probability that a chromophore with the center frequency of its ZPL at  $\nu_0$ , will absorb and be burnt by a photon of frequency  $\nu_b$ , that of the incident radiation. This portion of

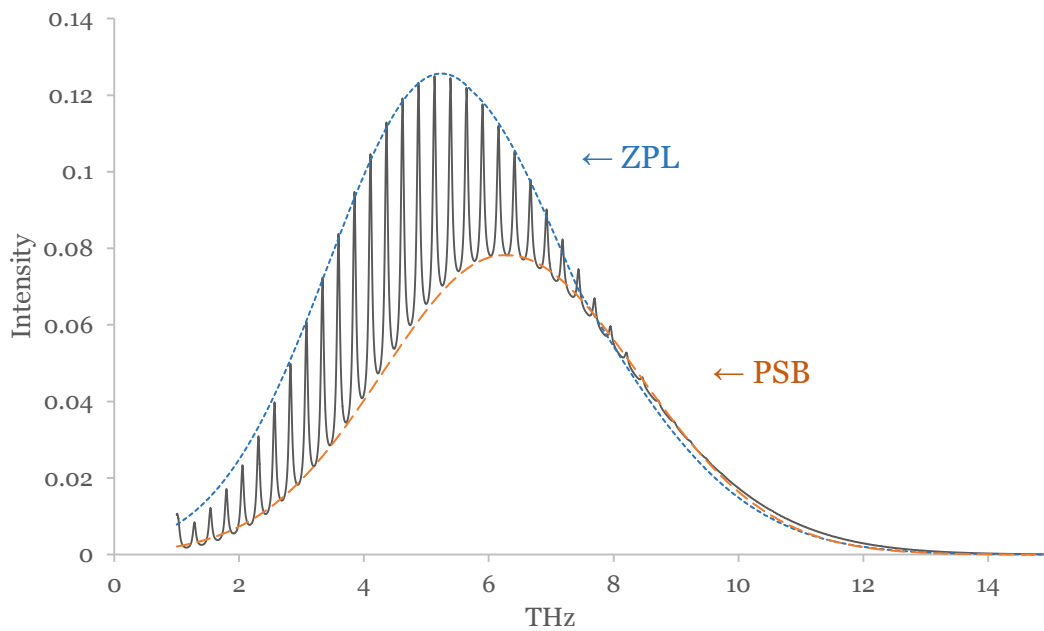


*Figure 1.8: Integration of the forty homogeneous line-shape functions displayed in figure 1.6. At higher frequencies, because of their additive nature, the phonon sidebands begin to overwhelm the total contribution to the inhomogeneous band profile in relation to the contribution from the ZPL's. Therefore, spectral holes should be burnt into the low energy side of the band, which is composed of predominantly the ZPL portion of the homogeneous line functions, allowing for the narrowest holes that approach the  $2\Gamma_H$  limit to be obtained.*

the hole shape equation accounts for any burning into the phonon sideband of a neighboring ZPL that is not centered at  $\nu_0$ . Burning into the phonon sideband ultimately results in a reduction of intensity of the neighboring ZPL and thus a broadening of the spectral hole is then observed. As displayed in figure 1.8, because of

the additive nature of the homogeneous line-shape functions that create the inhomogeneous band profile, at higher frequencies the contribution from the ZPL's are overwhelmed by the contribution from the phonon sidebands. For this reason, the narrowest holes are generally obtained when spectral hole-burning is performed on the red side of the band where the concentration of the higher energy phonon side bands is at a minimum. A similar contribution of the homogeneous line function also arises from the reading photon, and is related to the probability that a remaining absorber will be detected during this cycle. The relation defined in equation 1.5 will hold when the burning and reading cycles are performed at the same temperatures, minimizing any spectral diffusion and when burning times are short so the power broadening effects are negligible. Ideally, when these specifications are met the hole shape possesses a Lorentzian contribution from both the burning photon and the reading photon and is thus a convolution of the functions from each. In this case the spectral hole has a width that is twice the homogeneous linewidth,  $\delta = 2\Gamma_H$  [17, 27].

The method employed for this particular investigation is persistent photochemical spectral hole-burning. The specific process giving rise to the spectral hole formation is the tautomerization of the two protons on the inside of the porphyrin ring defining the x-axis of the plane, which upon illumination, photochemically shift to the y-axis of the plane. Although a photochemical process, this tautomerization can be likened to a 90-degree rotation of the porphine ring within the protein. Unlike typical photochemical hole-burning processes, the resultant photoproduct of this reaction resides within the inhomogeneous band, as opposed to being frequency shifted outside of the band [23, 27]. Although understanding the photoproduct is instructive, it is the

hole and its dynamics that are of primary consideration here. Because spectral holes serve as narrow frequency markers of electronic transitions and are extremely sensitive to any outside perturbations, and specifically in this investigation externally applied electric fields, it is this that will be utilized further for gaining insight of the molecular electric fields present within the active site of myoglobin.

## References:

- 1.) Angiolillo, Paul J., Vanderkooi, Jane M. (1998). "The Photoexcited Triplet State as a Probe of Chromophore-Protein Interaction in Myoglobin," *Biophysical Journal* 75, 1491-1502.
- 2.) Aragonès, Albert C., Haworth, Naomi L., Darwish, Nadim., Ciampi, Simone., Bloomfield, Nathaniel J., Wallace, Gordon G., Diez-Perez, Ismael., Coote, Michelle L. (2016). "Electrostatic catalysis of a Diels–Alder reaction," *Nature* 531, 88-91.
- 3.) Berezin, Mikhail Y., Achilefu, Samuel. (2010). "Fluorescence Lifetime Measurements and Biological Imaging," *Chemical Review* 110(5) 2641-2684.
- 4.) Bode B. M., Gordon, M.S. (1998). "MacMolPlt: a graphical user interface for GAMESS," *Journal of Molecular Graphics and Modeling* 16(3), 133-138.
- 5.) Brunori, Maurizio. (2010). "Myoglobin strikes back," *PROTEIN SCIENCE* 19, 195-201.
- 6.) Ceulemans, A., Oldenhof, W., Gorller-Walrand, C., Vanquickenborne, L. G. (1986). "Gouterman's "four-orbital" model and the MCD spectra of high-symmetry metalloporphyrins," *Journal of the American Chemical Society* 108 (6), 1155–1163.
- 7.) Chu, K., Vojtechovsky, J., McMahon, B.H., Sweet, R.M., Berendzen, J., Schlichting, I. (2000). "Crystal Structure of a New Ligand Binding Intermediate in Wildtype Carbonmonoxy Myoglobin," *Nature* 403 (6772) 921-923.
- 8.) de Silva, A. Prasanna., Rice, Terence E. (1999). "A small supramolecular system which emulates the unidirectional, path-selective photoinduced electron transfer (PET) of the bacterial photosynthetic reaction centre (PRC)," *Chemical Communications* 2, 163-164.
- 9.) Evans, Stephen V., Brayer, Gary D. (1988). "Horse Heart Myoglobin," *The Journal of Biological Chemistry* 263(9), 4263-4268.
- 10.) Fujita, Koji., Hirao, Kazuyuki., Tanaka, Katsuhisa., Soga, Naohiro., Sasaki, Hiroko. (1997). "Persistent spectral hole burning of Eu 3+ ions in sodium aluminosilicate glasses," *Journal of Applied Physics* 82(10), 5114-5120.
- 11.) Goldoni, A. (2001). "Porphyrins: fascinating molecules with biological significance," *ELETTRA Highlights Trieste* 2001-2002, 64-65.
- 12.) Gorokhovskii, A.A., Kaarli, R. K., Rebane, L.A. (1974). "Hole Burning in the contour of a pure electronic line in a Shpol'skii system," *JETP Letters* 20(7), 216-218.
- 13.) Gouterman, Martin. (1959). "Study of the Effects of Substitution on the Absorption Spectra of Porphin," *The Journal of Chemical Physics* 30(5), 1139-1161.



- 14.) Gouterman, M. (1978). Optical Spectra and Electronic Structure of Porphyrins and Related Rings. D. Dolphin (Ed.) *The Porphyrins Volume III*, 1–165. New York, NY Academic Press.
- 15.) Guex, N., Peitsch, M.C. (1997). “SWISS-MODEL and the Swiss-PdbViewer: An environment for comparative protein modeling,” *Electrophoresis* 18(15), 2714-2723. Swiss PDB Program At: <http://www.expasy.org/spdbv/>
- 16.) Gwaltney, Steven R., Bartlett, Rodney J. (1998). “Coupled-cluster calculations of the electronic excitation spectrum of free base porphin in a polarized basis,” *The Journal of Chemical Physics* 108(16), 6790-6798.
- 17.) Haarer, D. (1988). Photochemical Hole-Burning in Electronic Transitions. W. E. Moerner (Ed.) *Topics in Current Physics Persistent Spectral Hole-Burning: Science and Applications* 44, 79-125. Berlin Springer-Verlag.
- 18.) Hasegawa, Jun-ya., Takata, Koji., Miyahara, Tomoo., Neya, Saburo., Frisch, Michael J., Nakatsuji, Hiroshi. (2005). “Excited States of Porphyrin Isomers and Porphycene Derivatives: A SAC-CI Study,” *Journal of Physical Chemistry A* 109(14), 3187-3200.
- 19.) Hashimoto, Tomohiro., Choe, Yoong\_Kee., Nakano, Haruyuki., Hirao, Kimihiko. (1999). “Theoretical Study of the Q and B Bands of Free-Base, Magnesium, and Zinc Porphyrins, and Their Derivatives,” *Journal of Physical Chemistry A* 103(12), 1894-1904.
- 20.) Hayes, J. M., Jankowiak, R., Small, G.J. (1988). Two-Level-System Relaxation in Amorphous Solids as Probed by Nonphotochemical Hole-Burning in Electronic Transitions. W. E. Moerner (Ed.) *Topics in Current Physics Persistent Spectral Hole-Burning: Science and Applications* 44, 153-202. Berlin Springer-Verlag.
- 21.) Hoyt, L. F. (1934). “New table of the Refractive Index of Pure Glycerol at 20° C.,” *Industrial and Engineering Chemistry* 26(3), 329-332.
- 22.) Hughes, Joseph L., Krausz, Elmar. (2007). “Novel characteristics of persistent spectral hole-burning and hole-filling in Photosystem II core complexes,” *Journal of Luminescence* 127, 239-244.
- 23.) Jankowiak, R., Hayes, J. M., Small, G. J. (1993). “Spectral Hole-Burning in Amorphous Molecular Solids and Proteins,” *Chemical Reviews* 93(4), 1471-1502.
- 24.) Kendrew, J. C., Bodo, G., Dintzis, H. M., Parrish, R. G., Wyckoff, H., Phillips, D. C. (1958). “A three-dimensional model of the myoglobin molecule obtained by x-ray analysis,” *Nature* 181(4610), 662-666.
- 25.) Kendrew, J. C., Dickerson, R. E., Strandberg, B. E., Hart, R. G., Davies, D. R., Phillips, D. C., Shore, V. C. (1960). “Structure of myoglobin: A three-dimensional Fourier synthesis at 2 Å resolution,” *Nature* 185(4711), 422-427.

- 26.) Kobayashi, Hiroshi. (1959). "On the Electronic Spectra of Porphine," *The Journal of Chemical Physics* 30, 1362-1363.
- 27.) Kohler, B. E., Personov, Roman I., Woehl, Jorg C. (1995). Electric Field Effects In Molecular Systems Studied Via Persistent Hole Burning. Anne B. Meyers and Thomas R. Rizzo (Eds.) *Laser Techniques In Chemistry* 23, 283-323. New York John Wiley & Sons Inc.
- 28.) Kohler, M., Gafert, J., Friedrich, J., Vanderkooi, J. M., Laberge, M. (1996). "Stark Effect Experiments in Cytochrome c-Type Proteins: Structural Hierarchies," *Biophysical Journal* 71, 77-85.
- 29.) Leeson, Daan Thorn., Wiersma, Douwe A., Fritsch, Klaus., Friedrich, Josef. (1997). "The Energy Landscape of Myoglobin: An Optical Study," *Journal of Physical Chemistry B* 101(33), 6331-6340.
- 30.) Leontidis, Epameinondas., Suter, Ulrich W., Schutz, Martin., Luthi, Hans-Peter., Renn, Alois., Wild, Urs P. (1995). "The Mechanism of Spectral Shift and Inhomogeneous Broadening of an Aromatic Chromophore in a Polymer Glass," *Journal of the American Chemical Society* 117(28), 7493-7507.
- 31.) Lide, D. (2003). CRC handbook of chemistry and physics: A ready-reference book of chemical and physical data. (84th ed.). Boca Raton, Fla.: CRC Press. 10-250.
- 32.) Macfarlane, Roger M. (2007). "Optical Stark spectroscopy of solids," *Journal of Luminescence* 125, 156-174.
- 33.) Manas, Eric S., Wright, Wayne W., Sharp, Kim A., Friedrich, Josef, Vanderkooi, Jane M. (2000). "The Influence of Protein Environment on the Low Temperature Electronic Spectroscopy of Zn-Substituted Cytochrome c," *Journal of Physical Chemistry B* 104(29), 6932-6941.
- 34.) Meixner, Alfred J., Renn, Alois., Bucher, Stephan E., Wild Urs P. (1986). "Spectral Hole Burning In Glasses and Polymer Films: The Stark Effect," *Journal of Physical Chemistry* 90(26), 6777-6785.
- 35.) Meunier, Bernard. (1992). "Metalloporphyrins as versatile catalysts for oxidation reactions and oxidative DNA cleavage," *Chemical Review* 92 (6), 1411-1456.
- 36.) Moerner, W. E. (1988). Introduction. W. E. Moerner (Ed.) *Topics in Current Physics Persistent Spectral Hole-Burning: Science and Applications* 44, 1-15. Berlin Springer-Verlag.
- 37.) Moerner, W. E., Lenth, W., Bjorklund, G. C. (1988). Frequency Domain Optical Storage and Other Applications of Persistent Spectral Hole-Burning. W. E. Moerner (Ed.) *Topics in Current Physics Persistent Spectral Hole-Burning: Science and Applications* 44, 251-307. Berlin Springer-Verlag.

- 38.) Nakatsuji, Hiroshi., Hasegawa, Jun-ya., Hada, Masahiko. (1996). "Excited and ionized states of free base porphyrin studied by the symmetry adapted cluster-configuration interaction (SAC-CI) method," *The Journal of Chemical Physics* 104(6), 2321-2329.
- 39.) Namuangruk, Supawadee., Sirithip, Kanokkorn., Rattanatwan, Rattanawelee., Keawin, Tinnagon., Kungwan, Nawee., Sudyodsuk, Taweesak., Promarak, Vinich., Surakhot, Yaowarat., Jungsuttiwong, Siriporn. (2014). "Theoretical investigation of the charge-transfer properties in different meso-linked zinc porphyrins for highly efficient dye-sensitized solar cells," *Dalton Transactions* 43, 9166-9176.
- 40.) Nelson, D. L., Cox, M. M. (Eds.). (2008). *Lehninger Principles of Biochemistry* (5th ed.). New York: W. H. Freeman and Company.
- 41.) Palummo, Maurizia., Hogan, Conor., Sottile, Francesco., Bagalá, Paolo., Rubio, Angel. (2009). "Ab initio electronic and optical spectra of free-base porphyrins: The role of electronic correlation," *The Journal of Chemical Physics* 131, 084102-1 - 084102-7.
- 42.) Personov, R.I., Al'Shits, E.I., Bykovskaya, L.A. (1972). "The effect of fine structure appearance in laser-excited fluorescence spectra of organic compounds in solid solutions," *Optics Communications* 6(2), 169-173.
- 43.) Polticelli, Fabio., Battistoni, Andrea., O'Neill, Peter., Rotilio, Giuseppe., Desideri, Alessandro. (1998). "Role of the electrostatic loop charged residues in Cu, Zn superoxide dismutase," *Protein Science* 7, 2354-2358.
- 44.) Ponomarev, Yu. N., Petrova, T. M., Solodov, A. M., Solodov, A. A. (2010). "IR spectroscopy of water vapor confined in nanoporous silica aerogel," *OPTICS EXPRESS* 18(25),26062-26067.
- 45.) Purchase, R., Sellars, M.J., Krausz, E. Manson, N.B. (2000). "Electric-field-induced broadening of spectral holes in zinc phthalocyanine," *Chemical Physics Letters* 327, 189-196.
- 46.) Rebane, K. K., Rebane, L. A. (1988). Basic Principles and methods of Persistent Spectral Hole-Burning. W. E. Moerner (Ed.) *Topics in Current Physics Persistent Spectral Hole-Burning: Science and Applications* 44, 17-77 Berlin Springer-Verlag.
- 47.) Rebane, K. K. (2003). Purely electronic zero-phonon line as the foundation stone for high-resolution matrix spectroscopy, single-impurity-molecule spectroscopy, and persistent spectral hole burning. Recent developments," *LOW TEMPERATURE PHYSICS* 29(9-10), 838-843.
- 48.) Renge, Indrek. (2002). "Measurement of internal strain in polymers by means of optical hole burning," *Chemical Physics Letters* 357, 409-414.

- 49.) Rollakanti, Kishore R., Kanick, Stephen C., Davis, Scott C., Pogue, Brian W., Maytin, Edward V. (2013). "Techniques for fluorescence detection of protoporphyrin IX in skin cancers associated with photodynamic therapy," *Photonics & Lasers in Medicine* 2(4), 287–303.
- 50.) Rubio, Mercedes., Roos, Björn O., Serrano-Andrés, Luis., Merchán, Manuela. (1999). "Theoretical study of the electronic spectrum of magnesium-porphyrin," *The Journal of Chemical Physics* 110(15), 7202-7209.
- 51.) Schmidt, M.W., Baldrige, Kim K., Boatz, Jerry A., Elbert, Steven T., Gordon, Mark S., Jensen, Jan H., Koseki, Shiro., Matsunaga, Nikita., Hguyen, Kiet A., Su, Shujun., Windus, Theresa L., Dupuis, Michel., Montgomery, John A. (1993). "General atomic and molecular electronic structure system," *Journal of Computational Chemistry* 14(11), 134-1363.7
- 52.) Senge, Mathias O., Ryan, Aoife A., Letchford, Kristie A., MacGowan, Stuart A., Mielke, Tamara. (2014). "Chlorophylls, Symmetry, Chirality, and Photosynthesis," *Symmetry* 6, 781-843.
- 53.) Spellane, P. J., Gouterman, M., Antipas, A., Kim, S., Liu, Y. C. (1980). "Porphyrins. 40.' Electronic Spectra and Four-Orbital Energies of Free-Base, Zinc, Copper, and Palladium Tetrakis(perfluoropheny1)porphyrins," *Inorganic Chemistry* 19 (2), 386-391.
- 54.) Stubner, Markus., Hecht, Christoph., Schneider, Ellen., Friedrich, Josef. (2002). "Hole burning Stark-effect studies on aromatic aminoacids Part II. A comparative investigation of tyrosine and the BPTI-protein," *Physical Chemistry Chemical Physics* 4, 6080-6085.
- 55.) Suslick, Kenneth S., Chen, Chin Ti., Meredith, Gerald R., Cheng, Lap Tak. (1992). "Push-pull porphyrins as nonlinear optical materials," *Journal of the American Chemical Society* 114 (17), 6928–6930.
- 56.) Szabo, A. (1975). "Observation of hole burning and cross relaxation effects in ruby," *Physical Review B* 11(11), 4512-4517.
- 57.) Teale, F. W. J. (1959). "Cleavage of the haem-protein link by acid methylethylketone," *Biochimica et Biophysica Acta* 35, 543.
- 58.) Tokita, Y., Hasegawa, J., Nakatsuji, H. (1998). "SAC-CI Study on the Excited and Ionized States of Free-Base Porphin: Rydberg Excited States and Effect of Polarization and Rydberg Functions," *Journal of Physical Chemistry A* 102(10), 1843-1849.
- 59.) <http://www.rcsb.org/pdb/results/results.do?qrid=9BOCDD4A>

# I

## Chapter 2

# Mathematical Treatments for the Effect of Electric Fields Applied to Spectral Holes

## 2.1 Introduction

The spectral characteristics of atoms and molecules are directly related to the geometric distribution of the existing charges, and the ability of specific frequencies of light to impart to the electrons the necessary angular momentum required to link any of the various quantum states. As atoms and molecules are collections of charged particles, it is of no surprise that upon placement of a sample within an electric field, these charge distributions become perturbed. Resultantly, the existing quantum states and the frequency of incident radiation necessary to induce transition between those states, too, becomes perturbed. Any changes to intensity, shifting or splitting of spectral features caused by the presence of an external electric field applied to an atom or molecule is referred to as either the Stark effect, electrochromism or electroabsorption. Experiments on molecules involving external electric fields provide information indicating how a transition to an excited electronic state affects the dipole moment and polarizability of the molecule. The dipole moment is a measure of the degree of charge separation in a molecule, and the polarizability is the likelihood of the charge distribution in the

molecule to become distorted in the presence of an electric field. If the dipole moment and the polarizability are properties of the molecular system that are known, any resultant spectral shifts observed can be linked to the external fields required to induce said shifts. An understanding of these properties, their relationships, and how they change upon electronic excitation, shed light on both the electronic structure of molecules and how the molecules interact with and are affected by their environment. What follows is a brief overview of a few methods that have been and typically are used when analyzing the changing line-shapes of spectral holes when electric fields are applied to a sample in which a spectral hole was burnt.

## **2.2 Classical Approach**

The application of an electric field to a chromophore embedded within a host matrix will affect both the chromophore as well as the surrounding matrix. As the magnitude of the electric field is increased the electron distributions of the molecules making up the matrix as well as those of the embedded chromophores will deviate from the distributions existing in the field free case. Because the polarizabilities of the chromophore and matrix are unlikely to be exactly the same, the state energies, transition dipole moments and polarizabilities of the molecules that constitute the chromophore and matrix will undergo an adjustment. When the chromophore of interest possesses a permanent dipole moment, the ground and excited states of the chromophore will be affected by the applied electric field differently, if the permanent dipole moments are not the same in both states and the polarizabilities are not the same

in both states [9, 10, 20]. Under this situation, the transition frequencies will become modified and a spectral shift will then occur.

The change in state energy resulting from the application of an external electric field is traditionally quantified using a second order perturbation approach. If it is assumed that the molecule of interest is sufficiently small such that it experiences a homogeneous field, only three parameters are of necessity when evaluating the spectral shift. These are the total electric field at the site of the chromophore,  $\vec{E}$ , the difference of the permanent molecular dipole moment vectors,  $\Delta \vec{\mu}_{per}$ , and the difference of the polarizability tensors,  $\Delta \hat{\alpha}$ , of the two quantum states involved in the electronic transition being measured [12, 16].

$$\Delta\nu = -\frac{1}{h} ( \vec{E} \cdot \Delta \vec{\mu}_{per} + \frac{1}{2} \cdot \vec{E} \cdot \Delta \hat{\alpha} \cdot \vec{E} ) \quad (2.1)$$

Here, the shift of frequency caused by the difference of the permanent molecular dipole moments of the two states is first order with respect to the applied field, and the frequency shift caused by the difference of the polarizability tensors is second order with respect to the applied field. If the molecule of interest is centrosymmetric and possesses no intrinsic molecular dipole moment, according to the above formulation, it is the change of polarizability between the two states that accounts for the observed shift of frequency.

It becomes important at this point to question what exactly the electric field that is experienced by the chromophore at its embedded site within the matrix actually is. Based on the specific characteristics of the system under study, throughout the volume

of the entire sample in relation to each chromophore, the matrix may be mostly random as would be true in a solution or amorphous system, partially ordered, or even highly ordered as would be true in the case of a crystalline system. As the surrounding matrix is itself nothing more than an assemblage of molecules which are themselves collections of charged particles, the impact of the matrix on the observed electric field at the site of the chromophore is twofold. The particular arrangement of the charges in the molecules that make up the matrix will collectively induce their own electric field on the chromophore. Although the average electric field across the entire sample is zero, at the site of the individual chromophores, these local distributions of charge will have an influence. This can be considered as the internally generated electric field  $\vec{E}_{int}$ , which for situations where chromophores are situated in fairly homogeneous local environments, as is the case in doped crystals or when chromophores reside within proteins, is a field which affects all chromophores equivalently throughout the entirety of the sample. The second impact the matrix has on the field arises due to the fact that the matrix is a dielectric medium and acts as an insulator, partially shielding the externally applied electric field at the site of the chromophore. Therefore, the local electric field  $\vec{E}_{loc}$ , is the perceived portion of the external electric field that is felt by the chromophore. The total electric field  $\vec{E}_{tot}$ , that is experienced by the chromophore is then simply the vector sum of the internal and the shielded external field contributions.

$$\vec{E}_{tot} = \vec{E}_{int} + \vec{E}_{loc} \quad (2.2)$$

When this equality is factored into equation 2.1 describing the field dependent frequency shift, the following five term formulation is obtained [10].



$$\Delta\nu = -\frac{1}{h} \left( \vec{E}_{int} \cdot \Delta\vec{\mu}_{per} + \vec{E}_{loc} \cdot \Delta\vec{\mu}_{per} + \frac{1}{2} \cdot \vec{E}_{int} \cdot \Delta\hat{\alpha} \cdot \vec{E}_{int} \right. \\ \left. + \vec{E}_{loc} \cdot \Delta\hat{\alpha} \cdot \vec{E}_{int} + \frac{1}{2} \cdot \vec{E}_{loc} \cdot \Delta\hat{\alpha} \cdot \vec{E}_{loc} \right) \quad (2.3)$$

Under this formulation, it is easily observed that the first and third terms are representative of the purely molecular induced contribution to the frequency shift. The second and fifth terms are representative of the contribution to the frequency shift that are dependent solely upon the externally applied field. The fourth term is mixed, and describes the contribution to the frequency shift that is dependent upon both of the fields. This mixed term,  $\vec{E}_{loc} \cdot \Delta\hat{\alpha} \cdot \vec{E}_{int}$  is of most interest because it reveals information regarding the internal electric field, by application of the external field [14].

Just as the matrix plays a role in modulating the total electric field at the site of the chromophore, so too does it have an influence on the dipole moment. The total molecular dipole moment of a molecule residing in a host matrix consists of two components. The first component being that of the intrinsic or permanent dipole moment of the molecule itself,  $\vec{\mu}_{per}$ . The other component being the dipole moment which is induced by the matrix  $\vec{\mu}_{ind}$ , that dawns from the internal electric field that is imparted by the matrix to the molecule and the shielded external field.

$$\vec{\mu}_{ind} = \hat{\alpha}\vec{E}_{int} + \hat{\alpha}\vec{E}_{loc} \quad (2.4)$$

It is this induced dipole moment that allows frequency shifts that are linear in applied field to be observed in centrosymmetric molecules [16]. Upon insertion of identity 2.4, describing the matrix induced dipole moment, into equation 2.3, followed by grouping

like terms and factoring when possible, it can be seen that terms one and three of equation 2.3 can be combined into term one of the first equality of equation 2.5, and that terms two and five of equation 2.3, can be combined into term two of the first equality of equation 2.5. Term four becomes split between these two terms, with the contribution of  $\frac{1}{2} \cdot \vec{E}_{int} \cdot \Delta \hat{\alpha} \cdot \vec{E}_{loc}$ , residing within the first term and the contribution of  $\frac{1}{2} \cdot \vec{E}_{loc} \cdot \Delta \hat{\alpha} \cdot \vec{E}_{int}$  residing within the second term. The second equality displays the result of not splitting the total electric field into its respective components.

$$\begin{aligned} \Delta v &= -\frac{1}{h} \left\{ \vec{E}_{int} \left( \Delta \vec{\mu}_{per} + \frac{1}{2} \Delta \vec{\mu}_{ind} \right) + \vec{E}_{loc} \left( \Delta \vec{\mu}_{per} + \frac{1}{2} \Delta \vec{\mu}_{ind} \right) \right\} \\ &= -\frac{1}{h} \left\{ \vec{E}_{tot} \left( \Delta \vec{\mu}_{per} + \frac{1}{2} \Delta \vec{\mu}_{ind} \right) \right\} \end{aligned} \quad (2.5)$$

Based on equation 2.5, it can now be observed that the total apparent dipole moment of the molecule that interacts with the electric field is a linear combination of the permanent dipole moment  $\vec{\mu}_{per}$ , along with that which is induced by the matrix  $\vec{\mu}_{ind}$ . Again, the total electric field is simply the vectoral combination of the internally generated field along with the shielded externally applied electric field. The observed frequency shift due to the Stark effect then relies on contributions from these native and induced quantities.

What is shown in 2.5, represents a slightly generalized equation for quantifying frequency shifts, that presupposes that the local electric field  $\vec{E}_{loc}$ , at the site of the embedded chromophore is implicitly known. In practice this is infrequently ever the case other than the situation where a single molecule is placed within the field in vacuum, in which case the local field would then be exactly equal to the external field.

Therefore, approximations for estimating the effect of the chromophore being situated in a dielectric medium becomes of necessity. To account for the influence of the surrounding matrix on the externally applied field as observed by the chromophore, the external field is scaled by a quantity defined as the local electric field tensor  $\hat{f}_{loc}$ . The relationship between the applied field and the perceived field then is written as follows.

$$\vec{E}_{loc} = \hat{f}_{loc} \vec{E}_{ext} \quad (2.6)$$

The value assigned to  $\hat{f}_{loc}$  is dependent on the particular dielectric in which the chromophore is placed and accounts for the polarization of that medium in the presence of the electric field. Typically, this value is approximated using the Lorentz field correction. Under this approximation, the external field is turned on and the dielectric medium is allowed polarize. With the polarization locked, the chromophore is then observed as a point source sitting at the center of a spherical cavity that is carved out of the continuous dielectric medium. Only the polarization charges of the molecules existing on the surface of the spherical cavity contribute to the Lorentz field and any charges residing within the spherical cavity, which is assumed to be empty in this approximation, including the chromophore itself are assumed to have zero contribution or influence on the Lorentz field. Although this is a rather simplified approximation, this is the traditional approach used when modeling this parameter [3, 8, 14, 17, 18], with efforts to more accurately account for these effects being an ongoing area of research [11, 13]. In the Lorentz field correction approximation, the local electric field tensor is a scalar that is formulated by the following expression.

$$f_{loc} = \frac{(\epsilon+2)}{3} \quad (2.7)$$

Here  $\epsilon$  is the relative permittivity of the matrix in which the chromophore sits. In this particular investigation this would represent the relative permittivity of the protein environment as well as the glycerol water matrix. Efforts to experimentally measure the contribution of the low temperature relative permittivity of the glycerol water matrix for inclusion into this parameter for this investigation are more fully presented within chapter 8 of this document. Other more rigorous methods to account for the local field correction parameter  $\hat{f}_{loc}$ , can be applied to equation 2.6 to yield a different value of  $\vec{E}_{loc}$  and then substituted into equation 2.5 for calculation of the frequency shifts. The major caveat of this assumption rests in the fact that the molecule is required to behave as a point dipole which is not realistic on the scale of actual molecules [6, 18], and that the surrounding medium, which is highly structured in proximity to the chromophore, is assumed to be a dielectric continuum.

### 2.3 Molecular Resolution Approach

The molecular resolution approach to modeling the effects of an external electric field on the spectral characteristics of chromophores embedded in host matrices stems from the idea that since these systems are nothing more than collections of molecules, it should be possible to describe these systems using a quantum mechanical treatment. Because the spectral features of the system, and specifically, the spectroscopically observable transitions between states are what are of interest, the standard quantum mechanical formalism describing the state energies of the system can be used. The state

energies of the unperturbed system can be described by use of the time-independent Schrödinger equation.

$$H^0 | \Psi_n^{(0)} \rangle = \mathcal{E}_n^{(0)} | \Psi_n^{(0)} \rangle \quad (2.8)$$

When the Hamiltonian  $H^0$  operates on the state specific wave functions  $\Psi_n^{(0)}$ , the state specific energy values  $\mathcal{E}_n^{(0)}$  are returned. Here, the superscripts above refer to the unperturbed quantities.

In a similar fashion to the classical approach whereby the frequency shift that is observed due to the application of an external electric field is described using a perturbative process, so too can this methodology be implemented when describing the molecular system from a quantum mechanical as opposed to a classical standpoint. As with all perturbative processes, it is assumed that the perturbation represents a small offset from the initial unperturbed system, therefore the total Hamiltonian  $H$ , under the new condition, is obtained as a linear combination of the unperturbed Hamiltonian  $H^0$ , and the perturbative Hamiltonian  $H^1$ .

$$H = H^0 + H^1 \quad (2.9)$$

In the case of the Stark effect, the perturbed Hamiltonian is dependent upon the total electric field the molecule is experiencing and the distribution of charges throughout the molecule. The charge distribution within the molecule depends on all of the charges  $q_i$  existing within the molecule, and their locations in space, represented by their individual position vectors  $\vec{r}_i$ . To first approximation, the perturbation is

dominated by a dipole term, so that the Stark perturbation can be described by the interaction of the electric field  $\vec{E}$ , with the electronic dipole moment, and thus simply becomes  $-\vec{\mu} \cdot \vec{E}$ .

$$H^1 = H_{Stark} = -\vec{\mu} \cdot \vec{E} = -\sum_i q_i \vec{r}_i \cdot \vec{E} \quad (2.10)$$

Inserting the equality from equation 2.10 into 2.9 yields the perturbed Hamiltonian, and resting under the assumption that the states are non-degenerate, when this is then placed into equation 2.8, expanded, and like powers are equated, allows for the approximate solutions to the time-independent Schrödinger equation to be found. The new state energies accounting for the presence of the electric field up to the second order correction, are then defined as shown. [1, 15, 21].

$$\mathcal{E}_n = \mathcal{E}_n^{(0)} - \langle \Psi_n^{(0)} | \vec{\mu} \cdot \vec{E} | \Psi_n^{(0)} \rangle + \sum_{m \neq n} \left( \frac{|\langle \Psi_m | \vec{\mu} \cdot \vec{E} | \Psi_n \rangle|^2}{\mathcal{E}_n^{(0)} - \mathcal{E}_m^{(0)}} \right) \quad (2.11)$$

The first term above represents the contribution from the unperturbed state energies of the system  $\mathcal{E}_n^{(0)}$  in the field free case, resulting from inclusion of the original  $H^0$  term in the total Hamiltonian  $H$ . The next two terms represent the energy perturbation arising from the presence of the electric field. It can be observed in this formulation that the first order corrections, term two, rely on the electronic dipole moments of the respective states. The second order corrections, term three, rely on the electronic transition dipole moments between respective states.

As can be seen, the electronic dipole moments and transition moments of all of the states are quantities that are of necessity in this determination. To formally carry out

this calculation, the complete set of wave functions that completely span the space need to be known and in turn evaluated. In practice, a truncated basis is chosen and the perturbed energies according to that basis are found. Solving for the energies then requires the simultaneous solution to the resulting set of equations. In order to effectively and efficiently calculate the change in energy that results, the simplest approach is to set up the Hamiltonian as a matrix,  $\langle \Psi_m | H | \Psi_n \rangle$ , containing all of the necessary elements to be evaluated, running over all m and n, for the basis in which the new energies are to be found. Once this matrix is formed, the eigenvalues existing as the perturbed energies are simply determined by a numerical diagonalization of the matrix.

A few comments need to be made about the structure and components of the matrix. As it is the objective to determine the internal electric field that is present within the molecule, the perturbing electric field responsible for the Stark shift is viewed as that which appears in equation 2.2. Therefore, the total field  $\vec{E}$  is the vector sum of the local field  $\vec{E}_{loc}$ , which is the corrected externally applied electric field, equation 2.6, and the internal molecular electric field  $\vec{E}_{int}$ . Because the total field is viewed in this manner, the spectroscopically observable energies must already contain within them the contribution from the internal field perturbation term, namely  $\vec{E}_{int}$ , which cannot be turned off. Therefore, in the matrix displayed in equation 2.12, the elements appearing on the main diagonal  $W(n)$ , represent energies such that when the external field contribution  $\vec{E}_{loc}$  to the total electric field  $\vec{E}$  is set to zero, upon diagonalization, the spectroscopically observable energies are what results. The following change of notation,  $\vec{\mu}_{mn} = \langle \Psi_m | \vec{\mu} | \Psi_n \rangle$ , is used for brevity in the matrix. Here  $\vec{E}_{tp}$ , represents the total electric field that is projected onto the actual state specific transition dipole

moments. More regarding some of the specifics of these values are covered in section 2.5.

$$H = \begin{pmatrix} \mathbf{W}(\mathbf{gnd}) & -\vec{E}_{t_p}\vec{\mu}_{01} & -\vec{E}_{t_p}\vec{\mu}_{02} & -\vec{E}_{t_p}\vec{\mu}_{03} & -\vec{E}_{t_p}\vec{\mu}_{04} & \dots & -\vec{E}_{t_p}\vec{\mu}_{0n} \\ -\vec{E}_{t_p}\vec{\mu}_{10} & \mathbf{W}(\mathbf{1}) & -\vec{E}_{t_p}\vec{\mu}_{12} & -\vec{E}_{t_p}\vec{\mu}_{13} & -\vec{E}_{t_p}\vec{\mu}_{14} & \dots & -\vec{E}_{t_p}\vec{\mu}_{1n} \\ -\vec{E}_{t_p}\vec{\mu}_{20} & -\vec{E}_{t_p}\vec{\mu}_{21} & \mathbf{W}(\mathbf{2}) & -\vec{E}_{t_p}\vec{\mu}_{23} & -\vec{E}_{t_p}\vec{\mu}_{24} & \dots & -\vec{E}_{t_p}\vec{\mu}_{2n} \\ -\vec{E}_{t_p}\vec{\mu}_{30} & -\vec{E}_{t_p}\vec{\mu}_{31} & -\vec{E}_{t_p}\vec{\mu}_{32} & \mathbf{W}(\mathbf{3}) & -\vec{E}_{t_p}\vec{\mu}_{34} & \dots & -\vec{E}_{t_p}\vec{\mu}_{3n} \\ -\vec{E}_{t_p}\vec{\mu}_{40} & -\vec{E}_{t_p}\vec{\mu}_{41} & -\vec{E}_{t_p}\vec{\mu}_{42} & -\vec{E}_{t_p}\vec{\mu}_{43} & \mathbf{W}(\mathbf{4}) & \dots & -\vec{E}_{t_p}\vec{\mu}_{4n} \\ \vdots & \vdots & \vdots & \vdots & \vdots & \ddots & \vdots \\ -\vec{E}_{t_p}\vec{\mu}_{m0} & -\vec{E}_{t_p}\vec{\mu}_{m1} & -\vec{E}_{t_p}\vec{\mu}_{m2} & -\vec{E}_{t_p}\vec{\mu}_{m3} & -\vec{E}_{t_p}\vec{\mu}_{m4} & \dots & \mathbf{W}(\mathbf{N}) \end{pmatrix} \quad (2.12)$$

If the chromophore of interest is centrosymmetric or possesses certain types of symmetry, the matrix elements needing evaluation typically simplifies with many of the off diagonal elements becoming zero. What is shown above is for the general case that would reflect a matrix of the appropriate form for molecules lacking symmetry, as would be the case for molecules in real matrices in the solid state. Additional comments regarding this appear in chapter 9 of this document. This matrix approach for evaluating the internally generated molecular electric field present at the site of a probe molecule within a host system has been successfully implemented in the past by various researchers when studying both mixed glasses, specifically polyenes in alkane environments, as well as with various protein samples [5, 6, 7, 12].



## 2.4 Angular Dependencies of Hole-burning and Stark Profiles

Preliminary to any description of the expected line-shapes that arise due to application of the external electric field, it is important to understand the impact that various angular dependencies existing between the molecular orientation of the chromophores within the matrix, the excitation light used for the burning and reading cycles, and the applied electric field have, not only on the hole burning process but also on the Stark effect hole profiles. There are two primary vector quantities that play a fundamental role in the hole formation process and an additional vectoral relationship that influences the outcome of electric field application.

The spectral hole-burning process is one which is not only frequency selective but is also orientationally selective towards a specific subset of chromophores within the total illuminated population of chromophores in a sample. The frequency selectivity is directly understandable, as the excitation source used during the burning process can predominantly affect only those molecules possessing zero-phonon lines in resonance with the frequency of the source, with molecules that possess resonant phonon sidebands also making limited contribution to the hole as well. Again, because the chromophore molecules exist in anisotropic local environments, it is only the frequency differential between states that is selected for across the population of molecules, as opposed to any specified absolute energy value of either the ground or excited states of the molecules. Spectral hole-burning is almost exclusively conducted using polarized light, in which rests the orientation selectivity of the method. The laser polarization consequently causes preferred directional isolation by principally photobleaching only those absorbers with their transition dipole moment  $\vec{\mu}_{mn}$ , aligned with the polarization

vector  $\vec{E}_{h\nu-B}$ , of the burning light. Here, the indices on the transition moment do not run over all states but only between the two states m and n of the specific transition being probed during the hole-burning experiment. As already highlighted in equation 1.5, the hole shape for the burning contribution to a spectral hole profile partially relies on the inner product of these vector quantities, according to  $(\vec{\mu}_{mn} \cdot \vec{E}_{h\nu-B})^2$ . The contribution to hole shape due to the reading photon follows a similar formulation  $(\vec{\mu}_{mn} \cdot \vec{E}_{h\nu-R})^2$ , and although can possess a polarization different from that of the burning photon, is often of the same polarization [8, 19]. For purposes of simplicity, the “-B” and “-R” have been dropped from the index of the parameter describing the polarization of the light field  $\vec{E}_{h\nu}$ , for the remaining discussion.

In order to interpret the various effects resulting from application of an applied electric field to a sample in which a spectral hole has been burnt, it becomes of necessity to relate the molecular frame of reference to the laboratory frame of reference. This can be accomplished by use of the displayed coordinate system in figure 2.1. The light field propagates along the y-axis, with the applied electric field  $\vec{E}$ , existing along the z-axis between the copper electrodes, shown in amber. As the chromophores are placed in an amorphous matrix there is no preferred molecular orientation, and thus in a realistic sample a complete distribution of all possible molecular orientations are equally likely to exist. The transition dipole moment  $\vec{\mu}_{mn}$ , represented here is again only that of the specific transition being probed, which can be related to  $\vec{E}_{h\nu}$  by the specified angles and the matrices that are displayed in the figure. The subset of molecules possessing appropriate orientation to become saturated allowing hole formation are those for

which the overlap of these quantities are maximized. Therefore, the molecules most affected are those that have a transition moment aligned with the polarization of the light field. This process of selecting molecules possessing transition dipole moments that are collinear in the light field  $\vec{E}_{hv}$ , in turn results in the selection of the subset of molecules possessing a particular transition dipole moment  $\vec{\mu}_{mn}$ .

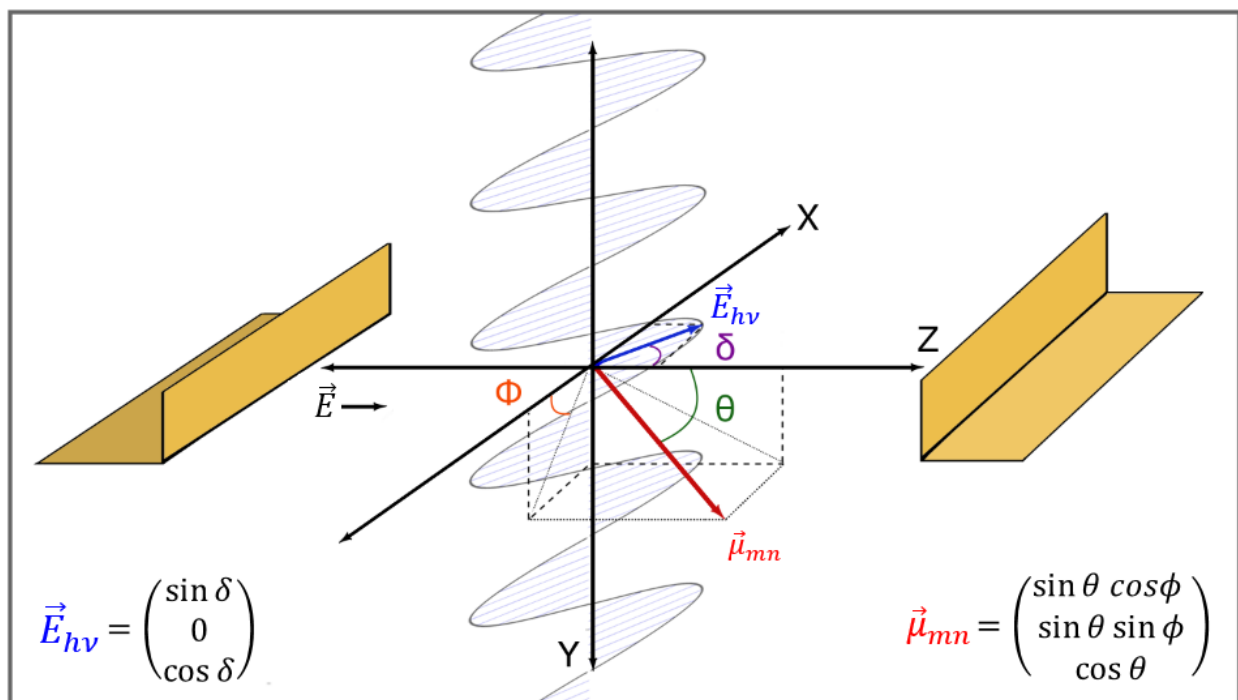


Figure 2.1: Vector representation of the important geometric relationships between the electric field, the source light and the chromophore. Displayed are the applied electric field  $\vec{E}$ , the polarization of the excitation and burning light  $\vec{E}_{hv}$ , and the molecular transition dipole moment  $\vec{\mu}_{mn}$ . The copper electrodes apply the external electric field along the z-axis. The light field interacting with the sample travels along the y-axis with polarization vector represented by  $\vec{E}_{hv}$ . The transition dipole moment  $\vec{\mu}_{mn}$  between the ground and first excited state of porphyrin describing the Qx transition, is the band into which spectral holes are burnt. The matrices depicted above describe the vector components of  $\vec{E}_{hv}$  and  $\vec{\mu}_{mn}$  in terms of the established angles. When used in tandem with the specified equations defining a molecule's contribution to hole shape, the interaction of these vector quantities for each individual chromophore dictate the weight with which that particular chromophore contributes to the resultant shape of the spectral hole during the orientational averaging process.

Traditionally, during a Stark experiment, the spectral hole is burnt, the external field is next applied, and the spectral hole is then read out while the field is still on. Various spectral effects can generally be expected based on the polarization of the light field used during the burning process as related to the direction of the applied electric field. In all cases, any modulation to the applied electric field breaks the accidental transition frequency degeneracy that was initially selected for during hole-burning, which results in a change to the hole profile as recorded in the field free case.

In the case that the light polarization is chosen in such a way as to ensure that the chromophore molecules selected during the burning process have a transition dipole moment that is oriented perpendicularly to the direction of the electric field  $\vec{E}$ , upon application of the electric field, spectral holes undergo broadening. The subset of molecules selected during the burning process, as existing in differing local environments, respond to the electric field slightly differently, with their individual state energies being affected asymmetrically across the entire subset. This is primarily due to the existence of randomized matrix fields, which leads to spectral shifts across the population of the chromophores that contribute to the spectral hole. Under this circumstance, a mostly linear relationship between the broadening of a spectral hole profile and the applied electric field is typically observed for chromophore molecules having either permanent or induced dipole moments, when existing in either amorphous glass matrices or in partially ordered environments such as in proteins [3, 4, 8, 19].

Of more interest is the situation where the polarization of the light field is chosen such that the transition dipole moment of the selected chromophore molecules is

aligned in a parallel configuration with that of the applied electric field,  $\vec{\mu}_{mn} \parallel \vec{E}_{loc}$ . In this case, upon application of the electric field, a splitting of the spectral hole profile is generally observed, unless it is masked by the electric field induced broadening of the hole. The subpopulation of these selected chromophores with a dipole moment difference  $\Delta\vec{\mu}$  (arising from the internal electric field  $\vec{E}_{int}$ ) aligned such that their vectorial orientation in relation to the local electric field  $\vec{E}_{loc}$  is additive, will resonate at

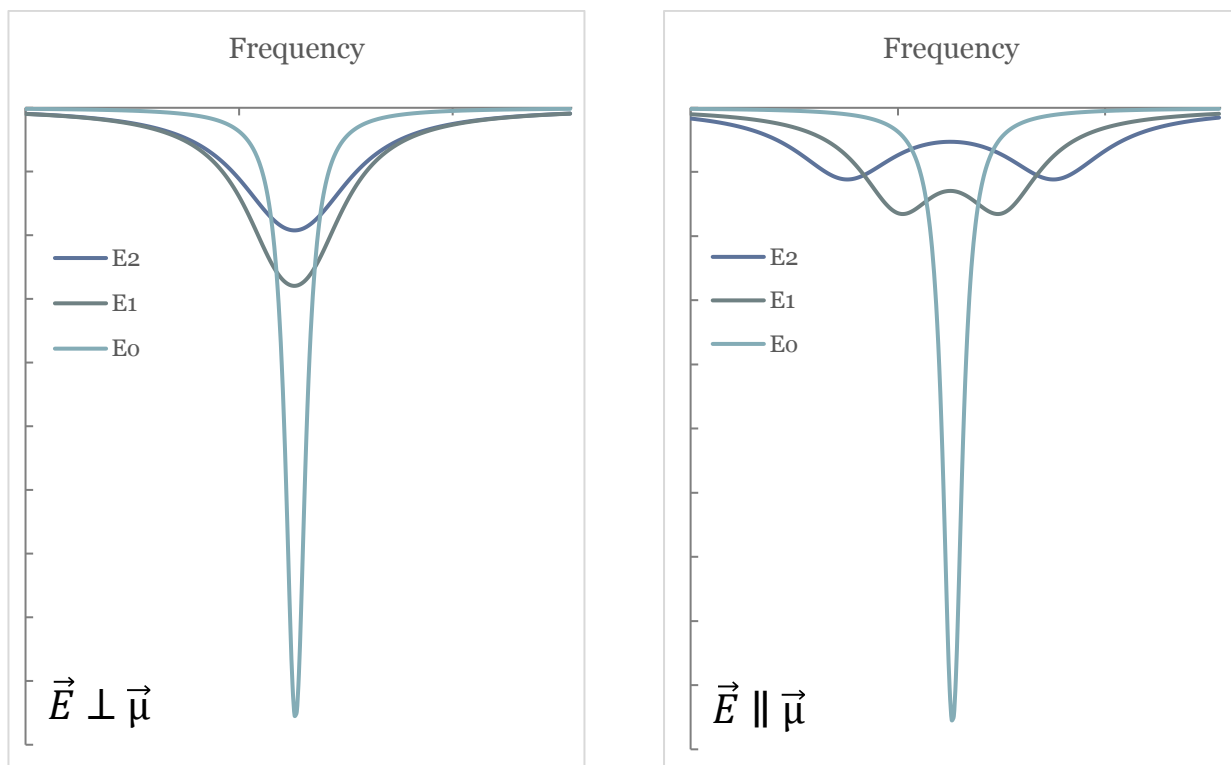


Figure 2.2: The effect of an externally applied electric field on a spectral hole. These hole profiles are simulated and represent the effect that increasing electric field strength,  $\vec{E}_0 < \vec{E}_1 < \vec{E}_2$ , has on hole profiles when applied both perpendicular and parallel to the polarization of the light used in the burning process. Left: When the applied electric field is perpendicular to the polarization of burning light, and consequently, perpendicular to the transition dipole moments of the population of chromophore molecules responsible for the spectral hole, the spectral hole undergoes broadening. Right: When the applied electric field is parallel to the polarization of burning light, and the transition dipole moments of the population of chromophore molecules responsible for the spectral hole, a splitting of the spectral hole is observed.

a decreased frequency. The subpopulation of chromophores with their dipole moment difference aligned such that their vectoral orientation in relation to the local electric is subtractive, then resonate at an increased frequency in the presence of the field. It has again been found that the relationship between the splitting of a spectral hole profile and the applied electric field is one that follows a mostly linear trend [3, 4, 19].

There are circumstances in which the aforementioned trends deviate. The total apparent molecular dipole moment difference  $\vec{\mu}$ , is a linear combination of the permanent dipole moment difference  $\Delta\vec{\mu}_{per}$ , and that which is induced by the matrix  $\Delta\vec{\mu}_{ind}$ . If the permanent molecular dipole moment difference is well defined and is dominant to the molecular polarizability difference, the first order effects as displayed in equation 2.1, are prevalent and the described splitting and broadening behavior for the parallel and perpendicular light and electric field configurations, is expected. If, however, the molecular polarizability difference is significantly high, the second order effects dominate and the field induced broadening becomes large. Here, the induced dipole moment arising from the molecular polarizability, equation 2.4, becomes dominant over the permanent molecular dipole moment, and the influence of randomized matrix fields is amplified. Therefore, in these cases a broadening of spectral hole profiles is expected for both parallel and perpendicular configuration modes [19].

In any Stark investigation, after the successive reading of a spectral hole profile at different magnitudes of applied electric field, it is necessary always to re-scan the hole profile with zero external field applied. Under ideal circumstances, the hole shape recorded at the end after applying the various fields should be the same as that which was initially recorded after the burning of the spectral hole. This practice allows the

magnitude of any additional saturation broadening and time broadening arising from the repeated reading of the hole profile to be monitored. If any shift in the center frequency of the hole is observed, it is known that a quadratic Stark effect has occurred. Any observed irreversible broadening of the hole is indicative of electric field induced configurational changes to the matrix environment surrounding the chromophore molecules, needing to be accounted for in any analysis of broadening or splitting phenomena.

## **2.5 The Molecular Resolution Modeling Process**

With the basic tenets of the analysis methodologies as well as the various angular dependencies which affect the resultant hole shape outlined, the actual process utilized for the evaluation of an internal molecular electric field is now a possibility. A generalized description of the process will be given first, followed by a procedural outline highlighting the necessary programmatic hierarchy of the calculation. The molecular resolution approach to determining the resultant line-shape of a spectral hole profile under the application of an external electric field requires evaluation of the system specific electric field perturbation Hamiltonian matrix. The perturbation matrix rests on two primary components, firstly the electric field and secondly the transition moment values between all of the states that are deemed important. The appropriately weighted contribution that any individual chromophore may make to the resultant line-shape must also be accounted for during the modeling process.

As for the electric field components of the Hamiltonian, in order for this analysis to yield the internal molecular electric field, the total electric field at the site of the chromophore molecule is viewed as the sum of the intrinsic field and the scaled externally applied field, equation 2.2. The scaling factor,  $\hat{f}_{loc}$ , which corrects the local electric field, must account for both the sample holder (cylindrical capillary) and the electrode (parallel plate) geometry, in addition to accounting for the use of the Lorentz cavity field approximation for the dielectric polarization of the surrounding matrix. A discussion regarding the contribution of the relative permittivity of the matrix towards the scaling factor appears in chapter 8 of this document and a discussion regarding the geometric contribution of the capillary can be found in reference [22].

As for the second component of the Hamiltonian, the various transition moment values between all excited states need to be calculated via external computational software packages. The calculations are performed for the free-base porphyrin molecule lacking any substituent groups, boxed in figure 1.1, existing in the gas phase. For all computational approaches used, the molecular axes of the porphyrin molecule is defined as the x-axis being situated between the hydrogen bound nitrogens, and the y-axis situated between the double bond nitrogens at the center of the porphyrin ring, with the z-axis normal to this plane. If the geometry of the porphyrin is optimized to that which exists purely in gas phase, the free-base porphyrin molecule is of  $D_{2h}$  symmetry. Under this symmetry class, the transition moments defining the four lowest optical transitions, namely those forming the Q and B-bands are completely polarized and exist along either the x or y-axis. Due to the symmetry, transition moments can exist only for transitions between the ground and excited states. Under this assumption of pure molecular



symmetry, a simplified matrix formulation describing the perturbing Hamiltonian is used. With the porphyrin described in this manner, the matrix takes on the following form, which has previously been used to great extent [5, 6, 12, 13, 22].

$$H = \begin{pmatrix} W(gnd) & -\vec{E}_x\vec{\mu}_{Q_x} & -\vec{E}_y\vec{\mu}_{Q_y} & -\vec{E}_x\vec{\mu}_{B_x} & -\vec{E}_y\vec{\mu}_{B_y} \\ -\vec{E}_x\vec{\mu}_{Q_x} & W(Q_x) & 0 & 0 & 0 \\ -\vec{E}_y\vec{\mu}_{Q_y} & 0 & W(Q_y) & 0 & 0 \\ -\vec{E}_x\vec{\mu}_{B_x} & 0 & 0 & W(B_x) & 0 \\ -\vec{E}_y\vec{\mu}_{B_y} & 0 & 0 & 0 & W(B_y) \end{pmatrix} \quad (2.13)$$

Here, the portion of the total electric field acting on a specific transition moment is simply the projection of the total electric field onto either the x-axis  $\vec{E}_x$  or the y-axis  $\vec{E}_y$ . This characterization, and therefore the use of this perturbation matrix is only strictly rigorous when the porphyrin ring possesses  $D_{2h}$  symmetry. However, protein induced ring distortions caused by the heme replaced protons, possible hydrogen bonding between close lying residues and the substituent propionate groups on the ring or other induced steric constraints can certainly lift this symmetry when the porphyrin resides within the myoglobin protein. As the hole-burning and Stark experiments are performed on real chromophores in real proteins, these symmetry-breaking distortions are certainly present and will influence the experimentally obtained spectra, which are utilized during the molecular resolution modeling process. In this case, off diagonal elements in the above Hamiltonian become non-zero and necessary to include.

Therefore, when the free-base porphyrin is allowed to take on a geometry realistically

representing one that would exist within the protein, the use of the Hamiltonian matrix appearing in equation 2.12 is necessary. When relaxing the assumption of pure  $D_{2h}$  symmetry, the transition moments used must be those that are calculated for the vertical transitions of the molecule possessing a native geometry that is not optimized in the gas phase.

The contribution that any individual chromophore may make to the resultant Stark line-shape must now be discussed. In a glassy matrix, no protein orientation is favored, thus an equal distribution amongst all possible molecular orientations exists. This is of primary influence on vector quantities that are fixed in the laboratory frame as related to those that are fixed in the molecular frame. In the laboratory frame, the light field propagates along the y-axis with polarization  $\vec{E}_{hv}$ . The external electric field, and thus its contribution to the local electric field  $\vec{E}_{loc}$  is along the z-axis. Therefore, these quantities, while fixed in the laboratory frame, appear to rotate with respect to the molecular frame. Within the molecular frame, regardless of absolute molecular orientation, the internal electric field  $\vec{E}_{int}$  is fixed [2, 3], as are the set of transition dipole moments  $\vec{\mu}_{mn}$ .

The probability that a particular color-center undergoes transition is a direct result of the interaction of the electric field vector of the excitation radiation (light polarization field vector) with the vector describing the transition moment of the color-center. As spectral hole-burning requires both a burn and read cycle, the probability that a chromophore will make a contribution to the collected Stark spectrum, then follows  $(\vec{\mu}_{mn} \cdot \vec{E}_{hv})^4$ , a squared expectation contribution from both the burn and read

process. To this is multiplied a factor that accounts for any deviation from the absolute polarization of the light field, as in this experiment, a Glan-Taylor prism is used for polarization of the light field. An application of Malus' law can be used to account for lack of perfect light polarization.

In order to equate these vector relationships for all chromophores present in a sample, the molecular plane is rotated through all possible molecular orientations as related to the laboratory frame. This is performed by using Euler angles. For each molecular plane orientation, a value for the total electric field is calculated accounting for the molecular fixed internal field, and the molecular observed rotating local field.

The process of fitting experimentally obtained Stark effect spectral holes with modeled line shapes, and thus the determination of the internal electric field, is an iterative mathematical process. As the external electric field is applied by the experimenter it is a specifically known quantity. The local field, therefore, derived from that quantity is also one which is in general approximately known. Using this as a fixed parameter, the internal field is guessed, which is a task that can be programmatically achieved by various methods, Nelder-Mead Simplex, Particle Swarm, etc. With this specific guessed internal field value,  $guess\vec{E}_{int}$ , the elements to appear on the main diagonal,  $W(n)$ , are calculated and stored for this particular guess of the internal field. For each possible molecular orientation, the total electric field is then calculated and the applicable Hamiltonian, equation 2.12 or equation 2.13, is populated with the total electric field value and the transition moments, and is then numerically diagonalized for all orientations. The resultant shift in transition energy between the ground and first excited state as related to the zero external field transition energy is calculated for each

orientation and weighted according to the probability that a molecule with the particular orientation will contribute to the Stark spectrum. These weighted shifts in transition energy from that of the zero-field, one from each possible molecular orientation, are then convolved with the best-fit Lorentzian profile of the original zero external electric field applied spectral hole. This modeled profile is then correlated to the actual experimentally obtained Stark spectrum. When this process is performed simultaneously on spectral holes for which different external electric fields were applied and the same value of the guessed internal field is found to yield modeled profiles that are highly correlated to all of the experimental profiles, confidence in the accuracy of the calculated internal field value is had. A procedural outline highlighting the necessary programmatic hierarchy of the calculation is shown in Appendix B.

Because this described molecular resolution approach is, in practice an elaborate physics driven line fitting methodology, a few comments regarding the accurate evaluation of the internal field value are necessary. There can only be confidence in any calculated internal field value if the values critical to its calculation rest on rigorous foundations.

The two quantities that have the greatest potential to lead to erroneous evaluations for the internal field,  $\vec{E}_{int}$ , are the local field tensor,  $\hat{f}_{loc}$ , and the set of transition moments,  $\vec{\mu}_{mn}$ , used in constructing the Hamiltonian. The local field tensor relies on the dielectric properties of the bulk matrix as well as that of the protein, in addition to specific geometric characteristics of the experimental setup. The transition moments will depend heavily on the particular geometric arrangement of the individual atoms making up the overall probe molecule, which in this case is the porphyrin core.

During the molecular resolution analysis procedure, the Hamiltonian matrix containing the non-experimentally measurable postulated state energies  $W(n)$ , which are under the influence of only the predicted internal electric field, must yield the state energies  $\mathcal{E}_n$  upon diagonalization. This set of state energies  $\mathcal{E}_n$  that serve as the target eigenvalues during the diagonalization, will profoundly influence the magnitude of any resultant shifts in transition energy between the ground and first excited state that are calculated for a particular electric field value. These state energies  $\mathcal{E}_n$ , must then reflect those that are spectroscopically obtainable. Additionally, these state energies should also be closely aligned to those that are calculated during the computational determination of the transition dipole moment values, as the state energies and transition moments are expectation values of the same wave function, and are thus inherently coupled to one another, with the importance of the energies scaling with the transition moments between the levels. The wave function and transition moments then can only be of quality if the calculated energies match those from experiment.

In a glassy matrix, the role of all possible molecular orientations are of importance. To accurately trace out the contribution from all possible color-centers, a complete orientation map needs to be used, especially when attempting to recover any fine characteristics of a Stark spectrum, specifically features sitting near the burn frequency. This amounts to implementing an angular step size that is ideally vanishingly small and approaching zero so that every possible molecular orientation is accounted for. Additionally, the weighting contributions need to reflect any deviation from perfect polarization of source light and the probability that any particular chromophore will contribute to the Stark profile.

## References

- 1.) Dirac, P. A. M. *The Principles of Quantum Mechanics*. Oxford: Clarendon Press, 1974. 167-184. Print.
- 2.) Gafert, J., Ober, C., Orth, K., Friedrich, J. (1995). "Thermal Broadening of an Optical Transition in a Chromoprotein between 50 mK and 15 K," *Journal of Physical Chemistry* 99(39), 14561-14565.
- 3.) Gafert, J., Friedrich, J., Parak, F. (1995). "Stark-effect experiments on photochemical holes in chromoproteins: Protoporphyrin IX-substituted Myoglobin," *Proceedings of the National Academy of Sciences USA* 92, 2116-2120.
- 4.) Gafert, Jurgen., Friedrich, Josef., Vanderkooi, Jane M., Fidy, Judit. (1995). "Structural Changes and Internal Fields in Proteins: A Hole-Burning Stark Effect Study of Horseradish Peroxidase," *Journal of Physical Chemistry* 99(15), 5223-5227.
- 5.) Geissinger, P., Kohler, Bryan E., Woehl, Jorg C. (1995). Electric Field and Structure in the Myoglobin Heme Pocket," *Journal of Physical Chemistry* 99(45), 16527-16529.
- 6.) Geissinger, P., Woehl, J. C., Prince, B. J. (2004). "A quantum-mechanical model for the determination of internal electric fields at protein active sites from the stark effect on persistent spectral holes," *Journal of Luminescence* 107, 220-229.
- 7.) Gradl, Gerhard., Kohler, Bryan E., Westetfield, Curtis. (1992). "Electric field splitting of the octatetraene 1 'A<sub>g</sub>→2 'A<sub>g</sub> transition in n-hexane," *Journal of Chemical Physics* 97(9), 6064-6071.
- 8.) Haarer, D. (1988). Photochemical Hole-Burning in Electronic Transitions. W. E. Moerner (Ed.) *Topics in Current Physics Persistent Spectral Hole-Burning: Science and Applications* 44, 79-125. Berlin Springer-Verlag.
- 9.) Hartmannsgruber, N., Maier, Max. (1992). "Wavelength dependence of electricfield effects on persistent spectral holes," *Journal of Physical Chemistry* 96(10), 7279-7286.
- 10.) Jankowiak, R., Hayes, J. M., Small, G. J. (1993). "Spectral Hole-Burning in Amorphous Molecular Solids and Proteins," *Chemical Reviews* 93(4), 1471-1502.
- 11.) Kirkwood, John G. (1939). "The Dielectric Polarization of Polar Liquids," *Journal of Chemical Physics* 7(10), 911-919.
- 12.) Kohler, B. E., Personov, Roman I., Woehl, Jorg C. (1995). Electric Field Effects In Molecular Systems Studied Via Persistent Hole Burning. Anne B. Meyers and Thomas R. Rizzo (Eds.) *Laser Techniques In Chemistry* 23, 283-323. New York John Wiley & Sons Inc.

- 13.) Kohler, Bryan E., Woehl, Jorg C. (1999). "Effects of Electrostatic Fields and Potentials on the Electronic Energies of Conjugated Organic Molecules," *Journal of Physical Chemistry A* 103(14), 2435-2445.
- 14.) Kohler, M., Friedrich, J., Fidy, J. (1998). "Proteins in electric fields and pressure fields: basic aspects," *Biochemica et Biophysica Acta* 1386(2), 255-288.
- 15.) Lennard-Jones, J. E. (1930). "Perturbation Problems in Quantum Mechanics," *Proceedings of the Royal Society of London. Series A* 129(811), 598-615.
- 16.) Meixner, Alfred J., Renn, Alois., Bucher, Stephan E., Wild Urs P. (1986). "Spectral Hole Burning In Glasses and Polymer Films: The Stark Effect," *Journal of Physical Chemistry* 90(26), 6777-6785.
- 17.) Onsager, Lars. (1936). "Electric Moments of Molecules in Liquids," *Journal of the American Chemical Society* 58(8), 1486-1493.
- 18.) Purchase, R., Sellars, M.J., Krausz, E. Manson, N.B. (2000). "Electric-field-induced broadening of spectral holes in zinc phthalocyanine," *Chemical Physics Letters* 327, 189-196.
- 19.) Ratsep, M. Wu, H.-M., Hayes, J. M., Blankenship, R. E., Cogdell, R. J., Small, G. J. (1998). "Stark Hole-Burning Studies of Three Photosynthetic Complexes," *Journal of Physical Chemistry B* 102(20), 4035-4044.
- 20.) Schindler, Florian., Lupton, John M., Muller, Josef., Feldmann, Jochen., Scherf, Ullrich. (2006). "How single conjugated polymer molecules respond to electric fields," *Nature Materials* 5(2), 141-146.
- 21.) Shankar, Ramamurti. Principles of Quantum Mechanics. New York: Springer, 1994. 451-471. Print.
- 22.) Woehl, J. C. (1996) *Measuring Internal Electrostatic Fields and Potentials at Molecular and Atomic Resolution using Hole Burning Spectroscopy*. Doctoral thesis. University of California-Riverside

## II

### Chapter 3

# Developing Temperature Cycling and Spectral Acquisition Software Platforms

## 3.1 Introduction

The ability to conduct experimental investigations lies not only in a researcher's fundamental understanding of the physical principles that dictate the mechanistic behavior of the system under study, but also lies in a researcher's ability to employ and integrate various laboratory components and instrumentation that allow for the effective collection of the appropriate data streams and information necessary for use in either proving or disproving the predetermined hypothesis. In many situations this could be as straightforward as using a single instrument and analyzing the output, however, as experiments become more and more sophisticated, the incorporation of greater numbers of instruments required for both experimental control and data collection becomes inevitable. The ability to integrate the operation of these different instruments into a manageable platform that allows for the seamless execution of input commands while maintaining high temporal inter-instrument resolution for data correlation becomes necessary to ensure the authenticity of the data obtained. The purpose for, and methods of program development, along with the completed block



diagrams displaying the internal workings of the developed virtual instruments (VI's) is discussed and highlighted herein.

### **3.2 Functional Requirements**

Obtaining information concerning molecular electric fields through the use of spectral hole-burning is a delicate task requiring the integration of several groups of specialized instrumentation. Three experimental aspects being of significant importance for carrying out hole-burning Stark spectroscopy, and temperature cycling studies are excitation control, emission collection, and temperature modulation. The data collected is in the form of a fluorescence excitation spectrum, whereby the excitation source is frequency scanned over the samples' absorption band and the corresponding fluorescence is simultaneously recorded. For this to occur, the coordination of a tunable frequency ring dye laser with an integrated wavelength meter that is precisely synchronized to a photon counter is critical. Additionally, the ability to record and modify the temperature of the sample throughout investigations is imperative.

### **3.3 Software Development**

In order for spectral information to be obtained, it was necessary for the Spectra-Physics Matisse DS tunable frequency dye laser scanning software, coupled to the HighFinesse WS-7 wavelength meter frequency measurement capabilities to be linked to the signal that is collected by two PerkinElmer SPCM-AQRH-16-FC avalanche photodiodes

(APD's), serving as the detectors. The software initially provided with the Matisse DS, already possessed the necessary plugin to allow for the HighFinesse WS-7 wavelength meter frequency readout during a frequency scan. It was therefore necessary to link this to the signal collected by the APD's. Initially it was thought that the Matisse software could be integrated with the software of the RHK Technology SPM 100 Controller, an instrument used when detecting the APD signal during image collection with the CTCSM (Cryogenic Temperature Confocal Scanning Microscope). Unfortunately, due to the proprietary nature of the RHK software, in addition to some patching and timing issues with the Matisse DS software, this turned out to be an impossibility. Thus, the initial decision to partner these existing programs was scrapped.

The new plan was to use the National Instruments LabView programming environment to develop an original software platform specifically tailored to the existing instrumentation. This allowed for the inclusion of even more precise control and data acquisition capabilities than just the simple spectrum (intensity vs. frequency), that had originally been the desired outcome. To this end, three programs have been developed in the National Instruments LabView environment, in order to address three specific aspects of the experiment. A fourth program that performs data smoothing and calculates the signal to noise ratio of the input data has been developed in the LabView environment for use in post processing of the experimental data sets. Figure 3.1 shows a simplified experimental schematic which displays the specific instruments addressed within each of the three developed programs. Block diagrams for each of the programs appear in the Appendix C.

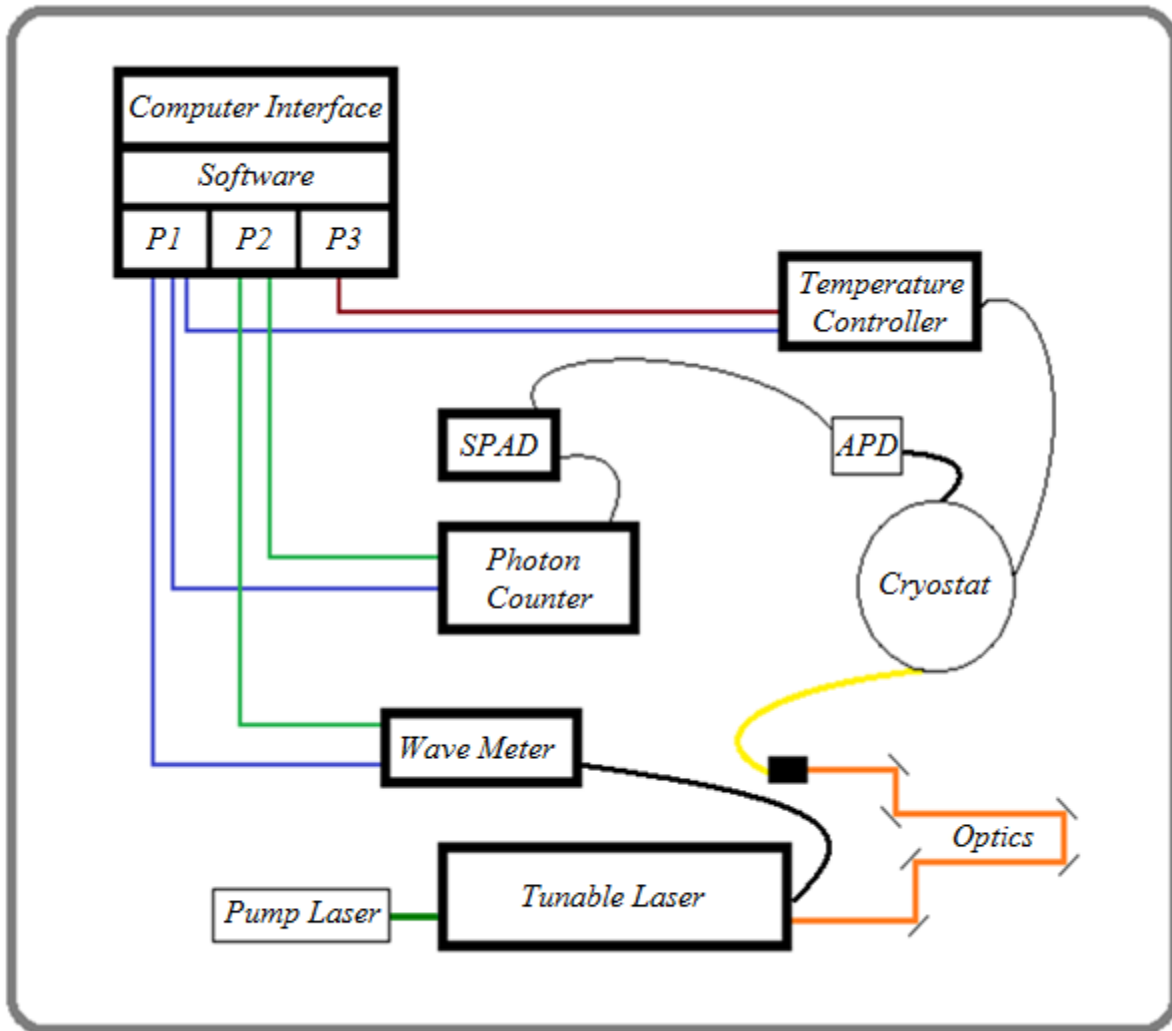


Figure 3.1: Schematic depicting experimental setup: The three programs developed are indicated as Software P1, P2 and P3. Solid blue, light green and red lines show which instrumentation is addressed in each program. Solid orange line is the laser beam, solid yellow line is an optical fiber, bold curved black lines are optical fibers, and light curved black lines are electrical connections. The SPAD supplies power to the APD's and relays the TTL signal produced by the APD's into the RHK Technology SPM 100 Controller.

### 3.3.1 Spectroscopy

The first program written, program P1, "Spectroscopy" is a platform used for acquiring spectral data. This program coordinates the HighFinesse WS-7 wavelength meter output with the sample's emitted fluorescent photons that are counted via a Stanford

Research Systems SR400 two channel gated photon counter that counts the signals collected by the two APD's. The program monitors the counted signal from each of the APD's as input 1 and input 2. These channels can serve as signal and reference or as two signal channels. All information is displayed in real-time. In addition to display of the

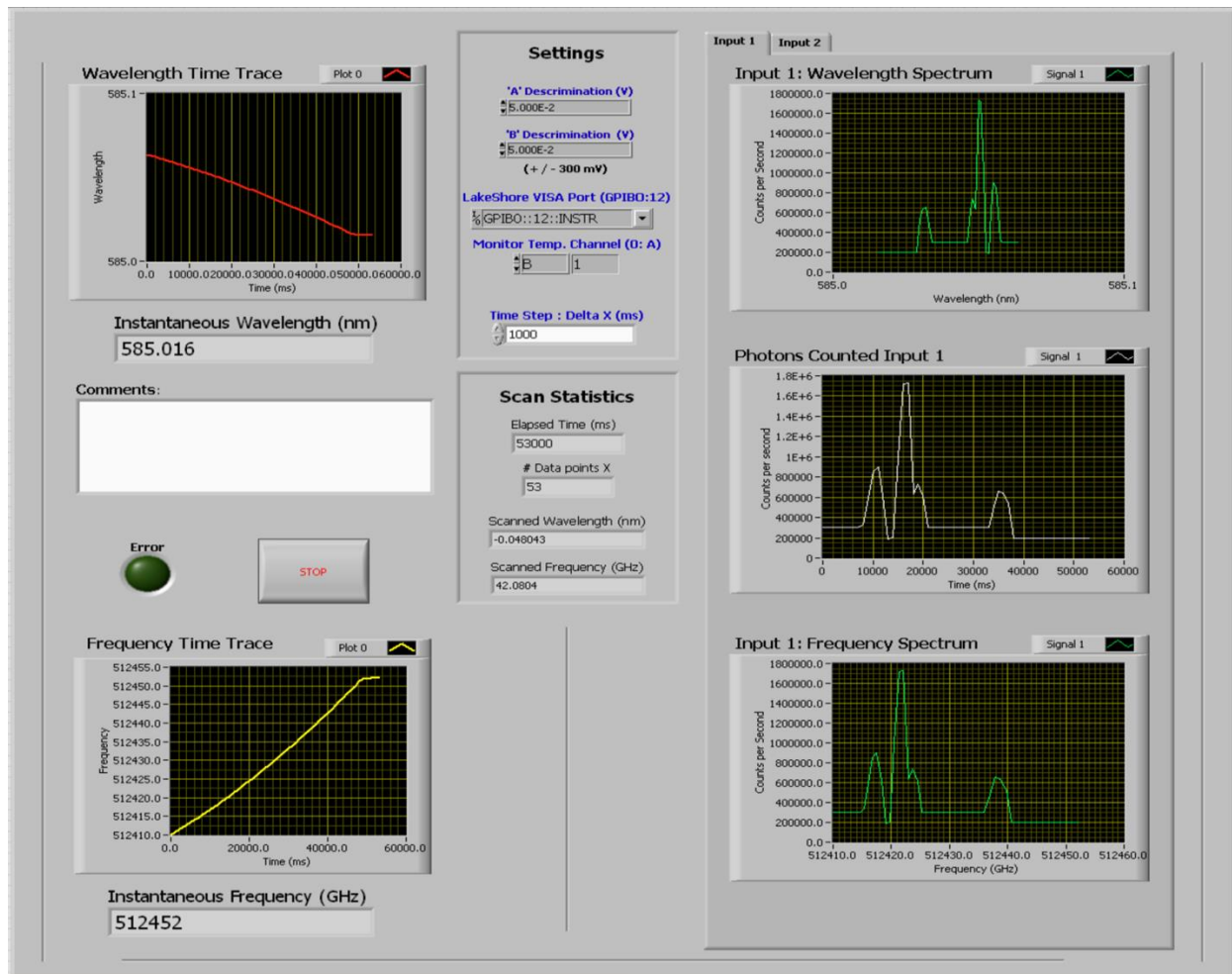


Figure 3.2: Screenshot of the user interface of program P1 "Spectroscopy". User sets timing of data acquisition, values for photon counter discrimination, and adds comments pertaining to the specific run. Recorded data is exported to spreadsheet.

standard spectrum, the scan of the laser source is displayed as wavelength and frequency vs. time. This is of use when monitoring the linearity of the scan process

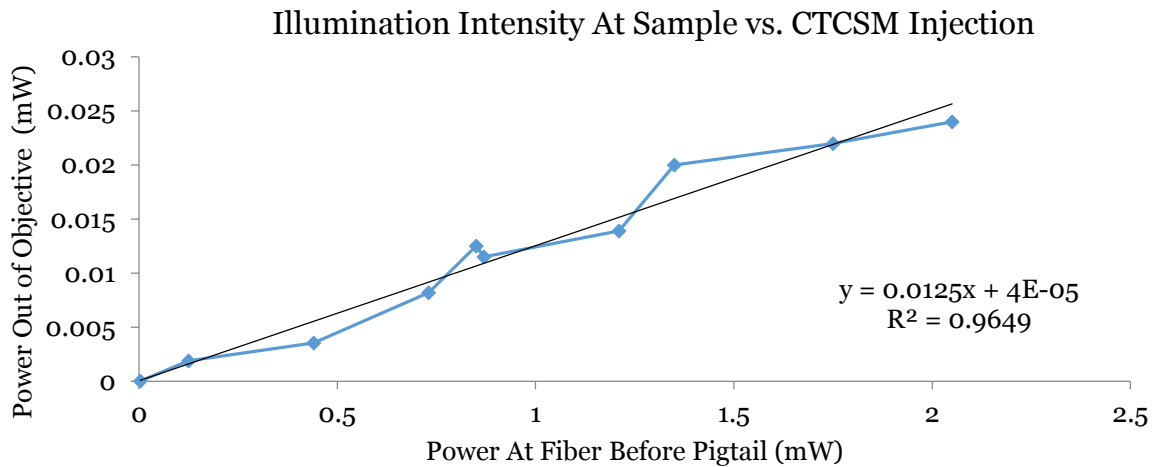
during a spectral scan. All of the data is saved to a spreadsheet file with counts input 1 and 2, wavelength, frequency, wavenumber, time, time stamp, and sample temperature information, as recorded with a Lakeshore 331 temperature controller. Any comments regarding scan parameters as entered by the user are also saved to the spreadsheet file. The scan statistics block displays to the user the number of data points taken during the experiment along with the total scanned wavelength in nanometers and the frequency in Gigahertz. Data acquisition timing control is set by user along with discriminator values for the Stanford Research Systems SR400 two channel gated photon counter. Additional information regarding appropriate time step and discriminator settings are discussed in chapter 5.2. The spectroscopy program front panel appears in figure 3.2 and an example spreadsheet of collected data is displayed in figure 3.3.

LabVIEW Measurement								
Writer_Version	2							
Reader_Version	2							
Separator	Tab							
Decimal_Separator	.							
Multi_Headings	Yes							
X_Columns	One							
Time_Pref	Absolute							
Operator	woehl-group							
Date	2/13/2013							
Time	13:55.7							
***End_of_Header***								
Channels	7							
Samples	225	225	225	225	225	225	225	225
Date	2/13/2013	2/13/2013	2/13/2013	2/13/2013	2/13/2013	2/13/2013	2/13/2013	2/13/2013
Time	13:56.6	13:56.6	13:56.6	13:56.6	13:56.6	13:56.6	13:56.6	13:56.6
Y_Unit_Label	ms	GHz	nm	cm-1	counts per sec	counts per sec	K	
X_Dimension	Time	Time	Time	Time	Time	Time	Time	
X0	0.00E+00	0.00E+00	0.00E+00	0.00E+00	0.00E+00	0.00E+00	0.00E+00	0.00E+00
Delta_X	1	1	1	1	1	1	1	1
***End_of_Header***								
X_Value	Time (ms)	Frequency (GHz)	Wavelength (nm)	Wavenumbers (cm-1)	Input 1 (cps)	Input 2 (cps)	Temperature (K)	Comment
0	0	512351.261	585.130712	17090.19848	340	16560	280.41	
1	100	512351.4399	585.130507	17090.20445	280	16740	280.41	
2	200	512351.5558	585.130375	17090.20831	150	15600	280.41	
3	300	512351.7909	585.130107	17090.21616	330	14460	280.41	

Figure 3.3: Example spreadsheet file with time and date stamp, time, frequency, wavelength, wavenumbers, counts per second, and temperature information, and comments. Spreadsheet output files produced by other developed programs appear similar to above.

### 3.3.2 Hole-Burning

The second program written, program P2, “Hole-Burning” is a platform that is used during the burning of the spectral hole. This allows the user to monitoring the hole-burning process during the burn. The initial intensity of emitted fluorescence is recorded and the depletion of the signal is displayed as the sample undergoes photo transformation. Any frequency drift of the laser that occurs during the burn is also



Before Injection (mW)	At Objective (mW)	Regression
2.05	0.024	0.025665
1.75	0.022	0.021915
1.35	0.02	0.016915
1.21	0.0139	0.015165
0.87	0.0115	0.010915
0.85	0.0125	0.010665
0.73	0.0082	0.009165
0.44	0.00355	0.00554
0.125	0.0019	0.0016025
0.0029	0.000009	0.00007625

Figure 3.4: Relationship of laser intensity incident upon sample out of objective at base of CTCSM in relation to laser intensity injected into the CTCSM. Intensity losses are due to optics contained within the CTCSM.

recorded, which is of necessity when analyzing characteristics of spectral hole width. The user again enters the data acquisition timing control and the appropriate discriminator values. The user also enters the laser power recorded by a power meter, measured at the output end of the optical fiber, prior to the pigtail used for injection into the CTCSM. This allows the total power delivered during the burn to be recorded. Laser intensity is stable over the course of the burning process which is usually between 6 and 24 seconds in length. To account for the loss of intensity due to the optics within the CTCSM, measurements were taken and a function describing the relative intensity prior

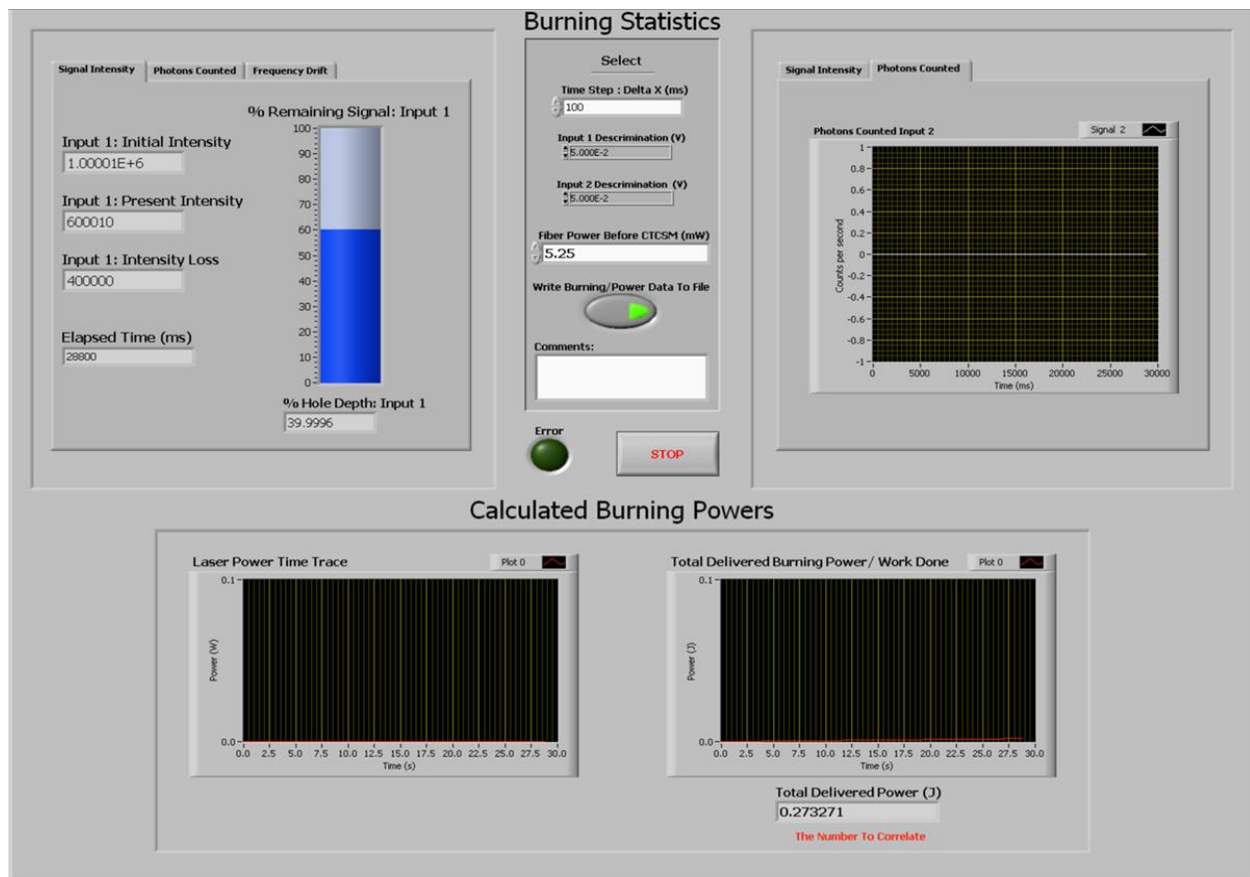


Figure 3.5: Screenshot of the user interface of program P2 "Hole-Burning". The user sets the time step for the data acquisition, and the laser power that was measured at the output end of the optical fiber by use of a power meter. The remaining signal, photons counted, frequency drift during burn, laser power and cumulative energy delivered to sample during the burning process are display. Data is exported to spreadsheet.

to injection into the CTCSM to the intensity at the sample was found and incorporated into the hole-burning program. Remaining signal, photons counted, frequency drift during burn, laser power and cumulative energy delivered to sample during the burning process are displayed in real-time. This information is again exported to the spreadsheet data file.

### 3.3.3 Temperature Cycling

The third program written, program P3, “Temperature Cycling” is a platform that assists in modulating the sample temperature by allowing users to control the heater ramping and PID temperature control values. This platform was adapted from a Lakeshore

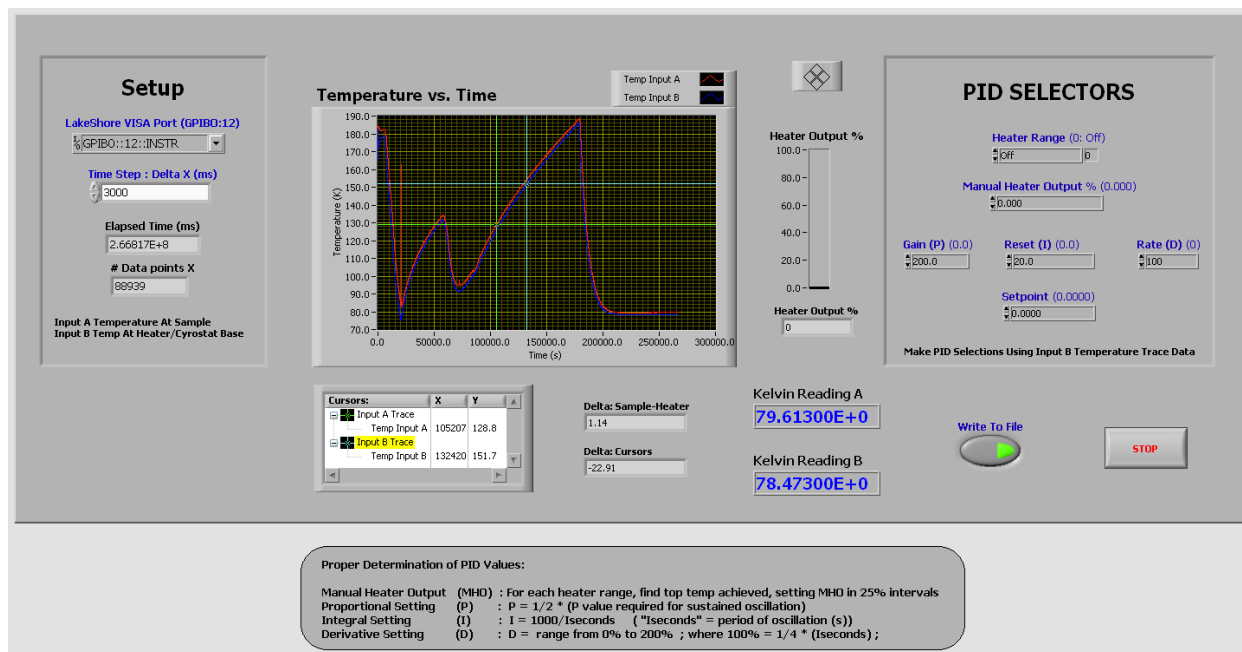


Figure 3.6: Screenshot of the user interface of program P3 “Temperature Cycling”. User sets timing of data acquisition and PID values. Control of heater range and heater output, used when performing temperature cycling studies, are also controlled here. Again, displayed data is exported to spreadsheet.



National Instruments LabView VI and was enhanced for more user control. The front panel displays a real-time trace of temperature vs. time. The user can change the heater range between low, medium, and high settings and the amount of heater output between 0-100%. Additionally, the user can input specific PID values for stabilized heater control in the particular temperature range of experimental operation. Temperature at the heater as well as the temperature at the sample are displayed and recorded. If desired, the temperature profiles can be saved to data files. The main benefit of this program lies in its ability to be used to enact specific thermal control of the sample. This is a main necessity when performing temperature cycling studies, which are used for investigating the potential energy surface of proteins around equilibrium conformations, and the possible conformational degrees of freedom existing in low lying energy states.

### **3.3.4 Signal Smoothing**

Most commercially available UV-Vis and fluorescence spectrometers have some form of signal averaging or smoothing functions built into the software. In some cases, the user may be unaware that this process is occurring if not required to manually set the smoothing or sampling parameters. As the software used for these experiments was developed in house, this feature was not incorporated. Initially, to overcome this issue the sampling and smoothing was manually performed for cleaning up the collected spectral profiles. All spectra would be repeatedly taken ten times, over the exact same frequency range at the same collection rate. The values were concatenated and then a

10-point boxcar style method was used to return the same number of points originally collected in a single spectrum. This procedure allowed for the enhancement and extraction of the true signal from the noisy data. Although this resulted in accurate and smoothed spectral profiles, this process was both labor and time intensive, and possibly

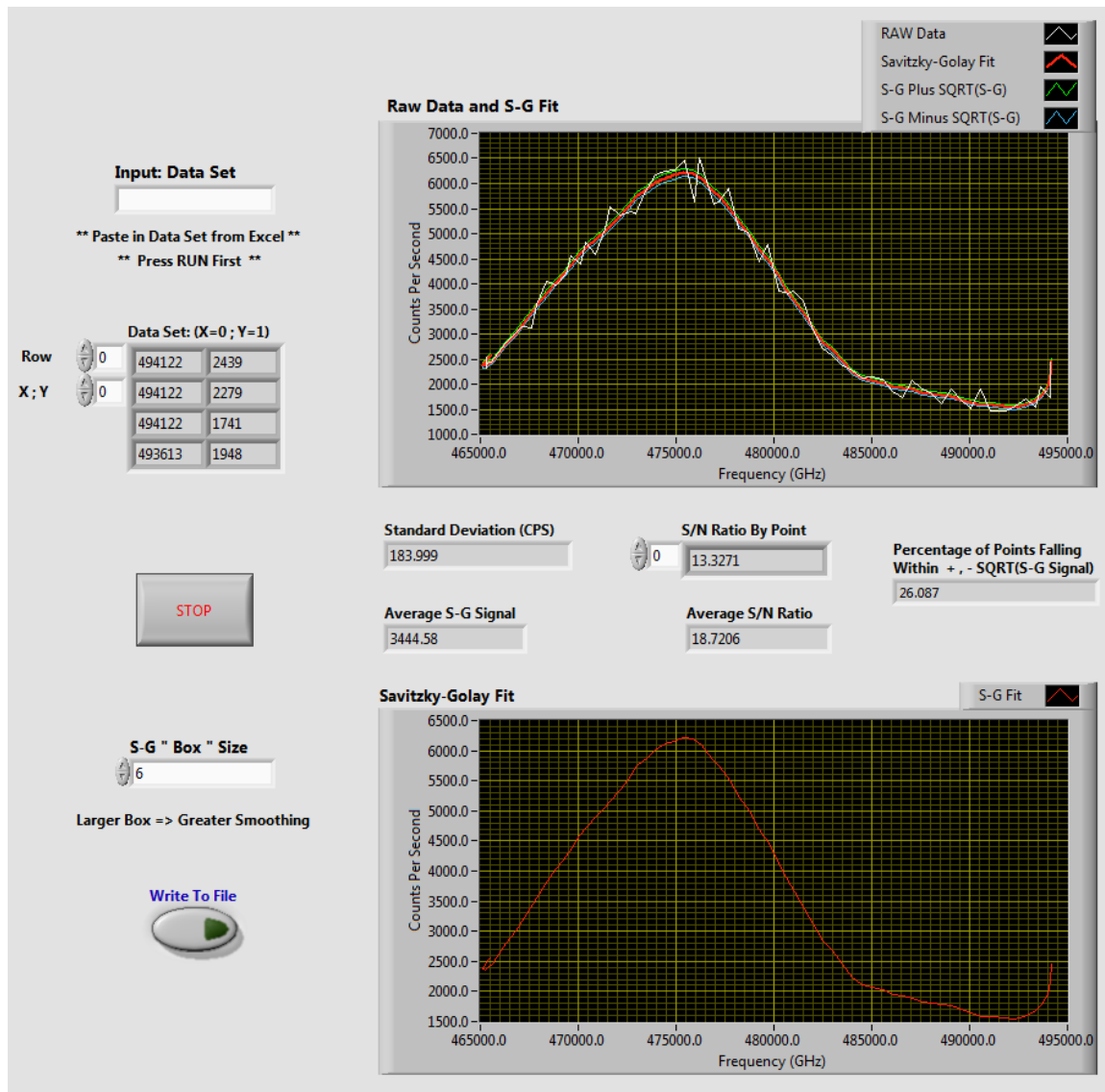


Figure 3.7: Screenshot of the user interface of the signal smoothing program. User enters the raw data set and selects the box size for the Savitzky-Golay smoothing algorithm. Raw data along with smoothed data and signal to noise characteristics are exported to spreadsheet.

detrimental to sample longevity. To get around this lengthy process, LabView was again used to create a smoothing filter and signal to noise ratio calculator that can be applied to collected spectra. The program uses a Savitzky-Golay weighted moving average filtering method. The Savitzky-Golay filter uses a third order polynomial, and the box size can be selected by the user, although the default is a box of size 6. As it is a standalone program, it can easily be used for any data set that a user would like to smooth and get S/N ratio information on. A screenshot of the user interface appears above.

## II

### Chapter 4

# **Extending Functionality of the Cryogenic Temperature Confocal Scanning Microscope**

## **4.1 Introduction**

We have developed and constructed a Cryogenic Temperature Confocal Scanning Microscope (CTCSM) for use in single molecule imaging studies as well as for use when performing Stark spectroscopy investigations on single molecules and heme proteins. This is a custom version of a conventional confocal microscope that is capable of operating in the cryogenic regime. Upon initial development, primary focus had been on the imaging capability of the microscope. A description of this work can be found in the doctoral dissertation of Yi Hu, [9]. The following highlights various modifications that were made to extend the functionality of the instrument and allow for enhanced experimental flexibility and data streams. The various mechanical modifications and additions made to the microscope, which are required when performing Stark spectroscopy, single molecule imaging, and spectral studies are reviewed. Of primary importance is the capability to collect a samples' spectral response in addition to its image, which has now been incorporated into the system. Due to the importance of the instrument to this investigation, a complete description of the final construction as well as spectral and image collection, acquired from cryogenic through room temperature

with this microscope, will be discussed. Although the CTCSM to this point has only been used for studies on fluorescent beads and doped glasses, the instruments' ability for imaging and spectral collection has broad applicability to diverse future experimental avenues.

## **4.2 Microscopy**

Optical light microscopy is a powerful tool that revolutionizes sciences' ability to probe the world of the small and gain an in-depth understanding of systems ranging from tissues and cells, to organelles and even single molecules. Microscopy allows researchers to directly visualize features that sit at the edge of the diffraction limit of light in size, systems that are larger than roughly 300 nm. In their simplest form, all microscopes use a series of lenses that work to expand the image of a specimen as it is illuminated with the goal to optimally enhance the contrast and resolution of the image.

Elementary microscopes possess an objective lens situated towards the sample, used to magnify the sample, and an ocular or eyepiece lens situated towards the observer, that is used to magnify the image of the sample as created by the objective lens. Originally these two optical elements were commonly separated by a reference distance of 160 mm known as the tube length. In the 1930's, infinity corrected objective lenses were developed by the German microscope manufacturer Reichert [10]. Standard objective lenses focus light rays emanating from a specimen to a focal spot between the objective and ocular lens. Infinity corrected objective lenses cause all light rays emanating from the sample to exit the objective in a parallel fashion, as though the focal

point of the objective were infinitely far away. This allows the distance between objective and ocular to be modulated and other optics to be incorporated into the light path. Infinity correction does, however, create the necessity of placing an additional optical element, known as a tube lens, between the infinity corrected objective and the ocular. Infinity corrected objective lenses are now standard and the lens separation characteristic of 160 mm is no longer stringently followed [17, 10, 7].

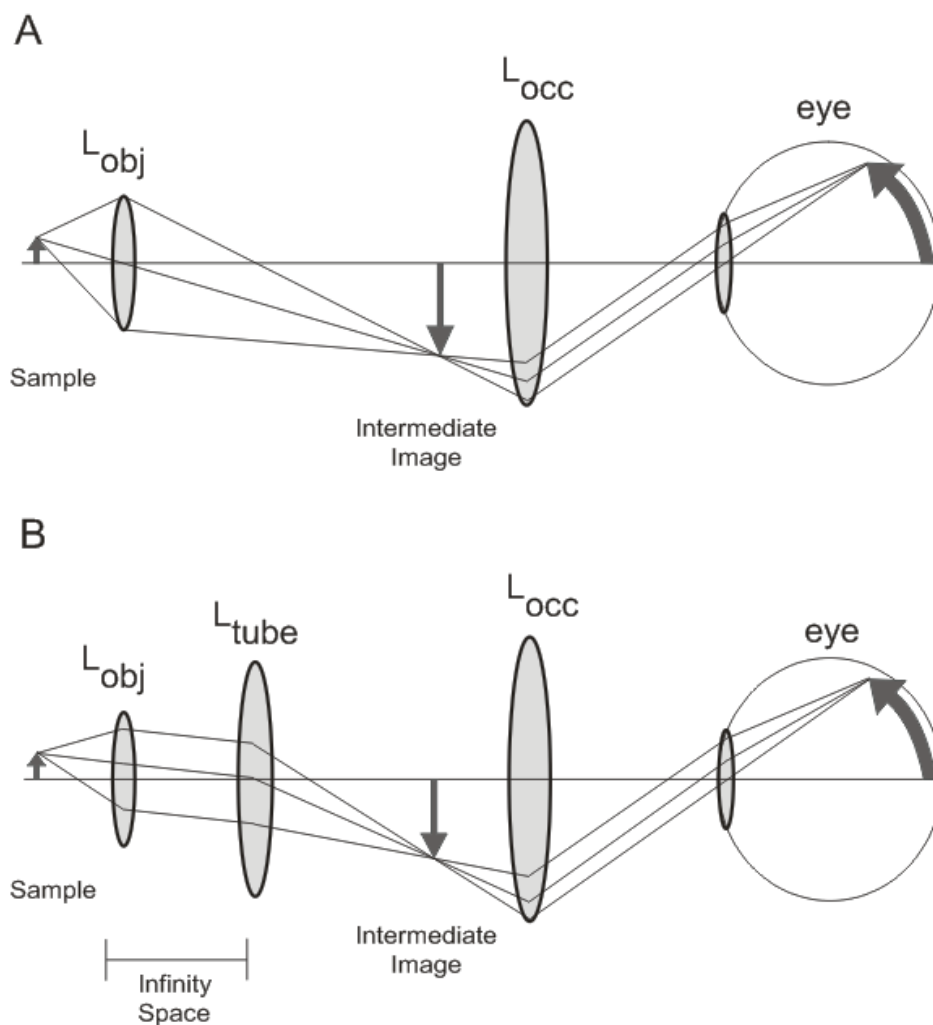


Figure 4.1: A: Ray diagram within a conventional microscope from the sample through the objective lens  $L_{obj}$  and ocular lens  $L_{occ}$  to the observer's eye. The intermediate image appears behind the objective at a distance equal to the back focal length  $f'$  of the objective plus the tube length of the microscope. B: Placement of the tube lens  $L_{tube}$  between the infinity corrected objective and ocular allows for inclusion of additional optical elements without affecting the effective tube length of the microscope.

In most imaging applications today, an electronic imaging device such as a CCD or electron multiplied CCD (EMCCD) camera is used to observe the intermediate image. The incorporation of such devices enhances the detection ability of low contrast and low light emitting samples by use of an integrated signal collection approach [5]. Although much advancement has been made throughout the field of microscopy, focus will be placed only on the basic operating principles of wide-field microscopy and the optical improvements gained through the use of confocal microscopy.

#### **4.2.1 Wide-Field Microscopy**

In wide-field microscopy, the entire specimen is bathed by the illumination source as it is imaged by the objective. Of the many illumination geometries that fit into this category, two of the most frequently used are dark-field and bright-field. In dark-field mode, the illumination source and objective are situated along different axial directions, where light that is reflected or scattered from the sample is the interest of investigation. When using bright-field mode, the illumination source and objective reside along the same axis. Light is either transmitted through sample from below, or the sample can be illuminated from above. In either arrangement it is the contrast or absorption of light that serves to provide detail about the sample. Acceptable recreation of the XY characteristics of the specimen will generally occur with each of these illumination geometries.

Illumination is frequently provided by an incoherent broadband source such as a tungsten or xenon arc lamp, however, laser sources are also used when fluorescently

tagged samples are studied. In fluorescent mode, all fluorophores within the sample are illuminated and some will fluoresce. In all cases, light that is absorbed or fluorescently originates from different planes within the sample is flattened to a 2D image. This is adequate in thin samples when discrimination in the Z direction is not critical for the experimenter. The compression of the image is the main contributor to the enhancement of any resultant blurring observed, which at best is limited only by the Abbe diffraction law. In thick samples, observing features that are reliably spatially resolved are not always a possibility.

Of main benefit to this branch of microscopy are the limited quantity of optical components required, the lack of need for specialized excitation sources and the low amount of excitation light that is generally required for an imaging application. These setups also allow for the high-throughput of samples and aside from fluorescent tagging, offer a non-invasive opportunity to gain image data [10].

#### **4.2.2 Confocal Microscopy**

Confocal microscopy is an imaging technique that uses the same underlying principles as wide-field microscopy, but allows for the spatial filtering of the out-of-focus light information that significantly contributes to loss of image clarity in the wide-field case. Now a fairly common technique used in most optical laboratory settings, the principle was first described in 1955 and patented in 1961 as a microscope apparatus by Dr. Marvin Minsky during his time as a Junior Fellow at Harvard [12]. Confocal microscopy's strength comes from inclusion of a pinhole aperture that is placed prior to



the detector. The pinhole is placed at the image plane and permits only the portion of signal light that resides in a conjugate focal plane to the point of focus in the sample under investigation to be collected.

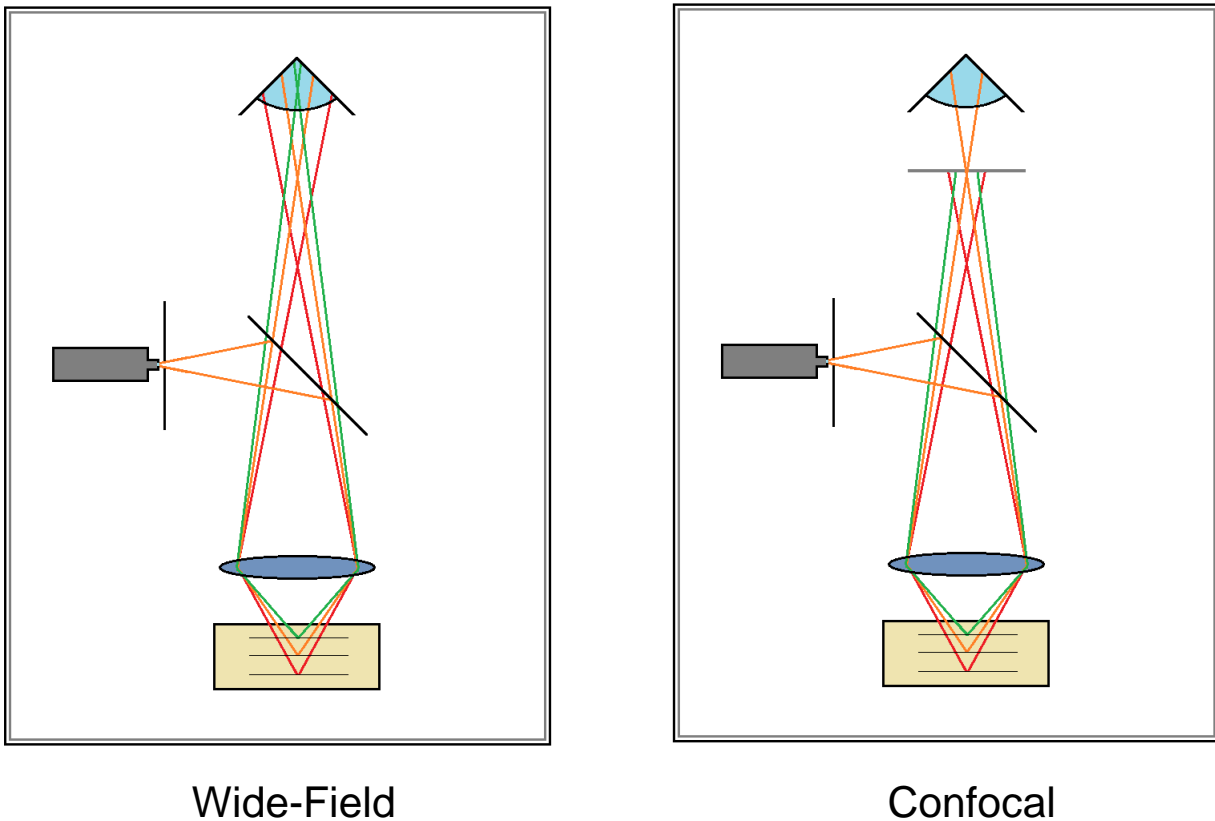


*Figure 4.2: Wide-Field microscopy, Left: Signal is collected from all depths within the entire sample simultaneously. The collection of out of focus light information leads to enhanced image blurring. Confocal microscopy, Right: Inclusion of pinhole aperture before detector spatially filters the out-of-focus light. Only the signal light that resides in a conjugate focal plane to the sample under investigation is collected, and the optical resolution of the sample is significantly enhanced.*

The optical setup in confocal microscopy is more involved than only the inclusion of a pinhole aperture for light discrimination purposes. These microscopes do not strictly, but generally use an epi-collection setup whereby the illumination source and signal collection occur from the same side, by use of the same objective element. This type of optical setup requires the introduction of dichroic mirrors into the pathway to

eliminate interaction of the excitation light with the detector. Although the optical resolution of the sample is significantly enhanced, the inclusion of the pinhole aperture allows only one point of the sample to be imaged at a time. As opposed to imaging the entire sample simultaneously as in wide-field, the image must be examined point by point usually by a raster scanning process. This process is performed by appending successive rows “Y” of parallel scans “X” together to create the image. This can be achieved by keeping the sample stationary and manipulating the excitation source, usually by translating in space a laser beam with actuated mirrors, or by using a Nipkow-disk to serve as the pinhole [6]. Conversely the optical arrangement can remain stationary and the sample stage can be raster scanned, as was the originally devised approach by Dr. Minsky referred to as “stage-scanning” [12]. The necessity for the mobile optical or stage components adds to the complexity of the method.

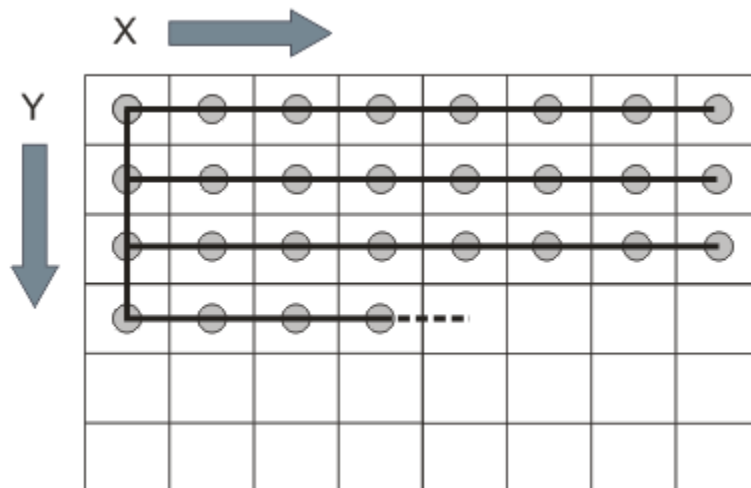


*Figure 4.3: Depiction of the raster scanning process. Either the source light or the sample is spatially translated in a pattern of successive rows Y, of parallel scans X. At each position within the sample, light information is collected and the image is created. Decreasing the step size in either direction increases the number of pixels in the image. This will create clearer and more detailed appearing images with enhanced contrast and perceived resolution.*

Of specific benefit, the confocal point by point collection characteristic serves as a means to optically section the sample. Since objective lenses have a focal point with a limited depth of field, the ability to investigate sample characteristics in the axial direction becomes a possibility [17]. No longer are 3D images flattened to 2D recreations, but each plane of a sample can be imaged with sample stage or objective lens translation in the Z direction. This Z-stacking imaging technique has found extensive use in biological research as well as in imaging the Z direction optical point spread function in optical systems [16, 15, 10]. The depth resolving capability is undoubtedly the most exciting advancement this microscopic method offers the scientist.

### **4.2.3 Optical Limitations**

All forms of optical microscopy rely on using a lens or a set of lenses to magnify the lateral appearance of objects under study as observed by the viewer. In the presence of perfect aberration free optics, the resolving capabilities of a light microscope are dictated only by the diffraction limit of light. Both the Abbe diffraction limit (diameter) and the Rayleigh criterion (separation) quantify this restriction [1, 14]. When a small emitter or point source of light is imaged, due to the occurrence of diffraction, the smallest spot-size that will be recreated by the optical imaging system is the diameter of resolution  $d$ . At minimum, with the use of perfect optics and within the visible light region, the diffraction limit translates to resolving structures that are approximately 150 nm to 350 nm in diameter. As described by the Abbe diffraction limit, the diameter of

resolution  $d$ , is directly related to the wavelength of source light  $\lambda$  used for illumination and inversely related to the index of refraction of the surrounding medium  $n$ , converging to a spot with angular resolution of  $\theta$ . The term,  $n \sin \theta$ , is equal to the numerical aperture  $NA$ , of the objective lens and is equal to one half of the maximum cone angle of acceptance for light into the particular objective being used.

$$d = \frac{\lambda}{2(n \sin \theta)} = \frac{\lambda}{2(NA)} \quad (4.1)$$

The minimum distance that two points sources can approach each other and their diffracted images still be resolved is the axial resolution limit and is defined by the Rayleigh criterion. This criterion states that the sine of the angle of resolution  $\theta$ ,

$$\sin \theta = 1.220 \frac{\lambda}{D} \quad (4.2)$$

is directly related to the wavelength  $\lambda$  of illumination and inversely related the objective lens diameter  $D$ . Due to the lateral intensity distribution in which image data are represented the minimum resolvable distance is defined as separation between the two points within the image at or greater than the first minimum of the intensity distributions of each emitter. Again with the use of perfect optics and within the visible light region, this correlates to two particles being resolvable at separations of greater than approximately 300 nm. The specific values for the diameter of resolution and minimum resolvable distance are dependent upon the individual microscope and illumination source properties.

Since the lenses that comprise the optical system are limited in angular size, they are not able to capture the entire light field emitted from a point source, resulting in imprecise focus back to a single point. Classically, the point spread function (PSF)

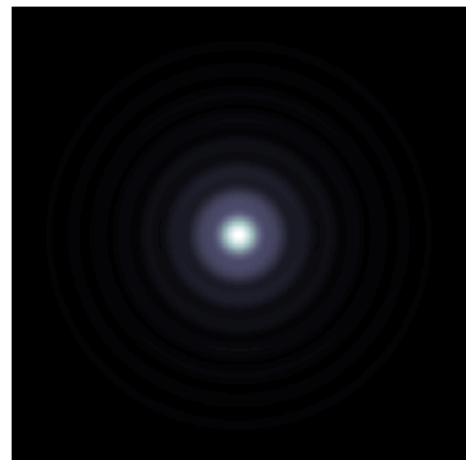
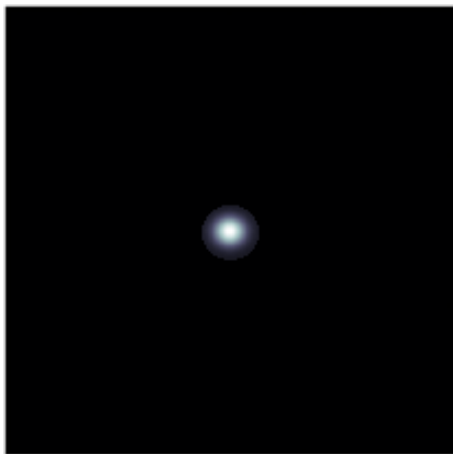
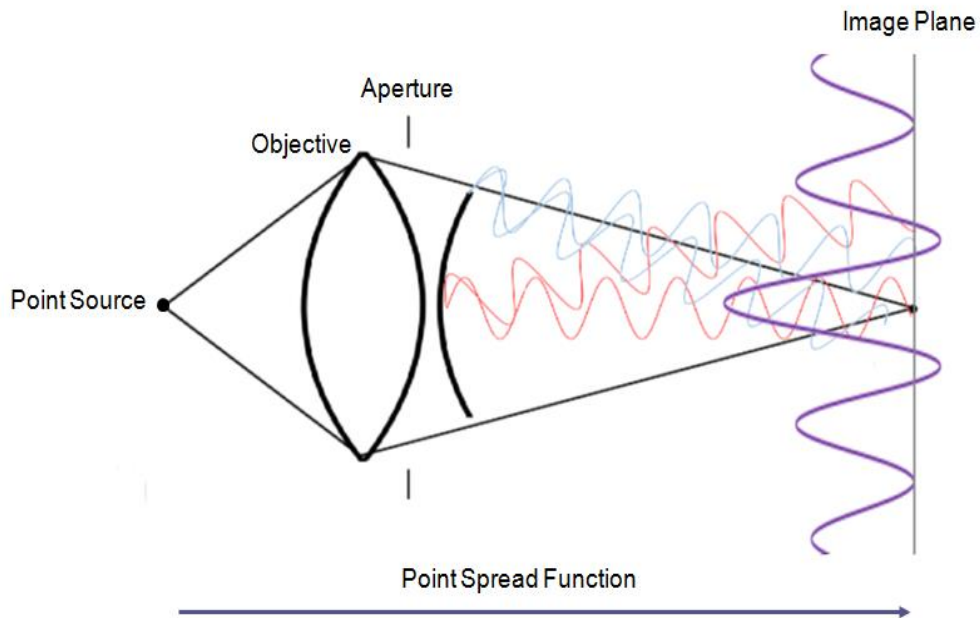


Figure 4.4: Top: Ray diagram of light emanating from a point source through an objective to the image plane. Because the objective collects only a portion of the spherical wave-front, light rays combine in a constructive and destructive fashion yielding the diffraction limited Airy pattern. Bottom left: Light emitting point source, expanded for clarity. Bottom right: Resulting image of the point source, now convolved with the point spread function of the imaging system.

provides a model of how light emitted from a point source is diffracted as it travels through the optical pathway of an imaging system. The PSF is representative of Fraunhofer diffraction, and in the focal plane, ideally can be described by the Airy pattern. The Airy pattern is a diffraction intensity distribution with a characteristic bright center known as the Airy disk, surrounded by alternating bright and dark diffraction rings [2]. The Airy disk equation is used to calculate the intensity of the optimally focused spot and diffraction rings in the resultant image of a point emitter as collected by an objective with a circular aperture. It relates the intensity  $I(r)$  at any radially specified distance  $r$ , to the position  $r_o$ , and magnitude of maximum intensity  $I_o$ , at the spots' center in the image. A Bessel function of the first kind  $J_1$ , is utilized in calculation of this intensity distribution.

$$I(r) = I_o \frac{J_1\left(\frac{r}{r_o}\right)}{\left(\frac{r}{r_o}\right)} \quad (4.3)$$

In modern microscopy, CCD, EMCCD and CMOS cameras are frequently employed as detectors to collect and record optical data. This enhances signal degradation as these detectors add not only pixilation but three additional sources of noise minimizing the overall quality of the image. These being dark noise, read noise and photon noise which all contribute to the PSF of the imaging system [13, 8]. Images experimentally obtained with microscopes can also possess uneven backgrounds and possess particles which undergo photobleaching [3].

Due to these various compounding affects, the fine detail of the diffraction rings is often lost, and it is standard practice to use a two dimensional Gaussian equation

instead of the Airy disk equation for modeling the PSF. The two dimensional Gaussian equation as used to approximate the Airy disk equation again models the intensity at any position  $I(x,y)$  around an imaged point source given the amplitude  $I_0$ , and position of maximum intensity  $x_0, y_0$ , using scale parameters  $\omega_x, \omega_y$ , that describe the circularity ( $\omega_x = \omega_y$ ) or ellipticity ( $\omega_x \neq \omega_y$ ), of the imaged point. Although the 2D Gaussian

$$I(x, y) = I_0 * e^{-\left(\left(\frac{(x-x_0)^2}{2\omega_x^2}\right) + \left(\frac{(y-y_0)^2}{2\omega_y^2}\right)\right)} \quad (4.4)$$

distribution reproduces the main disk of the Airy function, since it is only an approximation to the Airy function, authors have considered various modifications to the traditional formulation of the 2D Gaussian for establishing more accurate derivation of the various PSF parameters [19]. Other researchers have explored using alternate distributions [4] or have proposed the inclusion of some corrections to the 2D Gaussian distribution to account for the optics of the optical imaging system in the modeling of the PSF [11]. Considerable effort to find more powerful ways in which to accurately and computationally efficiently model the PSF remains an active branch of research with primary importance in particle tracking algorithms [3].

### 4.3 CTCSM

Conventional fluorescence wide-field optical microscopy suffers from diffraction limited resolution at sub-micrometer dimensions. To enhance the perceived angular resolution

and contrast of image data, minimization of scattered light that is responsible for amplifying background noise is crucial. This is of significant importance when imaging single molecules, nanoparticles, or weakly emitting fluorophores, especially when the emitters are contained within thick media. To achieve high-resolution imaging capabilities, a confocal setup was employed for the design of this microscope device. The Cryogenic Temperature Confocal Scanning Microscope (CTCSM) was designed as a fiber-based confocal microscope able to perform two dimensional and three dimensional sample scanning with the capability of operation in the cryogenic range. As with most microscopes, the CTCSM's utility as an imaging tool was of primary importance during initial development. The CTCSM, thus, could be used for investigations where the image generation of a specimen was the only data stream required by the experimenter. To expand experimental flexibility of the system, the capability of spectral collection was introduced to the CTCSM. This was achieved by the development of a software platform that coordinates several groups of specialized instrumentation used for acquiring the spectral data. The optical design allows for modulation to any desired angle, the polarization of the excitation light as incident upon the sample. High maintenance of the polarization is achieved because the polarization element interacts with the excitation light after the optical fiber and after the dichroic mirror. In addition to collection of the reference signal, electric fields can now be applied to the sample for performing Stark effect or electrochromism investigations.



### **4.3.1 Illumination**

The fiber coupled design of the CTCSM allows for the effortless inter-change between excitation sources used for illumination of the sample. Currently, three separate laser sources can be used for varied excitation. These include a Spectra-Physics Stabilite 2017 Argon Ion laser (514.5 nm, 488.0 nm, 465.8 nm), a Spectra-Physics Millennia Pro 6SJS (532 nm), or a Spectra-Physics Matisse DS tunable frequency dye laser (575 nm – 645nm). In most applications, however, the Argon Ion and Matisse DS are predominantly used. Laser light is coupled into the CTCSM through a Nufern 2.5  $\mu\text{m}$  Core Diameter 460-HP Select Cutoff Single-Mode Fiber.

### **4.3.2 Construction and Modifications**

Our custom designed and constructed low temperature confocal scanning microscope is a self-contained architecture whereby all of the necessary optical components are housed within the microscope as opposed to being a collection of optics situated on an optical table. It is primarily constructed of components from ThorLabs, with the optical elements from various sources. The 30 mm cage system is used, with cage cubes, construction rods and lens tubes providing the mechanical framework of the system. Of great advantage to this microscope is its modular design, allowing for some experimental flexibility. The microscope has two main sections. The head of the microscope, which remains outside of the cryostat and contains most of the optical elements, and the optical insert, which is placed within the cryostat during experiments. The head of the microscope is composed of a central axial scaffolding structure with an

excitation arm, two emission arms and a reference arm. The central axis is an arrangement of three C6W - 30 mm cage cubes which house the necessary filter and beam deflection elements, and provides support to the arms of the microscope. The optical insert portion uses construction rods to extend the length of the microscope so the objective and sample scan stage rest within the cryostat.

When light enters the microscope through the 2.5  $\mu\text{m}$  core diameter single-mode fiber, the diffuse beam is collected with a ThorLabs AC254-030-A achromatic doublet 25.4 mm diameter 30 mm focal length lens. A z-axis translation mount, SM1Z, is used to tune focus between the lens and the fiber to create a collimated beam upon entrance into the microscope. The collimated beam possesses a diameter of  $\sim 8.0\text{-}9.0$  mm which is slightly larger than the diameter of the back lens of the objective. Light travels in free space, optics aside, throughout the microscope until re-coupled into a detection fiber. When light leaves the excitation arm it enters the center cage cube, which houses the dichroic mirror. Light interacts with the dichroic mirror placed 45 degrees to the direction of propagation causing a 90 degree turn, sending the light down the optical insert to the objective and sample. To modulate the position of the beam on the dichroic filter, the excitation arm uses two kinematic micrometer drive translational mounts. A ST1XY-S allows for lateral translation of the beam on the dichroic and the KC1-T allows for tuning of the deflection angle off of the dichroic. These are modulated incrementally to allow for parallel and centered alignment to the optical axis of the objective. To allow for collection of a reference signal, the light that passes through the dichroic can be monitored. This light is passed through two iris elements used to attenuate the intensity

separated at a distance of two inches. This signal is coupled into a SPCM-QC9 optical fiber and can be recorded using a second APD.

The cage cube directly below the central cage cube contains a BP145B1 pellicle beam splitter placed 90 degrees to the dichroic mirror. This serves to deflect a portion of the emission beam out of the microscope in the original direction of beam propagation. This beam is observed with a viewing screen or with a CCD camera and is used to initially establish a rough focus of the sample stage to the objective. The reference signal can alternatively be collected at this position on the same side as the excitation arm should monitoring through the dichroic mirror prove difficult. During experiments with low intensity emitting fluorophores, the beam splitter can be removed, without any change in beam direction and position. In this case the reference must be placed behind the dichroic as originally described.

For hole-burning and single molecule experiments light polarization is critical. The excitation light can be actively modulated to produce a linearly polarized beam to any desired angle as incident upon the sample. This is achieved mechanically by rotation of a Glan-Taylor prism, positioned below the bottom cage cube, at the base of the head of the microscope, just prior to the flange coupling of the cryostat. The Glan-Taylor prism was procured from Casix, and sits within a one-inch lens tube and coupler and is placed between two 0.5-inch cage plates. The cage plates are held rigidly in place with 2.5-inch cage assembly rods at a distance that allows for the 1.035"-40 thread matched rotation of the lens tube. Up to three full revolutions, 1080 degrees, of smooth rotation is possible. Beam displacement upon rotation is negligible in comparison to the ~8.0 mm beam diameter causing only slight oscillation of the outer edge of the plane of

illumination hitting the back lens of the objective. The diameter of the back lens of the objective is 6.5 mm and when the CTCSM is aligned and collimated no deviation in focal point position is observed on the sample during prism rotation.

The optical insert is the portion of the microscope that is placed within the cryostat and holds the objective and sample stage translation actuators. The optical insert is 48 inches in length and is constructed using cage assembly rods. There are five evenly spaced CPO7 round cage plates that hold wg41050-A glass flat windows, all from ThorLabs, which aid in providing mechanical support to the optical insert. The top glass flat has an IR coating to help reduce thermal transport. The other four windows, although uncoated, do serve as thermal baffles when in the cryostat. Before being put into the cryostat the microscope is placed into a 47.7 mm inner diameter 50.7 mm outer diameter, 52-inch-long steel insert tube that keeps the microscope completely isolated from any cryogen. The presence of a low pressure helium exchange gas provides for heat transfer within the insert tube. A sixth CPO7 round cage plate holds the objective. The CTCSM uses a custom fabricated objective lens manufactured by Bernhard Halle Nachfolger GmbH N-SF6. The objective has a 60x magnification with a 0.64 numerical aperture and a 0.4 mm working distance, and was specifically made to be used over the thermal range of 1-300 K.

The sample can be placed on either cover glass as thin film or can be placed in either of two different sample holders used when the application of electric fields to the sample is necessary. The sample holders are discussed more completely in chapter 7. The various sample holders are magnetically affixed to the piezo-actuated scan stage. A stack of four Attocube nanopositioners are used for the sample translation and

positioning. For coarse adjustment, at the base of the stack sits a single ANPz101 for vertical adjustment, above which two ANPx101 positioners are situated 90 degrees to each other, and are used for in-plane lateral translation of the sample stage. The actual raster scan process uses a PI PT 130.14 piezo tube. This cylindrical piezo scanner is a four sided device that has segmented electrodes for axial and XY displacement. The voltages that drive this are applied with an RHK technology SPM 100. During the X and Y scan, there is also a small displacement in the Z direction, as the piezo ceramic cylinder expands and contracts with application of voltage. To allow for more reproducible scanning the fourth Attocube nanopositioner, an ANSxy100lr can be used instead of the PT 130.14. This scanner has active feedback control with a fine position range of 50x50  $\mu\text{m}$  at 300 K and 30x30  $\mu\text{m}$  at 4 K. This scanner has no Z direction displacement during the X and Y scan process. An Attocube ANC350 controller is used to control and apply voltages to all of the Attocube nanopositioners.

During cryogenic experiments, the lower portion of the CTCSM is inserted into a Janis research Dewar, a thermally controlled cryostat, where sample temperatures as low as 1 K can be achieved. Imaging has been successfully tested from ambient to 77 K, and spectral investigations have been performed from ambient to 1 K. Temperature of the sample is monitored using a DT-670-SD-1.4D sensor from Lake Shore Cryotronics. The sensor is positioned (at the sample) on the objective side of the sample to ensure accurate thermal readings of the portion of sample being optically or spectrally investigated. A complete description of sample heating and cooling behavior in the CTCSM when the microscope is within the Janis research Dewar is described in chapter

6. The application of high voltage to the sample at the base of the CTCSM during the cryogenic experiments is discussed more thoroughly in chapter 7.

The CTCSM is an epi-illumination design. The sample emitted signal is collected and re-collimated by the objective. After passing through the dichroic and emission filters, the signal is sent down the emission arm by reflection off of either a 25.4 mm Casix CAG0202 mirror or a Newport 05FC16PB.3 broadband polarizing cube beamsplitter. A ThorLabs AC127-025-A1 12.7 mm diameter achromatic lens with a 25 mm focal length is used to focus and couple the light information into an optical fiber. The SM1Z, z-axis translation mount is again used to achieve focus between the lens and the fiber. The microscope uses a 100  $\mu\text{m}$  core diameter SPCM-QC9 multimode optical fiber with 0.64 numerical aperture which serves as the detector aperture and light information is collected by two PerkinElmer SPCM-AQRH-16-FC Avalanche Photo Diodes (APD's), serving as the detectors. The TTL pulses generated by the APD's are sent through a DSN 100 Dual SPAD power supply and are passed by shunt connection to the RHK Technology SPM 100 Controller for imaging studies and to the Stanford Research Systems SR400 two channel gated photon counter for spectral studies.

The CTCSM is pictured in figure 4.5. The head of the microscope is first presented. Only a single emission arm is depicted, however, an additional emission arm can also be situated atop the microscope in a vertical orientation along the central axial scaffolding structure as created by the three cage cubes. The entire CTCSM, the microscope head joined to the optical insert, as well as the steel insert tube in which the optical insert portion is placed prior to introduction into the Janis research Dewar then follows. The sample scan stage and the piezo actuators used for both coarse alignment

and the raster scan process appear in close-up. The head of the microscope is shown in exploded view so the construction can be more easily visualized, along with a complete list of the components in sequential order, and appears within Appendix D.

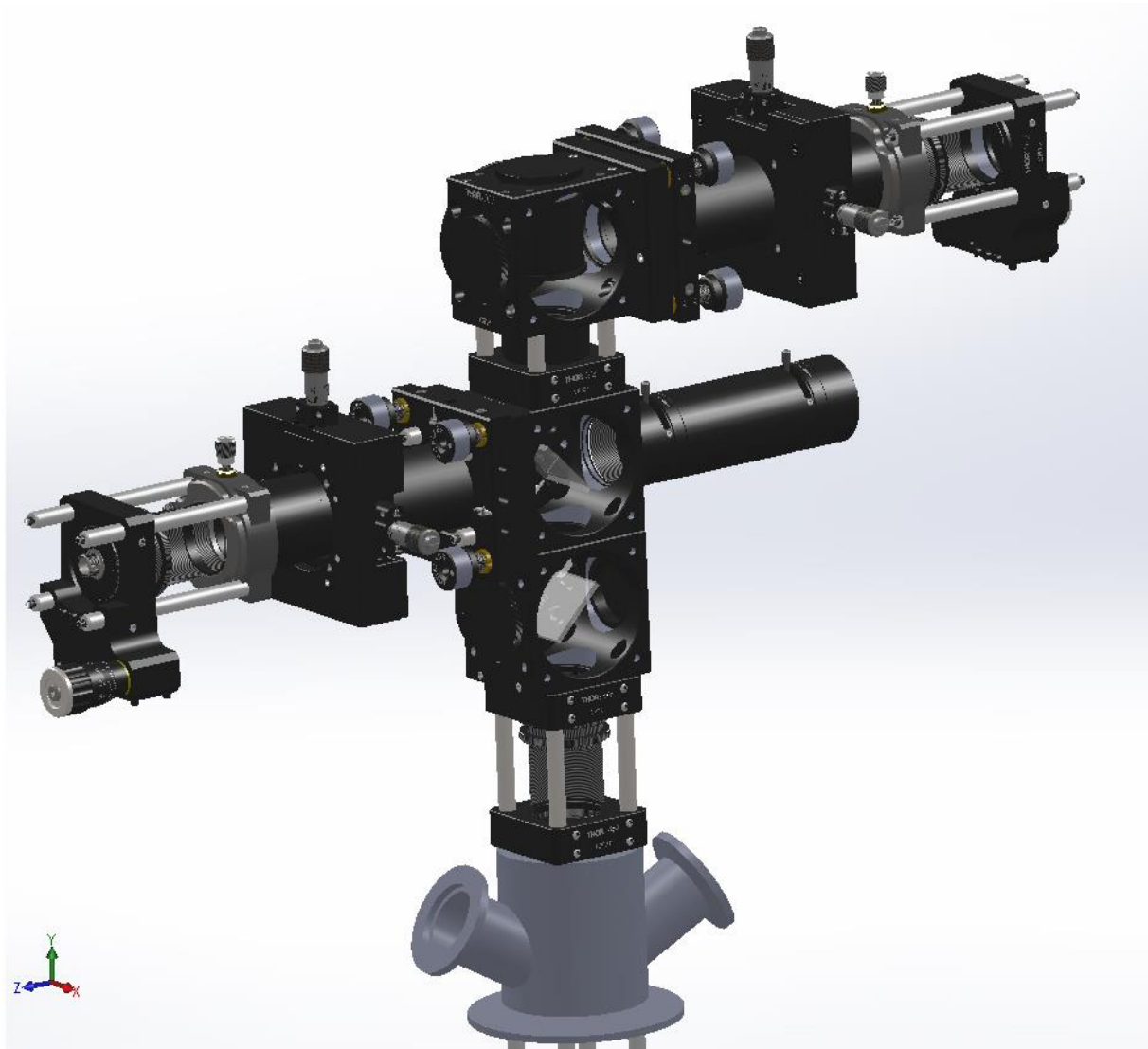


*Figure 4.5: The head portion of the CTCSM. Excitation arm (left), Emission arm (top right), Reference arm (bottom right), Axial scaffolding structure (center), Polarization modulator (center above cryostat flange). Light enters the microscope through the excitation arm and is deflected by a dichroic mirror in the central cage cube down towards the optical insert. The bottom cage cube contains a pellicle beam splitter used for deflection of a portion of the signal returning from the objective for rough focus purposes. The rotatable Glan-Taylor prism sits below the bottom cage cube. A mirror or additional polarization cube is housed in the top cage cube to send the signal light down the emission arm for collection by an optical fiber. A second emission arm can be placed vertically atop the microscope for polarization resolved signal collection.*



Figure 4.6: Left: The complete CTCSM, microscope head and the optical insert. Samples sit below the objective atop the positioners at the base of the optical insert portion of the CTCSM. Center: Insert tube that houses the optical insert when the microscope is used within the cryostat. Right: Close-up of the sample stage and piezo actuators used for coarse positioning and the raster process. Components as numbered 6. sample stage, 5. PI PT 130.14 piezo tube (raster scan), 4. ANSxy100lr (new raster scan positioner), 3. ANPx101 (X direction), 2. ANPx101 (Y direction), 1. ANPz101 (Z direction).



## 4.4 Image Collection

### 4.4.1 Calibration Grids

To assess the performance of the CTCSM and determine the appropriate voltages to be applied to the piezo tube to perform the raster scan process at various temperatures, in addition to parameterize the length scale of object features observed within an obtained image a calibration process was carried out. To achieve this task a Topometrix, model 10-10299 AFM calibration grid was used. The calibration grid has a repeating cross-hatched pattern with a total area of 2500x1500  $\mu\text{m}$ . When imaged, the cross-hatched pattern appears as squares and ridges. The squares portions are  $\text{SiO}_2$  and have dimensions of 5.8x5.8  $\mu\text{m}$  and the ridge portions are Si and have a width dimension of 3.2  $\mu\text{m}$ , with a pitch of 9.0  $\mu\text{m}$ . For this process, images were obtained at both 298 K and 82.5 K, room and liquid nitrogen temperatures. These images were recorded in reflection mode, with a glass flat installed in the optical pathway of the microscope as opposed to a dichroic element. The light source used in this study was the 514.5 nm laser line of the Spectra-Physics Stabilite2017 Argon Ion laser.

To obtain the images, the standard calibration grid was affixed to an 18x18 mm cover glass and then magnetically mounted to the piezo tube that is situated atop the Attocube translation scan stages. The calibration grid was positioned at the focal plane of the Bernhard Halle Nachfolger 60x objective and the image was scanned. In the room temperature image, an area of 25x25  $\mu\text{m}$  was scanned. For the low temperature calibration, the same process was followed but the microscope was placed within the

cryostat, a Janis research Dewar. An image area of 10x10  $\mu\text{m}$  was then scanned. Examples of these trials are depicted in figure 4.7.

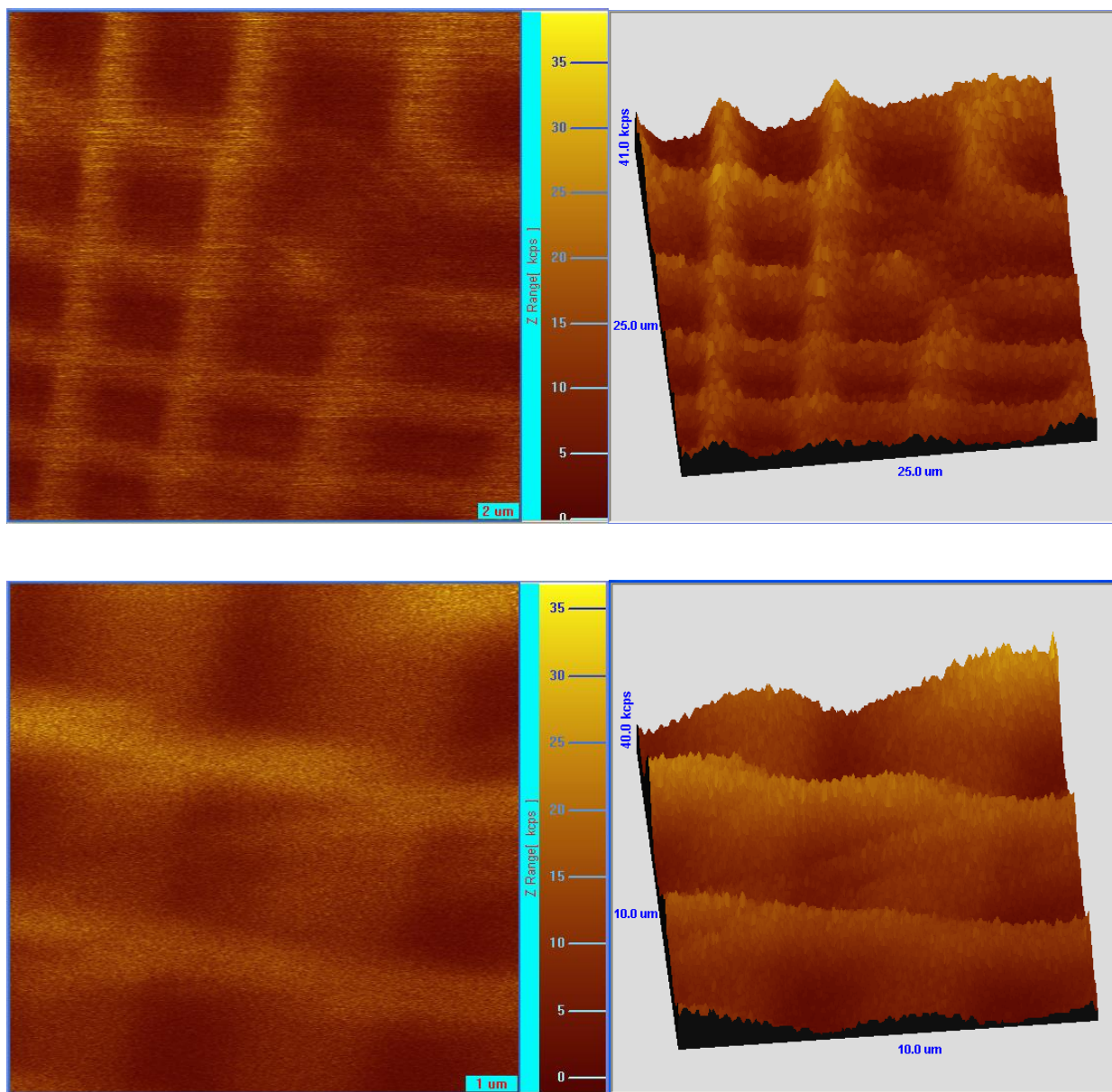


Figure 4.7: CTCSM images of Topometrix, model 10-10299 AFM calibration grid in reflection mode. Dimensions of squares 5.8x5.8  $\mu\text{m}$ , ridges have width of 3.2  $\mu\text{m}$ , and pitch of 9.0  $\mu\text{m}$ . Images taken using 100 mW laser intensity ( $\sim 1$  mW at sample), 514.5 nm, and 60x objective. Top left: image size 512x512 pixels, scan size 25x25  $\mu\text{m}$ , temperature 298 K. Top right: 3D of top left. Bottom left: image size 512x512 pixels, scan size 10x10  $\mu\text{m}$ , temperature 82.5 K. Bottom right: 3D of bottom left.

Successful capture of these images demonstrates that distinct regions within a sample can be individually investigated and addressed both at room and cryogenic temperature with this microscope. The analysis of many images, all similar to the ones displayed allowed the calibration factors for this microscope to be calculated. The scaling parameters for the skew correction in the X and Y directions of the image plane, relative to the theoretical performance of the piezo tube at different temperatures, were found by using 8 distinct images and averaging 100 sets of groups made of three data points each. The calibration was done for both the room and low temperature data. For this process, three points situated around each square region or each ridge region are picked to make a single three data point group. Then using a triangulation distance approach, whereby the actual measured distances between the three points are found and are then scaled by variables X and Y such that when inserted into the Pythagorean theorem equal the specified  $5.8\ \mu\text{m}$  square length or the specified  $3.2\ \mu\text{m}$  ridge length. Through an iterative approach the appropriate scale factors are found. The room temperature scale factors in the X direction were found to be 1.3741 and in the Y direction to be 1.7404. The low temperature scale factors in the X direction were found to be 1.867 and in the Y direction to be 2.491. When these values are entered into the RHK SPM 100 software during the scan process, the skew within the image is corrected for.

#### 4.4.2 Fluorescent Microspheres

To serve as a means to test the imaging capabilities of the CTCSM under more realistic conditions, fluorescent microspheres were the next samples used. For this battery of trials F8823 Yellow-green (505/515) 1.0  $\mu\text{m}$  carboxylate-modified microspheres, Fluospheres<sup>®</sup> by Invitrogen were imaged. Again, trials were performed at room and low temperatures, 298 K and 81.9 K

The microspheres were used directly from stock without any additional modification and were serially diluted (10  $\mu\text{L}$  to 1 mL) to a final concentration of  $2.0 \times 10^{-6}$  mg microspheres/mL using a pH 10.78 NaOH solution. As the exact composition of the microspheres is proprietary in nature no specific molar concentration can be calculated. To prepare the sample used for imaging, 1  $\mu\text{L}$  of the diluted microspheres sample was placed onto an 18x18 mm ozone cleaned cover glass to a sample thickness of approximately 0.05 mm. All fluorescent bead samples used for imaging were prepared in the same manner to the same specifications.

The absorbance and fluorescence characteristics of these specific microspheres again allowed for the 514.5 nm laser line of the Spectra-Physics Stabilite2017 Argon Ion laser to be used for the light source. To effectively collect only the fluorescent signal, the excitation filter hq515/10, dichroic mirror z514, and emission filter hq600, all from Chroma, were placed within the optical path of the microscope. The fluorescence was measured as a function of spatial translation of the sample stage during the raster process for image construction. Example room and low temperatures images follow.

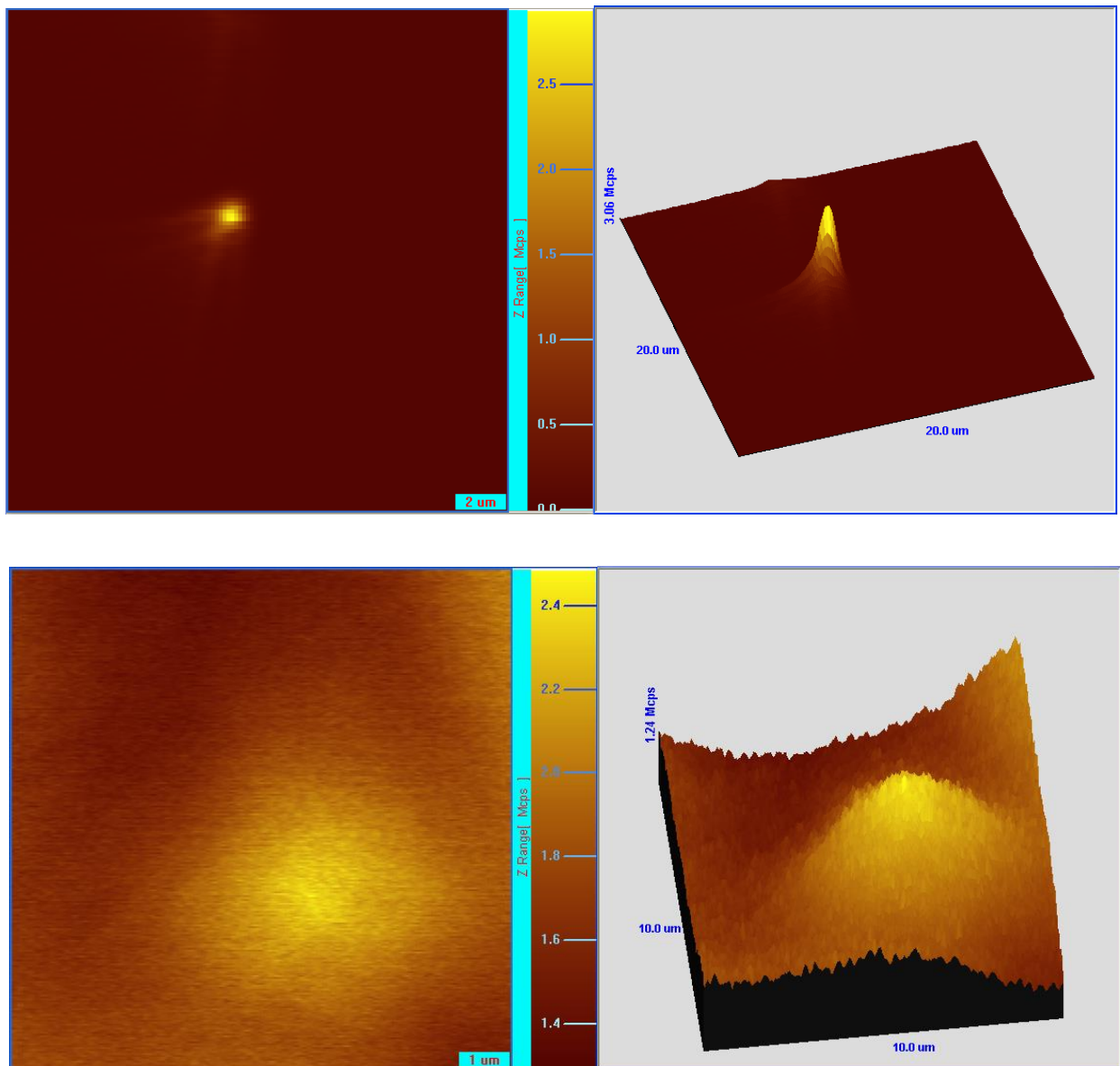


Figure 4.8: CTCSM images of 1.0  $\mu\text{m}$  Yellow-green (505/515) Fluospheres<sup>®</sup> in fluorescent mode. Images taken using 100 mW laser intensity ( $\sim 1$  mW at sample), 514.5 nm, and 60x objective. Filters: excitation hq515/10, dichroic z514, emission hq600. Top left: image size 128x128 pixels, scan size 20x20  $\mu\text{m}$ , temperature 298 K. Top right: 3D of top left. Bottom left: image size 256x256 pixels, scan size 10x10  $\mu\text{m}$ , temperature 81.9 K. Bottom right: 3D of bottom left.

Fluorescence cross sections of obtained images possess FWHM values that appropriately correlate to specified bead diameters for samples at room temperature.

The cross section of the low temperature image displayed below has a substantially

larger diameter than expected, most likely due to higher relative background intensity. Sample characteristics, however, are accurately reproduced in images obtained with the CTCSM.

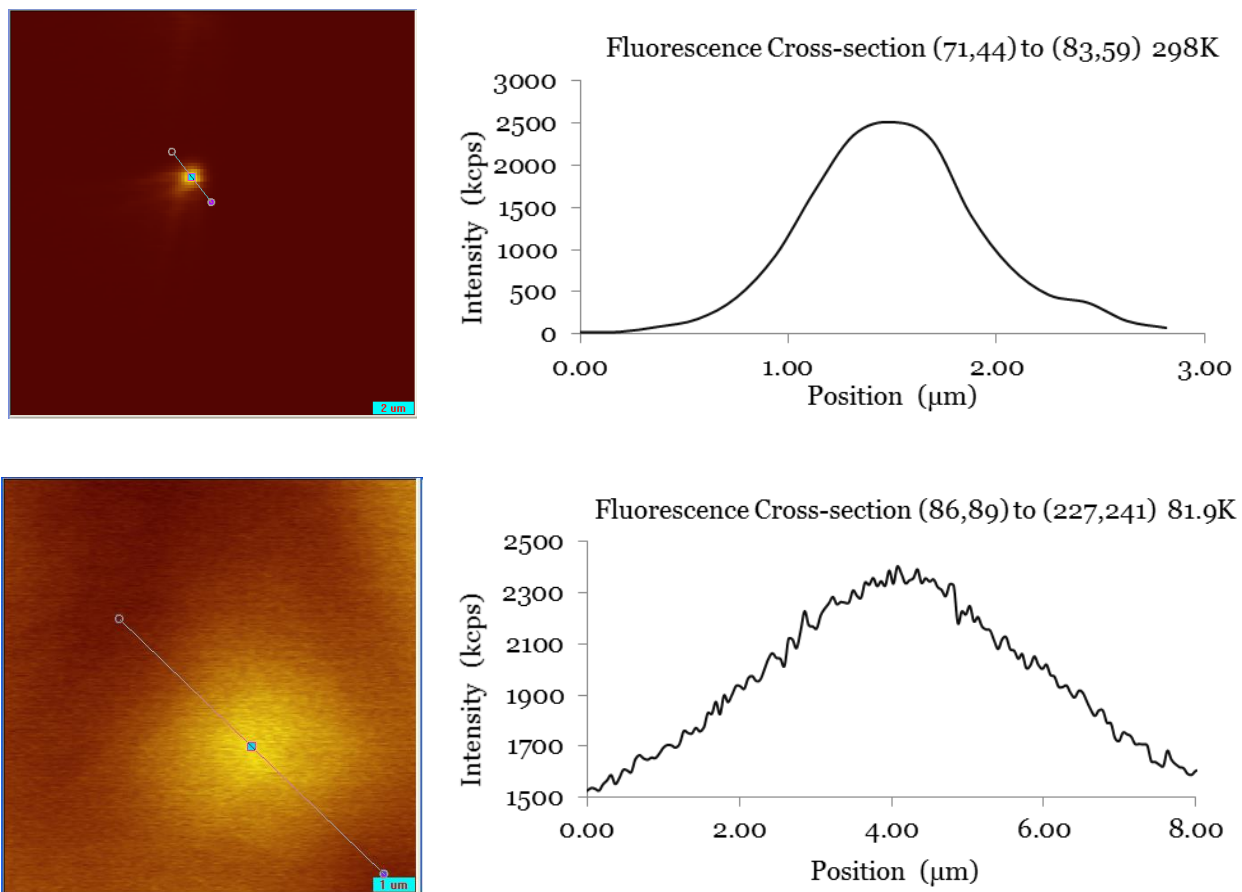


Figure 4.9: Room and low temperature fluorescent cross-sections of 1.0  $\mu\text{m}$  Yellow-green (505/515) Fluospheres<sup>®</sup> in fluorescent mode with CTCSM. Left: image sections depicted within plotted cross-sections appearing right. FWHM room temperature 0.91  $\mu\text{m}$ , low temperature 4.03  $\mu\text{m}$ .

## 4.5 Spectral Collection

Based on the successful collection of the image data from the calibration grids and the fluorescent microspheres, the microscope was deemed functional and focus shifted towards the integration of the spectral collection feature. This undertaking was of significant importance because the hole-burning investigations were to be performed within the CTCSM and spectral acquisition capability is required for these experiments. This task was achieved primarily through the development of the spectral collection program as discussed in Section 3.3.1.

Molecular glasses, specifically ZnPP in a 3:1 (volume:volume) glycerol:water matrix, were the first samples used to assess the performance of the optical setup, and the accurate coordination of the instrumentation using the developed *Spectroscopy* software. After a series of trials of various concentrations, it was found that sample concentrations greater than  $10^{-5}$  M possessed the necessary fluorescent intensity for detection in this particular setup. For the samples used, 1  $\mu$ L of sample was placed into the sample holder and installed into the CTCSM. Appropriate dichroic and emission filters were introduced into the beam path, and numerous fluorescence excitation spectra were collected. A complete list of matched filters and sample combinations can be found in Table 5.1.

Four examples depicting the spectral acquisition capabilities of the microscope appear below. The spectra were collected from samples within the CTCSM, using the developed *Spectroscopy* software. Displayed spectra are from samples of ZnPP and

PPIX-Mb, both in a 3:1 glycerol:water matrix. Spectra were obtained at various temperatures ranging from 5 K to 298 K.

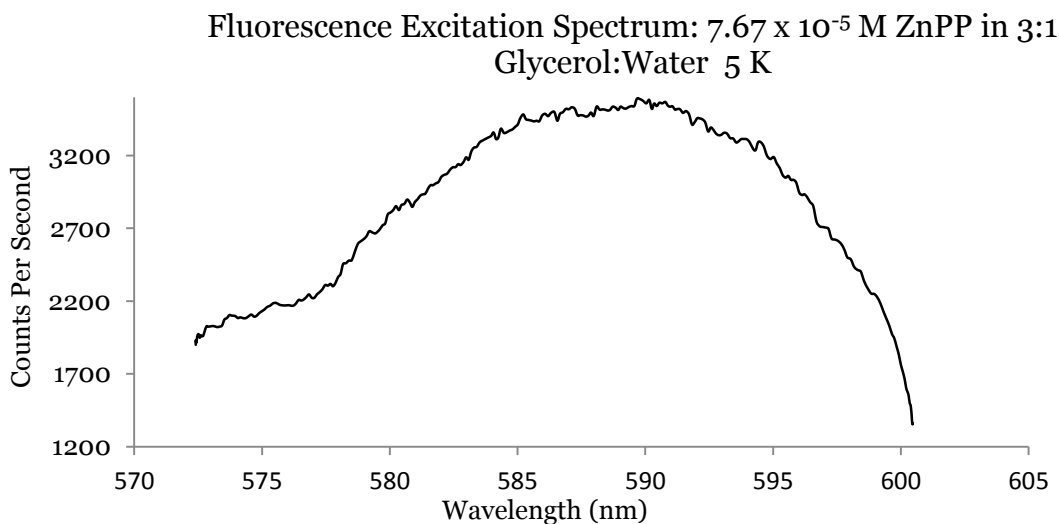
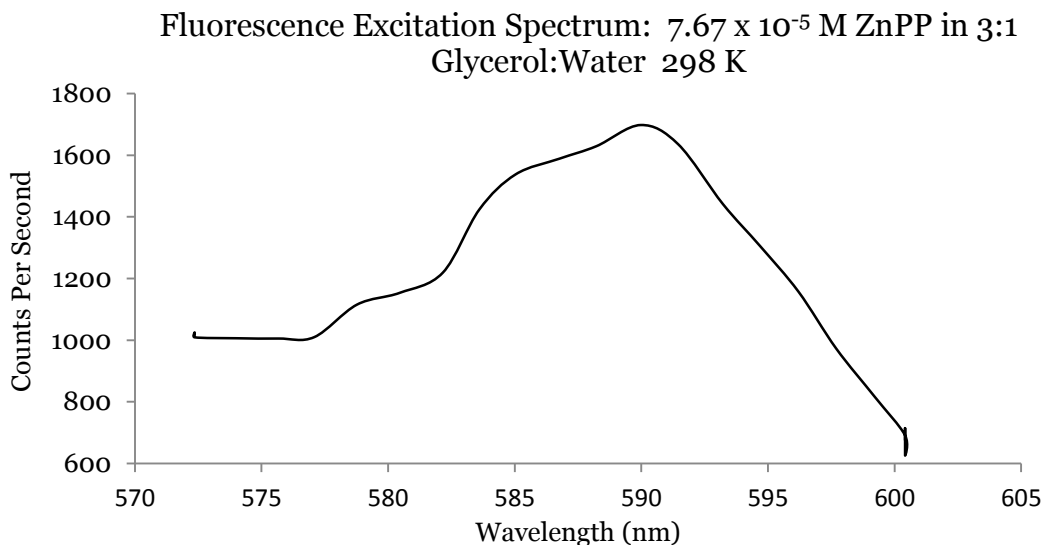


Figure 4.10: Example fluorescence excitation spectra of  $7.67 \times 10^{-5}$  M ZnPP in 3:1 glycerol:water acquired in CTCSM at room (top) and liquid helium (bottom) temperatures. Optical table neutral density filters: 0.1%; 1%, Time step/Integration time: 1000 ms, Scan increment: 200 (top) and 20 (bottom), Laser intensity: 100 mW ( $\sim 1$  mW at sample).



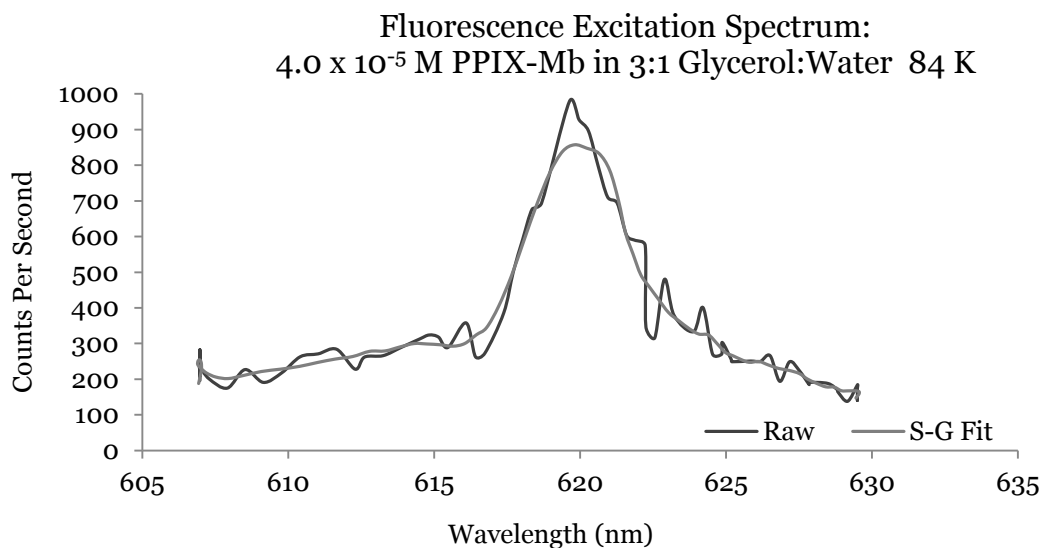
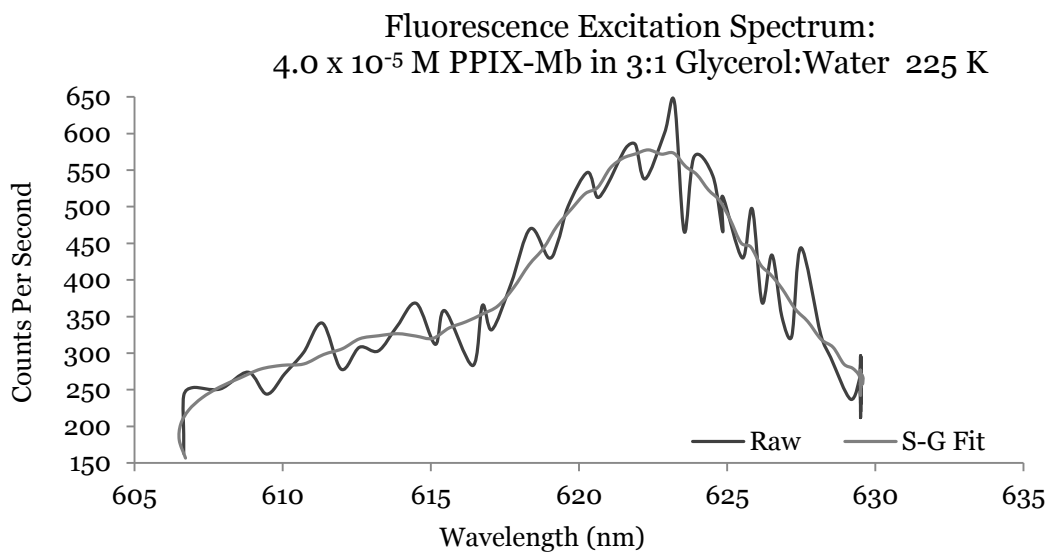
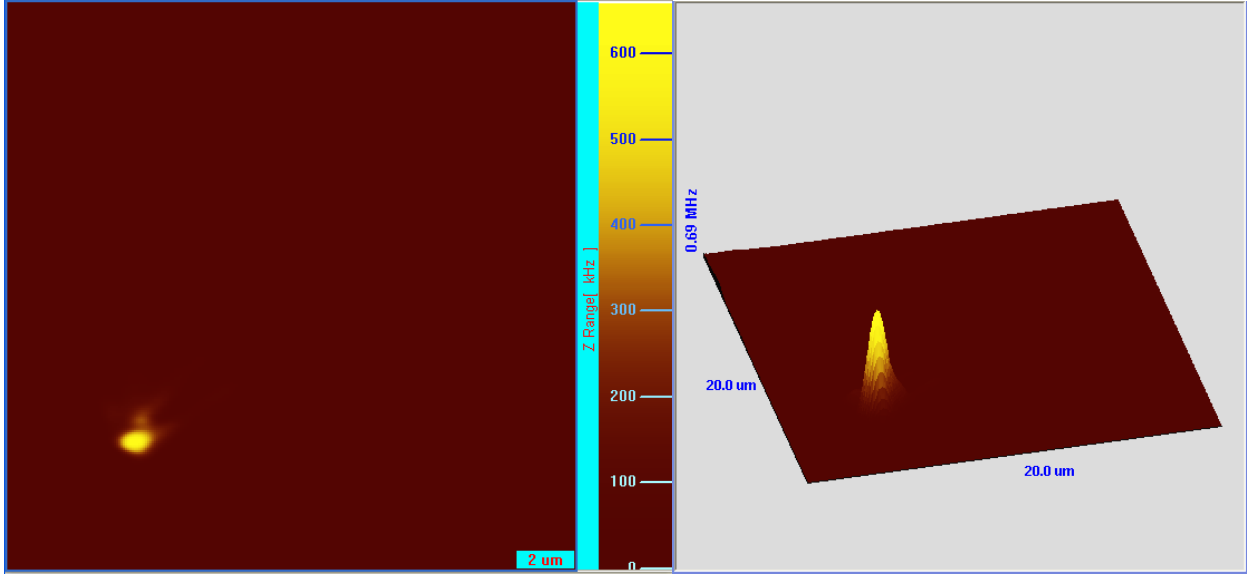


Figure 4.11: Example fluorescence excitation spectra of  $4.0 \times 10^{-5}$  M PPIX-Mb in 3:1 glycerol:water acquired in CTCSM with Optical table neutral density filters: 0.1%; 1%, Time step/Integration time: 1000 ms, Scan increment: 100, Laser intensity: 100 mW ( $\sim 1$  mW at sample). Spectral data are of the same sample at various low temperatures, 225 K (top) and 84 K (bottom). Raw data as well as the Savitzky-Golay fit of the data are displayed.

## 4.6 Image and Spectral Collection

To display the potential of the CTCSM to be used in experiments where simultaneous image and spectral data can be collected, F8821 Red (580/605) 1.0  $\mu\text{m}$  carboxylate-modified microspheres, Fluospheres<sup>®</sup> by Invitrogen were used. These trials were performed only at room temperature, 297 K. The absorbance and fluorescence of these specific microspheres are red shifted in relation to the microspheres previously used. The Fluospheres<sup>®</sup> were serially diluted from stock to a concentration of  $2.0 \times 10^{-6}$  g/mL with a pH 9.43 solution of NaOH. Based on the concentration, diameter, and the density of red fluorescent microspheres, according to a formula provided by Invitrogen, this correlates to approximately  $3.64 \times 10^6$  microspheres/mL of solution. Again, 1.0  $\mu\text{L}$  of the diluted sample was placed on ozone cleaned cover glass to a thickness of approximately 0.05 mm, and solvent allowed to evaporate overnight under refrigeration, leaving the microspheres physisorbed to the cover glass. The light source for this study was the Spectra-Physics Matisse DS tunable frequency dye laser, using laser dye *Rhodamine 6G*, R6G, and a wavelength of 580 nm. Collection of only the fluorescent signal was facilitated by inclusion of dichroic mirror ZT594rdc, and emission filter ET632/60m, again from Chroma, within the optical path of the microscope. No excitation filters were used. The fluorescence was measured as a function of spatial translation of the sample stage during the raster process for image construction. Numerous fluorescence excitation spectra and images were collected of these microspheres. Typical example image and spectral data appear in figure 4.12. Due to



Fluorescence Excitation Spectrum:  
F-8821 1.0 μm Red FluoSpheres 297 K

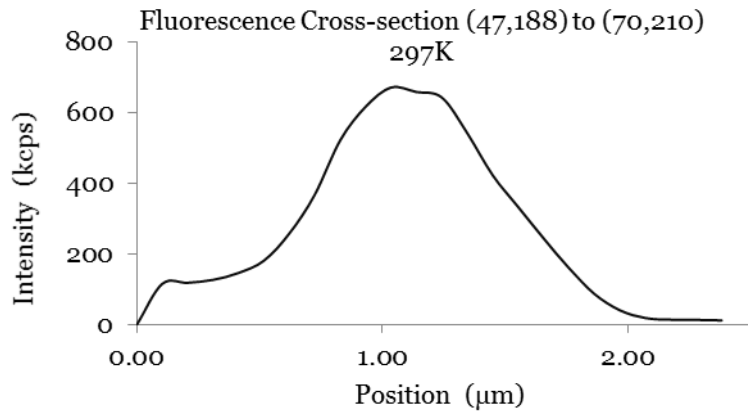
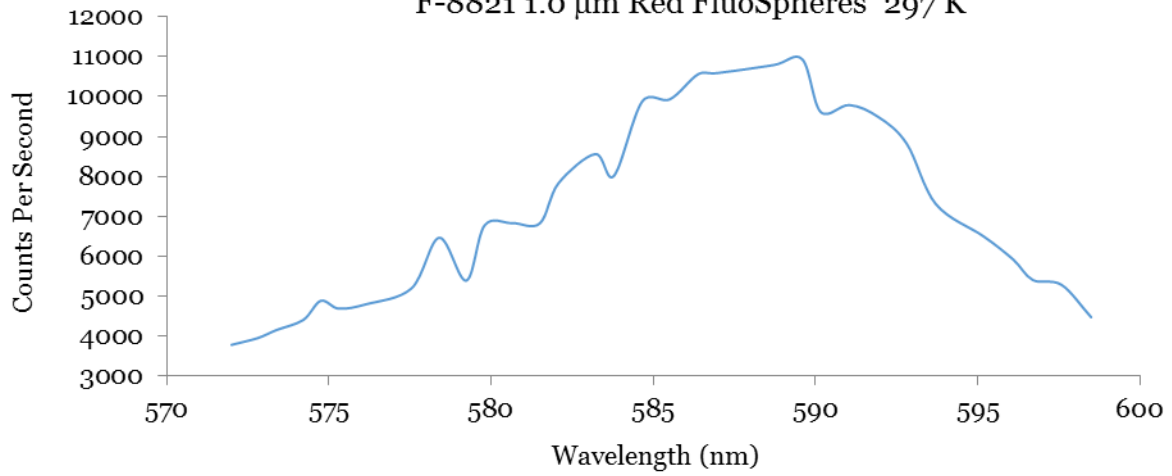


*Figure 4.12: CTCSM image of single 1.0  $\mu\text{m}$  Red (580/605) Fluospheres<sup>®</sup> in fluorescent mode. Image taken using 100 mW laser intensity ( $\sim 1$  mW at sample), 580 nm, and 60x objective. Filters: dichroic ZT594rdc, emission ET632/60m. Top left: image size 256x256 pixels, scan size 20x20  $\mu\text{m}$ , temperature 297 K. Top right: 3D of top left. Middle: Fluorescence excitation spectrum of the single fluorescent microsphere pictured in the top row. Spectrum was acquired in CTCSM with optical table neutral density filters: 0.1%; 1%, Time step/Integration time: 1000 ms, other optics as stated. Bottom Left: image section depicted within plotted cross-section appearing bottom right. FWHM 0.87  $\mu\text{m}$ .*

the successful collection of the fluorescence excitation spectra and image data of the fluorescent microspheres, there is no doubt that our system is fully functional and ready to use with more interesting specimens.

## **4.7 Outlook**

With the microscopes feasibility tested with numerous samples and the updated design features and functionality, the next step in regards to classifying the capabilities of this microscope is the successful acquisition of both image and spectral data for real samples instead of fluorescent microspheres. The first samples tested will most likely be various metal substituted and free-base porphyrin species in proteins and in glassy matrices.

A slight modification to the construction that would greatly streamline and allow for precise microscope alignment, especially when placed within the Janis research Dewar, would be the incorporation of a CCD camera placed at the top of the microscope head. This would allow the experimenter to observe the laser beam as it interacts with the back lens of the objective. Any beam offset from the optical axis of the objective could be observed and whatever translation necessary to centrally align the two could be made.

The new scan capabilities allowed for by the ANSxy100lr scan stage are most exciting. The sub nanometer resolution, calibrated steps and the PID control, will allow for precise raster scanning. The repeatability of this scan device in conjunction with its measured step sizes ensures scan and rescan of the same sample location. This can be used in accurately creating z-stack images. This feature can be used for modeling the point spread function of the microscope in the Z direction, and can be used for optically sectioning and looking at the depth profiles of various samples. This opens the door to the imaging and spectroscopy of substructures within samples. Also, point by point spectroscopy and imaging can allow the experimenter to create “spectral image slices” whereby a spectrum is taken at each point within the image and then the entire image can be viewed as stepped through the different wavelengths.

The ultimate goal, of course, will be to determine the potential for this microscope to be used in single molecule imaging and spectral collection studies.

## References:

- 1.) Abbe, Ernst. (1873). "Beiträge zur Theorie des Mikroskops und der mikroskopischen Wahrnehmung," *Archiv für Mikroskopische Anatomie* 9(1), 413-418.
- 2.) Airy, Sir George B. (1834). "On the Diffraction of an Object-Glass with circular aperture," *Transactions of the Cambridge Philosophical Society* 5, 283-291.
- 3.) Chenouard, Nicolas., Smal, Ihor., de Chaumont, Fabrice., Maška, Martin., Sbalzarini, Ivo F., Gong, Yuanhao., Cardinale, Janick., Carthel, Craig., Coraluppi, Stefano., Winter, Mark., Cohen, Andrew R., Godinez, William J., Rohr, Karl., Kalaidzidis, Yannis., Liang, Liang., Duncan, James., Shen, Hongying., Xu, Yingke., Magnusson, Klas E. G., Jaldén, Joakim., Blau, Helen M., Paul-Gilloteaux, Perrine., Roudot, Philippe., Kervrann, Charles., Waharte, François., Tinevez, Jean-Yves., Shorte, Spencer L., Willemse, Joost., Celler, Katherine., van Wezel, Gilles P., Dan, Han-Wei., Tsai, Yuh-Show., de Solórzano, Carlos Ortiz., Olivo-Marin, Jean-Christophe., Meijering, Erik. (2014). "Objective comparison of particle tracking methods," *Nature Methods* 11(3), 281–289.
- 4.) Claxton, Christopher D., Staunton, Richard C. (2008). "Measurement of the point-spread function of a noisy imaging system," *The Journal of the Optical Society of America A* 25(1), 159-170.
- 5.) Combs, Christian A. (2010). "Fluorescence Microscopy: A Concise Guide to Current Imaging Methods," *Current Protocols in Neuroscience* 50(2.1), 2.1.1–2.1.14.
- 6.) Egner, A., Andresen, V., Hell, S. W. (2001). "Comparison of the axial resolution of practical Nipkow-disk confocal fluorescence microscopy with that of multifocal multiphoton microscopy: theory and experiment," *Journal of Microscopy* 206, 24-32.
- 7.) Greb, Christoph. (2016). "Infinity Optical Systems: From infinity optics to the infinity port," *Optik & Photonik* 11(2), 34-37.
- 8.) Gustavo, Cancelo. et al. FERMILAB-PUB-11-391. Deep sub electron noise readout in CCD systems using digital filtering techniques. Retrieved April 2, 2015, from <http://lss.fnal.gov/archive/2011/pub/fermilab-pub-11-391.pdf>
- 9.) Hu, Yi. (2011). *Single molecule imaging and spectroscopy of protoporphyrin IX and its metal derivatives* (Doctoral dissertation). University of Wisconsin-Milwaukee.
- 10.) Inoué, Shinya., Oldenbourg, Rudolf. (1995). Microscopes. Michael Bass (Ed.) *Handbook of Optics. 2nd ed.* 17.1-17.52. New York McGraw-Hill, Inc.
- 11.) Miks, Antonin.; Novak, Jiri.; Novak, Pavel. (2007). "Calculation of point-spread function for optical systems with finite value of numerical aperture." *Optik* 118, 537-543.
- 12.) Minsky, Marvin. (1988). "Memoir on Inventing the Confocal Scanning Microscope," *Scanning* 10(4), 128-138.

Patent: US 3013467

13.) Paul, Perrine., Duessmann, Heiko., Bernas, Tytus., Huber, Heinrich., Kalamatianos, Dimitrios. (2010). "Automatic noise quantification for confocal fluorescence microscopy images," *Computerized Medical Imaging and Graphics* 34, 426-434.

14.) Rayleigh, Lord. (1896). "On the theory of optical images, with special reference to the microscope," *Philosophical Magazine* 42, 167-195.

15.) Shaw, Peter J. (2006) Comparison of Widefield/Deconvolution and Confocal Microscopy for Three-Dimensional Imaging. James B. Pawley (Ed.) *Handbook of Biological Confocal Microscopy*. 3rd ed. 453-467. New York SpringerScience+Business Media.

16.) SHOTTON, DAVID M. (1989). "Confocal scanning optical microscopy and its applications for biological specimens," *Journal of Cell Science* 94, 175-206.

17.) Webb, Robert H. (1996). "Confocal optical microscopy," *Reports on Progress in Physics* 59, 427-471.

18.) Xi, Peng., Rajwa, Bartlomiej., Jones, James T., Robinson, J. Paul. (2006). "The design and construction of a cost-efficient confocal laser scanning microscope," *American Journal of Physics* 75(3), 203-207.

19.) Zhang, Bo.; Zerubia, Josiane.; Olivo-Marin, Jean-Christophe. (2007). "Gaussian approximations of fluorescence microscope point-spread function models." *Applied Optics* 46(10), 1819-1829.

20.) [www.attocube.com](http://www.attocube.com)

21.) [www.b-halle.de](http://www.b-halle.de)

22.) [www.chroma.com](http://www.chroma.com)

23.) [www.janis.com](http://www.janis.com)

24.) [www.lakeshore.com](http://www.lakeshore.com)

25.) [www.newport.com](http://www.newport.com)

26.) [www.physikinstrumente.com](http://www.physikinstrumente.com)

27.) [www.thorlabs.com](http://www.thorlabs.com)

## II

### Chapter 5

## **Optimizing Signal Collection: Rates, Optics, and Hardware**

### **5.1 Introduction**

Spectral hole-burning is a delicate investigative process requiring a high degree of control over numerous characteristics of light emitted by the excitation source prior to interaction with the sample. Of greatest importance is the ability to linearly scan the coherent source over the desired frequency space with high resolution. High resolution is being defined here as the capability to perform scans with frequency steps on the order of 10 MHz  $\sim 1.0 \times 10^{-5}$  nm, and bandwidths of 100-200 kHz. Light source aside, the other specific qualities that need to be controlled are intensity and positional stabilization during the scan process, as well as the ability to manipulate the attenuation and polarization of the light. Various optical elements positioned on an optical table used for light modification prior to injection into the CTCSM microscope are used to achieve this control namely intensity and position stabilization units, and various polarization elements and neutral density filter combinations.

The imaging and spectral acquisition capabilities of the CTCSM, in conjunction with the perceived optimal optical pathway for beam position, intensity, and polarization control were initially tested with numerous samples, specifically 1 $\mu$ m



fluorescent beads and assorted samples of molecular glasses, PPIX and ZnPP in both DMSO and 3:1 glycerol:water. Most of these studies were performed at ambient temperature, and broadband spectra over tens of nanometers were collected at approximately 0.1 nm resolution over the tunable range of the laser source. Below is an example of a broadband spectrum collected within the CTCSM. To validate the accuracy of the collected signal, spectral features were compared to those obtained from a fluorescence excitation spectrum generated using a Fluorolog FL3-22 from Horiba Scientific.

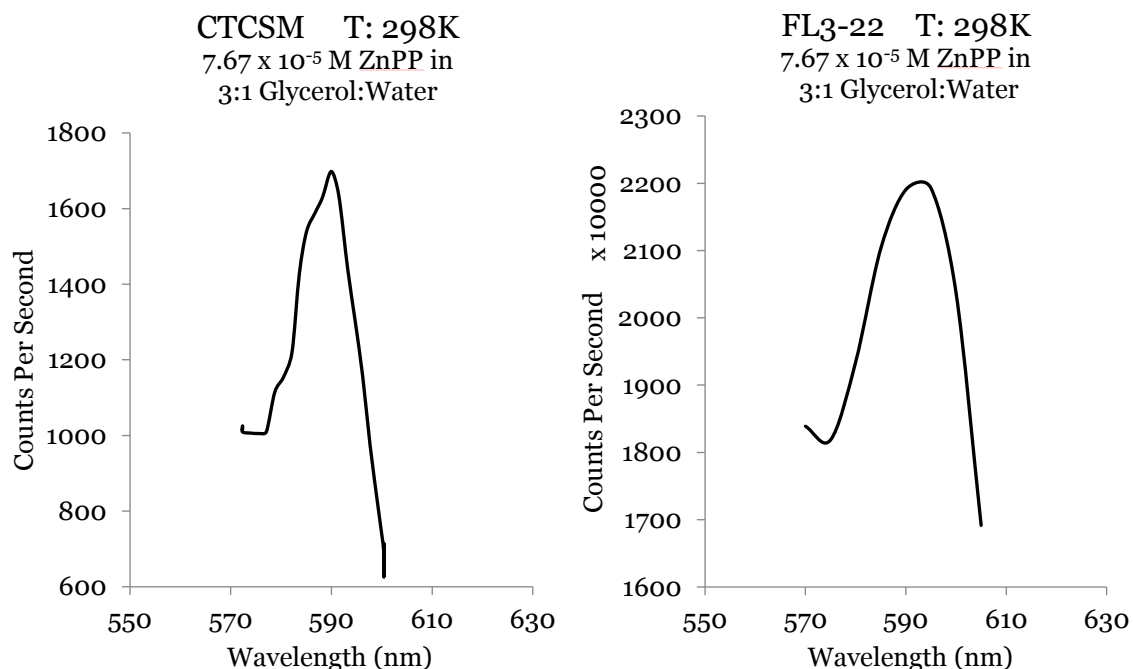


Figure 5.1: Left: Fluorescence excitation spectrum of  $7.67 \times 10^{-5}$  M ZnPP in 3:1 glycerol:water acquired in CTCSM at room temperature using filters Dichroic: ZT594rdc and Emission: FF01-731/137-25. Time step/Integration time: 1000 ms, Scan increment: 200. Right: Fluorescence excitation spectrum of  $7.67 \times 10^{-5}$  M ZnPP in 3:1 glycerol:water acquired in Horiba Scientific Fluorolog FL3-22 at room temperature using filters Dichroic: ZT594rdc and Emission: FF01-731/137-25. The FL3-22 fluorescence excitation spectrum was created by integrating the individual fluorescence spectra obtained, with excitation every 5 nm from 570 nm to 605 nm.

The many considerations necessary to refine the spectral response of the sample when performing high resolution scanning (scans of 10-100 GHz at approximately 10 MHz resolution) follows. Additionally, the optimization of both scan and collection rates, the optical pathway used and the various hardware parameters that need setting when performing these types of high resolution experiments is discussed.

## **5.2 Scan and Collection Rates**

The first order of importance at the onset of testing high resolution scanning is the determination of appropriate rates for scanning the tunable laser source and collecting the fluorescent signal. Since these two processes are performed with different instruments, and are not inherently correlated, it is necessary to understand how the resultant spectral signal is affected by changing collection and scan rates in relation to each other. As the source is scanned in frequency space and the sample illuminated, the fluorescence is detected with the two PerkinElmer SPCM avalanche photodiodes (APD's), which generate TTL pulses for each detected photon that are counted by a Stanford Research Systems SR400 two channel gated photon counter. By setting a counting rate on the SR400 as the laser is scanned, the fluorescent counts from different excitation frequencies are binned and then assigned to a single mean frequency value over the counting timeframe. This implies that high laser scan rates and long counting times would assign the fluorescent signal from a wide range of excitation frequencies to a single mean value. Although this procedure could aid in reducing random noise as a

larger integration time is being used, this also implies a potential for loss of spectral resolution. The four extreme cases along with implications appear below.

		Laser Scan Rate	
		Fast	Slow
Counting Integration Time	Fast	Frequency and counts closely correlated.  Low integration time ⇒Loss of fine spectral features ⇒High noise possibility ⇒Low overall signal	Frequency and counts closely correlated.  Low integration time ⇒Fine spectral features unpredictable ⇒High noise possibility ⇒Low overall signal
	Slow	Frequency and counts loosely correlated. ⇒Loss of fine spectral features  High integration time ⇒Greater random noise cancellation ⇒Greater noise from varied excitation binning ⇒Signal magnitude unpredictable	Frequency and counts closely correlated.  High integration time ⇒Retain most fine spectral features ⇒Greater random noise cancellation ⇒High overall signal

Figure 5.2: Tradeoffs between altering scan speed of the excitation source and the collection rate of the detected signal. The four extreme cases that could be encountered are represented.

Ideally, the scan and counting rates should be correlated in such a way as to assure the detected signal accurately represents the excitation frequency. Also, possible fine spectral characteristics need to be maintained while allowing for minimization of random noise and high overall collected signal. To find the optimum conditions, many coupled rates were looked into for their best agreement with the stated requirements. Figure 5.3 depicts representative traces taken over the same frequency range, which display tradeoffs with rate variation. The first two traces have the same scan rate, 493.7

MHz/s, and different integration times, 3000 ms and 1000 ms respectively. The third trace shares the integration time of the first trace with a scan speed decreased by one order of magnitude. It can be observed in the third trace that oversampling can introduce unnecessary noise that potentially obscures spectral features; however, in the first trace, undersampling generates smooth spectra that could lack important necessary detail. After many trials at varied rate combinations, it was initially thought that the truest spectral representations were achieved at 500 MHz/s with 2000 ms integration times. When the first hole burning trials concluded, the scan rate was found to be much too great to allow for the resolution necessary for spectral hole profiles to be detected and reasonably represented. Therefore, the scan rates were adjusted to the 20-80 MHz/s range and integration times were modified accordingly.

### **5.3 Spectral Shape and Filter Studies**

With the scan and collection rate issue sorted and the confidence that collected spectra would have minimal noise yet accurately retain spectral features, the first hole-burning trials were performed. The first samples used were found to be of concentrations lacking the necessary fluorescent intensity for successful detection in the CTCSSM. After a battery of concentration studies, appropriate ranges were determined. For the first hole-burning trials  $7.67 \times 10^{-5}$  M ZnPP in 3:1 glycerol:water at pH 7.3 was used. It was found that during the high resolution scans an irregular signal seemed to emerge in the spectra. This phenomenon would have been somewhat apparent from the scan rate testing that was just concluded, which displayed some similar features, as can be seen

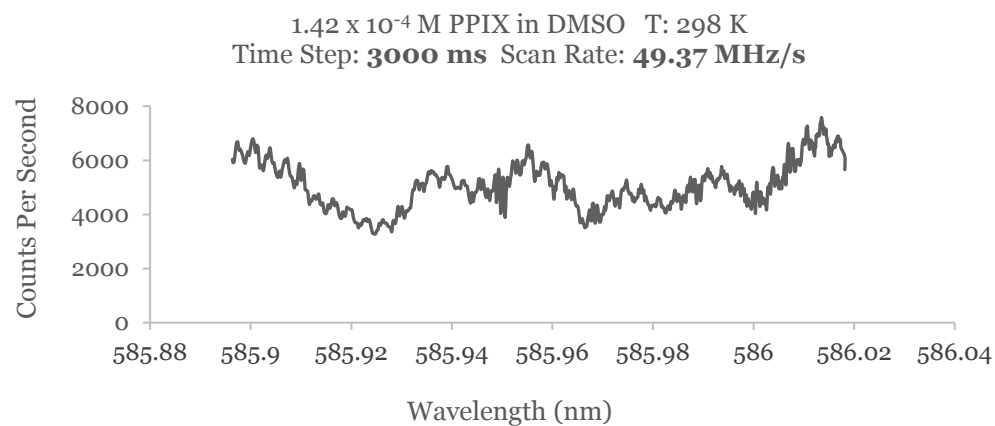
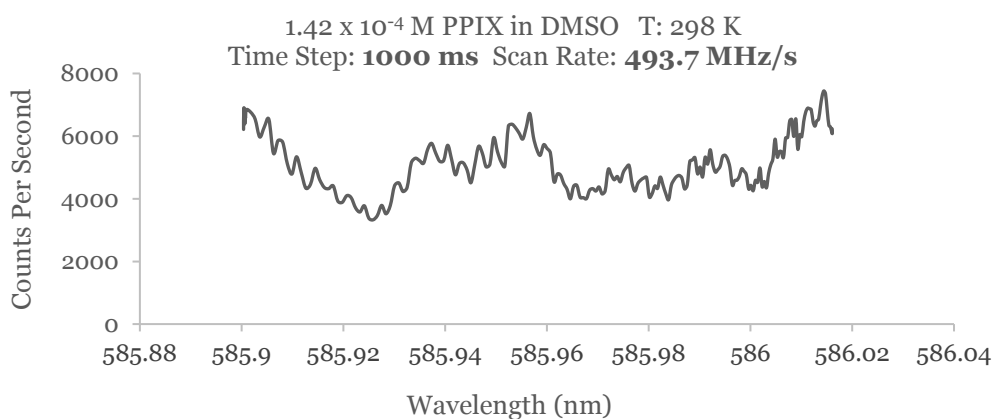
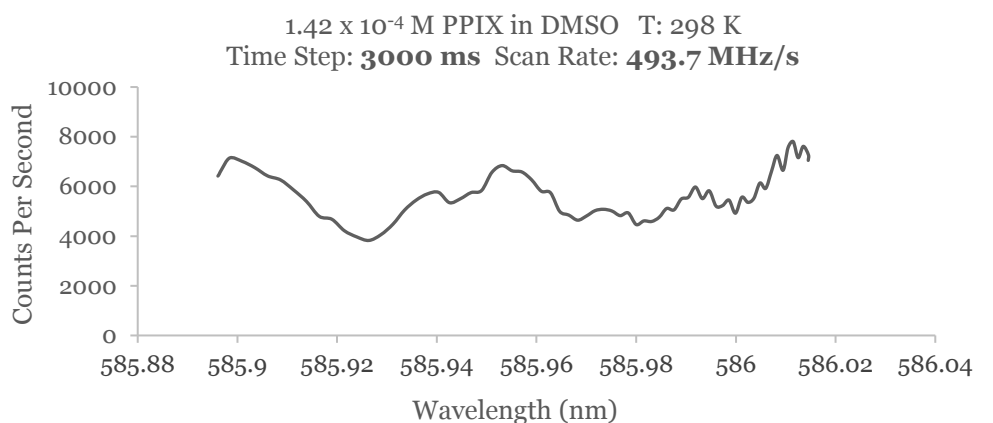


*Figure 5.3: Representative spectra of 1.42 x 10<sup>-4</sup> M PPIX in DMSO at various excitation scan and collection rate combinations. Observe the effects of undersampling in the first spectrum and oversampling in the third spectrum of the fluorescent signal and the substantial impact on resultant spectral signatures.*

within the traces, but this was overlooked. When the cryogenic temperature trials began it was thought that hole-burning could be conducted in the irregular profiles in regions that were of moderate flatness. At room temperature these fluctuations were present, yet it seemed that at liquid helium temperatures these features were amplified. Once at temperature, after a few scans to find a long frequency region of tolerable flatness, the first hole-burning attempts were made. Some results of this experiment are presented in figure 5.4. Observe the pre-burn and post-burn trace. The position of the attempted burn was 507547 GHz, the center of the range of reasonable flatness that spanned a 20 GHz window. It was thought that burning may have occurred yet, upon an extended scan of the presumed hole, an irrefutable oscillatory pattern emerged that aligned with the “hole” as can be seen in traces that follow.

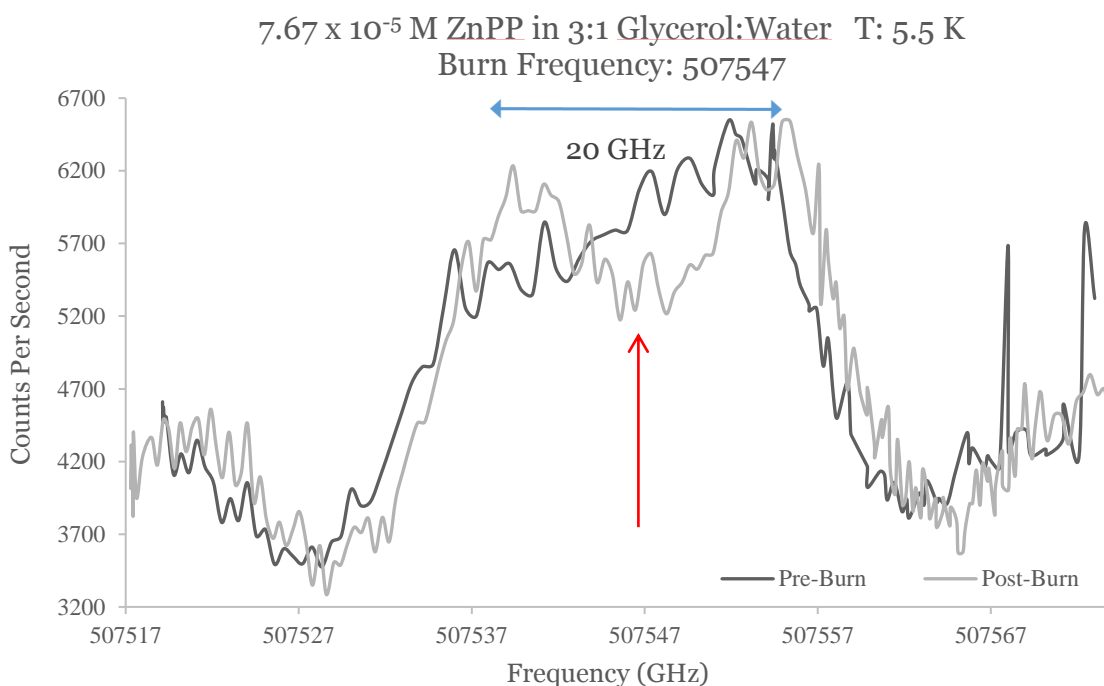
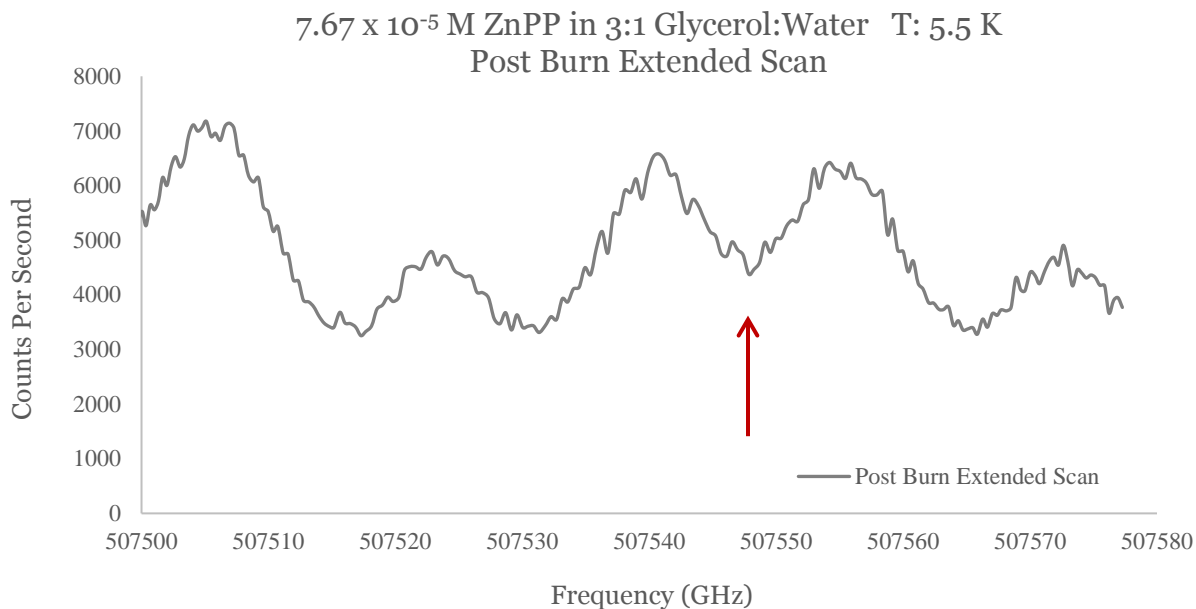


Figure 5.4: Pre-Burn and Post-Burn spectrum of  $7.67 \times 10^{-5}$  M ZnPP in 3:1 glycerol:water at 5.5 K. Observe a 20 GHz range of moderate flatness from 507537 to 507557 GHz in the pre-burn trace. Arrow indicates burn frequency, 507547 GHz. Spectral resolution  $\sim 15$  MHz.



*Figure 5.5: Extended scan of the above post-burn spectrum of 7.67 x 10<sup>-5</sup> M ZnPP in 3:1 glycerol:water at 5.5 K. Again, arrow indicates burn frequency. Spectral resolution ~ 15 MHz. Appearance of periodic spectral signal negates positive affirmation of successful spectral hole.*

As the polarization of excitation light was rotated by 90 degrees and the same trace re-scanned, a small shift in peak frequencies was observed. These findings led to some pressing concerns requiring answers prior to additional hole-burning experimentation. Was a hole actually burnt in the sample? There was a possible intensity dip, but the “hole” is very wide and not a Lorentzian profile. The signal looks very periodic; are the dips properties of the optical system or properties of the sample itself? Aside from these characteristics, changing the polarization appeared to have a spectral effect, yet without an application of external electric field the spectra should have been identical. To get to the bottom of these questions an extensive investigation of the optical pathway needed to be performed. To see if the oscillations were optics related, six filter combinations were evaluated. These included filter combinations that were matched for specific porphyrin species for the hole-burning trials in addition to

filter combinations that could potentially be matched for use when investigating other possible samples.

Correct Filters For Various PPIX Species:		
	Excitation/Dichroic	Emission
PPIX	Q647lp	FF01-675/67-25
PPIX Mb	Q647lp	FF01-675/67-25
PPIX DME	T660lpxrxt	FF01-731/137-25
ZnPPIX	ZT594rdc	ET632/60m
ZnPPIX Mb	ZT594rdc	ET632/60m
ZnPPIX DME	Dio1-R594-25x36	ET632/60m

*Table 5.1: Appropriate filter combinations for use with different intended Porphyrin species to be used for hole-burning investigations. Filters were obtained from Chroma and Semrock.*

All of these studies were performed at 298 K using the same sample. For consistency, the exact same frequency space at a span of 100 GHz was used for all trials. The six filter combinations were tested under both parallel and perpendicular excitation source conditions. For accuracy of determination, all spectra were taken tenfold. These experimental parameters were followed for the entirety of the filter and optical pathway studies that were to follow. Below is a summary of the first tests that maintained the complete optical pathway from laser to sample with only dichroic (Ex) and emission (Em) filters varied. The following spectra indicate that oscillations within the spectra are filter set independent. Polarization was shown to have little to no effect on the positions of peaks and troughs of the secondary spectral features. The observed intensity



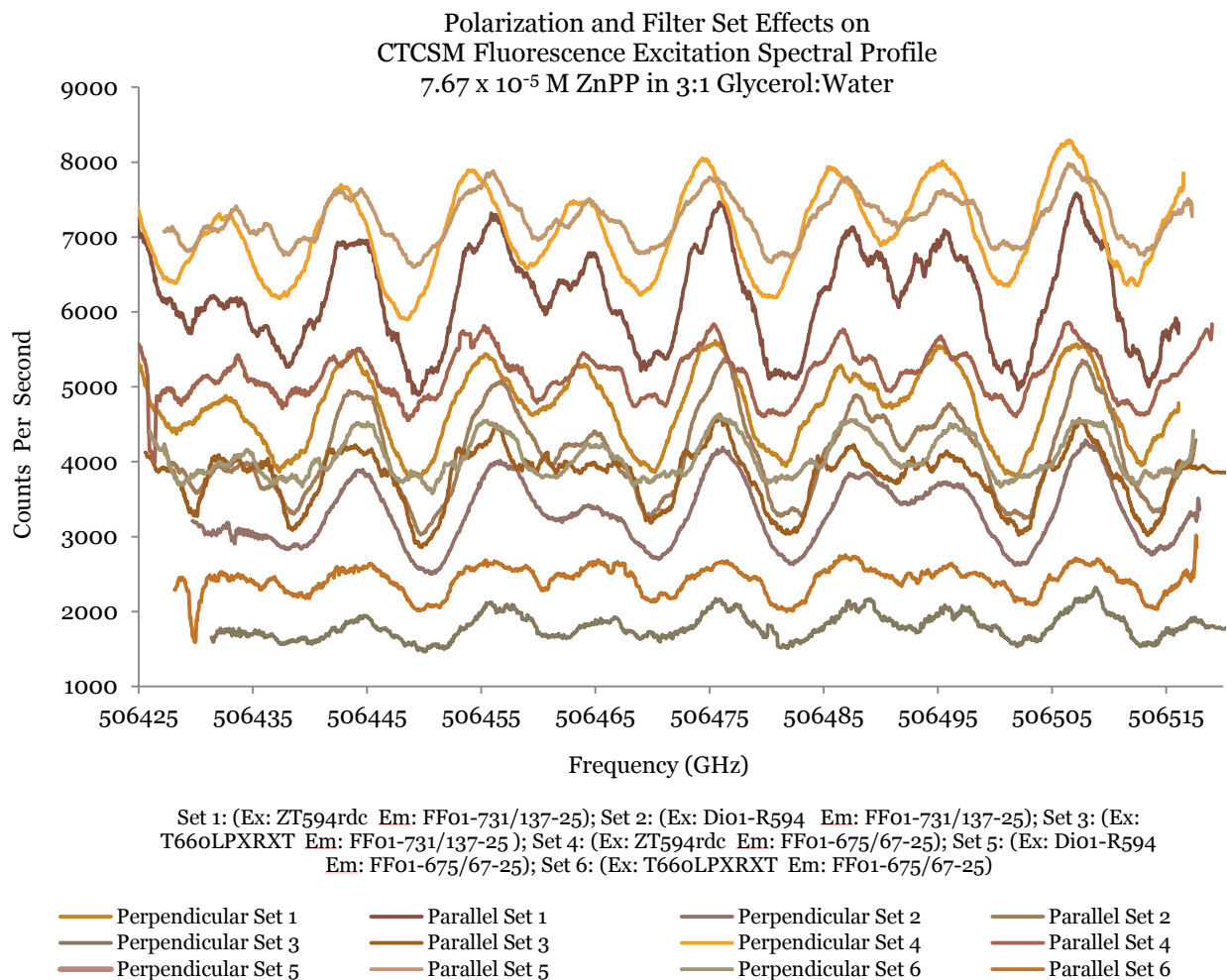


Figure 5.6: Effects of various filter sets on observed spectral signal. All spectra obtained at 298 K at resolutions of  $\sim 1$  MHz. Filter sets as indicated above. Set 1: (Ex: ZT594rdc Em: FF01-731/137-25); Set 2: (Ex: Di01-R594 Em: FF01-731/137-25); Set 3: (Ex: T66oLPXRXT Em: FF01-731/137-25); Set 4: (Ex: ZT594rdc Em: FF01-675/67-25); Set 5: (Ex: Di01-R594 Em: FF01-675/67-25); Set 6: (Ex: T66oLPXRXT Em: FF01-675/67-25).

variation is due to different optical densities of particular filter combinations in relation to a uniformly intense excitation source over the same frequency range, in addition to a polarization angle dependence to be discussed later. Different filter sets returning the same spectral profile seemed to indicate the source of oscillatory spectral features may

be characteristics of the sample itself. Yet lacking any physical explanation for this to be the case a more complete analysis of the optics needed to be conducted.

Filter studies proceeded as follows. The dichroic filters included in the test were a Dio1-R594 from Semrock, and a ZT594rdc, a T660LPXRXT, and a Q647lp, all from Chroma. The emission filters included in the test were an ET632/60m from Chroma, and a FF01-675/67-25, and a FF01-731/137-25, both from Semrock. All filters, the dichroic, emission and one colored filter, Schott RG665, were first singly tested in the microscope with sample. When only the dichroic filters were installed, the periodicity of the signal was replaced by only two large peaks over the same range. An example of this is displayed below.

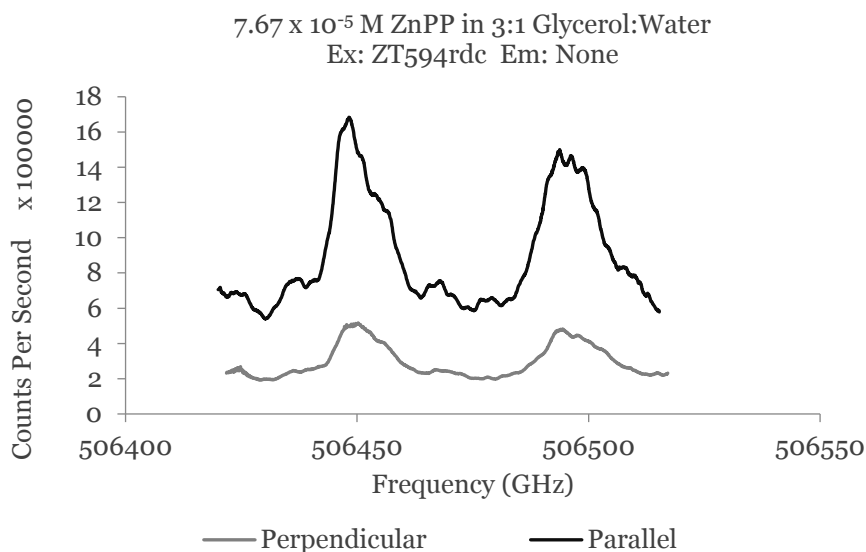
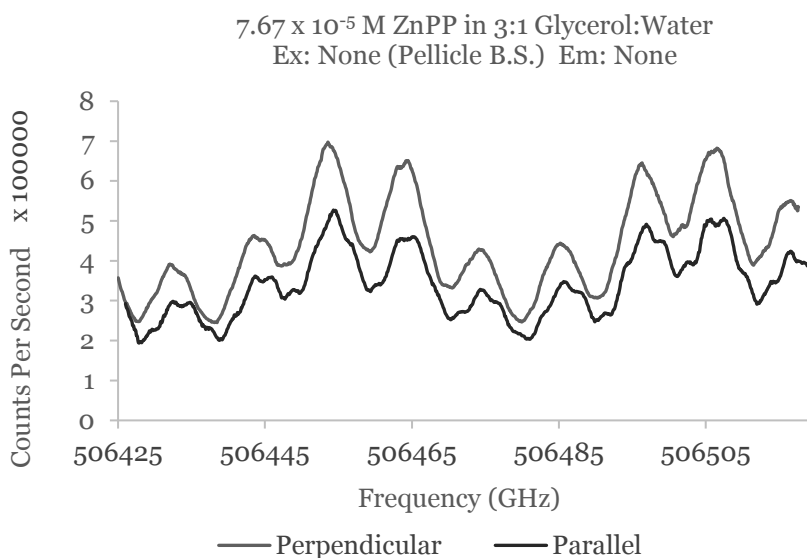


Figure 5.7: Spectral shape obtained in CTCSM using only dichroic filter with no emission filter present. Shape is representative of that obtained for all tested dichroic filters.

When testing the emission filters, the dichroic needed to be substituted with an optical element that would allow for the preservation of the optical pathway within the

microscope. To serve this purpose, the three emission filters and the color filter were tested first by using a glass flat for the stand-in element, and the filters then re-tested using a BP145B1 pellicle beam splitter from ThorLabs. The oscillatory pattern re-emerged although was not nearly as smooth as previous. The spectral results were similar regardless of glass flat or pellicle beam splitter for the replacement optic. Although not useful for experimental purposes, the next tests used neither dichroic nor emission filters, but only the glass flat or pellicle for pathway preservation. If the filters were the cause of the oscillation, removing both was expected to return a flat profile.



*Figure 5.8: Spectral shape obtained using no filters within the pathway. Observe presence of secondary oscillation with period similar to that seen in the emission filter free case.*

The detected signal, however, would be a combination of both fluorescence as well as excitation signal from lack of filters, and thus any periodicity that would be seen to remain would have been remnants of other portions of the filter free optical system, from laser to microscope. Above is an example of the filter free spectra obtained. The

original oscillation is shown to persist with yet another longer oscillation, similar to the dichroic only case superimposed upon it.

With no clear description of what was causing the spectral irregularities a new experimental plan was devised. The laser signal was monitored over the frequency range and found to be void of intensity variations matching the traces above, yet not completely void of some intensity variability. At this point, the laser was diverted around all of the stabilization and polarization optics on the optics table and the experiments performed again. This process was repeated, each time re-incorporating a portion of the optics; intensity stabilizer, position stabilizer, polarization optics back into pathway. A long process requiring the collection of many spectra, and optics pathway combinations, ultimately led to the ability to record signals lacking of these characteristics.

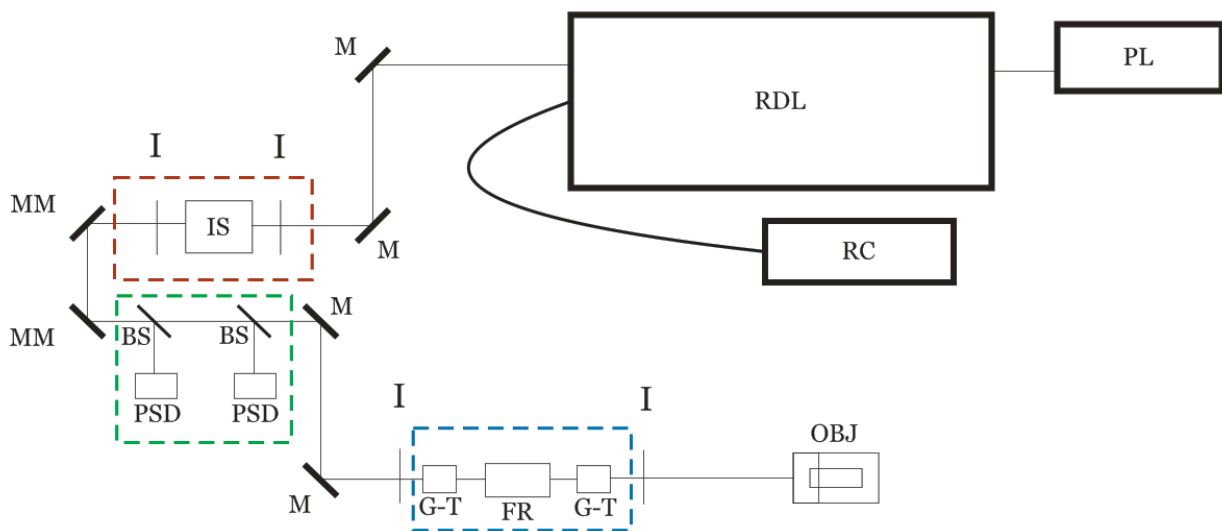


*Figure 5.9: Block diagram of components on optical table. PL: Pump Laser; RDL: Ring Dye Laser; RC: Reference Cavity; M: Silver Coated Mirror; I: Iris; IS: Intensity Stabilizer; MM: Motorized Mirror; BS: Beam Sampler; PSD: Position Sensitive Detector; G-T: Glan-Taylor Prism; FR: Fresnel Rhomb; OBJ: Objective. Orange square: Intensity stabilization optics; Green square: Position stabilization optics; Blue square: Polarization optics. Boxed portions were removed and then sequentially re-incorporated back into optical pathway during signal optimization studies.*

## 5.4 Final Optical Pathway

In the end, the Glan-Taylor prism on the optics table which was located immediately before the Fresnel rhomb was found to be the source of major influence. Upon its removal from the optical pathway, the major secondary spectral features had vanished. Although at both polarizations a small signature remains, the overall acquired spectral signal is predominantly flat in nature and completely usable for hole-burning trials, when deep holes are burnt. The matter of determining the source of the remaining periodicity is yet to be determined.

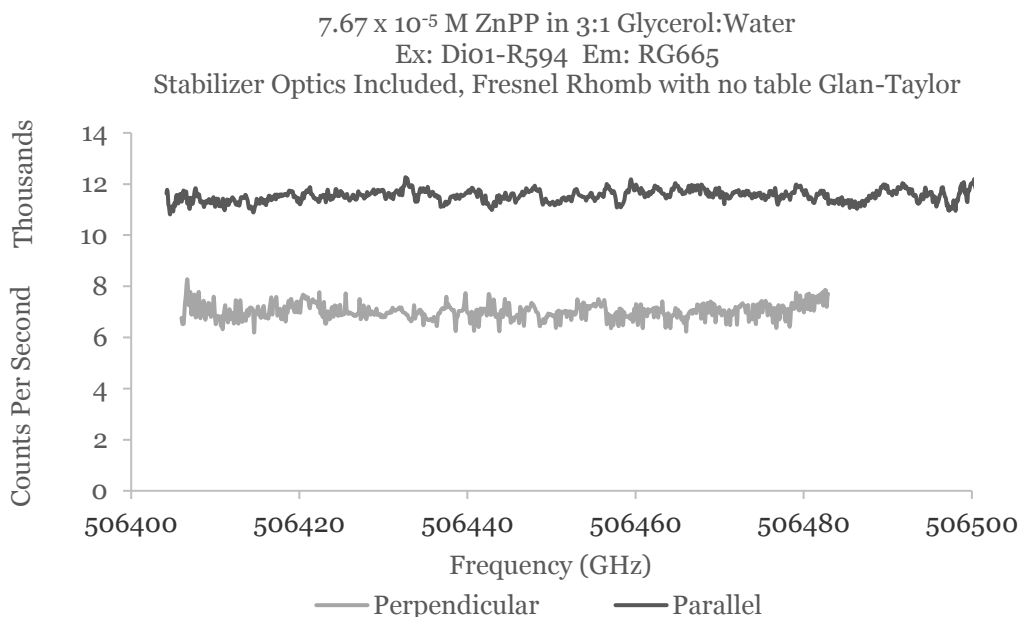


Figure 5.10: Parallel and perpendicular, excitation light polarization. 7.67 x 10<sup>-5</sup> M ZnPP in 3:1 glycerol:water at 298 K. Spectra obtained at 298 K with no windows present within CTCSSM, position and intensity stabilization optics included, along with table top Fresnel rhomb, but not the second optics table Glan-Taylor prism. Slight variation of spectral signal persists, however, lack of large variation within signal allows for possibility of successful spectral hole-burning studies.

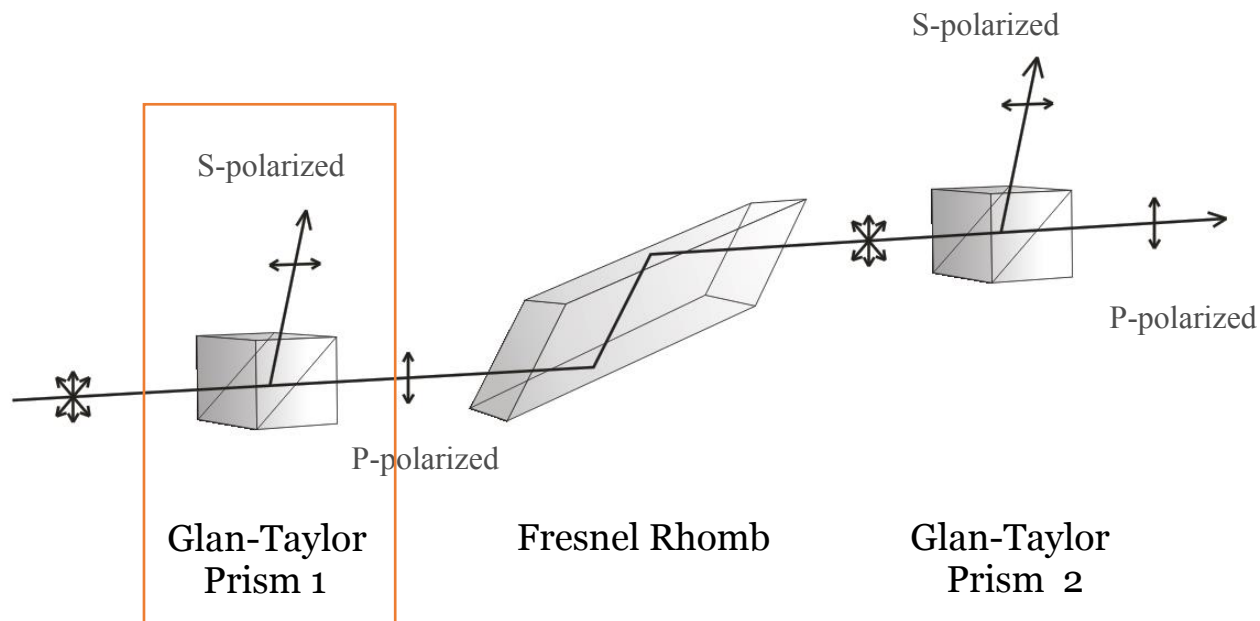
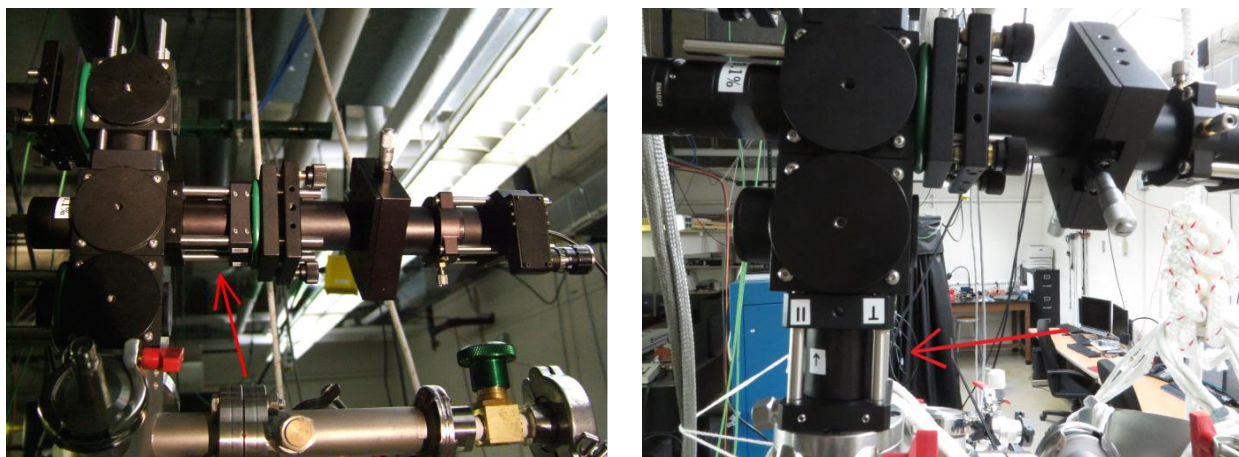


Figure 5.11: Polarization elements originally used within the optical pathway for control of the polarization of the excitation light. The second Glan-Taylor prism was moved from the optical table into the CTCSM. The first Glan-Taylor prism was eventually completely removed to eliminate the oscillatory behavior observed in collected spectra.

Removal of the Glan-Taylor prism from the optics table, and thus one less polarization element in the overall optical pathway, made necessary the re-investigation of the quality of the polarization of excitation light now incident upon the sample. To achieve this task a secondary polarizer was used as an analyzer and the ability to “null” the intensity was checked. It was observed that light within the CTCSM underwent a severe loss of polarization, on the order of 30-40% upon sample incidence. As strict polarization is necessary for cleanly split hole-profiles, this issue needed to be addressed. To resolve the problem, the polarization element within the excitation arm of the CTCSM was moved from before to after the dichroic filter. This is the position of the polarization modulator described within chapter 4. Three of the glass flats/windows within the optical insert of the microscope were removed. Although a secondary

function of these windows was to serve as partial thermal barriers for the sample, no significant sample heating has been observed in experiments that followed. These steps, resulted in a substantial increase  $> 95\%$  in maintenance of polarization as incident upon sample. As the Glan-Taylor prism now sits in the emission pathway, the fluorescent signal intensity is partially reduced and the effect of this secondary signal discrimination/selection process needs to be addressed within the calculations regarding the contributions of sub-ensembles of chromophores with various molecular orientations to resulting hole-profiles.



*Figure 5.12: Left: Previous location on the excitation arm of the CTCSM of the polarization modulator, housing the Glan-Taylor prism. Right: New location of the Glan-Taylor prism, after the dichroic mirror. The prism remains fully rotatable, allowing for any desired angle of linear polarization to be achieved*

With the optical pathway re-configured to alleviate collected spectra from erroneous secondary features arising from the optical properties of the experimental setup, and steps taken to assure accurate polarization at the sample, efforts moved towards signal to noise enhancement of collected data.

## 5.5 Hardware Methods

On the detection side of the experimental setup, a Stanford Research Systems SR400 two channel gated photon counter is used for counting TTL pulses generated by two PerkinElmer SPCM avalanche photodiodes (APD's), which detect the emitted fluorescent photons from the sample of interest. During the initial incorporation and testing this instrumentation, primary focus had been on the software development for correlating the counts as collected from the SR400 to the excitation wavelength, thus allowing for the production and recording of the spectral signal. Attention was given to the programmatic communication with the instrument and less attention to the signal input requirements, causing not only a necessary specification but also feature of the SR400 photon counter to be overlooked. Upon closer inspection it was found that the signal inputs could only accept and accurately count pulses within the range of -300 mV to +300 mV. As the TTL pulses generated by the APD's were  $\sim 2.5$  V, this indicated that any electrical noise generated by the APD's could incorrectly be counted as fluorescent signal, due to the relatively low 300 mV threshold. To address this, a voltage divider containing an 820-ohm resistor was constructed through which the APD's output signal is now passed prior to the input of the SR400. Figure 5.13 displays a trace from an oscilloscope showing the pulse before and after the resistor.

No phase change of the signal is observed to be present upon inclusion of the resistive element in the signal pathway, indicating that the reading of the scanning of the excitation source and the counted signal into the spectroscopy program does not require any temporal modification.



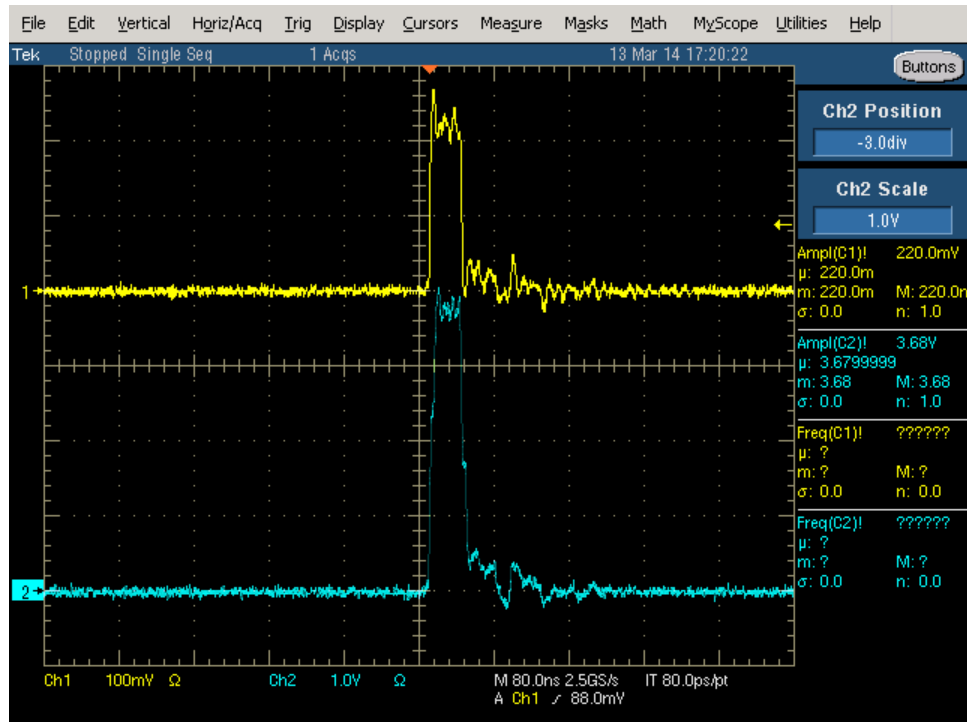
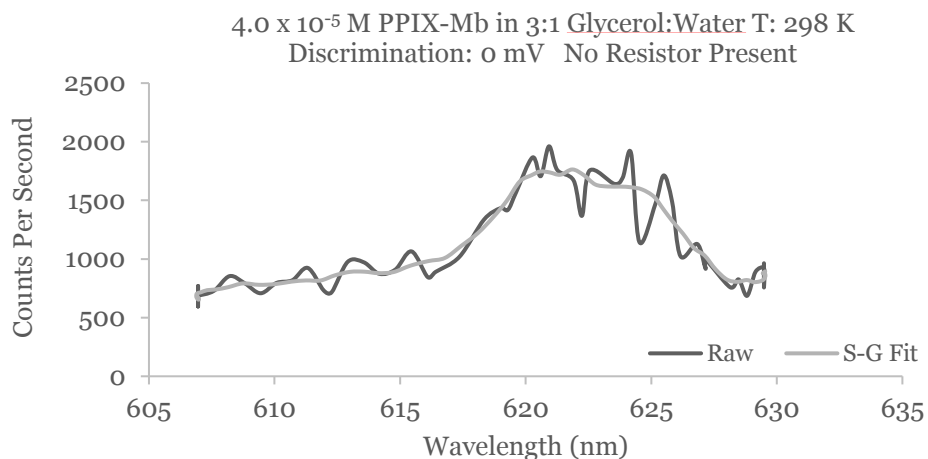
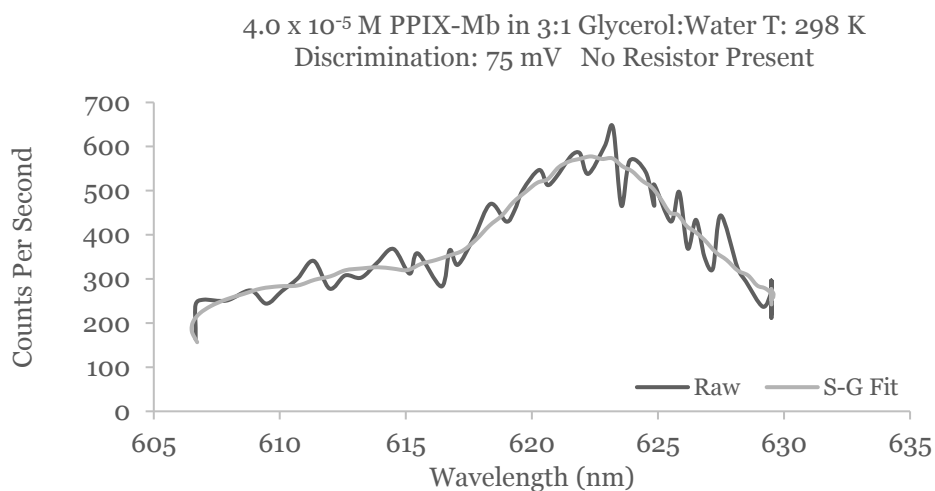


Figure 5.13: TTL pulse output from APD from detection of fluorescent signal. Blue trace: original pulse with amplitude of 3.68 V. Yellow trace: same pulse after passing through 820-ohm resistor with amplitude of 220.0 mV.

With the TTL pulses in the appropriate voltage range, threshold values for pulse discrimination could be investigated. This discrimination setting counts only those pulses that are above a user specified voltage cutoff. For these experiments the discriminator slope was set to rising edge, and spectral profiles of sample were taken at discrimination voltages set in steps of 10 mV increments over the discrimination range 0 mV to +300 mV. At 275 mV counts were minimal, and at 280 mV an upper threshold was found with no counts being recorded at or above this value. Example spectra appear in figure 5.14, along with statistics describing spectral noise. The entire experiment for all settings evaluated is then summarized in the following comparison of signal standard deviation in relation to discriminator value.



Standard Deviation (CPS)	Average S/N Ratio	Average S-G Signal	Percentage Points in +, - SQRT signal
123.0334	8.567389	1054.08	23.80952



Standard Deviation (CPS)	Average S/N Ratio	Average S-G Signal	Percentage Points in +, - SQRT signal
26.81241	11.9352	320.012	57.00935

Figure 5.14: Representative spectral profiles and statistics taken of PPIX-Mb sample at various discriminator settings on the SR400. Above: no discrimination. Below: 75 mV discrimination.

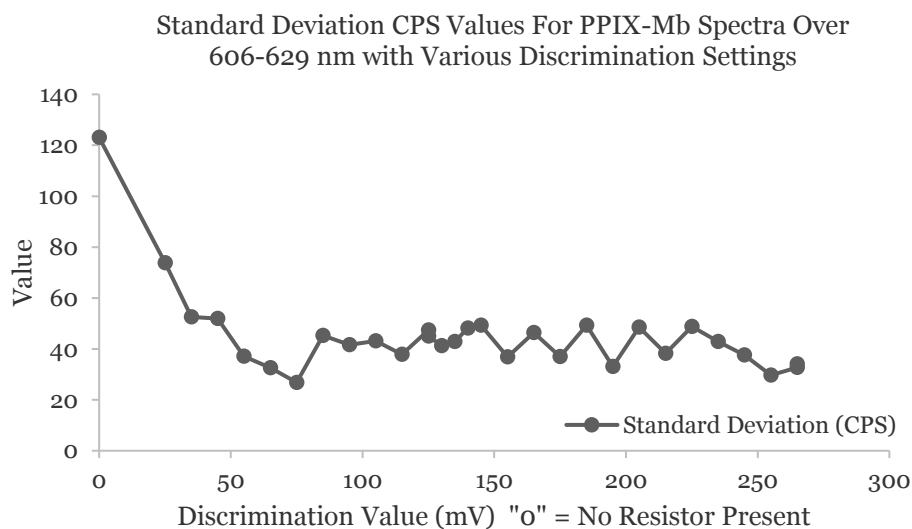


*Figure 5.15: Spectral standard deviation of PPIX-Mb sample excited over the range 606-629 nm at various discriminator settings on the SR400. Discrimination thresholds were evaluated at increments of 10 mV over the range of 0 mV to +300 mV. (Specifically: 0, 25, 35, 45,...,265, 275, 280, 285, 300 mV)*

In attempts to bracket discrimination parameters and count only pluses in-between a narrow range, the signal was “T” split after the resistor into input 1 and 2, to establish upper and lower discrimination bounds. Results from these trials were similar to those displayed above, and appeared to have little additional benefit to noise reduction than only setting a lower bound to input signal voltage for counting purposes. It was found that the 75 mV discrimination level represented the smallest standard deviation and the highest S/N ratios in recorded spectra. Therefore, the discrimination value of 75 mV was chosen as the default in all experiments that followed.

## II

### Chapter 6

# Modeling Cryogenic Heat Transfer for Predictive Thermal Regulation

## 6.1 Introduction

Conducting spectral experiments in the cryogenic regime offers two important benefits. Due to the significant minimization of phonon coupling, electronic transitions are able to approach their lifetime limited values, leading to less broadened spectral features. Furthermore, the conformational degrees of freedom existing in low lying energy states can be probed if the ability to systematically control and cycle the temperature of a sample is a possibility [7]. Possessing precise thermal control, however, requires the classification and regulation of the heating and cooling behavior of a sample's environment.

This investigation looks to formally model the thermal characteristics of a 9VSRD-SVT-22 Janis Research Dewar. Heat transfer occurs through multiple interfaces and phase boundaries between the sample, heater, and cryogen reservoir. The temperature within the cryostat is controlled by an internal heater and is monitored at both the heater and at the sample stage. Because the heating element is removed from the sample by multiple interfaces, establishing appropriate heater ramping techniques becomes necessary for quickly cycling the temperature at the sample. If this process is

performed correctly, the sample reaches the desired temperature without overshoot. Therefore, the establishment of a model that systematically predicts heat flows throughout the system is a necessity for maintaining appropriate heater control. The system is theoretically modeled, taking into account specific geometrical and material constraints, temperature-dependent heat transfer coefficients and thermal conductivities, for the conductive, convective and radiative heat transfer occurring. Transient and steady-state models are investigated for predictive ability and consistency to experimental data.

## 6.2 Heat

Heat is the form of energy that in the absence of work describes the interaction of a system with its surroundings, as the system changes from one equilibrium state,  $T_i(t_0)$  to another,  $T_f(t)$ , where  $t$  represents time and  $T$  indicates temperature. Here the subscripts on the temperature variable designate the initial and final temperature of the system. The larger the amount of heat energy contained within the medium, the greater the vibrational motion of the constituent particles making up solids and the greater the rate of diffusion and frequency of collisions in fluids, liquids and gasses. Heat transfer, deals specifically with the rates at which thermal energy flows within a medium or between systems. According to the second law of thermodynamics the driving force behind any heat transfer process is the existence of a spatial temperature differential and the tendency of heat to flow spontaneously and irreversibly from regions of high temperature to those of low temperature [2, 11]. This differential gives heat transfer both

a direction and a magnitude, making heat transfer a vector quantity, with a larger thermal differential yielding a higher rate of heat transfer. Of great importance when evaluating heat transfer amongst systems is the principle of conservation of energy, which dictates that the heat energy that flows into a system must remain in balance with the total sum of heat energy that becomes either stored or converted within the system and that which leaves the system. This equality is simply a restatement of the first law of thermodynamics, for a closed system in the absence of work. The process of energy transport can occur by molecular interactions, fluid flows, and electromagnetic waves [3, 8].

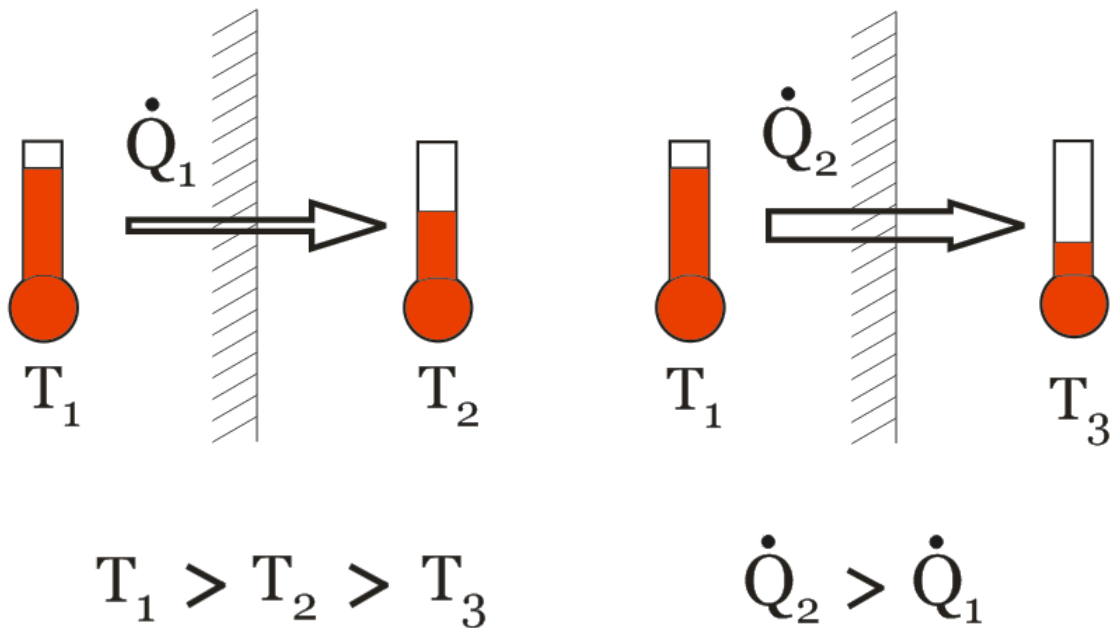


Figure 6.1: Direction and magnitude of heat transfer resulting from a thermal gradient across a boundary. The second law of thermodynamics dictates that heat flows from higher to lower temperatures giving the heat transfer a defined directionality. The heat transfer rate is dependent upon the magnitude of the thermal differential. These two results give heat transfer vector properties.

### 6.3 Heat Transfer Mechanisms

Thermal energy transfer can occur through three primary mechanisms; conduction, convection, and radiation. In most real systems heat transfer processes involve all three mechanisms and the total amount of heat that is transferred can be represented by the sum of the amount of heat that is transferred by each of the three mechanisms. The quantity of heat is denoted by the variable  $Q$ , with units J, and when the conductive, convective, and radiative terms are summed, the total heat takes the following form [8].

$$Q_{Tot} = Q_{Cond} + Q_{Conv} + Q_{Rad} \quad (6.1)$$

This relationship is easily extended to heat flow as opposed to heat. In this case  $\dot{Q}$ , when viewed as a rate, takes on the unit of watts, which is a joule per second,  $W = J/s$ .

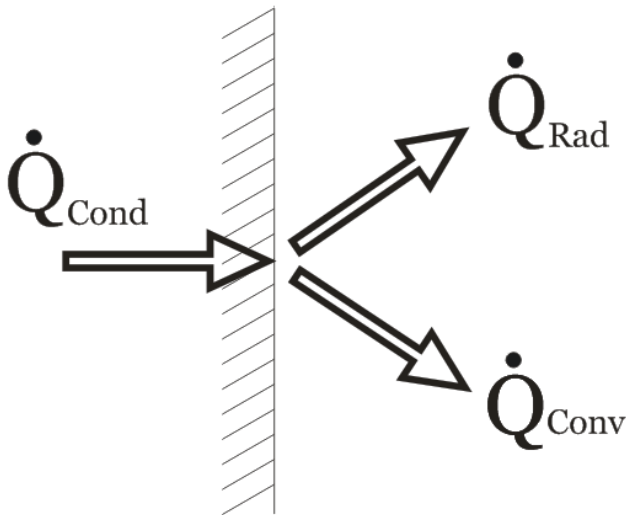


*Figure 6.2: The total heat that is transferred between temperature  $T_1$  and temperature  $T_2$  is the sum of heat flows by each of the three aforementioned mechanisms. The equality is mathematically stated in equation 6.1. Conduction is the mechanism of heat transfer in a solid. In fluids, both convective and radiative heat transfer processes occur. In vacuum, radiation is the only form of heat transfer.*

### 6.3.1 Conduction

Heat is representative of the randomized kinetic energy contained within a medium and can be related to the vibrational motions of the electrons, atoms and molecules that make up the medium. Conduction occurs when there is a direct transfer of thermal energy between particles possessing high kinetic energy, to neighboring particles possessing relatively lower kinetic energy [2]. This process occurs within solids between neighboring particles and also occurs in fluids between neighboring particles in the absence of fluid flow or bulk motions within the fluid.

The process of heat conduction was first formally described in 1822 in the book “Théorie Analytique de la Chaleur” by Jean Baptiste Joseph Fourier. The process of conduction is dependent on both the specific properties of the material and the geometry of the material involved. The overall flow of heat between two regions through a given space due to conduction is proportional to the temperature differential between the two and opposite in sign. This relationship is now known as Fourier’s law [8].

$$q = -k \frac{dT}{dx} \quad (6.2)$$

Here,  $q$  is the heat flux, which is the heat flow per unit area,  $\dot{Q}/dA$ , and has units of  $W/m^2$ , as  $\dot{Q}$  is viewed as a rate in this case. Upon rearrangement of the spatial terms, Fourier’s law takes the following form and the overall heat flow can be evaluated. The distance over which a thermal gradient exists in the direction of conduction across a medium is represented as a length  $L$ .

$$\dot{Q}_{net} = -k \frac{A}{L} \Delta T \quad (6.3)$$



The proportionality constant  $k$ , is the thermal conductivity, and has units of  $W/(m \cdot K)$ . Thermal conductivity is material dependent and describes how effective a medium is at the process of thermal transport. Similar to specific heat, the thermal conductivity of a material is dependent on the absolute temperature of the material. Large values of  $k$  signify efficient thermal transport across a medium. There exists a direct relationship between thermal conductivity and heat flow for a given temperature differential. When modeling heat transfer due to conduction, the thermal conductivity of a medium is an important parameter because it is the property that controls the flow of heat [3, 8, 11].

### **6.3.2 Convection**

Convection is the transfer of thermal energy that arises due to the physical mixing of the system, and can occur only in fluids. This can be through Brownian processes or mechanical agitation resulting in bulk fluid flows within a fluid or mixture of fluids. Convection also occurs as a fluid passes tangentially across a solid and fluid interface. In this case conduction occurs across the fluid boundary layer that develops at the interface existing between the two phases and the convective process is responsible for either bringing heat to or removing heat from that site [2, 3]. Convective processes can be naturally occurring, free convection, or instigated, forced convection. Because convection relies on the movement of fluids, the properties that dictate fluid flow characteristics become of predominant importance over the specific properties of the fluid when describing this form of heat transfer [8].

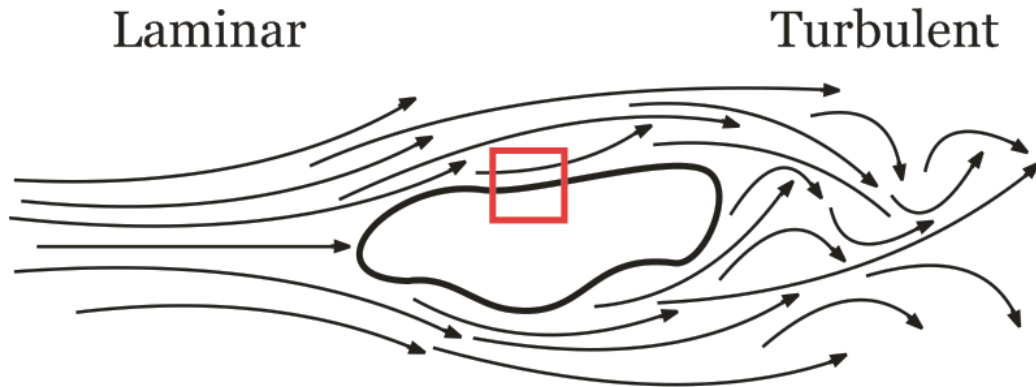


Figure 6.3: The convective heating or cooling of a body. Laminar flow dominates in regions of low Reynolds numbers where fluid viscous forces outweigh inertial forces. These regions are signified by nearly parallel fluid flow void of lateral mixing. At high Reynolds numbers, inertial forces dominate and flows becomes turbulent resulting in the formation of eddies. Despite depiction, the presence of a body in a flow does not necessarily induce turbulent flow. This is entirely fluid and velocity dependent. Both laminar and turbulent flow patterns facilitate convective heat transfer, yet to differing degrees.

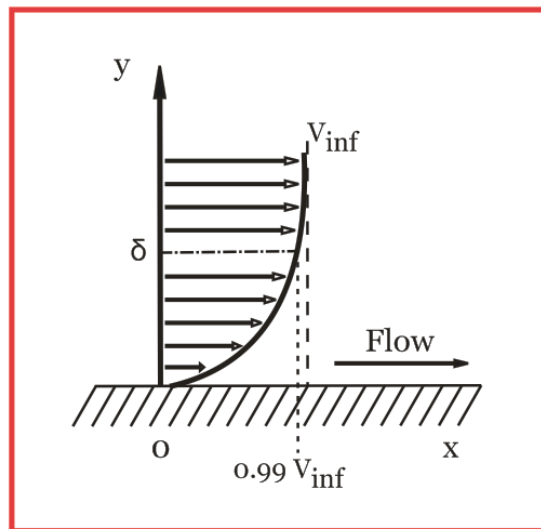


Figure 6.4: The development of a boundary layer as a fluid flows tangentially across a solid surface. Interactions between the fluid and surface reduce the propagation velocity of the fluid at the interface. The boundary layer thickness  $\delta$ , is defined as the distance from the surface to when the flow reaches 99% the flow rate of the bulk fluid. Conduction is the mode of transfer between the surface and the boundary layer. Convective processes facilitate heat transport. Depiction is representative of the interaction existing within the boxed region of the previous image.

Modeling heat transfer due to convection uses a relationship as devised by Isaac Newton and described in his 1701 work "Scala graduum Caloris. Calorum Descriptiones & signa" [10]. Similar to the findings of Fourier, albeit 121 years earlier, Newton observed that the change in temperature of a body over time was proportional to the temperature difference between the body and the surroundings.

$$\frac{dT_b}{dt} \propto T_b - T_{\text{inf}} \quad (6.4)$$

Where the temperature of the body is  $T_b$  and the temperature of the surroundings is  $T_{\text{inf}}$ . This can be placed in a more formal context by inserting Newton's proportionality into the first law of thermodynamics, relating heat flow  $\dot{Q}$  and internal thermal energy  $U$ , for a work free process. In this situation the temperature change over time for an incompressible material, where  $m$  is the mass and  $C$  is the specific heat of the material, is equivalent to the heat flow [8, 12].

$$\dot{Q} = \frac{dU}{dt} = mC \frac{dT}{dt} \quad (6.5)$$

When this substitution is made, this only states that a proportionality exists between the temperature difference and the heat flow. Although correct, convective heat transfer is quite a bit more complicated due to the physics occurring at the solid fluid boundary. The common formulation for this type of heat transfer, however, is known as Newton's law of cooling.

$$\dot{Q}_{\text{net}} = \bar{h} A (T_b - T_{\text{inf}}) \quad (6.6)$$

Here again  $\dot{Q}$  is the rate of heat transfer with the unit of watts, and  $A$  is the area of the surface through which the heat transfer takes place. To account for the interactions at the boundary the heat transfer coefficient  $\bar{h}$ , with units of  $W/(m^2 \cdot K)$  is introduced. This is an average quantity over the surface of the body. The position dependent heat transfer coefficient is  $h$ . The heat transfer coefficient exists as a constant of proportionality that indicates the diffusion of thermal energy across boundary layers occurring along the solid and fluid interface. Therefore, before a determination of  $\bar{h}$  or  $h$  becomes a possibility, an appropriate description of the forces dictating the fluids' condition at the interface becomes a necessity to the modeling the resultant heat flux. Heat transfer coefficients depend on specific system geometries and surface roughness; fluid properties such as density, viscosity, and specific heat, as well as the various characteristics of the fluids flow. Appropriate values for this coefficient can range over six orders of magnitude [3, 8]. The numerous dimensionless quantities that help determine which formulation should be used in the calculation of the heat transfer coefficient  $h$ , are discussed in section 6.4.

### 6.3.3 Radiation

All matter is made up of collections of charged particles. As an object gains thermal energy, the constituent particles making up the object gain kinetic energy and begin to vibrate. As temperature increases the particles vibrate more vigorously. These vibrating particles act as fluctuating or accelerated distributions of charge and give off energy in the form of electromagnetic radiation. The electromagnetic radiation given off by a

heated body is radiated in all directions and is known as thermal radiation. Therefore, all bodies that have temperatures above absolute zero emit thermal radiation. The amount of electromagnetic radiation given off by an object is related to the temperature of the object and the surface characteristics of the object [3].

An object that perfectly absorbs all electromagnetic radiation incident upon it, is known as a blackbody and has an absorptivity value of one,  $\alpha_b = 1$ . Black bodies are also perfect emitters of thermal radiation and have an emissivity of one,  $\epsilon_m = 1$ . The energy emitted by a blackbody is known as blackbody radiation. The maximum rate at which energy can be emitted in the form of blackbody radiation, and therefore the maximum rate at which thermal radiation can be emitted from a surface, is described by the Stefan-Boltzmann Law.

$$P = \sigma_{SB} AT^4 \quad (6.7)$$

This law states that the total radiated power emitted by a blackbody is directly related to the area of the emitting object  $A$ , and the fourth power of the absolute temperature  $T$ , of the object. The radiated power has units of  $W$ , and can be replaced by the variable  $\dot{Q}$ , the rate of heat transfer, to maintain convention. The  $\sigma_{SB}$  is the Stefan-Boltzmann constant, and has a value of  $5.670 \times 10^{-8} W/(m^2 \cdot K^4)$ . The above result is simply an integrated form of the Planck radiation formula over all wavelengths [8].

As all bodies at temperatures greater-than absolute zero emit some amount of thermal radiation, when modeling the heat transfer in real systems it becomes important to account for the radiation effects between bodies. In the simple case of two bodies, body one receives radiation from body two and simultaneously, body two

receives some thermal radiation from body one, which will change the overall rate of heat transfer in both directions. Additionally, real objects do not behave as perfect blackbody radiators and they neither perfectly absorb all incident electromagnetic radiation,  $\alpha_b \neq 1$ , nor do they perfectly emit thermal radiation,  $\epsilon_m \neq 1$ . To account for these effects the radiative heat transfer between two surfaces is modeled using the following relationship.

$$\dot{Q}_{\text{net}} = A_1 F_{1-2} \epsilon_m \sigma_{\text{SB}} (T_1^4 - T_2^4) \quad (6.8)$$

Again the total radiated power or rate of heat transfer is directly related to the area of the emitting object  $A_1$ , scaled by the Stefan-Boltzmann constant, and the difference of the fourth power of the absolute temperatures of the two objects,  $T_1$  and  $T_2$ . The scalar  $F_{1-2}$  is called the radiative view factor, the configuration factor, or the shape factor, and accounts for the radiative interaction between the two bodies. In this case,  $F_{1-2}$  represents the amount of radiant energy that leaves object one and is intercepted by object two.  $F_{2-1}$ , would indicate radiant energy leaving object two being transmitted to object one. The view factor is unitless in nature and is a calculated quantity. View factors are dependent upon the particular geometries of the interacting bodies, and therefore need to be determined for the specific system that is being studied [1, 3, 8, 12].

## 6.4 Dimensionless Quantities

Many aspects regarding the characteristics of heat transfer that occur within a system rely on the calculation and use of dimensionless numbers. Dimensionless quantities use

products and ratios of groups of variables that do possess units. These quantities are formulated in such a way that the final calculated values possess no units, when a consistent set of units are used in their calculation. Dimensionless numbers are used primarily for the determination of various properties regarding the flow of fluids that dictate convective behavior and play an important role in the determination of heat transfer coefficients and the appropriate forms of the equations necessary for use in their calculation. These quantities also find use when deciding if certain approximations defining conductive heat transfer behavior can be made. Of the many dimensionless quantities that exist in the field of heat transfer, the values that are of greatest importance to this particular investigation are presented [3, 8].

#### **6.4.1 Prandtl Number (Pr )**

The Prandtl number provides a measure of the diffusion rate of fluid momentum versus the diffusion rate of thermal energy in the fluid. Smaller Prandtl numbers, indicate higher convective ability of the fluid. These values are easily calculated using Sutherland's Law, the Eucken Correction and literature values for  $C_p$ . This dimensionless quantity is system specific in regards to system pressures and is of direct importance in evaluation of the Nusselt number  $Nu_L$ , and the heat transfer coefficient  $h$ .

$$Pr = \left( \frac{\nu}{\alpha} \right) = \frac{\mu C_p}{k} \quad (6.9)$$

The Prandtl number is directly related to the kinematic viscosity  $\nu$  and inversely related to the thermal diffusivity,  $\alpha$  of the gas, both quantities having units of  $m^2/s$ .

Here, the temperature dependent dynamic viscosity is  $\mu$  in kg/(m·s), the specific heat at constant pressure is  $C_p$  in J/(kg·K), and  $k$  is the thermal conductivity in W/(m·K). All quantities are properties of the fluid. Sutherland's Law is used for evaluating the dynamic viscosity and the Eucken Correction is used in calculation of the thermal conductivity. These are both presented later.

### 6.4.2 Reynolds Number (Re)

The Reynolds number is a ratio of inertial forces to viscous forces acting on a fluid. This ratio helps determine if the fluid behavior is laminar or turbulent flow. The critical Reynolds value is dependent on the geometry of the system, and for this study based on the cylindrical geometry of the research Dewar that value is  $5.0 \times 10^5$ . Laminar flow dominates in regions with Reynolds values less than the critical value and turbulent flow exists in regions above. This dimensionless number is again system specific in regards to pressure and container dimensions in addition to temperature, and must be evaluated for the particular system under study. This number is of importance in determining which method and formula will be used in the evaluation of  $Nu_L$ .

$$Re = \frac{\rho v L_c}{\mu} \quad (6.10)$$

In this relation,  $\rho$  is the density in kg/m<sup>3</sup>,  $v$  is the mean velocity of fluid flow in m/s,  $L_c$  is the characteristic length of the system in m, and  $\mu$  is again the dynamic viscosity.



### 6.4.3 Rayleigh Number (Ra)

The Rayleigh number is a relationship of buoyancy to viscosity within a fluid flow dictating the mode of thermal transport, convection versus conduction across the boundary layer and ultimately through the fluid. The critical Rayleigh range is about  $1.0 \times 10^4$ . Below this value conduction is dominant. This value is highly specific to geometrical and system parameters. Values change drastically throughout the system for each fluid and interface. This number is of direct importance in evaluation of  $Nu_L$ , and  $h$ .

$$Ra = \frac{g\beta\Delta TL^3}{\alpha\nu} \quad (6.11)$$

In this formulation,  $g$  is the acceleration of gravity in  $m/s^2$ ,  $\beta$  is the coefficient of thermal expansion for the fluid in  $1/K$ ,  $\Delta T$  is temperature difference between the heat transfer surface and the bulk fluid in  $K$ ,  $L$  is a geometry specific characteristic dimension in  $m$ ,  $\alpha$  is the thermal diffusivity in  $m^2/s$ , and the kinematic viscosity  $\nu$  is in  $m^2/s$ . The Rayleigh number is the product of the Grashof number  $Gr$  and Prandtl number  $Pr$ .

### 6.4.4 Nusselt Number ( $Nu_L$ )

The Nusselt number is a ratio of convective to conductive heat transfer across the fluid boundary layer. This number exists as a dimensionless form of the convective heat transfer coefficient  $h$ . The equation that defines this number is simply the ratio of the coefficients defining convective and conductive heat transfer accounting for the

characteristic length  $L_c$  over which the transfer occurs. Of great importance is that  $k_f$  in this equation is the thermal conductivity of the *fluid*.

$$Nu_L = \frac{hL_c}{k_f} \quad (6.12)$$

In the modeling of real systems, the Nusselt number is calculated first and is then used to determine the value of the heat transfer coefficient  $h$ . Different equations exist that allow for direct calculation of the Nusselt number. The flow characteristics that dominate within the fluid region dictate which basic form of equation is to be used. The flow characteristics depend on the calculated Prandtl and Rayleigh numbers for the system. Based on the values of these dimensionless numbers, the precise form of the equation to be used for calculating the Nusselt number is known.

#### 6.4.5 Biot Number (Bi)

The Biot number is again a ratio of convective to conductive heat transfer across the boundary layer. This value relates the heat transfer that occurs within a conducting body to the rate of heat transfer at the surface away from the body. It has the same formulation as the equation for the Nusselt number; however, it is the thermal conductivity  $k_s$  of the *solid* that is used.

$$Bi = \frac{hL_c}{k_s} \quad (6.13)$$

The Biot number determines whether or not the temperature within a body can be considered isotropic. This implies that the temperature at the surface of the body is

negligibly different than that of the body center and thus the temperature of the entire body can be considered to be the same. This is generally true for small or highly thermally conductive bodies. The isotropic assumption is true for Biot numbers less than 0.1, which implies that heat is transferred through the body faster than it leaves the body. Biot numbers larger than this critical value imply that heat is transferred away from the body faster than it is transferred within the body and therefore, thermal gradients begin to exist within the body. The value of the Biot number and the isotropic assumption become of great importance in modeling heat transfer under both steady state and transient formalisms.

#### **6.4.6 Fourier Number ( $F_0$ )**

The Fourier is a quantity that is used to represent dimensionless time. Its formulation uses the thermal diffusivity  $\alpha$ , a length component  $L$ , and a time component  $t$ , to return the dimensionless time. The thermal diffusivity itself can be broken into its constituent components,  $k$ ,  $\rho$ , and  $C_p$ .

$$F_0 = \frac{\alpha t}{L^2} = \frac{kt}{\rho C_p L^2} \quad (6.14)$$

### **6.5 Steady State and Transient Heat Transfer**

Thermal energy transport can be modeled under either steady state or transient conditions. A steady state process is one in which the heat flux either remains constant

or is assumed to remain constant at all locations within a medium. Different heat transfer rates are allowed to exist at different locations within a medium but these rates are not allowed to fluctuate during the heat transfer process. A steady state process is useful for applications where heat transfer occurs between two positions in space, each of which maintain a consistent temperature over time, regardless of the quantity of heat that is transferred. An example of this would be the heat that is transferred through a refrigerator door, where the temperature inside is maintained and the temperature outside remains effectively unchanged. The steady state solution is also used as a first approximation to heat transfer in a real system as the computation of analytical solutions is direct.

A transient process is one in which the heat flux, or rate of thermal transfer is allowed to vary during the process of thermal exchange. Temperature generally varies with both time and position in a transient process. Transient analysis is concerned with the instantaneous heat transfer rates at different points in a body. Due to the non-isotropic temperature variation across the body, isothermal surfaces within the body are used to assign the time and position dependent heat fluxes.

Although the modeling of real systems requires a transient analysis, frequently the system is first analyzed under steady state conditions due to the simplicity of the calculation. Additionally, modeling a system using the steady state formalism allows for determination of the initial thermal conditions likely to be present at the boundaries between media.

The distinction between the steady state and transient heat transfer can most easily be seen by looking at the equation for one-dimensional heat diffusion through a

plane by conduction. In this situation the region of interest is the volume element defined by the area  $A$  of thickness  $\Delta x$ . According to the first law of thermodynamics there must be an energy balance in the region such that the rate of heat conduction into the region minus the rate of heat conduction out of the region must be equal to the overall change in thermal energy within the region, during the specified time interval. Mathematically, this is equivalent to stating that the following must be true.

$$\dot{Q}_{in} - \dot{Q}_{out} = \frac{dU}{dt} \quad (6.15)$$

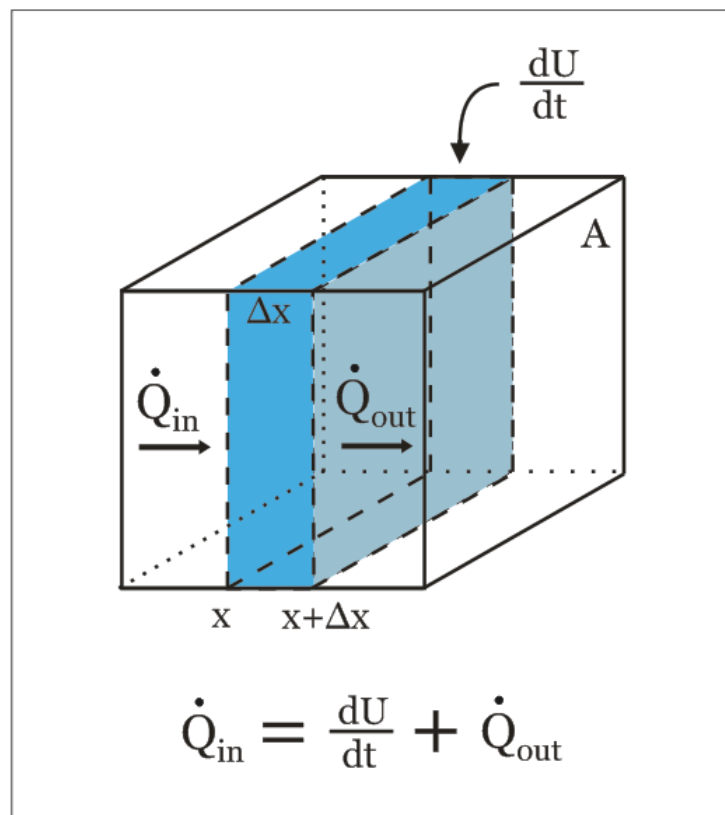


Figure 6.5: Net one-dimensional heat flow through a volume element of planar geometry. The region is defined by a surface of area  $A$ , and a thickness of  $\Delta x$ . By the first law of thermodynamics, a balance of energy exists if and only if, the heat that flows into a region is equivalent to the total sum of the heat energy which flows out of the region and the increase of internal energy that is contained within the region.

Solving for the equation for heat diffusion across this space simply requires Fourier's law to be equated to the first law of thermodynamics, relating the heat flow  $\dot{Q}$  and internal thermal energy  $U$ , during a work free process. Assuming that  $\rho$  represents the density of the material within the region, by using the definition of density, and separating the volume element into length and area terms, the mass can be replaced in equation 6.5 to yield the net gain of thermal energy within the region during the heat transfer.

$$\rho = \frac{m}{V} \Rightarrow m = \rho V \quad (6.16)$$

$$\dot{Q}_{net} = \frac{dU}{dt} = mC \frac{dT}{dt} = \rho A \partial x C \frac{\partial T}{\partial t} \quad (6.17)$$

To find the net difference of the thermal energy that entered the region to that which exited the region, Fourier's law, equation 6.3 is applied. Partial derivatives are utilized in the expression of Fourier's law to maintain generality.

$$\dot{Q}_{net} = \dot{Q}_{in} - \dot{Q}_{out} = -kA \frac{\partial T_x}{\partial x} - \left( -kA \frac{\partial T_{x+\Delta x}}{\partial x} \right) \quad (6.18)$$

These two identities for the net heat that is transferred are then equated.

$$kA \left( \frac{\partial T_{x+\Delta x}}{\partial x} - \frac{\partial T_x}{\partial x} \right) = \rho A \partial x C \frac{\partial T}{\partial t} \quad (6.19)$$

Each side is then divided by  $A \partial x$ , and the temperature term on the left hand side is grouped. Allowing both the thickness of the region and the change in time approach the limit yields the equation for one-dimensional heat diffusion.

$$\left(\frac{\delta}{\delta x}\right)\left(k\left(\frac{\delta T}{\delta x}\right)\right) = (\rho C)\left(\frac{\delta T}{\delta t}\right) \quad (6.20)$$

In the case of a transient analysis process, the term for the change in temperature over time remains as shown above. In the case of a steady state analysis this term is set to zero, as there is no overall change in the heat flux or net energy content contained within the medium in relation to time and the system is observed as steady.

$$\left(\frac{\delta}{\delta x}\right)\left(k\left(\frac{\delta T}{\delta x}\right)\right) = 0 \quad (6.21)$$

Under certain conditions temperature variation exists in a medium in relation to time but not in relation to position within the medium. When this is the case the temperature of the entire medium changes uniformly in time. Systems that possess these properties are called lumped systems. Under these circumstances the lumped capacitance approximation to the complete transient analysis can be performed [3, 12].

## 6.6 Lumped Capacitance

The lumped capacitance approximation can be applied to the situation of the convective heating or cooling of an object that has a low internal resistance to conduction. This means that the object being heated or cooled has a high thermal conductivity resulting in a high rate of conduction for the internal transfer of thermal energy within the body for the given temperature differential. Under this approximation, the temperature within the body does vary over time. In this case, the limiting term is not the thermal

conductivity of the body but the flow characteristics of the fluid and the respective heat transfer coefficient that dictate the transfer of heat.

Mathematically the lumped capacitance solution is obtained in the following way. Setting up the standard equality establishing the balance of energy as required by the first law, the heat transferred into the system utilizing a convective process is related to the internal energy gained within the system, as originally described in equation 6.5, making the appropriate substitution of the mass to density and volume. The temperature  $T_{inf}$  is representative of the bulk fluid temperature.

$$\dot{Q}_{in} = \frac{dU}{dt}$$

$$\frac{dU}{dt} = mC_p \left( \frac{dT}{dt} \right) = \rho VC_p \left( \frac{dT}{dt} \right)$$

$$\dot{Q}_{in} = hA (T_{inf} - T)$$

$$\Rightarrow hA (T_{inf} - T) = \rho VC_p \left( \frac{dT}{dt} \right) \quad (6.22)$$

Variables are separated and the constants and the time component are moved from the right hand side to the left hand side, with the opposite being performed for the thermal components.

$$-\left( \frac{hA}{\rho VC_p} \right) dt = \frac{dT}{T - T_{inf}}$$

Next, the left side is integrated with respect to time and the right with respect to temperature. The initial time is  $t=0$ , and initial temperature  $T_i$ . At some later time, the time is  $t$  and the temperature is  $T(t)$ , which establish the bounds of integration.



$$-\left(\frac{hA}{\rho V C_p}\right) \int_{t=0}^{t=t} dt = \int_{T_i}^{T(t)} \frac{1}{T - T_{inf}} dT$$

The exponential function is applied to both sides to get rid of the resulting natural log, ln, on the right hand side, the rules of subtraction and division for ln are applied and the equation is transposed for presentation purposes.

$$\Rightarrow \left(\frac{T(t) - T_{inf}}{T_i - T_{inf}}\right) = \exp^{-\left(\frac{hA}{\rho V C_p}\right)t} = \exp^{-\left(\left(\frac{hL}{k}\right) * \left(\frac{k}{\rho C_p L^2}\right)\right)t} = \exp^{-(Bi * Fo)} \quad (6.23)$$

Making the following insertions of an additional length quantity as well as inserting the thermal conductivity k, allows for the lumped capacitance model to be presented in terms of the Biot number and the Fourier number [8, 12].

## 6.7 Extended Dimensions and Geometries

All equations presented to this point have been for heat transfer in a single dimension. To allow for greater flexibility in modeling more complex heat flows, the equations are easily extended to higher dimensionality. Heat transfer is extended to a three-dimensional space by allowing the already vectorized quantity to possess components in each spatial dimension. The substitution below describes heat transfer in the direction normal  $\vec{Q}_n$ , to the isothermal plane at a point p in the medium.

$$\vec{Q}_n(p) = \dot{Q}_x \vec{i} + \dot{Q}_y \vec{j} + \dot{Q}_z \vec{k} \quad (6.24)$$

Heat flow through a spatial element requires the gradient. For this, the Laplacian which is the second partial derivative with respect to all independent variables is used

and the change of the flux through space is computed. The result for transient heat diffusion in a three-dimensional plane wall is presented. It can be observed that this is simply the expansion of equation 6.19 into the three-dimensional space. The last term on the left hand side describes the case where a heat generating element exists within the volume element being modeled.  $G$  is the rate of heat generation in the element. In the case of no internal heat generation, this term is set to zero.

$$\left(\frac{\delta}{\delta x}\right)\left(k\left(\frac{\delta T}{\delta x}\right)\right) + \left(\frac{\delta}{\delta y}\right)\left(k\left(\frac{\delta T}{\delta y}\right)\right) + \left(\frac{\delta}{\delta z}\right)\left(k\left(\frac{\delta T}{\delta z}\right)\right) + \left(\frac{G}{V}\right) = (\rho C_p)\left(\frac{\delta T}{\delta t}\right) \quad (6.25)$$

Of importance to the modeling of thermal properties in this study is the cylindrical geometry of the research Dewar. The following standard equalities are used for conversion between the rectangular and cylindrical coordinate systems.

$$x = r \cos\phi \quad y = r \sin\phi \quad z = z \quad (6.26)$$

The result for transient heat diffusion in a three-dimensional cylindrical wall follows. Again with no internal heat generation, the last term on the left hand side is set to zero. In the case of a steady state process, the right hand side of the expression is also set to zero, as would be true for equation 6.25. In cases where only radial heat transfer is important, or far outweighs that in the other directions, the other spatial components can be eliminated [3].

$$\left(\frac{1}{r}\right)\left(\frac{\delta}{\delta r}\right)\left(rk\left(\frac{\delta T}{\delta r}\right)\right) + \left(\frac{k}{r^2}\right)\left(\frac{\delta^2 T}{\delta \phi^2}\right) + \left(k\frac{\delta^2 T}{\delta z^2}\right) + \left(\frac{G}{V}\right) = (\rho C_p)\left(\frac{\delta T}{\delta t}\right) \quad (6.27)$$

$$\underbrace{\hspace{10em}} \quad \underbrace{\hspace{10em}}$$

= 0 for radial heat flux only      = 0 for Steady State

## 6.8 Thermal Resistance Networks

Heat flows through materials depend on thermal conductivities, and across interfaces on heat transfer coefficients, each of which reduce the maximum rate that heat is transferred through a system. When performing a multi-layer analysis, the objective is to determine how heat moves across a series of layers, each with their own thermal conductivity and heat transfer coefficients. As each additional layer is added there is an overall reduction in the rate that heat flows through the entire system. In these situations, it is useful to model the system as a series of resistances to heat flow that are encountered through and in-between each layer. The concept is analogous to the resistance to the flow of current in an electrical circuit.

Inherent surface roughness causes imperfect thermal contact between adjacent layers and reduces the efficiency of heat transport. This effect results in temperature drops at each thermal boundary in a resistance network. This is known as boundary resistance and is displayed as temperature discontinuities existing at the boundaries in a temperature position diagram.

To understand the resistances that are encountered, the resistance for conduction in a plane wall will be derived. The thermal resistances for the conductive, convective and the radiative processes are then presented for both planar as well as cylindrical geometries.

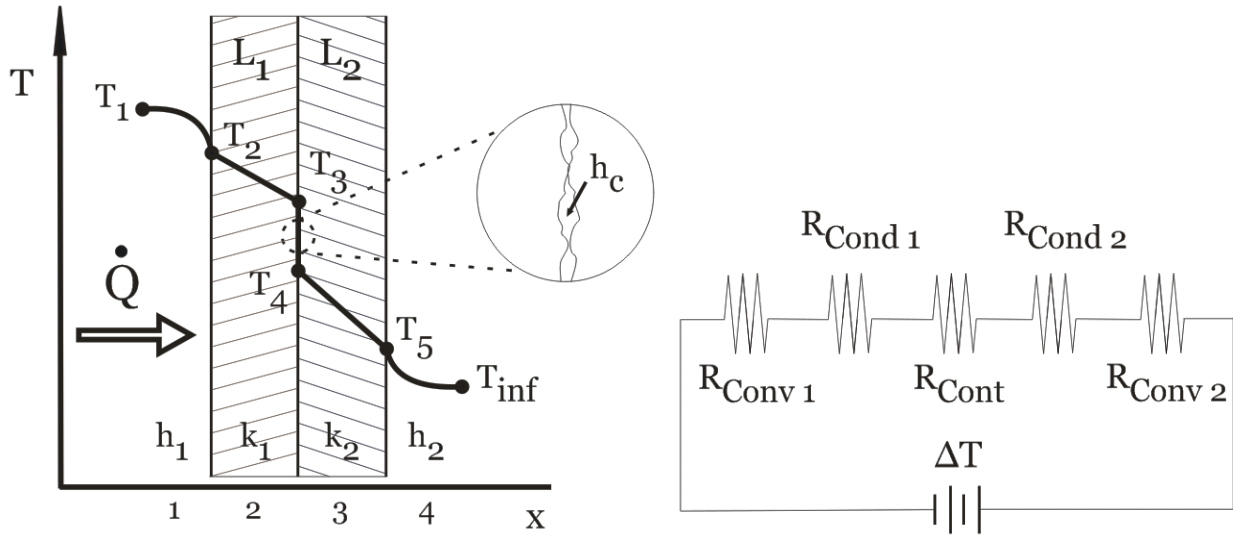


Figure 6.6: Left: Temperature profile of thermal gradients existing at and across each interface within a multilayer system. This system is composed of four distinct layers. Region one and four represent fluid layers with heat transfer coefficients  $h_1$  and  $h_2$  respectively. Regions two and three represent solid layers of thickness  $L_1$  and  $L_2$ , each layer possessing a different thermal conductivity. Observe the different temperature drops across each of these layers. Due to surface roughness, interstitial spaces exist between the solid layers and thermal contact is imperfect. Thermal transfer in this space is dictated by the heat transfer coefficient  $h_c$ . This results in the development of a thermal gradient at the interface. Right: Thermal resistance network for this system. Each layer, in addition to the contact resistance  $R_{cont}$  between the solid layers, contributes thermal resistance to the flow of heat.

For this derivation, figure 6.5 will be used and it will be assumed that there is no internal heat generation and no change in the overall internal energy of the enclosed volume element. An integration of Fourier's law, equation 6.2 and the fact that  $q = \dot{Q}/A$ , allows the net heat transfer through this region to be defined.

$$\int_x^{x+\Delta x} \dot{Q} \, dx = -kA \int_{T_x}^{T_{x+\Delta x}} dT$$

Let the distance from  $x$  to  $x+\Delta x$  be represented by the length  $L$ . Integration of both sides and a rearrangement of the temperatures to eliminate the minus sign on the right hand side yield the net heat flow.

$$\dot{Q}_{net} = kA \frac{T_x - T_{x+\Delta X}}{L} \quad (6.28)$$

Applying the concept of electrical circuits to this situation, and the relationship between voltage, current and resistance as defined by Ohm's law, the analogous relationship can be seen between a thermal gradient, the rate of heat transfer and the thermal resistance.

$$\text{Electrical} \quad V = iR \quad \text{Thermal} \quad \Delta T = \dot{Q}_{net} R \quad (6.29)$$

For the system described above, the thermal resistance can then be defined.

$$\text{Conduction} \quad R = \frac{L}{Ak} \quad (6.30)$$

A similar process can be performed for heat transfer by convection and radiation which yield the following resistances. In both cases the area of the surface over which heat is transferred is of importance.

$$\text{Convection} \quad R = \frac{1}{A_s h} \quad (6.31)$$

$$\text{Radiation} \quad R = \frac{1}{A_s F_{s-surr} \epsilon_m \sigma_{SB} (T_s + T_{surr})(T_s^2 + T_{surr}^2)} \quad (6.32)$$

For a geometric configuration with cylindrical characteristics, the planar surface area  $A$ , is substituted to reflect the area of the cylinder, by  $A=2\pi rL$ . Here the length of the cylinder as well as the inner radius,  $r_1$ , and outer radius,  $r_2$ , defining the cylinder are necessary to include for the evaluation of thermal resistances. These account for the change to the parameters defining the volume element caused by the changing radial characteristics of the cylinder as the heat is transferred towards or away from the center

of the cylinder. The forms of the expressions describing the encountered resistances, however, remain similar.

$$\text{Conduction} \quad R = \frac{\ln\left(\frac{r_2}{r_1}\right)}{2\pi Lk} \quad (6.33)$$

When similar substitutions and considerations for area and radial characteristics are taken into account, the following formulas for heat transfer resistances by convection and radiation can be found. In both cases the area of the surface over which heat is transferred is of importance [2, 3, 8, 12].

$$\text{Convection} \quad R = \frac{1}{2\pi r_s L_s h} \quad (6.34)$$

$$\text{Radiation} \quad R = \frac{1}{2\pi r_s L_s F_{s-surr} \epsilon_m \sigma_{SB} (T_s + T_{surr})(T_s^2 + T_{surr}^2)} \quad (6.35)$$

## 6.9 The Modeled System

In order to dependably and reproducibly modulate the temperature of the sample during hole-burning studies, in addition to possess the ability to effectively conduct temperature cycling investigations, it was necessary to classify the heating and cooling behavior of the cryostat. In particular, the system modeled for this investigation is a 9VSRD-SVT-22 Janis Research Dewar.

The temperature within the cryostat is controlled by an internal heater that is removed from the sample by three layers. These consist of a stainless solid layer

(SUS 304) sandwiched between two fluid layers of which are any combination of light vacuum, helium or nitrogen gasses. These regions are also removed from the cryogen reservoir, acting as the heat sink, by multiple layers of differing phase that need to be accounted for. The temperature is monitored at the heater with a LakeShore DT-670-SD-1.4L sensor, which is defined as the heater sensor and at the sample using a LakeShore DT-670-SD-1.4D sensor, being designated as the sample sensor. A Lakeshore 331 temperature controller is used to monitor the output signal of both sensors and to control the heating element contained within the research Dewar. The heating can be performed actively by the user, or the temperature can be set by using feedback control along with predetermined PID values. In practice, a combination of these methods are used, however, the end goal is automation of the process.

### **6.9.1 Temperature Cycling**

To successfully cycle between various temperature values during the cycling experiments or hole-burning investigations, the heater needs to be dependably modulated such that desired temperature set-points are quickly achieved without overshoot. This is of great importance when studying low lying energy barriers relating to conformational degrees of freedom in molecules during cycling experiments. To change the temperature of the sample, a three step process is used. Once the excursion temperature or new temperature is decided upon for the sample, the heater is ramped to a much higher temperature to quickly introduce heat into the system. Next, when the heater reaches a certain temperature as monitored by the heater sensor, the heater is

completely shut off. As the temperature at the heater sensor begins to fall, the excess heat in the system distributes, with the temperature at the sample continuing to increase until equilibrium between the two regions and sensors is reached. Lastly, using the feedback control in conjunction with the temperature specific PID values, the heater is again turned on and set to a temperature value slightly below the new equilibrium value. This maintains the sample at the new temperature. If the process is done perfectly, with the correct temperature ramp at the correct time and the feedback is activated at the correct time and temperature, the sample exactly reaches the desired excursion temperature. Figure 6.7 represents an example of two applications of this process to alter the sample temperature. Observe that the sample smoothly reaches the new temperature without any overshoot.

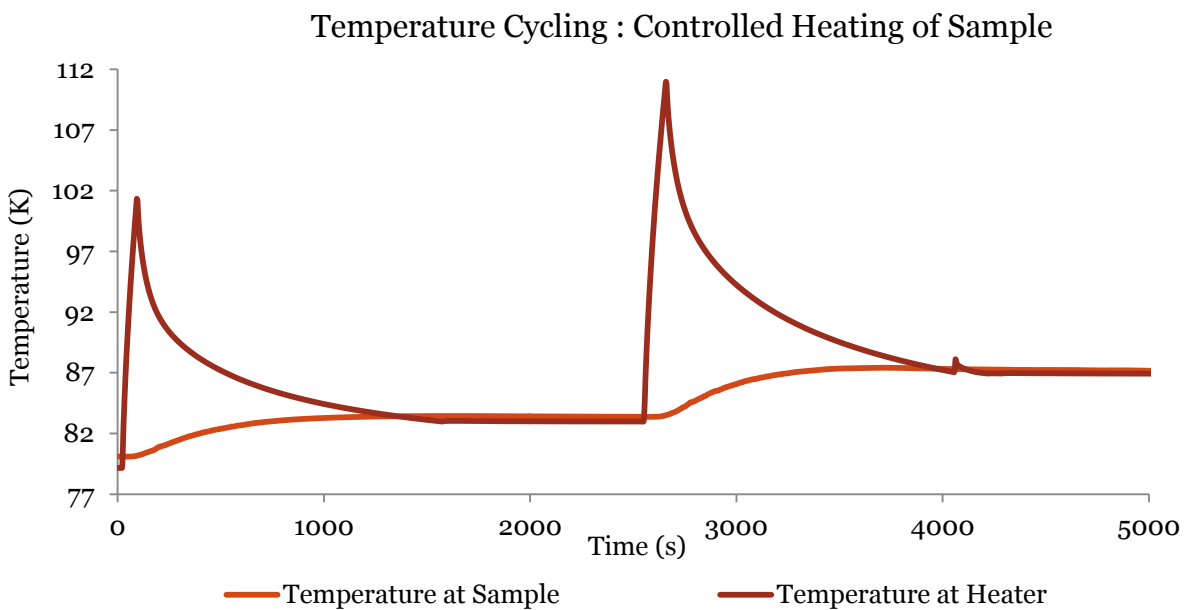
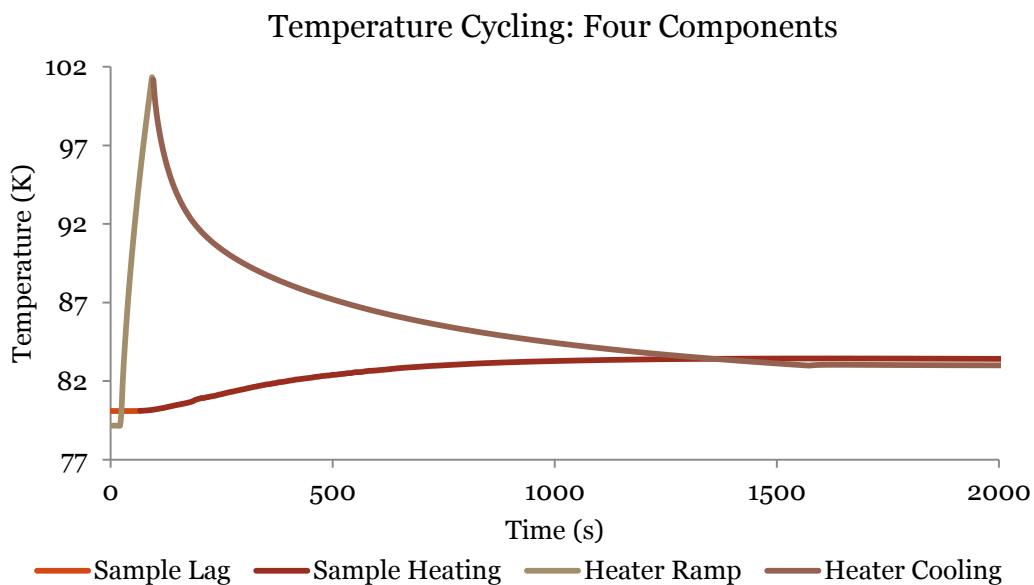


Figure 6.7: An example temperature profile of the controlled heating of the sample using the heater. The controlled cooling of the sample results in similar profiles. To minimize the time required to heat the sample, the heater is ramped and then turned off. The sample temperature continues to increase until thermal equilibrium is reestablished. Reduced heater output is then used to keep the sample at the heightened temperature.



Dependable thermal modulation of the cryostat requires controlled tuning of the internal heater, specifically in regards to heating powers and heating times. This requires that the heat transfer within the system be known. As can be seen in the previous figure, the cycling process can be broken into four distinct segments. These being, a function describing the ramp of the heater, a function describing the cooling at the heater, a function describing the increase in temperature at the sample, and lastly a description of the thermal and temporal lag between when the heater is turned on and when the sample temperature first starts to rise. For clarity, these four segments are explicitly displayed in the figure 6.8. The focus of this work has been on the determination of functions describing these four separate regions for the establishment of protocols to be used in automating the cycling process.



*Figure 6.8: The four segments of the temperature cycling curve that require modeling for predictive thermal regulation. The heater is first ramped to an increased temperature following the heater ramp segment. It is then completely turned off and the thermal energy allowed to disperse throughout the system. The loss of heat at the heater is observed as the heater cooling segment. The sample lag segment describes the temporal lag between the start of the heater ramp and the initial change in temperature at the sample. The sample heating segment reflects the increase of sample temperature to the predetermined set point value.*

## 6.9.2 Resistive Networks

When analyzing heat fluxes through multiple interfaces, conservation of energy dictates that the thermal gradients arising through a multi-layer system must possess energy balance. It then becomes instructive to model heat flows by analyzing the thermal resistivities encountered throughout the various layers and interfaces. By applying the concept of thermal resistance networks, the coupled thermal resistances of the multi-layer system can be calculated and the resultant heat fluxes can be determined.

As the resistances depend on material properties and the geometrical constraints of the medium under study, formulas for system specific resistance networks must be written. When the formulas are written, the system specific thermal conductivities and heat transfer coefficients must then be evaluated prior to use in the formulas. The values used must take into account the particular operational conditions of the system, such as the temperature ranges and fluid pressures in the system for which the heat transfer is being modeled. The values must not only reflect these conditions, but must also reflect the temperature varying properties of the materials making up the different layers.

Following is a depiction of the research Dewar that displays the interfaces providing thermal resistance to heat transfer. The actual schematic appears left. For clarity in regards to the various radial and length components that appear in the thermal resistive network at the positions of the sample sensor and the heater sensor, an expanded and simplified schematic appears to the right. The system consists of three concentric cylindrical layers of stainless steel, between which exist fluid layers of variable makeup. The sample sits within an exchange gas inside of the innermost

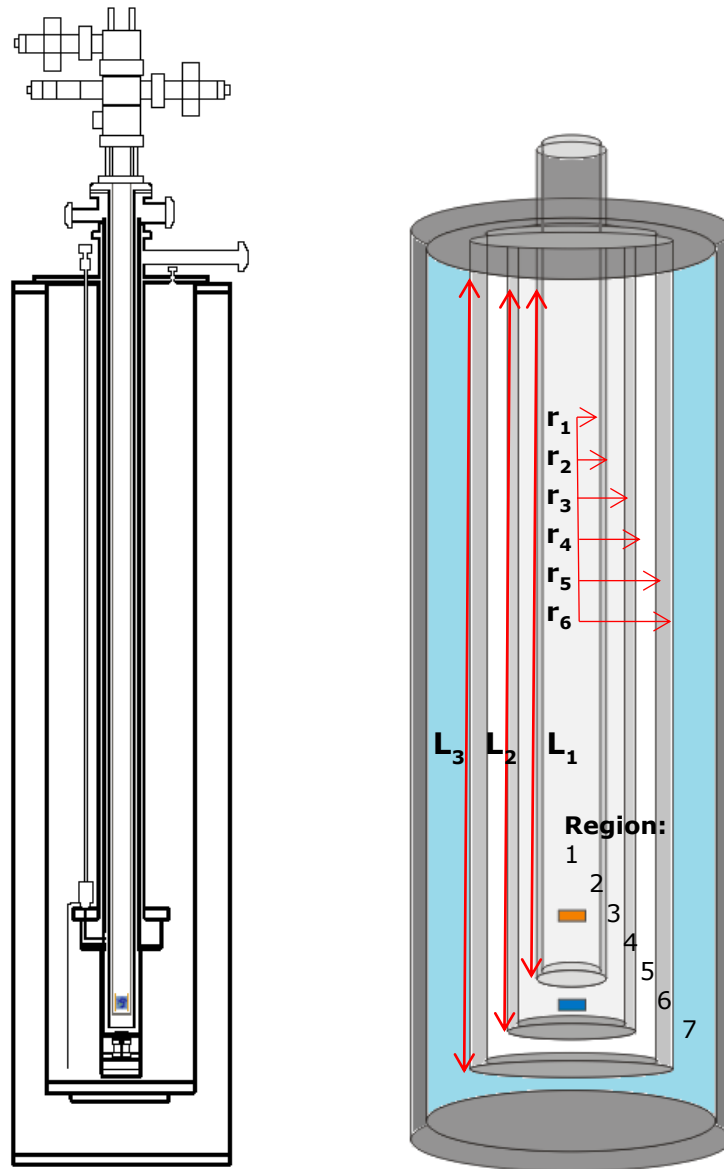


Figure 6.9: Left: CAD schematic of research Dewar. External components of the CTCSM are shown at the top of the diagram. Right: Various interfaces within Janis research Dewar providing thermal resistance to heat transfer. Orange and blue squares: positions of sample sensor and heater sensor/heater, respectively. Grey: stainless steel 304 walls. White: space for Air/Vacuum,  $N_2$ , or He gas. The lengths of the concentric cylinders are  $L_1$ ,  $L_2$ , and  $L_3$  with the inner and outer radii of the three cylinders represented by  $r_1$  through  $r_6$ . The outer vacuum jacket of the cryostat is not depicted in the simplified schematic appearing right. The actual quantities for the length and radial components are used for the analysis. Counting outwards, region 1 is annular volume at the sample; region 2 is the solid cylinder around region 1, etc. The liquid cryogen sits in region 7.

cylinder and is represented by the orange square. The position of the heater and heater sensor is shown as the blue square. Grey represents the cylindrical stainless steel 304 walls, and the white spaces are occupied by light vacuum, nitrogen or helium gas. Lastly, the light blue region is representative of the location of the cryogen reservoir, which is filled with either liquid nitrogen or liquid helium.

Many heat transfer relations were derived and equated for the analysis of this system. A complete description of all of the mathematical manipulations, formulas and equalities are not presented in the context of this document for brevity. Basic examples of the types of mathematical operations required during this investigation were, however, highlighted in the preliminary sections of this chapter. The results of this work and the equations that describe the thermal resistance through each of the cylindrical interfaces of this multi-layer system, at both the sample and at the heater are shown in the following networks.

In both networks,  $T_{inf}$  represents the temperature of liquid cryogen reservoir. In the first network,  $T_o$  represents the temperature at the position of the sample and in the second network,  $T_o$  is representative of the temperature at the position of the heater. In the first network, the differential between  $T_o$  and  $T_1$  is a convective term followed by a conductive term between  $T_1$  and  $T_2$ . The in-parallel terms that appear between temperatures  $T_2$  and  $T_3$  are a convective term on the top segment and a radiative term on the bottom segment. The terms in both the first and second networks follow a similar pattern for the remainder of the thermal pathway.

The resistive terms that appear for conduction and convection are similar to those found in equations 6.33 and 6.34. The resistive terms for radiation that appear in

the networks are a modification of equation 6.35. When  $T_s$  and  $T_{\text{surr}}$  are close, the approximation that they are effectively the same can be made. In this case,  $T_s$  and  $T_{\text{surr}}$  are replaced by a single temperature value,  $T_m$ . Substituting in  $T_m$  for both  $T_s$  and  $T_{\text{surr}}$  yields the reduced form of the cylindrical radiative thermal resistance.

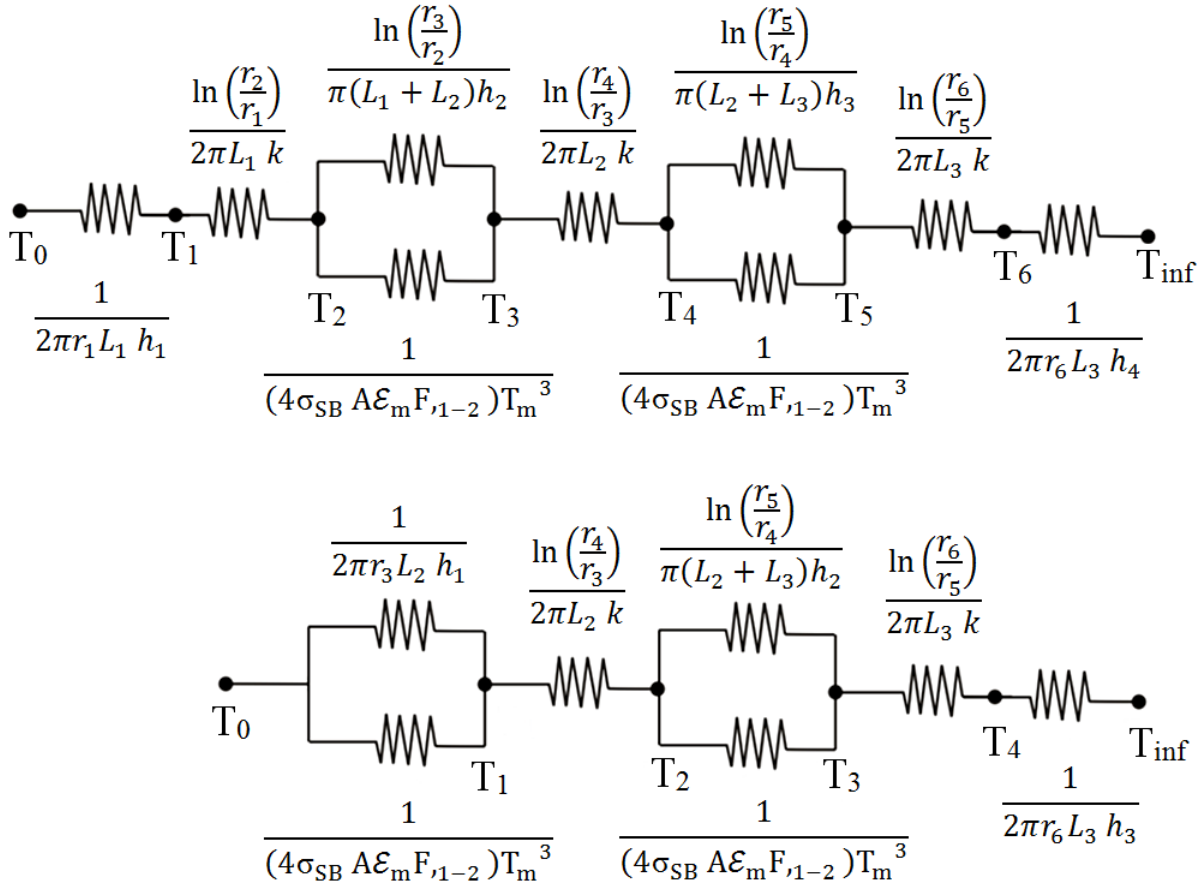


Figure 6.10: Thermal resistance networks for heat transfer occurring at the sample sensor (top) and the heater sensor (bottom) through the cylindrical interfaces within the research Dewar. Conductive, convective, and radiative resistances are displayed.

These relations are then used in conjunction with the equation for total heat transfer, where  $Q_{\text{Tot}}$  depends on the sum of the resistances shown in the above networks. The steady state solution for heat transfer in the system is calculated first and the various temperatures at each interfacial layer are found. The solution of the steady state

system, allows for the establishment of the boundary conditions necessary for the full solution to the transient heat flux differential. Solving the steady state equation of heat flows, requires a characterization of the thermal transfer properties of each component in the resistance network. Geometrical and material constraints for the system need to be classified for the specific temperature and pressure ranges within which experiments are conducted. For this particular system the thermal transfer properties of the resistance network needed to be characterized for the temperature range from 0 K to 300 K and fluids layers having pressures between 1  $\mu$ bar and 0.01 bar, which is equivalent to the range 0.1 pascal to 1000 pascal.

### **6.9.3 Thermal Conductivities**

The thermal conductivity  $k$ , of a material describes how effective the thermal energy transport process is across a medium. High  $k$  values signify efficient thermal transport. In this system, although  $k$  values are only used directly in calculating the resistances of the SUS 304 cylinders separating the gas spaces within the Dewar, they must also be established for the gas layers. This is due to the importance of the parameter in the evaluation of the gaseous heat transfer coefficients. Two methods for evaluating the values for the temperature dependant thermal conductivities of the SUS 304 layers to be used in the steady state calculation were looked at.

The first method used was application of a function developed by NIST, which was originally established based on the compilation of numerous experimentally collected data sets from various experimenters for different materials. The formulation

is an eighth order polynomial that has material specific coefficients and appears as follows [9].

$$\log k = -1.4087 + 1.3982 * \log(T) + 0.2543 * \log(T)^2 - 0.626 * \log(T)^3 + 0.2334 * \log(T)^4 + 0.4256 * \log(T)^5 - 0.4658 * \log(T)^6 + 0.165 * \log(T)^7 + -0.0199 * \log(T)^8 \quad (6.36)$$

The second method evaluated for determining the temperature dependant thermal conductivity was by the calculation of the low temperature electrical resistivity of the SUS 304 using the linear approximation, and then an application of the Wiedemann-Franz law. The linear approximation for electrical resistivity relates the resistivity of the material at any temperature  $\rho_r(T)$ , to the electrical resistivity of the material at a given reference temperature,  $\rho_{r0}$ . The units of resistivity are  $\Omega \cdot m$ . The scalar  $\alpha_r$ , is the temperature coefficient of resistivity at the given reference temperature. The expression for electrical resistivity is viewed as fairly accurate as long as the temperature T, does not deviate significantly from the reference temperature  $T_0$ . To impart as much accuracy to the linear approximation as possible, different reference temperatures and their corresponding  $\alpha_r$  values for SUS 304 were used over the investigated range. The same protocol, of using the most closely correlated values for the many other literature quantities required for inclusion into the various formulations during the investigation, was implemented whenever possible.

$$\rho_r (T) = \rho_{r0} [1 + \alpha_r (T - T_0)] \quad (6.37)$$

With the temperature dependent electrical resistivity found, the Wiedemann-Franz law was then used to determine the thermal conductivity. The Wiedemann-Franz law is a scaled temperature dependent ratio of the thermal conductivity k, to the electrical

conductivity  $\sigma$ ,  $(\Omega \cdot \text{m})^{-1}$ , of a metal. The constant of proportionality that relates the conductivity ratio to the temperature  $T$ , in Kelvin is the Lorentz number  $L_z$ , and has a value of  $2.44 \times 10^{-8} \text{ W} \cdot \Omega \cdot \text{K}^{-2}$ . There is an inverse relationship between conductivity and resistivity, therefore  $\sigma = 1/\rho_r(T)$ . The standard form of the Wiedemann-Franz follows.

$$\left(\frac{k}{\sigma}\right) = L_z T \quad (6.38)$$

The temperature varying thermal conductivity as determined by each method appears below. When performing the steady state and transient analysis for the heat transfer in the research Dewar, it was revealed that the NIST method for approximating the low temperature  $k$  values provided models that more closely reflected the experimentally obtained data. Therefore, there were the values used when specifying the thermal transfer characteristics of this system [5].

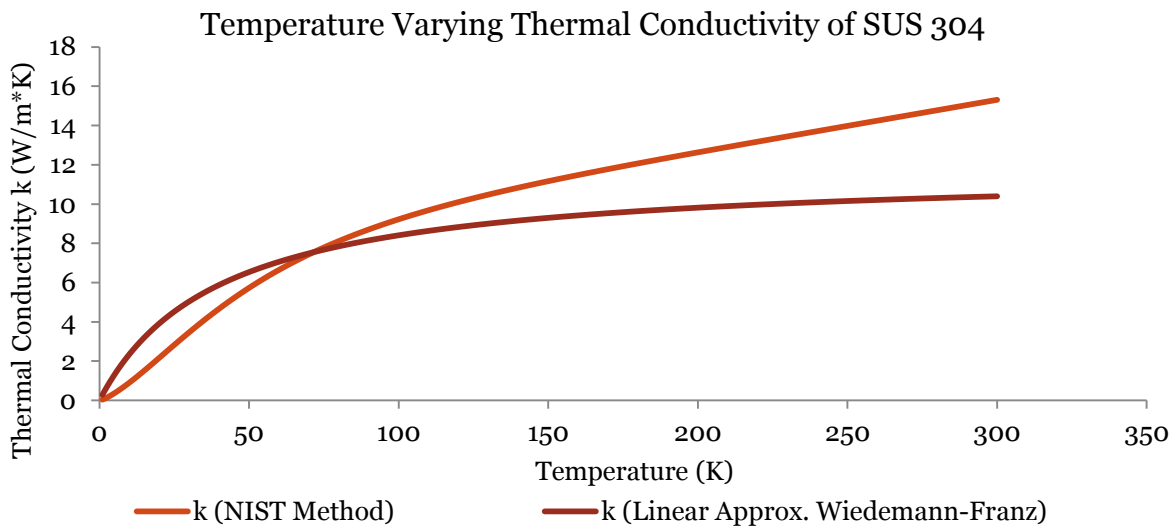


Figure 6.11: Temperature varying thermal conductivities of the SUS304 cylinders as determined by the NIST method as well as by application of the linear approximation for electrical resistivity used in conjunction with the Wiedemann-Franz law. It was found that the values as calculated by the NIST method yielded fits that more closely reflected experimentally obtained heating and cooling curves in this system.



The thermal conductivities for the various gaseous layers next needed to be evaluated. For gases existing at pressures below 0.10 the critical gas pressure, gas behavior is approximated as ideal behavior. As we operate at pressures at or below 0.01 bar = 1000 Pa when helium or nitrogen occupy these layers, and at most  $1.0 \times 10^{-4}$  bar = 0.1 Pa when low vacuum is used, this condition is certainly met. Therefore, the thermal conductivities for these gases were calculated under ideal conditions. By the use of Sutherland's viscosity law, a relationship between the actual dynamic viscosity and the absolute temperature of an ideal gas is found. The dynamic gas viscosity at any temperature T is  $\mu_v(T)$ , in units of kg/s·m. This value is related to the reference dynamic gas viscosity  $\mu_{v,ref}$ , of the particular gas as it exists at a specific reference temperature  $T_{ref}$ . The Sutherland constant S, is specific to the gaseous material being evaluated and exists in units of K.

$$\mu_v(T) = \mu_{v,ref} \left( \frac{T}{T_{ref}} \right)^{\frac{3}{2}} \left( \frac{T_{ref} + S}{T + S} \right) \quad (6.39)$$

The mean free path, which is the average distance a gas molecule travels between collisions with another gas molecule, is then calculated for the different gases used in this system. Here, l is the mean free path in m,  $k_b$  is Boltzmann's constant, P is the pressure of the gas in Pa, and D is the diameter of the gas molecule in question, modeled as hard sphere in m. As usual, the temperature T is in units of K.

$$l = \frac{k_b T}{\pi \sqrt{2} P D^2} \quad (6.40)$$

To take into account the internal degrees of freedom of polyatomic molecules, the Eucken correction for gas thermal conductivity is used. This expression yields the

necessary  $k$  values that are eventually used when calculating the heat transfer coefficients for the gaseous layers in the research Dewar.

$$k = \left( \frac{9\gamma - 5}{8} \right) \rho_p C_v \tilde{v} l \quad (6.41)$$

The Eucken correction relates the non-dimensional specific heat ratio  $\gamma = C_p/C_v$ , the ideal gas pressure  $\rho_p$ , in mol/m<sup>3</sup>, the specific heat at constant volume  $C_v$  in J/kg·K, the mean molecular velocity of the gas  $\tilde{v}$ , in m/s, and the mean free path, to the temperature dependent thermal conductivity. The relationship between the dynamic gas viscosity and the mean molecular velocity of the gas is as follows.

$$\mu_v(T) = \left( \frac{1}{2} \right) \rho_p \tilde{v} l \quad (6.42)$$

The thermal conductivities that were calculated for this system at experimental pressures, using the above expressions appear below. The literature values for the gas thermal conductivities at 1 atm are also displayed [8, 13, 15].

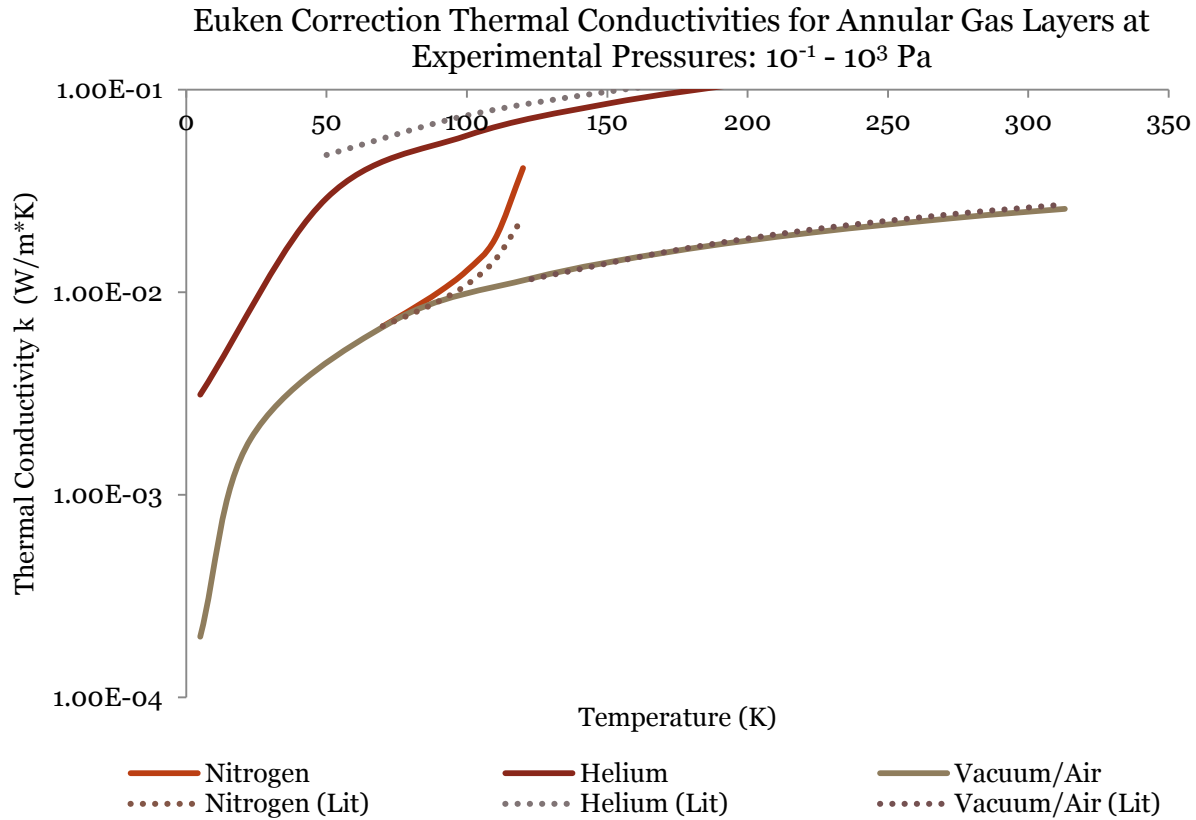


Figure 6.12: The calculated Eucken correction thermal conductivities for the annular layers for the various gaseous species at experimental pressures  $10^{-1} - 10^3$  Pa. The literature values for these species at 1 atm are included for comparison.

### 6.9.4 Heat Transfer Coefficients

The heat transfer coefficient is a constant of proportionality that indicates the diffusion of thermal energy across the boundary layer occurring along a solid and fluid interface. Before a determination of  $h$  is possible, however, an appropriate description of the forces dictating the fluids condition at the interface is a necessity to the modeling the resultant heat flux. To evaluate the particular characteristics of the fluid properties within the system, the various dimensionless numbers highlighted in section 6.4 must be calculated. Of specific interest are the Prandtl, Reynolds and Rayleigh numbers. For

this study, these values were determined for liquid helium and liquid nitrogen as well as gaseous helium, gaseous nitrogen and low vacuum or low pressure air. With these system specific values in hand, an understanding of the forces acting in the fluid layers can be known. Additionally, these values then guide which form of the Nusselt equation can be used for the actual determination of the heat transfer coefficients.

The Prandtl number relates the diffusion rate of momentum of the fluid to the diffusion rate of thermal energy in the fluid. Values of the Prandtl number that are lower than one, indicate a higher convection ability of the fluid and values in excess of one, indicate better conductive ability. It was found that for this system, when the cryogen reservoir contained liquid helium, Prandtl values fell between 0.49 and 0.81, with values falling between 1.74 and 2.74 for liquid nitrogen. The Prandtl numbers were then calculated for the annular spaces containing the different gasses. Each annular space, due to its different geometry, yields different values but the overall results across all layers fell within the following bounds over the entire investigated temperature range. Prandtl values for nitrogen were between 0.711 and 2.09 with the transition from the low to high regime occurring at a temperature 90 K. Helium gas had values between 0.663 and 0.667, and when low vacuum was used to occupy the annular spaces, values were found to be between 0.708 and 0.830.

The Reynolds number defines the type of flow in a fluid. Based upon the calculated Reynolds Numbers, displayed in table 6.1, Laminar flow dominates within the gaseous regions in the research Dewar.

System Specific Reynolds Numbers For Individual Fluids:				Laminar Flow Regime		Re < 5 x 10 <sup>5</sup>	
				Turbulent Flow Regime		Re > 5 x 10 <sup>5</sup>	
<b>Liquids:</b>		<b>Gases:</b>					
<b>Nitrogen</b>		<b>Nitrogen</b>		<b>Vacuum/Air</b>			
T (K)	Re (none)	T (K)	Re (none)	T (K)	Re (none)	T (K)	Re (none)
70	1.17 x 10 <sup>9</sup>	80	0.6888	2.3	1438.292	90	65.3186
77	1.59 x 10 <sup>9</sup>	90	0.6444	2.4	1379.585	100	61.7179
<b>Helium</b>		100	0.6088	2.6	1275.718	110	58.7718
T (K)	Re (none)	110	0.5797	2.8	1186.689	120	56.3168
2.3	7.27 x 10 <sup>9</sup>	120	0.5554	3	1109.53	123	55.6581
2.4	6.98 x 10 <sup>9</sup>	<b>Helium</b>		3.5	955.2131	150	50.9157
2.6	6.76 x 10 <sup>9</sup>	T (K)	Re (none)	4	839.4754	173	48.0434
2.8	6.72 x 10 <sup>9</sup>	50	1.83 x 10 <sup>9</sup>	4.2	800.8961	200	45.5146
3	6.76 x 10 <sup>9</sup>	100	2.0619	5	677.4426	223	43.8434
3.5	7.05 x 10 <sup>9</sup>	150	1.5388	23	170.2094	250	42.2739
4	7.56 x 10 <sup>9</sup>	200	1.4709	50	94.1244	273	41.1818
4.2	7.70 x 10 <sup>9</sup>	250	1.4109	70	75.6064	293	40.3716
		300	1.367	73	73.7038	300	40.1135
				77	71.3977	313	39.6648
				80	69.8195	350	38.5703

Table 6.1: Calculated Reynolds numbers for different fluids that could be present within the research Dewar. Fluids that possess turbulent flow characteristics are displayed in light blue and those that possess laminar flow appear in dark blue.

The Rayleigh number is again both system geometry and fluid dependant and describes the relationship between buoyancy and viscous forces acting on a fluid in a flow. Rayleigh numbers above  $1.0 \times 10^4$  indicate that heat transfer occurs primarily by conduction, with lower values pointing towards convection. Rayleigh numbers calculated for the cryogen reservoir indicate that convection dominates when either liquid nitrogen or liquid helium is used as the cryogen. Interestingly, regardless of

annular space, it was found that for the gasses, nitrogen, helium, or low vacuum, Rayleigh values indicate that conductive heat flows primarily dominate regardless of system temperature.

For this investigation, it was found that the Prandtl and the Reynolds numbers were fairly constant throughout the system for each fluid. The calculated Reynolds numbers, as displayed above, indicate that free Laminar flow dominates within the gaseous regions in the research Dewar. This result determines which basic form of the Nusselt equation is to be used in evaluation of heat transfer coefficients. Based on the calculated Prandtl and Rayleigh numbers for this particular system, the precise form of the Nusselt equation to be used for heat transfer analysis could be determined. The equation used to calculate the Nusselt number is the Churchill-Chu result, which is an extension of the Squire-Eckert approximation. The Squire-Eckert approximation is used when Laminar conditions exist in the boundary layer. The Churchill-Chu result is used in local heat transfer from a vertical isothermal wall with laminar natural convection for cylindrical geometries and accounts for real experimental data. This result can be used for all values of the Prandtl number and when Rayleigh numbers for the system are between the orders of  $10^{-1}$  to  $10^{12}$ . This formulation of the Nusselt number uses directly, the calculated values for the Rayleigh and Prandtl numbers.

$$Nu_L = 0.68 + 0.67 * \left( (Ra_L)^{\frac{1}{4}} \right) \left[ 1 + \left( \frac{0.492}{Pr} \right)^{\frac{9}{16}} \right]^{-\left( \frac{4}{9} \right)} \quad (6.43)$$

The temperature dependent Nusselt numbers which were obtained by the use of this result as well as the values for the thermal conductivities for the fluids obtained

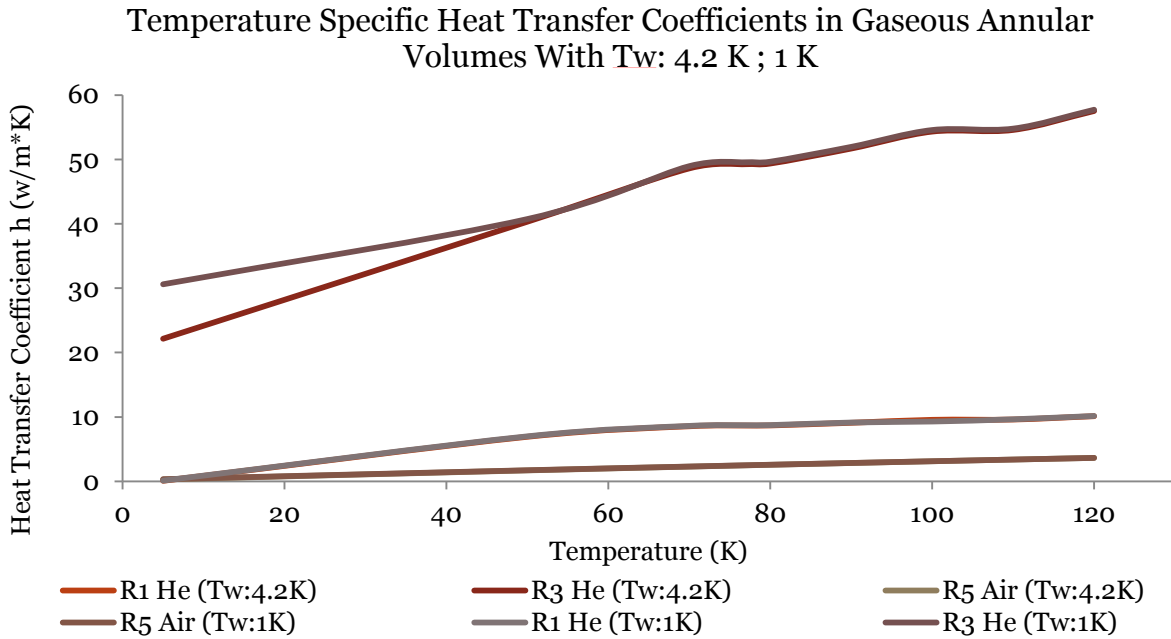
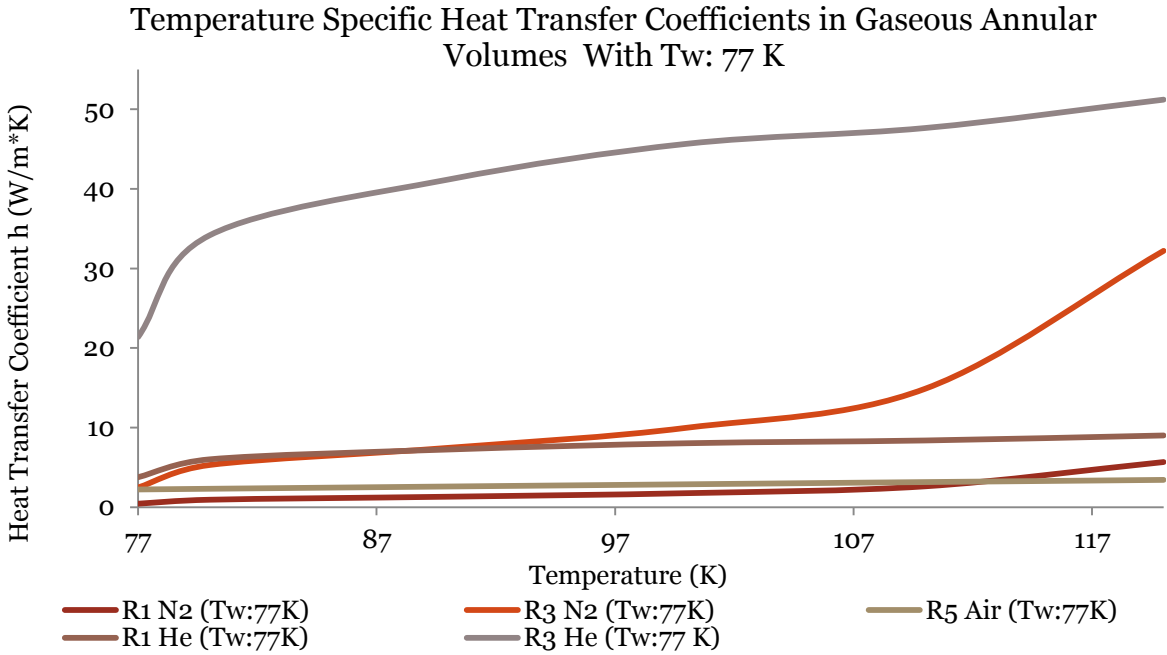


Figure 6.13: Top: Temperature specific heat transfer coefficient for each gas when liquid nitrogen is the cryogen and the wall temperature is 77 K. Bottom: same but liquid helium cryogen at 4.2 K or at 1 K.

through equation 6.41 were inserted into equation 6.12 for the evaluation of the heat transfer coefficients. The results that appear below display the heat transfer coefficient for each gas in each different annular region with the liquid cryogen being either liquid nitrogen or liquid helium [4, 5, 13]. Refer to description of figure 6.9 for regions.

### **6.9.5 Steady State Solutions**

With the classification of the temperature dependent thermal conductivities and heat transfer coefficients of the annular layers within the research Dewar, the solutions for steady state heat transfer in the system were calculated. The steady state solutions reveal the temperatures existing at the surface of each thermal transfer interface, as well as the temperature drop through each layer. These quantities establish the initial boundary conditions necessary for evaluation of the complete transient heat transfer differential equation. This was first performed for the situation where an exchange gas of nitrogen is used and the liquid cryogen is also nitrogen. The temperature profiles were first calculated using a fixed thermal conductivity value across all of the thermal interfaces. This was performed using thermal conductivity and heat transfer coefficients for the system at the temperatures 70, 77, 80, 90, 100, 110, and 120 K. Values over this range were chosen because the total thermal differential between the cryogen reservoir and the sample fell within the range of those bounds. Observing the temperature gradients developing across the layers using the fixed thermal conductivities, the thermal conductivity was allowed to fluctuate across each layer to reflect the temperature of the layer. Using this variable approach more accurately reflects the heat



transfer properties of the system during the heat transfer process. The result of the variable calculation appears in dark blue in the following plot. Observe the minimization of thermal fluctuation through the layers when this approach is taken. A completely legitimate classification requires the determination of thermal conductivities and heat transfer coefficients at all possible temperatures existing within the specified range [4, 5, 13, 15].

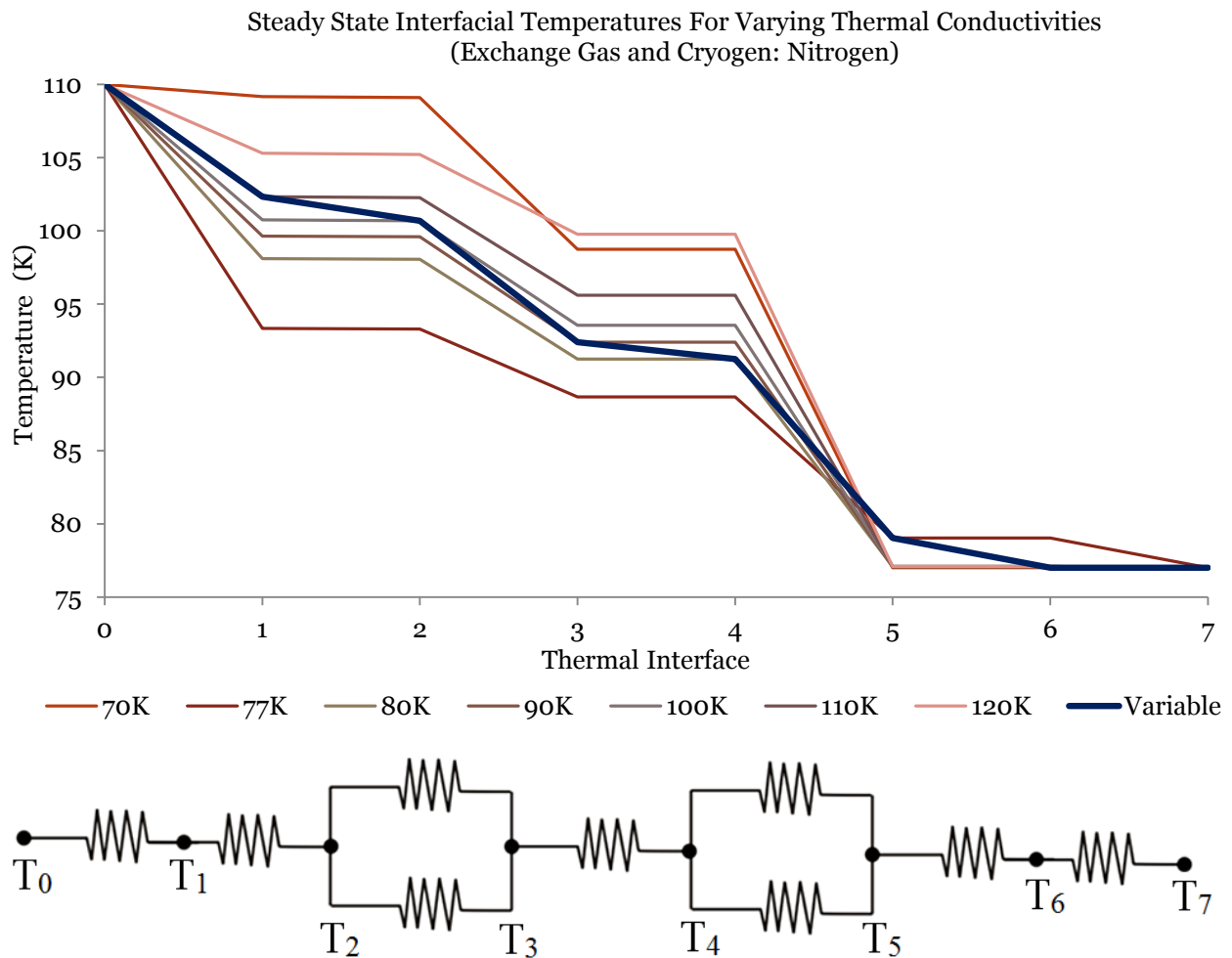


Figure 6.14: Top: Temperature profile of thermal gradients existing at and across each interface within the Janis research Dewar. Temperature profiles were calculated using fixed thermal conductivities across all of the thermal interfaces at the seven specified temperatures. The dark blue trace represents the thermal gradients across all thermal interfaces when a variable, temperature dependent thermal conductivity was used for calculation. Bottom: Thermal resistance network for above temperature profile.

In order to model the other possible situations that could be encountered in operation of the research Dewar, the process was performed using two additional exchange gas and cryogen combinations. These being the situation of an exchange gas of helium used with liquid cryogen nitrogen, and an exchange gas of helium used with liquid cryogen helium. The results of the similar analysis appear below. The values of

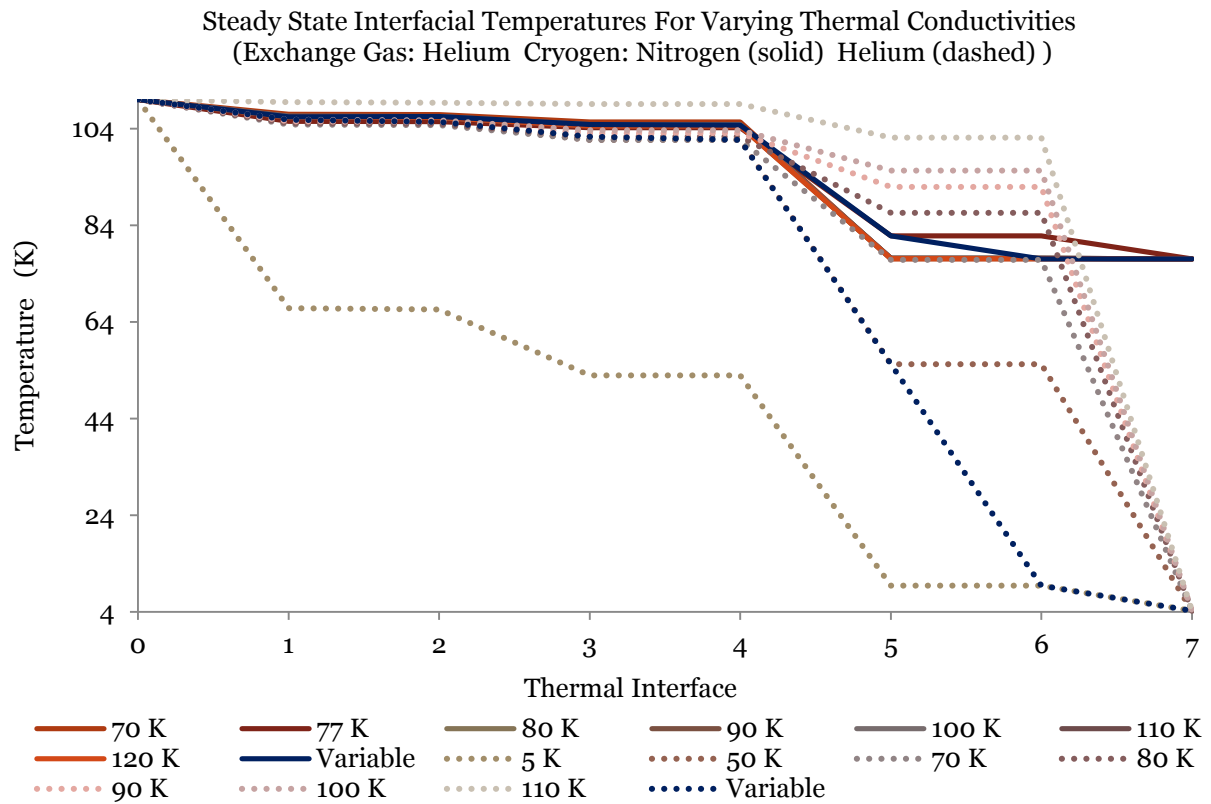


Figure 6.15: Temperature profile of thermal gradients existing at and across each interface within the Janis research Dewar. Solid line represents exchange gas helium and cryogen liquid nitrogen. Dotted line represents exchange gas helium and cryogen liquid helium. Temperature profiles were calculated using fixed thermal conductivities across all of the thermal interfaces at the seven specified temperatures. The dark blue traces represent the thermal gradients across all thermal interfaces when a variable, temperature dependent thermal conductivity was used for calculation.

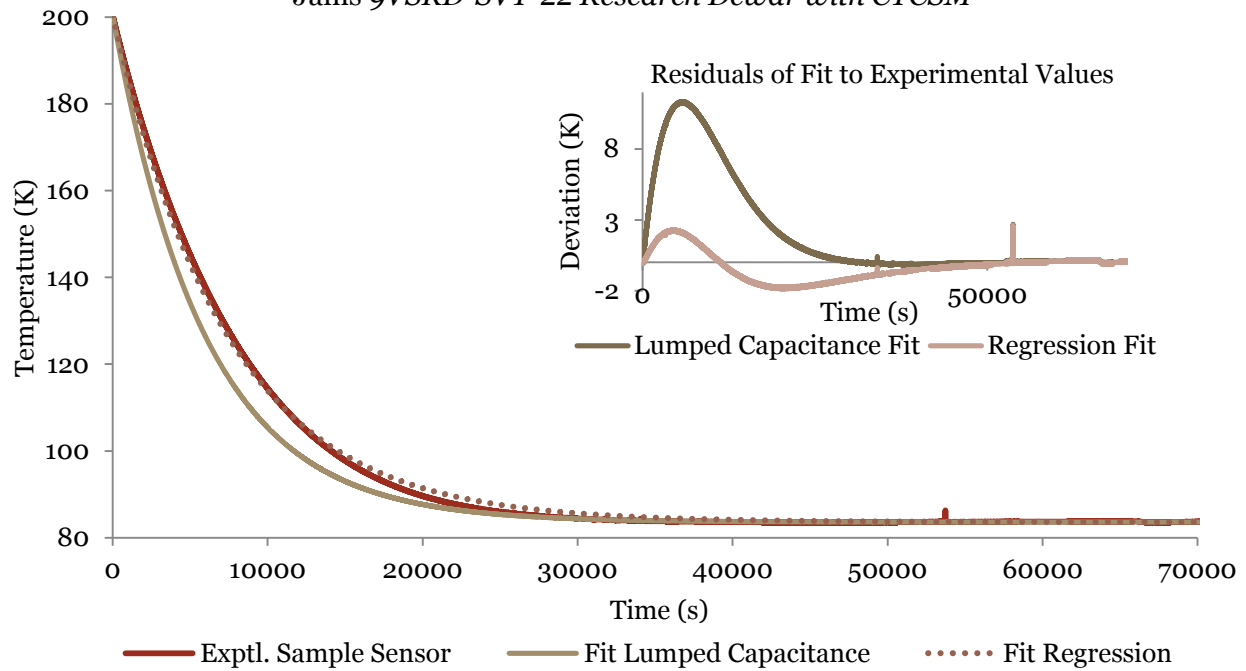
thermal conductivities and heat transfer coefficients used reflected a pertinent temperature range for the particular calculations. Although not displayed, the thermal resistance network remains the same as in the previous figure. Again, the dark blue trace is representative of using variable quantities.

### **6.9.6 Transient Approximation: Lumped Capacitance**

During a transient process, the rate of thermal transfer  $\dot{Q}$  is allowed to vary in relation to both temperature and position within a system over the course of thermal exchange. This is the behavior of heat transfer in real systems. An approximation to the complete transient formalism was made whereby thermal gradients within media, in this case within each individual annular volume, are assumed homogeneous and only temperatures at the multi-layer interfaces are accounted for. Each layer is viewed as a lumped system. This simplification is a possibility when the individual layers Biot number is  $< 0.1$ . For this investigation the Biot number was calculated for all gasses and all layers over the standard range of operating pressures. Biot numbers were found to satisfy this condition in all regions. During this analysis, the additional assumptions made were that only the heat transfer processes in the radial direction were accounted for, and the assumption of adiabatic behavior at the ends of the cylindrical volumes which were defined to be resistant to heat loss and heat transfer through the plane defining the cylindrical ends.

The results of this lumped analysis appear next. All resistances encountered by the three heat transfer mechanisms through all layers are taken into account as derived

**Sample Position Cooling Behavior**  
**Janis 9VSRD-SVT-22 Research Dewar with CTCSM**



**Temperature At Sample Sensor:**

**Lumped Capacitance Fit**

General model:

$$f(x) = 116.9 \cdot \exp(-0.0001679 \cdot x) + c$$

Coefficients (with 95% confidence bounds):

$$c = 85.67 \text{ (85.63, 85.72)}$$

Goodness of fit:

SSE: 2.958e+05

R-square: 0.9789

Adjusted R-square: 0.9789

RMSE: 3.555

**Regression Fit**

General model:

$$f(x) = 116.9 \cdot \exp(-b \cdot x) + 83.6$$

Coefficients (with 95% confidence bounds):

$$b = 0.0001352 \text{ (0.0001351, 0.0001353)}$$

Goodness of fit:

SSE: 2.547e+04

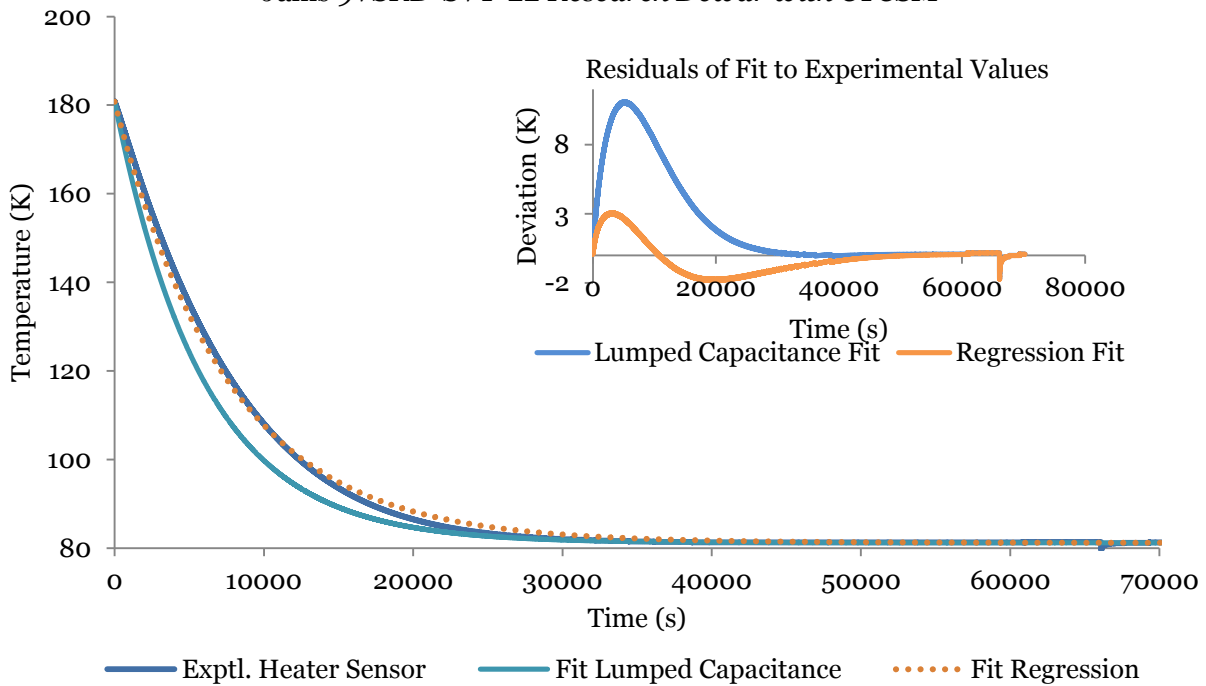
R-square: 0.9982

Adjusted R-square: 0.9982

RMSE: 1.043

Figure 6.16: Top: Cooling behavior at the position of the **sample** within the Janis 9VSRD-SVT-22 research Dewar containing the CTCSM. Fits to the cooling curve are modeled using the lumped capacitance transient approximation and using a standard regression approach. Top Right: Plot of residuals of fitting approaches to experimentally obtained results. Below: Fitting models used for the above fitted cooling curve and the goodness of fit parameters. Lumped capacitance uses a system determined (equation 6.23) fixed exponential term and a variable constant term. The regression approach uses a variable exponential term and a fixed constant term.

**Heater Position Cooling Behavior**  
*Janis 9VSRD-SVT-22 Research Dewar with CTCSM*



<b>Temperature At Heater Sensor:</b>	
<p><b>Lumped Capacitance Fit</b></p> <p>General model:  <math>f(x) = 99.6 * \exp(-0.0000972 * x) + c</math></p> <p>Coefficients (with 95% confidence bounds):  <math>c = 77.16 (77.11, 77.21)</math></p> <p>Goodness of fit:                      SSE: 3.572e+05                      R-square: 0.9663                      Adjusted R-square: 0.9663                      RMSE: 3.906</p>	<p><b>Regression Fit</b></p> <p>General model:  <math>f(x) = 99.6 * \exp(-b * x) + 81.3</math></p> <p>Coefficients (with 95% confidence bounds):  <math>b = 0.0001323 (0.0001322, 0.0001325)</math></p> <p>Goodness of fit:                      SSE: 3.205e+04                      R-square: 0.997                      Adjusted R-square: 0.997                      RMSE: 1.17</p>

Figure 6.17: Top: Cooling behavior at the position of the **heater** within the Janis 9VSRD-SVT-22 research Dewar containing the CTCSM. Fits to the cooling curve are modeled using the lumped capacitance transient approximation and using a standard regression approach. Top Right: Plot of residuals of fitting approaches to experimentally obtained results. Below: Fitting models used for the above fitted cooling curve and the goodness of fit parameters. Lumped capacitance uses a system determined (equation 6.23) fixed exponential term and a variable constant term. The regression approach uses a variable exponential term and a fixed constant term.

in the resistive networks diagramed in figure 6.10. Analysis was performed at the position of the sample figure 6.16, and at the heater figure 6.17, in the cryostat. The theoretically calculated lumped capacitance solutions in addition to standard least squares regression fits appear, along with the actual experimentally obtained cooling curves. A plot that shows the residuals of the fits and the fitting statistics for this analysis are also displayed below the displayed plots.

The cooling of the cryostat, as monitored at both the heater sensor as well as at the sample sensor, has been found to mostly follow the formulated lumped capacitance Newton-Richman relation, however, additional efforts are required to more accurately model the cooling behavior, as residuals between measured temperatures and fits occur at the base of the curves. These residuals are clearly observed in the adjoining residual plots to the fit. Despite this, the currently presented results are promising as the fitting statistics are of good quality. Removing the assumptions made, as stated above, in this analysis and fully accounting for the complete transient processes occurring in the system would undoubtedly shed light on the functional relation describing this heating and cooling occurrence.

### **6.9.7 Heater Ramp**

To characterize the ramp of the heater, temperature cycling trials without specific sample were carried out. The heater was ramped using differing heater powers and heater ranges. The heater settings are more fully described in section 6.9.9. Ramps were performed in a stepped fashion from low to high temperature out of order over the

course of many days. This was done to introduce randomness and to determine if different quantities of liquid cryogen contained within the reservoir play a noticeable role on the required ramp. Several different starting and ending temperature values were selected to test the consistence of the ramp of the heating element for introduction of thermal energy into the system. Next is an example of five separate ramping trials.

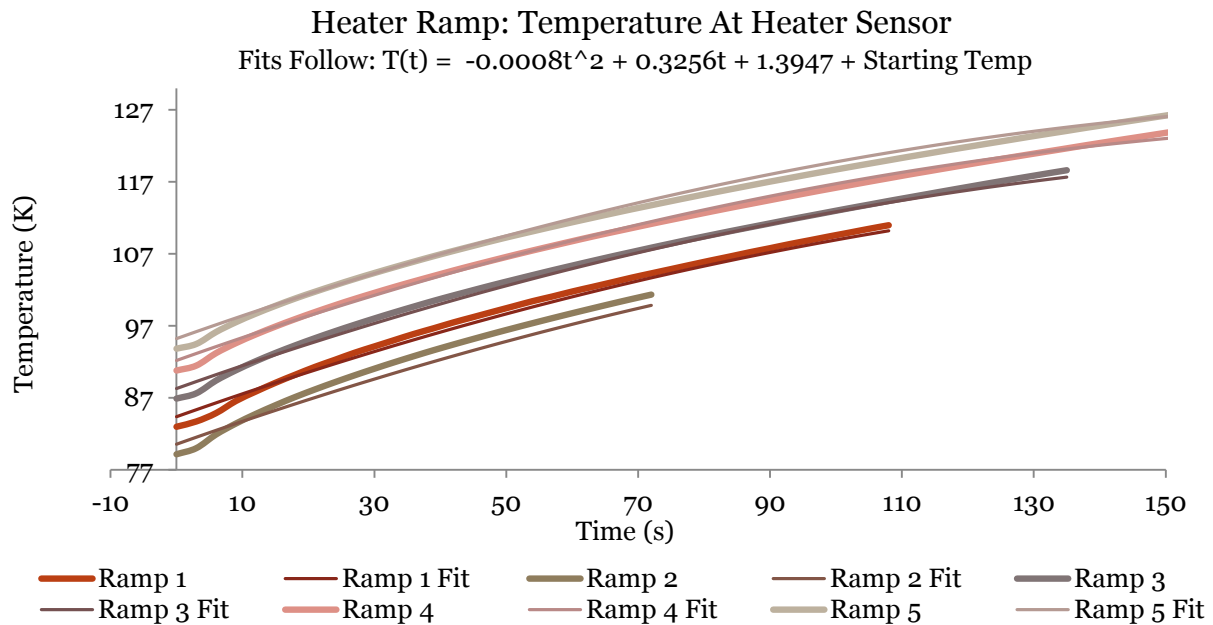


Figure 6.18: Five separate ramping cycles of the heater, and the temperature response as recorded at the heater sensor. Included polynomial fits. Ramping appears to follow the curve:  $T(t) = -0.0008t^2 + 0.3256t + 1.3947 + \text{Starting Temp}$ . This polynomial accurately predicts ramp characteristics for the range  $T = 80 \text{ K}$  to  $T = 150 \text{ K}$ .

It was found that the heater ramp basically follows the curve described by  $T(t) = -0.0008t^2 + 0.3256t + 1.3947 + T_0$ , with  $T_0$  being the temperature at the beginning of the ramp. This polynomial model was shown to be repeatable and appears to be accurate for the temperature range 80 K to 150 K. Additional work towards the accurate

modeling of ramping curves is still necessary in order to explain heating behavior over the entire thermal range of 0 K to 300 K.

### **6.9.8 Sample Lag**

As the sample stage is not located directly atop the heating element within the cryostat a temporal lag exists between the time the heater is first ramped and the time the sample begins to feel an effect. A parameterization of the thermal and temporal lag between the two is therefore of necessity if heat transfer between the heater and the sample is to be modeled, and is especially important if the heating of the sample is to become an automated process. Again numerous trials were conducted and an example plot of thermal lag at the sample is shown in figure 6.19. Time delays were determined by calculating the moving three-point slope across the different sample heating traces. To negate random thermal fluctuation, the start of a heating response at the sample was taken to be true when the slope of the sample temperature possessed a value of zero slope followed only by continuous positive slope. It was found that the time delay from the start of a heater ramp to the start of the thermal response detected at the sample is an average of 30 seconds, and generally falls within a range of 24-36 seconds. This delay appears consistent and is not temperature dependent over the range investigated.



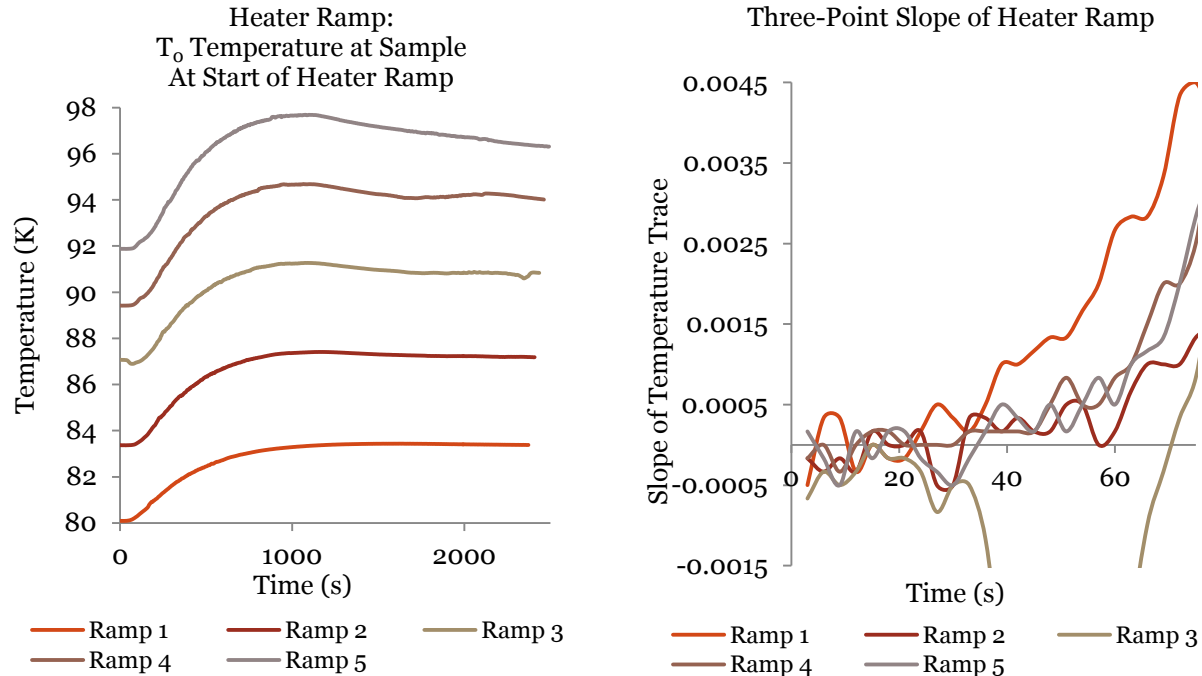


Figure 6.19: Left: Five separate heating response curves of the temperature at the sample in relation to a ramp of the heater. Right: Change in slope of the (left), temperature vs. time trace at the sample in relation to an induced heating by a ramp of the heater. A zero slope followed by continuous positive slope is indicative of initial sample heating and defines the thermal lag times. Lag times: Ramp 1, 24 s; Ramp 2, 33 s; Ramp 3, 72 s; Ramp 4, 15 s; Ramp 5, 36 s. Based on trials, temporal lag for initial heating of sample vs. start of heater ramp is approximately 36 s.

### 6.9.9 PID Parameters

To utilize the feedback control features of the Lakeshore 331 temperature controller, it was necessary to manually attain the appropriate PID values and heater output powers to be used for different temperature ranges. The heater output powers were first tested. The heater power can be set to three different ranges, low, medium, or high power. Within each range the user can set the percentage of the range to be used, zero to 100%. The low and medium ranges were tested from zero to 100%, at 25% increments. The high range was tested at only the 25% increment, as it was found to be

of excessive power. The maximum achievable temperature for each setting and time to reach the temperature was determined for each setting. It was found that in the liquid nitrogen range, the high temperature range most quickly allowed for thermal changes at the sample. In the liquid helium range, it was found that the medium range provided for the best results. A plot that displays the results of these trials performed in the liquid nitrogen range appears in Appendix E.

The PID values were then manually determined for the entire range of the cryostat. The process for establishing these values is described in the box “Proper Determination of PID Values” on the front panel of the temperature cycling program. This program is discussed along with a screenshot of the front panel in section 3.3.3. The actual process is iterative in nature with the formulas providing starting approximations for the values. At each temperature set point, the values are tested and modified until correct quantities are found that facilitate the quick attainment of the temperature set point. In the liquid helium range PID values were found at 2-3 degree intervals from 5 K to 35 K, and in 5 degree intervals from 40 K to 70 K. In the liquid nitrogen range, 77 K to 300 K, PID values were found at 5 degree intervals. A table that specifies all appropriate PID values and the corresponding heater output range allowing for precise temperature control appears in Appendix E.

## **6.10 Future**

The desired outcome of this study was the complete automation of this process whereby the user simply specified the new sample temperature and the rest was taken care of. At

this point, heat flows within the system have been most basically modeled and the building blocks for full programmatic control are known. So far, functions describing the sample and heater cooling, the heater ramping, the sample temporal lag, the interfacial temperature dependent boundary values, and the heater control and PID parameters have been determined. Best control will come only with modeling of the full transient solution. An approximation to the complete transient formalism using lumped capacitance was performed.

The results of the lumped capacitance approximation for the heat flows based purely on theoretical calculation, do match within reasonable limits to experimentally collected temperature profiles and are close to those fitted with a regression approach. The next step involves using the determined steady state parameters as boundary conditions and solving the non-homogeneous fifth and seventh order differential equations representing heat flows at both the heater sensor and sample sensors respectively. Since solutions to these higher order equations will be of the form of summed exponentials, it is no doubt that residuals to experimental curves will be at a minimum. Solving the complete solution to the 3D transient heat transfer of the system, including internal heat generation, should help accurately model both the heater ramping and sample heating curves. Effective fitting will allow for the quick cycling of the temperature at the sample based on applied heater powers by the heater, which is removed from the sample by multiple layers.

## References:

- 1.) Barron, Randall F. Cryogenic Heat Transfer. Ann Arbor: Taylor & Francis, 1999. 41-76. Print.
- 2.) Bell, Kenneth J. "Heat Transfer." Albright's Chemical Engineering Handbook. Boca Raton: CRC Press, 2009. 479-566. Print.
- 3.) Cengel, Yunus A. Heat Transfer: A Practical Approach. McGraw Hill Professional, 2003. Web.
- 4.) Donnelly. R. J., Barenghi. C. F. (1998). "The Observed Properties of Liquid Helium at the Saturated Vapor Pressure." *Journal of Physical and Chemical Reference Data* 27, 1217-1274. Print.
- 5.) Haynes, William M. CRC Handbook of Chemistry and Physics. 90th ed. Boca Raton: CRC Press, 2009. Print.
- 6.) Jain, Prashant K., Singh, Suneet., Uddin, Rizwan. (2009). "Analytical Solution to Transient Asymmetric Heat Conduction in a Multilayer Annulus," *Journal of Heat Transfer* 131, 011304-1-011307-7.
- 7.) Leeson, Daan Thorn., Wiersma, Douwe A., Fritsch, Klaus., Friedrich, Josef. (1997). "The Energy Landscape of Myoglobin: An Optical Study," *Journal of Physical Chemistry B* 101(33), 6331-6340.
- 8.) Leinhard IV, John H, and John H. Leinhard V. A Heat Transfer Textbook. Cambridge: Phlogiston Press, 2012. Web.
- 9.) Marquardt, E.D., Le, J.P., Radebaugh, Ray. (2000). "Cryogenic Material Properties Database", presented at 11th International Cryocooler Conference, Keystone, Co. June 20-22, 2000.
- 10.) Newton, Isaac. (1701). "Scala graduum Caloris. Calorum Descriptiones & Signa (Scale of the Degrees of Heat)." *Philosophical Transactions* 22(270), 824-829, English Translation in: Newton, Isaac. (1809) *Philosophical Transactions of the Royal Society of London, Abridged*, 4, 572-575.
- 11.) Ozisik, M. Necati. Heat Transfer. New York: Wiley-Interscience Publication, 1993. Print.
- 12.) Patankar, Suhas V. Numerical Heat Transfer and Fluid Flow. Washington: Hemisphere Publishing Corporation, 1980. Print.
- 13.) United States. WADD technical Report. Wright-Patterson Air Force Base, Ohio: 1960. Section 2 and Section 8. Report No.:60-56.
- 14.) [www.bnl.gov/magnets/staff/gupta/cryogenic-data-handbook/Section2.pdf](http://www.bnl.gov/magnets/staff/gupta/cryogenic-data-handbook/Section2.pdf)
- 15.) [www.engineeringtoolbox.com/air-properties-d\\_156.html](http://www.engineeringtoolbox.com/air-properties-d_156.html)

## II

### Chapter 7

# **Engineering a Solution for the Application of High Voltage Electric Fields: Sample Cells, Feedthroughs, Spectral Holes**

## **7.1 Introduction**

The experimental aspect of this investigation rests on the implementation of two spectroscopic techniques that when used in conjunction yield the necessary data required for determination of the internal molecular electric fields that are present at the site of a probe fluorophore. The two techniques being utilized are spectral hole-burning and Stark spectroscopy. In the simplest architecture, this requires an experimental condition where an electric field can be applied to a sample at an axis normal to the axis of propagation of the excitation light. The additional requirements existing in this investigation are that the electric field applied must be of high voltage (in excess of approximately 2000 V) and that the sample and electrodes must be housed within a minimal volume, which can be placed into a cryostat. A minimization of the quantity of sample required for an experimental trial is also of necessity.

The following is a description of the various sample cells fulfilling the stated stipulations that were designed, developed and tested for this study. Various issues concerning the application of high voltages to the sample, modifications made to the

electrical pathway and experimental setup, and the design of a high voltage feedthrough are described. The resultant spectral and Stark data acquired with each sample cell configuration along with the benefits and drawbacks of each are presented and discussed. The process that was devised for the successful and reproducible burning of spectral holes with this particular experimental setup is also highlighted.

## **7.2 Sample Cell Design**

The successful design and fabrication of a sample cell suited for use within the CTCSM, with the capabilities of both housing the sample in such a way as to allow interaction with the excitation light while allowing for the application of an externally applied electric field, was a task that took several design attempts. Originally, a preliminary design that was fabricated out of microscope slides cut to shape and bonded using Norland Optical Adhesive (NOA 61) featuring copper tape electrodes had been tried. The benefits of this design were the relatively low cost and ease of construction, with materials that are readily available in most chemistry departments and hardware stores. In practice, however, it was found that the design suffered from leakage, copper tape bonding, and electrical connection issues, and was thus infeasible. It was decided that a new and more rigorous approach was necessary, and that having the cell fabricated using either a milling or a 3D printing process would yield best results. This was the path taken for the first iteration of sample cells that would be used during Stark investigations.

The considerations taken into account during the development of the design were that the sample cell must be small enough to be situated at the base of CTCSM, allow for top illumination and collection, possess a small sample volume, have small separation between the electrodes to yield high electric fields for a given applied voltage, and provide some form of insulation of the field from the Attocube piezo actuators upon which the sample cell would be placed during experiments. Additionally, the electrodes needed to be made of a material that was thick enough to be used in high voltage applications and maintain its planar integrity during repeated thermal cycling.

The first iteration of sample cells consisted of three different variations to a single basic cell design. The SolidWorks platform was used to draft the three cell variations. The designs differed in distance between the parallel plate electrodes, and the number of samples that could be held at a single time within the sample cell. Many fabricators were contacted and different materials reviewed. Cost, speed of production and material specific electrical, thermal, and mechanical properties were of top priority. Eventually, it was found that based on stated priority, the designs would be 3D printed at the Milwaukee School of Engineering, MSOE Rapid Prototyping Center. Although many construction materials are offered, the material best suited for this experimental application was DuraForm PA Plastic. DuraForm PA has high tensile strength (43MPa) and low coefficient of thermal expansion ( $82.6 \mu\text{m}/\text{m}\cdot\text{C}$ ) important for low temperature environments, a low moisture absorption (0.07%) good for low sample absorption, a fairly low dielectric constant (2.73) good for shielding from the Attocube piezo positioners at the base of the CTCSM, and a high dielectric strength (17.3 KV/mm)

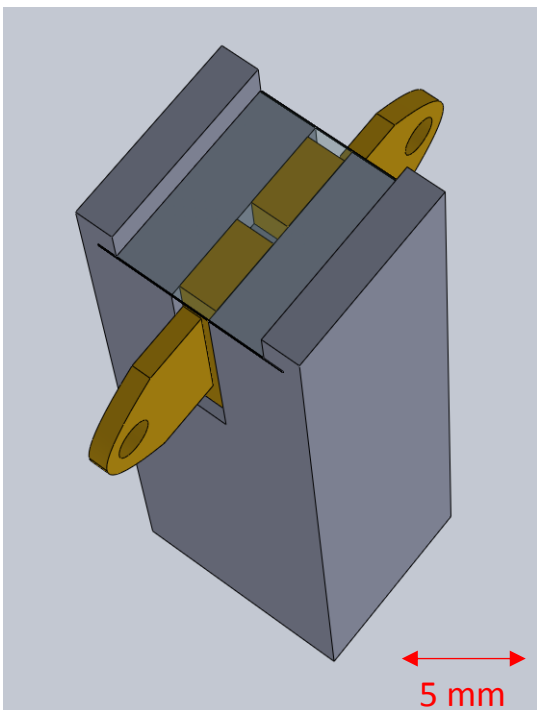
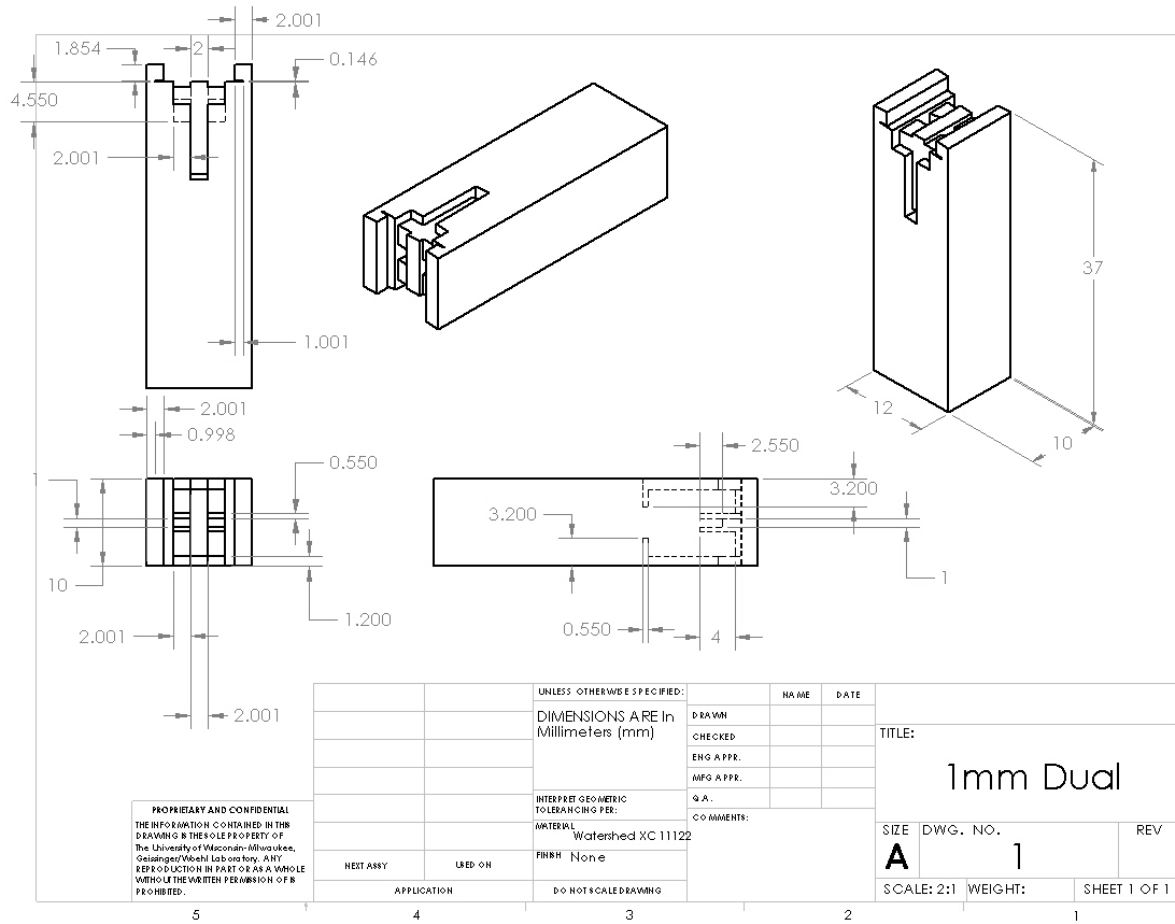


Figure 7.1: Above: SolidWorks CAD design of the 1mm dual channel sample cell. Diagram has units of mm. This variation has two channels, allowing for two samples to be held simultaneously. The electrode spacing is 1mm. DuraForm PA is the material used to 3D print these pieces. Left: Depiction of the 1mm single channel design variation. Copper electrodes clip into the 3D printed pieces. Sample sits in recess between electrodes. Coverglass slides into the top of the sample cell to keep the sample in place between the electrodes and isolated from the CTCSM objective.



important when applying high voltages to the sample. Additionally, the material has a fast rate of outgassing, a necessity when placing the sample in vacuum.

The electrodes, which were eventually clipped into the 3D printed DuraForm PA pieces, were handmade and fashioned out of 22 mil 99.9% pure copper alloy that was procured from the company Basic Copper. The 22 mil copper was chosen for its thickness and in turn robustness, necessary to withstand the repeated cooling cycles down to liquid helium temperatures while strictly maintaining its shape. The high electrical and thermal conductivity of copper provides for an excellent electrode material, while also allowing the sample to quickly thermally equilibrate with the surroundings as the electrodes are in direct contact with the sample.

A set of six sample cells, two of each of the three design variations were constructed. Variation 1 holds a single sample and has electrode spacing of 2mm, variation 2 holds a single sample with electrode spacing of 1mm, and variation 3 holds two samples with electrode spacing of 1mm. The small separation of electrodes allows for the efficient application of high electric fields to the sample under study. Electrodes are attached to special high voltage leads at base of CTCSSM using stainless steel screws and handmade copper washers. All of the cells were tested under high voltage conditions and were observed to capably produce high voltage electric fields across the sample between the parallel electrodes.

### **7.3 High Voltage**

To apply the high voltage to the electrodes at the sample, located at the base of the CTCSSM housed within our Janis research Dewar, several considerations were of

necessity. When the microscope is placed within the research Dewar, it is housed in a variable temperature insert tube that is an independent insert into the helium reservoir. The insert tube must be either under vacuum or contain an appropriate exchange gas upon insertion into the Dewar. For this task, to allow transmittance of an electric signal across this vacuum sealed barrier, a NW25 vacuum feed through flange equipped with an external MHV connector capable of transmitting high voltage signal was acquired from Nor-Cal Products and installed. Of major importance was selecting the appropriate leads to carry the voltage to the sample. It was found that leads made of a

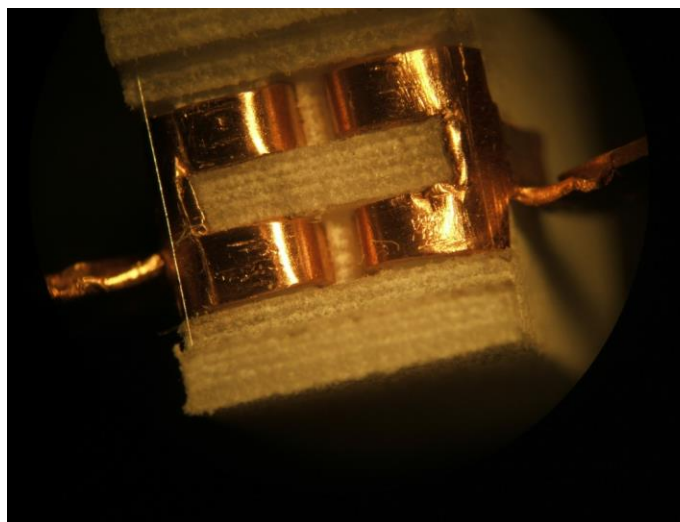


*Figure 7.2: Left: Sample cell attached at the base of the optical insert of the CTCSM. The low dielectric properties of the DuraForm PA provide for insulation between the high voltage at the electrodes and the piezo positioners upon which the sample cell sits just below the CTCSM objective. The electrical connections consist of the Kapton insulated voltage carrying lead at the far electrode, and the semi-rigid grounding connection (thick copper wire) which provides for additional positional stability of the affixed sample cell at the front electrode. Right: Close-up of dual channel sample cell with 1 mm electrode spacing. Cover glass is placed atop sample and slides into sample cell. The edge of the cover glass can be seen on the left side of the image.*

26 AWG stainless steel, stranded Kapton insulated high voltage wire, #100726, obtained from Accu-Glass Products, were best suited for the task. The stainless steel cable provides for good high voltage electrical conduction with low thermal conduction. The Kapton insulation is specifically made for high voltage, low temperature conditions, with a high outgassing rate, perfect for high vacuum applications. The flange and high voltage cable were mechanically affixed and then soldered using a solder comprising of a silver content greater than 5%.

Two different high voltage power supplies, a Stanford Research Systems PS325 capable of providing up to 2.5 kV or a Bertan 225-20R capable of providing up to 20 kV have been successfully tested and are available for use with our system. The Bertan has been modified to include the appropriate MHV connections allowing for the seamless switching between power supplies during an experiment if and when desired. Based on experimental findings, either can be used to supply voltages large enough to observe at least moderate splitting of spectral profiles.

## **7.4 Spectral Hole-Burning**

The burning of spectral holes is a balancing act between laser intensity and time. During the read cycles, the excitation beam must possess an intensity high enough to excite the sample to the extent that the collected spectra possess high signal to noise characteristics, yet low enough such that the repeated scanning of the spectrum does not overly photobleach the sample. The laser must be scanned during the read cycles at a rate slow enough for spectral hole profiles to be traced out with sufficient numbers of data points, yet fast enough to again minimize any afterburning effects. A discussion

regarding the selection of appropriate laser scan rates to achieve resolutions necessary for spectral hole profiles to be detected and not passed over appears in chapter 5.2.

During the burning process, an appropriate balance must be struck between the laser intensity and the burning time. These parameters must be tuned such that enough energy is deposited to the sample to cause a sufficient population of the molecules to undergo the photobleaching process, resulting in the creation of a narrow spectral hole of sufficient depth, without greatly oversaturating the sample such that a broadened hole shape results. Lastly, the intensities of the burn and read cycles must be chosen such that an appropriate intensity ratio between the two cycles can be achieved.

With the proper scan rates for the reading cycle already determined for this experimental setup, the remaining characterization of the hole-burning process requiring focus was the establishment of appropriate burn times and intensities that deliver the proper energy to a sample to yield deep and narrow hole profiles. Upon review of the literature [1, 2, 4-6, 8-10, 12] ratios of burn to read intensities fell in the range of 100 to 10,000 and burn times were reported between 10 seconds to several minutes. As these values are highly system (experimental setup and sample) dependent and ranges are broad, little information was known when first setting these parameters. As with all other aspects of this experimental process, a systematic approach was taken whereby a burn/read ratio was chosen and then a complete set of burn times attempted. Burn times ranged initially from 1 to 30 minutes, specifically: 1, 2, 5, 8, 10, 15, 20, 30 and ratios: 100, 200, 400, 1000, 2000, 6000, 10,000. These studies were carried out over a few different experimentation periods across several weeks. With little success, burning time frames under a minute were attempted. The first hole profiles obtained

appeared as only slight dips in intensity appearing at the burn frequency between the pre-burn and post-burn profiles. To determine if actual hole-burning occurred, a difference spectrum between the pre-burn and post-burn trace was calculated. A fitting of the difference spectrum with a Lorentzian revealed a moderate correlation to the expected hole shape and enough affirmation to claim that hole-burning had actually occurred with our system. Although all profiles from these sets of experiments were of unusable quality, it was determined that during future experiments burn times that were shorter than one minute would need to be investigated further. Additional modifications to the burning times and necessary filter combinations for attenuation of both the burning and reading intensities has led to many successful hole-burning trials. It was found that for the best results, the ratio of burning to reading intensity should fall between 30 and 1000, and the burn times should be in the range of 6 to 20 seconds. Between 18 and 40  $\mu\text{W}$  of intensity are required at the excitation arm of the CTCSM for the burning and reading of the spectral signal to be a possibility. Utilizing these experimental parameters, the process of hole-burning is completely repeatable with some necessary adjustments within the stated range to be determined at the onset of each experimentation period. Although microscope alignment takes considerable effort and can occasionally still pose problems to experimentation, the results are always of good quality when appropriate alignment and focus on the sample is achieved. As is always the case, alterations to the procedure that lead to the minimization of spectral noise should be looked into further.

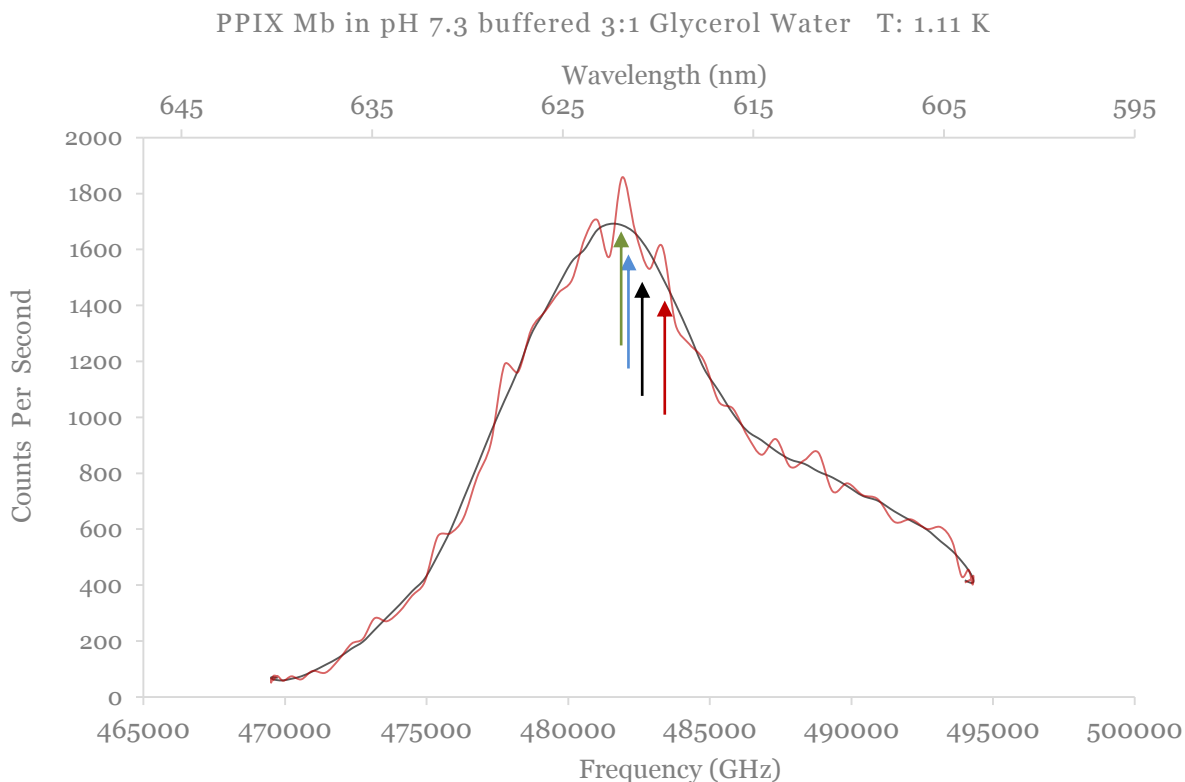
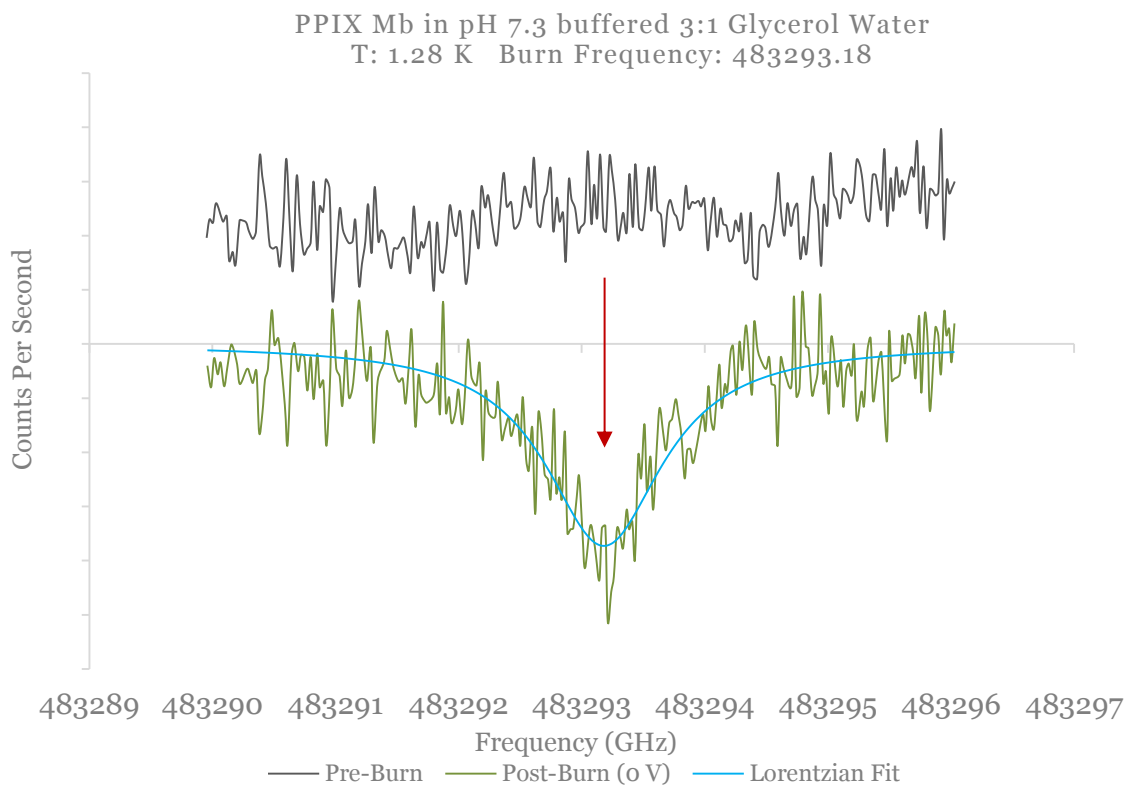


*Figure 7.3: Above: Qx band of PPIX in myoglobin at 1.11 K. The raw spectral data appears in red and a Savitzky-Golay smoothed trace of the data appears in grey. Colored arrows indicate the burning positions within the band for the representative hole profiles that follow. Red arrow figure 7.4; blue arrow figure 7.9; green arrow figure 7.12; black arrow figure 7.14.*

An example of the full Qx band of PPIX-Mb taken with the CTCSSM within the Janis research Dewar is shown in figure 7.3. Both the temperature dependence of the fluorescence excitation spectrum, as well as and the temperature dependence of the peak wavelength of the Qx transition of the PPIX-Mb sample, are displayed in Appendix A. In figure 7.3, the arrows indicate the positions in the band of the spectral holes that follow. All of the displayed hole profiles are of raw data with no smoothing filters employed. The tunable frequency ring dye laser that is used during these studies, has a laser line width of 87-150 kHz, at a resolution of 1 kHz. Some beam walk during the burning process does occur. The beam walk is always recorded for each burning process,

and is generally on the order of a few of MHz. The following profiles are representative of spectral holes taken in the CTCSM.



General model: Lorentzian Fit	<b>(0 V)</b>	483293.18	Goodness of fit:
$f(x) = I \cdot \frac{P1^2}{((x-P2)^2 + P1^2)}$			SSE: 4.748e+04 R-square: 0.9178 Adjusted R-square: 0.917 RMSE: 15.18
Coefficients (with 95% confidence bounds):			
I (Intensity)	= 186.4 (179.3, 193.4)		
P1 (HWHM)	= 0.58 (-0.612, -0.548)		
P2 (Peak)	= 4.833e+05 (4.833e+05, 4.833e+05)		

Figure 7.4: Shown above is a representative spectral hole, burnt into the Qx transition of PPIX-Mb. Arrow indicates position of burn. This spectral hole has a FWHM of 0.00148 nm = 1.16 GHz, and a relative depth of 47%. Fitting parameters along with fit statistics reveal good correlation to Lorentzian profile, and successful spectral hole-burning.

## 7.5 Problems with High Voltage Field

The typical experimental design utilized when conducting spectral hole-burning is one which features a bath cryostat for cooling the sample to temperatures where spectral holes can be burnt. In this type of design, the sample and high voltage carrying electrodes are immersed within the liquid cryogen, being in most practical applications liquid helium. Because the dielectric strength of the liquid phase far outweighs that of the gas [7], much higher voltage ranges can be applied to the liquid phase compared to the gaseous phase prior to dielectric breakdown. In this particular experimental setup, the sample and electrodes are removed from the liquid cryogen and sit at the base of the CTCSM within helium exchange gas. When Stark investigations began in helium

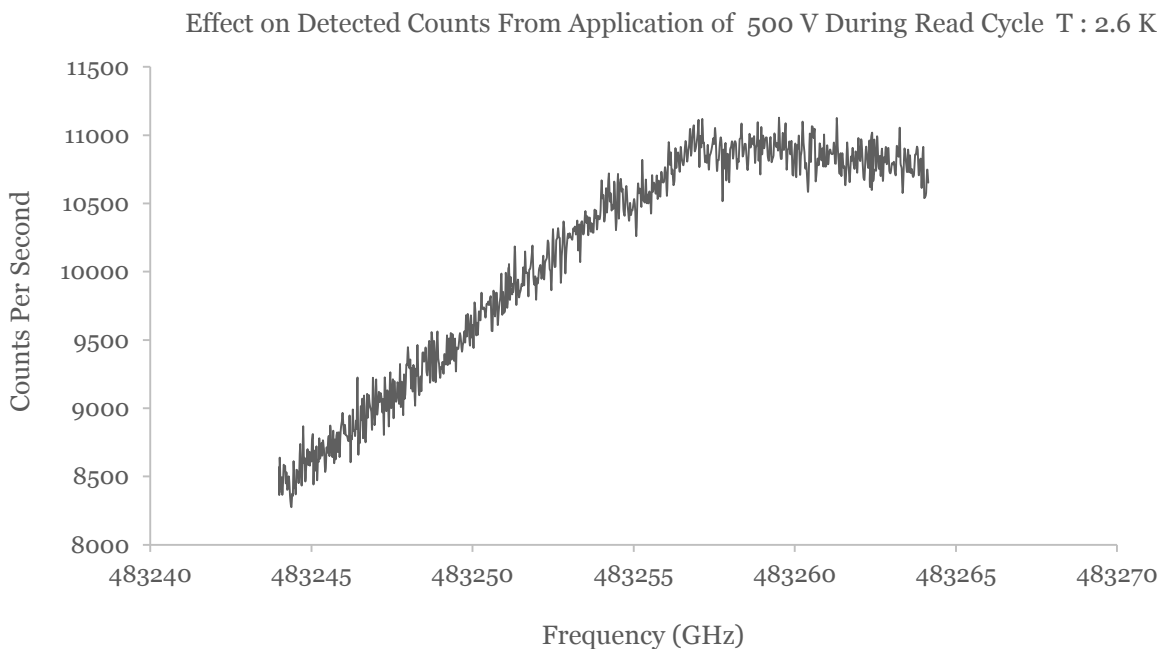


Figure 7. 5: Spectral trace observed during re-scan of a spectral hole burnt into the Qx band of a PPIX-Mb sample upon application of 500 V. Prior to voltage application, the counts were in the range of 4000 cps.



exchange gas at low temperature, it was found that upon application of relatively modest voltage ranges, 300-500 V/mm, the collected signal from the APD's displayed severe electrical noise. Figure 7.5 is a resulting spectral trace that was obtained when 500 V was applied to a sample of PPIX-Mb at low temperature.

When this type of response was not observed, increasing the voltage at the sample would cause the power supply to trip. The trip is indicative of some form of conductive pathway between the electrodes, and would most likely indicate an electric breakdown of the sample, of the exchange gas, or of some other connection in the electrical pathway. Based on the recorded spectra, it was thought that either there was some direct electrical connection or leak between the high voltage electrodes and the APD's, or that the signal being recorded was the exchange gas experiencing breakdown and emitting light, which was then detected. This was unfortunately a hurdle that was unforeseen until encountered, as voltages in excess of 4500 V/mm were attainable when the system was initially tested in an air atmosphere at 298 K. Steps thus needed to be taken to address the electrical issues if voltages were to be applied within the range necessary for successfully observing splitting of spectral hole profiles.

### **7.5.1 Cabling**

To determine if the electric breakdown was caused by a short occurring in the electrical pathway from the high voltage power supply to the electrodes at the sample, all components were disconnected and the reattached piecewise rebuilding the pathway. Upon the addition of each element back to the pathway, the maximum attainable

voltage prior to either breakdown or an upper limit of 4900 V, was established prior to reincorporation of the next piece in the pathway. These trials were performed in air of humidity 44-48 % at 298 K. Using this systematic approach, it was found that there was a negligible decrease in breakdown voltage, 4200 V, at the vacuum flange HV wire connection within the microscope. To prevent the possibility of electric field buildup at corners and sharp edges, this connection was re-soldered and sanded as were the electrodes at the sample cell. Kapton tape was then used for wrapping the exposed surfaces along the conduction path within the microscope, particularly at the electrodes and the exposed connection at the HV wire, vacuum flange connection. The shielding on HV wire was inspected for damage but none was found. During these tests it became apparent that trip conditions were minimized when the voltage was ramped at a few hundred volts per minute. Furthermore, to reduce the possibility of stray electrical noise from interacting with the APD's and the SR400 two channel gated photon counter, all connection BNC cables were shielded with tinned copper braid. While these methods seemed to limit the effects of runaway observed in the spectrum above, still only minimal voltages, 300-500 V, were achievable in helium atmosphere at cryogenic temperatures.

### **7.5.2 Sample Electrode Contact**

Sample-electrode interactions were next considered as the probable source of breakdown. In the initial design of the sample holder, the sample sits in direct contact with the copper electrodes. This is beneficial as there are no additional dielectric layers

between the sample and electrodes that need to be accounted for, however, since direct contact can enhance the occurrence of electrolysis this needed to be studied further. A series of tests were performed at room temperature in atmospheres of air and helium at ambient as well as reduced pressures to discover the source of the breakdown.

During optical investigations, the PPIX-Mb is placed at relatively low concentrations,  $10^{-4}$ - $10^{-5}$  mol/L, in a 3:1 (volume: volume) glycerol:water matrix. To determine if the breakdown was matrix or sample related, voltage tests were performed on pure glycerol, 3:1 glycerol:water, as well as PPIX-Mb in 3:1 glycerol:water. It was found that there was a small reduction in the maximum voltage that could be applied prior to breakdown with the introduction of pure glycerol or 3:1 glycerol:water to the sample cell, however, a substantial reduction in maximum voltage was observed when actual sample containing the PPIX-Mb was introduced. Although these same effects

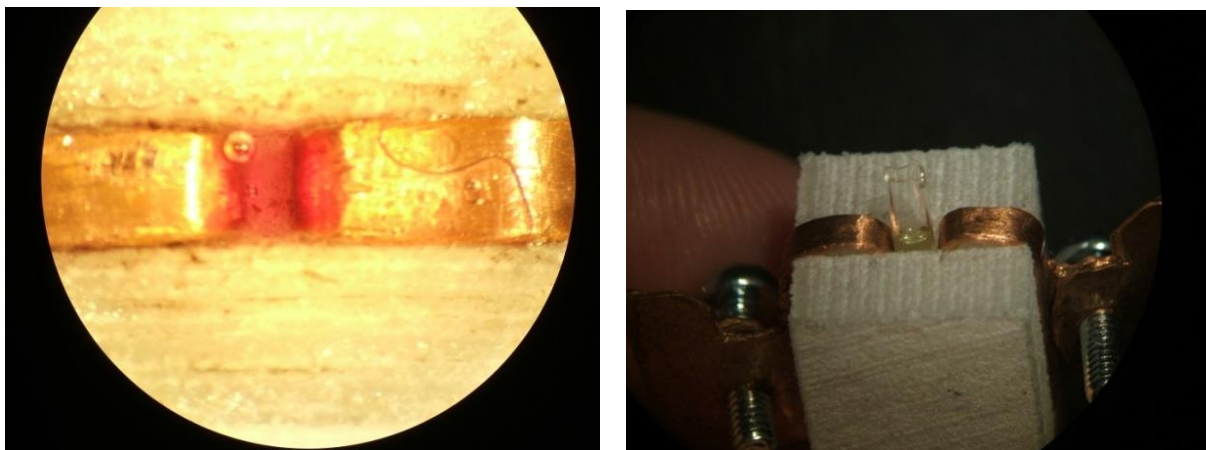


*Figure 7.6: Left: Original sample holder design. Sample rests in 1mm x 1mm x 1.5 mm channel in direct contact with copper electrodes. Right: Sample holder with electrode spacing of 2mm, sample in 1.5 mm OD KIMAX capillary, isolated from electrode contact. Image shows “tall” capillary for visual clarity.*

may not necessarily exist at cryogenic temperatures, it was deemed necessary to test if isolation of sample from the electrode surface could enhance attainable fields. Initial thoughts to apply some form of coating to the electrodes, although tried, created more uncertainty than comfort. These considerations were, imprecise thickness of coating, surface inhomogeneity arising from cooling and contracting, coating degassing rates, possible chemical reaction with sample or electrode surface, and its own breakdown potential, all important when calculating accurate electric fields at the sample. A different direction was needed.

Isolation testing began with sample placed into a 1.5 mm outer diameter KIMAX cylindrical borosilicate glass capillary that was situated between the electrodes. Figure 7.6 shows images of sample in direct contact with the electrodes and the setup for initial trials with sample placed within the cylindrical capillary. Maximum voltages that could be applied to the sample situated in the cylindrical capillary prior to breakdown were then looked into further in environments of air and helium at both 1 atm and reduced pressures. The results of only a few of these tests appear in table 7.1.

Condition		V <sub>max</sub>	Condition		V <sub>max</sub>
<b>T = 298 K P = 1000 mbar Air</b>			<b>T = 298 K (capillary between electrodes)</b>		
HV Line (no cell)		4900	PPIX-Mb	P = 10 <sup>-4</sup> mbar Air	3500
Air	44% humidity	4130	PPIX-Mb	P = 10 <sup>-4</sup> mbar He	2600
Glycerol	(bare electrodes)	3600	<b>New Cell (capillary between electrodes)</b>		
PPIX-Mb	(bare electrodes)	635	PPIX-Mb	T = 1.2 K P ~ 100 mbar He	500
PPIX-Mb	(nail polish electrodes)	828	PPIX-Mb	T = 11.3 K P = 10 <sup>-3</sup> mbar He	2200
PPIX-Mb	(capillary between electrodes)	3900			

Table 7.1: Above: Abridged attainable maximum voltages prior to breakdown, or trip condition for various cell configurations and conditions.

All of the trials indicated that if high voltages were to be applied to the sample, it would be necessary to isolate the sample from direct contact with the bare electrodes. An example trace that displays the results of the improvements made to the electrical connections and cables of the electrical pathway in addition to the isolation of the sample from the electrode surface appears next. Observe the difference from the result as recorded by the APD's upon application of the voltage to the sample as depicted within figure 7.5.

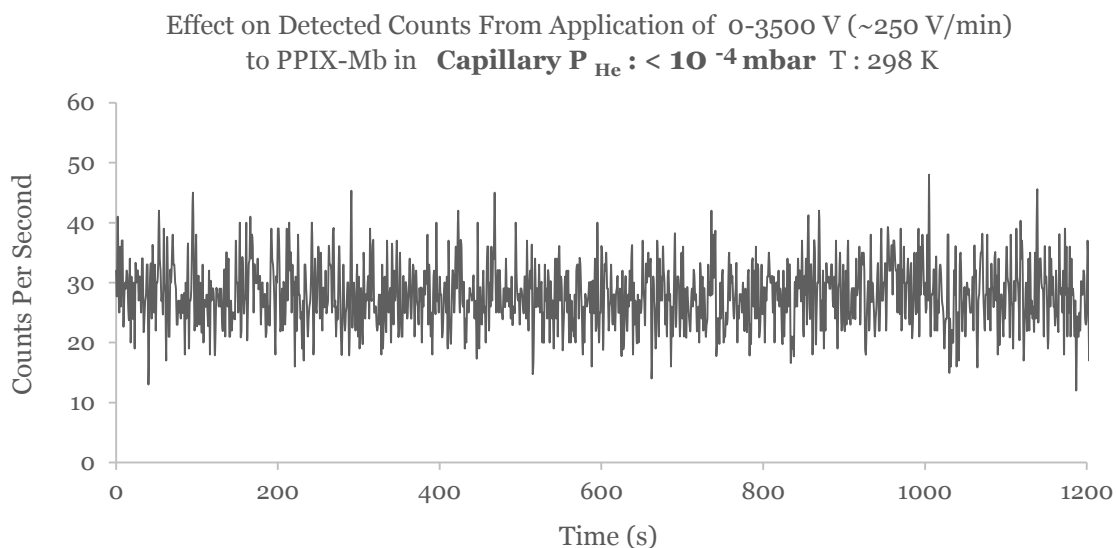


*Figure 7.7: Sample trace showing no APD runaway with improvements to connections, shielding of electrical pathway, and isolation of sample from direct contact with electrode surface.*

## 7.6 New Sample Cell

Based on the results from the trials performed at room temperature, and the substantial enhancement of allowable voltage application ranges, a new sample cell that completely isolates the sample from the electrodes was designed. In this cell design, the sample is

placed in a square borosilicate capillary of 1mm ID x 1.4mm OD from Wale Apparatus. The capillary is open-ended on both sides, and sits horizontally. It was found that without an angle of  $> 3$  degrees, the sample experiences no noticeable flow over a three-day period. The sample cell is constructed from microscope slides cut to size and again features electrodes made of 22 mil copper. The sample cell is magnetically affixed to the piezo actuators at the base of the CTCSM and connects to the electrical leads by use of stainless steel screws and copper washers. Black fabric tape is used to eliminate reflections from the top surface of the cell. A CAD schematic as well as an image of the constructed cell are shown in figure 7.8.

The re-design of the sample cell offered five main advantages over that of the previous design. As the sample is isolated from the electrode surface, electrolysis of sample is minimized. This is beneficial for sample integrity in addition to limiting the occurrence of breakdown, as was shown with the initial maximum voltage trials on sample contained in the cylindrical capillary. The process of loading the sample into the cell is much easier and the probability of bubble formation upon introduction of sample is significantly reduced with this new design. A representative bubble can be seen in the image of the original holder, figure 7.6 left. This means less sample is wasted during the filling process. Additionally, since the sample is entirely contained within the capillary it is removable and can possibly be reused as long as the sample can withstand the thermal cycling. For protein samples this may not be achievable, but with other samples this possibility can certainly be realized. Installation and alignment of the new holder into the CTCSM is simpler as sample track illumination is observable from the side of the cell. Additionally, the working surface area of the sample as seen by the excitation

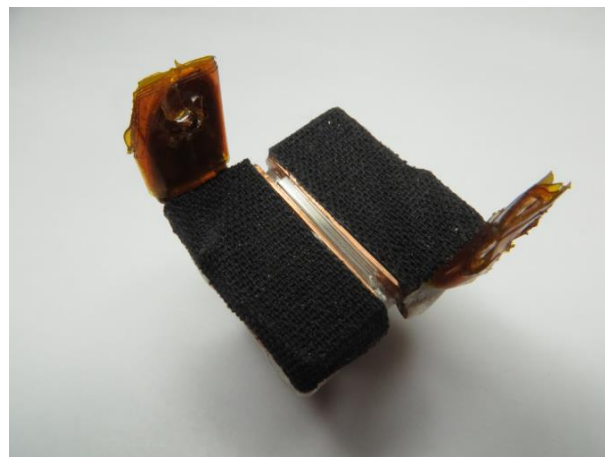
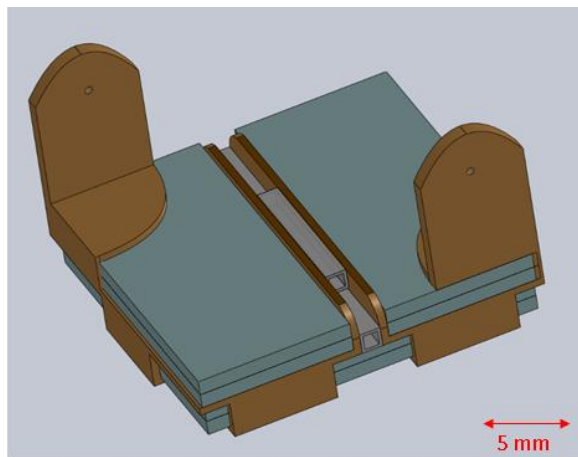
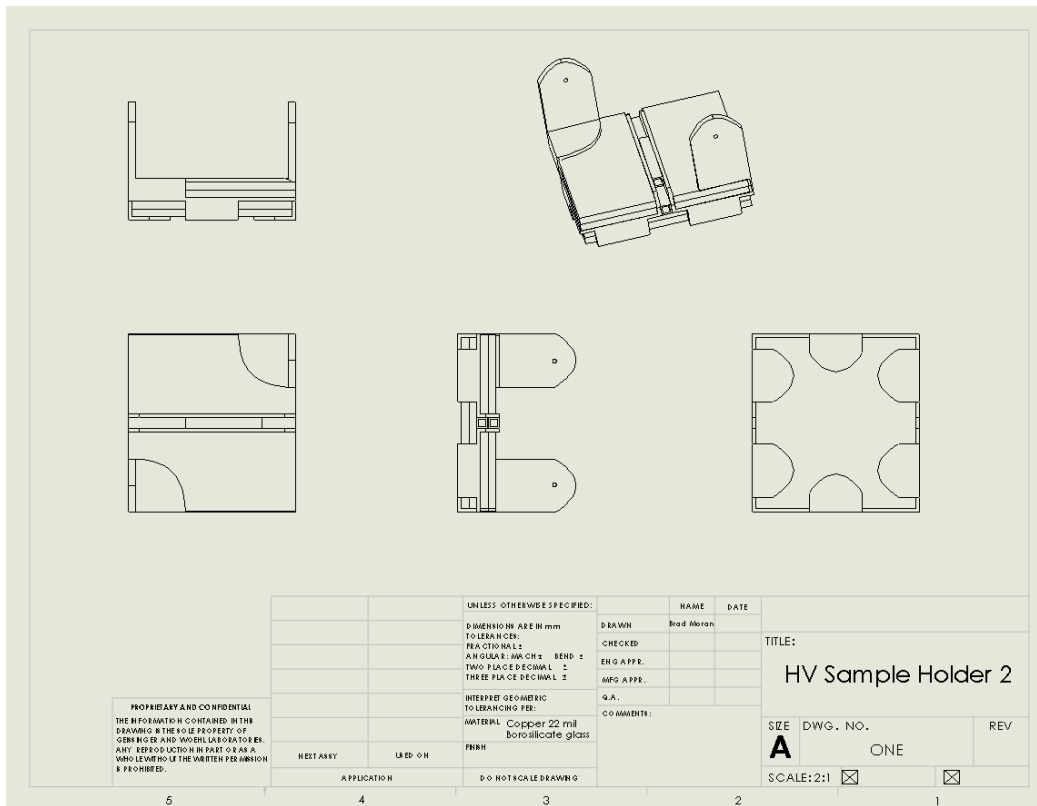
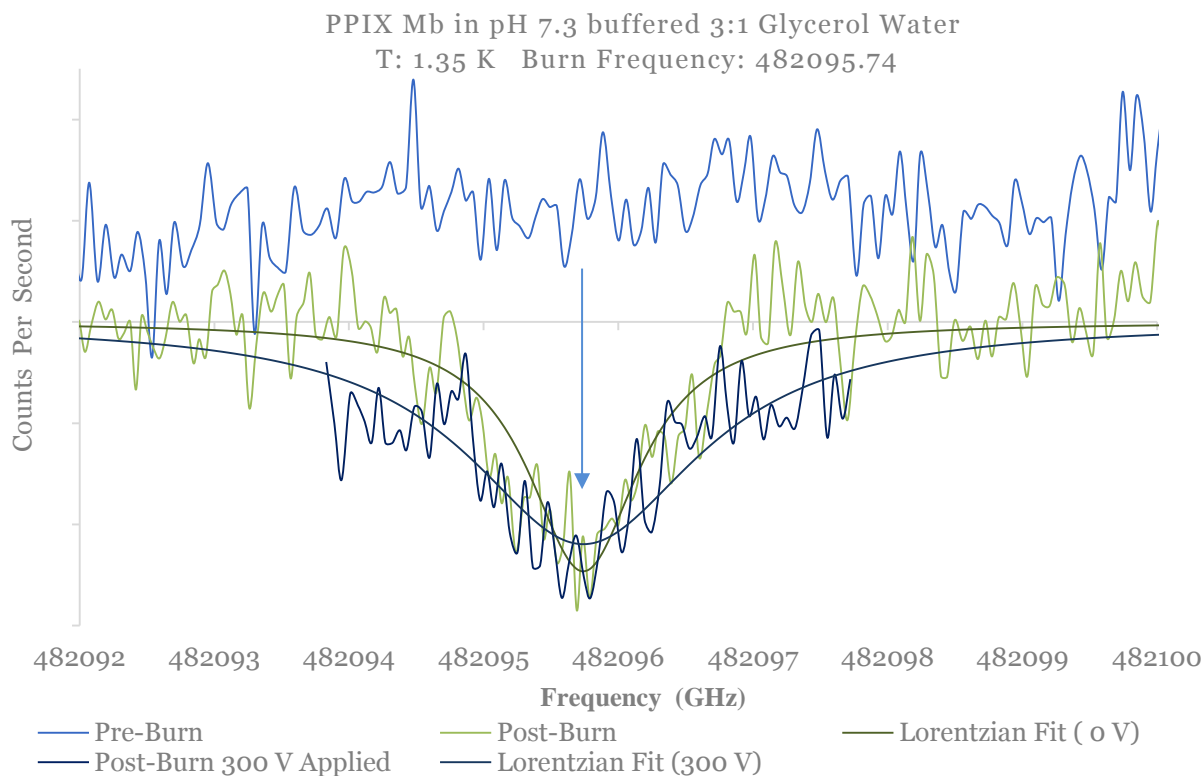


Figure 7.8: Above: Newly designed sample holder. Sample rests within 1.4 mm x 1.4 mm x 10 mm square borosilicate glass capillary, isolated from direct contact with Cu electrodes.

beam has increased. This sample holder can also be used any time a solution or thick media is to be studied with the CTCSM as opposed to investigating only thin films deposited on the surface of coverglass, which is the standard sample mounting technique.

This cell has been successfully used during many hole-burning studies and performs very well. During these studies the sample is in an environment of helium exchange gas that is at a pressure of 100 mbar and a temperature of approximately 1 K. Unfortunately, it was found that under these conditions application of only 500 V to the sample resulted electric breakdown of the helium gas. When the pressure of the exchange gas was reduced to  $10^{-4}$  mbar and below, it was possible to apply voltages in excess of 3000 V to the sample without any breakdown of the helium exchange gas. During the pumping process, from 100 mbar to  $10^{-4}$  mbar, due to lack of appropriate exchange gas, temperature fluctuations of up to 10 K at sample have been observed. During the evacuation of exchange gas all spectral holes have been observed to spontaneously fill and at temperatures ranging from 4-6 K begin to completely disappear. As a result, despite numerous attempts with a parallel configuration of the excitation light polarization and the externally applied electric field, no effective splitting of spectral holes has been observed with this cell, again due to the reduced voltages that can be applied prior to breakdown. This phenomenon is not any longer a result of interactions between the sample and electrodes but is specifically due to breakdown issues concerning the helium exchange gas. The development and implementation of a fairly rapid pressure modulation protocol within the sample chamber to achieve appropriate voltage ranges is a task that still needs additional effort





General model: Lorentzian Fit <b>(0 V)</b>	482095.74	Goodness of fit:
$f(x) = I \cdot (P1^2 / ((x - P2)^2 + P1^2))$		SSE: 1.353e+06 R-square: 0.7089 Adjusted R-square: 0.7062 RMSE: 79.7
Coefficients (with 95% confidence bounds):		
I (Intensity) = 491.6 (435.5, 547.6)		
P1 (HWHM) = 0.5012 (0.4203, 0.5821)		
P2 (Peak) = 4.821e+05 (4.821e+05, 4.821e+05)		

General model: Lorentzian Fit <b>(300 V)</b>	482095.74	Goodness of fit:
$f(x) = I \cdot (P1^2 / ((x - P2)^2 + P1^2))$		SSE: 4.754e+05 R-square: 0.6047 Adjusted R-square: 0.5935 RMSE: 81.83
Coefficients (with 95% confidence bounds):		
I (Intensity) = 438.9 (395.3, 482.6)		
P1 (HWHM) = 1.055 (0.8855, 1.224)		
P2 (Peak) = 4.821e+05 (4.821e+05, 4.821e+05)		

Figure 7.9: Spectral hole, burnt into the Qx transition of PPIX Mb. Laser polarization parallel to applied electric field (300 V). Low magnitude of externally applied field resulted only in broadening of hole-profile. Spectral splitting is expected at enhanced externally applied field values. Hole (0 V): FWHM 0.00128 nm = 1.0024 GHz; with a relative depth of 18%. Hole (300 V): FWHM 0.00269 nm = 2.11 GHz; with a relative depth of 16%. Lorentzian fit parameters and fitting statistics for the above spectral hole with 0 V applied and 300 V applied.

if Stark investigations on spectral holes are to be a possibility using the existing experimental setup. In figure 7.9 is a typical spectral hole that was obtained when sample was housed in this sample cell. The result of application of a relatively modest voltage, 300 V, to the sample does reveal a broadening effect indicating that the cell does effectively apply an electric field to the sample and performs as expected. The 0 V and 300 V applied spectral holes were each fit with a Lorentzian to confirm the expected shape characteristics of spectral holes and to most basically show the occurrence of the broadening. The fits along with the fitting statistics are displayed with the spectral profile. There is no doubt that this cell design could be successfully used to split the spectral hole profiles if the exchange gas pressure issues could be ameliorated.

## **7.7 Glass Cryostat**

After attempts to apply high voltages to the sample by electrodes exposed to an environment of exchange gas were unsuccessful a new approach for cooling the sample was taken. The new approach would be to modify the experimental setup and abandon use of the Janis research Dewar and instead use a bath cryostat. The choice was made to take advantage of the greater dielectric strength of the liquid to gas phase of helium in order to apply higher voltages to the immersed sample and electrodes. This choice of experimental setup was also known to have worked as it had been implemented successfully in previous experiments [1-3, 11].

The dual reservoir cryostat, made of Pyrex, is approximately one meter in height, and features quartz windows at its base. Windows exist on three sides of the cryostat,

with two sides along the same principal axis and one side on a normal axis allowing for front face, transmission, or the standard 90-degree collection modes. The quartz windows are interchangeable and are secured to the body of the cryostat using the low pressure vacuum epoxy Torr-seal. The cryostat is shielded using black tape to minimize cryogen boil off due to ambient light. The outer jacket holds liquid nitrogen and the inner jacket typically holds between 7-9 liters of liquid helium. Best results with this cryostat are obtained when the vacuum jacket is in the range  $10^{-6}$  to  $10^{-7}$  mbar. When vacuum is applied to the helium reservoir, boil off generally ranges from 1/3 to 2/5 of the initial liquid volume and temperatures between 1-2 K are easily achievable. At these specifications useable experimental time frames generally range between 7 to 10 hours before the liquid level falls below the electrodes at the sample.

Due to the clearance height above the cryostat that is necessary for the transfer tubes used for filling with liquid cryogens and the sample insert rod, the cryostat is situated off of a traditional optics table. A cage structure to support the cryostat below which a small floating table for the placement of optical components was constructed. The cage structure is on caster wheels so the cryostat and immediate optics can be easily maneuvered and transported. The source and signal are carried to and from these optics by optical fibers. The specific fibers used for this purpose are discussed in chapter 4.3.

The switch to the glass cryostat required an optical method alternate to the CTCSM to be used for sample illumination and signal collection. For this purpose, the head portion of the CTCSM was unmounted from the optical insert. The top and bottom cage cube were removed and the emission arm was moved to the top side of the central cage cube. The polarization modulator was moved directly below the central cage cube.

A 60 mm lens was attached after the polarizer and is used to focus the beam onto the sample within the cryostat. The entire unit rotated on its side, these optics are affixed to the floating table below the cryostat. The sample is placed in a 1.5 mm outer diameter KIMAX cylindrical borosilicate glass capillary and sits between planar copper electrodes that have a spacing of 1.5 mm, which are in direct contact with the capillary walls.

Of main benefit aside from being able to apply higher voltages to the sample due to liquid immersion, is the possibility for multiple collection modes not realizable in the Janis research Dewar. The presence of the parallel plate electrodes negates the possibility of 90-degree signal collection. The reflected signal is collected back through the optics just described. To allow for collection of the transmission signal, a second emission arm was placed on the transmission side of the cryostat and affixed to the floating table. The second emission arm is set up conjunction with a 60 mm lens with both the fiber coupler of the emission arm and the sample placed at twice the focal length of the lens. When the optics are arranged in this way, the fluorescent signal can be collected under both reflection and transmission modes. A schematic of the entire experimental setup appears next.

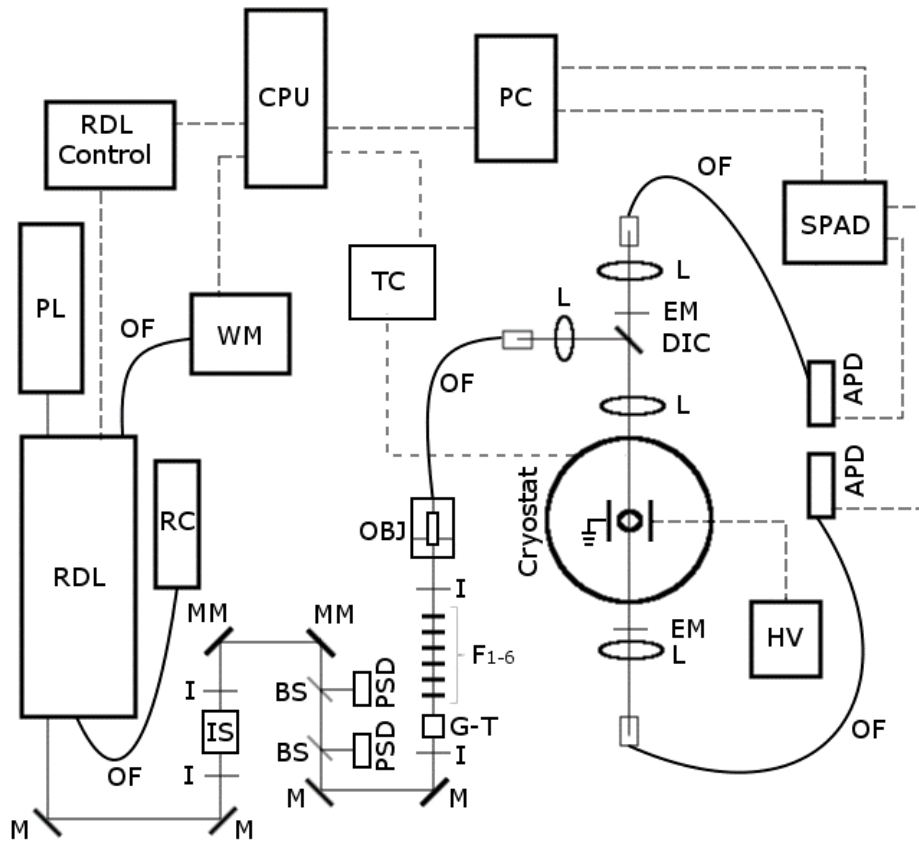


Figure 7.10: Experimental setup for hole-burning with glass cryostat. When Janis Dewar is used, transmission signal, (bottom right) is not present. PL: Pump Laser; RDL: Ring Dye Laser; M: Mirror; I: Iris; IS: Intensity Stabilizer; MM: Motorized Mirror; BS: Beam Sampler; PSD: Position Sensitive Detector; G-T: Glan-Taylor Prism; F1-6: Neutral Density Filters; OBJ: 10x Objective; OF: Optical Fiber; L: Lens; DIC: Dichroic Mirror; EM: Emission Filter; HV: High Voltage Power Supply; APD: Avalanche Photodiode; SPAD: APD Power Supply; PC: Photon Counter; CPU: Computer; RDL Control: Dye Laser Control Box; TC: Temperature Controller; WM: Wave meter; RC: Reference Cavity. The laser beam is depicted as a solid line, dotted lines are electrical connections.

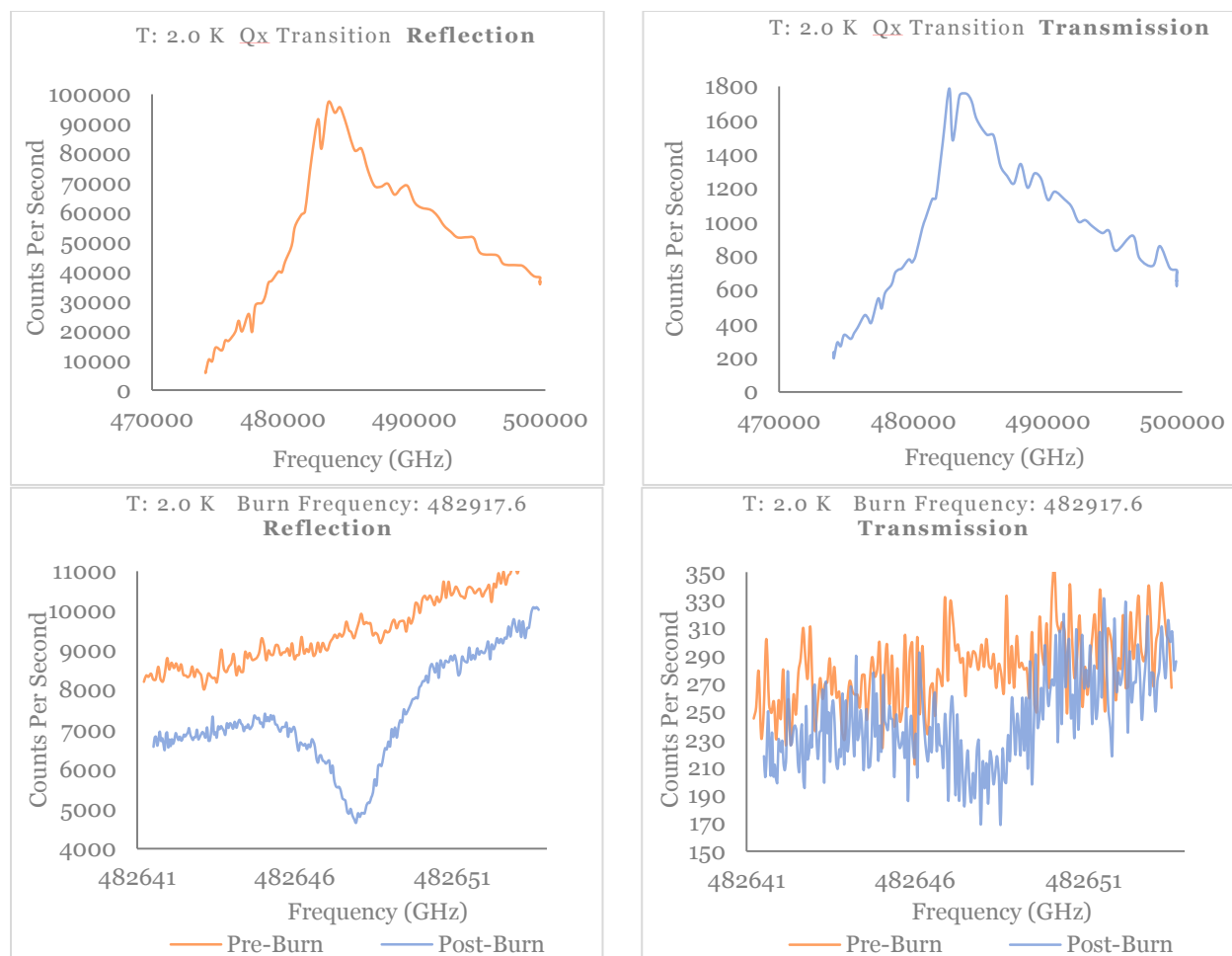


Figure 7.11: Representative spectra of PPIX Mb in pH 7.3 buffered 3:1 Glycerol Water at 2 K, depicting the possible collection modes when sample is placed in the glass cryostat. The reflected and transmitted signal are acquired simultaneously. The top row displays nearly identical spectra of the entire Q<sub>x</sub> band and the bottom row displays a representative single spectral hole as collected by each mode. The transmitted signal suffers from enhanced noise. Additional efforts placed on alignment of the optics positioned on the transmission side of the cryostat does reduce the noise, yet signal intensity generally remains an order below that of the reflected signal.

Above are resultant spectral profiles that were collected simultaneously in reflection and transmission modes. Depicted are an example of the entire Q<sub>x</sub> band as well as of a spectral hole that was burnt. It can be seen that the same overall spectral characteristics are present in both collection schemes but the transmission signal is of significantly lower intensity than that of the reflected signal and does suffer noise.

When the glass cryostat was brought into commission it already possessed a high voltage feedthrough. The feedthrough was constructed out of a hollow  $\frac{1}{4}$  inch aluminum cylinder approximately one meter in length that contained a wound stainless steel wire serving as the conductor. Both ends of the aluminum cylinder were capped with ceramic feedthrough insulators through which the conduction wire was passed. Solder and epoxy were used to create the seal at these junctures. The aluminum cylinder was evacuated prior to use for high voltage applications. For incorporation into the electrical pathway a MHV connector was added at the external end of the feedthrough and experiments proceeded.

Preliminary trials indicated that the feedthrough performed quite well. It was initially found that application of voltages in excess of 3500 V to the sample was a possibility. Because exact voltages necessary to induce splitting of spectral hole profiles were unknown, the first investigations used more modest voltages generally below 2000 V. During experimentation it was discovered that, most likely due to submersion in liquid helium, the epoxy creating the seal at the end of the feedthrough had cracked. Upon this occurrence and introduction of helium gas into the aluminum cylinder from the cryogen reservoir, breakdown resulted and again only minimal voltages could be applied to the sample. Efforts were made to rectify this issue by application of new solder and epoxy at the juncture. Upon submersion into the liquid helium, however, cracks would always form causing similar issues regarding breakdown at voltages below the necessary threshold for collection of usable experimental data.

Although representing a great increase in the magnitude of voltage that could be applied prior to breakdown in relation to the previous sample cell designs, the collected

spectra indicate that voltages of magnitudes below 2000 V are not in the range allowing for split conditions. An example of some of the larger voltages that were applied to a spectral hole and the resulting broadening observed appears in figure 7.12.

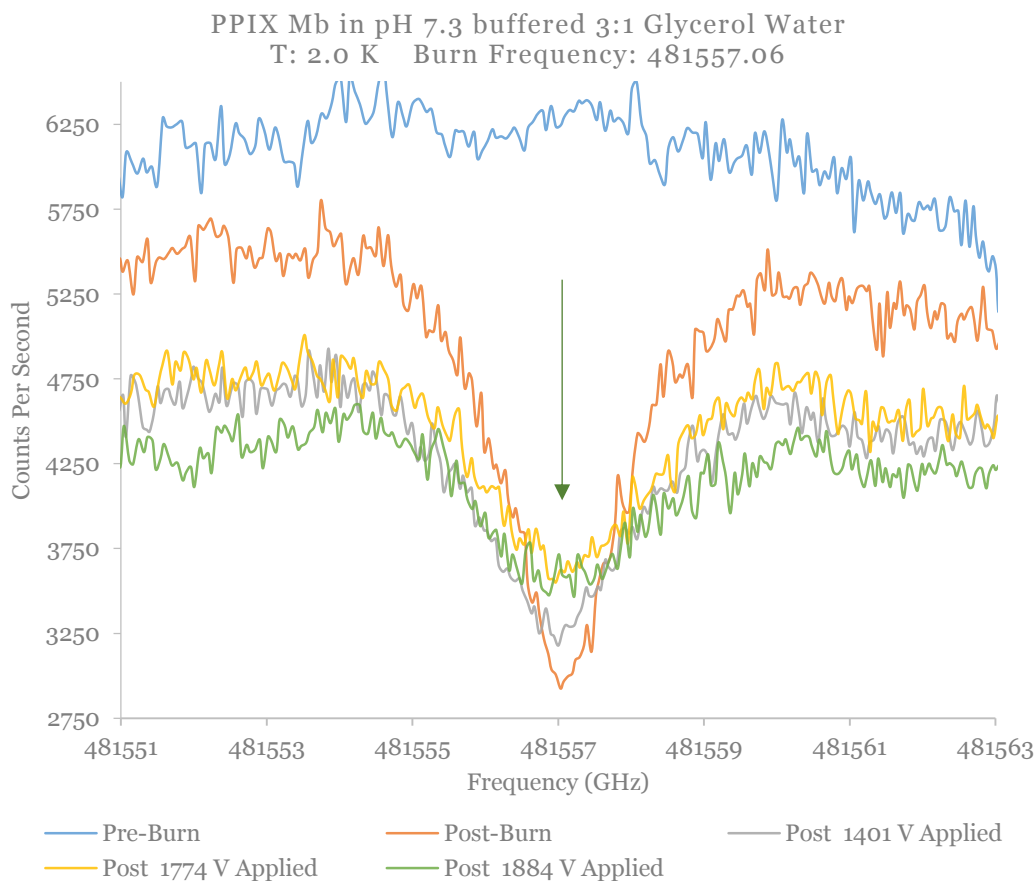


*Figure 7.12: Spectral hole, burnt into the Qx transition of PPIX Mb and resultant broadening of hole profile with application of electric field. Laser polarization parallel to applied electric field. Hole (Post-Burn): FWHM 0.00218 nm = 1.689 GHz; with a relative depth of 44%. Hole (1401 V): FWHM 0.00276 nm = 2.13 GHz; with a relative depth of 31%. Hole (1774 V): FWHM 0.0032 nm = 2.48 GHz; with a relative depth of 26%. Hole (1884 V): FWHM 0.00332 nm = 2.57 GHz; with a relative depth of 24%. At these voltages only broadening of hole profile was observed, profile splitting is expected at enhanced externally applied field values.*



## 7.8 New High Voltage Feedthrough

In order to apply voltages within the acceptable range for splitting hole profiles a new method for transmitting the voltage to the electrodes was necessary. In the original feedthrough, due to the close proximity and lack of an insulating barrier, there existed a large probability of the occurrence of arcing between the conduction wire and the surrounding aluminum cylinder. To negate the possibility of gas breakdown, the conductor needed to be completely surrounded by an insulating medium or surrounded by vacuum. While the original design of the high voltage feedthrough did place the conductor in vacuum, a more permanent method of sealing the vacuum volume capable of withstanding submersion into a 1 K liquid environment needed to be found.

Opposed to the aluminum cylinder of the original, the new feedthrough needed to be constructed out of primarily insulator with only a small conducting element at its center. To completely alleviate the chance of gaseous breakdown the first thought was to embed a conductor within a glass rod. Investigation revealed that a direct seal could be created between the glass and conductor if the glass was aluminosilicate and the metal conductor was molybdenum. Proving difficult materials to work with for the scale required for the feedthrough, a different path was chosen.

Abandoning a direct seal between conductor and glass made available many materials and simplified fabrication efforts. As with the original design, this required an evacuation space surrounding the conductor. Again rigorously sealing the ends of the feedthrough to ensure maintained vacuum was of chief concern. It was found that a housekeeper seal should be used for a vacuum quality glass to metal contact. The

stainless housekeeper seal situated at the base of the designed feedthrough was procured from Larson Electronic Glass. The body of the feedthrough is a 1/2 inch 7740 Pyrex cylinder that is approximately 1 meter in length, with a NW16 to Pyrex adaptor at the top. A NW 16 T-flange, allows for an evacuation port and an electrical port. A Swagelok valve is used at the evacuation port to isolate the feedthrough. The electrical port is fitted with an MHV NW16 flange from Nor-Cal Products. Running along the center of the Pyrex cylinder is a 1/8-inch stainless steel conduction rod. The conduction rod is welded to the stainless housekeeper seal ensuring no possibility of leakage. The voltage is transmitted between the feedthrough and the parallel plate electrodes by a Kapton insulated 26 AWG stainless steel wire from Accu-Glass Products, that is

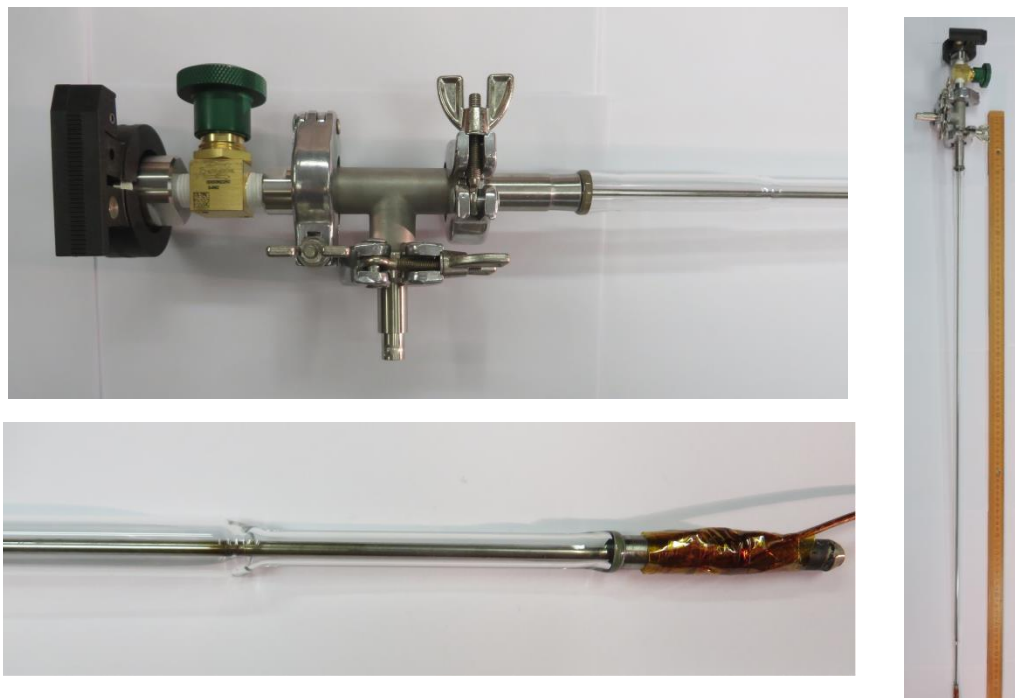


*Figure 7.13: The developed high voltage feedthrough. Right: The entire feedthrough, just over 1 meter in length, is inserted into bath cryostat. Top: close-up of vacuum components at top of feedthrough. Bottom: close-up of the base of the feedthrough. Observe the 1/8-inch stainless conduction rod. Welded endcap ensuring no leakage image right.*

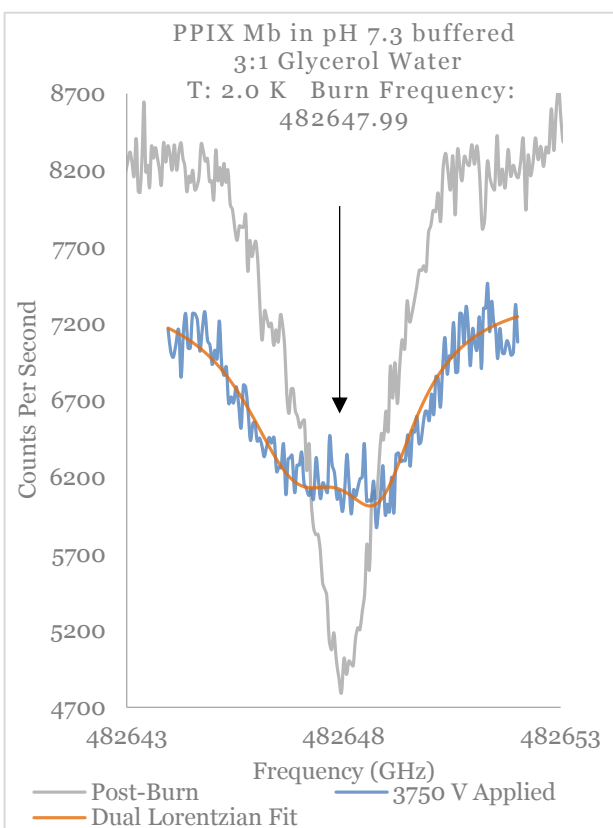
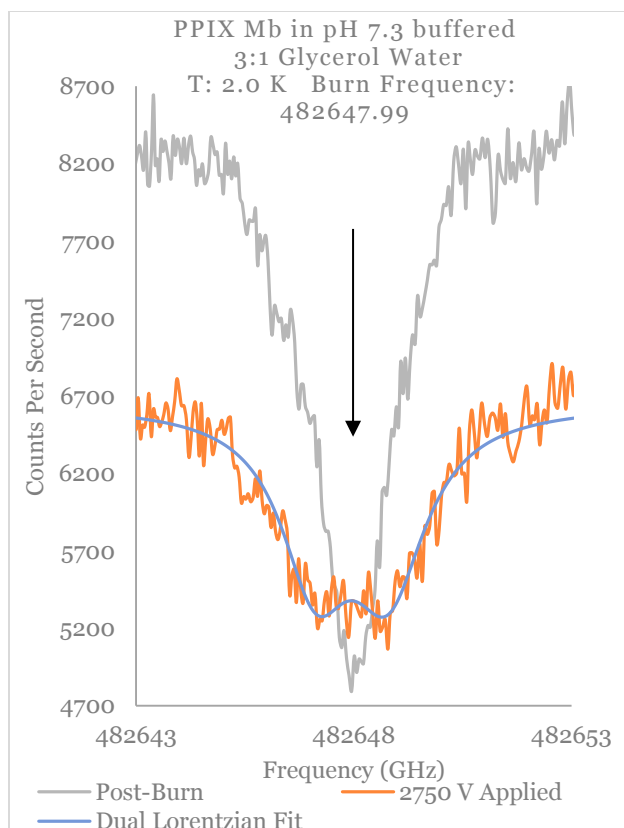
mechanically affixed to the feedthrough and wrapped with Kapton tape. The opposite side of the wire is fitted with an eyelet and connection to the electrodes is by means of a screw. The electrodes are again planar copper plates between which the cylindrical sample capillary is placed.

This feedthrough has been tested and performs beyond expectation. When a vacuum of  $10^{-5}$  mbar or better exists within the feedthrough no breakdown has been observed. Successful application of up to 5000 V to the sample has been realized. This feedthrough allows the entire voltage range necessary for the splitting of spectral hole profiles to be explored.

## **7.9 Split Hole Profiles**

The inclusion of the new high voltage feedthrough into the electrical pathway has allowed for experimentation with voltages well within the range necessary to induce the splitting of spectral holes. To systematically narrow the range of voltages and to potentially gain insight to the relationship between applied field and induced splitting, a stepped voltage protocol was tested. During these studies, the voltages applied were at intervals of 250 V between 1750 V and 5000 V.

Immediately following are two examples of representative splits that have been obtained utilizing the above stated procedure. The split profiles depicted are of the same spectral hole at applied voltages of 2750 v and 3750 V during the read cycles, corresponding to an applied electric field of approximately  $1.83 \times 10^6$  V/m and



<b>(2750 V → 1.83 x 10<sup>6</sup> V/m)</b>	482647.99	Goodness of fit:
General model: Lorentzian Fit		
$f(x) = I1*((P1^2)/((x-P2)^2+P1^2)) + I2*((P3^2)/((x-P4)^2+P3^2))+6647$		
I1 (Intensity) = -1039 (-1167, -911.2)		SSE: 3.399e+06 R-square: 0.9297 Adjusted R-square: 0.9277 RMSE: 138.2
I2 (Intensity) = -1099 (-1232, -966)		
P1 (HWHM) = 1.056 (0.8761, 1.236)		
P2 (Peak) = 4.8264738e+05 (4.826e+05, 4.826e+05)		
P3 (HWHM) = 0.9641 (0.7945, 1.134)		
P4 (Peak) = 4.8264860e+05 (4.826e+05, 4.826e+05)		

<b>(3750 V → 2.50 x 10<sup>6</sup> V/m)</b>	482647.99	Goodness of fit:
General model: Lorentzian Fit		
$f(x) = I1*((P1^2)/((x-P2)^2+P1^2)) + I2*((P3^2)/((x-P4)^2+P3^2))+7435$		
I1 (Intensity) = -1018 (-1153, -883.1)		SSE: 2.595e+06 R-square: 0.9084 Adjusted R-square: 0.9047 RMSE: 132.9
I2 (Intensity) = -1002 (-1165, -839.4)		
P1 (HWHM) = 1.522 (1.19, 1.855)		
P2 (Peak) = 4.8264703e+05 (4.826e+05, 4.826e+05)		
P3 (HWHM) = 1.105 (0.8564, 1.353)		
P4 (Peak) = 4.8264875e+05 (4.826e+05, 4.826e+05)		

*Figure 7.14: Above, is a representative spectral hole, burnt into the Qx transition of PPIX-Mb. Arrow indicates position of burn. This spectral hole has a FWHM of 0.00249 nm = 1.93 GHz, and a relative depth of 42%. Application of 2750 V and 3750 V resulted in successful splitting of the spectral hole. These applied voltages correspond to applied electric fields of approximately  $1.83 \times 10^6$  V/m and  $2.50 \times 10^6$  V/m, respectively. Each of the split profiles were most basically modeled using a sum of Lorentzian profiles. Lorentzian fit parameters and fitting statistics appear for each split profile.*

$2.50 \times 10^6$  V/m respectively. After application of external field to any spectral hole, the holes are always re-scanned to monitor the effects of after burning and to reassure that the original hole can be regained. These split profiles have been most basically fitted with dual Lorentzian functions simply to more clearly observe the presence of the resulting split. The fit functions along with the standard goodness of fit parameters for each of the resulting fits are also displayed. Again the quality of the fit parameters appear to indicate fairly accurate fits and does indicate that successful splitting was achieved. A representative split hole profile that is blue shifted from the split hole profiles appearing above, that displayed splitting upon application of 2500 V, correspond to an applied electric field of approximately  $1.67 \times 10^6$  V/m at the sample, appears in Appendix F. Based on these experiments it is thought that with this particular experimental setup, an application of 2500 V is representative of the minimum voltage that is necessary to apply to the sample to observe any splitting behavior.

Regarding voltages above the immediately presented range, it has been observed that application of voltages in excess of 4000 V generally tend to broaden a spectral hole to such an extent that it appears similar in profile to pre-burn traces yet existing at a lower intensity, similar to what one would expect from a baseline shift. To investigate if the broadening of hole profiles at voltages of this magnitude simply split the hole

beyond the standard scan window of approximately 10-15 GHz, with the hole being placed at the center, extended scans ranges of up to 30 GHz were looked at. Despite the expectation that this would reveal a larger scale splitting of the hole profiles, results have been too inconclusive for a definitive interpretation explaining this result to be made. Further efforts along this line of inquiry should be pursued.

Although the observed splitting is on par with some results obtained by previous experimenters [3,11], the lack of complete and well defined splits that have thus far been realized indicate that some modification to the current methodology is necessary. Due to the fairly large range over which voltages were initially investigated, the chosen step size of 250 V may be too large to tease out the desired splitting characteristics. Additional experimentation that more accurately investigates the effects of smaller increments needs to be carried out. The particular optical setup being used also focuses the excitation beam at the sample and only collects fluorescent signal from the molecular population existing in the focal volume. It is possible that the probed volume represents an ensemble that is too small and is lacking of the necessary differentiation of random molecular orientations to create cleanly split the profiles. Attempts have been made to defocus the excitation and collection beams to include a larger subset of molecules within the probe volume but again no successes on this front have been made.

There are two easily realizable experimental modifications that may produce better splits. If the focusing lens on the excitation side is removed, the illuminated area of sample would be approximately equal to the surface area of the excitation beam. This much larger probe volume would likely result in a population possessing the appropriate orientational diversity to be simultaneously be studied. This modification would require

transmission collection of the fluorescent signal, most likely by use of a PMT. Secondly, past experiments have applied electric field only at angles strictly parallel or perpendicular to the polarization of the burn and read light. Due to the complete rotational freedom as afforded by the polarization modulator, other angular offsets besides these two can now be explored to reveal the angular dependence of splitting.

## References

- 1.) Gafert, J., Friedrich, J., Parak, F. (1995). "Stark-effect experiments on photochemical holes in chromoproteins: Protoporphyrin IX-substituted Myoglobin," *Proceedings of the National Academy of Sciences USA* 92, 2116-2120.
- 2.) Gafert, J., Ober, C., Orth, K., Friedrich, J. (1995). "Thermal Broadening of an Optical Transition in a Chromoprotein between 50 mK and 15 K," *Journal of Physical Chemistry* 99(39), 14561-14565.
- 3.) Geissinger, P., Kohler, Bryan E., Woehl, Jorg C. (1995). Electric Field and Structure in the Myoglobin Heme Pocket," *Journal of Physical Chemistry* 99(45), 16527-16529.
- 4.) Kohler, M., Gafert, J., Friedrich, J., Vanderkooi, J. M., Laberge, M. (1996). "Stark Effect Experiments in Cytochrome c-Type Proteins: Structural Hierarchies," *Biophysical Journal* 71, 77-85.
- 5.) Kohler, Bryan E., Woehl, Jorg C. (1999). "Effects of Electrostatic Fields and Potentials on the Electronic Energies of Conjugated Organic Molecules," *Journal of Physical Chemistry A* 103(14), 2435-2445.
- 6.) Leeson, Daan Thorn., Wiersma, Douwe A., Fritsch, Klaus., Friedrich, Josef. (1997). "The Energy Landscape of Myoglobin: An Optical Study," *Journal of Physical Chemistry B* 101(33), 6331-6340.
- 7.) Lide, D. (2003). *CRC handbook of chemistry and physics: A ready-reference book of chemical and physical data*. (84th ed.). Boca Raton, Fla.: CRC Press. 15-34 to 15-36.
- 8.) Meixner, Alfred J., Renn, Alois., Bucher, Stephan E., Wild Urs P. (1986). "Spectral Hole Burning In Glasses and Polymer Films: The Stark Effect," *Journal of Physical Chemistry* 90(26), 6777-6785.
- 9.) Purchase, R., Sellars, M.J., Krausz, E. Manson, N.B. (2000). "Electric-field-induced broadening of spectral holes in zinc phthalocyanine," *Chemical Physics Letters* 327, 189-196.
- 10.) Ratsep, M. Wu, H.-M., Hayes, J. M., Blankenship, R. E., Cogdell, R. J., Small, G. J. (1998). "Stark Hole-Burning Studies of Three Photosynthetic Complexes," *Journal of Physical Chemistry B* 102(20), 4035-4044.
- 11.) Woehl, J. C. (1996) *Measuring Internal Electrostatic Fields and Potentials at Molecular and Atomic Resolution using Hole Burning Spectroscopy*. Doctoral thesis. University of California-Riverside
- 12.) Zollfrank, J., Friedrich, J., Parak, F. (1992). "Spectral hole burning study of protoporphyrin IX substituted myoglobin," *Biophysical Journal* 61, 716-724.



# III

## Chapter 8

# A Capacitive Cell for the Assessment of Dielectric Permittivity

## 8.1 Introduction

The dielectric permittivity of a material is a quantity that provides a measure of the material's response to an externally applied electric field. This field can exist either in the form of a propagating light field or in the form of a traditional electric field established between a pair of electrodes. The specific value of the permittivity, aside from being a property that is material dependent, is also a value that is highly dependent upon not only the absolute temperature of the material but also upon the frequency of the interacting electric field. The dielectric permittivity thus becomes an especially important parameter to accurately quantify when conducting spectroscopic investigations on samples that are immersed within various media and at varying temperatures [13, 26].

Unfortunately, the thermal range over which these values are readily available is frequently limited. Therefore, a determination of this quantity for various solutions that are commonly used in the formation of spectroscopic glasses, in which chromophores can be embedded, across a vast temperature range could potentially be of great benefit to many researchers. This discussion highlights the creation, development and

experimental testing of a capacitive cell that is capable of being used from cryogenic to ambient temperature for the determination of a material's dielectric permittivity. This cell has been shown to successfully yield values for this quantity for various media that are in accordance with those found in the literature, while also offering the ability to provide measures for these values over the entire working temperature range of the instrument, from 1-300 K.

## 8.2 Capacitors

In general, any two conductors that are separated by a distance can form a capacitor. Although capacitors can take on many forms, the simplest design that can be used to create a capacitor is a pair of parallel plates that share an area of overlap ( $A$ ) and are separated by a distance ( $d$ ). When these plates are connected to a voltage source, such as a battery, charges begin to migrate between the two plates with the positive charges  $+q$  accumulating on one of the plates and the negative charges  $-q$  accumulating on the other. If the voltage source is then removed, generally by a switch, the charges will remain positioned on the outer surface of the respective plates towards the inner surface of the capacitor as long as neither plate is grounded. Ideally, a capacitor has no losses and will maintain a constant voltage until it is discharged. The voltage differential created by the charges residing on the plates will be equal to the voltage drop existing across the battery that was used to initially charge the plates. The separation of charge that exists between the two plates leads to the development of an electric field  $\vec{E}$ ,

between the plates. Thus, the primary function of a capacitor is to store electrical potential energy in the form of an electric field so that it can be used at a later time.

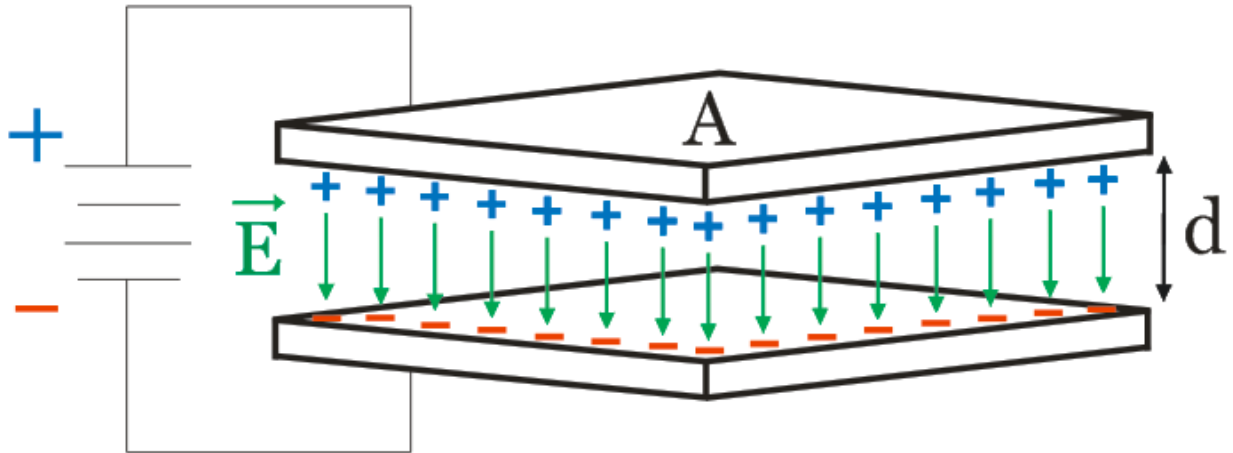


*Figure 8.1: Parallel plate capacitor. The capacitor is formed by two parallel plates that share an area of overlap  $A$ , and are separated by a distance  $d$ . After connection to a voltage source, charges accumulate on the inner surface of the plates. Due to the separation of charge that is established, an electric field  $\vec{E}$  develops between the plates. The magnitude of the electric field is directly proportional to the voltage differential of the plates and inversely proportional to their distance from one another.*

The capacitance  $C$  of a system provides a measure of the system's ability to store an electric charge. The total charge  $Q$  that can be stored for a specified voltage differential  $V$  results in the capacitance. The units are coulombs per volt  $C/V$ , which is equivalent to a farad  $F$ , the unit that capacitance is typically reported.

$$C = \frac{Q}{V} \tag{8.1}$$

For a capacitor possessing a parallel plate geometry, as depicted in figure 8.1, the amount of charge that can be stored for a given voltage is directly related to the area of

overlap of the plates and is inversely proportional to the distance between the plates. In the case that vacuum exists between the plates of the capacitor, the capacitance is based purely on the geometry of the capacitor and can be calculated as follows.

$$C = \epsilon_0 \left( \frac{A}{d} \right) \quad (8.2)$$

In this equality, the geometric characteristics of the plates are scaled by the vacuum permittivity (or the permittivity of free space)  $\epsilon_0$ , having a value of  $8.85418 \times 10^{-12}$  F/m, to yield the total capacitance of the capacitor. Therefore, the capacitance value can be modulated by altering the size of the plates and the distance between them.

### 8.3 Dielectrics in Capacitors

When the space between the plates of a capacitor is occupied by a dielectric material as opposed to a vacuum, a change in the value of capacitance will be observed. Whether the dielectric consists of molecules possessing a permanent dipole moment or consists of molecules in which a dipole moment can be induced, the electric field that exists between the plates of the capacitor will polarize the molecules of the dielectric, causing the molecules to orient to the electric field. Because each molecule once polarized will create its own electric field, upon orientation to the field, the polarized molecules will collectively establish an electric field that is opposed to that of the capacitor. As the electric field between the plates must remain unchanged, this polarization induces the flow of additional charges to the surface of the plates to maintain an inter-plate voltage differential that is equal to that of the battery that is used to charge the capacitor.

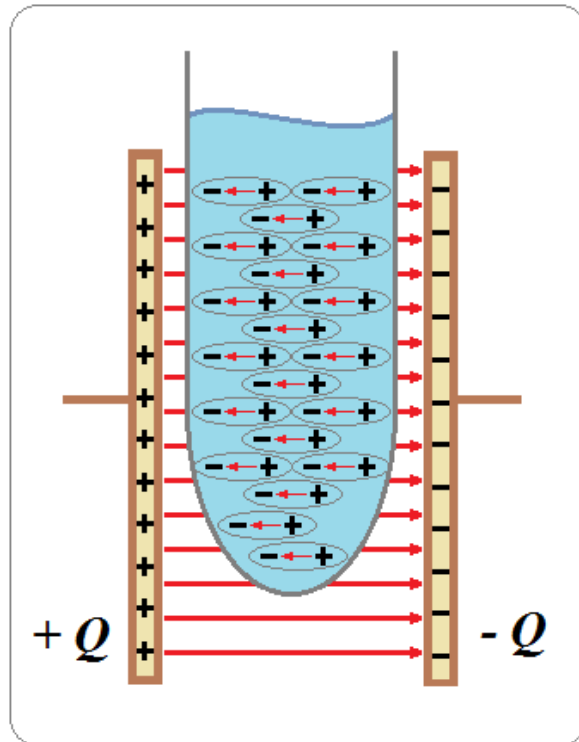


*Figure 8.2: Placement of a dielectric material between the plates of a parallel plate capacitor. The polarizable molecules of the dielectric upon orientation towards the external field will collectively establish a counter field that reduces the net field between the plates. To maintain the voltage differential between the plates additional charges flow to the respective plates.*

Therefore, the presence of a dielectric material between the plates of a capacitor allows the quantity of charge that resides on the plates to increase. A measure of the ability of a medium to enhance the charge that is stored on the plates in relation to that which is stored when there is only vacuum between the plates defines the relative permittivity  $\epsilon_r$  of that medium. The relative permittivity is thus a quantity of importance when assessing the polarizability of specific materials in the gaseous, liquid, or solid state [2, 13, 26].

Under this circumstance, the previous formulation for calculating the capacitance of a capacitor with parallel plate geometry can be used if it is additionally scaled by the relative permittivity  $\epsilon_r$ , of the dielectric medium that exists between the plates.

$$C = \epsilon_r \epsilon_0 \left( \frac{A}{d} \right) \Rightarrow \epsilon_r = \frac{Cd}{A\epsilon_0} \quad (8.3)$$

The value of the relative permittivity of vacuum is always one, with all other dielectric materials having a value of relative permittivity being greater than one. As shown, by this slight rearrangement of the equation, if the geometric characteristics of the capacitor are known and the capacitance of the capacitor can be measured, the relative permittivity of the dielectric medium existing between the plates can then be calculated. The product of the vacuum permittivity  $\epsilon_0$ , and the relative permittivity  $\epsilon_r$ , is equal to the frequency-dependent absolute permittivity  $\epsilon$  of the material.

$$\epsilon = \epsilon_r \epsilon_0 \quad (8.4)$$

In order to maximize the capacitance of this type of capacitor, the area of the plates can be increased, the distance between the plates can be minimized, or a dielectric material with a larger value of relative permittivity can be placed between the plates, or any combination of the three.

### 8.3.1 Dielectrics and Hole-Burning

During the hole-burning investigations, the sample is placed between two planar electrodes which are used to create the high fields (by applying high voltage) necessary to induce spectral shifts according to the Stark effect. The chromophore of interest is

any of various types of porphyrin analogs, chapter 1.3, that are substituted into the myoglobin protein. The substituted myoglobin is then placed within a 3:1 glycerol:water host matrix, creating the resultant sample. Finally, sample is located within a cylindrical borosilicate capillary that rests between the electrodes. All of these factors need to be taken into account for an accurate representation of the electric field that is acting upon a given chromophore.

This situation is akin to that of a parallel plate capacitor containing a dielectric. Upon application of a potential difference to the electrodes the entire matrix, including the protein as well as the glycerol:water, that surrounds the chromophores will polarize to the electric field of the capacitor. When utilizing the Lorentz field approximation for determining the electric field that exists within the dielectric, this polarization of the medium results in a modified distribution of charge residing on the surface of the Lorentz cavity. This adjustment of surface charge on the cavity alters the electric field that exists within the cavity and interacts with the chromophore. Any chromophore that is placed within a dielectric will then observe an electric field that is different from the one that is expected due to the applied voltage and plate separation alone. Again, as the objective of this investigation is to determine the molecular electric field that is present within the active site of the protein  $\vec{E}_{int}$ , it is necessary to tease apart the composite electric field  $\vec{E}_{tot}$ , that is responsible for the observed spectral shifts into its respective components, namely the internal and local  $\vec{E}_{loc}$ , electric fields. Accurate quantification of the magnitude of the externally applied electric field  $\vec{E}_{ext}$  that is felt by the chromophores embedded within the matrix, rests upon correct assignment of the local field tensor  $\hat{f}_{loc}$ .

$$\begin{aligned}
\vec{E}_{tot} &= \vec{E}_{int} + \vec{E}_{loc} \\
&\quad \underbrace{\hspace{10em}} \\
\vec{E}_{loc} &= \hat{f}_{loc} \vec{E}_{ext} \\
&\quad \underbrace{\hspace{10em}} \\
\hat{f}_{loc} &= (\epsilon_r + 2)/3
\end{aligned}
\tag{8.5}$$

In this formulation, under the assumption of the Lorentz approximation for the cavity field at the site of the chromophores, the relative permittivity of the surrounding matrix is needed. In the case that an alternate methodology is used for calculating the cavity field, a value for the relative permittivity would still be a requirement.

Ideally, the  $\epsilon_r$  used in equation 8.5 should reflect the relative permittivity of the protein as well as the glycerol:water matrix. Under the Lorentz field approximation, the surrounding medium is viewed as continuous, which is an appropriate description for the glycerol:water matrix, and does represent an appropriate methodology for describing the effect of the surrounding bulk matrix on the observed electric field. Utilizing this approximation for the structured protein that surrounds the chromophore, however, would represent a serious oversimplification. The Lorentz approximation, therefore, should not be used in any case to describe the protein and a model that is based on a non-continuous structure would be necessary to implement when evaluating the effect of an external electric field at the site of the protein embedded chromophore. Measuring the relative permittivity of proteins is a problem that has been investigated for a long time [37] from both experimental [18] as well as from theoretical standpoints [8, 20, 28, 29], and continues to be a topic of great research interest. It is not addressed



specifically here, and only the host matrix is investigated, with knowledge that work on assignment for this quantity for proteins is a task that is necessary when moving forward with this study. Because of the thermal range in which hole-burning experiments are performed, in addition to the surrounding matrix being a solution as opposed to a pure solvent, values for the relative permittivity of the glycerol:water matrix are not available in the literature. As the mathematical approach to analyzing the experimentally obtained Stark profiles and ultimately the calculated internal molecular electric field value rests heavily on an accurate assignment of this parameter, its finding is of significant importance. Therefore, to ensure the accuracy of the relative permittivity  $\epsilon_r$  value that is used during the analysis process, it should necessarily be experimentally measured under conditions similar to those in which the hole-burning experiment is conducted.

## **8.4 Design of Capacitance Cell**

In order to perform the measurement of the low temperature relative permittivity of the matrix and provide some accuracy to the value that is used during the line-shape analysis, a capacitance cell needed to be designed and tested. The considerations of principal concern during the design phase were the size of the instrument, the magnitude of the capacitance values measured, and the mechanical strength of the instrument. The capability of the instrument to be used to study the relative permittivity of other various solutions and glasses in addition to that of the glycerol:water was also of importance influencing the design process.

These concerns required various conditions to be met by the design. First, the total size of the instrument needed to be small enough to fit within the cryostat that is used during the low temperature studies. Secondly, the instrument needed to be capable of producing capacitance values large enough to minimize measurement noise and outweigh any stray capacitance of the overall measurement system. To achieve this, the capacitor needed to possess plates with a large surface area and small plate separation. The plate separation, however, needed to remain large enough so that the dielectric solution being tested would be able to easily enter in-between the plates, regardless of viscosity, which for the case of the glycerol:water solution is relatively high. The design also needed to be capable of keeping the dielectric located between the plates consistently when the dielectric is in solution phase, during the phase transition, and also when in solid phase. It was also desired that only modest sample volumes would be required for measurement. The last concern to be addressed was the mechanical strength. The instrument needed to be fabricated out of materials that are durable enough to withstand repeated thermal cycling from 1-300 K, with the assurance that the plates would remain planar, and maintain their consistent and parallel separation.

Due to the size constraints imposed by the internal geometry of the cryostat, the Janis research Dewar, it was determined that multiple capacitors should be used to provide for an increased overall plate size, in order to enhance the measurable capacitance, while staying within the allowed geometric bounds. As displayed in figure 8.3, capacitors can be connected in either parallel or in series configurations.

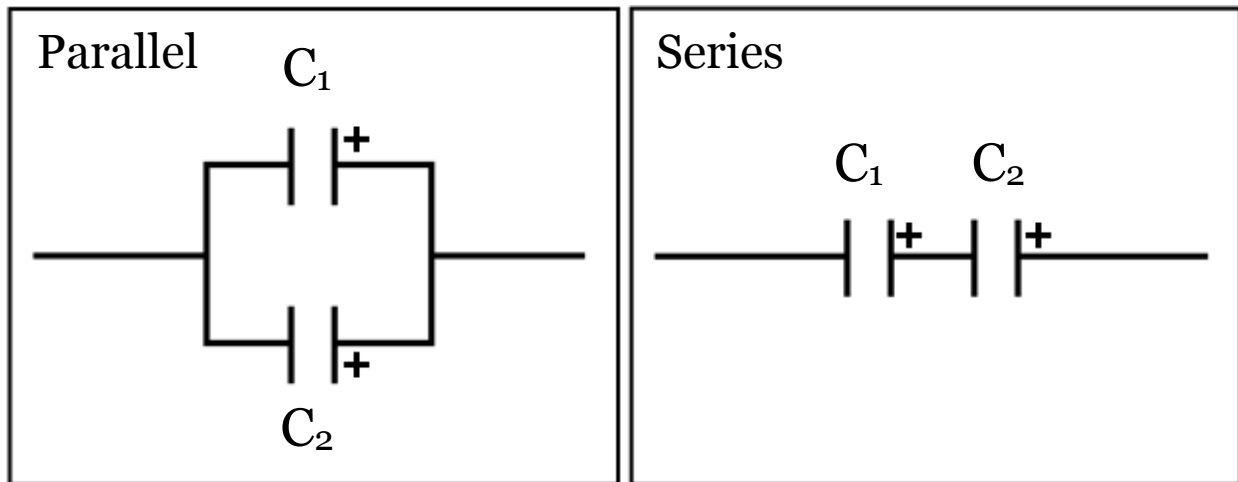


Figure 8.3: Capacitors connected in parallel and in series configurations.

When capacitors are connected in parallel, the respective halves of all of the capacitors are in direct connection to the respective poles of the voltage source. Therefore, the voltage drop across each of the capacitors that are connected in parallel, is equal to the total voltage drop  $V_T$ , across the source and can be viewed as a constant. The total charge  $Q_T$ , that is stored across all of the plates of all of the capacitors, is therefore the sum of the charges that are stored on each of the capacitors,  $Q_T = Q_1 + Q_2 + \dots + Q_n$ . Utilization of these facts along with equation 8.1, it can be observed that the total capacitance of a set of  $N$  capacitors connected in parallel, after dividing through by voltage, is equal to the sum of the capacitance of each individual capacitor.

$$\begin{aligned}
 Q_n &= C_n V_T \\
 \Rightarrow C_T &= C_1 + C_2 + \dots + C_N
 \end{aligned}
 \tag{8.6}$$

Under this connection scheme, the capacitance is additive, and results in a capacitance value that is greater than any of the individual capacitors alone. As can be observed in

the figure, this connection scheme acts to effectively increase the overall plate area of the resultant capacitor.

When capacitors are connected in series, the respective halves of all of the capacitors are in connection with each other, as opposed to the respective poles of the voltage source. Therefore, the charging current through all of the capacitors must be the same, resulting in the total charge  $Q_T$ , being the same for all capacitors, which can be viewed as a constant. The voltage drop across each capacitor is then different, with the restriction that the total voltage drop across all of the capacitors must be equal to the total voltage drop across the voltage source,  $V_T = V_1 + V_2 + \dots + V_n$ . Again, rearrangement of equation 8.1 reveals that the total capacitance of a set of  $N$  capacitors connected in series is inversely related to the sum of the capacitance of each of the individual capacitors.

$$\begin{aligned} V_n &= \frac{Q_T}{C_n} \\ \Rightarrow \frac{1}{C_T} &= \frac{1}{C_1} + \frac{1}{C_2} + \dots + \frac{1}{C_N} \end{aligned} \quad (8.7)$$

Utilizing these facts, it was determined that the most efficient way to enhance the overall capacitance of any constructed capacitor, while minimizing the overall footprint of the device, was to use a design of interlaced capacitors connected in parallel. This design scheme enhances the total capacitance value while limiting the total volume of the instrument. As can be seen in figure 8.4, which displays the charge accumulation of capacitors connected in this manner, the number of capacitive regions created is equal to one less than the total number of capacitor plates used.

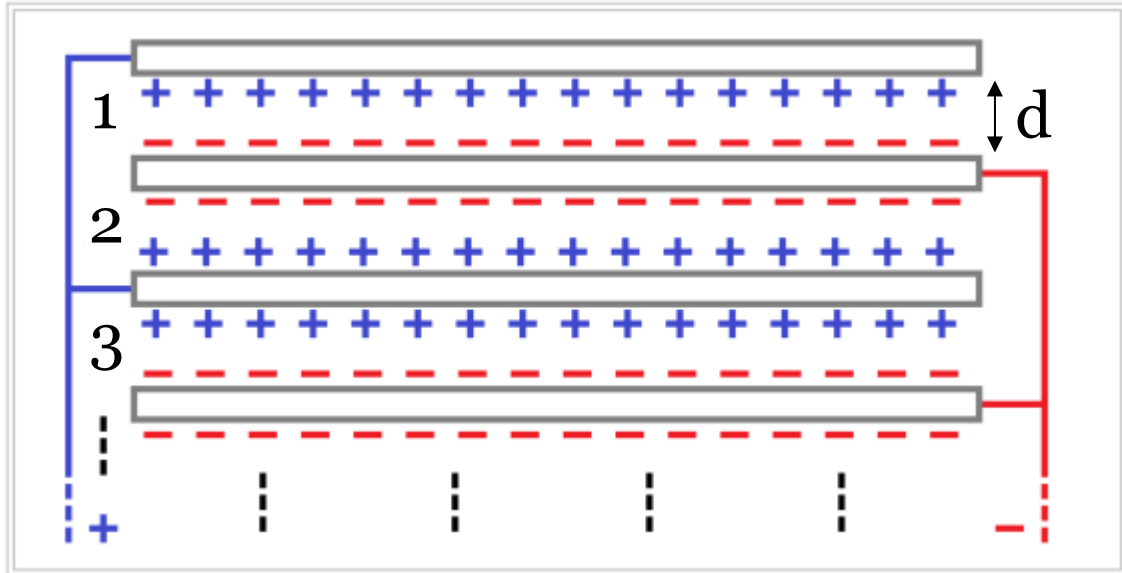


Figure 8.4: Schematic of charge accumulation on multiple parallel plate capacitors that are connected in parallel. Connection in parallel allows for additive capacitance across the capacitors. The total number of capacitors created in this arrangement is equal to the total number of plates minus one,  $\text{capacitors} = \# \text{ plates} - 1$ .

To give the instrument analytical integrity, and assure for consistency in plate area and plate separation across all of the plates to be used in constructing the device, it was determined that the components should be precision machined. The entire capacitance cell was drafted using the SolidWorks platform, the design of which was then utilized during the CNC milling process. The design resembles a three-dimensional rectangle, consisting of a steel post at each of the four longer sides, with square bases made of Teflon at either end. The capacitive region of the measurement cell is located within this rigid housing, which gives the device mechanical strength during the thermal cycling, in addition to providing for electrical connection. The capacitor consists of 46 identical machined aluminum plates that are successively stacked on the support posts, with a 90-degree rotation between each plate. The plates are separated by stacked machined washers used to provide the homogeneous inter-plate spacing. The 90-degree

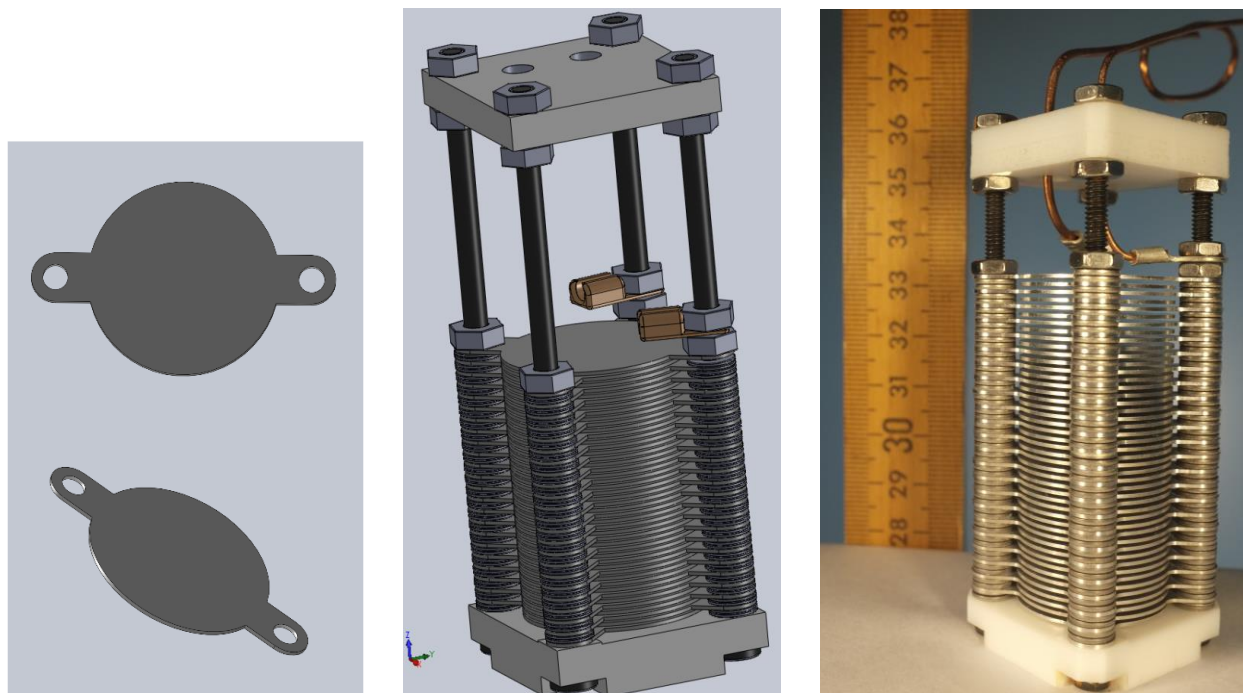


Figure 8.5: Left: SolidWorks design of an individual capacitor plate, top and tilt view. When plates are successively stacked with a 90-degree rotation the capacitor plate area of overlap is circular. Center: SolidWorks design of entire instrument, used for the CNC fabrication of the capacitor plates and the Teflon bases. Right: An image of the completed capacitance cell. The total height is 76.2 mm, containing 46 plates of diameter 22.86 mm with homogeneous spacing of 0.53 mm. This geometry yields a total capacitive area of 410.4 mm<sup>2</sup> and a theoretical capacitance in air of 310.46 pF at 298 K. The instrument sits in a Vitlab 50mL beaker for solution measurements.

rotation between each plate allows for electrical connection between all plates oriented along one of the diagonals with isolation from the plates oriented along the other diagonal. The parallel connection is achieved by connecting the support posts that are across the opposite diagonals of the capacitance cell to the respective terminals of the voltage source, with these electrical connections shown in copper color in figure 8.5. Displayed are the SolidWorks drafts of an individual capacitor plate, along with the entire capacitance cell. An image of the completed capacitance cell is also shown.

The total height of the completed capacitive cell is 76.2 mm. It contains 46 plates that are each 22.86 mm in diameter and are machined from aluminum - alloy 3003-

H14. Machined washers made of SAE 304 stainless steel provide a homogeneous spacing of 0.53 mm between all of the plates. As described in figure 8.4, the instrument then has 45 parallel plate capacitor regions, yielding a total capacitive area of 410.4 mm<sup>2</sup>. The theoretical capacitance of this device in air is 310.46 pF. The capacitance cell is placed in a Vitlab 50mL beaker that is used to hold the various dielectric samples during the solution as well as the solid phase measurements. Sample volumes of approximately 30 mL are required for measurements with this instrument.

Because the measured value of capacitance is highly dependent on the geometric properties of the capacitance cell, it is important to determine the change to the measured capacitance value that would be expected to occur during the cooling process to 1 K. Any changes to the geometry of the capacitance cell would be due to the thermal expansion properties of the various materials used in the construction. Of most importance to the measured capacitance value are changes occurring to the aluminum – alloy capacitor plates, and to the stainless steel washers that provide homogeneous spacing between the plates, as these dictate the plate area and separation distance of the capacitor, equation 8.3.

To model the expected mechanical changes to the instrument that would occur, an understanding of the thermal expansion coefficients of these two materials was necessary. For this purpose, a fourth order polynomial with material specific coefficients, as described by a NIST study [24], was used. The formula appears in table 8.1, along with the applicable coefficients for the stainless steel, of which the spacers

<b>Material Properties : Thermal Expansion</b>				
UNITS :	unitless, eg. m/m		Data Range (K) :	4 - 300
$\{(L_T - L_{293})/L_{293}\} = (a + bT + cT^2 + dT^3 + eT^4) \times 10^{-5}$				
<b>6061-T6 Aluminum</b>			<b>304 Stainless Steel</b>	
a	$-4.13 \times 10^2$		a	-295.46
b	$-3.06 \times 10^{-1}$		b	-0.40518
c	$8.80 \times 10^{-3}$		c	0.009401
d	$-1.06 \times 10^{-5}$		d	$-2.11 \times 10^{-5}$
e	0		e	$7.88 \times 10^{-8}$

Table 8.1: Coefficients and formula for modeling the temperature dependent length of 304 stainless steel and 6061-T6 aluminum alloy, based on the thermal expansion properties of the material over the temperature range 4-300 K. Formula and coefficients from NIST, reference 24.

are made, and for an aluminum alloy similar to the one used for fabrication of the capacitor plates. Here,  $L_T$  is representative of the length of the material at a given temperature  $T$ , in relation to the originally measured length  $L_{293}$ , as existing at a temperature of 293 K. Using these relationships, the expected temperature dependent contraction of the individual plate thickness as well as the surface area of the capacitor plates was calculated, in addition to the expected contraction of the thickness of the individual spacers. Based on the resultant modifications to the geometry, the expected value for the capacitance of air, which would be theoretically measured by the instrument, based on geometry alone, was calculated over the thermal range of 4-300 K.



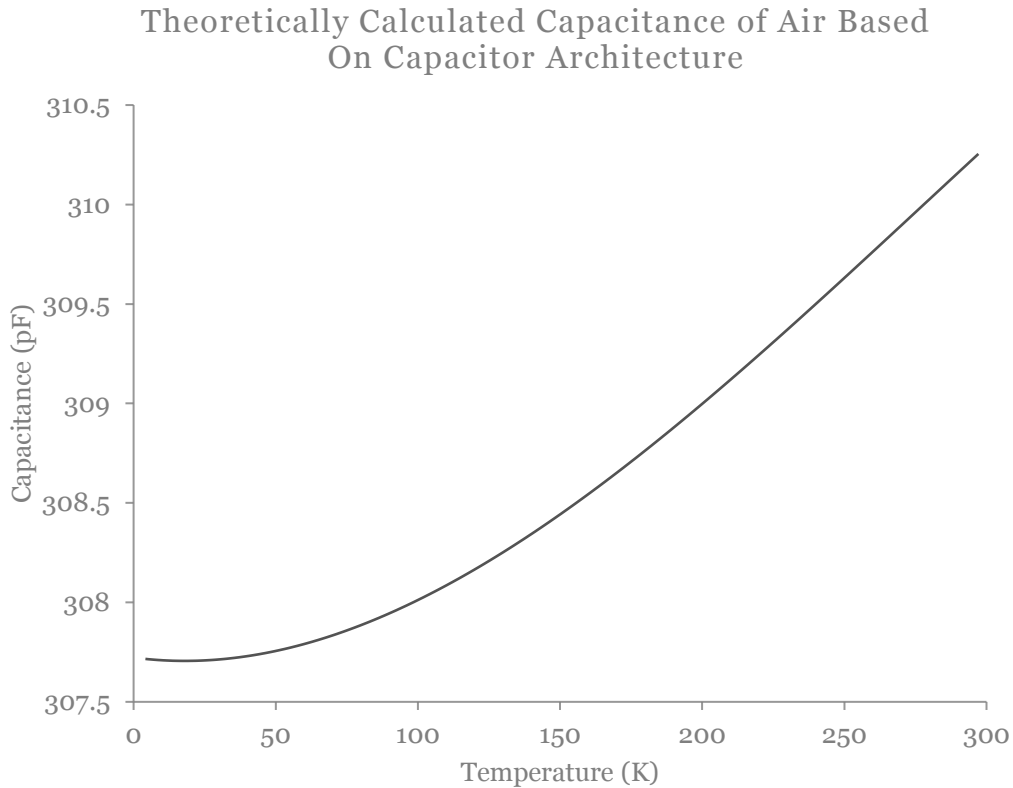


*Figure 8.6: Theoretically calculated capacitance of air based on the temperature dependent architecture of the capacitance cell.*

It was determined that the effects of the thermal expansion properties of the materials used for the construction of this instrument resulted in a negligible change to the measured capacitance over the instruments' entire useful thermal range. It was found that the measured capacitance change in pF was for the most part beyond the sensitivity of the device with the utilized measurement methodology, sections 8.5 and 8.6. This analysis has, however, provided for a correction accounting for the temperature dependent architecture of the instrument, which can be applied to the measured capacitance values based on the temperatures range in which any given measurement is made.

## 8.5 Measurement Methods

Rough capacitive measurements with the completed capacitance cell were first made using a CircuitMate CM20 Digital Capacitance Meter. These preliminary measurements served to confirm both that the capacitor was in working condition and that the measured capacitance value returned, with air as the dielectric, was in accordance with the theoretically calculated value based on the geometry of the device. This exercise also aided in guiding initial input parameters and in choosing the necessary resistive elements to be incorporated into the measurement circuit for the more rigorous approaches that were surveyed for possible use during the actual experimental process. Two methods, one DC and the other AC in nature, were initially reviewed for the capacitance and relative permittivity determination.

In addition to the constructed capacitance cell, the following is a list of the components that were used to perform the measurement of the dielectric constant of the various dielectric materials that were investigated.

Tektronix AFG3101 Waveform Generator

Tektronix TDS5052B Oscilloscope

Resistor 1K ohm 0.6W  $\pm 0.01\%$  RADIAL Metal Foil Y0062-1.0KA-ND

Resistor 820 ohm 0.25W  $\pm 5\%$  AXIAL Carbon Film CF14JT820R

POMONA BNC Coaxial Cable 2249-C

Cryogenic Service Wire KAPTON 24 AWG - TYP35-15

Janis 9VSRD-SVT-22 Research Dewar

Lakeshore 331 Temperature Controller

LakeShore DT-670-SD-1.4D Temperature Sensor

### 8.5.1 DC Approach-RC Time Constant

Measurement of the capacitance of a capacitor can be performed in a closed circuit, consisting of a power supply or voltage source  $V_s$ , a mechanical switch, a resistor  $R$  of known resistance, and the capacitive element  $C$ , all of which are connected in series. An example of this simple circuit, known as an RC circuit, is shown in figure 8.7. The switches are used to initiate the charging or discharging processes. If a DC power supply is used, the closing and opening of the switches necessary for the charging and discharging of the capacitor can be simulated if a square-wave potential can be supplied by the power supply. In this case, the switches can be removed from the circuit with the following derivations still remaining consistent. In order to describe the various time constants defining the behavior of the RC circuit, which are of necessity in determining the value of capacitance of the capacitor, it is beneficial to look at the charging and discharging of the capacitive element separately.

According to Kirchhoff's voltage law, the sum of all of the voltages existing around a closed loop must be equal to zero. For the circuit describing the charging of the capacitor, top of figure 8.7, since the total voltage differential within the circuit cannot exceed the voltage differential of the power supply that is used to charge the circuit, this requires that the voltage across the power supply  $V_s$ , be equal and opposite to the sum of the voltage  $V_R$  across the resistor  $R$ , and the voltage  $V_C$  across the capacitor  $C$ .

$$V_S - V_R - V_C = 0 \quad (8.8)$$

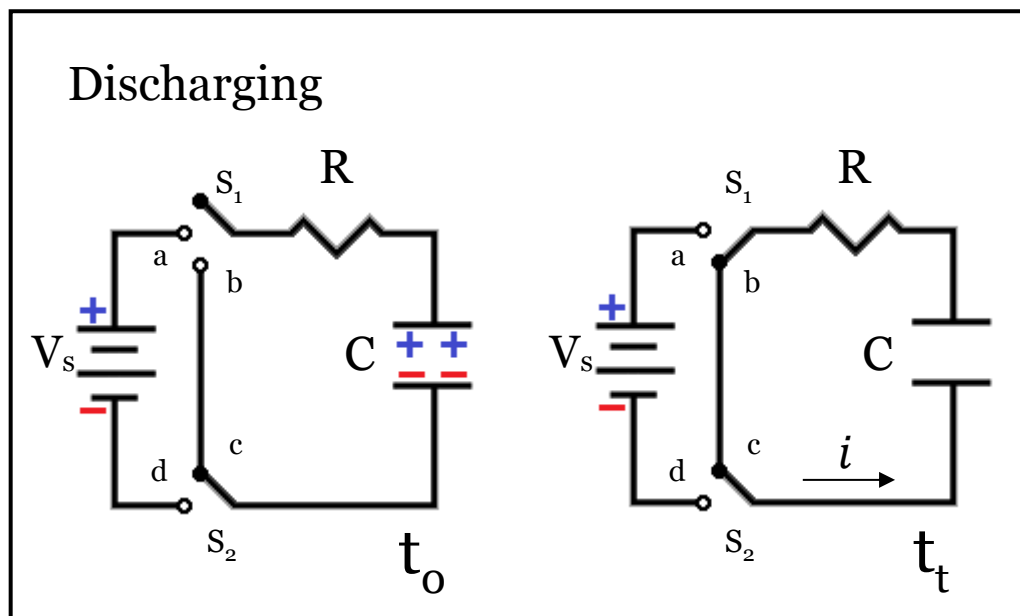
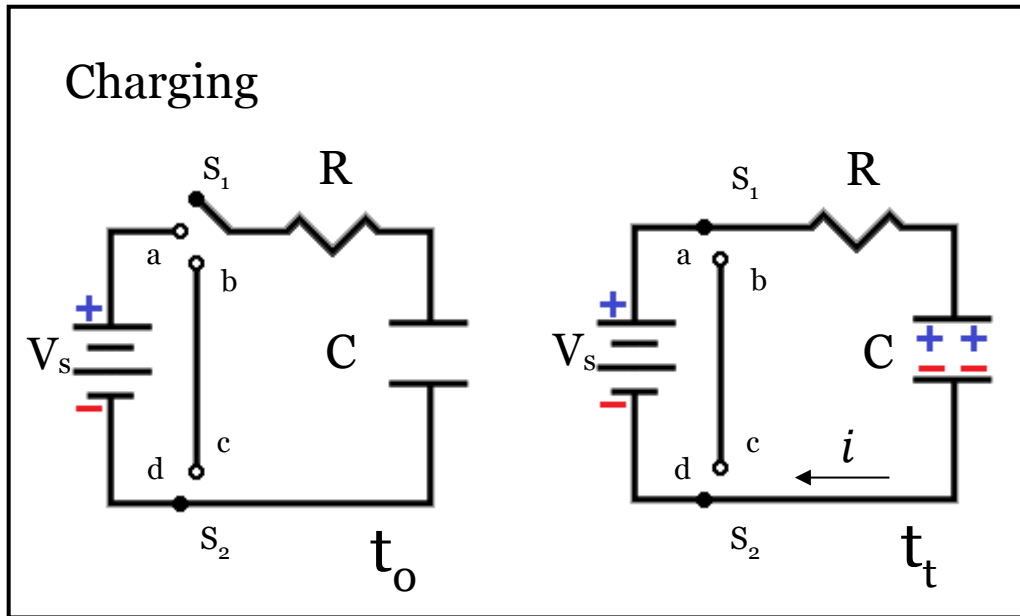


Figure 8.7: RC circuit used for the charging and discharging of a capacitor. Top: Initially at time  $t_0$ , the switch  $S_1$  is open. As soon as switch  $S_1$  is closed, current begins to flow in the direction indicated and the capacitor continues to charge until the voltage across the capacitor is equal to that of the power supply, at time  $t_t$ . Bottom: Initially at time  $t_0$ , the switch  $S_2$  is positioned at point c, and switch  $S_1$  is open, effectively removing the power supply from the circuit. When switch  $S_1$  is positioned at point b, current begins to flow in the indicated direction and the capacitor continues to discharge until the voltage across the capacitor is zero at time  $t_t$ .

In the figure,  $V_S$  is representative of the potential of the power supply in volts. The voltage across the resistor  $V_R$ , is found using Ohm's law, which states that the voltage difference between any two points in a conductor is directly proportional to the current  $i$  in amperes through, and the resistance  $R$  in ohms of the conductive path between the two points. Utilizing the fact that current is a measure of the flow of charge  $q$ , Ohm's law can be written in the following form.

$$V = iR = \frac{dq}{dt}R \quad (8.9)$$

Upon rearrangement of equation 8.1, it can be seen that the voltage across the capacitor  $V_C$ , is equal to the charge  $q$  in coulombs on the capacitor, divided by its capacitance  $C$  in farads. Kirchhoff's voltage law for this charging RC circuit is then as follows.

$$V_S - \frac{dq}{dt}R - \frac{q}{C} = 0 \quad (8.10)$$

Initially, at time zero  $t_0$ , before the switch  $S_1$  is moved to position a, there exists no current flow in the circuit and the capacitor has no charge accumulation or voltage differential between the plates. As soon as the switch is moved to position a, the circuit is a closed loop and current begins to flow in the direction indicated within the figure. Charges will continue to accumulate on the plates of the capacitor with the voltage differential between the plates continuing to increase until a value that is equal to the potential difference of the power supply is reached, at which time the capacitor is fully charged.

To determine the quantity of charge  $q$  residing on, or the voltage differential  $V_C$  between the plates of the capacitor at any given time  $t$  during the charging process,

equation 8.10 must be changed to a usable form. The second term is added to both sides of the equation. The resistance and time components are then moved to the left hand side, with all of the other portions of the left hand side being moved to the right hand side, to yield the following.

$$\int_0^t \frac{dt}{R} = \int_0^q \frac{dq}{V_s - \frac{q}{C}} \quad (8.11)$$

Integration bounds have been added to reflect the accumulation of charge  $q$ , on the plates of the capacitor, as the capacitor charges in time. Integration of the left hand side is trivial, with the integration of right hand side performed using a u-substitution for the denominator.

$$\text{LHS:} \quad \int_0^t \frac{dt}{R} \Rightarrow \frac{t}{R} \quad (8.12)$$

$$\text{RHS:} \quad \text{Let} \quad U = V_s - \frac{q}{C}$$

$$\frac{dU}{dq} = -\frac{1}{C} \rightarrow dq = -CdU$$

$$\int \frac{-CdU}{U} \rightarrow -C \ln \left( V_s - \frac{q}{C} \right) \Big|_0^q$$

$$\Rightarrow -C \left( \ln \left( V_s - \frac{q}{C} \right) - \ln(V_s) \right) \quad (8.13)$$

The integrated forms of the left hand side, equation 8.12, and the right hand side, equation 8.13, are then equated and the  $-C$  is moved to the left hand side. Applying the

rules of the natural log, the right hand side is written in its fractionalized form. To both sides the exponential function is then applied to remove the natural log to yield the following.

$$e^{-\frac{t}{RC}} = \frac{(V_s - \frac{q}{C})}{(V_s)} \quad (8.14)$$

This equation is then rearranged such that the exponential term and the terms describing the voltage across the power supply appear on the same side, with the  $\frac{q}{C}$  on the opposite. Both sides are then multiplied by the capacitance value to solve solely for the time dependent charge on the capacitor. Since the fully charged capacitor will have a potential difference between its plates equal to that of the power supply, using the identity of equation 8.1, allows for the total charge  $Q$  stored on the capacitor to be found.

$$q = CV_s \left(1 - e^{-\frac{t}{RC}}\right) \Rightarrow q = Q \left(1 - e^{-\frac{t}{RC}}\right) \quad (8.15)$$

This now provides for a relation between the quantity of charge residing on the capacitor at any given time during the charging process  $q$ , to the total amount of charge that can be stored on the capacitor. Because charge is not a directly measurable quantity, if both sides of this equation are divided by the capacitance, the usable form of the equation, which indicates the magnitude of the voltage across the capacitor  $V_C$  at any given time  $t$  during the charging process in relation to the potential difference of the power supply  $V_s$ , the resistance  $R$  of the resistive element, and the capacitance of the capacitor  $C$  is finally found.

$$V_C = V_s \left(1 - e^{-\frac{t}{RC}}\right) \quad (8.16)$$

When a capacitor is fully charged, the electrical potential energy it contains is stored in the form of an electric field. In order to utilize this stored energy, the capacitor can be discharged. Assuming that the capacitor was just charged by the method described above, the potential difference between the plates of the capacitor  $V_C$  is equivalent to the potential of the power supply  $V_S$  that was used to charge the capacitor. The appropriate circuit to discharge this capacitor is shown at the bottom of figure 8.7. To discharge this capacitor, switch  $S_1$  is first opened, and switch  $S_2$  is moved from position d to position c. This serves to disconnect the power supply from the circuit. At time  $t_0$  the entire voltage drop of the capacitor will exist across switch  $S_1$ , as there is no current flow through the resistor  $R$ . As soon as this switch  $S_1$  is moved to position b, current will begin to flow in the direction indicated in the figure and the capacitor will begin to discharge through the resistor.

As with the case of charging the capacitor, according to Kirchhoff's voltage law the sum of all of the voltages existing around this new closed loop must be equal to zero. For the case of the discharging circuit as shown, this implies the following equality be satisfied.

$$V_C + V_R = 0 \quad (8.17)$$

In order to translate this equation to a usable form that describes the quantity of charge residing on, or the voltage differential between the plates of the capacitor at any given time during the discharge process, the same identities discussed above regarding Ohm's law, the current and equation 8.1, are used to rewrite these two voltages with the following substitution of applicable variables.



$$\frac{q}{C} + \left(\frac{dq}{dt}\right)R = 0 \quad (8.18)$$

As before this equation is rearranged to separate the time and charge terms and the appropriate integration bounds are chosen. In this situation, at time  $t_0$  the plates of the capacitor already possess a maximum total charge accumulation of  $Q$  related to the capacitance and original charging voltage of the capacitor. The quantity of charge residing on the plates at some later time  $t$ , is then described by  $q$ .

$$\begin{aligned} -\int_0^t \frac{dt}{RC} &= \int_Q^q \frac{dq}{q} \\ \Rightarrow -\frac{t}{RC} &= \ln\left(\frac{q}{Q}\right) \end{aligned} \quad (8.19)$$

To eliminate the natural log, the exponential function is applied to both sides of the equation and the time-dependent quantity of charge residing on the plates is isolated.

$$q = Q \left( e^{-\frac{t}{RC}} \right) \quad (8.20)$$

To view the voltage form of this equation, both sides of 8.20 can now be divided by the capacitance  $C$  of the capacitor, and again by use of the identity of equation 8.1, the formula is converted to a form which describes the time-dependent voltage differential  $V_C$  across the plates of the capacitor.

$$V_C = V_S \left( e^{-\frac{t}{RC}} \right) \quad (8.21)$$

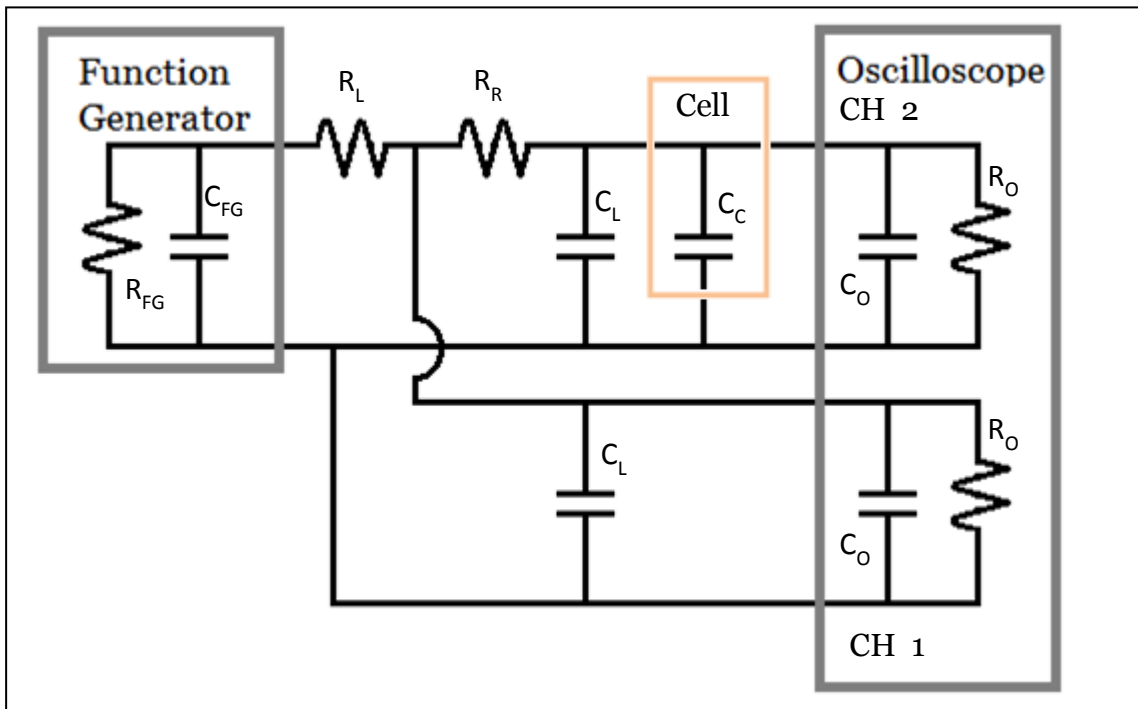
With the relationships for the time-dependent voltage across the capacitor during both the charging and the discharging of a capacitor now established, a discussion of their application to the determination of the relative permittivity of a material can now proceed. Because the potential difference between the plates of a capacitor depends entirely on the quantity of charge stored on the plates, charge must first move to the plates before a voltage is established. Therefore, current must lead the voltage, when the potential difference between plates either builds to a maximum during a charging event or decreases to a minimum during a discharging event. In an RC circuit, the time constant  $\tau$  is a measure of the temporal lag in the charging or discharging of a capacitor across a resistor by a power supply. The time constant is equal to the resistance times the capacitance of the circuit.

$$\tau = RC \quad (8.22)$$

At five time constants,  $5\tau$ , the circuit comes to within X % of the steady state condition ( $X = e^{-5} \cong 0.7\%$ ). At one time constant,  $\tau = RC$ , and when used in conjunction with the relationship between voltage and time as established according to equation 8.16 for a charging capacitor or equation 8.21 for a discharging capacitor, allows for calculation of the desired quantity. If the time varying voltage across the capacitor can be measured and the resistance value is known, the time constant can be found and the capacitance of the capacitor can be calculated. Using this calculated capacitance, an application of equation 8.3 will yield the relative permittivity of the dielectric material contained between the plates of the capacitor.

To put this process of determining capacitance by measurement of the RC time constant to the test, the first trials with the capacitor utilized ambient air at a temperature of 293 K and a humidity of 12-16% as the dielectric medium. The initial trials were performed as benchtop measurements without use of the Janis research Dewar. These trials were conducted periodically over a three-day period to monitor the consistency of the determined value of the measurement. The equipment used in addition to the constructed capacitance cell during these tests appears in the list of the components at the beginning of section 8.5. During these trials, the reference resistor used was the 820 ohm 0.25W  $\pm 5\%$  AXIAL Carbon Film CF14JT820R resistor. The setup used for both the charging and discharging of the capacitor appears at the bottom of figure 8.8. Because the function generator and the oscilloscope possess a self-capacitance ( $C_{FG}$ ,  $C_O$ ) and self-resistance ( $R_{FG}$ ,  $R_O$ ), and the electrical leads required for connection of the various components in the circuit also possess a self-capacitance ( $C_L$ ) and self-resistance ( $R_L$ ), these need to be accounted for in the analysis if the capacitance of the measurement cell ( $C_C$ ) is to be accurately determined. The equivalent circuit accounting for these capacitive and resistive elements in the closed circuit are displayed at the top of figure 8.8.

## Circuit



## Setup

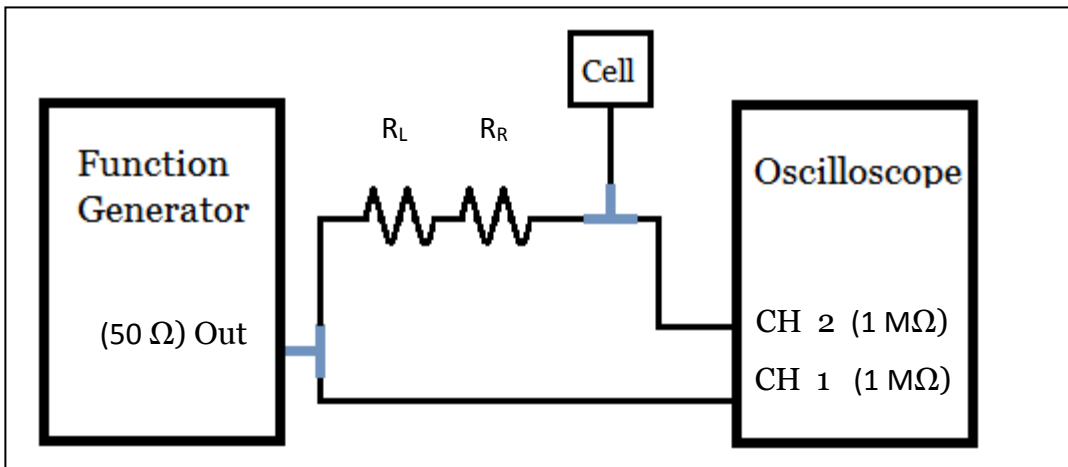
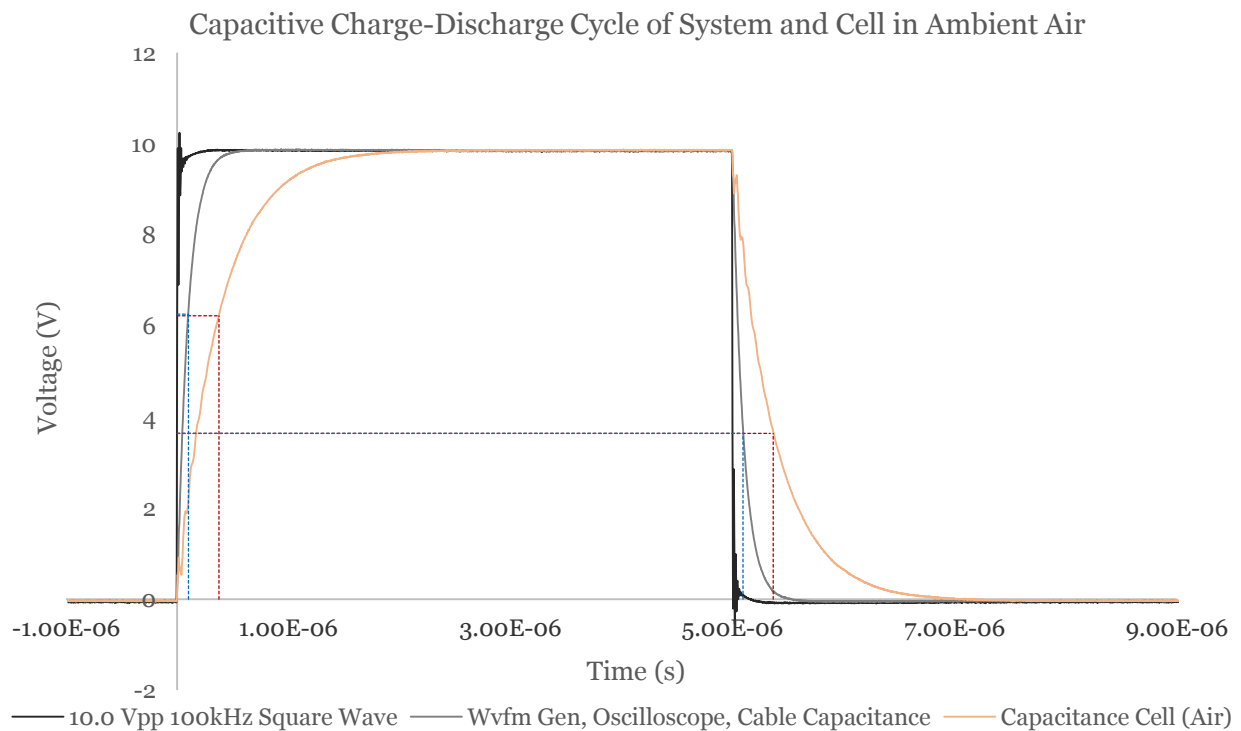


Figure 8.8: Top: Complete circuit for the measurement of the RC time constant indicating the additional capacitive and resistive contributions of the function generator  $C_{FG}$  and  $R_{FG}$ , and oscilloscope  $C_O$  and  $R_O$ , and the additional capacitive contribution  $C_L$  of the BNC and other electrical leads used for connection of the various components. The resistance values for these instruments were verified by measurement and are indicated in the bottom schematic. The reference resistor is shown as  $R_R$ , the resistance of the leads is  $R_L$ , and the capacitance of the developed measurement cell as  $C_C$ . Bottom: Experimental setup used for the measurement of the RC time constant. During the initial benchtop trials with ambient air as the dielectric medium, an 820 ohm 0.25W  $\pm 5\%$  AXIAL Carbon Film CF14JT820R was used for the reference resistor  $R_R$ . Representative example data appears in figure 8.9. For all remaining trials, the 1K ohm 0.6W 0.01% RADIAL Y0062-1.0KA-ND was used as the reference resistor.

No switches are included in the closed loop circuit displayed in the schematic above. Rather than switches, the function generator was set to deliver a square-wave signal. The square-wave signal acts as a pseudo DC signal for the measurement as it ideally is akin to switching a true DC signal on and off by means of a switch in a repeated manor. For these trials, the signal used was 10.0 Vpp (volts peak to peak) with a 5.0 V offset and a frequency of 100 kHz. The oscilloscope was set to signal averaging and the charging and the discharging of the capacitor under these conditions was recorded. The reference resistor used was measured and was found to possess a resistance of ~824-839 ohm. This variability of the reference resistor was taken into account during



*Figure 8.9: Representative trace of system and cell capacitive charging and discharging in ambient air. Square-wave excitation 10.0 Vpp, 5.0V offset, 100kHz; using an 820-ohm reference resistor before the capacitance measurement cell. The dotted traces indicate the measured voltage and time when  $\tau = RC$ .*

the analysis of the time constant, and the relative permittivity. A representative trace from these trials appears in figure 8.9. All trials looked at the charging as well as the discharging cycle of the capacitor. Effectively allowing two measurements to be made, namely the charging time constant as well as the discharging time constant.

Because no function generator generates a perfect square-wave with a slope of infinity, it is necessary to record the actual pulse that is being delivered to the circuit. This is the actual square-wave that used to charge and discharge the capacitor, and is shown in black. To understand the capacitance contributions to the circuit from the function generator, oscilloscope and the electrical leads, from here on described as the system, a measurement must be conducted first with the entire circuit except for the capacitance measurement cell. This trace appears in grey. Lastly, the capacitance measurement cell, from here on described as the cell, is included into the circuit and the measurement performed again. This trace appears in pink. To determine the capacitive contribution of just the capacitance measurement cell, the time constants need to be analyzed for all three traces and the difference determined. When this is done, it is possible to calculate only the capacitance of the measurement cell and the relative permittivity of the dielectric medium of the capacitor. The dotted lines indicate the time constants for the respective traces. A summary of the results from the analysis of this set of trials, all of which yielded traces similar to that shown in the figure, appears in table 8.2 in section 8.5.3, along with comments regarding use of this particular experimental approach for determination of the relative permittivity.

## 8.5.2 AC Approach-Capacitive Reactance

Similar to the to the previous case whereby the capacitance of a capacitor could be measured if the capacitive element  $C$  was connected in series with a resistor  $R$  of known resistance and a power supply generating a DC signal, so too will this circuit allow the capacitance of a capacitor to be measured if the power supply instead generates an AC signal. An AC signal is defined by the situation where the polarity of the applied voltage or the direction of the current in a circuit is continually switched at a given frequency. Because the voltage that is output by the power supply continually alternates between positive and negative polarity, the current in the circuit follows an alternating pattern, and the capacitor will continuously charge and discharge. The direction of the potential difference established across the plates of the capacitor, and thus the direction of the electric field that is stored between the plates, will also switch according to the cycle of the applied voltage.

Most simply, in a purely resistive AC circuit, the voltage and the current possess the same phase and can be modeled by a sine wave. In a purely capacitive AC circuit, the current leads the voltage by a phase of 90 degrees and the current is modeled by a cosine wave and the voltage is modeled by a sine wave. In a circuit that has both resistive and capacitive components, as is the case for the circuit used in this measurement, the current will again necessarily lead the voltage as charges need to be present on the plates of the capacitor before a voltage differential can develop across the plates. Therefore, a phase shift will be present between the input and output voltages of the circuit as well as between the current and the voltage in the circuit. The magnitude of

the observed phase shifts is dependent upon the magnitude of the resistance and the magnitude of the capacitance in the circuit, in addition to the frequency of the AC signal that is being applied.

A complete description of the fundamentals of AC circuit theory is well beyond the scope of this document. What is presented here is a brief introduction to some of the various quantities that arise in RC circuits when driven with time varying signals, their underlying relationships, and a few of the pertinent equations used in the analysis process for the determination of the capacitance of an unknown capacitor. The curious reader is encouraged to further explore references 1 and 11 for additional information regarding this topic, and reference 35, from which the following analysis method was most basically described. For this discussion, the circuit displayed at the top of figure 8.7, can again be used, with the understanding that the switch will always remain closed and that the power supply will generate an AC signal. Kirchhoff's voltage law dictates that the sum of the voltages existing around this closed loop must be equal to zero, and equation 8.8 will again be used as a starting point. With slight rearrangement, the time varying voltage of the power supply is observed to be equal to the time varying voltage across the resistor and the capacitor.

$$V_S = V_R + V_C \quad (8.23)$$

The voltage across the resistor  $V_R$ , can again be described by Ohm's law, equation 8.9. In an AC circuit, the voltage across the capacitor  $V_C$ , although still equal to the ratio of the charge  $Q$ , stored on the plates of the capacitor to the value of the capacitance  $C$ , equation 8.1, is instead described by the capacitive reactance. The capacitive reactance



$X_C$ , describes the ratio between the magnitude of the voltage, and the magnitude of the current in a capacitor, and provides a measure of the capacitors' opposition towards changes in current and voltage. This opposition arises from the development of the electric field that is stored in the capacitor, which resists changes to voltage and current in the circuit. Similar to resistance, the unit of capacitive reactance is the ohm.

$$X_C = \frac{1}{j2\pi fC} = \frac{1}{j\omega C} \quad (8.24)$$

Because current is denoted with  $i$ , in the equation above,  $j$ , serves as the imaginary number, namely  $j = \sqrt{-1}$ . The frequency of the AC signal, in hertz is described by  $f$ , and the value of the capacitance is  $C$  with the units of farad. The frequency is generally combined with the  $2\pi$  so that the frequency term is instead represented as the angular frequency  $\omega$ . The capacitive reactance acts as a scalar in the voltage to current relationship, similar to that of a resistor. Inserting these identities into equation 8.23, results in the following formulation for the voltages within the circuit.

$$V_S = iR + iX_C = i(R + X_C) = iZ \quad (8.25)$$

As opposed to performing the substitution for the current and carrying out the necessary integration of the various terms as was done in the case of the DC power supply, a process which does yield very usable formulations for the time varying voltages and current at different points in the circuit, instead an alternate method is followed so that a new quantity can be defined. By factoring out the current  $i$ , the total effective opposition to current flow in the circuit is instead grouped into a single term that is

given the name impedance  $Z$ . This action results in the establishment of a more generalized formulation of Ohm's law that takes into account time varying signals and accounts for the inclusion of components into a circuit that possess a reactance. The inclusion of  $j$  in the formula for capacitive reactance, equation 8.24, means that capacitive reactance is a quantity that exists along the imaginary axis. Therefore, the impedance consists of a real component, the resistance, and an imaginary component, the reactance, which can be capacitive or inductive in nature. Here only the capacitive form of the reactance will be of importance.

$$Z = R + X_C = Re(Z) + Im(Z) \quad (8.26)$$

The impedance is a complex number that is obtained by orienting the resistance (abscissa) and the reactance (ordinate) along their respective axes of the complex plane. The process allows for the magnitude of the impedance  $|Z|$ , to be found by use of the Pythagorean theorem, and the angle of impedance  $\varphi$ , to be found using basic trigonometric relationships.

$$|Z| = \sqrt{R^2 + X_C^2} \quad (8.27)$$

$$\varphi = \tan^{-1} \left( \frac{X_C}{R} \right) \quad (8.28)$$

With the basic equation and relationships regarding the behavior of resistors and capacitors in AC circuits defined, the pertinent formulas used for the analysis of this circuit can be described. In this circuit, the power supply, the resistor, and the capacitor are connected in series. This connection scheme is similar to a voltage divider, where

the second in series resistor is replaced with a capacitor. In actuality, this RC circuit behaves similar to a passive RC low pass filter. Below is the standard formulation for a voltage divider where the amplitude of the input voltage is represented by  $V_1$ , the amplitude of the output voltage is represented by  $V_2$ , and the two in series resistors are represented as resistor one  $R_1$  and resistor two  $R_2$ . In the case that the second resistor  $R_2$  is replaced with a capacitor, the impedance  $Z_C$  of the capacitor can be substituted into the relation.

$$V_2 = \left( \frac{R_2}{R_1 + R_2} \right) V_1 \quad \text{since: } R_2 = Z_C \quad \rightarrow \quad V_2 = \left( \frac{Z_C}{R_1 + Z_C} \right) V_1 \quad (8.29)$$

Upon rearrangement of the second equation, the impedance of the capacitor can be defined in terms of the resistor  $R_1$ , which can be re-defined as the reference resistor  $R_{ref}$ , and in terms of the measured amplitudes of the input and output voltages  $V_1$  and  $V_2$ .

$$Z_C = \left( \frac{V_2}{V_1 - V_2} \right) R_{ref} \quad (8.30)$$

In order to use the measured voltages, the known resistance, and the calculated impedance to find the capacitance value of the unknown capacitor, a few steps must be taken. The magnitude of the impedance in equation 8.27, was found by taking the square root of the impedance squared, equation 8.26. By using the same mathematical operation on equation 8.30, and switching from rectangular to polar form to describe the variables, which, requires then usage of the complex conjugate, or more simply  $|Z| = \sqrt{ZZ^*}$ , the magnitude of the impedance for the capacitor in the RC circuit used during this investigation can be formulated as follows.

$$|Z_C| = \frac{V_2 R_{ref}}{\sqrt{V_1^2 - 2V_1 V_2 \cos \theta + V_2^2}} \quad (8.31)$$

Here  $|Z_C|$  is the magnitude of the impedance of the capacitor,  $R_{ref}$  is the magnitude of the reference resistor in the circuit. The amplitude of the output voltage of the power supply is  $V_1$  and the amplitude of the voltage across the capacitor is  $V_2$ . The phase difference between the maxima of the two measured voltages is represented by the phase shift  $\theta$ . The cosine of the phase shift appearing in the mixed term captures only the real portion of the voltages. With the impedance of the capacitor defined this way, the angle of impedance  $\angle_Z$  can then be found by taking the difference of the originally determined phase shift of the voltages, and the polar form of the capacitive reactance and the resistance written in terms of voltages.

$$(\angle_Z) = \theta - \tan^{-1} \left( \frac{-V_2 \sin \theta}{V_1 - V_2 \cos \theta} \right) \quad (8.32)$$

When the two previous equations, defining the magnitude and angle of impedance are inserted into the formula for the complex impedance in polar form appearing below, the total impedance of the capacitor can be calculated.

$$Z_C = |Z_C| \cos(\angle_Z) + j |Z| \sin(\angle_Z) \quad (8.33)$$

The necessary relations required for the determination of the capacitance of the capacitor are now established. Since both equation 8.26 and equation 8.33 describe the impedance, they are first equated to one another with the understanding that it is only the impedance of the capacitor that is being evaluated. Next, the real component of the impedance, reflecting the resistance, is linked to the cosine term, and the imaginary

component of the impedance, reflecting the reactance, is linked to the sine term. Pulling these equations apart and performing the necessary rearrangement finally allows for the equivalent series resistance of the impedance  $R_{ESR}$ , and the capacitance  $C$ , of the unknown capacitor to be found. These results appear in the following two relations:

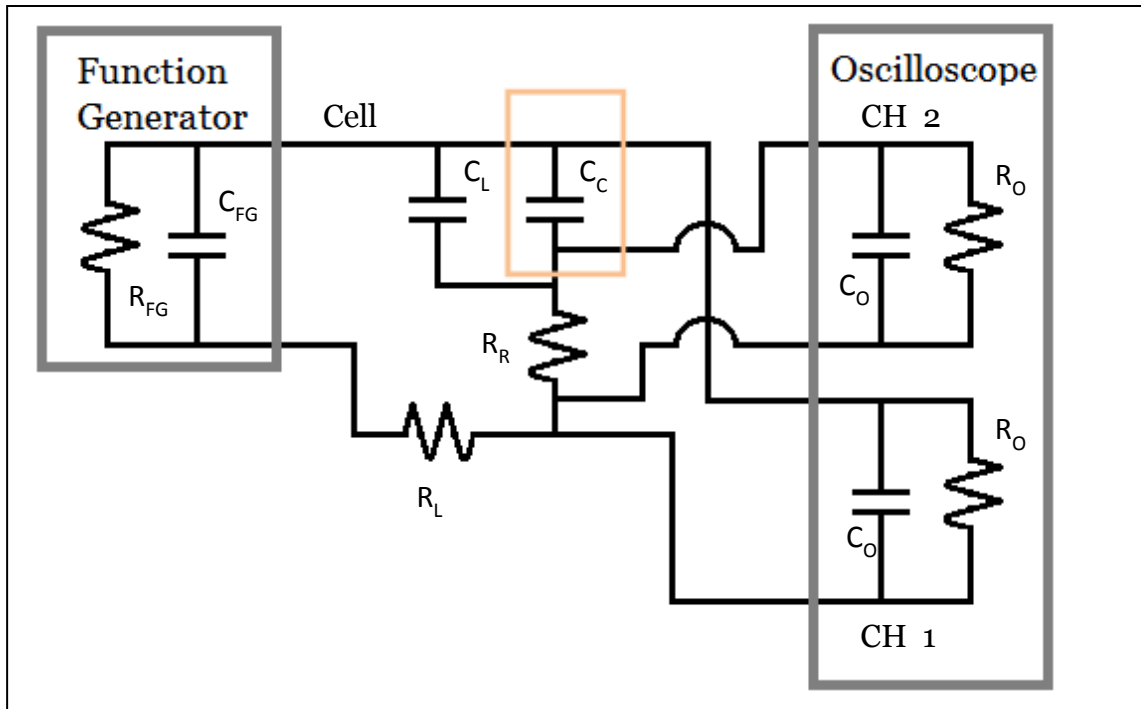
$$R_{ESR} = Z \cos(\phi_Z) \quad (8.34)$$

$$C = \frac{-1}{\omega |Z| \sin(\phi_Z)} \quad (8.35)$$

The process of measuring the input voltage, and the voltage across the capacitor, to calculate the magnitude and phase angle of the impedance of the AC charge and discharge cycle can thus be used for a frequency dependent determination of the capacitance.

To put this process of determining capacitance by measurement of the capacitive reactance to test, the trials with the capacitor were again conducted with ambient air at a temperature of 293 K and a humidity of 12-16%, as the dielectric medium. The trials were also performed as benchtop measurements without use of the Janis research Dewar, and were conducted immediately following the DC-trials during the same three-day period, with the same equipment being used and only the circuit configuration and the output signal of the function generator varied accordingly. The setup used for these AC-trials is depicted at the bottom of figure 8.10, with the equivalent circuit displaying the additional capacitive and resistive contributions of the various components of the circuit appearing at the top of the figure. The same issues as previously discussed are

## Circuit



## Setup

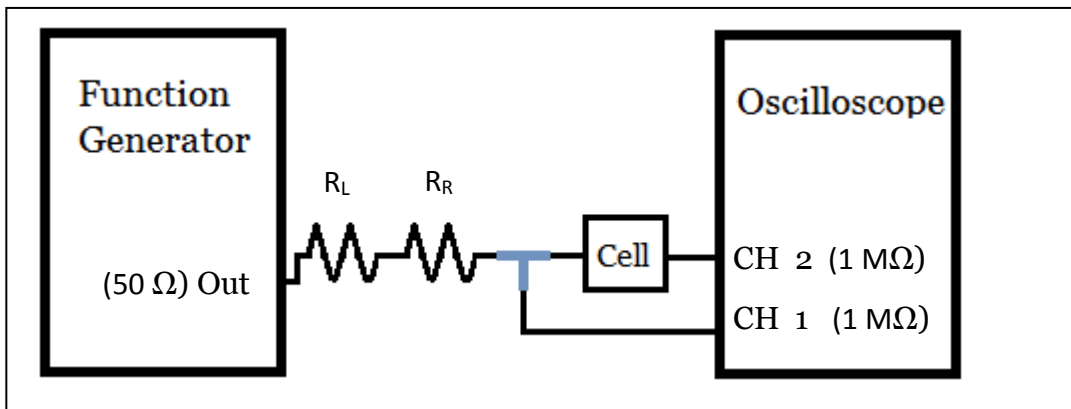
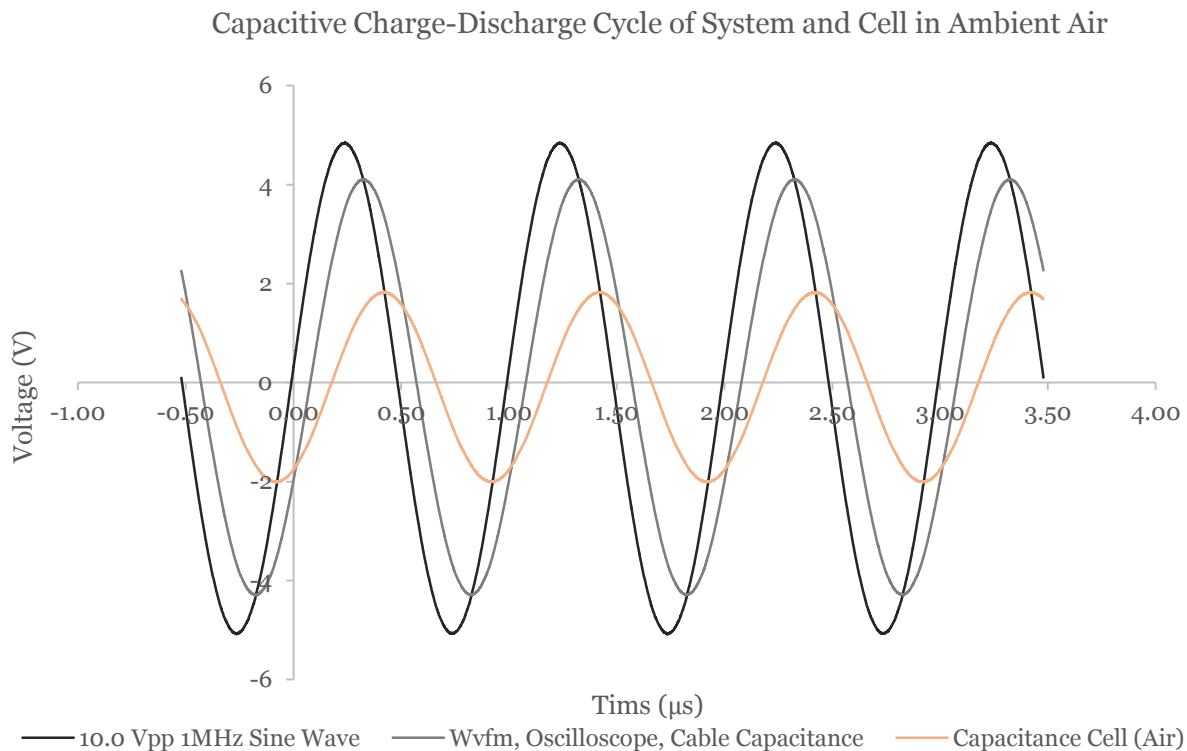


Figure 8.10: Top: Complete circuit for the measurement of the capacitive reactance indicating the additional capacitive and resistive contributions of the function generator  $C_{FG}$  and  $R_{FG}$ , and oscilloscope  $C_O$  and  $R_O$ , and the additional capacitive contribution  $C_L$  of the BNC and other electrical leads used for connection of the various components. The resistance values for these instruments were verified by measurement and are indicated in the bottom schematic. The reference resistor is shown as  $R_R$ , the resistance of the leads is  $R_L$ , and the capacitance of the developed measurement cell as  $C_C$ . Bottom: Experimental setup used for the, measurement of the capacitive reactance. During the benchtop trials with ambient air as the dielectric medium, an 820 ohm 0.25W  $\pm 5\%$  AXIAL Carbon Film CF14JT820R was used for the reference resistor  $R_R$ .

again present in this setup and again need to be accounted for during the measurement and analysis process.

For these trials, the function generator was set to deliver a sinusoidal signal of 10.0 Vpp at a frequency of 1 MHz. The oscilloscope was set to signal averaging and the charging and the discharging of the capacitor under these conditions was recorded. As the capacitive reactance measurement requires knowledge of the differential of the amplitude of the measured voltage and the phase shift of the AC signal, again multiple traces needed to be acquired for the measurement. A representative trace from this set of experiments appears in figure 8.11. Here the AC signal produced by the function



*Figure 8.11: Representative trace of system and cell capacitive charging and discharging in ambient air. Sine-wave excitation of 10.0 Vpp, 1MHz; using an 820-ohm reference resistor before the capacitance cell.*

generator appears in black. To determine the capacitance contribution to the circuit from the system, again a measurement must be conducted first with the entire circuit except for the capacitance measurement cell. The trace accounting for this capacitance appears in grey. The final measurement is that of the capacitance measurement cell, included into the circuit. This trace is displayed in pink. The capacitive contribution of just the capacitance measurement cell is determined by performing the necessary calculations of the capacitive reactance between three various signals. When this is done, the capacitance of the measurement cell can be calculated along with the relative permittivity of the dielectric medium of the capacitor.

All trials yielded traces similar to that shown in figure 8.11, with a summary of the results from this methodology appearing in table 8.2 of the next section. Comments regarding utilization of this experimental approach for determination of the relative permittivity are also discussed.

### **8.5.3 Comparison of Methods**

Based strictly on the geometry of the developed capacitance measurement cell, a value of 310.46 pF is the theoretically expected capacitance using air as a dielectric at 298 K. These investigations were conducted at a temperature of 293K, and this minor thermal differential is not expected to cause measurable deviation from the expected theoretical capacitance value, specifically with regards to the sensitivity of this instrument and the analysis process being used. The sensitivity of this instrument is discussed further in the following section. When relating the measured value of the relative permittivity of air to



values that are found in the literature, as a means to comment on the efficacy of this particular measurement, the effects of the presence of humidity during the trials is not known, as humidity is not a parameter that is always stated in other studies on the topic. They will, however, be assumed to be negligible.

The results of the various trials using both the DC-approach of measuring the RC time constant and the AC-approach of measuring the capacitive reactance appear in table 8.2. The presented values reflect a summary of this initial set of benchtop experiments. It can be observed that measurement of the RC time constant for the charging and the discharging of the capacitor results in values for the relative permittivity that rest on either side of the literature value. Taking the average of these two measurements then yield a relative permittivity value that is aligned fairly close to the literature value. When the capacitive reactance is instead measured, it can

<b>Capacitance Cell Measured Dielectric Constants:</b>						
<b>Dielectric Material</b>	<b>Method</b>	<b>Theoretical</b> (capacitor geometry)		<b>Measured</b>		<b>% Error</b>
		<b>C (pF)</b>	<b><math>\epsilon_r</math></b>	<b>C (pF)</b>	<b><math>\epsilon_r</math></b>	
<b>Air</b> <i>Temperature:</i> 293 K <i>Humidity:</i> 12-16%	<b>RC Time Constant</b>					
	Charging	310.46	1.00059	309.11	1.0035	0.2908
	Discharging	310.46	1.00059	305.96	0.9955	-0.5087
	Average				0.9995	-0.1089
	<b>Capacitive Reactance</b>	310.46	1.00059	325.05	1.0476	4.6982

Table 8.2: Summary of the measured capacitance values by various methods. The displayed values for the dielectric constant of ambient air at 293 K were calculated using the measured capacitance values and the geometry of the capacitance cell. The percent errors reflect the deviation of the experimentally measured relative permittivity to those reported in reference 9.

immediately be seen that although the value for the relative permittivity is of decent quality, it is further from the literature comparison. This set of trials seemed to indicate that between these two measurement approaches, more accurate determinations dawned from measurement of the RC time constant.

It was thus decided that the investigation into the relative permittivity of the various dielectric materials would be conducted using only measurement of the RC time constant. Aside from the accuracy of the measurement, this approach was chosen as it offered multiple benefits in relation to measurement of the capacitive reactance. Measuring the response of the dielectric under application of a DC voltage more closely reflects that of the actual experimental conditions, under which a DC voltage is applied to the sample during the hole-burning investigations. Because the full step function response of the capacitor is measured for each data set collected, both the charging and the discharging of the capacitor could be evaluated. This allows for two measurements to be made for each collected data set, which not only increase the number of data points taken but allows for measurement of the average charge and discharge response of the capacitor to be determined. Lastly, the necessary mathematics required for analysis of the data is more direct, requiring less manipulations prior to reaching the desired value.

## **8.6 Calibration of Measurement**

The initial set of benchtop experiments confirmed that the developed capacitance cell was capable of providing accurate evaluation of the relative permittivity of air when the

RC time constant for the charging and the discharging of the capacitor was measured, and the average value of the time constant was used during the analysis process. Because the remainder of experiments required the capacitance cell to be introduced into the Janis research Dewar, a battery of preliminary investigations was of necessity to assure the continued accuracy of the measurement under these new conditions. In order to situate the capacitance cell at the base of the cryostat, the optical objective and the sample scan stage were removed from the optical insert portion of the CTCSM, as described in chapter 4. The 50mL Vitlab beaker, within which the capacitance cell and the dielectric material under test is placed during capacitance measurements, was suspended from the support rods with waxed braiding. Due to the placement of the capacitance cell at the base of the cryostat, electrical leads of extended length in relation to those initially used during the benchtop trials were required for connecting the various components of the RC circuit. Additionally, the 820 ohm 0.25W  $\pm 5\%$  AXIAL Carbon Film CF14JT820R resistor was removed from the RC circuit and was replaced with the 1K ohm 0.6W  $\pm 0.01\%$  RADIAL metal foil Y0062-1.0KA-ND resistor, which was incorporated into the circuit as the reference resistor for enhanced accuracy of measurement.

The first set of tests were to investigate if the measured capacitance value was dependent upon where the capacitance cell was located during the measurement. Again prior to being placed into the research Dewar, the optical insert and capacitance cell needed to be placed first into the insert tube, displayed in figure 4.6, and then into the Dewar. Measurements were taken at three different locations to monitor any changes in the capacitance value. The first location was with the capacitance cell suspended from

the optical insert of the microscope which is designated as "Outside" in figure 8.12. The second location was after the optical insert and capacitance cell were placed inside of the insert tube, which is indicated as "In Tube" in the figure. The last location that was measured is designated as "Cryostat", and was a measurement that was taken after the insert tube was placed into the cryostat. In order to be able to understand any additional affects that would result from cryopumping which would be present during the low temperature studies, measurements were also taken inside of the cryostat at reduced pressures within the insert tube, to monitor if any changes to the measured

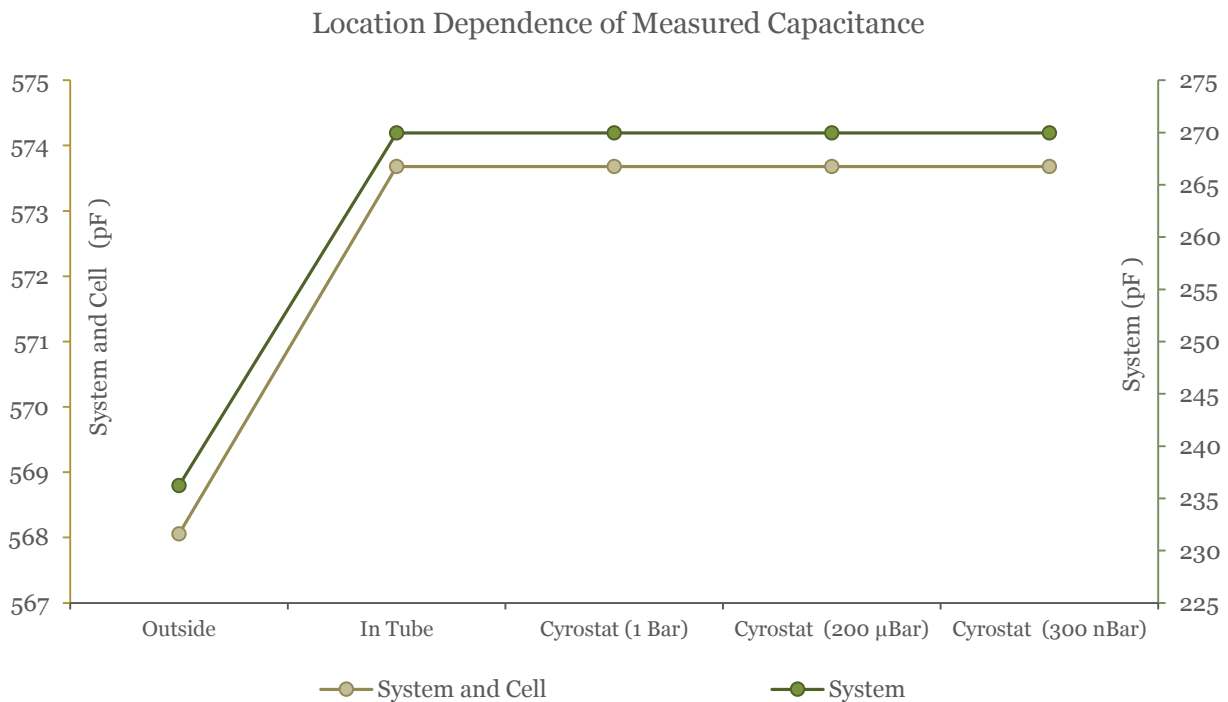


*Figure 8.12: Location and pressure dependence of the measured capacitance value at ambient temperature. The system capacitance consists of the total sum of the self-capacitance of the function generator, the oscilloscope and the electrical leads used to connect the various components of the RC circuit. The system and cell consists of the system capacitance as well as the additional capacitance of the capacitance cell when it is incorporated into the circuit. The only shift in measured capacitance occurs after the optical insert, containing the electrical leads and optionally the capacitance cell, is placed within the insert tube. Over the pressure range investigated, there was no observed pressure dependence on the measured capacitance value.*

capacitance value would result due to the presence of a reduced pressure environment. Trials were again performed with just the electrical leads, to capture the capacitance of the measurement system, indicated as the "System" data set, as well as with the actual capacitance cell, indicated as the "System and Cell" data set. These trials seemed to indicate that a change in the measured capacitance value occurred only after placement of the optical insert into the insert tube, with all other locations and pressures resulting in no change to the measured capacitance value.

As displayed in this particular data set, placement of the optical insert into the insert tube had a significantly larger effect on the capacitance of the system  $\sim 30$  pF, in comparison to that of the system and cell  $\sim 6$  pF. This was due the electrical leads of extended length not initially being fastened with any rigor to the optical insert during these first trials, when the pressure dependence was examined. In other trials that followed, when the pressure experiments were not repeated, once effort was made to securely fasten the electrical leads to the optical insert with string, the change in the measured capacitance of the system was in line with the location dependent  $\sim 6$  pF differential observed for the system and cell after placement into the insert tube. It is thought that this additional  $\sim 6$  pF capacitance is due to an increased capacitance of the system and cell with respect to the grounded metal insert tube. This entire set of trials revealed that there was no pressure dependence to the capacitance measurement and that once the optical insert and capacitance cell were placed into the insert tube, no additional changes to the measured capacitance value occurred.

The next set of experiments were performed to investigate if there existed a temperature dependence to the measured capacitance of the electrical leads used in

connection of the various components within the RC circuit. An accurate assessment of this quantity was of primary importance because it is representative of the system capacitance that would need to be subtracted from any capacitance that was measured with the capacitance cell. For these trials the capacitance cell was removed from the circuit and the capacitance of just the connection leads down to the base of the cryostat was measured. Measurements were taken during both cooling and heating cycles to determine if the direction of the thermal change would have any additional influence on the capacitance. These trials consisted of a total of 19 measurements that were taken throughout a six-day period. During this study, the thermal range investigated spanned from ambient temperature to 100 K. The function generator was set to deliver a square

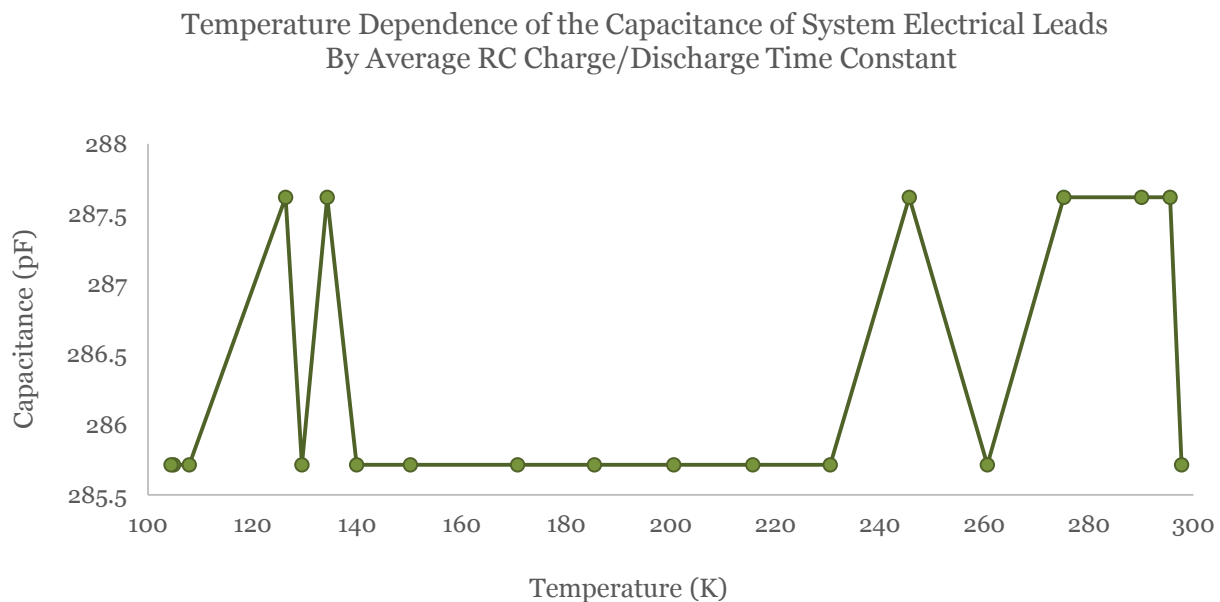


*Figure 8.13: The temperature dependence throughout the liquid nitrogen range of the capacitance of the electrical leads used to connect the various components within the RC circuit, including the leads that extend to the base of the research Dewar. This is representative of the capacitance of the measurement system, which must be accounted for when determining the magnitude of the contribution of the capacitance measurement cell alone, in relation to the total measured capacitance. The jumps in the capacitance trace are equivalent to a differential of 1.905 pF. The magnitude of the differential is dependent upon the frequency of the square wave pulse used during the measurement process, which for these trials was 100 kHz.*

wave of amplitude 5.0 V<sub>pp</sub>, using a 2.5 V offset, and a frequency of 100 kHz. The results of these experiments that monitored the change in the system capacitance in regard to the temperature inside the cryostat appear in figure 8.13. In this data, the jumps correspond to a difference of 1.905 pF, which is equivalent to a percent difference of only 0.665 %. Although the thermal range studied was moderate in comparison to the entire range in which experiments would be conducted, these trials revealed that the capacitance of the electrical leads were temperature independent.

The temperature dependence of the measured capacitance value of the capacitance cell was the next item to be investigated. Based on calculation, it was already determined that there would be approximately a 2.5 pF change over the entire thermal range between 1 K and 300 K in the measured capacitance of the instrument due to the thermal expansion characteristics of the various materials used to construct the device, figure 8.6. As with any newly developed instrument it was, however, necessary to experimentally classify the actual effect that varying the temperature of the device would have on the measured capacitance. During these trials, the capacitance of the electrical leads to the base of the cryostat in addition to the empty capacitance cell were measured. Because these trials would be conducted throughout the temperature range from approximately 100-300 K, in order to eliminate the possibility of any water vapor condensing and solidifying on the plates of the capacitor yielding an inaccurate measurement, as opposed to using standard room air to serve as the dielectric medium, 1 atm of nitrogen gas was backfilled into the insert tube. The effects of both the cooling as well as the heating the instrument were monitored during this set of studies, which consisted of 12 measurements that were taken as the device cooled from room

temperature to 100 K, and 11 measurements that were taken as the device returned to room temperature. Again, for these trials the function generator was set to deliver a square wave of amplitude 5.0 Vpp, using a 2.5 V offset, and a frequency of 100 kHz. The cumulative results of these cooling and heating experiments that indicate the temperature dependence of the measured cell capacitance in a nitrogen atmosphere are displayed in figure 8.14. In this data, the jumps again correspond to a difference of 1.905 pF, being equivalent to a percent difference of 0.6231 %. Using this data, it is observed that the average value of the capacitance that was measured over the thermal range is 305.671 pF which, result in a relative permittivity of 0.985150. If the expected thermal contraction of the capacitance cell is taken into account, this results in a value of

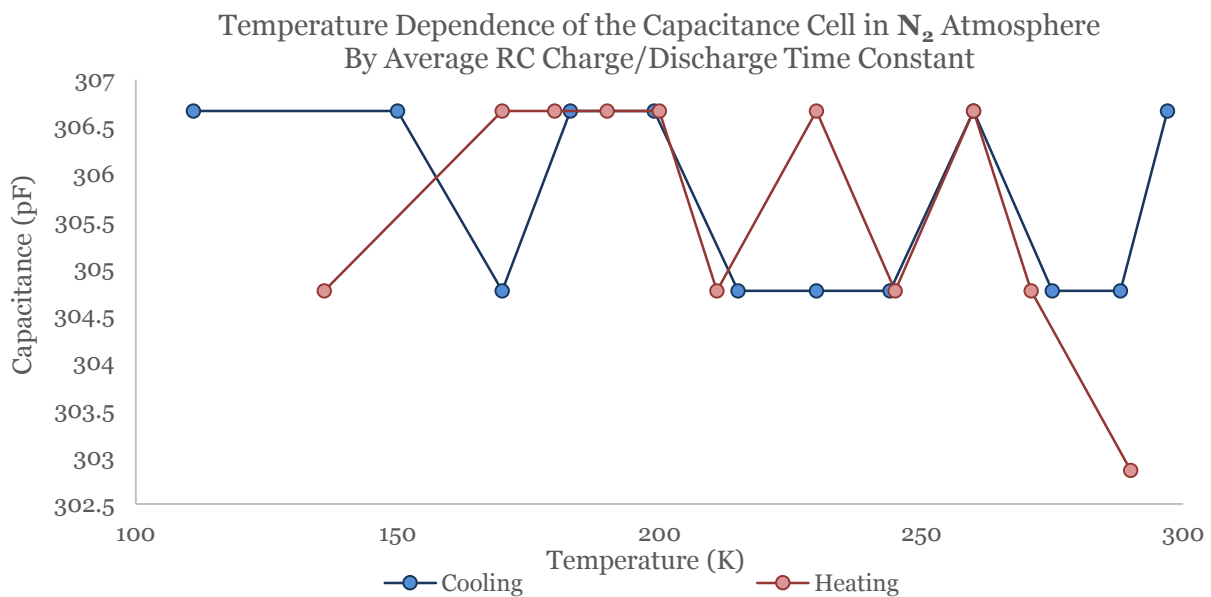


Figure 8.14: The temperature dependence throughout the liquid nitrogen range of the capacitance measurement cell using nitrogen gas as the dielectric medium within the capacitance cell. The measurements performed during both the cooling and heating of the instrument indicate that no apparent geometric deviation of the instrument occurs throughout the thermal range. The jumps in the capacitance trace are equivalent to a differential of 1.905 pF. The magnitude of the differential is dependent upon the frequency of the square wave pulse used during the measurement process, which for these trials was 100 kHz.



0.991596 for the relative permittivity of the nitrogen gas. The literature value for the relative permittivity of nitrogen, which is stated for a pressure of 1.02 atm at a temperature of 298.43 K, is 1.00052 [14]. Comparison of the evaluation made with this instrument to the literature value reflects a percent error in measurement of 0.892%. Some deviation, however, should be expected due to the difference in measurement pressure and temperature that exist between the two compared values.

As the instrument had proved to provide accurate measurements of the relative permittivity for dielectric materials in the gas phase, the next experiments focused on conducting an investigation on a dielectric in the solid phase. The most suitable material for this purpose was water in the ice phase, as it was not only a natural choice but also because it would eventually be a principal component in the solution sample that was the basis for this entire investigation. For these studies, an Arium 611 VF purifier was used to produce the purified 18 M $\Omega$ ·cm water that would serve as the sample. The water was degassed prior to placement within the 50 mL Vitlab beaker containing the capacitance cell. The water and capacitor were flash frozen by submersion into a liquid nitrogen bath after which the ice was checked to assure that it was free of bubbles or any other defects, and possessed a homogeneous and high quality optical clarity. The capacitance cell and ice sample were then placed into the cryostat that was already at 77 K. This set of experiments was conducted over a period of 50 days during which the temperature was never allowed to rise above 200 K. During this period, 46 measurements were taken out of thermal order, during both the heating and the cooling of the sample. The sample temperature was monitored at the sample, and the temperature was either regulated using the LakeShore 331 temperature controller, or

underwent a natural heating or cooling process. Throughout the entire set of experiments, measurements were taken only after it was known that thermal equilibrium had been reached within the entirety of the sample in order to assure a consistent evaluation of the dielectric properties of the material. For these trials the function generator was set to deliver a square wave of amplitude 5.0 Vpp, using a 2.5 V offset, and a frequency of 5 kHz. The frequency was changed in order to more closely simulate a DC signal, as relative to the previous sets experiments. A thorough

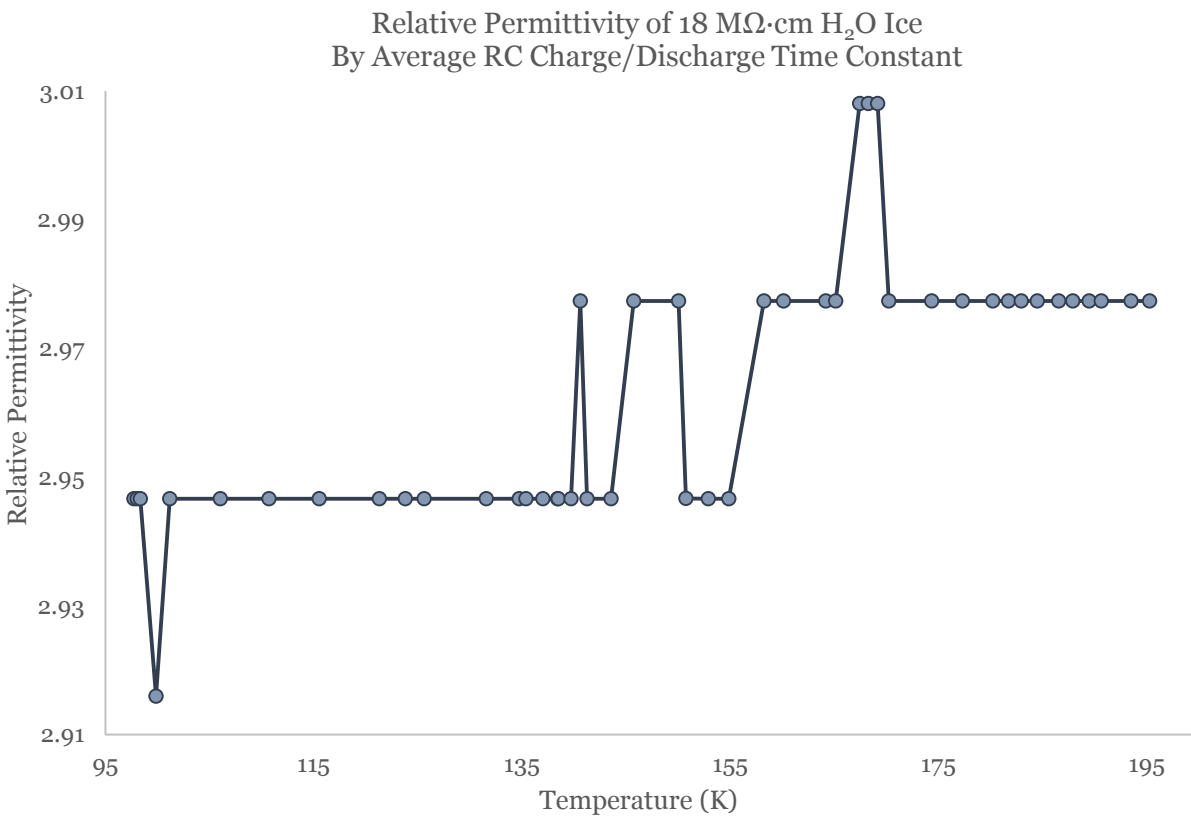


Figure 8.15: The measured relative permittivity of 18 MΩ·cm water within the thermal range of 97.7 K to 195.31 K. Displayed are the results of 46 separate measurements that were taken throughout a period of 50 days out of thermal order, during both the heating and the cooling of the sample. The jumps in the above trace are equivalent to a differential in capacitance of 9.5 pF, resulting in a differential of 0.0307 in the value of the relative permittivity. The magnitude of the differential is dependent upon the frequency of the square wave pulse used during the measurement process, which for these trials was 5 kHz. A direct relationship appears between the temperature and the measured relative permittivity. The average value of the relative permittivity throughout this thermal range is equivalent to 2.963.

investigation into the true frequency dependency of this measurement process was carried out and is further discussed in the next section of this chapter. The cumulative results of this set of measurements, which indicate the temperature dependence of the value of the relative permittivity of ice phase pure 18 M $\Omega$ ·cm water, is displayed in figure 8.15. The observed jumps correspond to a difference in measured capacitance of 9.5 pF, which corresponds to a change of 0.0307 in the value of the relative permittivity and a percent difference in the measured relative permittivity of 1.036 %. The average value for the relative permittivity is 2.963, across the entire thermal range 97.73 K – 195.31 K looked at. From the data points taken, a direct relationship between the temperature and the measured value for the relative permittivity does appear, which is exactly in line with what is expected regarding the relative permittivity of a material.

A comparison of the average value that was determined for the relative permittivity of ice, to those that appear within the literature allows the quality of this particular measurement to be assessed. A brief summary of a few of the many values that are available in the literature are provided in table 8.3. The values presented for comparison represent work spanning several decades with evaluations for this quantity made in similar temperature ranges, using similar capacitance measurement techniques. No existing experimental data could be found that had precise overlap across either the thermal ranges investigated and reported on, or with other experiments that were conducted using the particular type of capacitor and circuit that was used during this investigation. What can be observed in the table is the relatively broad range of evaluations for the relative permittivity of ice that appear in the literature. The quantity for the relative permittivity that was determined in this study is

in close proximity to the range that other literature values are reported. Aside from the data presented in reference 17, the general trend of a decreasing temperature resulting in a decreasing relative permittivity value seems to strengthen the results of this investigation as it was carried out in a slightly lower temperature range than was found in the literature and resulted in a slightly lower evaluation for the relative permittivity.

<b>Relative Permittivity Values: ICE</b>						
$\epsilon_r$	Temperature (K)		Method	Author	Year	Ref.
<b>3.8</b>		<b>173.5</b>	<b>5 kHz</b> Three-Terminal Coaxial Capacitor Transient	Johari, G. P. et al.	1981	17
<b>3.9</b>		<b>181.5</b>	<b>5 kHz</b> Three-Terminal Coaxial Capacitor Transient			
<b>3.1</b>		<b>207.35</b>	Parallel Plate Transient “infinite frequency limit”	Auty, R. P. et al.	1952	3
<b>3.13</b>		<b>210</b>	<b>5 GHz</b> Resonator	Matsuoka, T. et al.	1996	25
<b>3.28 -&gt; 3.05</b>		<b>233</b>	<b>5 kHz</b> Parallel Plate Oscillator Circuit	Fen-Chong, T. et al.	2005	7
<b>3.216</b>		<b>268.1</b>	<b>5 MHz</b> Two-Terminal Coaxial Capacitor	Johari, G. P.	1976	16
<b>3.33</b>		<b>268.1</b>	<b>500 kHz</b> Two-Terminal Coaxial Capacitor			
<b>3.15</b>		<b>273</b>	Statement as opposed to measurement	Jiang, J. H. et al.	2004	15
<b>2.963</b>		<b>97.7 – 195.3</b>	<b>5 kHz</b> Parallel Plate Capacitor	This Work		

*Table 8.3: Commonly accepted values appearing in the literature for the relative permittivity of water in the solid, ice phase. Measurement methodologies, as well as investigated thermal ranges vary according to the particular experiment, with no exact overlap between either parameter, and this particular investigation. Work was selected for inclusion for this comparison to reflect similar thermal ranges and measurement techniques in addition to being selected to represent measurement for this quantity across several decades of experiments. This current work represents a determination for the relative permittivity that is within the range of accepted values that appear throughout the literature.*

## 8.7 Sample of Interest 3:1 Glycerol:Water

Based on the success of the previous sets of experiments and the ability of the capacitance cell to provide accurate assessments of the relative permittivity of ambient air, nitrogen gas, and ice phase  $18 \text{ M}\Omega\text{-cm}$  water, experimental efforts towards the determination of the relative permittivity of the 3:1 glycerol:water could finally commence. As it was the primary objective of this investigation to determine the relative permittivity of the surrounding matrix within which the PPIX-Mb is placed during the hole-burning investigations, this study was carried out using the same source chemicals that were used during preparation of the samples that the hole-burning studies were performed on. The glycerol component used in preparation of the test solution was Alfa Aesar 32450 ultrapure spectrophotometric grade, lot: Jo3Z560, which was used directly from stock. The water component of the test solution was again  $18 \text{ M}\Omega\text{-cm}$  water that was purified using the Arium 611 VF purifier, which was degassed prior to mixing with the glycerol.

Prior to placement within the research Dewar, the 3:1 glycerol:water test solution and capacitor were, as with the  $18 \text{ M}\Omega\text{-cm}$  water sample, flash frozen by submersion into a liquid nitrogen bath. The solid phase glycerol:water was checked and was found to possess a homogeneous and high quality optical clarity, that was free of any defects. As with the previous experimental trials, the capacitance cell and sample were placed into the cryostat that was already at a temperature of  $77 \text{ K}$ . The experiments were conducted over a period of 120 days during which the temperature was never allowed to rise above  $230 \text{ K}$  [19]. Throughout the experimental period, measurements were again taken out of thermal order during both the heating and the cooling of the sample. Experimental

efforts during this set of trials were focused towards measurement of both the temperature as well as the frequency dependence of the determined relative permittivity value.

The temperature was monitored at the sample, and the sample was allowed to heat and cool through a natural process, or by thermal regulation using the LakeShore 331 temperature controller. To assure a consistent evaluation of the dielectric properties of the material, measurements were taken only after thermal equilibrium had been reached within the entirety of the sample. For all of the trials conducted, the function generator was set to deliver a square wave of amplitude 5.0 V<sub>pp</sub>, using a 2.5 V offset. A variable set of frequencies were used, with the specific set being dependent upon the specific category of the investigation, with the primary focus being either temperature or frequency.

### **8.7.1 Temperature Dependence**

The temperature dependence of the relative permittivity of the 3:1 glycerol:water sample was a fairly comprehensive investigation that was conducted throughout two general temperature ranges. The two thermal ranges studied reflect the low temperature end of the working thermal ranges of the liquid cryogen that was used to cool the research Dewar. Within the liquid helium thermal range, experimental measurements were performed at 9 different temperatures throughout the range of 1.034 K to 37.168 K. Within the liquid nitrogen thermal range, experimental measurements were performed at 33 different temperatures throughout the range of 82.225 K to 200.610 K. During all

of the investigations on the temperature dependence of the relative permittivity, measurements at each temperature were taken at each of 11 distinct frequencies. For enhanced temporal resolution in regard to determination of the RC time constant, the charging as well as the discharging behavior of the capacitor were measured separately. The set of frequencies studied during these trials followed a pseudo log scale and included the frequencies 5 Hz, 10 Hz, 20 Hz, 50 Hz, 100 Hz, 200 Hz, 500 Hz, 1 kHz, 2 kHz, 5 kHz, 10 kHz.

The cumulative results of these sets of trials appear in figure 8.16. In the plot immediately below, a magnification of the measurements that were taken within the liquid helium thermal range is displayed. Although a gap between 35 K and 85 K exists in the studied thermal range, based on the entirety of the surrounding data values and the apparent slope of the determined relative permittivity values, estimates for likely valuations for the relative permittivity in this range can safely be inferred. Despite numerous repeated measurements, the peak representing a differential of  $\sim 0.30$  in the value of the relative permittivity, that appears at  $\sim 172$  K continues to persist. The glycerol:water sample under study is prepared to the specification of 3:1 (volume:volume), which equates to a percent mass ratio of approximately 79:21, and a mole fraction of approximately 43:57. A glycerol:water solution at this mixing ratio does have a freezing point of 243.35 K [19]. The presence of this peak can easily be correlated to the findings of other authors that were investigating the glass characteristics of glycerol:water samples at similar and overlapping mixing ratios. The peak appearing at the temperature of  $\sim 172$  K in this study appears to be a measurement signifying the glass transition temperature  $T_G$  of the sample, as it closely follows the evaluations of the

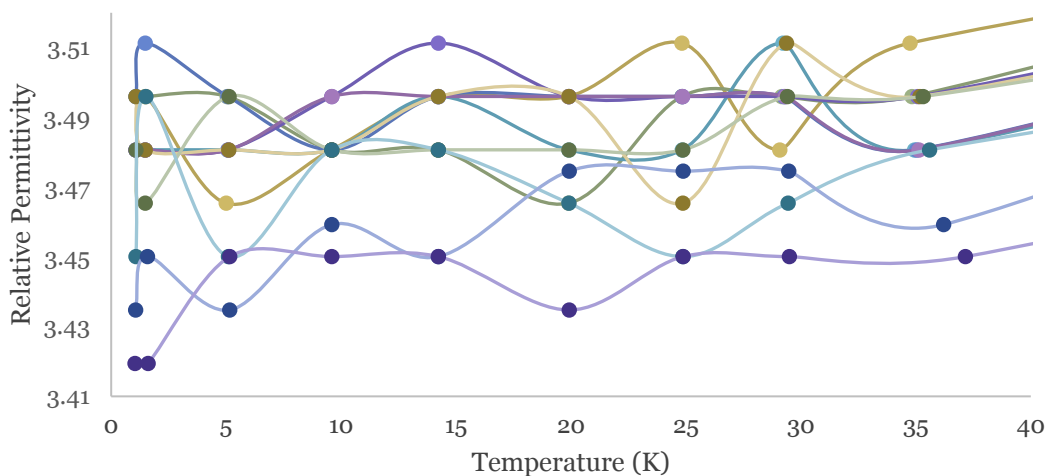
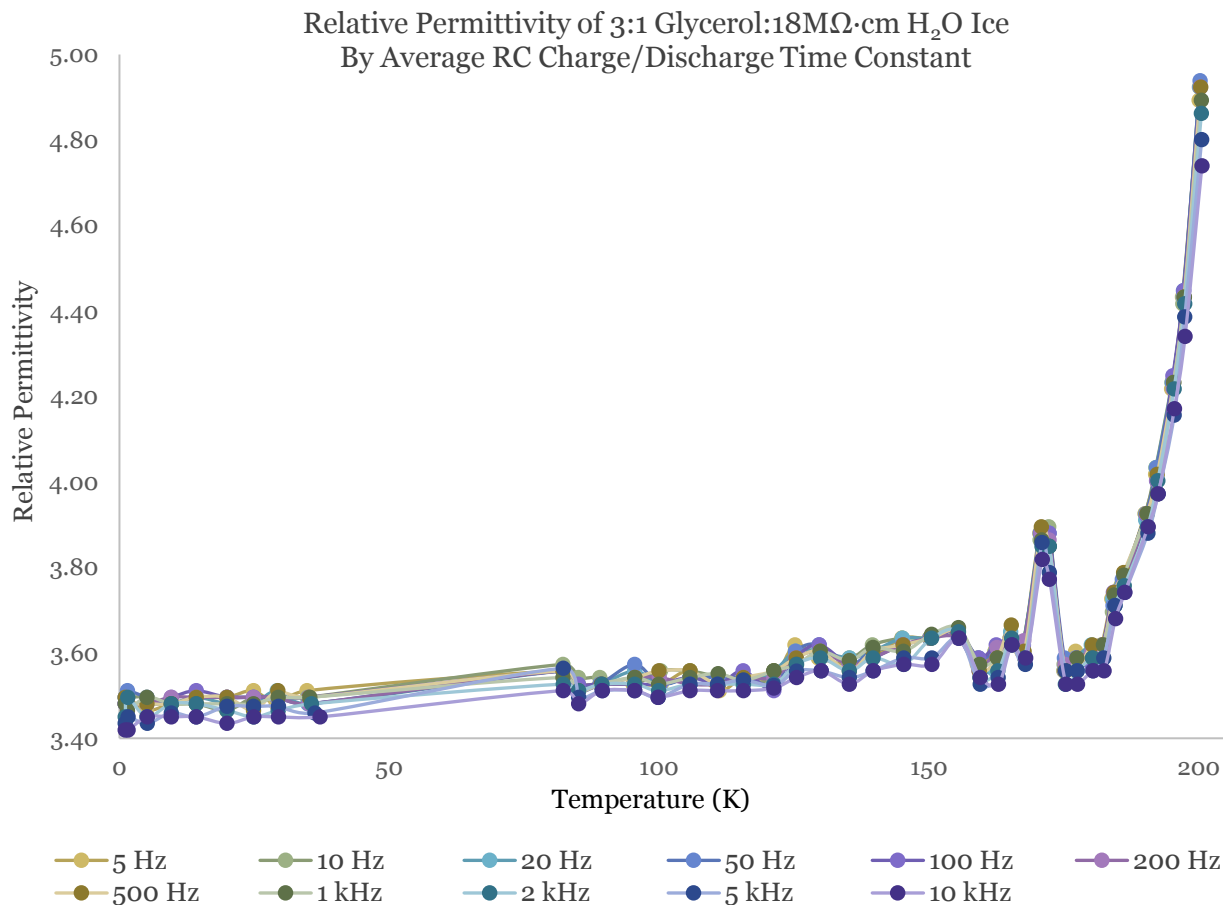


Figure 8.16: The temperature dependence of the relative permittivity of a 3:1 glycerol:water ice sample. This study consists of 42 separate measurements that were all taken at 11 different frequencies, out of thermal order, during both the heating and the cooling of the sample. Top: All 42 measurements, 33 of which occurred between the temperatures of 82.225 K to 200.610 K. Bottom: The nine measurements that were made throughout the range of 1.034 K to 37.168 K.



transition temperature  $\sim 173$  K that have been reported by other researchers [12, 27, 30, 31]. As for the determination of the transition temperature that was made during this study, additional measurements that completely trace over this thermal range would undoubtedly need to be performed prior to making any definitive explanations as to the underlying reason for its presence or its exact meaning in regard to the particular glass characteristics of this sample. This initial finding does, however, reveal that this instrument could have the potential to be used for investigating other various characteristics of a sample in addition to valuations of a sample's relative permittivity.

### **8.7.2 Frequency Dependence**

Investigation into the temperature dependence of the relative permittivity of the 3:1 glycerol:water sample was again conducted throughout two general temperature ranges. Within the liquid helium thermal range, measurements were performed at 4 different temperatures throughout the range of 1.034 K to 37.168 K. Within the liquid nitrogen thermal range, experimental measurements were performed at 3 different temperatures throughout the range of 92.336 K to 159.22 K. During this set of investigations on the frequency dependence of the relative permittivity, measurements at each temperature were taken at each of 45 distinct frequencies. Again to enhance the temporal resolution of the measurement, the charging as well as the discharging behavior of the capacitor were measured separately. During these trials, aside from the first six lower frequencies studied, measurements occurred at intervals of 250 Hz up to a frequency of 10 kHz. The

investigated set of frequencies that were studied include 5 Hz, 10 Hz, 20 Hz, 50 Hz, 100 Hz, 200 Hz, 500 Hz, 750 Hz, ..., 9750 Hz, 10 kHz.

The results of the sets of trials carried out within the liquid nitrogen range appear in figure 8.17, and the results of those experiments carried out in the liquid helium range appear in figure 8.18. In both figures, the temperatures are recorded as ranges as opposed to single values because accumulation of the charging and discharging data set at each of the 45 frequencies took approximately 90 minutes to complete and some thermal variation occurred over that timeframe. In all seven of the data traces, a clear indirect relationship between the relative permittivity of the material and the measurement frequency can be observed. Additionally, this data reinforces the results of the previous temperature investigation, whereby a direct relationship is again observed between a decreasing magnitude of the relative permittivity value at decreasing temperature values. The dotted lines that appear across the data sets are a least squares regression fourth order polynomial meant only to guide the eye. The smaller plots directly below each of the main plots in each of the figures display a magnification of the frequency dependence of the relative permittivity of only the six lowest frequencies investigated.

In order to introduce some estimates of the possible error associated with the measurements, the error bars were added using a jackknife resampling technique, which is a statistical methodology. For this particular implementation of the technique, of the 45 data points in a given data set, 33 of the points (approximately 75%) were selected at random. This new set of the 33 randomly selected points was then fit to a least squares

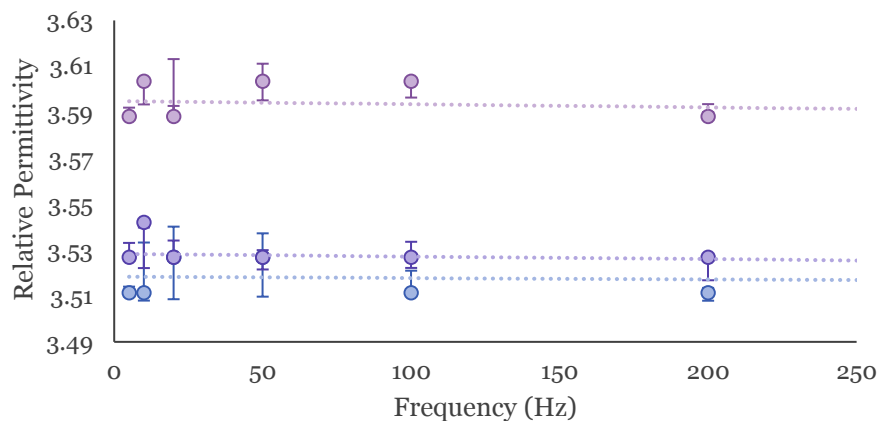
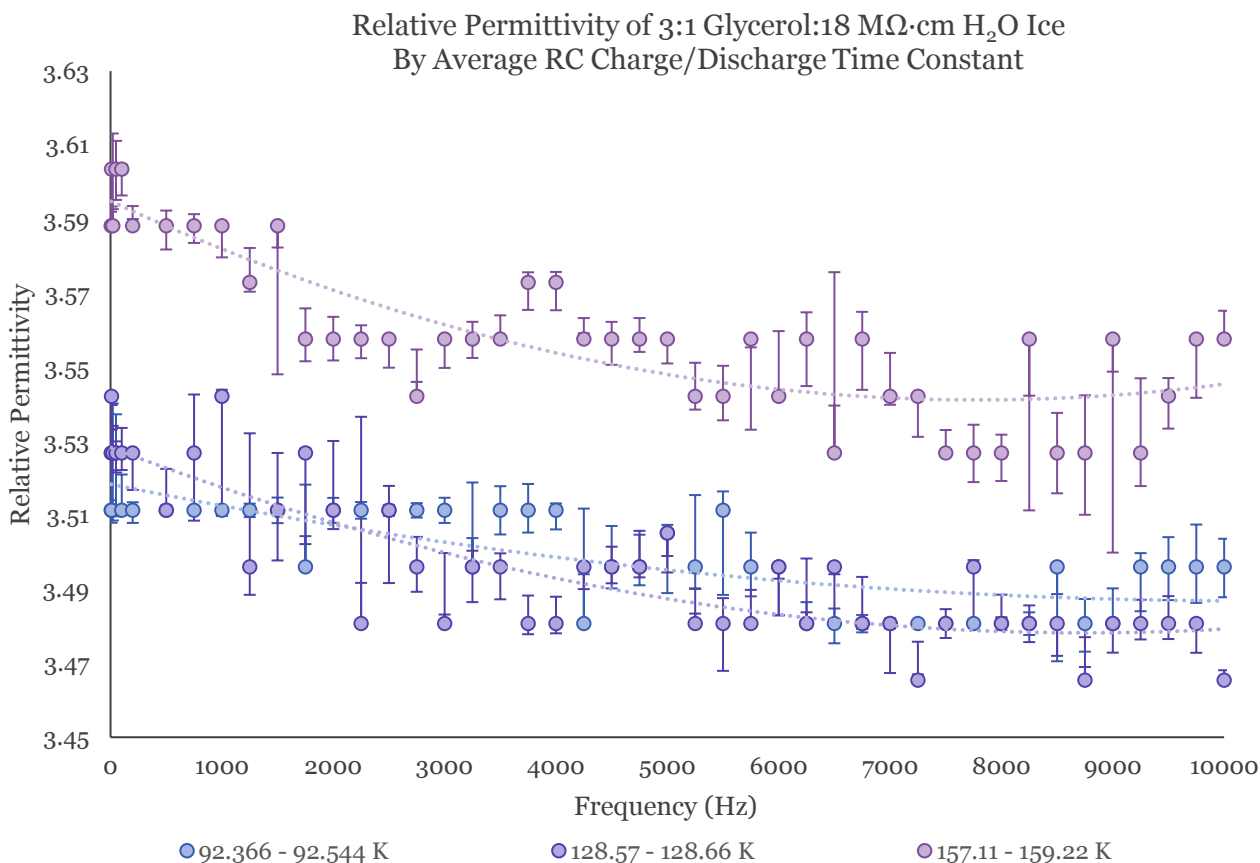
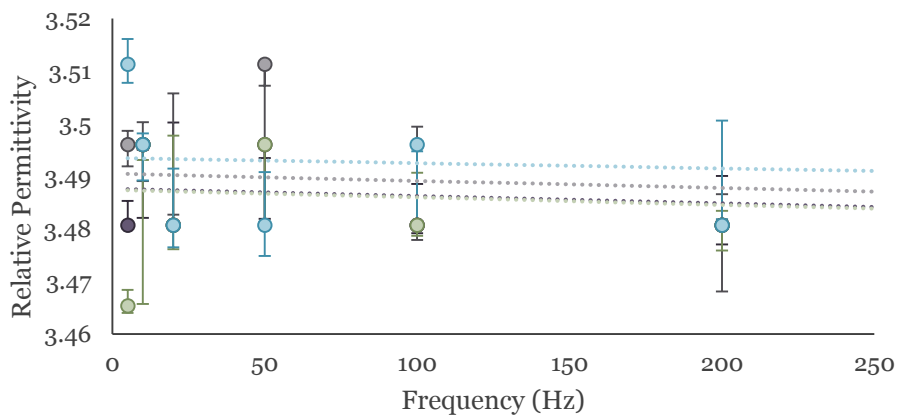
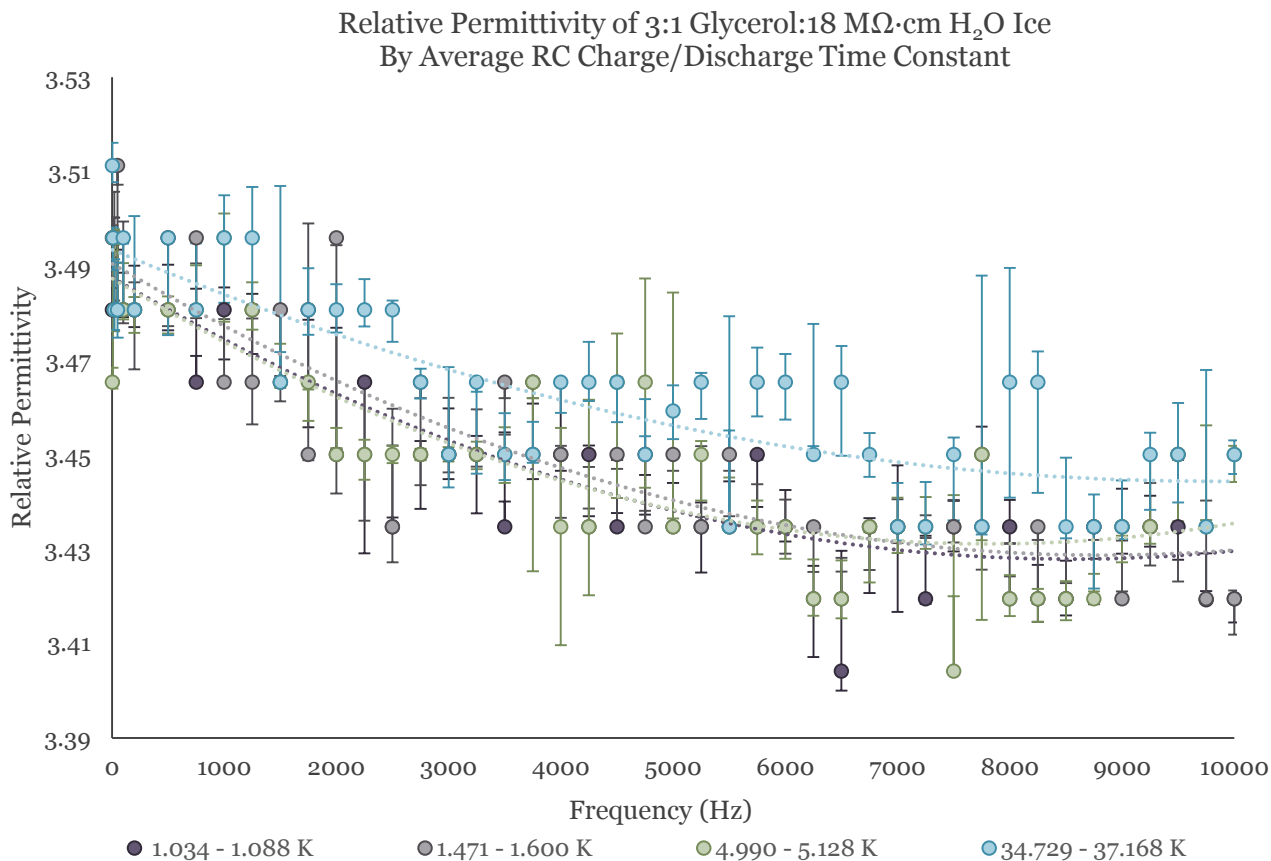


Figure 8.17: The frequency dependence of the relative permittivity of a 3:1 glycerol:water ice sample. This study consists of 45 separate frequency measurements that were taken at 3 different temperature ranges, within the liquid nitrogen thermal range Top: The 45 measurements, for each of the three investigated temperature ranges. Bottom: Magnification of the six lowest frequency measurements appearing in the above plot. The dotted lines appear only for guidance and represent a least squares regression fourth order polynomial fit to the data. Error bars represent the 95 % confidence interval, and were created using jackknife resampling, a statistical resampling technique.



*Figure 8.18: The frequency dependence of the relative permittivity of a 3:1 glycerol:water ice sample. This study consists of 45 separate frequency measurements that were taken at 4 different temperature ranges, within the liquid helium thermal range Top: The 45 measurements, for each of the four investigated temperature ranges. Bottom: Magnification of the six lowest frequency measurements appearing in the above plot. The dotted lines appear only for guidance and represent a least squares regression fourth order polynomial fit to the data. Error bars represent the 95 % confidence interval, and were created using jackknife resampling, a statistical resampling technique.*

regression fourth order polynomial. The y-value (relative permittivity) of the least squares regression at each of the x-values (frequency) of the original 45 points of total data set was stored. This process, of a random selection of 33 points, regression fit and storing of regression y-value at the 45 original x-values, was repeated one billion times. This resampling process allows for a distribution of likelihood of the y-value (relative permittivity) to be created at each x-value (frequency). The error bars presented are then the standard 95% confidence interval of the distribution of likelihood at each of the individual frequencies. The jackknife (sample subset), like the bootstrap (sample with replacement), is a statistics technique that allows estimations of population statistics to be made using information from only a sample distribution. The program for performing this operation in this investigation was written by this author, but further information regarding this technique can be found in these references [32, 33, 36].

### **8.7.3 Experimental Permittivity**

The principal objective of this inquiry was to experimentally evaluate the relative permittivity of a solution of 3:1 glycerol:water under conditions that were similar, if not identical to those existing at the sample when the Stark investigations on spectral hole profiles are carried out. With an accurate measurement of this quantity, insight into the influence that the bulk matrix surrounding the chromophore has on the externally applied electric field in relation to the local electric field that is actually experienced at the site of the chromophore can be known. A complete understanding of the true local electric field existing at the chromophore will require experimental efforts focused on

investigating the relative permittivity of the surrounding protein itself, in addition to implementing a correction factor to the macroscopic field that is based on a more rigorous foundation than can be afforded by the Lorentz cavity field approximation. A realistic assessment for the relative permittivity of the glycerol:water, however, should enhance the credibility of any valuations of the internal molecular electric field that are calculated through use of the molecular resolution approach for the analysis of spectral hole profiles that are collected when external electric fields at various magnitude are applied to the sample.

To most directly measure the relative permittivity under nearly identical conditions to those existing during the hole-burning experiments, two low temperature low frequency measurements of the relative permittivity were taken. As with the previous trials, the function generator was set to deliver a square wave of amplitude 5.0 Vpp, using a 2.5 V offset, and the charging as well as the discharging behavior of the capacitor were measured separately. The low temperature low frequency measurement was performed at 1.034 K using a frequency of 2 Hz. The second measurement was performed at a temperature of 1.088 K and at a frequency of 5 Hz. These two measurements yielded for the relative permittivity of the 3:1 glycerol:water matrix values of 3.465 and 3.480 respectively. These results are presented in figure 8.19. Because a DC voltage is applied to the sample during the Stark investigations, the relative permittivity that was determined when the square wave was applied at a frequency of 2 Hz should most closely resemble the conditions under which the actual experiments are performed. Hole-burning can generally be performed at temperatures in the range of 1-3 K.

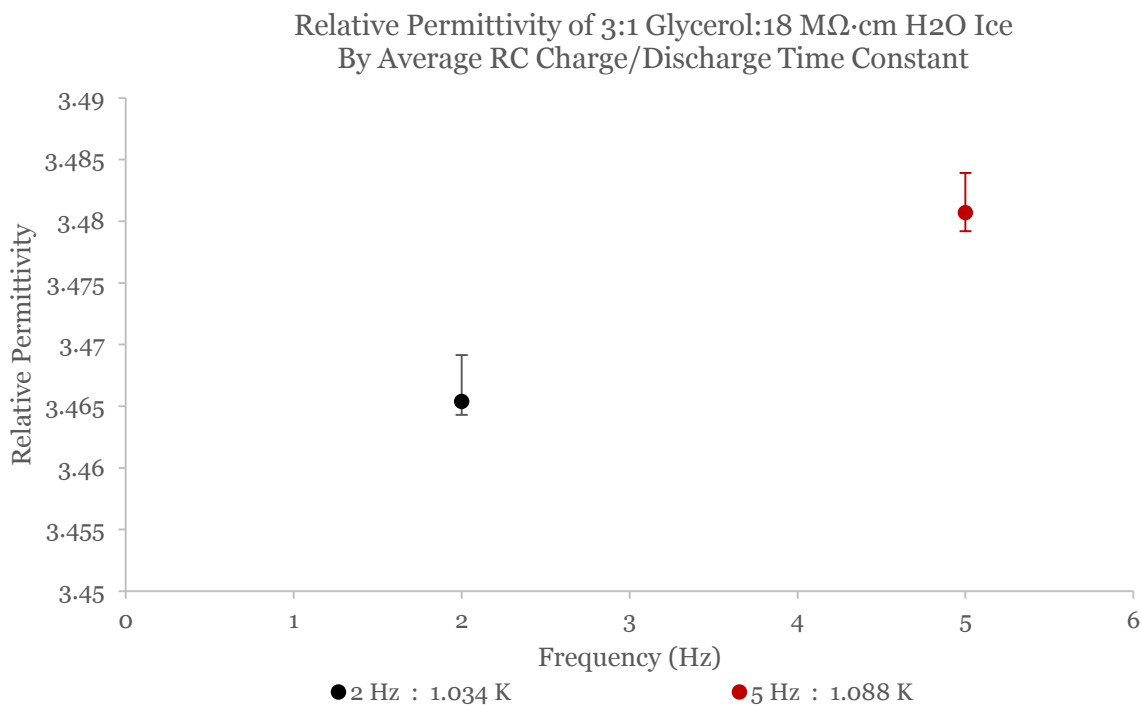


*Figure 8.19: The relative permittivity of 3:1 glycerol:water ice. These two measurements represent the low temperature and low frequency relative permittivity of the glycerol:water matrix that is used to contain the sample (PPIX-Mb) during the spectral hole-burning and Stark investigations. During the molecular resolution approach to calculating the internal molecular electric field, for the most realistic valuation of the relative permittivity of the surrounding matrix, the value of 3.465 should be used, as this measurement was obtained under environmental conditions that closely reflect those under which the sample exists during the hole-burning and Stark experiments. Error bars represent the 95 % confidence interval, and were created using jackknife resampling, a statistical resampling technique.*

## 8.8 Moving Forward

The objective of this investigation was to develop an instrument that was capable for use in the measurement of the relative permittivity of various solutions from ambient to cryogenic temperatures. The developed capacitor has been shown to yield evaluations of the relative permittivity of gas phase species, namely air and nitrogen, as well as the relative permittivity of solid phase 18 M $\Omega$ ·cm H<sub>2</sub>O, all of which are in accordance with valuations appearing in the literature. Based on the success of these measurements,

there is confidence in accuracy of the determined and reported value for the relative permittivity of the 3:1 glycerol:water. In order to further affirm the validity of the measurement, additional pure solvents should be tested throughout commonly investigated temperature ranges, so that comparisons can be made between values existing in the literature and the values determined with this instrument. The most logical next step would be to measure the temperature and frequency dependence of pure glycerol. A confirmation with literature values would serve not only to validate the capacitance cell as an instrument with analytical integrity, but would also serve to enhance confidence in the determined value of the relative permittivity of the glycerol:water solution. After that set of tests, other solvents that are commonly used to create spectroscopic glasses should be looked into.

Until this date, the capacitance cell has only successfully been used to test solid phase and gas phase dielectrics. All solution phase studies have resulted in evaluation of the relative permittivity that were on the order of an order of magnitude too large. This is a common problem in the literature and is expected to arise from electrode polarization [4, 6, 10]. As such, the current design of the capacitance cell allows only for invasive measurement, and solution phase measurements are not a possibility. To allow for investigations on solution phase dielectrics to be taken, a protective layer should be added to the surface of the capacitor plate, to block their direct contact with solution and reduce ionic leakage current in the solution. This is an inquiry that is presently underway.

In order to allow for AC frequency independent measurements of the capacitance, a Schering bridge circuit, pictured in figure 8.20, should be incorporated



into the system. This is a commonly used bridge circuit that allows for the determination of the capacitance of an unknown capacitor. The bridge consists of four arms, and has a relatively simple construction. Here, the arm numbers are indicated by the subscripts of the impedances,  $Z$ . The first arm of the bridge consists of the capacitance  $C_1$  of a known capacitor, with the total impedance of the arm represented by  $Z_1$ . The second arm of the bridge consists of the capacitance  $C_T$  of the unknown capacitor, and the in series resistance  $R_T$  that describes the loss of the capacitor, where the total impedance of the arm is represented by  $Z_2$ . The third arm of the bridge consists of a variable capacitor with capacitance  $C_3$ , which is connected in parallel with a variable

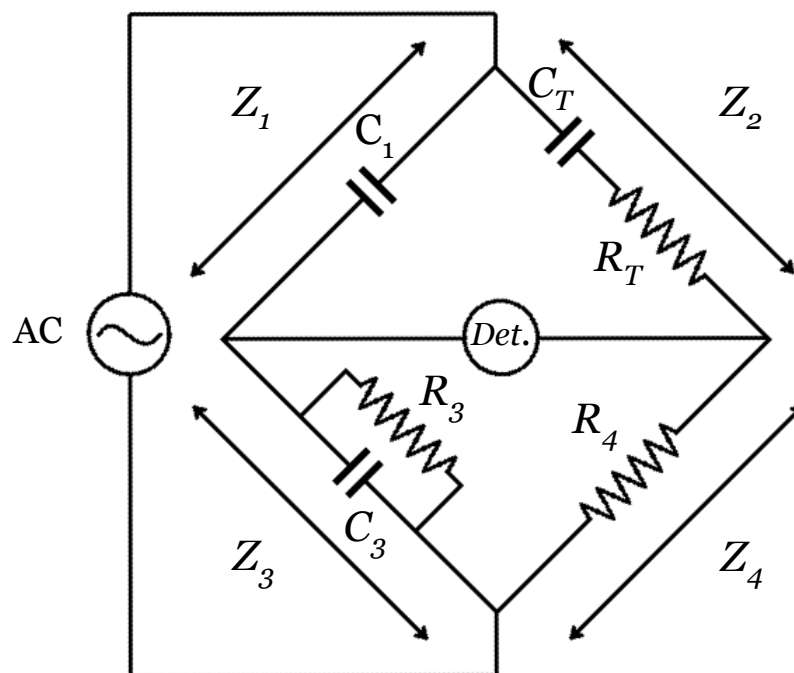


Figure 8.20: Schematic representation of the Schering bridge circuit that allows for the frequency independent determination of the capacitance of an unknown capacitor. In this circuit, the unknown capacitor under test is  $C_T$  which possesses an in series resistance  $R_T$  representing the loss in the capacitor.

non-inductive resistor of resistance  $R_3$ . The total impedance of arm three is represented by  $Z_3$ . The fourth arm of the bridge possesses a total impedance of  $Z_4$ , and consists of only a single a resistor  $R_4$ , with a non-inductive resistance. An AC power supply is connected across the bridge from the node existing between arm one and arm two, to the node existing between arm three and arm four. The detector, *Det.*, typically a galvanometer, is connected across the opposite diagonal of the bridge, from the node existing between arm one and arm three, to the node existing between arm two and arm four.

Through an iterative process of tuning the variable resistor  $R_3$  and the variable capacitor  $C_3$  of arm three, the impedance across the different arms of the bridge is modulated until a balance of the bridge has been achieved and the detector yields a null reading, indicating a voltage drop of zero across the detector. In this case, the complex impedance of the different arms is matched according to the following equation.

$$Z_1 Z_4 = Z_2 Z_3 \quad (8.36)$$

Inserting into the above equality the actual contributions defining the impedance of each arm, namely the resistance for the resistors and the capacitive reactance for the capacitors, taking into account the rules for in series and in parallel resistive and capacitive elements, yields the following equality. In this equation, the terms are ordered and bracketed such that they correlate respectively to the impedances listed in the previous equation.

$$\left(\frac{1}{j\omega C_1}\right) (R_4) = \left(R_T + \left(\frac{1}{j\omega C_T}\right)\right) \left(R_3 + \left(\frac{1}{j\omega C_3}\right)\right)^{-1} \quad (8.37)$$

Upon equating the real and imaginary terms in equation 8.37, equations that solve for the value of the resistance  $R_T$  and the capacitance  $C_T$  of the unknown capacitor can be found as follows.

$$R_T = R_4 \left( \frac{C_3}{C_1} \right) \quad (8.38)$$

$$C_T = C_1 \left( \frac{R_3}{R_4} \right) \quad (8.39)$$

When the detector reads a value of zero and the impedance within the arms of the bridge are in balance, the values of the of the variable resistor  $R_3$  and the variable capacitor  $C_3$  are recorded. Because the resistance of resistor  $R_4$  and the capacitance of capacitor  $C_1$ , are known, these four values are then inserted into the above equations to solve for the capacitance  $C_T$  of the unknown capacitor, equation 8.39, and the value of the in series resistance  $R_T$  describing the loss of the capacitor, equation 8.38. By utilizing this method for determination of the unknown capacitance, capacitance values in agreement to  $\sim 0.01\%$  of their true value can be expected [5, 6, 21-23, 34].

## References

- 1.) Alexander, Charles K., and Matthew N.O. Sadiku, *Fundamentals of Electric Circuits*. Boston: McGraw-Hill Higher Education, 2007. Print.
- 2.) Altmann, R. B., Renge, I., Kador, L., Haarer, D. (1992). "Dipole moment differences of nonpolar dyes in polymeric matrices: Stark effect and photochemical hole burning. I," *Journal of Chemical Physics* 97(8), 5316-5322.
- 3.) Auty, Robert P., Cole, Robert H. (1952). "Dielectric Properties of Ice and Solid D<sub>2</sub>O," *The Journal of Chemical Physics* 20(8), 1309-1314.
- 4.) Baudot, A., Bret, J.L. (2003). "A simple capacitive cell for the measurement of liquids dielectric constant under transient thermal conditions," *CryoLetters* 24(1), 5-16.
- 5.) Bera, S. C., Chattopadhyay, S. (2003). "A modified Schering bridge for measurement of the dielectric parameters of a material and the capacitance of a capacitive transducer," *Measurement* 33(1), 3-7.
- 6.) Braunstein, J. et al. Presented at 21st Southeastern Regional ACS Meeting, Richmond, Va., Nov. 5-8, 1969, Division of Chemical Education Paper No. 110.
- 7.) Fen-Chong, Teddy., Fabbri, Antonin. (2005). "Freezing and thawing porous media: experimental study with a dielectric capacitive method," *Comptes Rendus Mecanique* 333, 425-430.
- 8.) Gunner, M. R., Alexov, Emil., Torres, Eduardo., Lipovaca, Samir. (1997). "The importance of the protein in controlling the electrochemistry of heme metalloproteins: methods of calculation and analysis," *Journal of Biological Inorganic Chemistry* 2, 126-134.
- 9.) Hector, L. Grant., Woernley, Donald L. (1946). "The Dielectric Constants of Eight Gases," *Physical Review* 69(3-4), 101-105.
- 10.) Heidari, M., Azimi, P. (2011). "Conductivity Effect on the Capacitance Measurement of a Parallel-Plate Capacitive Sensor System," *Research Journal of Applied Sciences, Engineering and Technology* 3(1), 53-60.
- 11.) Herrick, Robert J., *DC/AC Circuits and Electronics: Principles & Applications*. USA: Thomson/Delmar Learning, 2003. Print.
- 12.) Inaba, Akira., Andersson, Ove. (2007). "Multiple glass transitions and two step crystallization for the binary system of water and glycerol," *Thermochimica Acta* 461(1-2), 44-49.
- 13.) Jackson, John David. *Classical Electrodynamics*. New York: Wiley, 1962. Print.

- 14.) Jensen, J.E., Tuttle, W.A., Stewart, R.B., Brechna, H., Prodel, A.G. (Eds.). (1980). Brookhaven National Laboratory Selected Cryogenic Data Notebook Volume I Sections I-IX, VI-H-2.5. BNL 10200-R. Brookhaven National Laboratories Laboratory Associated Universities Inc.
- <https://www.bnl.gov/magnets/staff/gupta/cryogenic-data-handbook/Section6.pdf>
- 15.) Jiang, Jonathan H., Wu, Dong L. (2004). "Ice and Water Permittivities for Millimeter and Sub-millimeter Remote Sensing Applications," *Atmospheric Science Letters* 5(7), 146-151.
- 16.) Johari, G. P. (1976). "The dielectric properties of H<sub>2</sub>O and D<sub>2</sub>O ice Ih at MHz frequencies," *The Journal of Chemical Physics* 64(10), 3998-4005.
- 17.) Johari, G. P., Whalley, E. (1981). "The dielectric properties of ice Ih in the range 272-133K," *The Journal of Chemical Physics* 75(3), 1333-1340.
- 18.) Kukic, Predrag., Farrell, Damien., McIntosh, Lawrence P., García-Moreno, Bertrand E., Jensen, Kristine Steen., Toleikis, Zigmantas., Teilum, Kaare., Nielsen, Jens Erik. (2013). "Protein Dielectric Constants Determined from NMR Chemical Shift Perturbations," *Journal of the American Chemical Society* 135(45), 16968-16976.
- 19.) Lane, Leonard B. (1925). "Freezing Points of Glycerol and Its Aqueous Solutions," *Industrial and Engineering Chemistry* 17(9), 924.
- 20.) Li, Lin., Li, Chuan., Zhang, Zhe., Alexov, Emil. (2013). "On the Dielectric "Constant" of Proteins: Smooth Dielectric Function for Macromolecular Modeling and Its Implementation in DelPhi," *Journal of Chemical Theory and Computation* 9(4), 2126-2136.
- 21.) Linear Technology, Appl. Note 43, 1-48.
- 22.) Malmberg, Cyrus G., Maryott, Arthur A. (1950). "Dielectric Constants of Aqueous Solutions of Dextrose and Sucrose," *Journal of Research of the National Bureau of Standards* 45(4), 299-303.
- 23.) Malmberg, C. G., Maryott, A. A. (1956). "Dielectric constant of water from 0° to 100 °C," *Journal of Research of the National Bureau of Standards* 56(1), 1-8.
- 24.) Marquardt, E. D., Le, J. P., Radebaugh, Ray. (2000). "Cryogenic Material Properties Database," 11th International Cryocooler Conference, Keystone, Co., June 20-22, 2000.
- 25.) Matsuoka, Takeshi., Fujita, Shuji., Mae, Shinji. (1996). "Effect of temperature on dielectric properties of ice in the range 5-39 GHz," *Journal of Applied Physics* 80(10), 5884-5890.
- 26.) Mehta, Mehta Neeraj. Textbook Of Engineering Physics, Part 2. New Delhi: Asoke K. Ghosh, 2009. 85-116. Print.

- 27.) Murata, Ken-ichiro., Tanaka, Hajime. (2012). "Liquid–liquid transition without macroscopic phase separation in a water–glycerol mixture," *Nature Materials* 11(5), 436-443.
- 28.) Nielsen, J. E., Andersen, K.V., Honig, B., Hooft, R.W.W., Klebe, G., Vriend, G., Wade, R.C. (1999). "Improving macromolecular electrostatic calculations," *Protein Engineering* 12(8), 657-662.
- 29.) Pitera, Jed W., Falta, Michael., van Gunsteren, Wilfred F. (2001). "Dielectric Properties of Proteins from Simulation: The Effects of Solvent, Ligands, pH, and Temperature," *Biophysical Journal* 80(6), 2546–2555.
- 30.) Popov, Ivan., Greenbaum (Gutina), Anna., Sokolovcd, Alexei P., Feldman, Yuri. (2015). "The puzzling first-order phase transition in water–glycerol mixtures," *Physical Chemistry Chemical Physics* 17, 18063-18071.
- 30.) Rasmussen, Don H., MacKenzie, Alan P. (1971). "The Glass Transition in Amorphous Water. Application of the Measurements in Problems Arising in Cryobiology," *The Journal of Physical Chemistry* 75(7), 967-973.
- 32.) Shao, Jun., Wu, C. F. J. (1989). "A General Theory for Jackknife Variance Estimation," *The Annals of Statistics* 17(3), 1176-1197.
- 33.) Shao, Jun., and Dongsheng Tu, *The Jackknife and Bootstrap*. New York: Springer-Verlag, 1995. Print.
- 34.) Table of Dielectric Constants of Pure Liquids, N.B.S. Circular 514. 1951.
- 35.) Tektronix, Appl. Note 75W-28152-1, 1-10.
- 36.) Wu, C. F. J. (1986). "Jackknife, Bootstrap and Other Resampling Methods in Regression Analysis," *The Annals of Statistics* 14(4), 1261-1295.
- 37.) Wyman, Jeffries. (1931). "Studies On The Dielectric Constant Of Protein Solutions: I. Zein," *The Journal of Biological Chemistry* 90(2), 443-476.

# III

## Chapter 9

### **Transition Moments and Energies of Free Base Porphyrin Possessing In-Protein Structural Characteristics**

#### **9.1 Introduction**

The fundamental aim of this research seeks to quantitatively determine the internal molecular electric fields that are generated by proteins within active regions. The specific system of interest is the oxygen binding site of the oxygen storage protein myoglobin. The high resolution spectroscopic technique, spectral hole-burning, is used in conjunction with electric field measurements based on the Stark effect and a unique analysis to study the impact that these internal electric field distributions play. The chromophore which serves as the probe of the internally generated electric field within the active site is free base porphyrin, an analogue of the native heme. As the investigation is performed using real samples, the experimentally collected data reflects real porphyrin in a real protein environment. For the quantum mechanical treatment that is employed during the analysis of the experimental data to yield a physically meaningful result, the boundary conditions, appearing in the form of the transition energies as well as the transition dipole moments, must be accurate. The molecular

structure of porphyrin that is used during the computational determination of these values, therefore, must reflect the structural characteristics existing in the protein.

This work focusses on implementing post Hartree-Fock methods that take electron correlation into account when calculating the transition energies and the state-specific dipole and transition dipole moment values of the molecule. Both the configuration interaction, as well as the coupled-cluster approaches, at various levels of electronic excitation, have been investigated. The ability of each of the various approaches to accurately reproduce valuations for quantities that are spectroscopically observable serve as the marker by which the quality of the different methods explored are assessed. The selection of an appropriate molecular geometry for the porphyrin probe, possessing structural characteristics realistic to those that exist within the myoglobin protein, used when carrying out the computational studies, is discussed. The current findings from this set of studies and the future direction of this line work are then highlighted.

## **9.2 The Molecular Geometry of Porphyrin**

The accurate evaluation of the internal molecular electric field present within the active site of the myoglobin protein as determined by implementation of the molecular resolution approach, chapter 2, to the analysis of spectral hole profiles obtained under applied external electric fields of various magnitude depends heavily upon the state specific energies and the state specific transition dipole moment values utilized for establishment of the applicable Hamiltonian matrix, which upon diagonalization yields



the desired quantity of interest, the internal electric field. Therefore, the determination of a suitable molecular geometry for the free base porphyrin, of which only the porphine core is considered during the computational process, to serve as the base molecular structure upon which the state energies and the state specific transition dipole moment values are theoretically calculated, requires judicious consideration.

A prerequisite to any choice of the appropriate base molecular geometry to utilize during the computational studies is an understanding of the geometric variability that exists within the molecule. In the vapor phase, and in environments that are free from external forces, the porphine macrocycle is typically considered to be a member of the  $D_{2h}$  point group and possess a geometry that is planar or nearly planar [10, 17, 58]. This classification is based generally in both theoretical work as well as in some early crystallographic studies [18, 54, 58]. With the advent of enhanced crystallographic resolution, detailed three-dimensional diffraction data reveals that the porphine macrocycle deviates from a planar configuration and has a broad adaptability towards the environment that it is situated within [23, 34, 58]. It is now thought that the biological functionality of these molecules can be partially attributed to their geometric tunability [49, 50]. In most porphyrin crystals that have been analyzed, the macrocycle has been observed to possess a “ruffled” conformation. This ruffling is thought to arise from angular strain that is caused by the  $\sigma$ -bonding pattern existing throughout the molecule [20, 23, 35]. Therefore, the molecular geometry of the porphine core of a porphyrin molecule would not be expected to be confined to a planar geometry in a realistic solid-phase sample. Despite these findings, much of the theoretical work

regarding this class of molecules has been performed using representative model structures that are planar and highly symmetric [12].

It is now widely accepted that most varieties of porphyrins possess non-planar geometric character when existing in prepared porphyrin crystals. Although the results from these studies on porphyrin crystals are representative of the molecular conformational variability in the solid phase, the geometric characteristics that exist in porphyrin crystals does not necessarily reflect the characteristics of porphyrin when it is present in proteins. Therefore, an evaluation of the geometric variability existing across this class of molecules when contained in protein environments was viewed as a necessity before any determination regarding the base molecular structure to utilize during the computational analysis could be made.

### **9.2.1 The In-Protein Structural Characteristics of Porphyrin**

Although many studies report on the non-planar character of porphyrins in protein environments [2, 24, 27, 52], the underlying objective of this portion of this study was to answer the question, “What does porphyrin actually look like in myoglobin?”. In order to gather insight to the molecular geometry possessed by porphyrin when existing in myoglobin, myoglobin crystal structures were reviewed regardless of the species of origin, if the protein existed in its native state or if residue alterations had been made to the protein, or if the porphyrin was in either the ligated or the unligated form. During this inquiry, a survey of the molecular characteristics of porphyrin, across all of the

crystal structures for myoglobin that appear in the RCSB-PDB (Research Collaboratory for Structural Bioinformatics Protein Data Bank), was performed.

It was decided that the most direct way to observe the variability of the molecular geometry of the porphyrin macrocycle as it exists in the different myoglobin environments would be to place a best fit surface to the atoms of the porphine core of the porphyrin macrocycle, free of any substituent groups or a central metal atom. To provide for the most faithful representation of the macrocycle, the myoglobin crystallographic structures obtained from RCSB-PDB were used directly with no alterations to any of the atomic positions by use of force fields or other energy optimization algorithms. Using the Avogadro molecular editor and visualization application [21], the downloaded crystal structure was opened and the entire protein was cut away leaving only the porphyrin ring. The ring was then translated such that the origin resided at the center of the four central nitrogens of the porphyrin ring, with the distal side of the porphyrin ring oriented to the plus z direction. The molecule was then oriented such that the propionic acid side chains bonded to the porphyrin ring resided along the negative x-axis and the positive y-axis. It was assured that the nitrogens situated along the x-axis resided strictly along the x-axis with no character in the y or z direction. The nitrogens along the y-axis were kept planar to each other but due to the various characteristics of the many porphyrin macrocycles, these two nitrogens were not necessarily confined to having zero x-axis or zero z-axis character, as any alteration of the relative atomic positions could not be made if an accurate representation of the geometry of the macrocycle was to be understood. Lastly, the substituent groups and

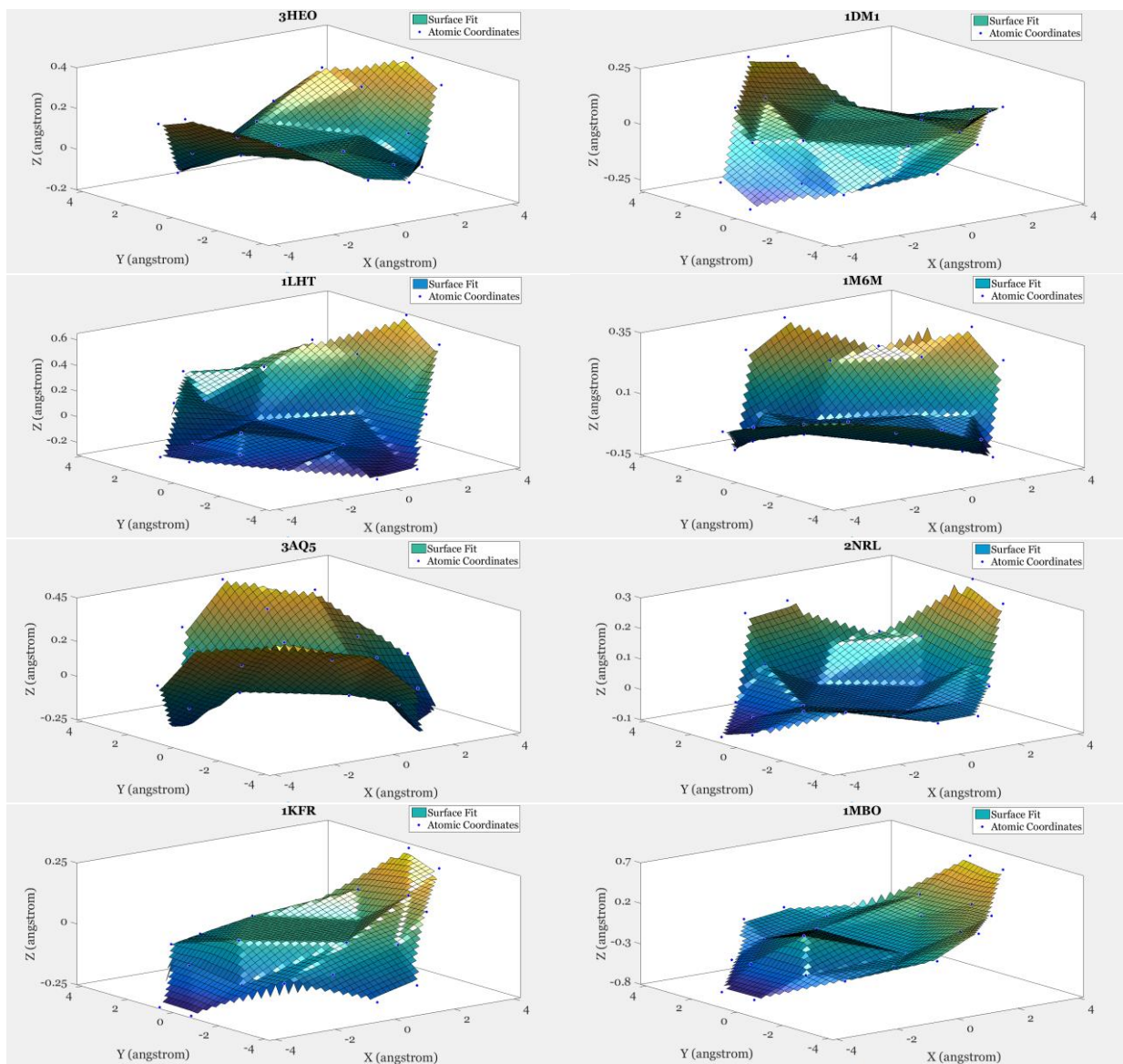


Figure 9.1: Representative surface fits to the atomic positions of the porphine core of the porphyrin macrocycle in myoglobin. For each species of origin available in the RCSB-PDB, one surface is displayed. The displayed surfaces include, top left to bottom right (species of origin, PDB identification code and the crystal structure resolution): *Equus caballus* (horse): 3HEO at 2.00 Å [63], *Aplysia limacina* (slug sea hare): 1DM1 at 1.99 Å [13], *Caretta caretta* (loggerhead turtle): 1LHT at 2.00 Å [39], *Sus scrofa* (wild boar): 1M6M at 1.80 Å [31], *Tetrahymena pyriformis* (ciliate protozoa): 3AQ5 at 1.78 Å [25], *Thunnus atlanticus* (blackfin tuna): 2NRL at 0.91 Å [48], *Physeter catodon* (sperm whale): 1MBO at 1.60 Å [41], other porphyrins (not of the above): 1KFR at 1.85 Å [38]. In all of the displayed plots above, the porphine ring is positioned such that the two propionic acid side chains bonded to the porphyrin ring would be oriented towards the front of the image. Across the 380 fits that were performed, additional surface variability that cannot be observed in the above fits did exist. Legends display “Surface Fit”, top, and “Atomic Coordinates”, bottom. The axes have the units of angstrom.

central metal atom were removed so that only the porphine core of the porphyrin ring remained. Using Matlab, a best fit surface was then fit to the atomic coordinates of the remaining porphine core.

During this study the entire RCSB-PDB was surveyed and 380 fits were performed following the process described above, for all of the myoglobin crystal structures across all of the different species of origin. This number of myoglobin crystal structures that were reviewed for each species included *Equus caballus* (horse): 66, *Aplysia limacina* (slug sea hare): 7, *Caretta caretta* (loggerhead turtle): 2, *Sus scrofa* (wild boar): 17, *Tetrahymena pyriformis* (ciliate protozoa): 5, *Thunnus atlanticus* (blackfin tuna): 8, *Physeter catodon* (sperm whale): 238, other porphyrins (not of the above): 9. Of the total structures that were reviewed, 8 of the crystal structures were of apo species that were void of the porphyrin group, which could not be fit to a surface. Twenty-six of the reviewed crystal structures possessed multiple myoglobin domains, thus, for those structures the multiple porphyrin planes were independently fit. For a basic visualization of the results of this inquiry, a small sample that is representative of the typical results of this fitting procedure appears in figure 9.1. For all of the projections illustrated in the above figure, the porphine ring is positioned such that the two propionic acid side chains bonded to the porphyrin ring would be oriented towards the left side of the image with the side chains being bonded to the macrocycle at approximately position (-1, 4) for the y-axis oriented chain and at approximately position (-4, 1) for the x-axis oriented chain, with the porphyrin positioned distal side up. For each species of origin available in the RCSB-PDB, only one surface is displayed.

The displayed surface fits reveal that a high degree of geometric variability exists throughout the porphyrin macrocycle when it is present in the protein environment.

### **9.2.2 Selection of an Appropriate Candidate**

During the experimental process, protoporphyrin IX is substituted into the myoglobin protein and acts as the investigatory probe of the internal electric field. As the experimental data is used in conjunction with the results of the theoretical computations during the analysis, a consistent evaluation of the internal field value can result only if a structural equivalency exists between the molecular protoporphyrin IX being spectroscopically analyzed during the experiment and the porphine core that is used for the calculation of the state energies and the transition dipole moments. Ideally, the greatest accuracy using this combined experimental and analysis approach would result if the exact molecular coordinates of the protoporphyrin IX as it exists within the myoglobin under the precise thermal conditions that the hole-burning and Stark experiment is conducted at could be known. Unfortunately, within the literature there is no crystal structure for protoporphyrin IX substituted myoglobin, PPIX-Mb. This, therefore, makes the selection of an appropriate substitute for the core molecular structure to use when carrying out the theoretical computations a necessity. Any selected substitute for this purpose must then uphold some specific qualifications if it is to justly represent the geometric characteristics of the molecule as it exists under the context of the experiment. The following qualifications were viewed as being of primary importance and were the qualifications under which the substitute was chosen. All of

the qualifications amount to the restriction that the crystal structure must reflect the sample that is used during the hole-burning experiment. The crystal structure of the myoglobin should arise from the same species, the porphyrin must be in the unligated form, the myoglobin should have no residue alterations, and the crystal structure should be from myoglobin that was in the same pH range and be at a similar temperature during the crystallography process as to that which is present during the hole-burning experiments. Of the 66 crystal structures for *Equus caballus* (horse) myoglobin that appear in the RCSB-PDB, the best suited candidate that most fully upheld these criterion was the structure 1DWT, as first described by K. Chu *et al.* (2000) [6].

The myoglobin that is used in preparation of the sample upon which the spectroscopic investigations are performed is horse heart myoglobin, M1882 from Sigma-Aldrich. After substitution of the protoporphyrin IX into the myoglobin, the sample is buffered to a pH of 7.3, and is then placed within the 3:1 glycerol:water matrix. As previously indicated, the hole-burning and electric field experiments are carried out at 1-3 K. The crystal structure that provides for the closest correlation, and in turn should best represent the molecular characteristics of the experimental molecule, is 1DWT. This particular crystal structure was obtained through X-ray diffraction with a resolution of 1.40 Å. The crystallization experiments were performed using a sample of horse heart myoglobin from Sigma-Aldrich that was buffered to a pH of 7.5, and during the diffraction experiment, the data collection temperature was 88 K. This particular crystal structure is representative of the photorelaxed horse heart myoglobin CO complex. According to the original publication regarding the 1DWT structure, “no electron density associated with CO is seen at the distal side of the haem, but a new peak

interpreted as CO\* appears below the haem” [6]. No residue alterations were made to this protein and aside from the presence of the CO, based on all of the other aspects under which the crystallographic experiment was performed, 1DWT does provide for a reasonable substitute for establishing the molecular geometry of the porphyrin in the native protein environment that, although is not an exactly perfect match for the parameters of this particular experimental investigation, is at least a plausible

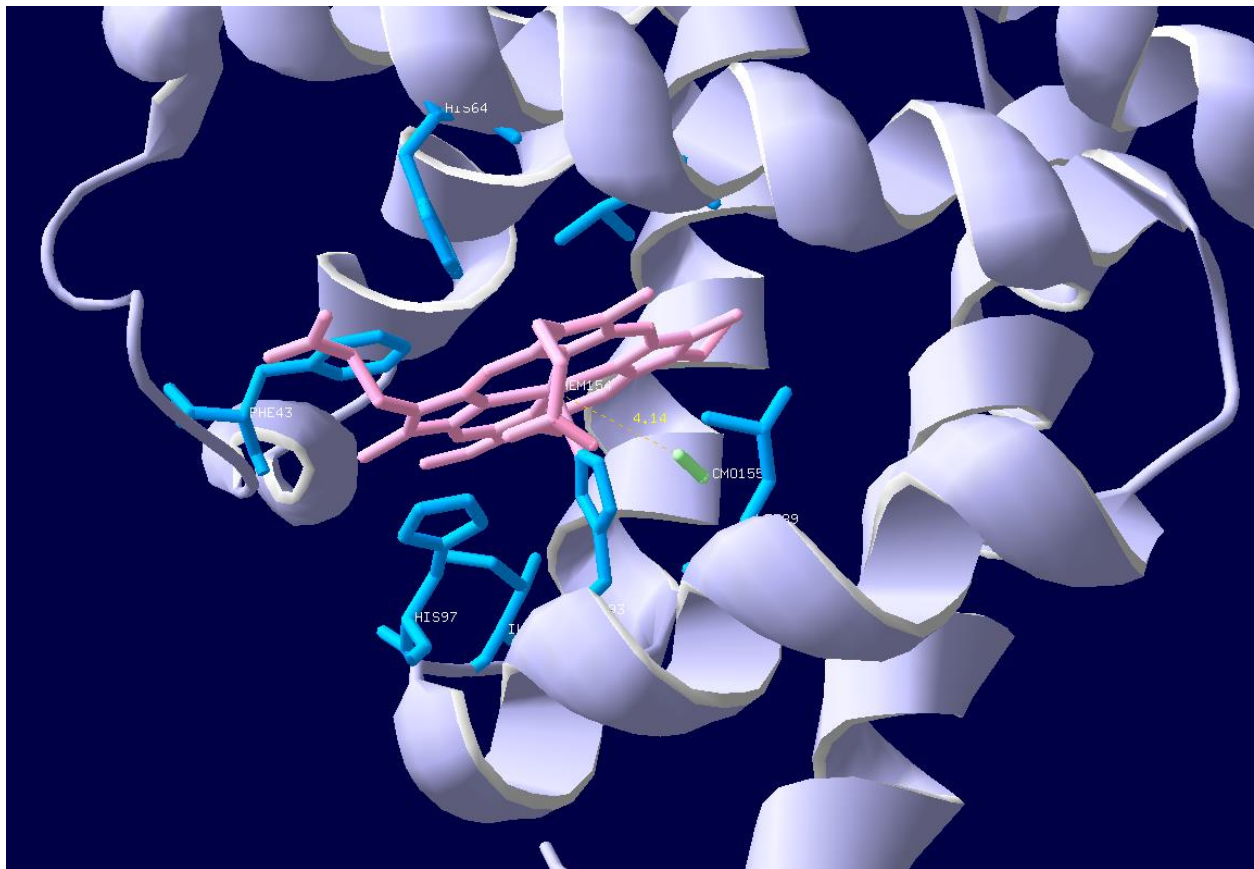


*Figure 9.2: Close up of the oxygen binding site of horse heart myoglobin as described by the 1DWT crystal structure [6]. The native heme appears in pink, and the CO is shown in green. The CO is removed from the center of the porphyrin ring by a distance of 4.14 Å. The protein residues also existing within this range to the center of the porphyrin ring are shown in light blue. No electron density associated with the CO appears on the distal side of the porphyrin plane. This image was created using the Swiss-PdbViewer application [19].*



substitute. To more clearly illustrate the location of the CO within the binding cavity, an image was generated using the Swiss-PdbViewer application, and the original information as provided within the 1DWT crystal structure data [19, 6]. In the preceding figure, the protein appears in light grey, with the native heme displayed in pink. The CO appears in green and resides 4.14 Å away from the center of the porphyrin ring. The protein residues that are within the same proximity as the CO to the center of the porphyrin ring are displayed in light blue.

The coordinates to define the porphyrin molecule that were used throughout the computational investigations discussed here were taken directly from those that appear in the structure 1DWT. To create the free base form of the molecule for the calculation process, the iron was removed and was replaced with two inner hydrogens on opposite nitrogens that would henceforth define the x-axis of the molecule. The hydrogens were placed within the porphyrin molecule according to the positions of the inner hydrogens at the designated bond lengths and bond angles as specified by B. Chen (1972) [5]. The methyl, vinyl and propionic substituents were removed, and because the vinyl and propionic groups are significantly twisted out of the plane of the molecule and do not contribute to the conjugation within the molecule, they are treated as a part of the protein environment when using this specific analysis methodology. The periphery of the porphyrin was then populated as necessary with hydrogens for the correct bonding character for the atoms of the molecule.

In order to most faithfully represent the molecule as it would be found within the myoglobin under true experimental conditions, no geometry optimization was performed on the molecular structure that was used for calculating the transition dipole

moments and the state energies for the analysis. The coordinates that were used throughout all of the computational studies appears in Appendix G. With one exception only, a geometry optimization of this structure was performed using a 6-311G basis set at the MP2 level of perturbation theory and by means of a vibrational analysis calculation, the resulting geometry was found to represent the stationary point [3, 47].

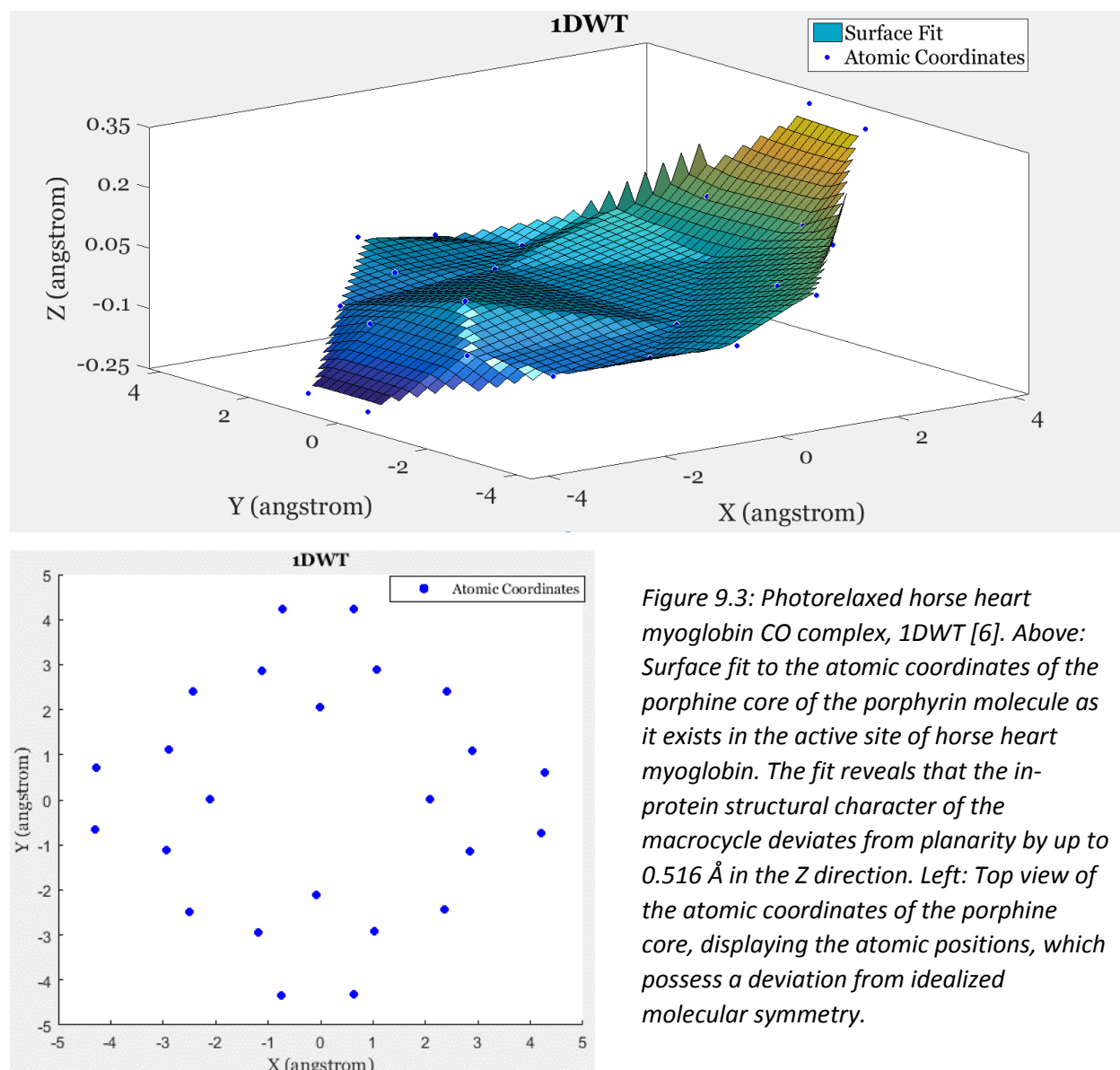


Figure 9.3: Photorelaxed horse heart myoglobin CO complex, 1DWT [6]. Above: Surface fit to the atomic coordinates of the porphine core of the porphyrin molecule as it exists in the active site of horse heart myoglobin. The fit reveals that the in-protein structural character of the macrocycle deviates from planarity by up to 0.516 Å in the Z direction. Left: Top view of the atomic coordinates of the porphine core, displaying the atomic positions, which possess a deviation from idealized molecular symmetry.

This brief set of studies using this optimized structure was performed for comparative purposes only and are discussed more fully in section 9.4.1 of this chapter. The results of these investigations, along with the comparisons between the quantities that were calculated using the optimized and the non-optimized molecular structure are highlighted.

Displayed in figure 9.3 is the best fit surface to the atomic positions of the porphine core of the porphyrin macrocycle as defined within the 1DWT crystallographic structure of photorelaxed horse heart myoglobin [6]. Although the geometric character of this macrocycle could be viewed as being nearly planar, in the Z direction the macrocycle deviates from planarity by up to 0.516 Å. This surface fit illustrates the ruffled nature of the porphyrin macrocycle as it exists in myoglobin. The top view of the atomic positions in the above figure displays that the molecule possess deviation from an idealized molecular symmetry.

### 9.3 Electronic Structure Theory

A complete determination of all of the properties that describe a molecular system is often not a possibility through experimental means alone. Therefore, computational approaches must be used that allow for the theoretical calculation of the various molecular quantities that are of interest to the experimenter. At the heart of all problems in computational chemistry is the Schrödinger equation. Although the time-dependent form of the Schrödinger equation can be and is used, it is not necessary here because we are dealing with stationary states. In addition, the Born-Oppenheimer

approximation can be employed, so that the electronic motion can be separated from the nuclear motion, which makes the equations more tractable. Therefore, the properties of interest can be arrived at by solving for the solutions to the time-independent Schrödinger equation.

$$H | \Psi_n \rangle = \epsilon_n | \Psi_n \rangle \quad (9.1)$$

According to this relation, the state specific energy values  $\epsilon_n$  are found when the state specific wave functions  $\Psi_n$  are operated upon by the Hamiltonian  $H$ , which is the operator that describes the energy of the system [9, 33]. Frequently, in addition to the state energy, other various quantities of the molecular system are desired. When this is the case, the particular molecular properties of interest can be evaluated by use of a more generalized formulation of the above equation.

$$\langle \Psi_n^* | \mathcal{O} | \Psi_n \rangle = \beta_n \langle \Psi_n^* | \Psi_n \rangle \quad (9.2)$$

In this most basic formulation, when the operator  $\mathcal{O}$  acts on the state specific wave functions  $\Psi_n$ , the scalars  $\beta_n$ , representing the state specific eigen values of the operator are returned as the observables. The observables that are returned by finding the solution to equation 9.2 depend upon which operator is applied to the wave function. When implementing either equation 9.1 or 9.2, any observables that are returned are only strictly accurate if the true wave function  $\Psi$  is known.

The true wave function contains all of the possible information regarding the system at any given time, and therefore can allow any given property of the system to be calculated by application of the applicable operator. In practice, determination of the

true wave function by analytical means is only possible in the simplest of cases, such as the case of the particle in a box, or more interestingly the case of the hydrogen atom, as well as some other simplified situations. Therefore, approximations must inevitably be made in the construction of a wave function that can reasonably describe the properties of a more complicated and realistic molecular system. The technique that is generally employed for establishing a molecular wave function is known as the LCAO-MO approach, which rests in using a linear combination of atomic orbitals to generate the resultant molecular orbitals [33, 51].

$$\phi_n = \sum_{i=1}^N \alpha_{ni} \varphi_i \tag{9.3}$$

Here, the  $\alpha_{ni}$  represent the characteristic coefficients that are used to scale the contribution of each of the  $N$  one electron atomic orbitals or basis functions  $\varphi_i$  that are used in construction of the effective one electron molecular orbital  $\phi_n$  that is in itself a one electron wave function. In the case that the molecule under study has multiple electrons, the many electron wave function of the system can then be established by taking the anti-symmetrized product of the individual one electron molecular orbitals  $\phi_n$  that contribute to the system. This amounts to forming and then eventually solving the Slater determinant of the system to yield the many electron wave function  $\Phi$ .

The quality of the many electron wave function that is established through the LCAO-MO approach, which exists only as an approximation of the true wave function, can be assessed according to the variational principle, and the wave function can then be improved upon by using the variational method. According to this principle, the ground

state energy serves as a gauge of the quality of the wave function. The variational principle states that the ground state energy as calculated with the true wave function  $\Psi$ , will exist as a lower bound to the ground state energy that can be calculated with any other trial wave function  $\Phi$  [51]. Mathematically, the variational principle takes on the following formulation.

$$\frac{\int \Phi^* H \Phi dr}{\int \Phi^* \Phi dr} \geq \epsilon_0 \quad (9.4)$$

As before, the Hamiltonian operator is specified as  $H$ , and  $\epsilon_0$  is the true ground state energy that would be calculated if the true wave function  $\Psi$  were known. When the trial wave function  $\Phi$  is operated upon by the Hamiltonian, the expectation value for the ground state energy in relation to that particular trial wave function can be calculated. The evaluation for the ground state energy that is returned will always be greater than the true ground state energy, unless the trial wave function is the true wave function. This integration is performed over the spatial coordinates  $r$ , and the denominator in equation 9.4 functions to normalize the energy.

The best trial wave function is then determined by using a variational process. The trial wave functions  $\Phi$  are optimized in an iterative fashion until the lowest value for the energy of the ground state is returned. This optimization procedure is carried out by systematically varying the characteristic coefficients  $\alpha_{ni}$  that are used to scale the basis functions in the LCAO-MO approach to construct the molecular orbitals. During each iteration, a new Slater determinant describing the many-electron wave function of the system is generated, and the determinant is then evaluated to solve for the new molecular orbitals and values for the state energies. This method of improving the wave

function by the variational approach is known as the self-consistent field method and is the basis of the Hartree-Fock approximation, that is used to yield the Hartree-Fock wave function  $\Psi_{HF}$  [56].

Aside from simply varying the characteristic coefficients of the basis functions to create better descriptions of the molecular orbitals and in turn the trial wave function, other methods that fall under two primary categories are frequently employed. These methods, which allow for even greater approximations to the true wave function of the system to be made, rely upon either improvements to the basis set or rely upon improvements to the level of theory used in the computation. Improvements to the quality of basis set modify the position in space that the electrons are able to occupy around the molecule. Improvements to the level of theory used in the computation modify the way in which the electron-electron interaction term of the Hamiltonian is accounted for. Under the most basic theoretical treatment, the Hartree-Fock method, all of the electrons experience only the mean potential field that is created by all of the other electrons, which results in the motion of the electrons within the molecule to not be correlated to one another. Higher order theoretical approaches use different methods to move past the mean field approximation for the electrons. Many computational studies investigating real molecular systems use both of these improvement schemes in order to increase the completeness by which the wave function is defined, so that the most realistic evaluations for the various molecular properties can be calculated.

The volume in space that the electrons are able to exist within around the molecule is ultimately defined by the effective molecular orbitals  $\phi_n$  that are used.

Originally, the basis functions  $\varphi_i$  that were used in construction of molecular orbitals were hydrogen-like one electron atomic orbitals, or Slater-type orbitals, for which the Schrödinger equation could be solved analytically [8]. Due to the computational efficiency of using Gaussian functions, and the ability of these functions to yield analytic solutions for all of the necessary integrals that must be performed, Gaussian functions are typically used as opposed to Slater-type functions when describing the atomic orbitals. Generally, a linear combination of primitive Gaussian functions is used to create a contracted basis function, which is then in turn used to represent the one electron atomic orbitals that are then used to establish the molecular orbitals. Plane wave solutions are also commonly used to serve as the basis functions out of which the effective molecular orbitals can be constructed.

To improve the description of the position of the electron density in space, higher order basis sets can be and generally are implemented during computational investigations. These larger basis sets utilize multiple Gaussian functions and sets of Gaussian functions to model the Slater-type atomic orbitals that are used in creation of the molecular orbitals. Additionally, polarization functions that give higher angular momentum character to electrons existing in low-order orbitals can be added to give the electrons the capability to exist in more varied volumes that they may be likely to exist within around the atomic positions when in various bonding situations. When modeling excited states, since the electrons are located further away from the nucleus, lose functions that allow electron density to exist at locations that are further away from the nucleus are typically added to the description of the atomic orbital. Thus, the inclusion of any functional types that allow the electrons the ability to possess amplitude at



distances away from the nuclear coordinates of the molecule, and occupy volumes with more varied spatial character, becomes very important when performing calculations regarding the energies or other molecular properties of excited states. Many basis sets exist that can be used in computational studies. Typically, the basis sets that are the most descriptive and have the greatest flexibility for assigning electron density to varied locations in space yield the highest quality wave functions and in turn the best computational results.

The second primary improvement that can be made to the description of the wave function relies on accounting for the electron-electron interactions that exist around the molecule in a more complete fashion. To date, many methods have been devised to deal with the electron correlation energy. Typically, these approaches either implement different perturbative treatments to deal with the correlation energy or utilize computational approaches that build the wave function differently. Similar to the LCAO-MO approach, rather than constructing the wave function using a single Slater determinant, these methods generally attempt to construct better approximations to the true wave function by taking scaled linear combinations of many Slater determinants, each of which distribute the population of the electrons across the occupied and unoccupied states differently [53, 56]. Each of the different methods that are available for treating the electron correlation energy have benefits as well as drawbacks. Typically, the tradeoff being that an improvement in the quality of the result comes at the cost of greatly increased computational expense. This expense is in regard to either the computational memory that is required or the time that is required to conduct the calculation. Of the developed approaches, there is generally a more complete

description of this electron correlation as one moves across the different theoretical approaches according to Hartree-Fock < MP2~CIS~MP3~CCD < CISD < CCSD < MP4 < CCSD(T) < MP5~CISDT~CCSDT < MP6 < MP7 < CISDTQ~CCSDTQ, of which the scaling of the computational cost, memory and time, also closely follows. The role of the computational chemist is to determine the necessary tradeoff that can be made in regard to the computational accuracy and the computational cost of a particular calculation. This is specifically in relation to the chemical accuracy of the returned result that is required by the experimenter to solve the particular chemical problem at hand [8].

This particular investigation focused on studying the effects of using basis sets with varying levels of descriptive ability, as well as implementing various computational approaches that account for the electron correlation energy differently, when calculating the transition energies as well as the state specific dipole and transition dipole moment values of free base porphyrin possessing in-protein structural character. The computational approaches reviewed fall under two main categories, namely, configuration interaction, and coupled-cluster, of which the results of these studies are discussed in detail in the following sections.

## 9.4 Configuration Interaction Approaches

Configuration interaction, CI, attempts to describe electron correlation and regain the energy losses that arise from the over-counting of the electron-electron repulsion effects. To achieve this, the configuration interaction methodology uses a weighted linear combination of Slater determinants, each describing differing electron

occupations across the occupied and the virtual orbitals. The true solution will only occur if full CI is performed, whereby all of the possible occupation combinations of all of the electrons across the occupied and virtual orbitals are included in the calculation. In practice, except for the smallest of molecular systems, full CI is not a possibility and a truncated version of this process must be performed. These truncated CI approaches build the wave function out of Slater determinants that allow only a limited number of electrons to possess different occupations across the occupied and virtual orbitals. These truncations typically fall under the categories of CIS (configuration interaction singles), CISD (singles and doubles), CISDT, (singles, doubles, and triples) and CISDTQ (singles, doubles, triples, and quadruples); however, the number of electrons allowed to possess different occupation can sometimes be extended even further.

The configuration interaction method to construct the wave function is performed by using the following weighted linear combination scheme. The Slater determinant representing the many electron trial wave function that was created using

$$\Psi_{CI} = \mathbf{a}_i \Psi_{HF} + \sum_i^{occ} \sum_r^{vir} \mathbf{a}_i^r \Psi_i^r + \sum_{i<j}^{occ} \sum_{r<s}^{vir} \mathbf{a}_{ij}^{rs} \Psi_{ij}^{rs} + \dots \quad (9.5)$$

the LCAO-MO approach, described in the previous section, which places all of the available electrons into occupied orbitals, appearing as  $\Psi_{HF}$ , is the standard Hartree-Fock wave function. The next term represents the set of terms that would be included under a CIS approach. Here, the index  $i$  runs over all of the electrons in occupied orbitals and the index  $r$  runs over all of the unoccupied or virtual orbitals. A Slater determinant that places one of the electrons from an occupied orbital  $i$  into an

unoccupied orbital,  $r$  is represented as  $\Psi_i^r$ . Because this second term is a sum, the number of Slater determinants that need to be calculated grows quickly, since there will be a Slater determinant representing each individual electron in an occupied orbital being placed into each of the possible virtual orbitals. The next term is additionally included if the CISD approach is being used. This creates the Slater determinants  $\Psi_{ij}^{rs}$ , that remove one electron from occupied orbital  $i$ , and one electron from occupied orbital  $j$ , and places them into virtual orbitals  $r$  and  $s$ , respectively. The different  $\alpha_i$  terms that appear throughout the equation are the CI coefficients, which are used to scale the contribution of the various Slater determinants in the linear combination used for constructing the CI wave function. As with the standard Hartree-Fock approach, the variational method is again used to optimize the CI coefficients to determine the particular wave function that returns the lowest evaluation of the ground state energy. Therefore, at all of the various levels of excitation, CI uses a linear combination of excitations to improve on Hartree-Fock reference wave function [8, 56].

### 9.4.1 Configuration Interaction Singles

The configuration interaction singles (CIS) methodology was the first computational approach investigated for its ability to accurately reproduce experimental valuations for spectroscopically observable transition energies of the porphyrin probe molecule. Under a CIS treatment, a linear combination of singly excited determinants that are scaled by the optimized configuration interaction coefficients are added to the base Hartree-Fock

reference wave function to create the CIS wave function. A CIS treatment amounts to using only the first two terms of equation 9.5 for establishing the wave function.

During this set of studies, GAMESS and Firefly, two related but different quantum chemistry applications, were used. The General Atomic and Molecular Electronic Structure System, GAMESS, is developed and maintained by the Mark Gordon research group at Iowa State University, for which a site license is available at no cost to both academic and industrial users [15, 47]. This program can be obtained at <http://www.msg.ameslab.gov/GAMESS/>. Firefly is a computational chemistry program that was developed for high performance on Intel-compatible processors, and was originally based on the source code ISUQCG of the 1999 version of GAMESS. Firefly is developed by the Firefly Project Team under the coordination of lead developer Dr. Alex A. Granovsky, where there has been significant change to and development of the source code over the past 16 years [1]. Firefly is a freely available application that can be obtained at <http://classic.chem.msu.su/gran/gamess/index.html>. Because of the relation of Firefly to the early versions of GAMESS, the input files necessary to prepare for running a calculation are very similar to those that are used in the GAMESS application. Although both of these quantum chemistry programs offer much of the same functionality, each application has its own strengths with differing capabilities in relation to the more advanced theoretical treatment methods that can be performed, and the way in which the calculations are programmatically carried out. Therefore, with these two quantum chemistry applications at hand, an investigator has the ability to perform computations utilizing almost any theoretical approach that currently exists.

Of the primary benefits that exist when performing a calculation at the CIS level of theory is that the preparation of the input file required to run the calculation is extremely simple, with the decisions necessary to be made by the experimenter regarding the molecular and chemical parameters of the calculation being very limited in scope. The principal component is a specification of the number of excited states for which the property of interest (operator-dependent) is to be calculated. Additionally, because only a single electron is excited at a time into the unoccupied or virtual space, for the construction of the new determinants, the overall number of determinants that will be necessary to form and calculate stays relatively low. This is due to the limited number of possible combinations of electronic excitations that could be carried out. The scaling of a CIS calculation is on the order of  $N^5$ , where  $N$  is the number of electrons in the molecule. A result of this low scaling level is that very large basis sets can be implemented, and that the memory requirements and the length of time required for performing computations, even with very large basis sets that include large virtual spaces, remains low. The greatest benefit of this approach is that expectation values for properties can be calculated for in excess of 1000 excited states with relative ease. The main drawback to performing computation at this level of theory is that the accuracy of CIS is only on the order of a standard Hartree-Fock calculation. Due to the limited number of excitations included, the CIS level of theory is incapable of capturing any of the correlation between excited states. Therefore, since true excited states can only be effectively modeled using linear combinations of determinants possessing multi-excited electrons, CIS generally will not give good approximation for the excited states unless they are low lying [8, 15, 53].

The set of studies that were performed under this level of theory focused on modulating both the quality of the basis set used in the computation as well as investigating how the results of the computation were affected by requesting properties to be calculated for greater numbers of excited states of the virtual space. As with all of the following studies that are discussed, the state energies as well as the state specific dipole moments and the transition dipole moments were computationally evaluated. The metric of quality being the transition energy of the four observable optical transitions of porphyrin, namely the Soret transitions,  $B_y$  (425.86 nm) and  $B_x$  (429.52 nm), and the Q-band transitions,  $Q_y$  (541.65 nm) and  $Q_x$  (620.27 nm) [62]. Although not experimentally observable, the anticipated splitting of the Soret transition is stated, with the experiment resulting in a degenerate  $B_x$ ,  $B_y$  peak appearing at  $\sim 430$  nm.

Displayed in table 9.1 is a representative summary of the initial set of CIS calculations performed. The basis set comparison, shown first and third, displays the effect of using a moderately sized basis set, 6-311++G(d,p), that includes some polarization and diffuse character, and a larger Dunning basis set, aug-cc-pCVDZ, possessing polarization and diffuse character that was specifically designed and tailored for use with theoretical methods that include correlation [11]. If calculations using aug-cc-pCVDZ, aug-cc-pCVTZ, and aug-cc-pCVQZ are performed, extrapolation to the CBS, complete-basis-set limit, can be made. The effect of requesting the calculation of properties for a greater number of states of the virtual space can be observed in the first and second portions of the table. Here, the state energies appear in hartrees, and the state transitions are highlighted in light blue and are presented in nm. The transitions

Original Structure: 1DWT									RPN
<b>150 STATES</b>									
<b>6-311++G(d,p)</b>									
	<b>hartree (H)</b>	<b>(nm)</b>		<b>X</b>	<b>Y</b>	<b>Z</b>	<b>NORM</b>		
<b>Gnd</b>	-983.38								
<b>EX 1</b>	-983.294	529.63	$\mu$ 0-1	-1.072	0.0119	-0.015	1.0723	DEBYE	
<b>EX 2</b>	-983.29	506.07	$\mu$ 0-2	0.0499	-2.348	0.1093	2.3515	DEBYE	
<b>EX 3</b>	-983.225	294.22	$\mu$ 0-3	-8.284	0.1782	0.0031	8.2854	DEBYE	
<b>EX 4</b>	-983.218	281.41	$\mu$ 0-4	-0.307	2.3345	-0.088	2.3563	DEBYE	
<b>500 STATES</b>									
<b>6-311++G(d,p)</b>									
	<b>hartree (H)</b>	<b>(nm)</b>		<b>X</b>	<b>Y</b>	<b>Z</b>	<b>NORM</b>		
<b>Gnd</b>	-983.38								
<b>EX 1</b>	-983.294	529.63	$\mu$ 0-1	1.0721	-0.012	0.0145	1.0723	DEBYE	
<b>EX 2</b>	-983.29	506.07	$\mu$ 0-2	-0.05	2.3484	-0.109	2.3515	DEBYE	
<b>EX 3</b>	-983.225	294.22	$\mu$ 0-3	8.2835	-0.178	-0.003	8.2854	DEBYE	
<b>EX 4</b>	-983.218	281.41	$\mu$ 0-4	0.3074	-2.335	0.0882	2.3563	DEBYE	
<b>150 STATES</b>									
<b>aug-cc-pCVDZ</b>									
	<b>hartree (H)</b>	<b>(nm)</b>		<b>X</b>	<b>Y</b>	<b>Z</b>	<b>NORM</b>		
<b>Gnd</b>	-983.283								
<b>EX 1</b>	-983.198	533.22	$\mu$ 0-1	1.1829	-0.017	0.0127	1.1831	DEBYE	
<b>EX 2</b>	-983.194	510.43	$\mu$ 0-2	0.0493	-2.423	0.1095	2.4256	DEBYE	
<b>EX 3</b>	-983.129	295.36	$\mu$ 0-3	8.3219	-0.199	-0.003	8.3243	DEBYE	
<b>EX 4</b>	-983.121	281.62	$\mu$ 0-4	0.0992	-2.522	0.0948	2.5261	DEBYE	

Table 9.1: State energies, transition energies, and transition dipole moment values for the optical transitions ( $Q_x$ ,  $Q_y$ ,  $B_x$ ,  $B_y$ ) of porphine, possessing the molecular geometry of 1DWT. Calculations were performed using the configuration interaction singles (CIS) approach. The first two portions of the table display the effect of calculating properties for a larger number of excited states using the same basis set. The first and third portion of the table display the effect of using basis sets of differing size and quality during the calculation.



correspond as follows,  $Q_x=EX_1$ ,  $Q_y=EX_2$ ,  $B_x=EX_3$ ,  $B_y=EX_4$ . The calculated transition moments are highlighted in light grey.

It can be observed that the norm of the transition moments are almost exactly consistent across the different calculations. Requesting properties for a greater number of states of the virtual space has no impact on the calculated state energies or transition energies, and has no impact on the numerical magnitude of the transitions moments. The results of this study indicate that the directionality of the calculated transition moments is dependent on both the number of virtual states for which properties are requested as well as the basis set that used during the calculation. As is expected with this molecule, all evaluations for the transition moments follow a polarization that is predominantly  $(EX_1, EX_2, EX_3, EX_4) = (X, Y, X, Y)$ . Deviation from pure  $(X, Y, X, Y)$  transition moment polarization is to be expected as the molecule is not perfectly planar or symmetric, see figure 9.3, which should naturally result in some off directional character. Although it would be expected that the energy of the ground state would be lower in value when the calculation is performed using the more complete aug-cc-pCVDZ basis set, in comparison to the 6-311++G(d,p) basis set, a slight increase of about 0.091 hartree in the energy of the ground state is observed. The relative performance between these two basis sets has been reported to deviate from what is expected in some studies [59]. The transition energies that were computed using the aug-cc-pCVDZ basis set were, however, of slightly better quality, based on what is observed in experiment.

Using the CIS theoretical approach only, a set of calculations were performed with a base molecular structure that was optimized from the 1DWT crystal structure

geometry. The geometry optimization, although performed using a relatively small 6-311G basis set, was carried out at the MP2 level of perturbation theory. A vibrational analysis was carried out and the resulting geometry was found to represent the stationary point. This brief set of studies that utilized this optimized structure were performed only for comparative purposes, of which the results appear in table 9.2. Here only the effect of requesting the calculation of properties for a greater number of states

Optimized Structure: 1DWT				RPN-OPT				
<b>150 STATES</b>								
<b>6-311++G(d,p)</b>								
	<b>hartree (H)</b>	<b>(nm)</b>		<b>X</b>	<b>Y</b>	<b>Z</b>	<b>NORM</b>	
<b>Gnd</b>	-983.4363							
<b>EX 1</b>	-983.3515	537.19	$\mu$ 0-1	2.0397	-8E-04	-0.093	2.0418	DEBYE
<b>EX 2</b>	-983.3472	511.54	$\mu$ 0-2	-9E-04	1.5855	-0.014	1.5856	DEBYE
<b>EX 3</b>	-983.2783	288.42	$\mu$ 0-3	9.5435	0.0027	-0.1001	9.5441	DEBYE
<b>EX 4</b>	-983.2703	274.51	$\mu$ 0-4	0.0027	-12.57	0.0926	12.572	DEBYE
<b>500 STATES</b>								
<b>6-311++G(d,p)</b>								
	<b>hartree (H)</b>	<b>(nm)</b>		<b>X</b>	<b>Y</b>	<b>Z</b>	<b>NORM</b>	
<b>Gnd</b>	-983.4363							
<b>EX 1</b>	-983.3515	537.19	$\mu$ 0-1	-2.04	0.0008	0.0934	2.0418	DEBYE
<b>EX 2</b>	-983.3472	511.54	$\mu$ 0-2	0.0009	-1.586	0.0141	1.5856	DEBYE
<b>EX 3</b>	-983.2783	288.42	$\mu$ 0-3	-9.544	-0.003	0.1001	9.5441	DEBYE
<b>EX 4</b>	-983.2703	274.51	$\mu$ 0-4	0.0027	-12.57	0.0926	12.572	DEBYE

Table 9.2: State energies, transition energies, and transition dipole moment values for the optical transitions ( $Q_x$ ,  $Q_y$ ,  $B_x$ ,  $B_y$ ) of porphine, possessing a molecular geometry that was optimized from the original 1DWT geometry. Calculations were performed using the configuration interaction singles (CIS) approach. The effect of calculating properties for a larger number of excited states using the same basis set can be observed. As compared to the results displayed in table 9.1 that were obtained using the unoptimized molecular geometry, the optimized geometry produces slightly better valuations of the transition energies in relation to what is spectroscopically observable. Again the directionality of the transition moments changes when properties for a greater number of states are calculated.

of the virtual space was looked into. These studies were again performed using the 6-311++G(d,p) basis set so that comparisons could be made to the findings illustrated in table 9.1. These calculations yielded evaluations for the ground state energy that were slightly lower by approximately 0.0564 hartree than those found using the unoptimized geometry of the molecule, which from a variational standpoint indicates that any molecular parameters calculated may be of slightly better quality in relation to the true values. Although the  $Q_x$  and  $Q_y$  transition energies were in slightly better agreement to the spectroscopically observable result, the  $B_x$  and  $B_y$  transition energies were slightly worse, than what was calculated using the unoptimized geometry. Again, no difference of state energy, transition energy, norm of transition moment, or the numerical magnitude of the transition moments is observed by requesting properties for a larger subset of the virtual space during the calculation. As with the unoptimized molecular structure, the polarization of the transition moments is again found to be (X, Y, X, Y). Similar to the calculation that utilized the unoptimized molecular geometry, the directionality of the transition moments again shift when values for additional states are requested for in the calculation, but in a direction that is opposite to that which was found in the previous set of results, as displayed in table 9.1.

If the valuations of the transition moments and state energies that are found by performing calculations at the CIS level of theory are to be used when implementing the molecular resolution approach to the fitting of spectral holes, additional efforts need to be made to determine the cause of the shift in sign of the transition moments that occurs as the evaluation of more states are requested and if the change in directionality follows any periodic behavior.

## 9.4.2 Configuration Interaction Singles Doubles

The next set of studies focused on utilizing the CISD approach that includes both singly as well as doubly excited determinants in creation of the CI wave function. This treatment includes all of the fully displayed terms in equation 9.5. Unlike the CIS methodology, carrying out this type of calculation requires much greater attention to determining which electrons may be chemically relevant in the calculation, and decisions must be made with regard to which electrons will be active and allowed to populate which portion of the unoccupied orbitals in the virtual space, making preparation of the input file more involved. This is true for any level of CI moving past singles excitation. This does, however, allow for greater control and flexibility in performing the calculation by the experimenter. The scaling of a CISD calculation is on the order of  $N^6$ . Choosing to limit the active electrons and the explored virtual space in effect amounts to performing a restricted active space configuration interaction RAS-CI calculation, again at any level of CI excitation (CISD, CISDT, ...) beyond the singles category [40]. The primary benefit of performing a CISD calculation opposed to only a CIS calculation is that the inclusion of determinants possessing more electronic excitations allows more of the electron correlation as well as correlation between excited states to be captured.

Because this methodology makes necessary the determination of the number of doubly occupied core (DOC), electron orbitals from the HOMO down that are allowed to populate the virtual space, this represents another set of variable parameters (which electrons, which virtual space) that become necessary to investigate in relation to the valuations for the calculated expectation values. To systematically explore the effect that

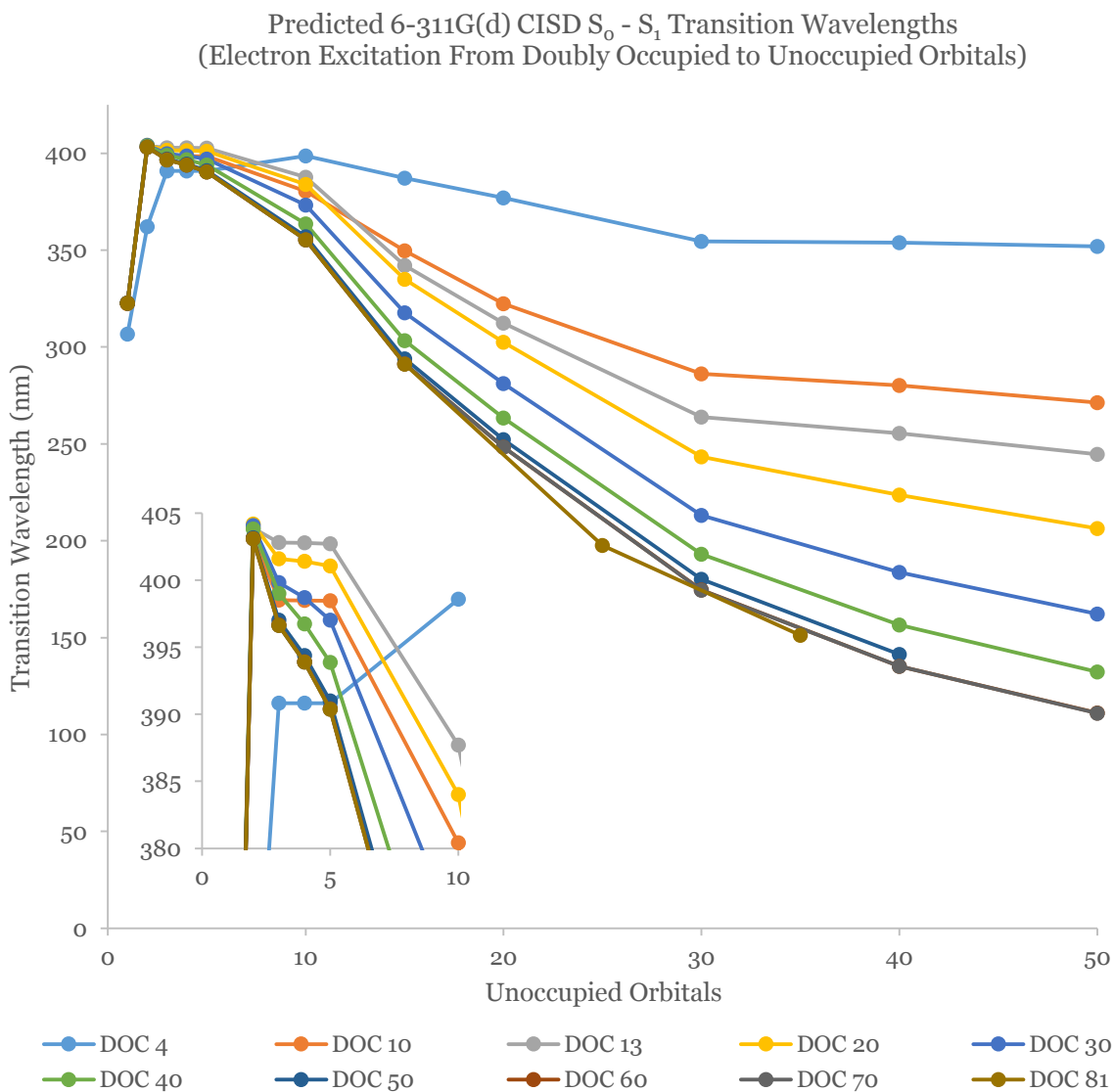


Figure 9.4: Predicted Qx transition wavelengths by CISD using the 6-311G(d) basis set. Electron were excited from doubly occupied core orbitals, HOMO down, into unoccupied orbitals from the LUMO upwards. Ten different active electron groups were allowed to populate up to the first 50 orbitals of the virtual space. The inset displays a magnified view of the first portion of the data.

modifying the number of the doubly occupied core electron orbitals that were included in the calculation had, a set of studies that varied this parameter was conducted. Here, ten different sets of electrons from doubly occupied core orbitals were looked at, which ranged from inclusion of only the electrons from the highest 4 doubly occupied core orbitals HOMO to HOMO-3, (8 total active electrons), down to an inclusion of all of the electrons of the molecule in the active space. Specifically, the different sets of electrons included in the space of active electrons were the groups, DOC: 4, DOC: 10, DOC: 13, DOC: 20, DOC: 30, DOC: 40, DOC: 50, DOC: 60, DOC: 70, DOC: 81. Calculations were performed with the ten different active electron groups being allowed to explore a virtual space of the unoccupied orbitals from the LUMO upwards that included specifically, VIR: 1, VIR: 2, VIR: 3, VIR: 4, VIR: 5, VIR: 10, VIR: 15, VIR: 20, VIR: 30, VIR: 40, VIR: 50. Therefore, only up to inclusion of the first 50 excited states, to create Slater determinants for construction of the CISD wave function was investigated.

The state energies, dipole and transition dipole moments were again calculated. What appears in figure 9.4, are the calculated transition energies for the Q<sub>x</sub> optical transition of porphyrin, by constructing the CISD wave function using the above stated combinations of different groups of active electrons allowed to populate a differing virtual space. The calculated transition energies for the Q<sub>y</sub>, B<sub>x</sub>, and B<sub>y</sub> optical transitions appear in Appendix G. These figures display the results that were obtained using a modest yet descriptive basis set, 6-311G(d). It can be observed that inclusion of a relatively small number of active electrons ( $\geq$  DOC: 13) and a relatively small virtual space (between VIR: 4 and VIR: 10) yielded the highest quality transition energy values. The limited number of necessary active electrons from doubly occupied orbitals seems

to be consistent with the idea that much of the chemical properties of a molecule would be determined predominantly by the behavior of the valence electrons of the molecule as opposed to that of the electrons embedded within the core orbitals of the molecule. The cause, however, of the decrease in the quality of the calculated transition energy that is observed to occur as the number of unoccupied orbitals that are included in the active space is increased, which effectively expands the number of configurations included within the calculation, is unknown.

As with the CIS method, an investigation into the basis set dependence of the evaluations of the state energies, dipole and transition dipole moments as calculated using the CISD methodology was again conducted. For this study the basis sets that were examined, in order of improving quality and descriptive ability were, 6-311G(d), 6-311G(d,p), and 6-311++G(d,p). The quality of basis set that these computations can be performed with can still be improved during future investigations. The results of the basis set study appear in table 9.3. It can be observed in the third entry of the table that when the same basis set, 6-311++G(d,p) was used, the result of the CISD calculation with the active space determined by, DOC: 13  $\rightarrow$  VIR: 4, yields a ground state energy that is within 0.022 hartree of the ground state energy that was calculated using the optimized molecular structure and the CIS level of theory. The transition energies, however, are highly inaccurate as compared to what is expected from experiment. More work that focuses on utilizing larger basis sets should first be explored using the current active space, as these moderate active spaces seems to return the best energies. After that, the effect of including different active spaces into the calculation should be looked into. The transition moments are still dominantly polarized following the expected

Original Structure: 1DWT								RPN
<b>100 STATES</b>								
<b>6-311G(d)</b>								
	<b>hartree (H)</b>	<b>(nm)</b>		<b>X</b>	<b>Y</b>	<b>Z</b>	<b>NORM</b>	
<b>Gnd</b>	-983.3962							
<b>EX 1</b>	-983.2831	402.784	$\mu$ 0-1	0.8893	-0.0234	0.0302	0.8901	DEBYE
<b>EX 2</b>	-983.2708	363.174	$\mu$ 0-2	0.0398	-1.7845	0.1163	1.7888	DEBYE
<b>EX 3</b>	-983.2180	255.595	$\mu$ 0-3	-1.4221	-0.5936	0.0282	1.5413	DEBYE
<b>EX 4</b>	-983.2165	253.456	$\mu$ 0-4	0.1451	0.1692	0.0088	0.2231	DEBYE
<b>100 STATES</b>								
<b>6-311G(d,p)</b>								
	<b>hartree (H)</b>	<b>(nm)</b>		<b>X</b>	<b>Y</b>	<b>Z</b>	<b>NORM</b>	
<b>Gnd</b>	-983.4230							
<b>EX 1</b>	-983.3101	403.790	$\mu$ 0-1	0.9057	-0.0237	0.0287	0.9065	DEBYE
<b>EX 2</b>	-983.2977	363.709	$\mu$ 0-2	-0.0425	1.7981	-0.1174	1.8024	DEBYE
<b>EX 3</b>	-983.2453	256.412	$\mu$ 0-3	-1.4300	-0.5909	0.0278	1.5475	DEBYE
<b>EX 4</b>	-983.2438	254.257	$\mu$ 0-4	-0.0957	-0.1557	-0.0090	0.1830	DEBYE
<b>100 STATES</b>								
<b>6-311++G(d,p)</b>								
	<b>hartree (H)</b>	<b>(nm)</b>		<b>X</b>	<b>Y</b>	<b>Z</b>	<b>NORM</b>	
<b>Gnd</b>	-983.4147							
<b>EX 1</b>	-983.3028	407.139	$\mu$ 0-1	-0.7503	0.0041	-0.0242	0.7507	DEBYE
<b>EX 2</b>	-983.2941	377.732	$\mu$ 0-2	0.0364	-1.8151	0.1082	1.8187	DEBYE
<b>EX 3</b>	-983.2376	257.260	$\mu$ 0-3	-1.4025	-0.5238	0.0441	1.4978	DEBYE
<b>EX 4</b>	-983.2308	247.754	$\mu$ 0-4	-4.3978	-0.0917	-0.0269	4.3988	DEBYE

Table 9.3: State energies, transition energies, and transition dipole moment values for the optical transitions (Qx, Qy, Bx, By) of porphine, possessing the molecular geometry of 1DWT. Calculations were performed using the configuration interaction singles and doubles (CISD) approach with an active space determined by, DOC: 13  $\rightarrow$  VIR: 4. Displayed are the effect of using basis sets of differing size and quality during the calculation. The ground state energy shows improvement to what was determined using the CIS approach. Similar trends as displayed in tables 9.1 and 9.2 regarding the shift in directionality of the transition moments, continues to occur when the properties are evaluated using CISD.



(X, Y, X, Y) convention, and again appear not to vary in magnitude across the different basis sets utilized during this study to any great extent. It can be observed, however, that when the smaller basis sets, namely 6-311G(d) and 6-311G(d,p), are used that the transition dipole moments for the Q and B transitions are of the same magnitude.

### 9.4.3 Configuration Interaction Singles Doubles Triples

As a rule, adding determinants that have more excited character allows for more of the electron correlation energy to be captured. Therefore, adding the triples correction and performing calculations using CISDT would be expected to produce results of higher quality than either CIS or CISD. The scaling of a CISDT calculation is on the order of  $N^8$ . The calculated transition energies for the Q<sub>x</sub> optical transition of porphyrin, by construction the CISDT wave function, again using the stated combinations of different groups of active electrons and virtual spaces, is displayed in figure 9.5. As compared to the previous results calculated using CISD, all of the CISDT transition energies show great improvement. Of specific interest is that calculation with the active space determined by, DOC: 13 → VIR: 30, yields a value for the Q<sub>x</sub>, B<sub>x</sub>, and B<sub>y</sub> transition energies that are of higher quality than those that were calculated using the CIS method, even though the basis set used in this calculation was less complete than the basis set used when the CIS calculation was performed. The calculated transition energies for the Q<sub>y</sub>, B<sub>x</sub>, and B<sub>y</sub> optical transitions are again displayed in Appendix G. Utilizing CISDT, basis set improvements are still a possibility for future studies.

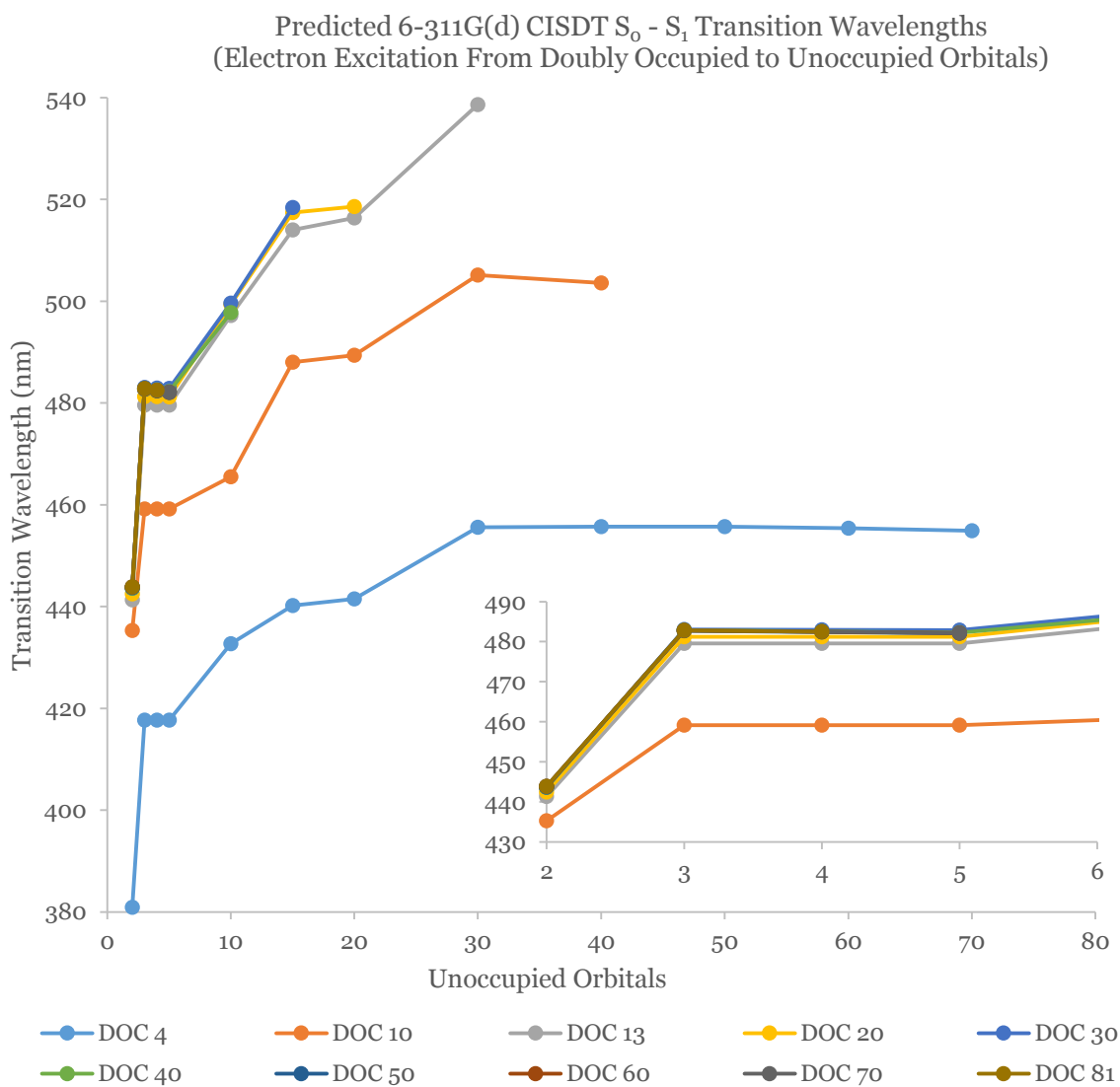


Figure 9.5: Predicted  $Q_x$  transition wavelengths by CISDT using the 6-311G(d) basis set. Electron were excited from doubly occupied core orbitals, HOMO down, into unoccupied orbitals from the LUMO upwards. Ten different active electron groups were allowed to populate up to the first 50 orbitals of the virtual space. The inset displays a magnified view of the first portion of the data.

#### 9.4.4 Configuration Interaction Singles Doubles Triples Quadruples

The last configuration interaction approach investigated was the quadruple level of excitation. The calculated Qx transition energies, by construction the CISDTQ wave function using the various combinations of different active electrons and virtual spaces, is displayed in figure 9.6. The calculated transition energies for the Qy, Bx, and By optical transitions are again displayed in Appendix G. As compared to the previous results of the other levels of excitation using configuration interaction, the CISDTQ energies show a decrease in quality as compared to the CISDT results. Although the values are not terrible, they are certainly not of any usable quality. The scaling of a CISDTQ calculation is on the order of  $N^{10}$ . Due to the sheer size of the calculation, there is not any possibility to improve the quality of the basis set used, as during the current computation the quantity of memory addresses required for storing the necessary integrals was already exceeded. When these calculations were performed, the memory that was available was too limiting. As can be observed in figure 9.6, the active space that could be explored was greatly reduced as the inclusion of additional doubly occupied core orbitals into the active space at the upper end was confined to DOC: 40 → (VIR: 2, VIR: 3, VIR: 4), DOC: 50 and 60 → (VIR: 2, VIR: 3), and DOC: 70 and 81 → (VIR: 2). Due to the exceedingly large size of this calculation and the vast magnitude of computational resources both in regard to memory as well as the time required for a calculation to be completed, the CISDTQ approach should most likely be abandoned at least when studying the porphine core of porphyrin, which is a fairly large molecule from a computational standpoint. Perhaps this method can be revisited in the years to come when the available computational resources are greater.

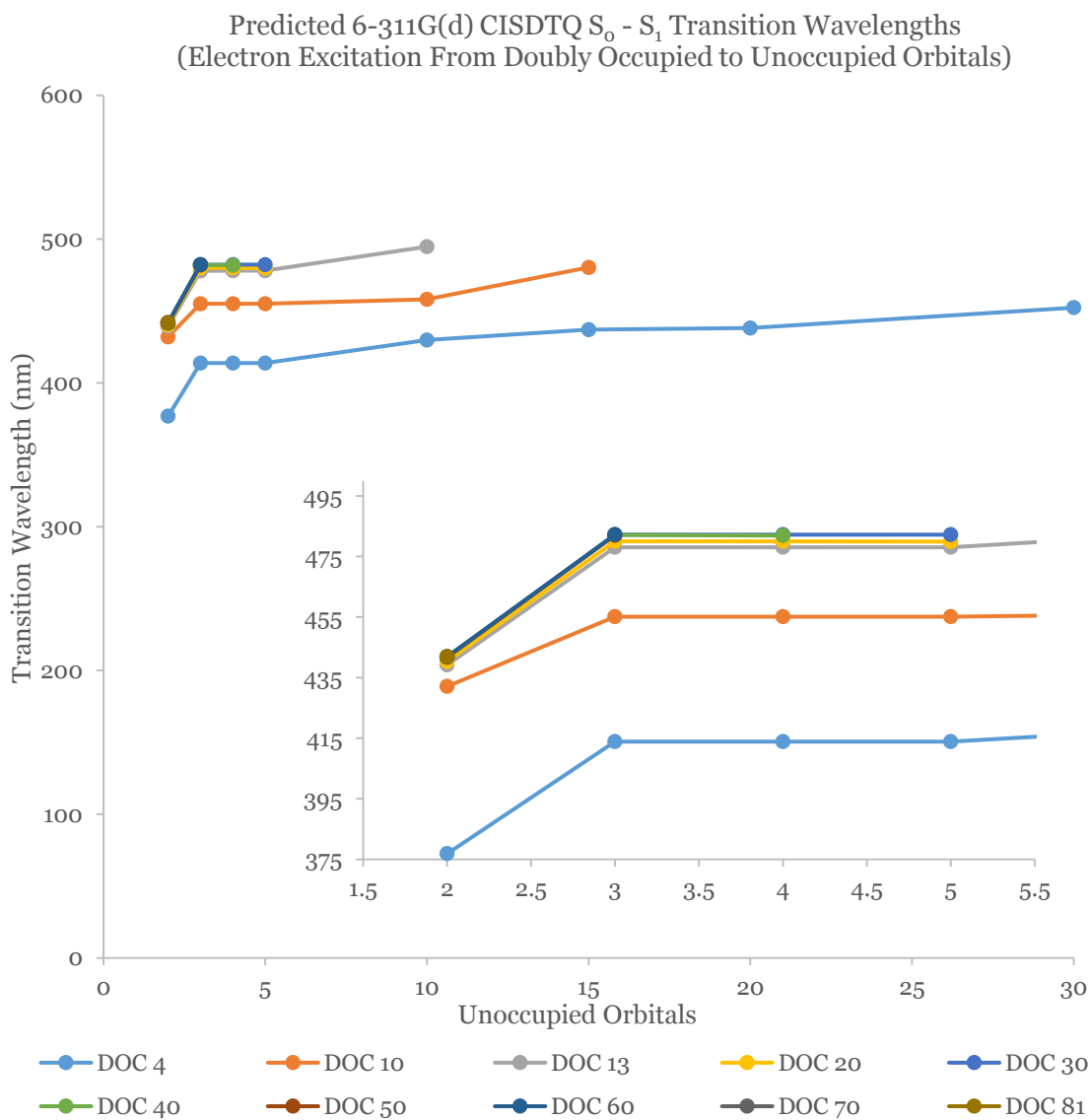


Figure 9.6: Predicted Qx transition wavelengths by CISDTQ using the 6-311G(d) basis set. Electron were excited from doubly occupied core orbitals, HOMO down, into unoccupied orbitals from the LUMO upwards. Ten different active electron groups were allowed to populate up to the first 50 orbitals of the virtual space. The inset displays a magnified view of the first portion of the data. Due to the large scaling of this method,  $N^{10}$ , where  $N$  is the number of electrons, calculations could only be performed with all of the different active electron groups populating only a limited portion of the virtual space.

## 9.5 Coupled-cluster Approaches

The various treatments that fall under the category of coupled-cluster represent some of the most successful and highly accurate approaches available for formulating the many-electron wave function to date. Similar to configuration interaction (CI), coupled-cluster theory (CC) focuses on correcting for the electron correlation that is not accounted for when the wave function is formulated using Hartree-Fock theory alone. Just as in CI, coupled-cluster makes use of the excitation operator, which is represented as  $T_n$ . The associated subscript relates to the number of electron excitations that the particular excitation operator describes. Here,  $T_1$  represents the single excitation,  $T_2$  represents the double excitation, etc. Performing a full CI calculation requires the inclusion of all of the possible excitations, and combinations of excitations, for the  $N$  electrons of the molecular system. The necessary excitation operator required to carry out the calculation, in the case of full CI, is equivalent to the sum of the  $N$  individual  $T_n$ . This is the total excitation operator  $T$  that is displayed in equation 9.6.

$$T = T_1 + T_2 + \dots + T_N \quad (9.6)$$

Using this operator, an application of  $1+T$  to the Hartree-Fock wave function results in an equivalent formulation to that which was presented in equation 9.5. Therefore, if a calculation was to be performed at the CISD level of theory, only the  $T_1$  and  $T_2$  terms of  $T$  would be used. The effect that each of these individual excitation operators in equation 9.6 has on a wave function is shown in equation 9.7, where only the first and second terms are displayed fully. These excitation operators remove  $n$  electrons from occupied orbitals and place them into unoccupied orbitals, creating a

new Slater determinant for each various electron occupation combinations. Again, the indexes  $i$  and  $j$  run over all of the occupied orbitals, and the indexes  $r$  and  $s$  run over the virtual or unoccupied orbitals. Analogous to the case of CI, the  $t_i$  terms that appear in the equations are the coefficients that scale the contribution of the various Slater determinants in the linear combination. The values of  $t_i$ , however, are determined by iteratively solving the coupled equations that result when the Hamiltonian is applied to the coupled-cluster wave function in a self-consistent process [8, 53, 56].

$$T_1 \Psi_{HF} = \sum_i^{\text{occ}} \sum_r^{\text{vir}} t_i^r \Psi_i^r \qquad T_2 \Psi_{HF} = \sum_{i < j}^{\text{occ}} \sum_{r < s}^{\text{vir}} t_{ij}^{rs} \Psi_{ij}^{rs} \qquad (9.7)$$

Different from CI, coupled-cluster theory does not use the excitation operator  $T$ , regardless of imposed truncation, as a linear combination directly but instead relies on an exponential treatment of this operator, as applied to the Hartree-Fock reference wave function. As opposed to an explicit use of the exponential function, however, coupled-cluster arrives at the wave function by implementing a power series expansion of the exponential. For clarity, the power series expansion of only the  $T_2$  operator, as would be applicable in the coupled-clusters double (CCD) method is shown [7, 8].

$$\Psi_{CCD} = e^{T_2} \Psi_{HF} = \left( 1 + T_2 + \left( \frac{T_2^2}{2!} \right) + \left( \frac{T_2^3}{3!} \right) + \dots \right) \Psi_{HF} \qquad (9.8)$$

It is easily observed in this formulation that by implementing the series expansion of the exponential, there is a repeated application of the excitation operator, which, in this case is the  $T_2$  operator. The repeated application, occurs through the squaring, cubing, etc. of the operator in the series expansion. This is the process that

allows for the creation of the “disconnected coupled clusters”, which account for the multiple pairwise interactions occurring between the electrons. Equation 9.9 displays the effect that squaring the  $T_2$  operator, as occurs in the third term of the overall expansion of the exponential, will have on the resulting set of the Slater determinants that the term describes.

$$T_2^2 = \sum_{i<j,k<l}^{occ} \sum_{r<s,p<q}^{vir} t_{ij}^{rs} t_{kl}^{pq} \Psi_{ijkl}^{rspq} \quad (9.9)$$

Through the repeated application of the operator in this fashion, the electron correlation energy is re-captured more quickly than when performing only a basic linear combination of the excitation operators, as was shown in equation 9.6, which is the standard when the configuration interaction method is performed at any of the different levels of excitation. What can be observed in equation 9.9, is that squaring the  $T_2$  operator yields a term that would be similar to the result of an application of the  $T_4$  operator. Here again the Hartree-Fock determinant is used, but now products of the coupled-cluster coefficients  $t_i$  are used as an approximation of the coefficients that would be used for scaling the determinants of a higher order excitation. Therefore, under this methodology, the coefficients that scale these fourth order electron excitation terms are a product of coefficients that scale two second order electron excitations. These coefficients are therefore not linearly independent parameters that can be modulated separately [53]. This protocol of representing higher order excitations and approximating the applicable scaling coefficients by use of lower order coefficients is

carried out for all of the powers that are represented in the series expansion of the exponential function.

The original idea for using this type of approach in coupled-cluster comes from statistical mechanics, where the Mayer-Mayer cluster expansion implements this type of treatment when establishing the partition function that is used when modeling gasses at higher pressures that are under non-ideal conditions. This cluster expansion revealed that under non-ideal conditions, the occurrence of two-particle interactions as well as two two-particle interactions or binary collisions were far more likely than any single three-particle interaction. Therefore, multiple low order interactions were found to be of greater importance than any higher order interaction for describing the behavior of the system, where it was also found that higher order coefficients were well approximated by and closely correlated to the products of low order coefficients.

Analogous to this situation, much of the electron correlation energy existing in real molecules that would need to be accounted for in a true wave function, would also more likely be attributed to the interaction of two electrons with one another, or multiple sets of two electron interactions, as opposed to any single three electron interaction. It was these principles that the originators of coupled-cluster theory used as a foundation for creating the disconnected coupled clusters of pairwise electron interaction during the development of this theoretical approach for describing a wave function [7, 36, 37, 53].

This technique is unlike other post Hartree-Fock theoretical approaches, such as multireference configuration interaction (MRCI) and multi-configurational self-consistent field (MCSCF) that re-optimize the coefficients that are used to scale the atomic orbitals that make up the molecular orbitals appearing in the Slater determinants possessing differing electron orbital occupations. Because the Hartree-



Fock molecular orbitals are used directly without any further optimization, coupled-cluster is considered as a single reference approach to modeling the wave function.

As additional excitation operators, such as the  $T_1$  and  $T_3$  operators, are added to the calculation the higher order electron excitations are more fully described, capturing more of the correlation energy and producing more valid approximations of the true wave function. A result of this, however, is that the size of the computation becomes exceeding large. In practice, the excitation operator is always truncated as coupled-cluster is an exceedingly computationally expensive methodology requiring vast memory resources with computations taking extended periods of time. Typically, the truncation must be made at or below the triples level, with the possibility for additional excitation operators to be included only for calculations that are performed on systems consisting of a few atoms.

Of the primary benefit to the different approaches falling under the category of coupled-cluster are that for all levels of excitation the resulting wave functions are size extensive, meaning that electron density is appropriately assigned such that the energy of the total system will be equivalent to the energy of the constituent parts of the system, which is true also in the case of full CI, but not true for any truncations of CI. The excitation operators that are typically included in establishing the coupled-cluster wave function generally are limited to single, double, and triple excitations, with the methods CCSD, CCSD(T), CCSDT being the most frequently implemented. Rather than using a true triples application, the CCSD(T) approach uses a perturbative treatment for capturing the triple excitation correlation. The triples correction and its variants such as CCSD(T), represent the gold standard for single reference approaches and are viewed as the gold standard for excited state calculations [8, 29, 53, 56].

### 9.5.1 EOM-CCSD(T) and Variants

The equation-of-motion EOM variety of coupled-cluster, using either the singles, doubles, triples or any combination of these three excitation operators, is implemented when calculations on excited states, ionized systems, radical species, or charge transfer systems are performed [30, 32, 46]. Due to the method's ability to yield computed results that are highly accurate when compared to experimentally obtained data, EOM-CCSD is frequently used as a benchmark for evaluating the quality of other computational approaches. EOM-CCSD has been shown to outperform both truncated CI approaches as well as various DFT approaches [4, 60].

This study utilized EOM-CCSD, CR-CCSD(T)\_L [43, 44], and variants of EOM-CCSD(T) that included, CR-EOM-CCSD(T) ID/IB, CR-EOM-CCSD(T) IID/IA, and DELTA-CR-EOM-CCSD(T) DEL(IA), for state energy and transition moment calculations. A full mathematical and operational description of these approaches can be found elsewhere [29, 42, 45, 61]. Here the CR methods use completely renormalized (CR) determinants. All of these EOM-CCSD and EOM-CCSD(T) variants are effective in accounting for dynamical electron correlation effects. The ID/IB and the IID/IA methods are mixed approximations that use different perturbative treatments for inclusion of the triple excited corrections (T) to the approximate wave functions used in determination of the vertical excitation energies [29]. To account for the fact that excited states can have significantly different electronic structure character than ground states, these different variants of EOM-CCSD(T) perform direct calculation of the excitation energies as opposed to implementing a subtraction of the excited and ground state energy as is done in the CI approaches [60]. The DELTA-CR-EOM-CCSD(T)

DEL(IA) method, implements the triples corrections directly to the EOM-CCSD excitation energies rather than the total EOM-CCSD energies. In some cases, this method allows for a balance in the quality of the calculation of the excited states for molecular systems that possess excited states of singly excited character and excited states of doubly excited character. The scaling of a EOM-CCSD(T) calculation is on the order of  $N^8$  [32].

To allow for a comparison of the quality of the state energies and transition dipole moments as calculated using these coupled-cluster approaches, the same basis set 6-311G(d) that was used throughout the configuration interaction studies was again employed. Basis set improvements can be made in future investigations that utilize coupled-cluster for calculating properties of the porphyrin system. The calculated Qx transition energies, using the various combinations of different active electrons and virtual spaces, is presented in figure 9.7. The calculated transition energies for the Qy, Bx, and By optical transitions are again displayed in Appendix G.

For ease of comparison across the different EOM-CCSD(T) variants that were explored, all of the results were plotted together. Due to the significant number of traces that appear in the figure, the specific data point markers have been removed so the data can more easily be viewed. Figure 9.8 which displays the calculated ground state energies, includes markers corresponding to the points where each calculation was performed in figure 9.7. In the two figures, 9.7 and 9.8, the similar colors represent the same groups of active electrons from doubly occupied core orbitals, and the different line types indicate the different EOM variants that were used to perform the calculation. As with the configuration interaction studies, similar sets of active electron groups,

Predicted 6-311G(d)  $S_0 - S_1$  Transition Wavelengths  
 EOM-CCSD (—) CR-EOM-CCSD(T) IID/IA (---)  
 CR-EOM-CCSD(T) ID/IB (- -) DELTA-CR-EOM-CCSD(T) DEL(IA) (.....)

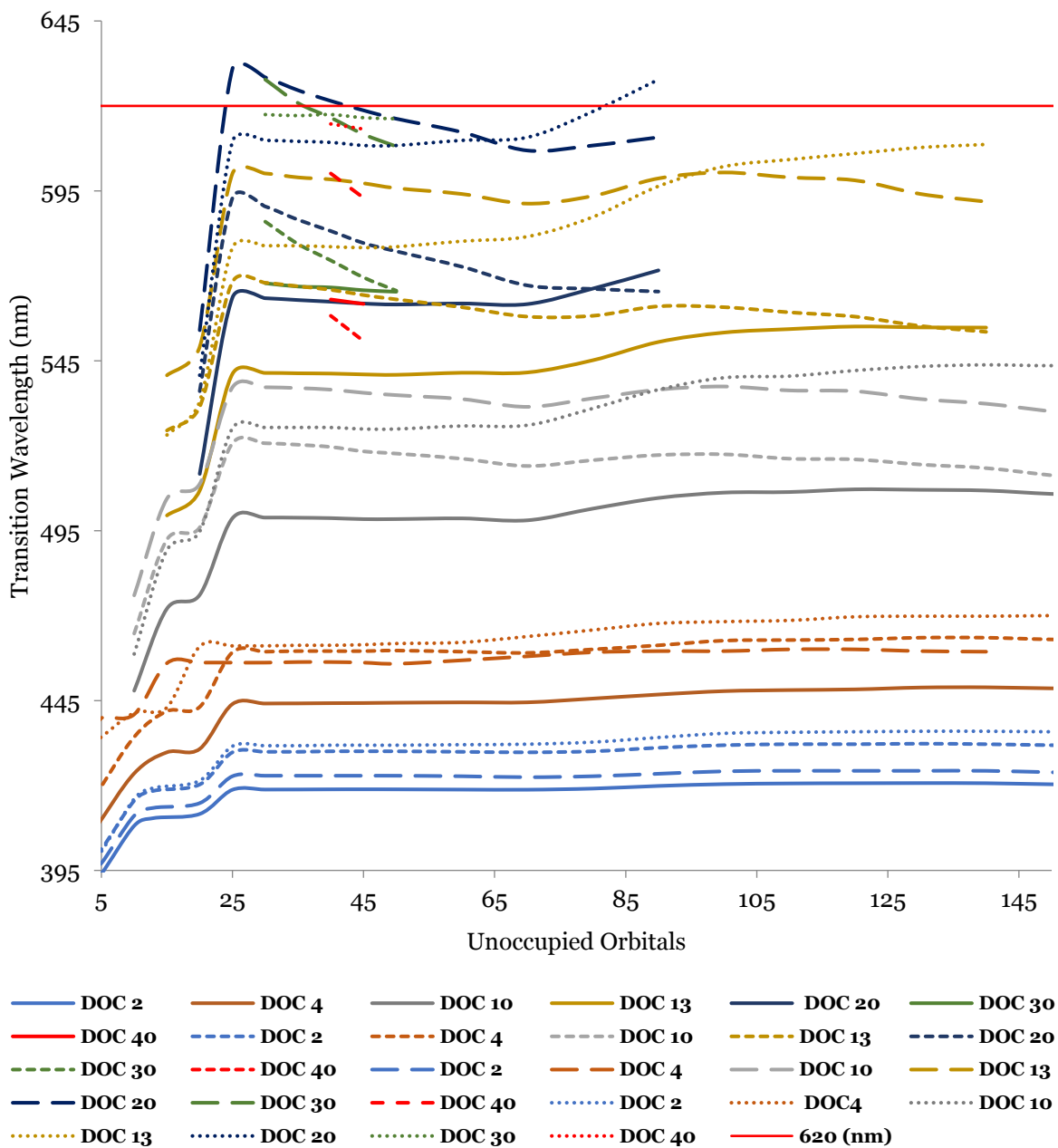


Figure 9.7: Predicted Qx transition wavelengths by EOM-CCSD, CR-EOM-CCSD(T) ID/IB, CR-EOM-CCSD(T) IID/IA, and DELTA-CR-EOM-CCSD(T) DEL(IA), using the 6-311G(d) basis set. Electrons were excited from doubly occupied core orbitals, HOMO down, into unoccupied orbitals from the LUMO upwards. Seven different active electron groups were allowed to populate orbitals of the virtual space. Marker positions of the different calculations performed appear in figure 9.8. The experimental Qx transition energy is depicted as the red horizontal line. Several of the selected active spaces, when used with these variants of EOM-CCSD(T), were able to yield transition energies that closely reflect this experimental value.

DOC: 2, DOC: 4, DOC: 10, DOC: 13, DOC: 20, DOC: 30, DOC: 40, were allowed to populate the varying virtual space of unoccupied orbitals. Because of the way the coupled-cluster calculation is performed, the explored virtual space must be equal to or exceed the number of orbitals that have been chosen to be active. Therefore, as more DOC electrons become active, the minimum number of the virtual orbitals that are necessary to include in the calculation increases. This is the reason that the traces in the figures display a shift of the first calculated value in relation to the x-axis, as more active orbitals are included within the active space of the calculation. The virtual space of the unoccupied orbitals from the LUMO upwards that was explored during these trials included those that were previously described, with additional virtual spaces at intervals of 10, between VIR: 60 to VIR: 150, being included until issues regarding excessive computational demands were encountered. Utilizing these approaches, it was found that once more than 30 doubly occupied core orbitals were selected as active, the size of the virtual spaces that could be included in the calculation became limited. The red horizontal line in figure 9.7 represents the spectroscopically observable Q<sub>x</sub> transition energy for porphyrin. Therefore, the coupled-cluster approach is capable of producing accurate computational valuations of the transition energy. Similar to the case of the calculations utilizing the CISDT approach, the most spectroscopically accurate evaluations for the energy occurred again when only a limited set of electrons from doubly occupied core orbitals were selected as active, with the necessary space of virtual orbitals included also being modest. A selection of the active space existing between DOC: 20 → VIR: 25 - VIR: 50, allowed for the most accurate evaluations to be computationally obtained. Future studies should be conducted within this, or in a close

Predicted 6-31G(d) Ground State Energy (H)  
 EOM-CCSD (-) And CR-CCSD(T)\_L (-·-)

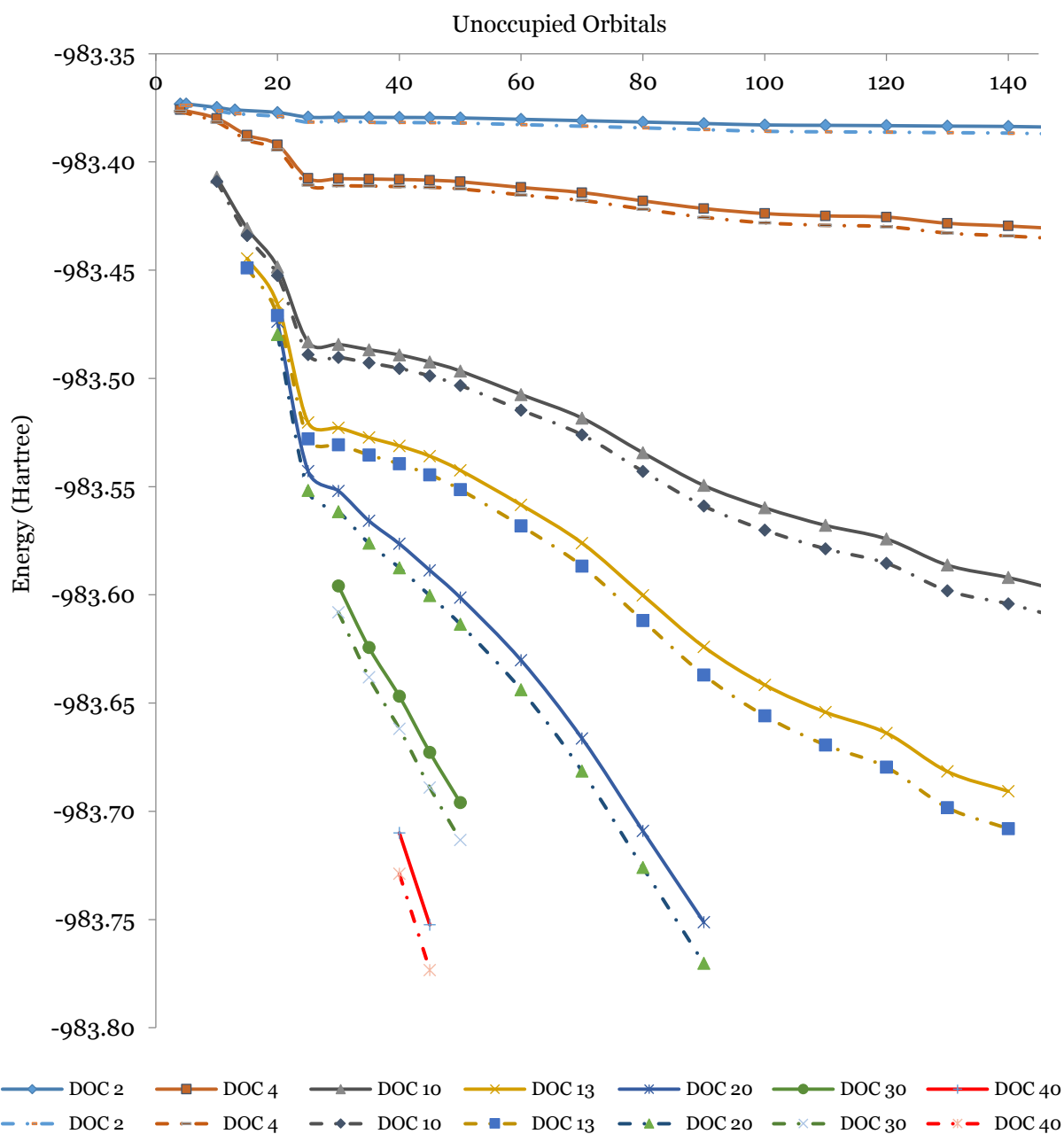


Figure 9.8: Comparison of calculated ground state energies as calculated by the EOM-CCSD and the CR-CCSD(T)\_L methods using the 6-31G(d) basis set. This figure indicated that including greater numbers of occupied and unoccupied orbitals into the active space of the calculation returns lower evaluations of the ground state energy. Improvement to the basis set will undoubtedly lead to further decrease in determined values for the ground state energy.

proximity to this active range, with primary investigative efforts focused on improving the quality of basis sets implemented during the computation.

Appearing in figure 9.8 are the calculated ground state energies that were determined using the EOM-CCSD and the CR-CCSD(T)\_L methods, in conjunction with the 6-311G(d) basis set. This data indicates that as the size of the active space is increased, and greater numbers of occupied and unoccupied orbitals are included into calculation, lower evaluations of the ground state energy are returned. It can be observed that the gain in energy minimization that is obtained by expanding the number of doubly occupied orbitals in the active space from DOC: 10 to DOC: 13, an increase of 3 active orbitals is approximately one half of the gain in energy minimization that was obtained moving from DOC: 4 to DOC: 10, an increase of 6 active orbitals, resulting in a nearly equivalent gain in energy minimization of  $\sim 0.0122$  h per additional active occupied orbital over this entire orbital space. The gain in energy minimization obtained by expanding the active space from DOC: 13 to DOC: 20, an increase of 7 active orbitals, resulted in a gain of energy minimization of  $\sim 0.004$  h per additional active occupied orbital. Therefore, the number of doubly occupied orbitals that should be included in the active space should be at minimum DOC: 13, in order to obtain the greatest descriptive ability while still maintaining the smallest set of active doubly occupied orbitals. Improvement to the basis set will undoubtedly lead to further decrease in determined values for the ground state energy, and should be looked into further.

Displayed in figure 9.9 are the norm of the transition moments obtained using the EOM-CCSD method, with the 6-311G(d) basis set, for the optical transitions of porphine, allowing 20 doubly occupied orbitals to occupy a varying number of

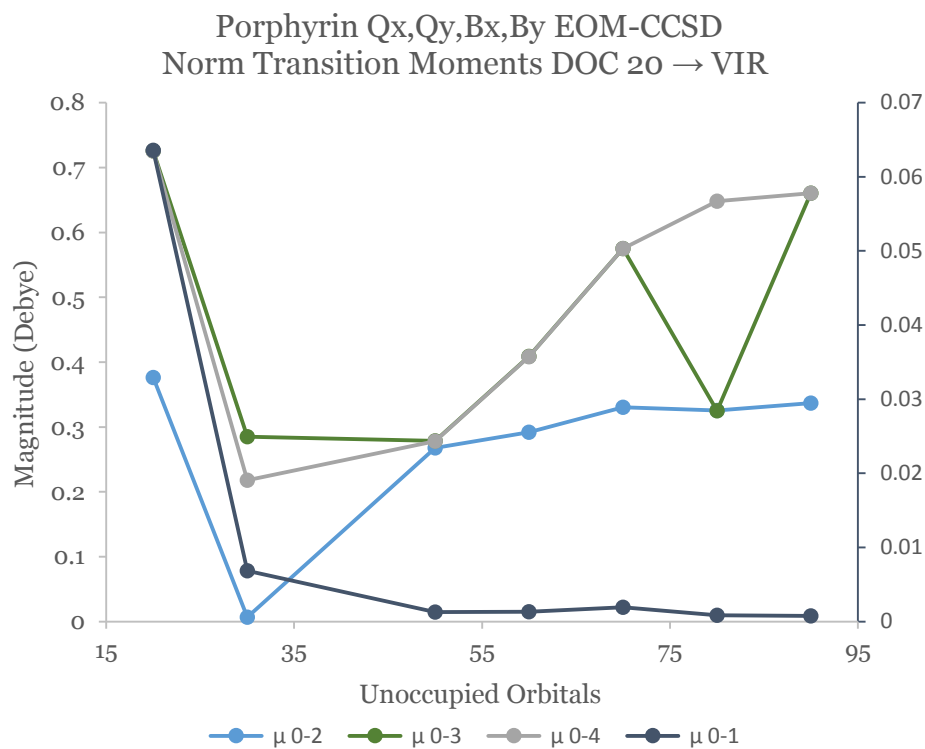


Figure 9.9: Norm of the transition moments of the first four optical transitions of porphine allowing 20 doubly occupied orbitals (40 electrons, HOMO down) to occupy a differing number of unoccupied orbitals in the virtual space (LUMO upwards) for capture of the electron correlation energy by EOM-CCSD, 6-311G(d).

unoccupied orbitals in the virtual space (LUMO upwards). Aside from the calculated norm value for the  $\mu$  0-3 transition of VIR: 80, this initial set of data suggests that after the inclusion of approximately 80 to 90 unoccupied orbitals into the active space, the magnitude of the dipole moments predominantly stabilize and approach their limiting values. Due to the minimal number of data points in this stabilized region, this statement should be taken with caution. Additional calculations that investigate the inclusion of unoccupied orbitals in the range of VIR: 80 – VIR: 120 should be performed, before any definitive conclusions as to VIR: 90 being representative of the



lower limit of the number of unoccupied states that need to be included in the active space to achieve a stabilized magnitude of the transition moment, can be confidently stated.

In order for comparison to be made with the results of the configuration interaction studies, table 9.4 provides a representative example of the magnitudes and directionality of the transition dipole moments for the optical transitions of porphine. The coupled-cluster computations that were performed always return degenerate energies for the Bx and By transitions. The directionality of the transition moments typically but not always, follows a (X, Y, X, X) polarization, with some active spaces returning the expected (X, Y, X, Y) polarization. Computations that utilize larger basis

Original Structure: 1DWT							RPN
EOM-CCSD							
6-311G(d)		(20 → 20)					
	hartree (H)	(nm)		X	Y	Z	NORM
Gnd	-983.4738						
EX 1	-983.3848	511.697	μ 0-1	0.0636	0.0001	0.0001	0.0636 DEBYE
EX 2	-983.3610	403.843	μ 0-2	0.0018	0.3761	0.0016	0.3761 DEBYE
EX 3	-983.3240	304.14	μ 0-3	0.7234	0.0573	0.0001	0.7257 DEBYE
EX 4	-983.3240	304.14	μ 0-4	0.7235	0.0569	0.0001	0.7258 DEBYE

Table 9.4: Representative state energies, transition energies, and transition dipole moment values for the optical transitions (Qx, Qy, Bx, By) of porphine, possessing the molecular geometry of 1DWT. Calculations were performed using the EOM-CCSD approach with an active space determined by, DOC: 20 → VIR: 20. All of the coupled-cluster computation that were performed thus far have yielded degenerate energies for the Bx and By transitions. The directionality of the transition moments typically follows a (X, Y, X, X) polarization. Additional computations that utilize larger basis sets and an increased active space should be performed to determine if this trend continues.

sets and include an increased active space should be performed to determine if this trend continues. Coupled-cluster allows the active spaces to be chosen using non-sequential sets of orbitals. The next sets of computational studies need to focus on using an active set of most likely DOC: 20, and choosing an active space that uses a non-sequential set of unoccupied orbitals, or sets of non-sequential sets of unoccupied orbitals in the active space. This methodology can be used to investigate state degeneracies.

## 9.6 Comparison of Methods

Two metrics can be used to assess the likely quality of a transition dipole moment value that is calculated by a particular computational method: the calculated ground state energy, and the calculated state transitions energies. The variational principle places the true ground state energy as a lower bound to any ground state energy that can be calculated by the use of an approximate wave function. The computational method that produces the most accurate wave function will have the lowest evaluation of the ground state energy. Transition moments are found when the dipole moment operator is applied to the wave function. Therefore, better wave functions should yield more accurate transition dipole moments, which are the primary quantity of interest during these computational investigations. A second marker to assess the quality of a particular computational method is the ability of the method to calculate values for the ground and excited state energies, and specifically the transition energies between states, which are in close correlation to the spectroscopically observable transition energies. These are the

measures that can be used to compare and differentiate between the computational methods that were investigated, to determine which methodology should be used to calculate transition moments of the greatest physical accuracy for use in any analysis concerning spectral hole-burning profiles.

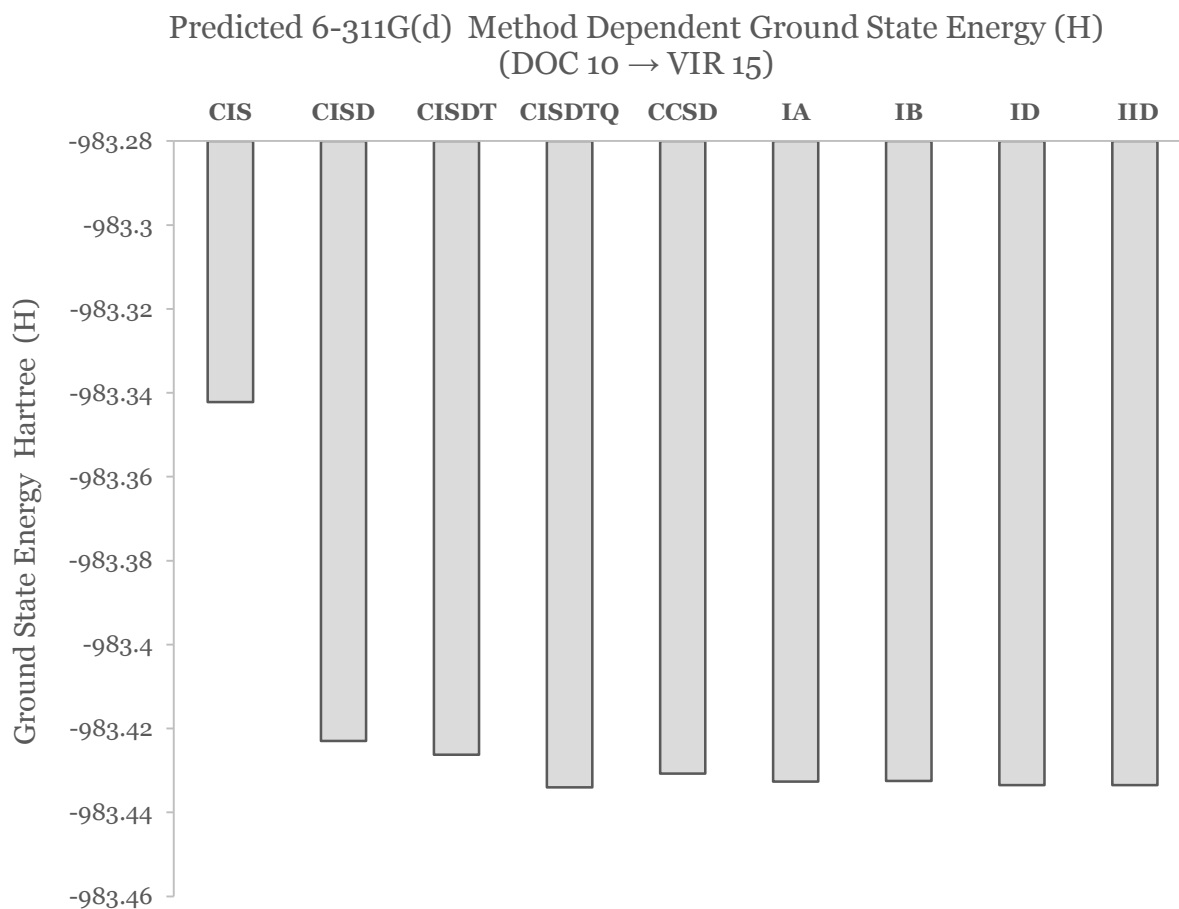


Figure 9.10: Performance comparison across the investigated methods. The calculated ground state energy determined by each of the investigated computational approaches using the 6-311G(d) basis set, and the same active space DOC: 10 → VIR: 15. The difference between the ground state energy calculated using the CIS approach and the CISDTQ approach is about 2.5 eV or 240 kJ/mol.

Displayed in figure 9.10 is a performance comparison of the calculated ground state energy determined by each of the investigated computational approaches. These are not necessarily representative of the lowest possible ground state energy that was computationally obtained by each of the methods, but does provide for a consistent comparison across methods, as these ground state energies were all obtained by use of the same basis set 6-311G(d), and the same active space DOC: 10 → VIR: 15. It can be observed that implementing higher order methods (> CIS) that effectively take electron correlation into account, specifically in-between excited states, leads to an increase in the quality of the wave function that results in a substantial decrease in the calculated ground state energy. The difference between the ground state energy calculated using the CIS approach and the CISDTQ approach, is about 2.5 eV or 240 kJ/mol. Although coupled-cluster is not variational by construction, the ground state energy as determined by the different coupled cluster methods remains greater than the ground state energy as determined by the CISDTQ approach, which is variational. This indicates that the ground state energies determined by the coupled-cluster approaches, also would consequently remain above the unknown true ground state energy.

Table 9.5 displays a performance comparison of the ability of all of the various investigated computational methods to calculate values for the transition energies between states, which are highlighted in blue. Although the same basis set was used across all of these computations, the results represent inclusion of different active spaces during the calculations. The active spaces that produced the most experimentally accurate valuations for these energies using the configuration interaction methods are represented here. A consistent active space is displayed across all of coupled-cluster

methods. Highlighted in grey are the spectroscopically observable transitions [62]. This comparison reveals that the coupled-cluster approaches typically outperform the truncated configuration interaction methods.

<b>Predicted Q<sub>x</sub>, Q<sub>y</sub>, B<sub>x</sub>, B<sub>y</sub> Transitions For Porphine With 1DWT Geometry</b>						
<b>6-311G(d)</b>						
<b>CI</b>		<b>CIS</b>	<b>CISD</b>	<b>CISDT</b>	<b>CISDTQ</b>	<b>EXPTL.</b>
(OCC.→VIR.)			(13 → 4)	(13 → 30)	(13 → 10)	
		(nm)	(nm)	(nm)	(nm)	(nm)
<b>EX 1</b>		526.835	402.784	538.628	494.801	620.27
<b>EX 2</b>		501.838	363.174	412.203	408.784	541.65
<b>EX 3</b>		291.774	255.595	301.915	302.668	429.52
<b>EX 4</b>		279.833	253.456	290.326	294.319	425.86
<b>6-311G(d)</b>						
<b>EOM-CC</b>		<b>CCSD</b>	<b>CCSD(T)</b>	<b>CCSD(T)</b>	<b>CCSD(T)</b>	<b>EXPTL.</b>
(OCC.→VIR.)		(20 → 50)	ID/IB (20 → 50)	IID/IA (20 → 50)	DEL(IA) (20 → 50)	
		(nm)	(nm)	(nm)	(nm)	(nm)
<b>EX 1</b>		561.562	577.208	616.224	608.362	620.27
<b>EX 2</b>		403.755	400.466	425.040	416.194	541.65
<b>EX 3</b>		316.835	325.418	350.139	332.041	429.52
<b>EX 4</b>		316.835	325.418	350.139	332.041	425.86

Table 9.5: Performance comparison across investigated methods. Calculated state energies, highlighted in blue, for the optical transitions (Q<sub>x</sub>, Q<sub>y</sub>, B<sub>x</sub>, B<sub>y</sub>) of porphine, possessing the molecular geometry as described by 1DWT, determined by each of the investigated computational approaches. The utilized basis set remained consistent across all computations, but the displayed results do represent inclusion of different active spaces during the calculations. For the configuration interaction methods, the active spaces that produced the most experimentally accurate valuations are represented here. For the coupled-cluster methods, a consistent active space across all investigated variants was chosen for display. In relation to the spectroscopically observable transitions [62], highlighted in grey, this comparison reveals that the coupled-cluster approaches generally outperform the truncated configuration interaction methods at least when this basis set is utilized.

Based on the results of figure 9.10 and table 9.5, transition dipole moments that are evaluated using these coupled-cluster approaches should be more representative of the transition dipole moments existing within the porphine molecule as it exists in its protein environment.

## 9.7 Next Steps

As the dipole and transition dipole moments of molecules cannot be easily measured through experimental means, they represent quantities that must be determined computationally using a theoretical approach. The computational studies that were carried out and discussed here represent only the first necessary steps towards an accurate quantification of the state energies, and the state specific dipole and transition dipole moments of the porphine core of the protoporphyrin IX as it exists in myoglobin. During the experimental process, a real protoporphyrin IX molecule acts as the sensor towards the internally generated molecular electric field within the active site of the real myoglobin protein. Therefore, any values for the internally generated electric field  $\vec{E}_{int}$  that are calculated through the analysis of experimentally collected hole-burning profiles by use of the molecular resolution approach can only be taken as physically meaningful if the transition dipole moments  $\vec{\mu}_{mn}$  that were used during the molecular resolution analysis were computationally determined for a porphine molecule possessing realistic geometric character.

The ability of a particular method to calculate state energies for the molecule that are in close approximation to those that are spectroscopically observable is the primary

metric by which the various computational approaches can be compared. In regard to the studies that have already been completed, it can be observed that based on the quality of the computational results, the dipole and transition dipole moments values need to be calculated using computational methodologies that take electron correlation into account. This initial work indicates that the number of the electronic states that are included in the calculation has a significant impact on the values of the state energies, dipole and transition dipole moments that are computationally arrived at when utilizing these post Hartree-Fock methods. It can be observed in figure 9.10 that the trends for state energies and undoubtedly also for the dipole and transition dipole moments are not necessarily consistent across the computational methodologies. The fewest states that are necessary to include in the calculation prior to arriving at valuations of the state energies that are in acceptable proximity to the experimentally attainable results is a determination that needs to be made, which will most likely be found to be method dependent. Therefore, the number of states that are necessary to include will likely need to be determined for each computational method that is used for the calculation of values.

Despite crystallographic structures already being representative of equilibrium geometry, the next step in regard to classifying the most chemically accurate state energies and transition dipole moment values to use in the molecular resolution analysis will be performing a complete optimization of the entire structure of the protein including the porphyrin ring. A complete optimization of the entire protein structure is a possibility if the fragment molecular orbital (FMO) method is used. The fragment molecular orbital method was originally described by Kitaura [28], and allows for

computational investigations on large macromolecules such as DNA or even large proteins [26]. The method operates by partitioning the molecule into fragments across bonds, thus creating many small fragment molecules. The desired calculation is then performed upon on each fragment molecule or on small groups of fragment molecules, while taking into account the electrostatic environment that is imposed by all of the other fragment molecules. The calculation is performed iteratively until the electron densities across the different fragments becomes matched [16]. This method has proven to produce high quality results for biomolecules and even for solvated species [14, 22, 57]. Partitioning and solvating the protein can be performed using the molecular modeling and visualization program Facio [55].

Many theoretically rigorous methods do exist that allow for the calculation of state energies and state specific dipole and transition dipole moments. Beyond the FMO optimization protocol, additional high order correlative methods need to be investigated. Specifically, the methods that should be performed and evaluated include MCSCF over CISD, XMCQDPT2, and CASPT2. Although a few initial assessments were made using these various methodologies, a complete investigation regarding these has yet to be completed. In regard to the configuration interaction and coupled-cluster methods discussed above, additional states to include during the calculation process as well as implementing higher order basis sets need to be investigated using the CISDT and the EOM-CCSD(T) methods. Only at the end of this complete set of studies can any confidence in the values of the interstate transition dipole moments used during the molecular resolution analysis be had.



## References

- 1.) Alex A. Granovsky, Firefly version 8, www  
<http://classic.chem.msu.su/gran/firefly/index.html> **FIREFLY - CI**
- 2.) Beames, J. M., Hudson, A. J. "The isolation of porphyrins in the gas phase using pulsed-laser desorption," Central Laser Facility Annual Report (2007-2008), 179-181.
- 3.) Bode B. M., Gordon, M.S. (1998). "MacMolPlt: a graphical user interface for GAMESS," *Journal of Molecular Graphics and Modeling* 16(3), 133-138.
- 4.) Caricato, Marco., Trucks, Gary W., Frisch, Michael J., Wiberg, Kenneth B. (2011). "Oscillator Strength: How Does TDDFT Compare to EOM-CCSD?," *Journal of Chemical Theory and Computation* 7(2), 456-466.
- 5.) Chen, Betty M. L., Tulinsky, A. (1972). "Redetermination of the Structure of Porphine," *Journal of the American Chemical Society* 94(12), 4144-4151.
- 6.) Chu, K., Vojtechovsky, J., McMahon, B.H., Sweet, R.M., Berendzen, J., Schlichting, I. (2000). "Crystal Structure of a New Ligand Binding Intermediate in Wildtype Carbonmonoxy Myoglobin," *Nature* 403 (6772) 921-923. (1DWT)
- 7.) Cizek, Jiri. (1966). "On the Correlation Problem in Atomic and Molecular Systems. Calculation of Wavefunction Components in Ursell-Type Expansion Using Quantum-Field Theoretical Methods," *The Journal of Chemical Physics* 45(11), 4256-4266.
- 8.) Cramer, Christopher J. Essentials of Computational Chemistry: Theories and Models 2<sup>nd</sup> Edition. United Kingdom: John Wiley and Sons Ltd, 2004. Print.
- 9.) Dirac, P. A. M. The Principles of Quantum Mechanics. Oxford: Clarendon Press, 1974. 167-184. Print.
- 10.) Dolphin, David., Felton, Ronald H. (1974). "The Biochemical Significance of Porphyrin  $\pi$  Cation Radicals," *Accounts of Chemical Research* 7(1), 26-32.
- 11.) Dunning, Thom H. (1989). "Gaussian basis sets for use in correlated molecular calculations. I. The atoms boron through neon and hydrogen," *Journal of Chemical Physics* 90(2), 1007-1023.
- 12.) Edwards, W. Daniel., Weiner, Brian., Zerner, Michael C. (1986). "On the low-lying states and electronic spectroscopy of iron(II) Porphine," *Journal of the American Chemical Society* 108(9), 2196-2204.
- 13.) Federici, L., Savino, C., Musto, R., Travaglini-Allocatelli, C., Cutruzzolà, F., Brunori, M. (2000). "Engineering His(E7) affects the control of heme reactivity in *Aplysia limacina* myoglobin," *Biochemical and Biophysical Research Communications* 269(1), 58-63. (1DM1)

- 14.) Fedorov, Dmitri G., Nagataab, Takeshi., Kitauraab, Kazuo. (2012). "Exploring chemistry with the fragment molecular orbital method," *Physical Chemistry Chemical Physics* 14(21), 7562–7577.
- 15.) Gordon, M.S., Schmidt, M.W. (2005). Advances in electronic structure theory: GAMESS a decade later. C.E.Dykstra, G.Frenking, K.S.Kim, G.E.Scuseria (Eds.) *Theory and Applications of Computational Chemistry: the first forty years* 1167-1189. Amsterdam Elsevier.
- 16.) Gordon, Mark S., Fedorov, Dmitri G., Pruitt, Spencer R., Slipchenko, Lyudmila V. (2011). "Fragmentation Methods: A Route to Accurate Calculations on Large Systems," *Chemical Reviews* 112(1), 632-672.
- 17.) Gouterman, Martin. (1959). "Study of the Effects of Substitution on the Absorption Spectra of Porphin," *The Journal of Chemical Physics* 30(5), 1139-1161.
- 18.) Gouterman, M. (1978). Optical Spectra and Electronic Structure of Porphyrins and Related Rings. D. Dolphin (Ed.) *The Porphyrins Volume III*, 1–165. New York, NY Academic Press.
- 19.) Guex, N., Peitsch, M.C., Schwede, T. (2009). "Automated comparative protein structure modeling with SWISS-MODEL and Swiss-PdbViewer: A historical perspective," *Electrophoresis* 30(S1), S162-S173.
- Swiss PDB Program At: <http://www.expasy.org/spdbv/>*
- 20.) Hamor, T. A., Caughey, W. S., Hoard, J. L. (1965). "The Crystal and Molecular Structure of Nickel (II) 2,4-Diacetyldeuteroporphyrin-IX Dimethyl Ester," *Journal of the American Chemical Society* 87(11), 2305-2312.
- 21.) Hanwell, Marcus D., Curtis, Donald E., Lonie, David C., Vandermeersch, Tim., Zurek, Eva., Hutchison, Geoffrey R. "Avogadro: an advanced semantic chemical editor, visualization, and analysis platform," (2012). *Journal of Cheminformatics* 4:17.
- 22.) Heifetz, Alexander., Chudyk, Ewa I., Gleave, Laura., Aldeghi, Matteo., Cherezov, Vadim., Fedorov, Dmitri G., Biggin, Philip C., Bodkin, Mike J. (2016). "The Fragment Molecular Orbital Method Reveals New Insight into the Chemical Nature of GPCR–Ligand Interactions," *Journal of Chemical Information and Modeling* 56(1), 159-172.
- 23.) Hoard, J. L., Hamor, M. J., Hamor, T. A., Caughey, W. S. (1965). "The Crystal Structure and Molecular Stereochemistry of Methoxyiron (III) Mesoporphyrin-IX Dimethyl Ester," *Journal of the American Chemical Society* 87(11), 2312-2319.
- 24.) Hobbs, John David., Shelnut, John A. (1995). "Conserved nonplanar heme distortions in cytochromes c," *Journal of Protein Chemistry* 14(1), 19-25.
- 25.) Igarashi, J., Kobayashi, K., Matsuoka, A. (2011). "A hydrogen-bonding network formed by the B10-E7-E11 residues of a truncated hemoglobin from *Tetrahymena pyriformis* is critical for stability of bound oxygen and nitric oxide detoxification," *Journal of Biological Inorganic Chemistry* 16(4), 599-609. (3AQ5)

- 26.) Ikegami, Tsutomu., Ishida, Toyokazu., Fedorov, Dimitri G., Kitaura, Kazuo., Inadomi, Yuichi., Umeda, Hiroaki., Yokokawa, Mitsuo., Sekiguchi, Satoshi. "Full Electron Calculation Beyond 20,000 Atoms: Ground Electronic State of Photosynthetic Proteins," Presented at SC05 International Conference for High Performance Computing, Networking, Storage and Analysis, Seattle, WA., Nov.12 - 18, 2005, Proceedings of the 2005 ACM/IEEE conference on Supercomputing
- 27.) Jentzen, Walter., Ma, Jian-Guo., Shelnut, John A. (1998). "Conservation of the Conformation of the Porphyrin Macrocycle in Hemoproteins," *Biophysical Journal* 74(2), 753-763.
- 28.) Kitaura, K., Ikeo, E., Asada, T., Nakano, T., Uebayasi, M. (1999). "Fragment molecular orbital method: an approximate computational method for large molecules," *Chemical Physics Letters* 313(3-4) 701-706.
- 29.) Kowalski, K., Piecuch, P. (2004). "New coupled-cluster methods with singles, doubles, and noniterative triples for high accuracy calculations of excited electronic states," *The Journal of Chemical Physics* 120(4), 1715-1738.
- 30.) Krylov, Anna I. (2008). "Equation-of-Motion Coupled-Cluster Methods for Open-Shell and Electronically Excited Species: The Hitchhiker's Guide to Fock Space," *Annual Review of Physical Chemistry* 59, 433-462.
- 31.) Krzywd, S., Murshudov, G. N., Brzozowski, A. M., Jaskolski, M., Scott, E. E., Klizas, S. A., Gibson, Q. H., Olson, J. S., Wilkinson, A. J. (1998). "Stabilizing bound O<sub>2</sub> in myoglobin by valine68 (E11) to asparagine substitution," *Biochemistry* 37(45), 15896-15907. (1M6M)
- 32.) Kucharski, Stanisław A., Włoch, Marta., Musiał, Monika., Bartlett, Rodney J. (2001). "Coupled-cluster theory for excited electronic states: The full equation-of-motion coupled-cluster single, double, and triple excitation method," *Journal of Chemical Physics* 115(18), 8263-8266.
- 33.) Levine, Ira N. Quantum Chemistry 3<sup>rd</sup> Edition. Newton, Massachusetts: Allyn and Bacon Inc., 1983. Print.
- 34.) Li, Xiao-Yuan., Czernuszewicz, Roman S., Kincaid, James R., Spire, Thomas G. (1989). "Consistent Porphyrin Force Field. 3. Out-of-Plane Modes in the Resonance Raman Spectra of Planar and Ruffled Nickel Octaethylporphyrin," *Journal of the American Chemical Society* 111(18), 7012-7023.
- 35.) Little, Robert G., Ibers, James A. (1975). "Crystal and Molecular Structure of the Free Base Porphyrin, Mesoporphyrin IX Dimethyl Ester," *Journal of the American Chemical Society* 97(19), 5363-5369.
- 36.) Mayer, Joseph Edward, and Maria Goeppert Mayer, Statistical Mechanics. New York: John Wiley and Sons, Inc., 1940. Print.
- 37.) Mayer, Joseph E., Montroll, Elliott. (1941). "Molecular Distribution," *Journal of Chemical Physics* 9(1), 2-16.

- 38.) Milani, Mario., Pesce, Alessandra., Dewilde, Sylvia., Ascenzi, Paolo., Moens, Luc., Bolognesi, Martino. (2002). "Structural plasticity in the eight-helix fold of a trematode haemoglobin," *Acta Crystallographica Section D* 58(4), 719-722. (1KFR)
- 39.) Nardini, Marco., Tarricone, Cataldo., Rizzi, Menico., Lania, Amalia., Desideri, Alessandro., De Sanctis, Gianpiero., Coletta, Massimo., Petruzzelli, Raffaele., Ascenzi, Paolo., Coda, Alessandro., Bolognesi, Martino. (1995). "Reptile heme protein structure: X-ray crystallographic study of the aquo-met and cyano-met derivatives of the loggerhead sea turtle (*Caretta caretta*) myoglobin at 2.0 Å resolution," *Journal of Molecular Biology* 247(3), 459-465. (1LHT)
- 40.) Olsen, Jeppe., Roos, Björn O., Jorgensen, Poul., Jensen, Hans Jorgen Aa. (1988). "Determinant based configuration interaction algorithms for complete and restricted configuration interaction spaces," *Journal of Chemical Physics* 89(4), 2185-2192.
- 41.) Phillips, Simon E.V. (1980). "Structure and refinement of oxymyoglobin at 1.6 Å resolution," *Journal of Molecular Biology* 142(4), 531-554. (1MBO)
- 42.) Piecuch, P., Kucharski, S.A., Kowalski, K., Musial, M. (2002). "Efficient computer implementation of the renormalized coupled-cluster methods: the R-CCSD[T], R-CCSD(T), CR-CCSD[T], and CR-CCSD(T) approaches," *Computer Physics Communications* 149(2), 71-96.
- 43.) Piecuch, P., Wloch, M. (2005). "Renormalized coupled-cluster methods exploiting left eigenstates of the similarity-transformed Hamiltonian," *The Journal of Chemical Physics* 123(22), 224105.
- 44.) Piecuch, P., Wloch, M., Gour, J.R., Kinal, A., (2005). "Single-reference, size-extensive, non-iterative coupled-cluster approaches to bond breaking and biradicals," *Chemical Physics Letters* 418, 467-474.
- 45.) Piecuch, P., Gour, J.R., Wloch, M. (2009). "Left-eigenstate completely renormalized equation-of-motion coupled-cluster methods: Review of key concepts, extension to excited states of open-shell systems, and comparison with electron-attached and ionized approaches," *International Journal of Quantum Chemistry* 109(14), 3268-3304.
- 46.) Rowe, D. J. (1968). "Equations-of-Motion Method and the Extended Shell Model," *Reviews of Modern Physics* 40(1), 153-166.
- 47.) Schmidt, M.W., Baldrige, Kim K., Boatz, Jerry A., Elbert, Steven T., Gordon, Mark S., Jensen, Jan H., Koseki, Shiro., Matsunaga, Nikita., Hguyen, Kiet A., Su, Shujun., Windus, Theresa L., Dupuis, Michel., Montgomery, John A.(1993). "General atomic and molecular electronic structure system," *Journal of Computational Chemistry* 14(11), 134-1363.7 ***GAMESS- EOMCCSD(T) and Variants***
- 48.) Schreiter, Eric R., Rodríguez, Mari ´ a M., Weichsel, Andrzej., Montfort, William R., Bonaventura, Joseph. (2007). "S-nitrosylation-induced conformational change in blackfin tuna myoglobin," *The Journal of Biological Chemistry* 282(27), 19773-19780. (2NRL)

- 49.) Senge, Mathias O. (2006). "Exercises in molecular gymnastics—bending, stretching and twisting Porphyrins," *Chemical Communications* 3, 243-256.
- 50.) Senge, Mathias O., Ryan, Aoife A., Letchford, Kristie A., MacGowan, Stuart A., Mielke, Tamara. (2014). "Chlorophylls, Symmetry, Chirality, and Photosynthesis," *Symmetry* 6(3), 781-843.
- 51.) Shankar, Ramamurti. Principles of Quantum Mechanics. New York: Springer, 1994. 451-471. Print.
- 52.) Shelnut, John A., Song, Xing-Zhi., Ma, Jian-Guo., Jia, Song-Ling., Jentzen, Walter., Medforth, Craig J., Medforth, Craig J. (1998). "Nonplanar porphyrins and their significance in proteins," *Chemical Society Reviews* 27(1), 31-42.
- 53.) Simons, Jack. An Introduction to Theoretical Chemistry. Cambridge University Press, 2003. Print.
- 54.) Simpson, William T. (1949). "On the Theory of the  $\pi$ -Electron System in Porphines," *The Journal of Chemical Physics* 17(12), 1218-1221.
- 55.) Suenaga, M. (2005). "Facio: New Computational Chemistry Environment for PC GAMESS," *Journal of Computer Chemistry, Japan* 4(1), 25-32.
- 56.) Szabo, Attila, and Neil S. Ostlund. Modern Quantum Chemistry: Introduction to Advanced Electronic Structure Theory. Mineola, N.Y.: Dover Publications, 1996. Print.
- 57.) Ueno-Noto, Kaori., Takano, Keiko. (2016). "Water Molecules Inside Protein Structure Affect Binding of Monosaccharides with HIV-1 Antibody 2G12," *Journal of Computational Chemistry* 37(26), 2341-2348.
- 58.) Webb, Lawrence E., Fleischer, Everly B. (1965). "Crystal Structure of Porphine," *The Journal of Chemical Physics* 43(9), 3100-3111.
- 59.) Wiberg, Kenneth B. (2004). "Basis set effects on calculated geometries: 6-311++G\*\* vs. aug-cc-pVDZ," *Journal of Computational Chemistry* 25(11), 1342-1346.
- 60.) Wiberg, Kenneth B., Wang, Yi-Gui., De Oliveira, Anselmo E., Perera, S. Ajith., Vaccaro, Patrick H. (2005). "Comparison of CIS- and EOM-CCSD-Calculated Adiabatic Excited-State Structures. Changes in Charge Density on Going to Adiabatic Excited States," *The Journal of Physical Chemistry. A* 109(3), 466-477.
- 61.) Wloch, M., Gour, J.R., Kowalski, K., Piecuch, P. (2005). "Extension of renormalized coupled-cluster methods including triple excitations to excited electronic states of open-shell molecules," *The Journal of Chemical Physics* 122(21), 214107-1 - 214107-15.
- 62.) Woehl, J. C. (1996) *Measuring Internal Electrostatic Fields and Potentials at Molecular and Atomic Resolution using Hole Burning Spectroscopy*. Doctoral thesis. University of California-Riverside
- 63.) Yi, Jun., Heinecke, Julie., Tan, Hui., Ford, Peter C., Richter-Addo, George B. (2009). "The distal pocket histidine residue in horse heart myoglobin directs the o-binding mode of nitrite to the heme iron," *Journal of the American Chemical Society* 131(50), 18119-18128. (3HEO)

# III

## Chapter 10

### **Concluding Remarks**

Enzymatic proteins are liaisons of chemical reactivity. Despite being composed of only a small set of constituent molecules, proteins represent a class of macromolecules that enjoy an overwhelming abundance of structural diversity. The specific activity of a protein is determined by its well-defined structure. Not only is it their ability to maintain a specific shape, but their ability to create within themselves unique microenvironments that give these proteins the capability to participate in a wide range of chemical processes. Due to the specific geometric arrangement and the electrostatic nature of the pocket residues within the active regions, it is easy to conceive that internally generated electric fields at these sites may contribute to, facilitate, or even play a principle role in the specific functionality of the protein. The underlying objective of this investigation is to study the impact that these internal electric field distributions play by quantitatively determining and describing the molecular electric fields that are present. The target protein of initial interest is the oxygen storage protein myoglobin.

To achieve this aim, the high resolution spectroscopic technique, spectral hole-burning, is used in conjunction with electric field measurements based on the Stark effect, and a quantum mechanics based analysis methodology. Experiments of this nature require the integration of an elaborate set of instrumentation, which grant the

investigator the ability to possess precise control over the environmental conditions of the sample. As described throughout this document, much of the effort that was put towards investigating these internal molecular electric fields fell under the category of tailoring the various aspects of the existing and newly developed instrumentation so that the collection of the experimental data was a real possibility. Additionally, much effort was devoted towards investigating methods for establishing the valuations for various quantities, existing as necessary input parameters during the molecular resolution analysis of the data, which were either rigorously determined through experimental means, or were based upon rigorous theoretical foundation. Any determined value of the internal molecular electric fields present within the active site can only be viewed as being realistic or accurate if this is the case.

Gaining the capability to collect experimental data required first the ability to collect spectral data. This was achieved by developing a software platform coordinating the scan of the tunable frequency ring dye laser as integrated to a wavelength meter, with a photon counter that measures the signals collected by the avalanche photodiodes, used as detectors of the sample's emitted fluorescent photons. Development of this software platform extended the functionality of the cryogenic temperature confocal scanning microscope, giving the instrument the ability to collect a sample's spectral response in addition to its image, providing the instrument a broad applicability to diverse future experimental avenues. Of considerable importance was the development of a high voltage feedthrough capable of delivering voltages of up to 5000 V to the sample as positioned within the research Dewar, allowing for experiments that utilize the Stark effect to be performed. Lastly, protocols for the burn time and light intensities

necessary for burning deep and narrow spectral holes were developed such that the burning of spectral holes with this particular experimental setup is now highly repeatable. All of the efforts expended here thus gives to future experimenters the necessary capabilities to perform these experiments from the start, without requiring from them years of work before a single spectrum can even be recorded.

The values of primary importance existing as necessary input parameters during the molecular resolution analysis of the data are the magnitude of the externally applied electric field, in addition to the state energies and the transition dipole moments of the porphyrin probe. The magnitude of the externally applied electric field that is felt by the chromophores embedded within the matrix rests upon the correct assignment of the relative permittivity of the matrix that surrounds the chromophore. A capacitive cell, for the determination of a materials dielectric permittivity, was developed in order to experimentally determine a valuation for the relative permittivity, at 1 K, of the 3:1 glycerol:water matrix within which the sample is embedded. As for the state energies and the transition dipole moments of the porphyrin probe, numerous post Hartree-Fock methods that take electron correlation into account were assessed for their possible use when calculating the values for these quantities that should be used during the analysis of the effect of external electric fields applied to spectral holes. The current findings from this set of studies indicate that high order methods such as the EOM-CCSD(T) should be used moving forward, as it was determined that this category of computational methods accurately reproduce valuations for the spectroscopically observable transition energies. Additional computational work on this front is necessary



before realistic valuations for the internal molecular electric field existing at the oxygen binding site of myoglobin should be reported.

# Appendix A

## **Substitution Process and Temperature Dependence of Q<sub>x</sub> Transition**

Presented below is an abridged procedure for the substitution of protoporphyrin-IX into native myoglobin, to yield the PPIX-Mb sample that is used during hole-burning investigations. This substitution process is modeled on the methodology outlined by Teale 1959 [57], and also that of Angiolillo 1998 [1]. References appear at the end of chapter 1. The temperature dependence of the fluorescence excitation spectrum and the peak wavelength of the Q<sub>x</sub> transition of the PPIX-Mb sample then follows.

### **Substitution Process**

- Mb is used directly from stock without additional purification
- Mb in chilled Tris-buffer (pH 7.0)
- The pH lowered to 3.8–4.0 with 1 M HCl
- Separatory funnel extraction with chilled 2-butanone / methylethylketone  $\leq$  (2 times the solution volume)
- Extraction process is repeated under maintained pH until a colorless layer can be obtained
- The apoMb is dialyzed with water
- 1 M ammonium hydroxide is added until pH 7.0 is achieved
- Porphyrin replacement prepared by dissolving the porphyrin in dimethylformamide or dimethylsulfoxide at pH of 7.0
- The dissolved porphyrin is added to the apoMb and placed on ice with continual stirring for approximately 1 hour
- This yields the porphyrin substituted species
- Full combination porphyrin/Mb is assessed spectrophotometrically
- The substituted Mb is then washed with Tris buffer at pH 7.0 in a cold room

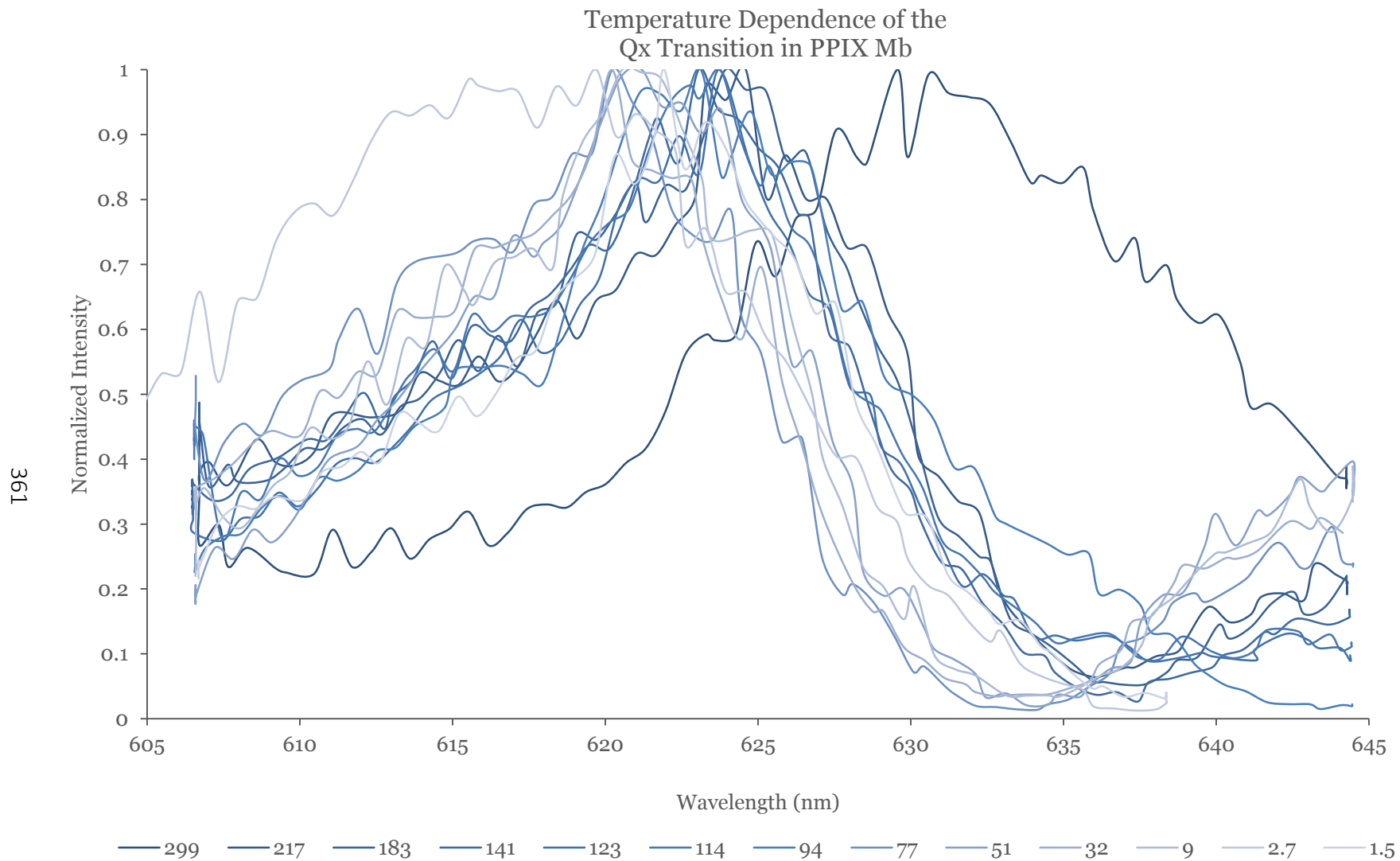


*Figure A.1: Temperature dependence of the Qx transition of the protoporphyrin-IX substituted myoglobin sample used during the spectral hole-burning investigations. The names of the traces are representative of the temperature in K that the spectra were acquired at.*

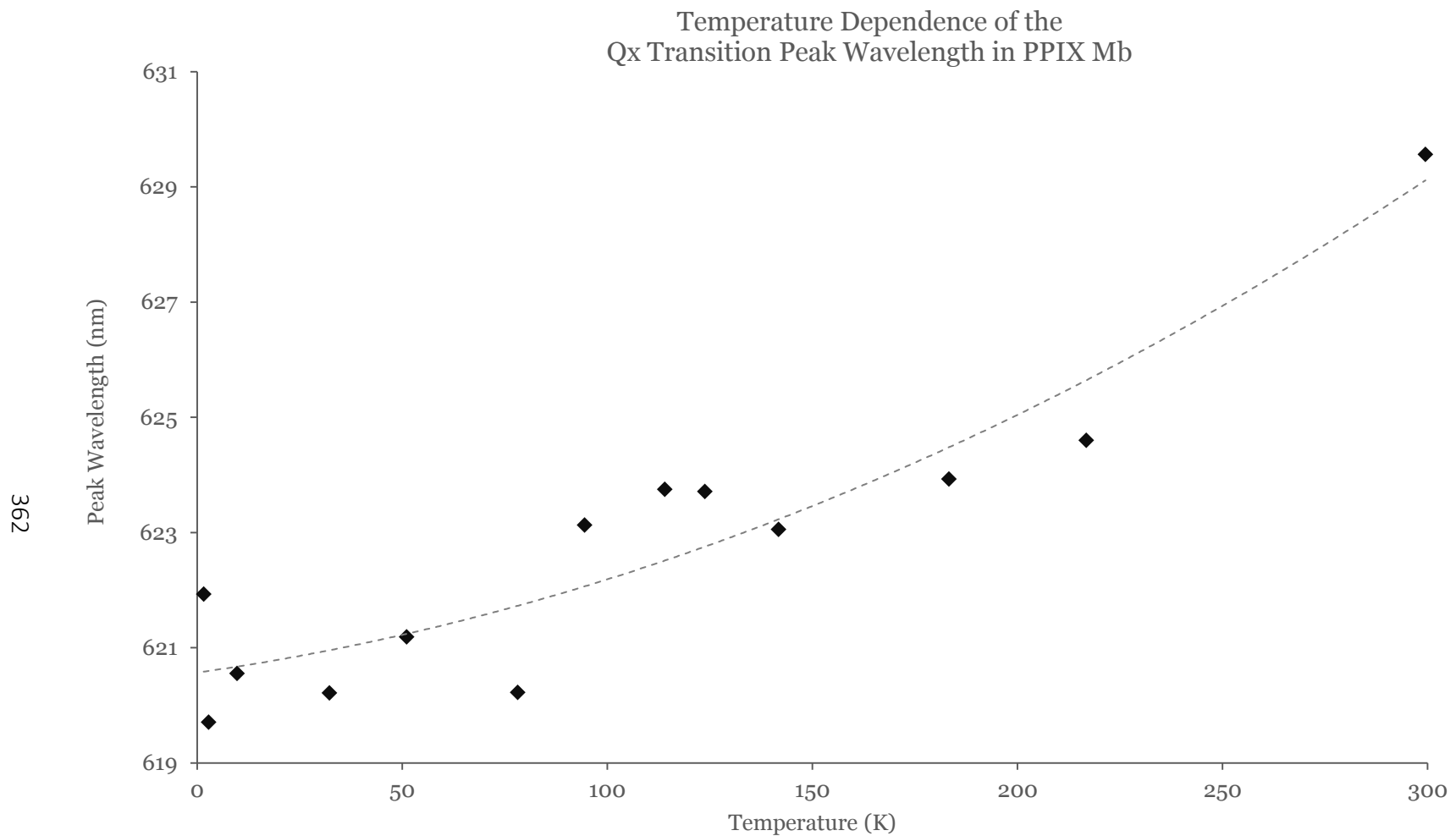


Figure A.2: Temperature dependence of the peak wavelength of the Qx transition of the protoporphyrin-IX substituted myoglobin sample used during the spectral hole-burning investigations. Peak wavelengths were taken from the fluorescence excitation spectra appearing in figure A1. To guide the eye, the data was fit using a second order polynomial,  $y = 6 \times 10^{-5}x^2 + 0.01x + 620.57$ ;  $R^2 = 0.8725$ , and appears as the dotted trace.

# Appendix B

## **Programmatic Hierarchy for Molecular Resolution Approach**

Following is a procedural outline that highlights the necessary programmatic hierarchy for fitting the experimentally obtained spectral hole profiles, to which external electric fields have been applied, with the modeled line-shapes that allow for the internal electric field to be determined. This iterative mathematical process for evaluating the experimentally obtained spectral hole profiles is required when the molecular resolution approach is utilized during the analysis.

## Programmatic hierarchy:

### User Input:

- Voltage applied
- Polarization direction (parallel, perpendicular, angle)
- Energy states vector
- Transition moment matrix
- Hole profiles: zero field, applied field
- Orientation step size

### Calculation:

For All spectra (each with different applied E-field, or applied E-field/burn polarization angle)

Calculate local electric field Eloc

Account for

- Voltage applied
- Sample geometry (capillary and dielectric matrix)

Specify burn and Efield polarization

Initialize state energy and transition moment matrices

Baseline adjustment of Raw Data

Lorentzian fit of zero field hole (stored to vector)

Start internal field determination Loop

Programmatically select Eint value (guess-PSO)

If first loop iteration (Eint only)

Determine protein field free energies (FFE)

Project Eint onto mu

Yields Hamiltonian

Call energy states vector

Symbolically solve Hamiltonian to yield energy states vector

Populate identity with "new" eigen values (FFE)

Store as "Eint guess dependent" energy matrix

else (Eloc+Eint)

Start porphyrin orientation loop

For each step (using step size)

Establish Euler rotation matrix,

Rotate all mu vectors (mu\_rot\_array)

Rotate Eint vector (Eint\_rot)

Sum Eloc to Eint\_rot "rotated Eint Guess dependent"

Yields Etot array

Project Etot onto mu\_rot

Yields total Hamiltonian

Diagonalize

Weighting of orientations (Ephoton dot mu S0->S1)

Delnu

Delta (field on (1,1) (2,2)) (field off (1,1) (2,2)) from each diagonalized matrix

Store as points with ((Delnu,Weight)

Convolve with zero field hole, Lorentzian

Calculate residuals/GOF/ least squares between two data sets

if convergence end

else programmatically select Eint Value (guess-PSO)

# Appendix C

## **Block Diagrams for Developed Programs**

Appearing here are the completed block diagrams for the four developed programs that were discussed in chapter 3.

Program P1, “Spectroscopy” is a platform used for acquiring spectral data. The block diagram appears in figures C1 (top half), and C2 (bottom half).

Program P2, “Hole-Burning” is a platform that is used during the burning of the spectral hole. The block diagram appears in figures C3 (top left portion), C4 (top right portion), C5 (bottom left portion), and C6 (bottom right portion).

Program P3, “Temperature Cycling” is a platform that assists in modulating the sample temperature by allowing users to control the heater ramping and PID temperature control values. The block diagram appears in figure C7.

Program P4, “Signal Smoothing” is a platform that is used in preliminary analysis, and allows for data smoothing and the determination of the signal to noise ratio for the data set. The block diagram appears in figure C8.

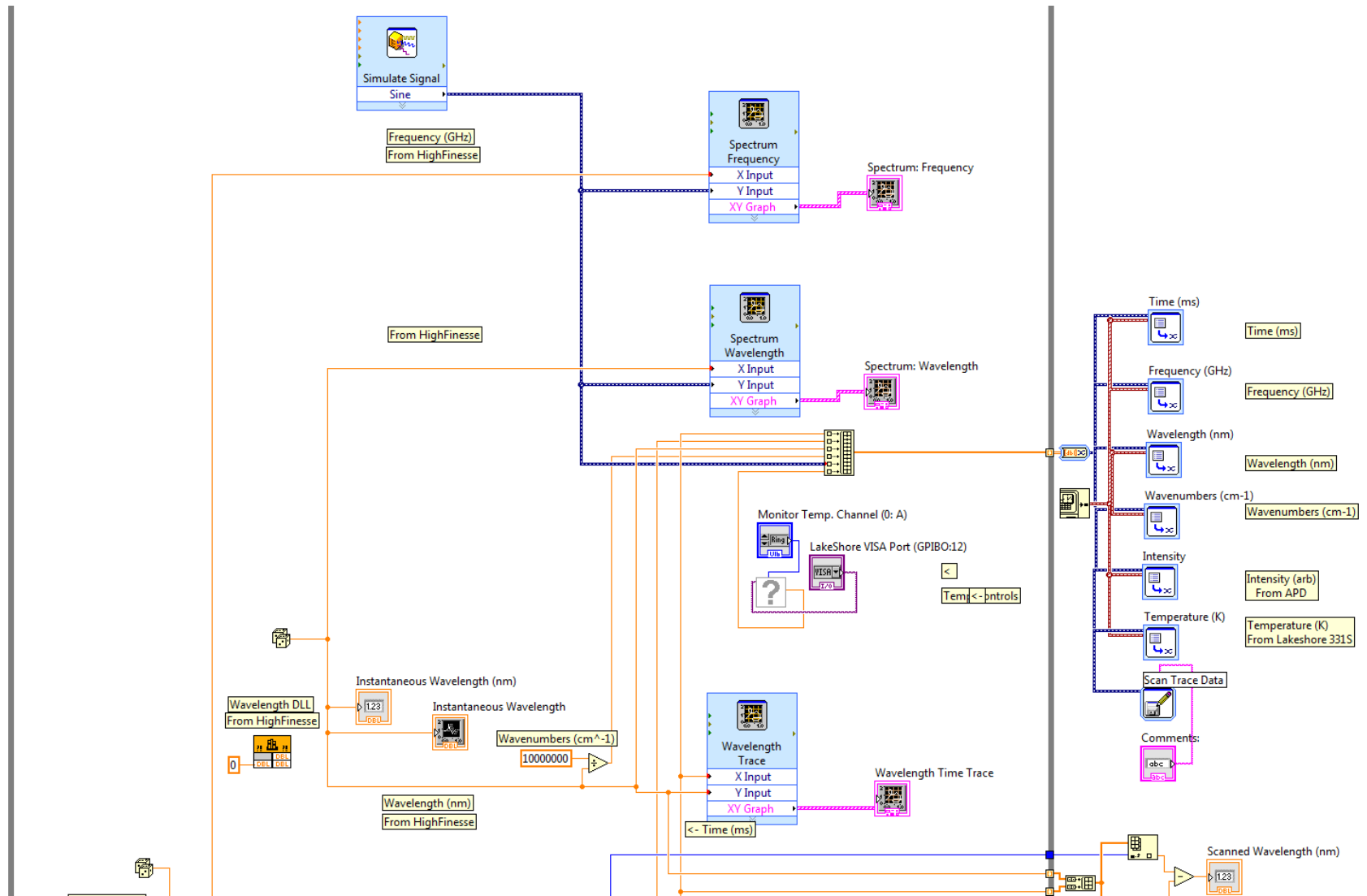
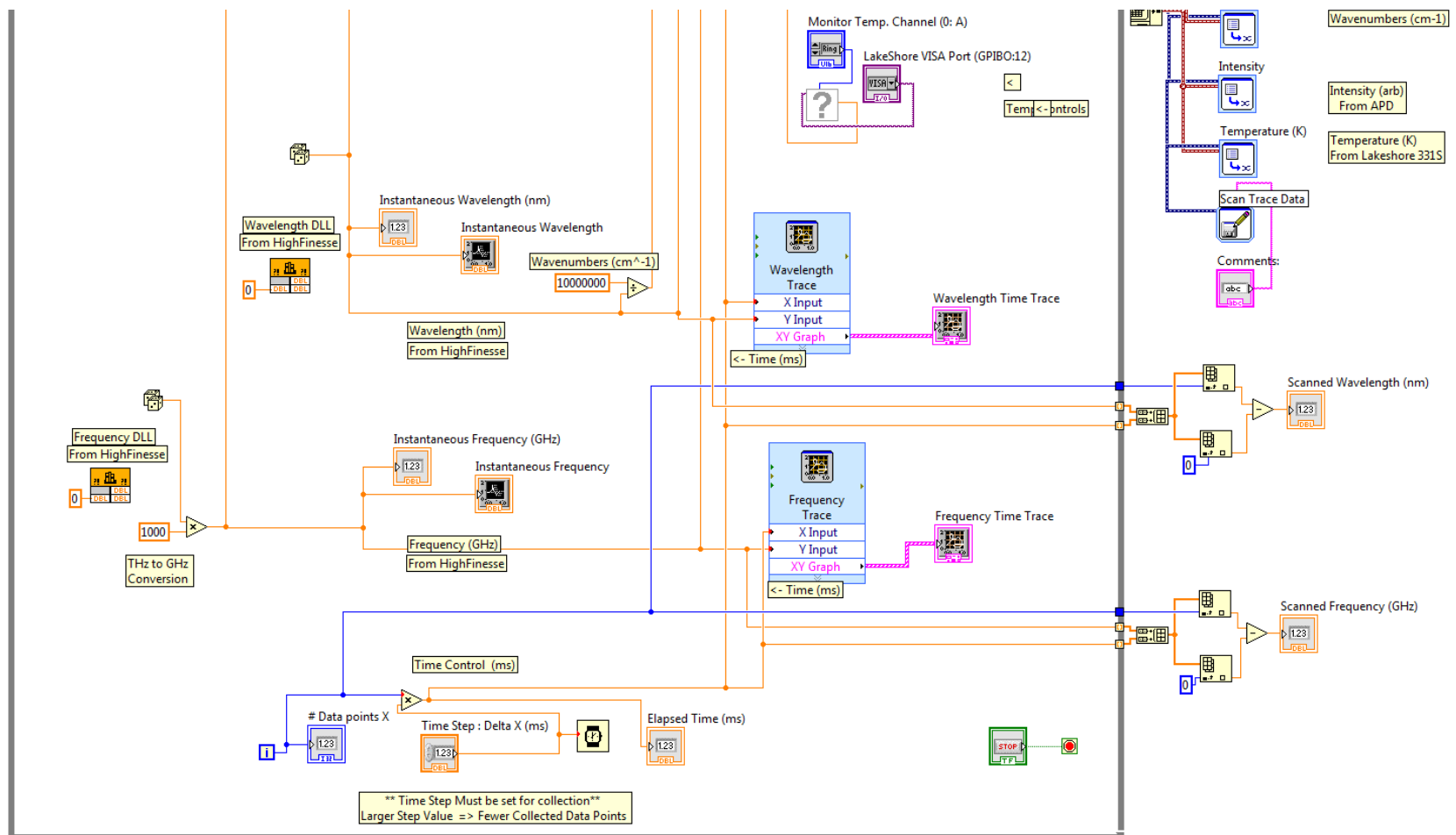


Figure C.1: Top half of program P1 "Spectroscopy". The user interface of this block diagram is displayed in figure 3.2.





Location of Lakeshore 331S VI Library

C:\Program Files\National Instruments\LabVIEW 2012\instr.lib\Lake Shore Cryotronics 331\Examples

To Work Properly: Must Choose Visa (Set up with NI MAX and GPIB) in drop down on "Application Temp Controller" Front Panel

To remove this feature from this Spectroscopy program, Remove above Temp Dynamic Data VI and 2 temp controls in While loop, just left

Figure C.2: Bottom half of program P1 "Spectroscopy". The user interface of this block diagram is displayed in figure 3.2.

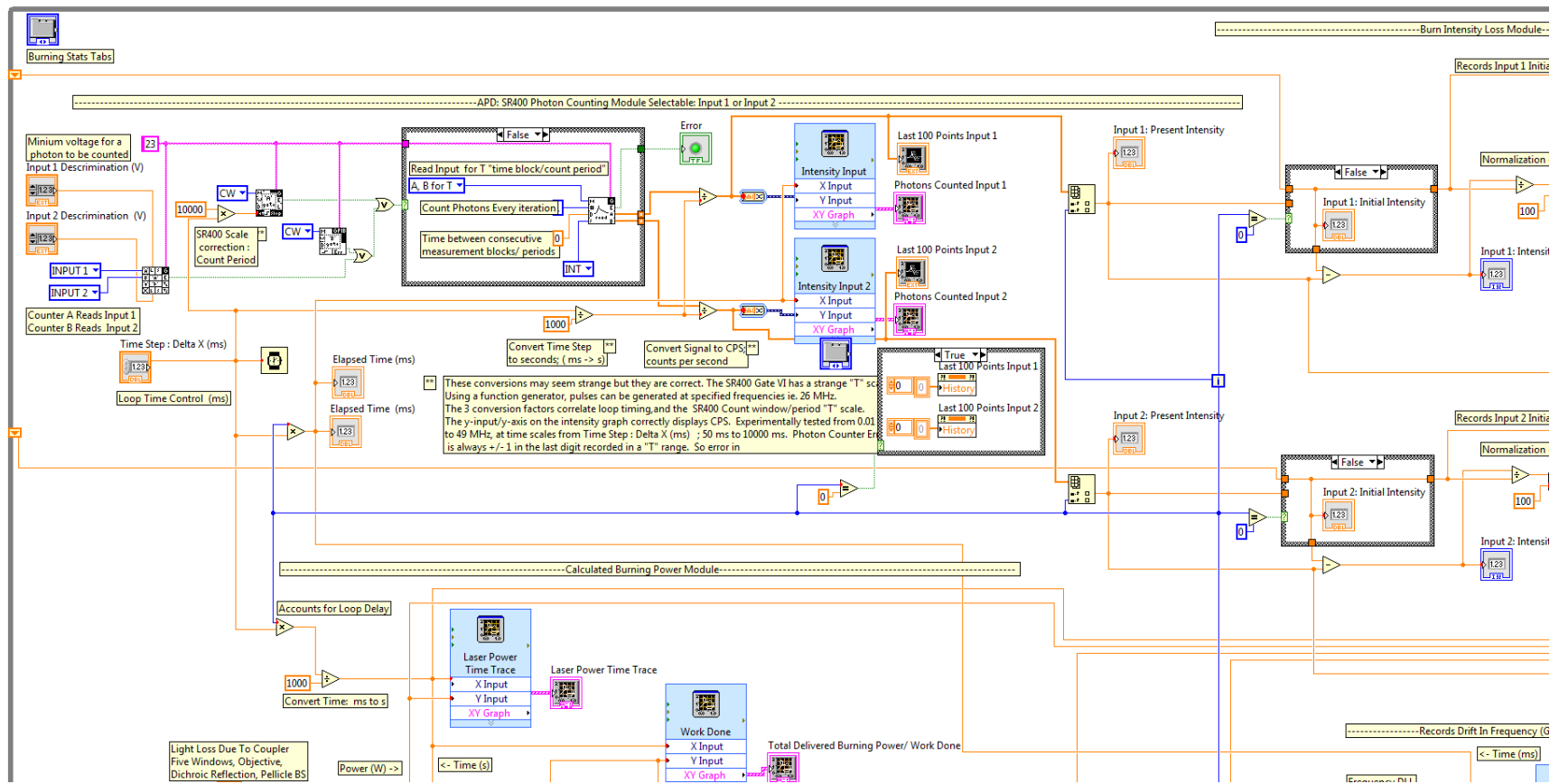


Figure C.3: Top left of program P2 "Hole-Burning". The user interface of this block diagram is displayed in figure 3.5.

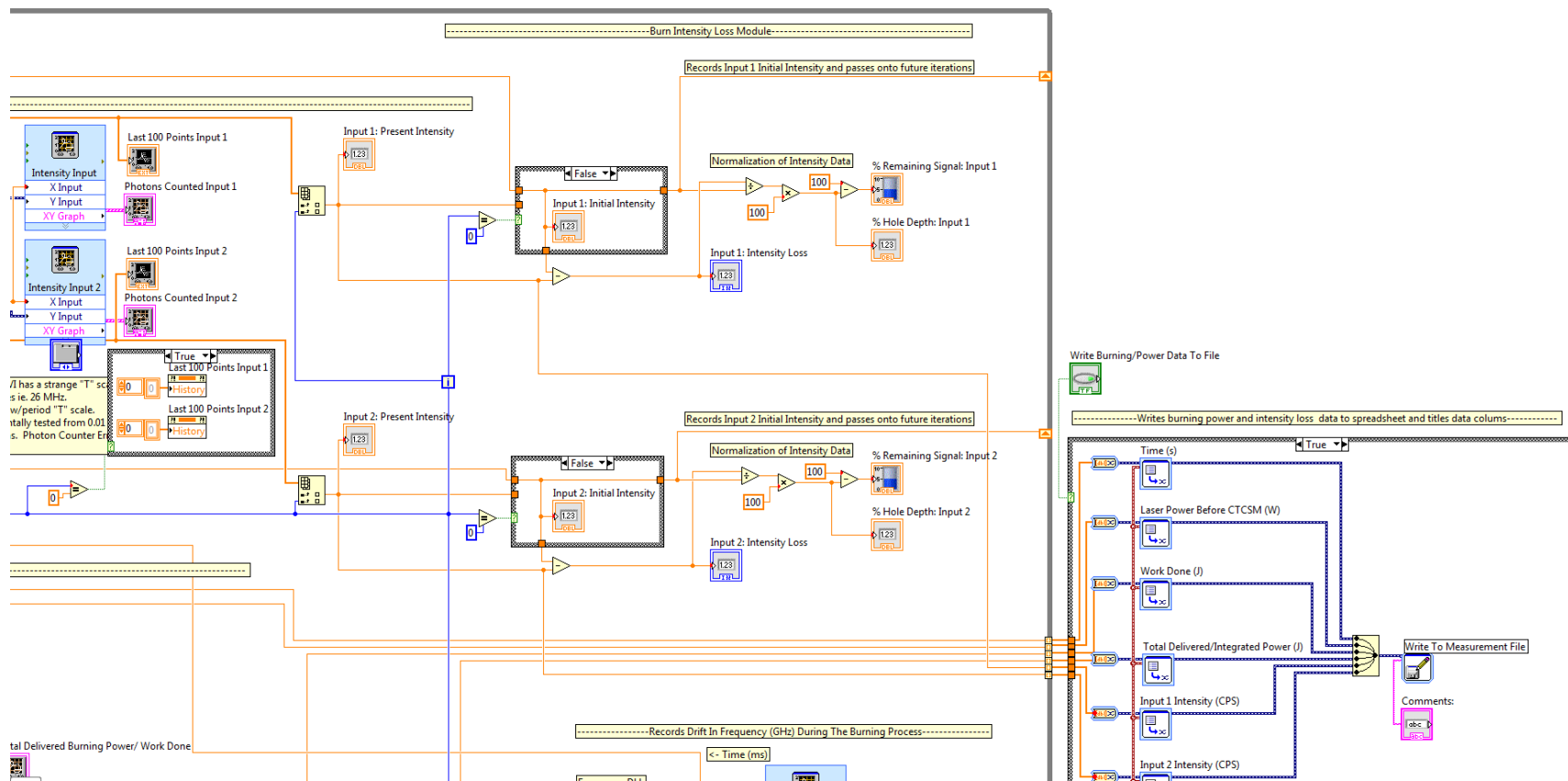


Figure C.4: Top right of program P2 "Hole-Burning". The user interface of this block diagram is displayed in figure 3.5.

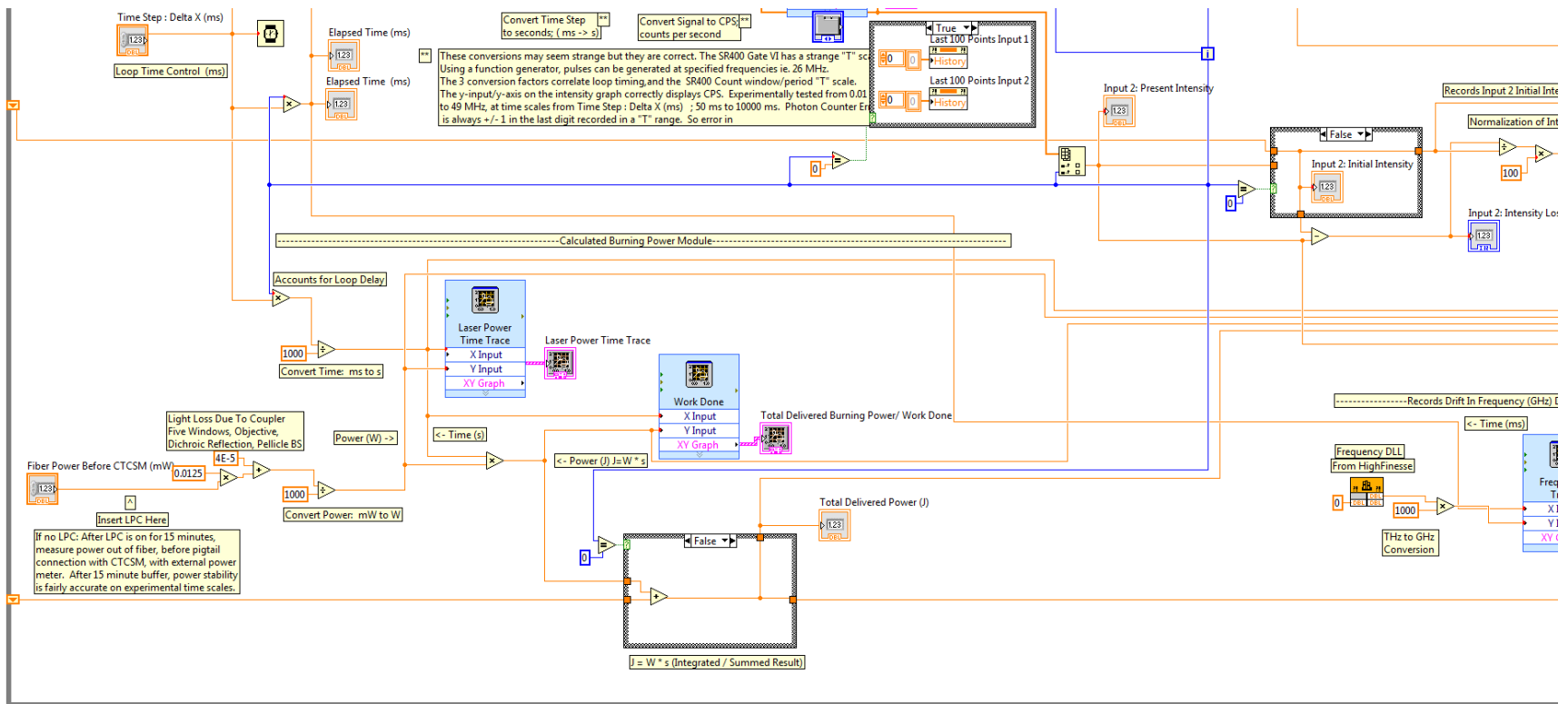


Figure C.5: Bottom left of program P2 "Hole-Burning". The user interface of this block diagram is displayed in figure 3.5.

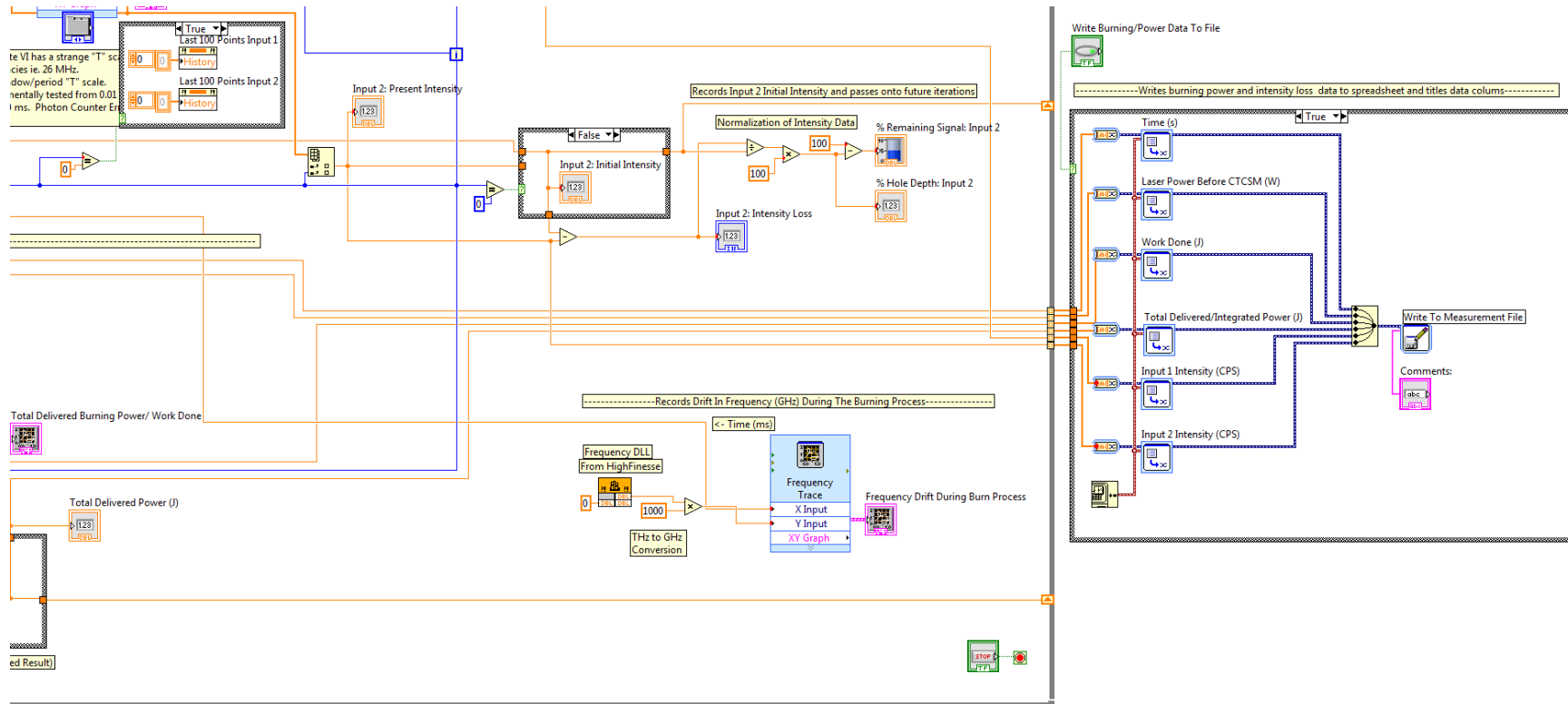


Figure C.6: Bottom right of program P2 “Hole-Burning”. The user interface of this block diagram is displayed in figure 3.5.

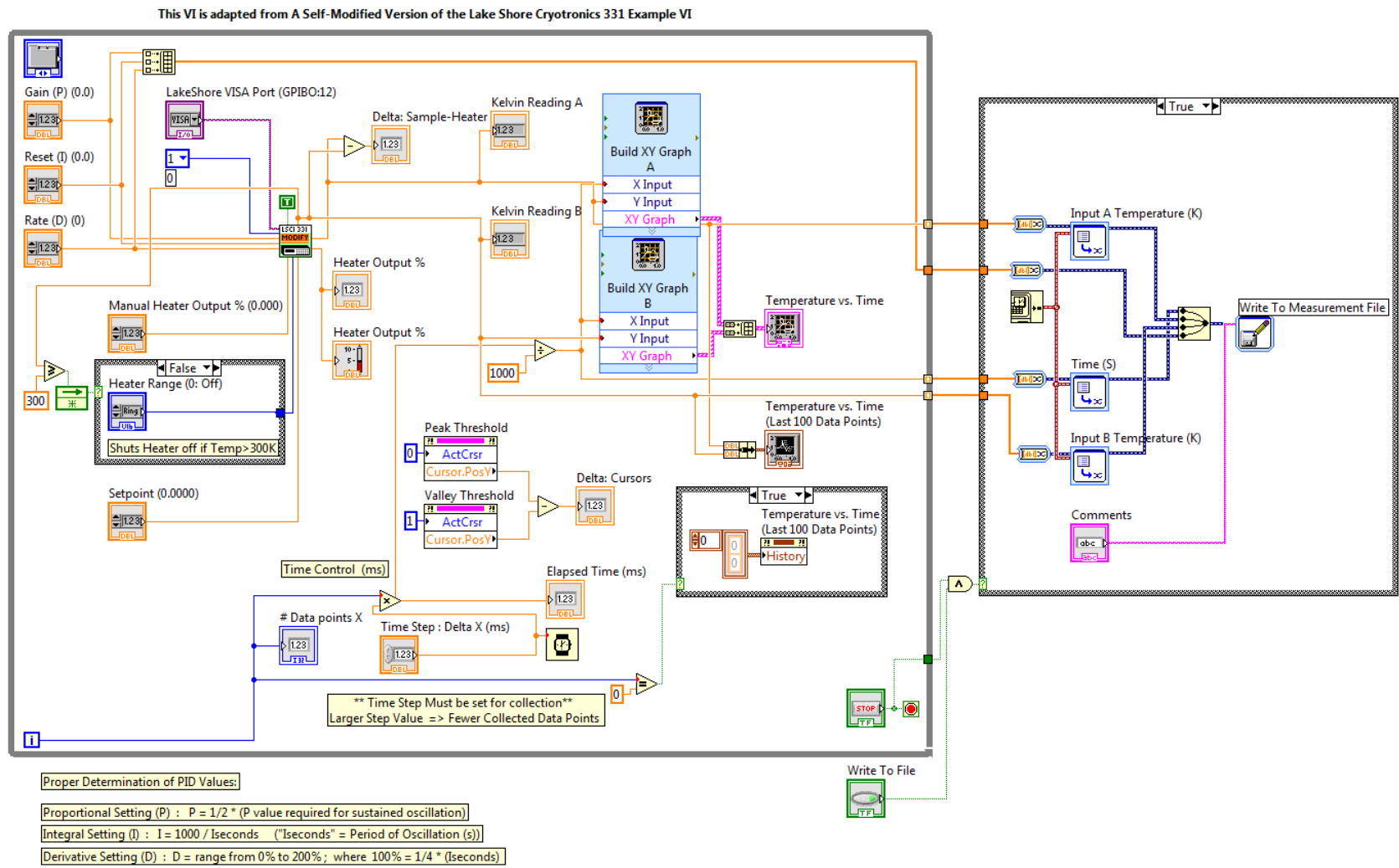


Figure C.7: Program P3 "Temperature Cycling". The user interface of this block diagram is displayed in figure 3.6.

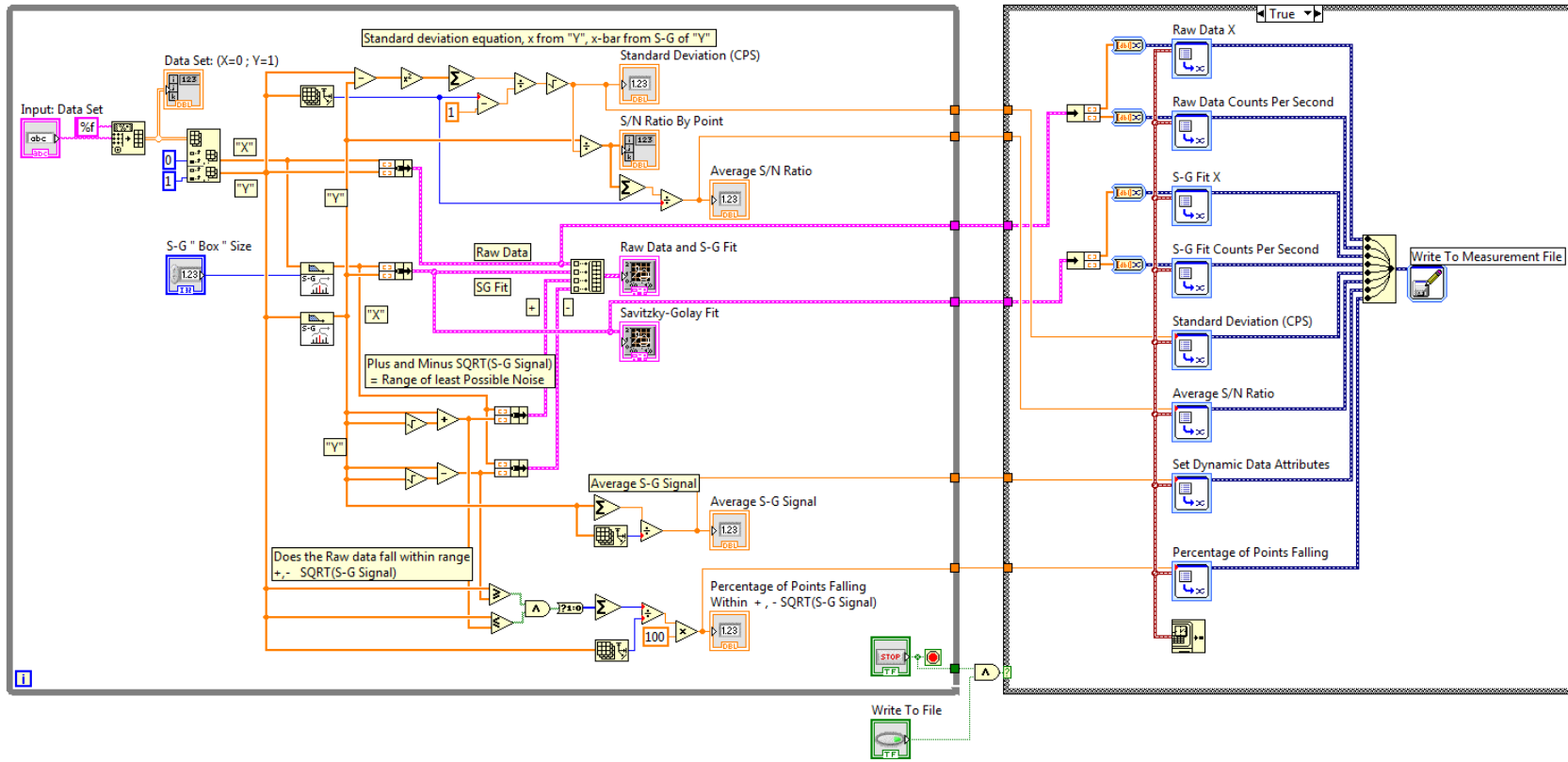


Figure C.8: Program P4 "Signal Smoothing". The user interface of this block diagram is displayed in figure 3.7

# Appendix D

## CTCSM Microscope Head and Component List

The head portion of the CTCSM microscope is displayed in exploded view in figure D.1 so that the construction can be more easily visualized. Below is a complete list of the components, separated into segments, that are utilized in the construction of the microscope. The segments are indicated in figure D.1.

### Emission Arm

SM1FC - FC/PC Fiber Adapter Plate	
SM1Z - Z-Axis Translation Mount, 30 mm Cage Compatible	
SM1L10 - SM1 Lens Tube, 1.00" Thread Depth,	
SM1T2 - SM1 (1.035"-40) Coupler	
ER3 - Cage Assembly Rod, 3" (76.2 mm) Long, Ø6 mm	4 each
HPT1 - 30 mm Cage Assembly, XY Translating Lens Mount	
SM1S10 - SM1 Lens Tube Spacer	
ST1XY-S - XY Translator with Micrometer Drives	
SM1S20 - SM1 Lens Tube Spacer	
KC1-T - Kinematic, SM1-Threaded, 30 mm-Cage-Compatible Mount	
ER1 - Cage Assembly Rod, 1" (25.4 mm) Long	4 each

### CUBE-Top

C6W - 30 mm Cage Cube, Ø6 mm Through Holes	
SM1PM10 - SM1 Lens Tube Mount for 8 mm and 10 mm Mounted Polarizing Prisms	
SM1CP2 - Externally SM1-Threaded End Cap	2 each
B3C - Fixed Cage Cube Platform for C4W/C6W	2 each
SM1L05 - SM1 Lens Tube	
CP02T - SM1-Threaded 30 mm Cage Plate, 0.5" Thick	
ER1 - Cage Assembly Rod, 1" (25.4 mm) Long	4 each

### CUBE-Center

ER1 - Cage Assembly Rod, 1" (25.4 mm) Long	4 each
C6W - 30 mm Cage Cube, Ø6 mm Through Holes	
FFM1 - Cage-Compatible Dichroic Filter Mount	
B3C - Fixed Cage Cube Platform for C4W/C6W	2 each

### CUBE-Bottom

ER05 - Cage Assembly Rod, 1/2" (12.7 mm) Long	4 each
C6W - 30 mm Cage Cube, Ø6 mm Through Holes	
FFM1 - Cage-Compatible Dichroic Filter Mount	
B3C - Fixed Cage Cube Platform for C4W/C6W	2 each
SM1CP2 - Externally SM1-Threaded End Cap	2 each



### **Polarization Modulator**

CPo2T - SM1-Threaded 30 mm Cage Plate, 0.5" Thick

SM1T2 - SM1 (1.035"-40) Coupler

SM1L10 - SM1 Lens Tube, 1.00" Thread Depth,

Glan-Taylor prism inside

ER2 - Cage Assembly Rod, 2" (50.8 mm) Long, Ø6 mm

CPo2T - SM1-Threaded 30 mm Cage Plate, 0.5" Thick

### **Excitation Arm**

SM1FC - FC/PC Fiber Adapter Plate

SM1Z - Z-Axis Translation Mount, 30 mm Cage Compatible

SM1T2 - SM1 (1.035"-40) Coupler

SM1L10 - SM1 Lens Tube, 1.00" Thread Depth,

ER3 - Cage Assembly Rod, 3" (76.2 mm) Long, Ø6 mm

HPT1 - 30 mm Cage Assembly, XY Translating Lens Mount

SM1S10 - SM1 Lens Tube Spacer

ST1XY-S - XY Translator with Micrometer Drives

SM1S20 - SM1 Lens Tube Spacer

KC1-T - Kinematic, SM1-Threaded, 30 mm-Cage-Compatible Mount

ER1 - Cage Assembly Rod, 1" (25.4 mm) Long

4 each

### **Reference Arm**

SM1L05 - SM1 Lens Tube, 0.50" Thread Depth

SM1D12 - SM1 Lever-Actuated Iris Diaphragm

SM1L20 - SM1 Lens Tube, 2.00" Thread Depth

SM1D12 - SM1 Lever-Actuated Iris Diaphragm

SM1L05 - SM1 Lens Tube, 0.50" Thread Depth

SM1FC - FC/PC Fiber Adapter Plate

### **Optical Insert**

ER12 - Cage Assembly Rod, 12"

16 each

CPo7 - Similar 1.8" Outer Diameter Round Cage Plate with SM1 Internal Thread Window Holders

CPo7 - Similar 1.8" Outer Diameter Round Blank Cage Plate, 0.35" Thick  
Base for piezo actuators

### **Focusing Lens-Glass Cryostat Setup**

#### **Bottom/After Cube**

CPo2T - SM1-Threaded 30 mm Cage Plate, 0.5" Thick

ER2 - Cage Assembly Rod, 2" (50.8 mm) Long, Ø6 mm

SM1L10 - SM1 Lens Tube, 1.00" Thread Depth,

Glan-Taylor prism inside

CPo2T - SM1-Threaded 30 mm Cage Plate, 0.5" Thick

SM1L05 - SM1 Lens Tube, 0.50" Thread Depth

SM1T2 - SM1 (1.035"-40) Coupler

SM1L05 - SM1 Lens Tube, 0.50" Thread Depth

Newport LH-1

Newport LH-0.5

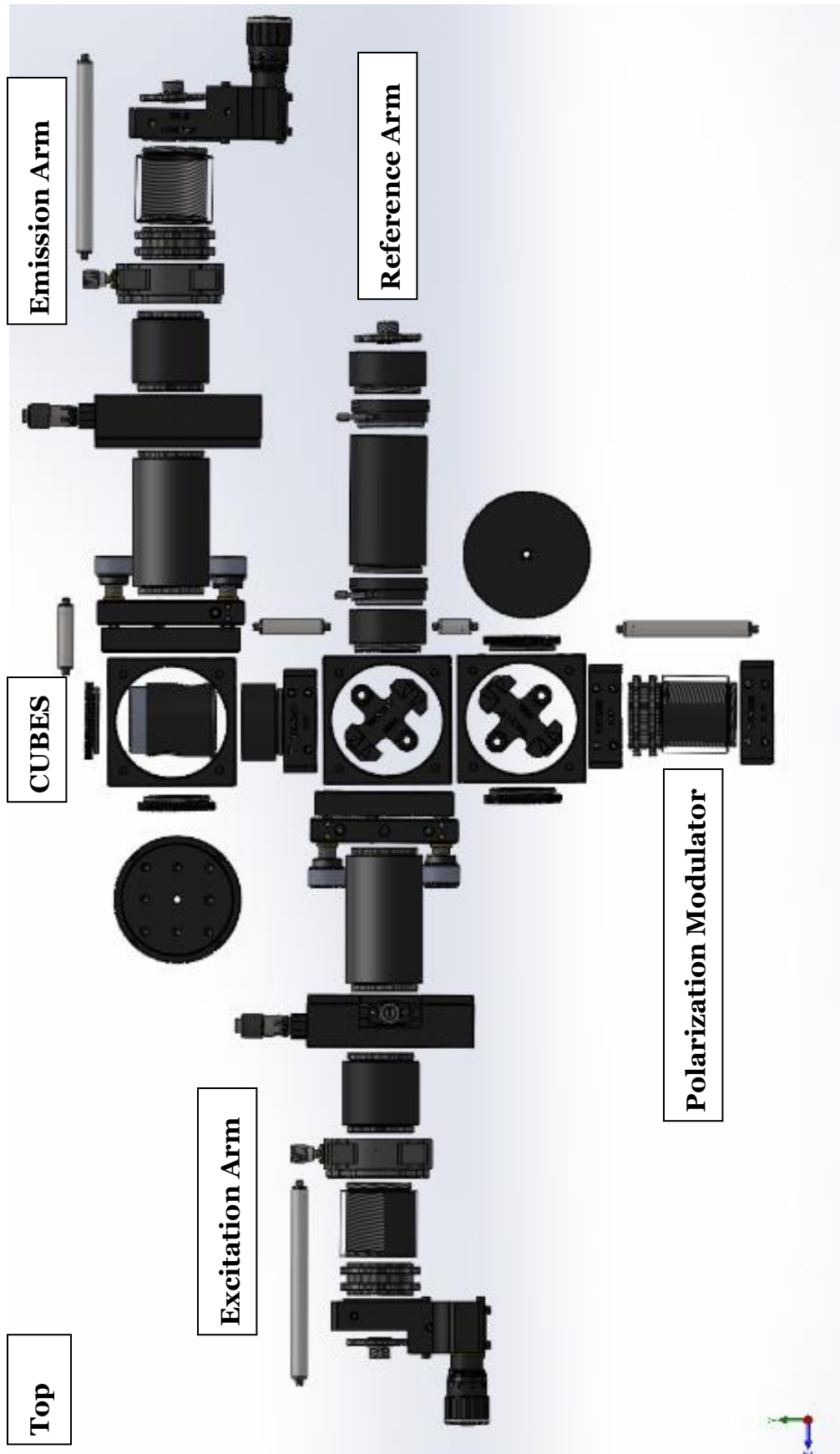


Figure D.1: The head of the CTCSM presented in exploded view. The displayed segments correspond to the respective component lists.

# Appendix E

## Thermal Modulation Parameters for the Heater Ramp and Temperature Specific PID Settings

Following is a plot that displays the maximum achievable temperature and the time that is required for a given temperature to be reached within the Janis research Dewar, dependent upon the utilized heater output setting and heater range setting. The temperature specific PID values and the corresponding heater output range allowing for precise temperature control is then presented in tabular form.

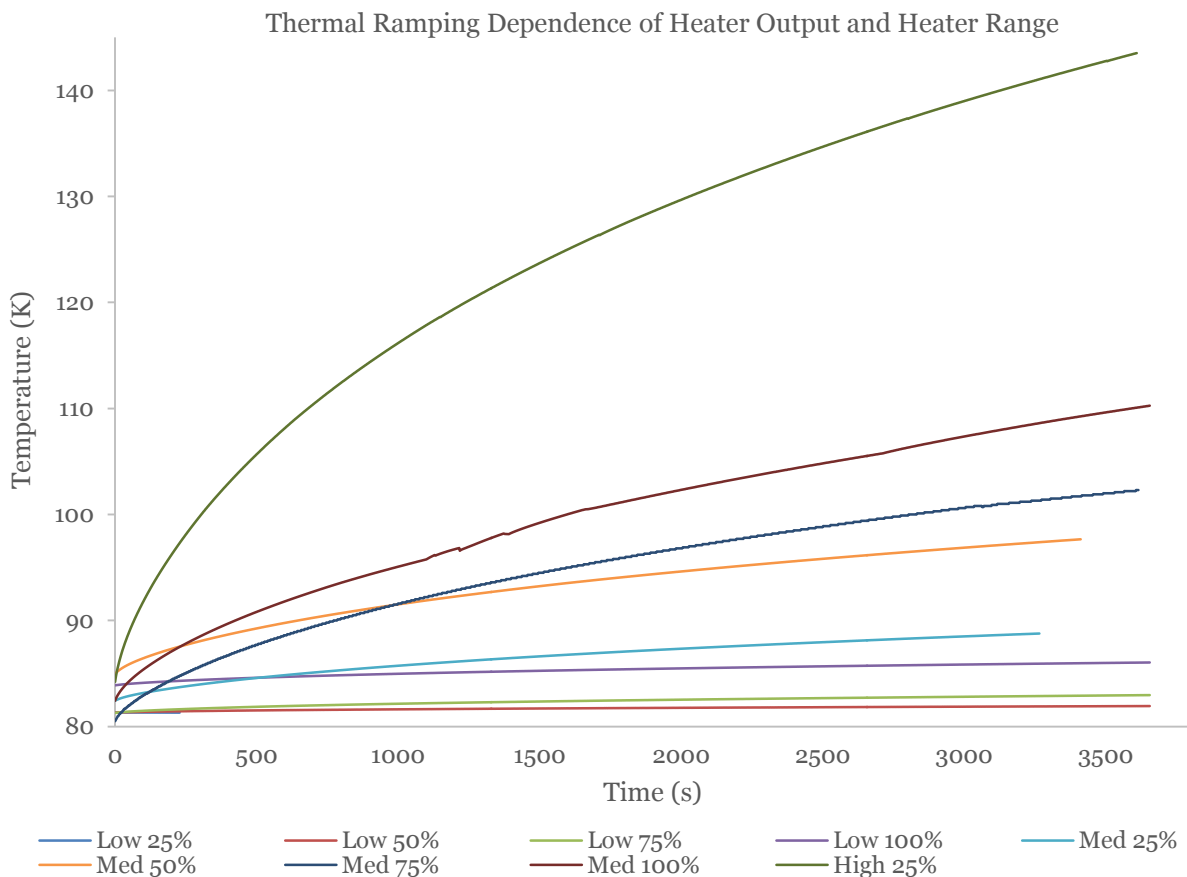


Figure E.1: Thermal ramping dependence of Janis research Dewar based on the specified heater output power and the heater range. The resistive heating element can be modulated within three ranges that correspond to: Low = 500 mW, Med = 5 W, High = 50 W. The heater power is specified as a percentage of total power for a given heater range.

**PID Value Settings For Various Temperature Regions:  
LakeShore 331S Temperature Controller  
Janis 9VSRD-SVT-22 Research Dewar**

<b>Temp (K)</b>	<b>P</b>	<b>I</b>	<b>D</b>	<b>Heater Range</b>
<b>5</b>	20	50	100	Medium
<b>7</b>	75	15.4	100	Medium
<b>10</b>	300	15.4	100	Medium
<b>12</b>	75	84.3	100	Medium
<b>15</b>	300	84.3	100	Medium
<b>17</b>	450	124.7	100	Medium
<b>20</b>	675	81.3	100	Medium
<b>22</b>	1000	68.9	100	Medium
<b>25</b>	500	21.7	100	Medium
<b>27</b>	750	25.9	100	Medium
<b>30</b>	750	25.9	100	Medium
<b>32</b>	1000	22.1	100	Medium
<b>35</b>	1000	17.1	100	Medium
<b>40</b>	1000	17.1	100	Medium
<b>45</b>	1000	17.1	100	Medium
<b>50</b>	1000	17.1	100	Medium
<b>55</b>	1000	17.1	100	Medium
<b>60</b>	500	20	100	Medium
<b>65</b>	500	20	100	Medium
<b>70</b>	500	20	100	Medium
<b>80</b>	200	20	100	High
<b>85</b>	200	20	100	High
<b>90</b>	200	20	100	High
<b>95</b>	250	20	100	High

**PID Value Settings For Various Temperature Regions:  
LakeShore 331S Temperature Controller  
Janis 9VSRD-SVT-22 Research Dewar**

<b>Temp (K)</b>	<b>P</b>	<b>I</b>	<b>D</b>	<b>Heater Range</b>
100	1000	20	100	High
105	1000	77.4	100	High
110	1000	71.7	100	High
115	1000	62.4	100	High
120	1000	56.6	100	High
125	1000	47.4	100	High
130	1000	48.9	100	High
135	1000	54.9	100	High
140	1000	44.9	100	High
145	1000	42.9	100	High
150	1000	40.5	100	High
155	1000	38.2	100	High
160	1000	37.2	100	High
165	1000	34.3	100	High
170	1000	33.5	100	High
175	1000	31.3	100	High
180	1000	28.9	100	High
185	1000	26.7	100	High
190	1000	25.2	100	High
195	1000	24.2	100	High
200	1000	22.1	100	High
205	1000	21.5	100	High
210	1000	19.3	100	High
215	1000	17.7	100	High
220	1000	17.1	100	High

<b>PID Value Settings For Various Temperature Regions: LakeShore 331S Temperature Controller Janis 9VSRD-SVT-22 Research Dewar</b>				
<b>Temp (K)</b>	<b>P</b>	<b>I</b>	<b>D</b>	<b>Heater Range</b>
<b>225</b>	1000	15.5	100	High
<b>230</b>	1000	15.6	100	High
<b>235</b>	1000	13.1	100	High
<b>240</b>	1000	13.8	100	High
<b>245</b>	1000	13.8	100	High
<b>250</b>	1000	13.3	100	High
<b>255</b>	1000	11.3	100	High
<b>260</b>	1000	11.3	100	High
<b>265</b>	1000	11.3	100	High
<b>270</b>	1000	8.5	100	High
<b>275</b>	1000	8.3	100	High
<b>280</b>	1000	8.3	100	High
<b>285</b>	1000	8.3	100	High
<b>290</b>	1000	8.3	100	High
<b>295</b>	1000	8.3	100	High
<b>300</b>	1000	8.3	100	High

*Table E.1: Determined PID value settings for Janis 9VSRD-SVT-22 Research Dewar and Lakeshore 331 Temperature Controller for various temperature regions from 5 K to 300 K. Medium heater range is used in the liquid helium range as it allows for fast equilibration times while not imparting unnecessary additional thermal energy to the cryostat thereby minimizing cryogen losses. High heater range is utilized within the liquid nitrogen range because it yields the fastest equilibration times.*

# Appendix F

## Split Hole Profile

Following is an example of the splitting of a spectral hole upon application of 2500 V. This split hole profile is representative of a split hole profile that is blue shifted from the split hole profiles appearing in chapter 7.

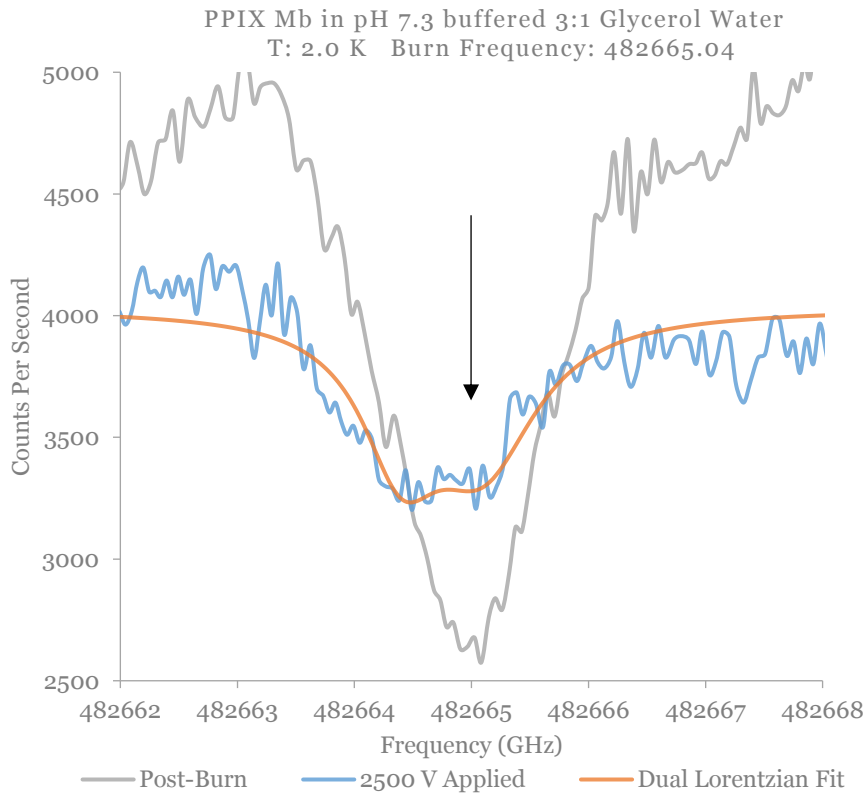


*Figure F.1: Spectral hole, burnt into the Qx transition of PPIX-Mb. Arrow indicates position of burn. This spectral hole has a FWHM of 0.00193 nm = 1.50 GHz, and a relative depth of 46%. The applied voltage corresponds to an applied electric field of approximately  $1.67 \times 10^6$  V/m. This split profile was most basically modeled using a sum of Lorentzian profiles. The Lorentzian fit parameters and the fitting statistics appear the table below.*

<b>(2500 V → 1.67 x 10<sup>6</sup> V/m)</b>	482665.04	Goodness of fit:
General model: Lorentzian Fit		
$f(x) = I1*((P1^2)/((x-P2)^2+P1^2))$ $+ I2 *((P3^2)/((x-P4)^2+P3^2)) + 4030$		
I1 (Intensity) = -544.5 (-760.6, -328.3)		SSE: 1.001e+06
I2 (Intensity) = -595.8 (-769.3, -422.2)		R-square: 0.8798
P1 (HWHM) = 0.4094 (0.2289, 0.5898)		Adjusted R-square: 0.8727
P2 (Peak) = 4.827e+05 (4.827e+05, 4.827e+05)		RMSE: 99.07
P3 (HWHM) = 0.5702 (0.3439, 0.7965)		
P4 (Peak) = 4.827e+05 (4.827e+05, 4.827e+05)		

# Appendix G

## **Computational Studies: Molecular geometries and Method Dependent Q<sub>x</sub>, Q<sub>y</sub>, B<sub>x</sub>, and B<sub>y</sub> Transition Energies**

Here are the coordinates of the porphine core as obtained from the 1DWT crystal structure data, that were repositioned according to the procedure discussed in chapter 9.2.1, and utilized during the computational investigations. Presented first are the unoptimized coordinates, with the optimized coordinates presented second. Following the coordinates are the calculated transition energies for the Q<sub>x</sub>, Q<sub>y</sub>, B<sub>x</sub>, and B<sub>y</sub> optical transitions by the various computational methods.



COORDINATES OF ALL ATOMS ARE (ANGS)

ATOM	CHARGE	X	Y	Z
C	6.0	2.39200	-2.40500	0.02100
C	6.0	-2.48100	-2.43800	0.07800
C	6.0	-2.40700	2.40900	-0.08600
C	6.0	2.43300	2.41200	-0.06600
N	7.0	-0.00500	-2.07900	-0.03800
C	6.0	1.09700	-2.86800	0.01700
C	6.0	0.68600	-4.24500	0.13400
C	6.0	-0.68300	-4.25500	0.14700
C	6.0	-1.13600	-2.88900	0.04400
N	7.0	-2.09600	-0.03100	0.03800
C	6.0	-2.94600	-1.12900	0.06400
C	6.0	-4.32300	-0.68100	0.01500
C	6.0	-4.30100	0.69500	-0.06400
C	6.0	-2.89300	1.09000	-0.03700
N	7.0	0.02900	2.11000	0.00000
C	6.0	-1.09700	2.88400	-0.08600
C	6.0	-0.70400	4.25100	-0.27000
C	6.0	0.64800	4.30400	-0.29900
C	6.0	1.13000	2.92000	-0.10400
N	7.0	2.07200	0.00000	0.00000
C	6.0	2.90000	1.08900	0.00000
C	6.0	4.26400	0.63200	-0.01000
C	6.0	4.23500	-0.71800	-0.05100
C	6.0	2.85400	-1.11600	-0.00800
H	1.0	1.22900	-0.06000	0.17900
H	1.0	-1.24700	-0.00900	-0.11800
H	1.0	5.05200	-1.34700	-0.10300
H	1.0	5.10800	1.22500	0.01000
H	1.0	1.22900	5.14600	-0.43100
H	1.0	-1.34300	5.05600	-0.36400
H	1.0	1.30600	-5.06700	0.19600
H	1.0	-1.28400	-5.09100	0.21800
H	1.0	-5.16300	-1.28000	0.03500
H	1.0	-5.11700	1.32300	-0.12900
H	1.0	-3.20300	-3.17400	0.11800
H	1.0	-3.13500	3.14000	-0.12900
H	1.0	3.17500	3.12900	-0.09100
H	1.0	3.12100	-3.13500	0.05000

*Table G.1: Atomic coordinates of the porphine core of the porphyrin molecule as it exists in the active site of horse heart myoglobin. Atomic coordinates were obtained from the crystal structure 1DWT. The molecule was repositioned as described in chapter 9.2.1.*

\*\*\*\*\* EQUILIBRIUM GEOMETRY LOCATED \*\*\*\*\*

COORDINATES OF ALL ATOMS ARE (ANGS)

ATOM CHARGE X Y Z

ATOM	CHARGE	X	Y	Z
C	6.0	2.44232	-2.45872	-0.09770
C	6.0	-2.44119	-2.45690	0.13165
C	6.0	-2.44537	2.45946	-0.07362
C	6.0	2.44486	2.46033	0.03772
N	7.0	0.00049	-2.03148	0.01334
C	6.0	1.10428	-2.88136	-0.09179
C	6.0	0.68501	-4.28785	-0.01470
C	6.0	-0.68364	-4.28703	0.08070
C	6.0	-1.10318	-2.87963	0.13291
N	7.0	-2.12562	0.00000	0.00000
C	6.0	-2.91382	-1.13667	0.13752
C	6.0	-4.28851	-0.68977	0.07733
C	6.0	-4.28881	0.69188	-0.01805
C	6.0	-2.91574	1.13845	-0.10720
N	7.0	-0.00034	2.03084	-0.01400
C	6.0	-1.10953	2.88059	-0.00359
C	6.0	-0.68596	4.28727	-0.05077
C	6.0	0.68543	4.28729	-0.02047
C	6.0	1.10896	2.88009	-0.04071
N	7.0	2.12562	0.00000	0.00000
C	6.0	2.91548	1.13999	0.09113
C	6.0	4.28885	0.69283	0.00695
C	6.0	4.28889	-0.69006	-0.07032
C	6.0	2.91439	-1.13835	-0.12314
H	1.0	1.10861	-0.00226	0.01613
H	1.0	-1.10849	-0.00178	-0.01626
H	1.0	5.14940	-1.34068	-0.16822
H	1.0	5.15027	1.34589	0.07479
H	1.0	1.35252	5.14142	-0.06654
H	1.0	-1.35288	5.14226	-0.02272
H	1.0	-5.15052	1.34365	-0.09484
H	1.0	-5.14867	-1.33969	0.18215
H	1.0	-1.34501	-5.14111	0.18008
H	1.0	1.34629	-5.14342	-0.09811
H	1.0	3.20853	3.23849	0.06606
H	1.0	-3.20920	3.23696	-0.11350
H	1.0	-3.20184	-3.22991	0.24453
H	1.0	3.20315	-3.23309	-0.19888

*Table G.2: Atomic coordinates of the porphine core of the porphyrin molecule as it exists in the active site of horse heart myoglobin. Atomic coordinates were obtained from the crystal structure 1DWT. These coordinates represent the optimized geometry that was obtained using a 6-311G basis set at the MP2 level of perturbation theory, and found to be a stationary point by means of a vibrational analysis calculation.*

Predicted 6-311G(d) CISD  $S_0 - S_1$  Transition Wavelengths  
 (Electron Excitation From Doubly Occupied to Unoccupied Orbitals)

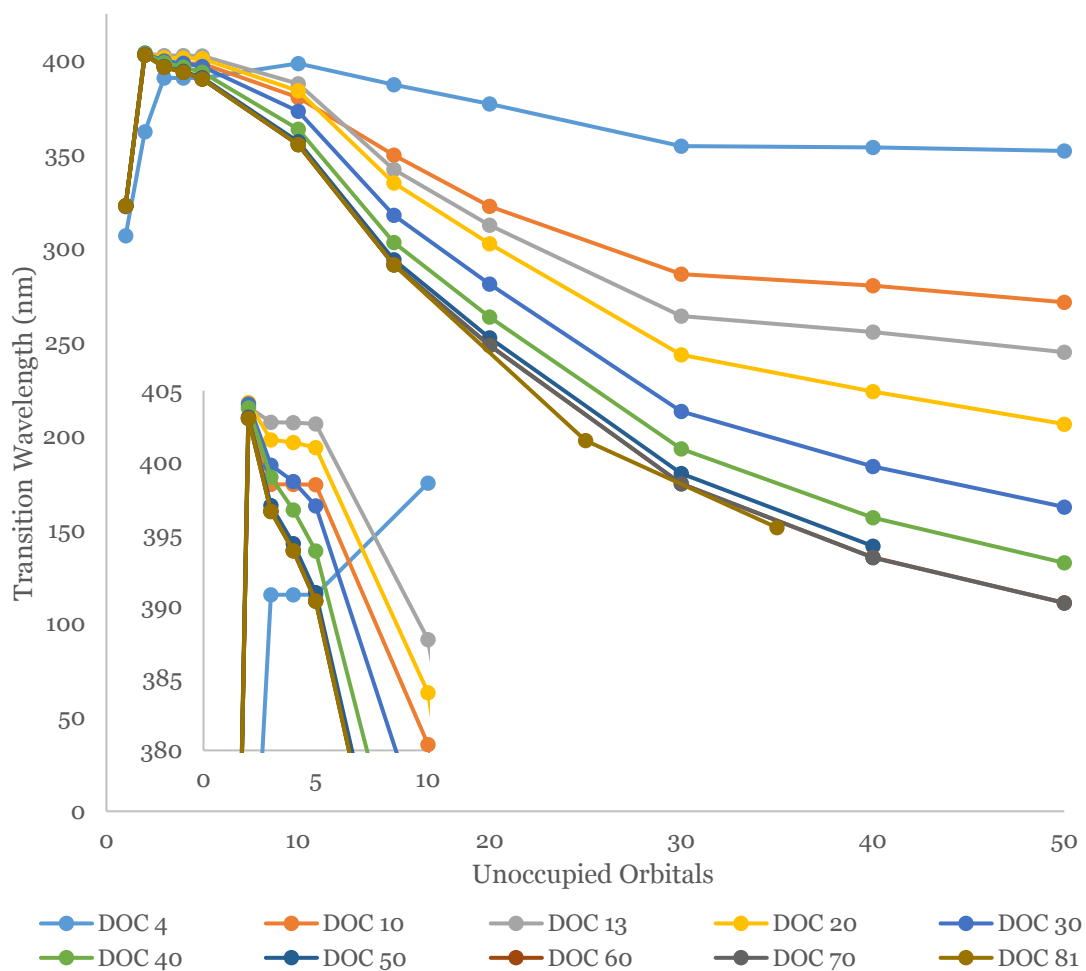


Figure G.1: Predicted Qx transition wavelengths by CISD using the 6-311G(d) basis set. Electrons were excited from doubly occupied core orbitals, HOMO down, into unoccupied orbitals from the LUMO upwards. Ten different active electron groups were allowed to populate up to the first 50 orbitals of the virtual space. The inset displays a magnified view of the first portion of the data.

Predicted 6-311G(d) CISD  $S_0 - S_2$  Transition Wavelengths  
 (Electron Excitation From Doubly Occupied to Unoccupied Orbitals)

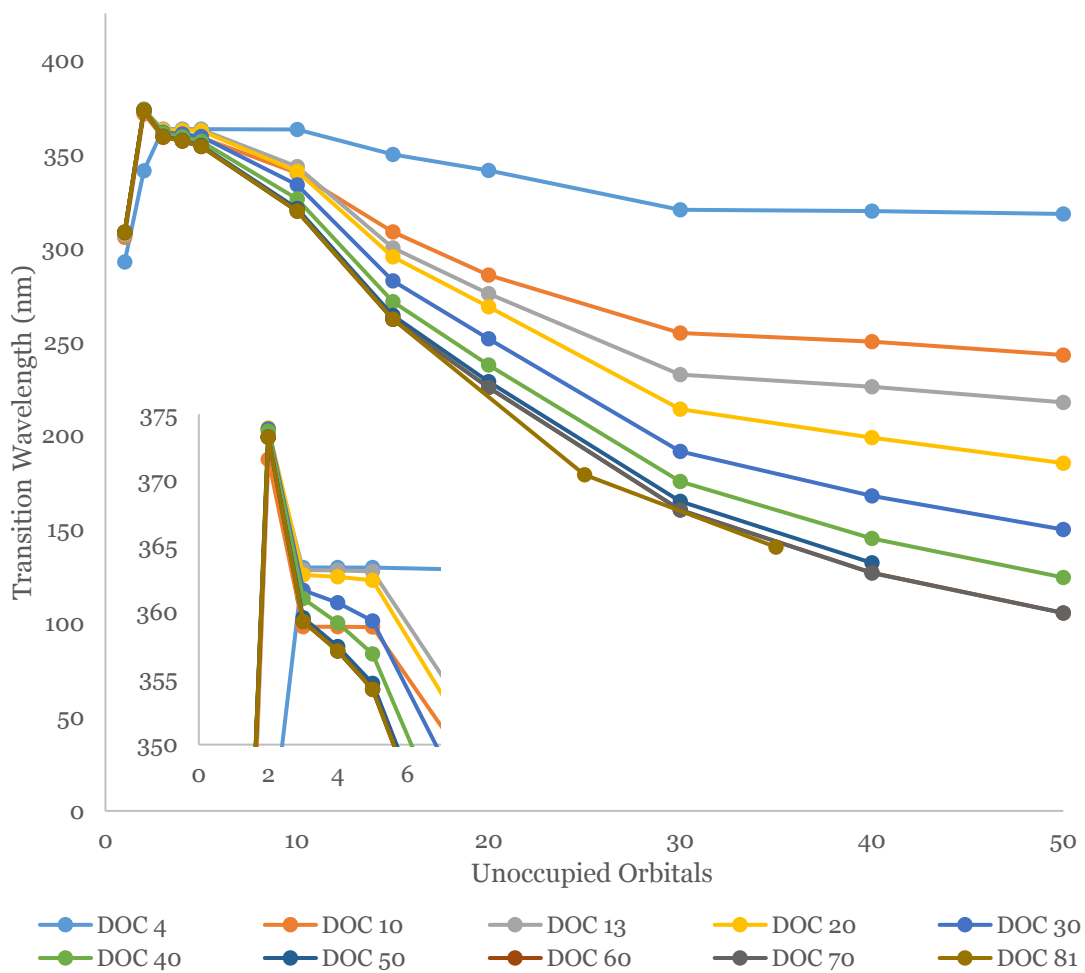


Figure G.2: Predicted  $Q_y$  transition wavelengths by CISD using the 6-311G(d) basis set. The inset displays a magnified view of the first portion of the data.

Predicted 6-31G(d) CISD  $S_0 - S_3$  Transition Wavelengths  
 (Electron Excitation From Doubly Occupied to Unoccupied Orbitals)

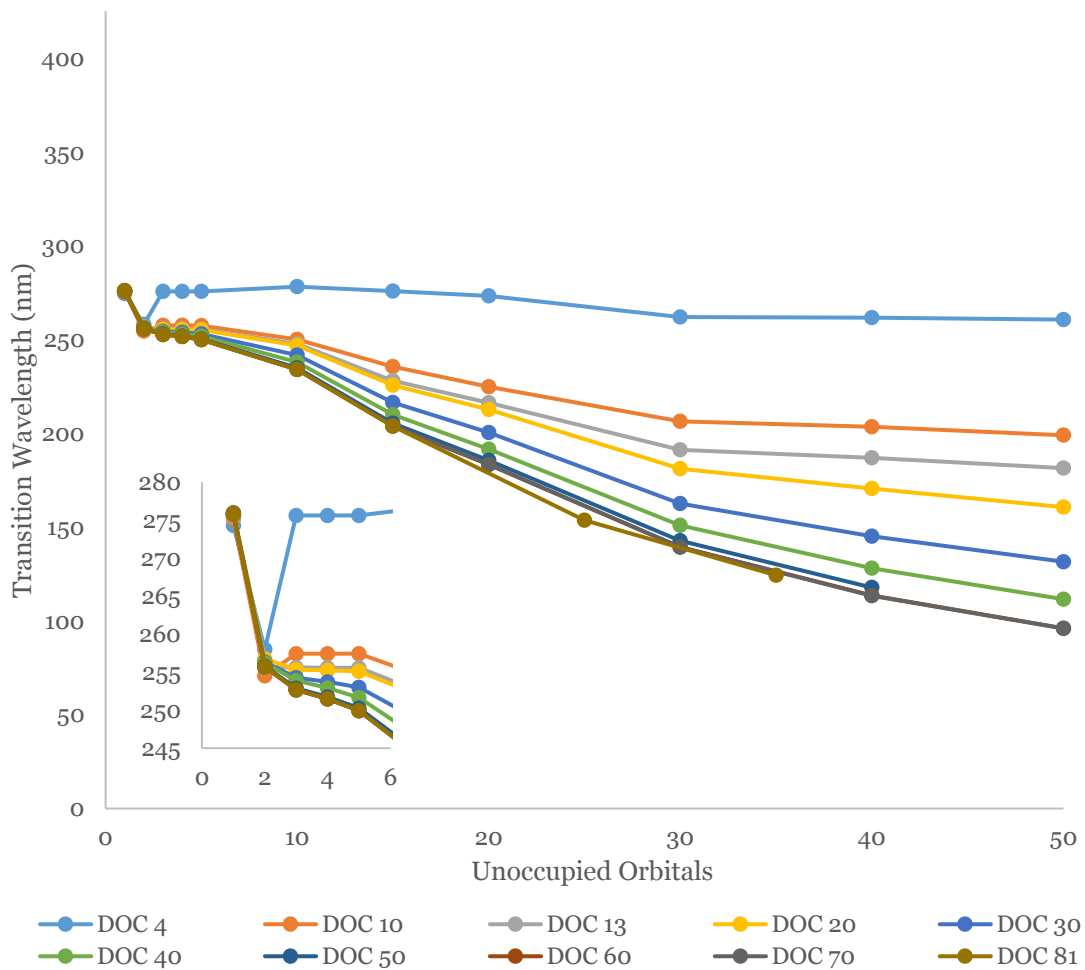


Figure G.3: Predicted  $B_x$  transition wavelengths by CISD using the 6-311G(d) basis set. The inset displays a magnified view of the first portion of the data.

Predicted 6-311G(d) CISD  $S_0 - S_4$  Transition Wavelengths  
 (Electron Excitation From Doubly Occupied to Unoccupied Orbitals)

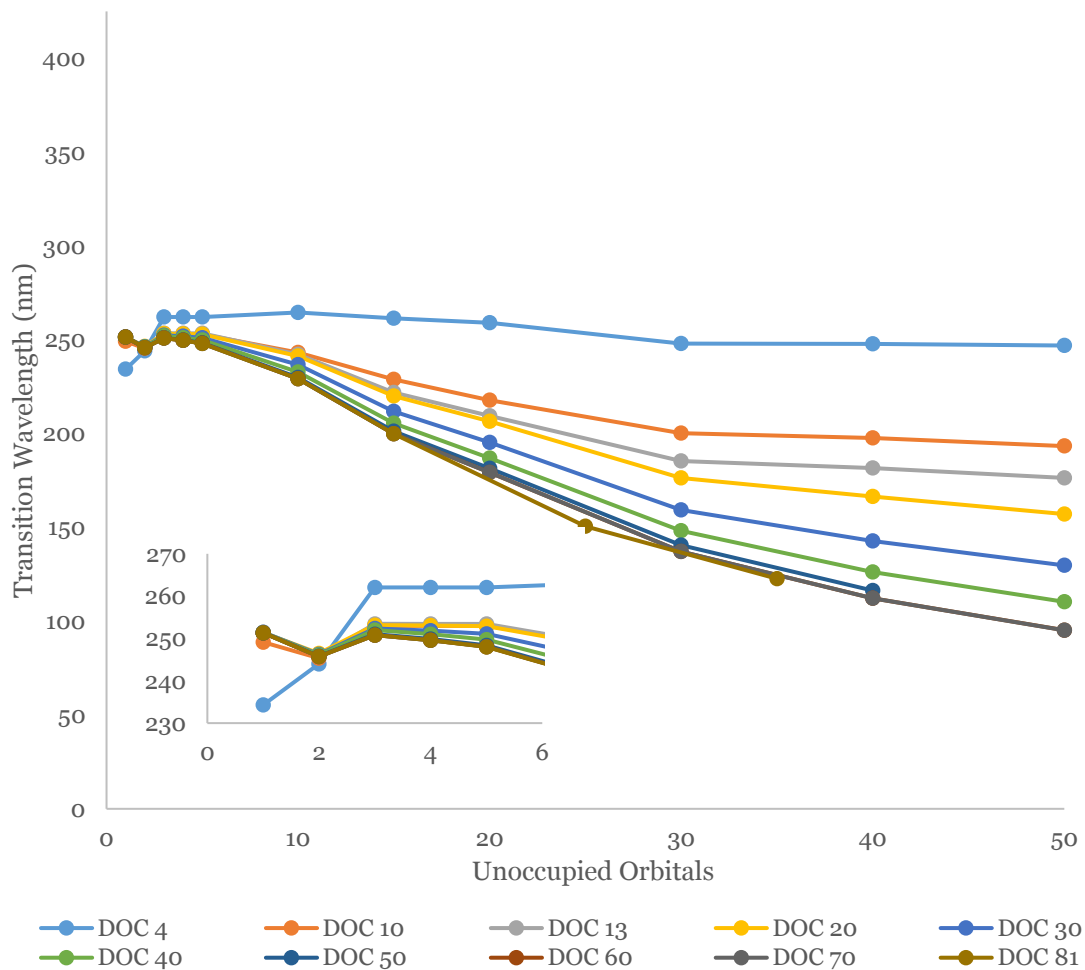


Figure G.4: Predicted By transition wavelengths by CISD using the 6-311G(d) basis set. The inset displays a magnified view of the first portion of the data.

Predicted 6-311G(d) CISDT  $S_0 - S_1$  Transition Wavelengths  
(Electron Excitation From Doubly Occupied to Unoccupied Orbitals)

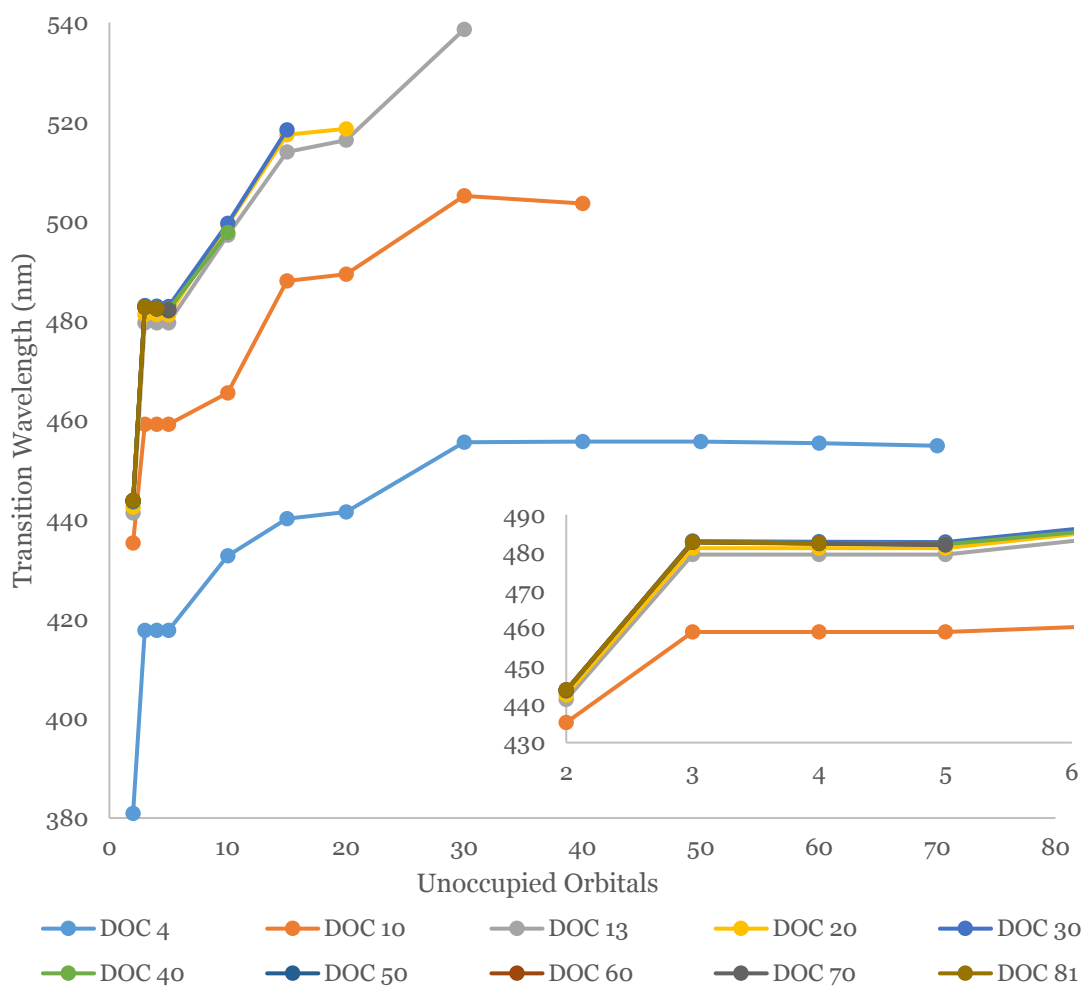


Figure G.5: Predicted Qx transition wavelengths by CISDT using the 6-311G(d) basis set. Electrons were excited from doubly occupied core orbitals, HOMO down, into unoccupied orbitals from the LUMO upwards. Ten different active electron groups were allowed to populate up to the first 50 orbitals of the virtual space. The inset displays a magnified view of the first portion of the data.

Predicted 6-31G(d) CISDT  $S_0 - S_2$  Transition Wavelengths  
 (Electron Excitation From Doubly Occupied to Unoccupied Orbitals)

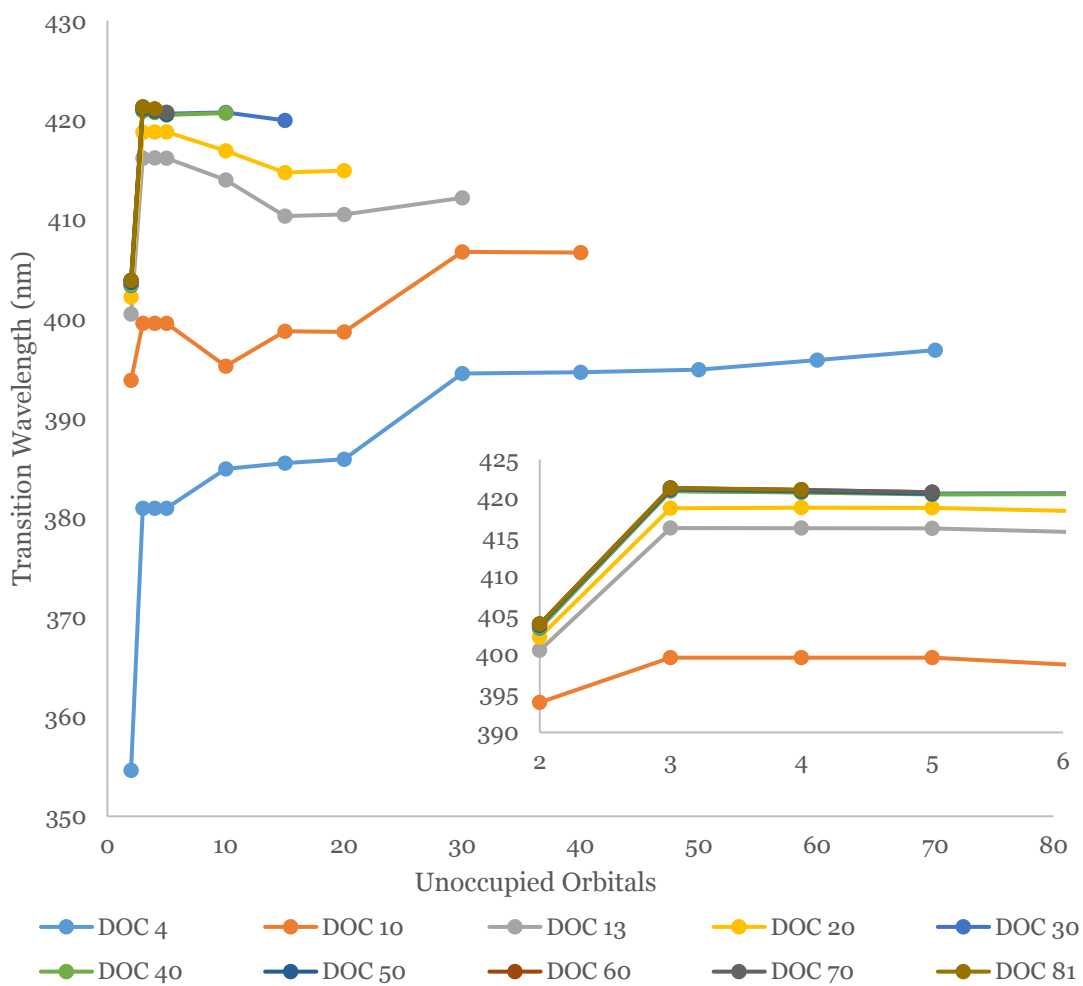


Figure G.6: Predicted  $Q_y$  transition wavelengths by CISDT using the 6-31G(d) basis set. The inset displays a magnified view of the first portion of the data.



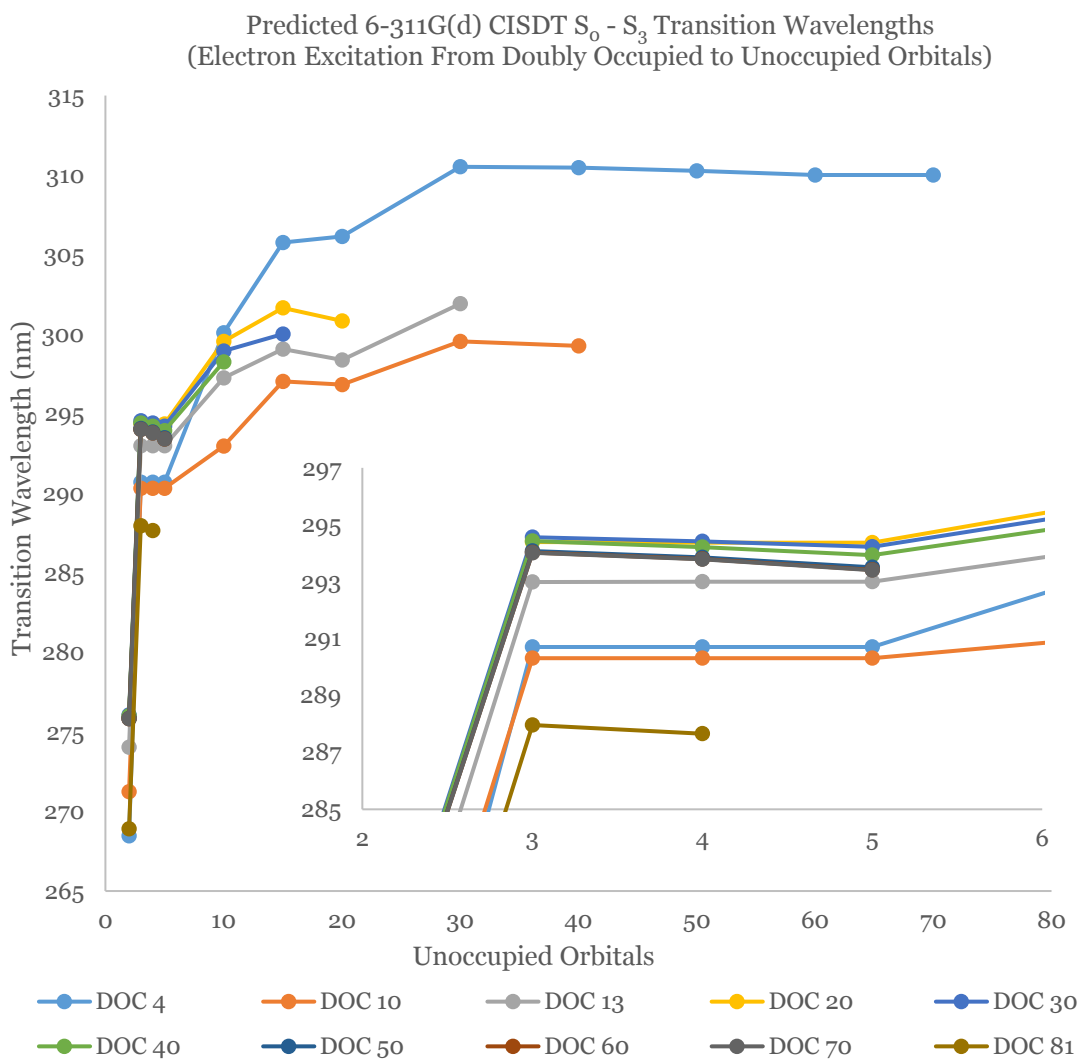


Figure G.7: Predicted Bx transition wavelengths by CISDT using the 6-311G(d) basis set. The inset displays a magnified view of the first portion of the data.

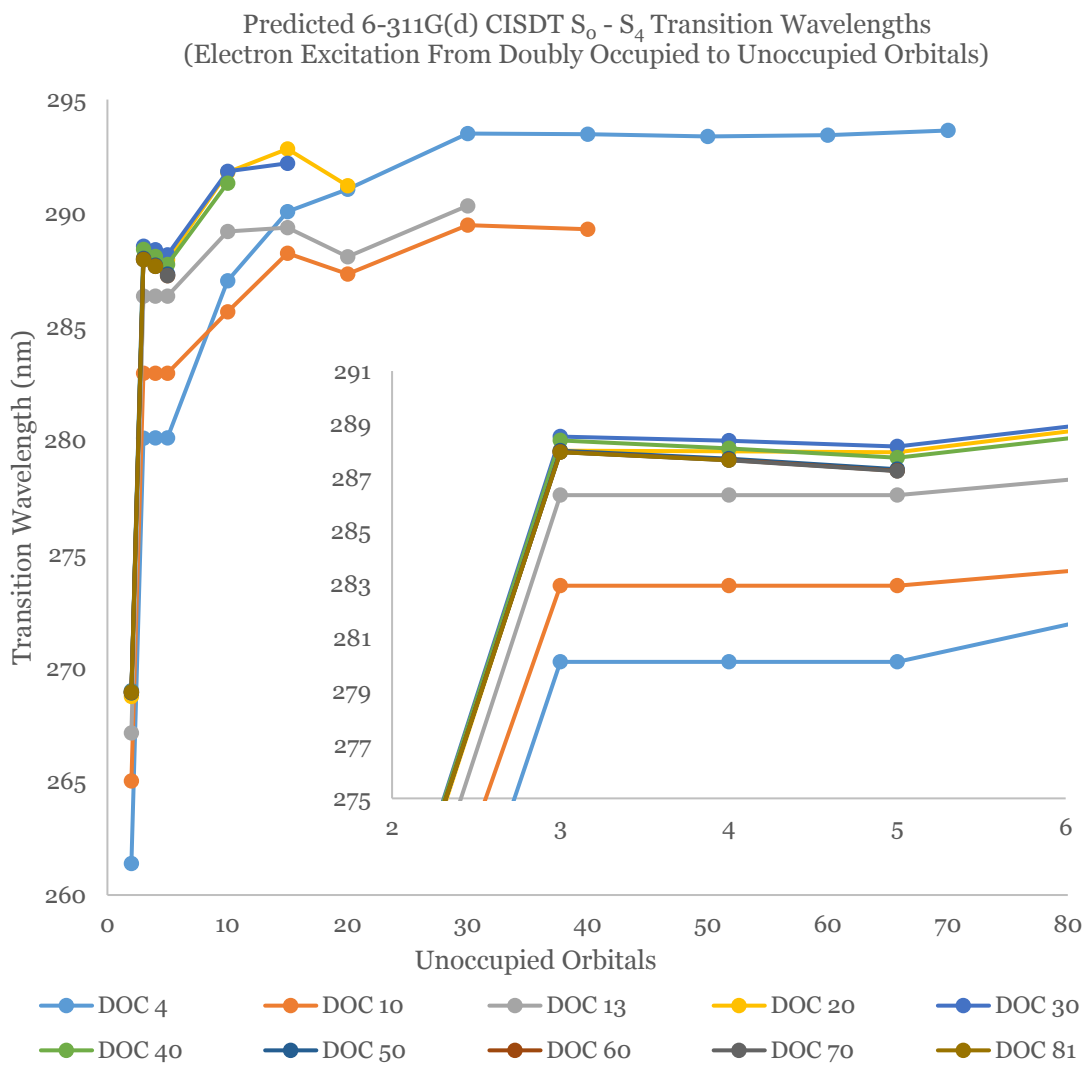


Figure G.8: Predicted By transition wavelengths by CISDT using the 6-311G(d) basis set. The inset displays a magnified view of the first portion of the data.

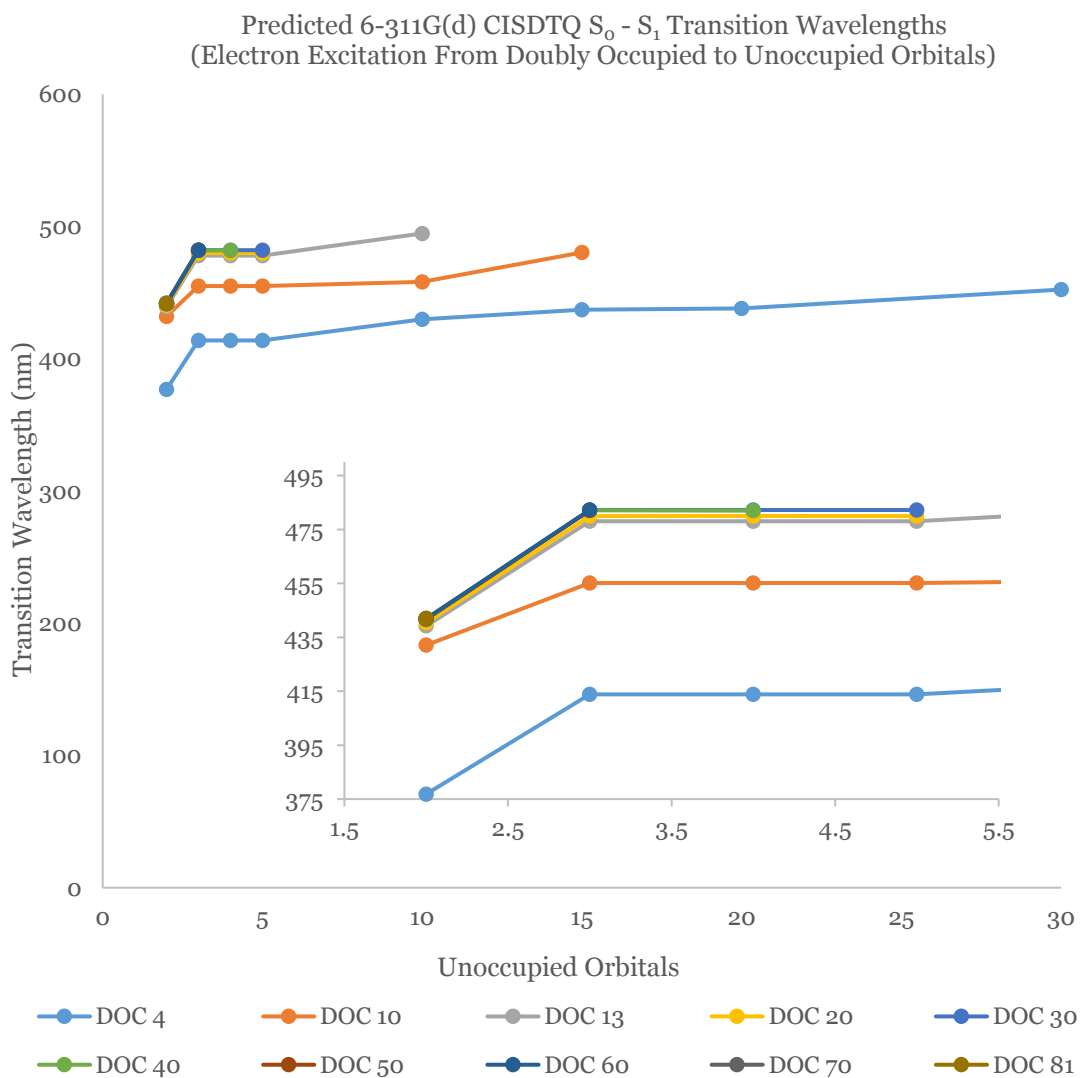


Figure G.9: Predicted Qx transition wavelengths by CISDTQ using the 6-311G(d) basis set. Electrons were excited from doubly occupied core orbitals, HOMO down, into unoccupied orbitals from the LUMO upwards. Ten different active electron groups were allowed to populate up to the first 50 orbitals of the virtual space. The inset displays a magnified view of the first portion of the data.

Predicted 6-311G(d) CISDTQ  $S_0 - S_2$  Transition Wavelengths  
(Electron Excitation From Doubly Occupied to Unoccupied Orbitals)

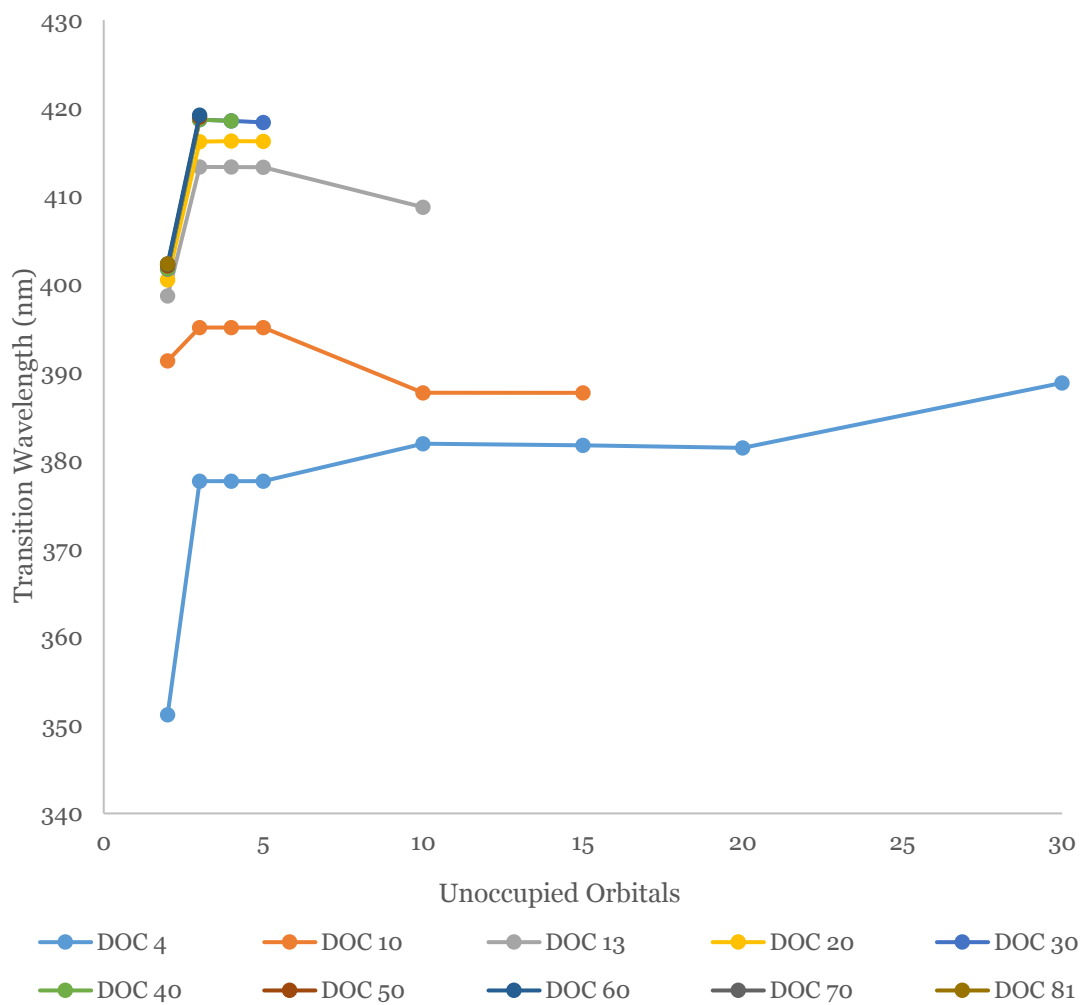


Figure G.10: Predicted  $Q_y$  transition wavelengths by CISDTQ using the 6-311G(d) basis set.

Predicted 6-311G(d) CISDTQ  $S_0 - S_3$  Transition Wavelengths  
 (Electron Excitation From Doubly Occupied to Unoccupied Orbitals)

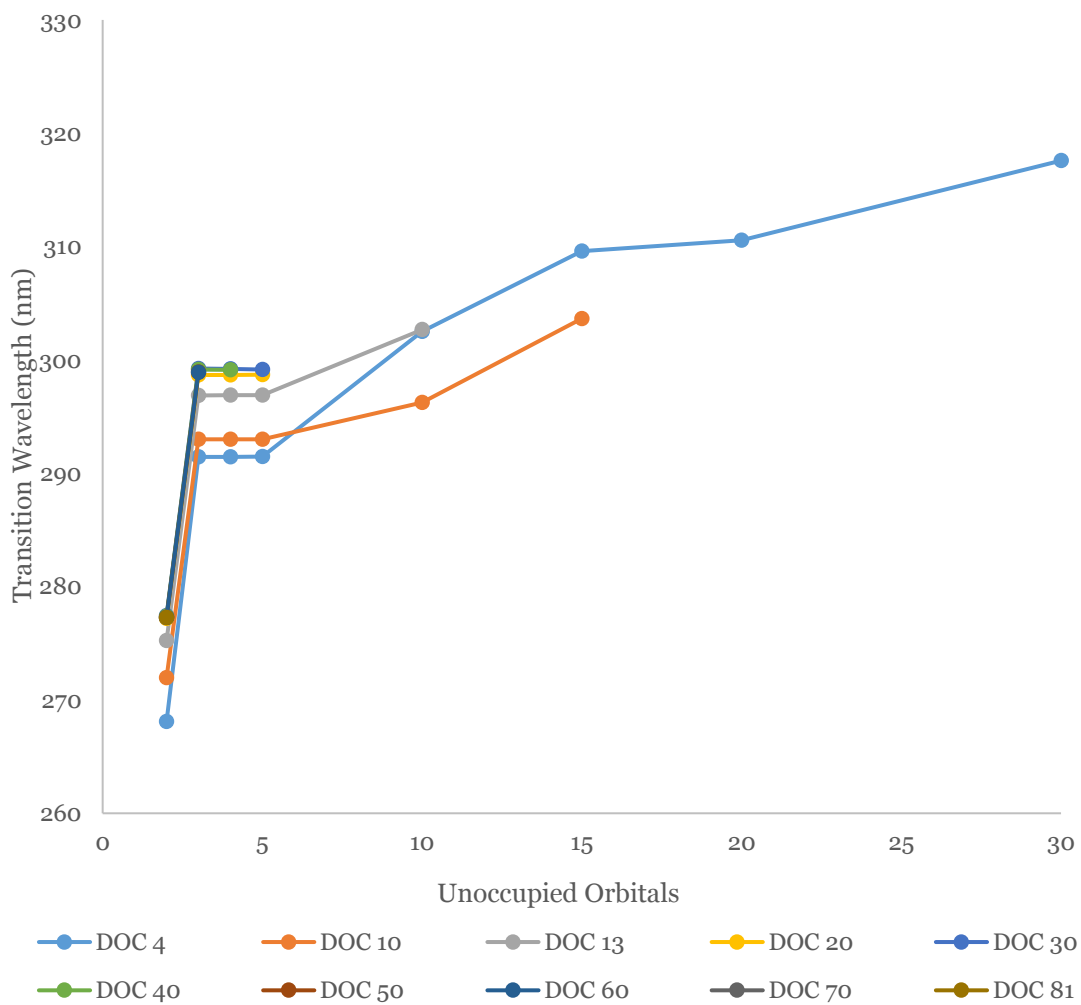


Figure G.11: Predicted Bx transition wavelengths by CISDTQ using the 6-311G(d) basis set.

Predicted 6-311G(d) CISDTQ  $S_0 - S_4$  Transition Wavelengths  
 (Electron Excitation From Doubly Occupied to Unoccupied Orbitals)

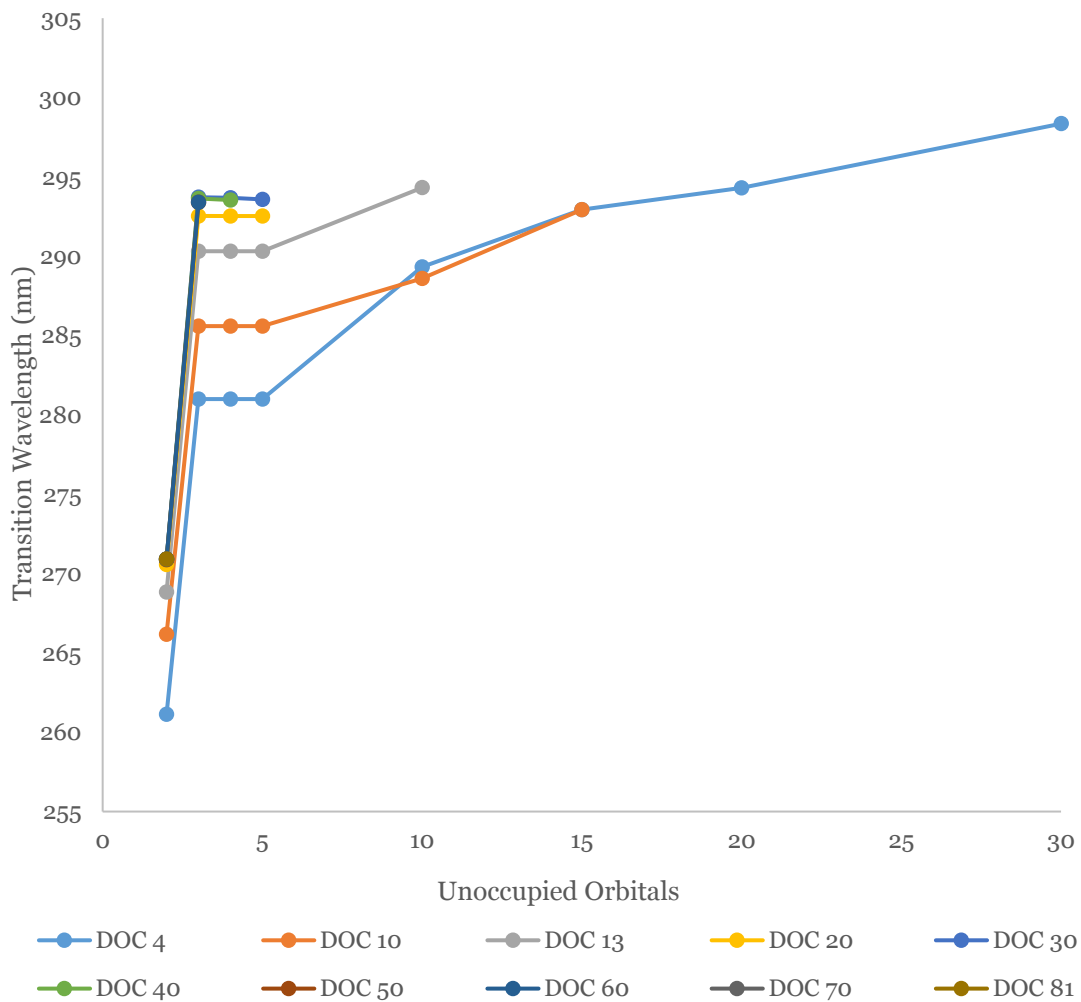


Figure G.12: Predicted By transition wavelengths by CISDTQ using the 6-311G(d) basis set.

Predicted 6-311G(d)  $S_0 - S_1$  Transition Wavelengths  
 EOM-CCSD (-) CR-EOM-CCSD(T) IID/IA (- -)  
 CR-EOM-CCSD(T) ID/IB (- -) DELTA-CR-EOM-CCSD(T) DEL(IA) (.....)

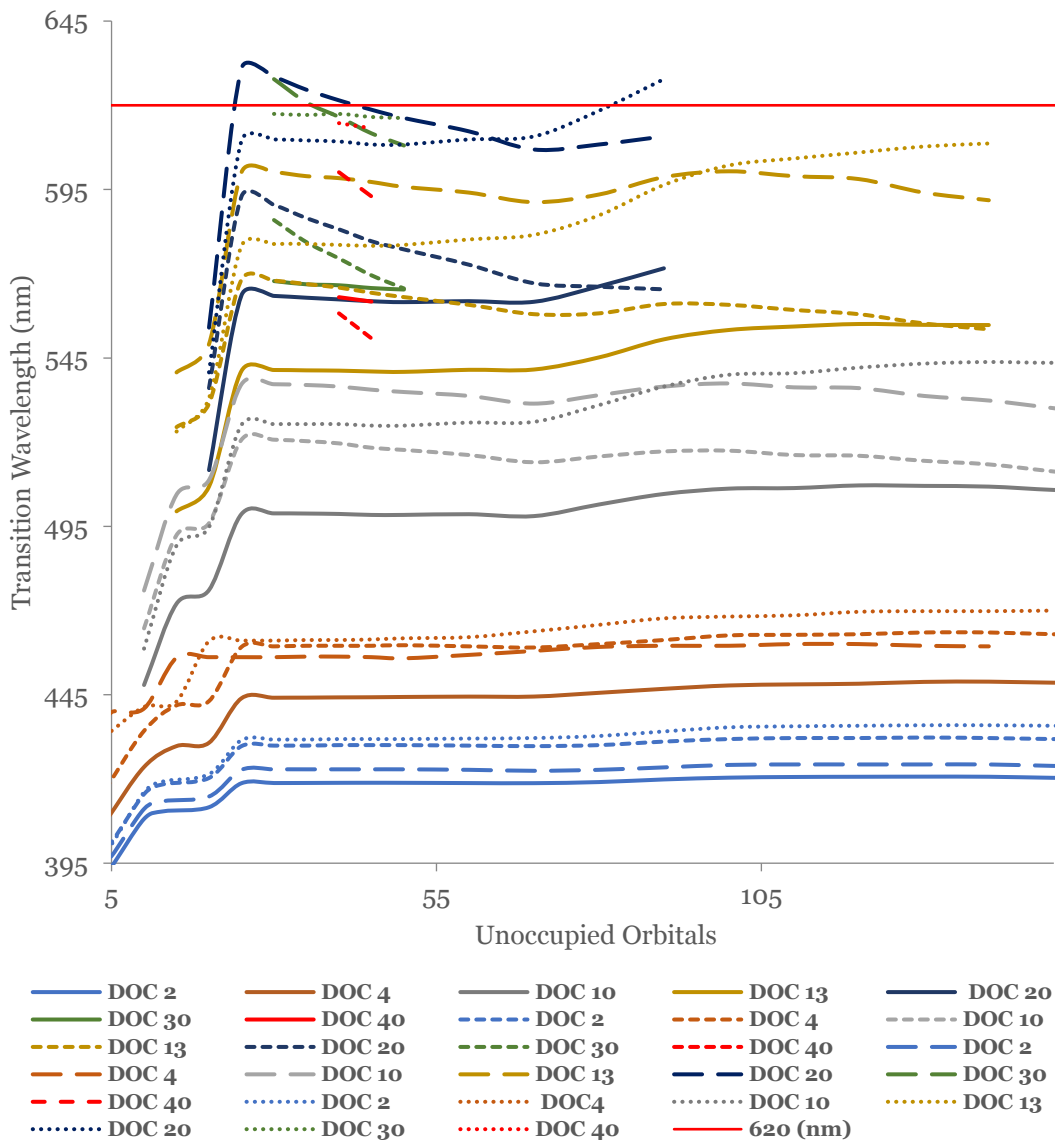


Figure G.13: Predicted Qx transition wavelengths by EOM-CCSD, CR-EOM-CCSD(T) ID/IB, CR-EOM-CCSD(T) IID/IA, and DELTA-CR-EOM-CCSD(T) DEL(IA), using the 6-311G(d) basis set. Electrons were excited from doubly occupied core orbitals, HOMO down, into unoccupied orbitals from the LUMO upwards. Seven different active electron groups were allowed to populate orbitals of the virtual space. Marker positions of the different calculations performed appear in figure 9.8. The experimental Qx transition energy is depicted as the red horizontal line.

Predicted 6-311G(d)  $S_0 - S_2$  Transition Wavelengths  
 EOM-CCSD (-) CR-EOM-CCSD(T) IID/IA (- -)  
 CR-EOM-CCSD(T) ID/IB (- -) DELTA-CR-EOM-CCSD(T) DEL(IA) (.....)

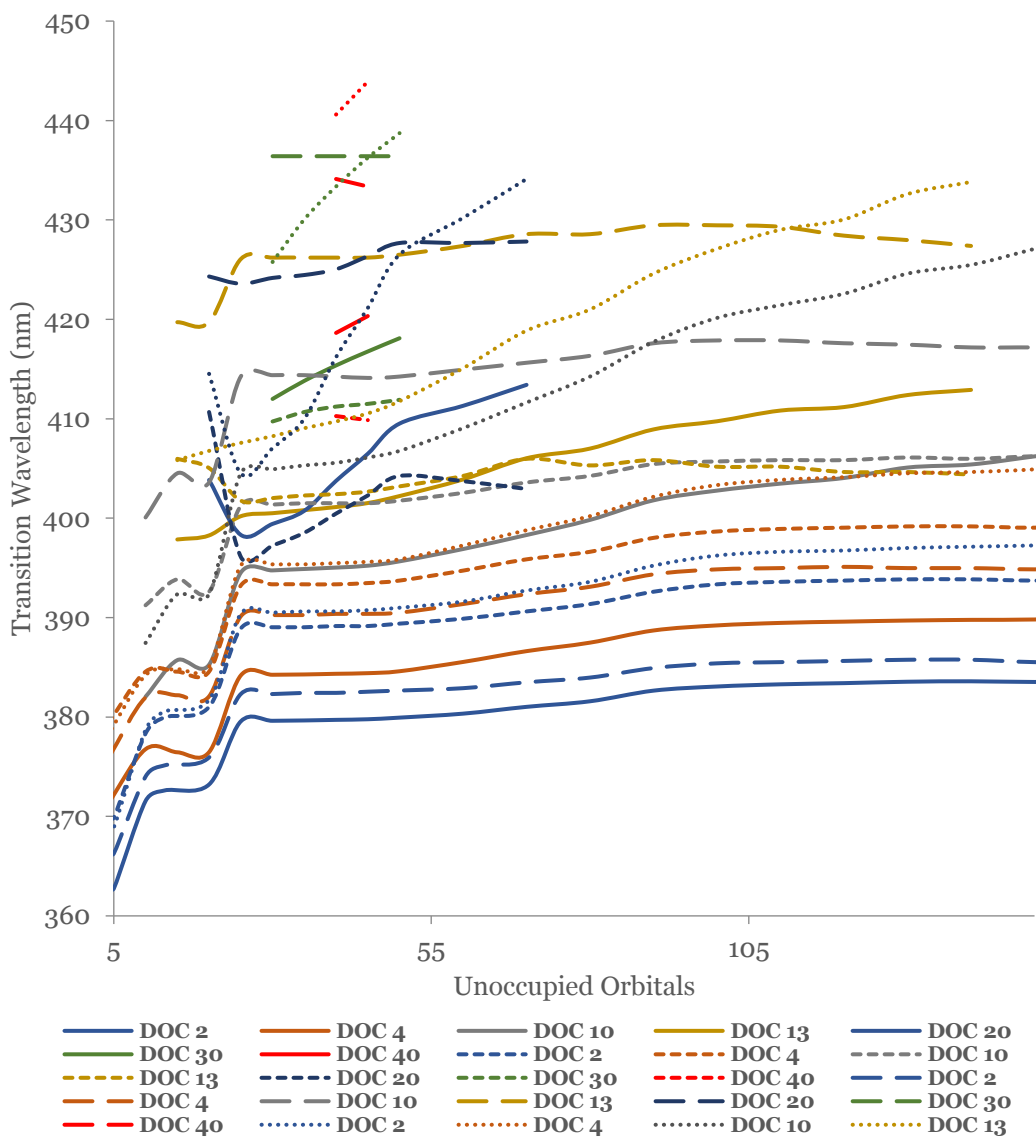


Figure G.14: Predicted  $Q_y$  transition wavelengths by EOM-CCSD, CR-EOM-CCSD(T) ID/IB, CR-EOM-CCSD(T) IID/IA, and DELTA-CR-EOM-CCSD(T) DEL(IA), using the 6-311G(d) basis set. According to experiment, the peak wavelength of this transition occurs at 541 nm.



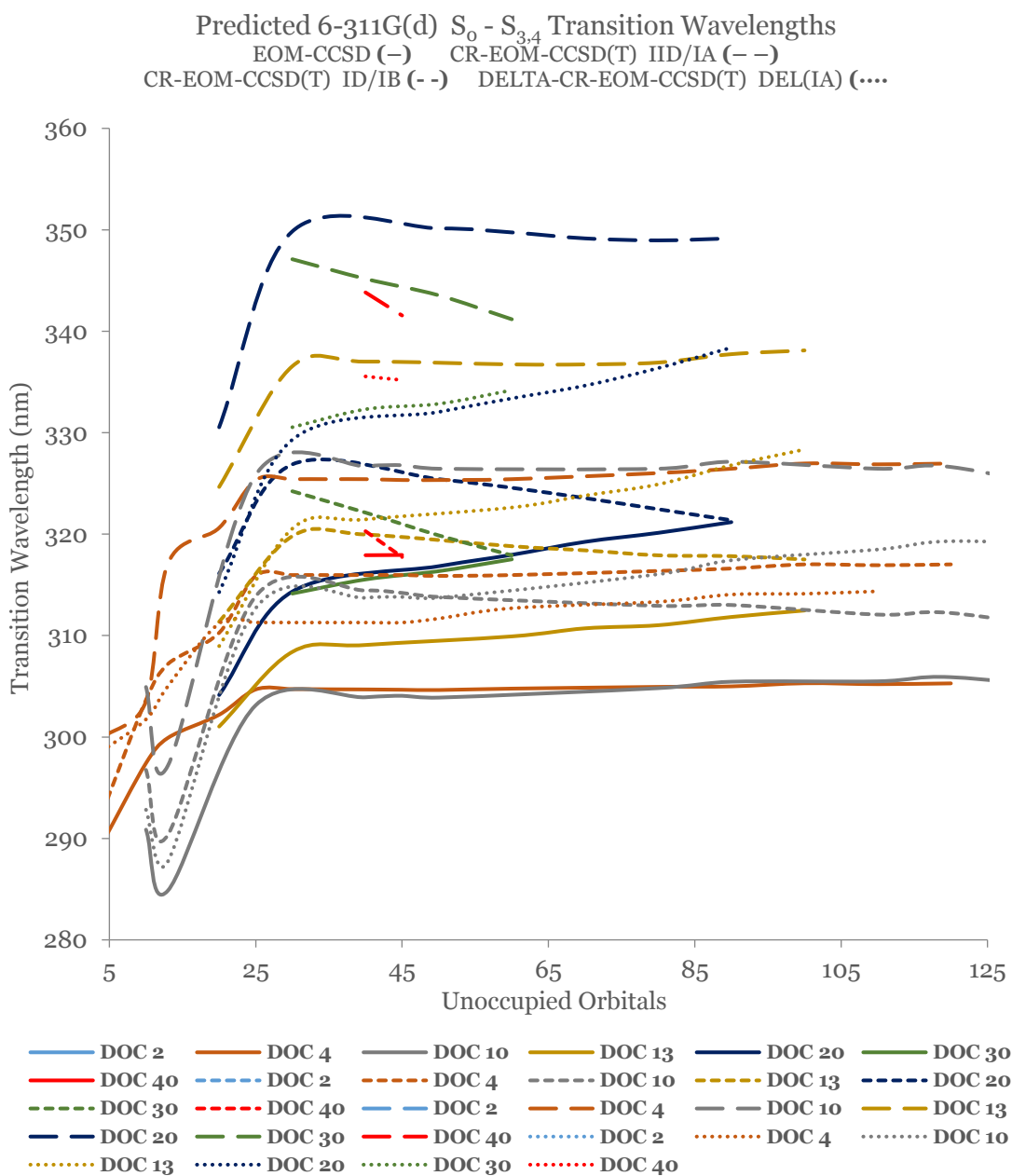


Figure G.15: Predicted  $B_x$ ,  $B_y$  transition wavelengths by EOM-CCSD, CR-EOM-CCSD(T) ID/IB, CR-EOM-CCSD(T) IID/IA, and DELTA-CR-EOM-CCSD(T) DEL(IA), using the 6-311G(d) basis set. The coupled-cluster computations that were performed always return degenerate energies for the  $B_x$  and  $B_y$  transitions. According to experiment, these transitions also result in a degenerate peak, with a peak wavelength of 427 nm. Alternate theories predict that the  $B_x$  transition occurs at 429 nm, and that the  $B_y$  transition occurs at 425 nm.

## **Bradley M. Moran**

Department of Chemistry and Biochemistry  
University of Wisconsin-Milwaukee  
Chemistry Building, Room 336  
3210 N. Cramer Street  
Milwaukee, WI 53211  
(414)229-5223  
bmmoran@uwm.edu

### **Education:**

*University of Wisconsin-Madison; Madison, WI; B.S. in Mathematics. May 2005*

*University of Wisconsin-Milwaukee; Milwaukee WI; MBA. In Finance and Investment Strategy. December 2006*

### **Awards:**

Louise Arndt Fellowship 2011  
Louise Arndt Fellowship 2016  
SciX 2013 Poster Award Winner-Third Place  
SciX 2014 Poster Award Winner-Second Place  
SciX 2014 Society for Applied Spectroscopy Poster Award Winner

### **Teaching Experience:**

University of Wisconsin-Milwaukee  
Chem 102 General Chemistry: Fall 2014  
Chem 103 Survey of Biochemistry: Smr. 2010  
Chem 104 General Chemistry and Qualitative Analysis:  
Fall 2009; Fall 2015; Spr. 2016; Smr. 2016; Fall 2016  
Chem 221 Elementary Quantitative Analysis: Spr.2011; Spr. 2013; Spr. 2014; Spr. 2015

### **Services and Activities:**

SAS Member 2010-Current  
SAS Treasurer for the UW-Milwaukee Chapter 2010-2011  
Coblentz Society Member 2013-Current  
SAS High School Outreach 2011 (2 schools),  
TA Mentorship Program: Mentor 2011-2013, 2015

### **Poster Presentations:**

“Fostering a fundamental understanding of NMR in undergraduate laboratory courses” John A. Frost, Bradley M. Moran UWM Awards Day 2010

“Determination of Internal Electric Fields in Protoporphyrin IX with Hole-Burning Spectroscopy” Bradley M. Moran, Hannah E. Wagie UWM Awards Day 2010

“Fostering a fundamental understanding of NMR in undergraduate laboratory courses” Bradley M. Moran, John A. Frost Chemistry in Southeastern WI Poster Mixer 2010

“Initial Calibration and Imaging for Custom Low Temperature Confocal Laser Scanning Microscope” Bradley M. Moran, Yi Hu, Jörg C. Woehl, and Peter Geissinger UWM Awards Day 2011

“Calibration and Imaging with Cryogenic Temperature Confocal Laser Scanning Microscope” Bradley M. Moran, Yi Hu, Jörg C. Woehl, and Peter Geissinger FACSS 2011 Reno, NV.

“Calibration and Imaging with Cryogenic Temperature Confocal Laser Scanning Microscope” Bradley M. Moran, Yi Hu, Jörg C. Woehl, and Peter Geissinger ACS Younger Chemists Committee Poster Mixer 2011

“Development of a Cryogenic Temperature Confocal Laser Scanning Microscope for Investigating Molecular Electric Fields” Bradley M. Moran, Yi Hu, Hannah E. Wagie, Peter Geissinger, and Jörg C. Woehl Biophysical Society 56th Annual Meeting 2012 San Diego, Ca.

“Characterizing Methods of Fit for Resolving Optical Point Spread Functions” Bradley M. Moran, Peter Geissinger, Jörg C. Woehl UWM Awards Day 2012

“Evaluating Optical Point Spread Function Fitting Methods” Bradley M. Moran, Peter Geissinger, Jörg C. Woehl SciX 2012 Kansas City, Mo.

“Developing Spectral and Temperature Cycling Acquisition Software for Cryogenic Hole Burning Stark Spectroscopy Studies” Bradley M. Moran, Peter Geissinger, Jörg C. Woehl UWM Awards Day 2013

“Developing Cryogenic Temperature Hole Burning Stark Spectroscopy Temperature Cycling and Spectral Acquisition Software Platforms” Bradley M. Moran, Peter Geissinger, Jörg C. Woehl ACS-Great Lakes Regional Meeting 2013 La Crosse, Wi.

“Modeling Heat Transfer through Multiple Interfaces of Differing Phase for Predictive Temperature Cycling Regulation” Bradley M. Moran, Peter Geissinger, Jörg C. Woehl SciX 2013 Milwaukee, WI. *Winner of Third Place Conference Poster Award.*

“Modeling Cryogenic Heat Transfer for Predictive Thermal Regulation” Bradley M. Moran, Peter Geissinger, Jörg C. Woehl ACS Younger Chemists Committee Poster Mixer 2013

“Extending Confocal Laser Scanning Microscope Functionality: Spectral and Imaging Acquisition from Cryogenic to Ambient Temperature” Bradley M. Moran, Peter Geissinger, Jörg C. Woehl UWM Awards Day 2014

“Assessing Intrinsic Active Site Electric Fields via Stark Deconvolution” Bradley M. Moran, Hannah Wagie, Peter Geissinger, Jörg C. Woehl SciX 2014 Reno, NV. *Winner of Second Place Conference Poster Award and Society for Applied Spectroscopy Poster Award.*

“A Capacitive Cell for the Assessment of Dielectric Permittivities” Bradley M. Moran, Peter Geissinger, Jörg C. Woehl UWM Awards Day 2015

“Coupled-Cluster and Configuration Interaction Transition Moments and Energies of Free Base Porphyrin Possessing In-Protein Structural Characteristics” Bradley M. Moran, Peter Geissinger, Jörg C. Woehl UWM Awards Day 2016

“Transition Moments and Energies of Free Base Porphyrin Possessing In-Protein Structural Characteristics by the Coupled-Cluster and Configuration Interaction Methods” Bradley M. Moran, Peter Geissinger, Jörg C. Woehl UWM Graduate Student Research Symposium 2016

### **Presentations:**

“Single Molecule Magnets” Graduate Seminar Spring 2011